Transactions of the ASME®

Technical Editor
H. L. JULIEN (1998)

Associate Technical Editors
Advanced Energy Systems
M. J. MORAN (1999)
Gas Turbine
D. COOKE (1999)
H. NELSON (1999)
J. PETERS (1999)
J. N. SHINN (1996)
Internal Combustion Engines
D. ASSANIS (1999)
Power
D. LOU (1998)

BOARD ON COMMUNICATIONS
Chairman and Vice President
R. MATES

OFFICERS OF THE ASME
President, **R. J. GOLDSTEIN**
Executive Director, **D. L. BELDEN**
Treasurer, **J. A. MASON**

PUBLISHING STAFF
Managing Director, Engineering
CHARLES W. BEARDSLEY
Director, Technical Publishing
PHILIP DI VIETRO
Managing Editor, Technical Publishing
CYNTHIA B. CLARK
Managing Editor, Transactions
CORNELIA MONAHAN
Production Coordinator
VALERIE WINTERS
Production Assistant
MARISOL ANDINO

Transactions of the ASME, Journal of Engineering for Gas Turbines and Power (ISSN 0742-4795) is published quarterly (Jan., April, July, Oct.) for $175.00 per year by The American Society of Mechanical Engineers, 345 East 47th Street, New York, NY 10017. Periodicals postage paid at New York, NY and additional mailing offices. POSTMASTER: Send address changes to Transactions of the ASME, Journal of Engineering for Gas Turbines and Power, c/o THE AMERICAN SOCIETY OF MECHANICAL ENGINEERS, 22 Law Drive, Box 2300, Fairfield, NJ 07007-2300.
CHANGES OF ADDRESS must be received at Society headquarters seven weeks before they are to be effective. Please send old label and new address.
PRICES: To members, $40.00, annually: to nonmembers, $175.00. Add $30.00 for postage to countries outside the United States and Canada.
STATEMENT from By-Laws. The Society shall not be responsible for statements or opinions advanced in papers or . . . printed in its publications (B7.1, par. 3).

INDEXED by Applied Mechanics Reviews and Engineering Information, Inc. Canadian Goods & Services Tax Registration #126148048

Journal of Engineering for Gas Turbines and Power

Published Quarterly by The American Society of Mechanical Engineers

VOLUME 119 • NUMBER 1 • JANUARY 1997

TECHNICAL PAPERS

(Contents continued on p. 264)

(Contents continued)

S. F. Duffy

J. L. Palko

Civil Engineering Department,
Cleveland State University,
Cleveland, OH 44115

J. B. Sandifer

C. L. DeBellis

M. J. Edwards

Babcock & Wilcox,
Research and Development Division,
Alliance, OH 44601

D. L. Hindman
Babcock & Wilcox,
Lynchburg Research Center,
Lynchburg, VA 24506

Trends in the Design and Analysis of Components Fabricated From CFCCs

Continuous fiber ceramic composite materials (CFCCs) are being considered for an increasing number of commercial applications. They provide the potential for lighter, stronger, more corrosion-resistant components that can perform at higher temperature for long periods of time. Global competitiveness demands a shortening of the time for CFCC commercialization. Thus, considerable effort has been expended to develop and improve the materials, and to a lesser extent, to develop component design methods and data bases of engineering properties. To shorten the time to commercialization, project efforts must be integrated, while balancing project resources between material development and engineering design. Currently a good balance does not exist for most materials development projects. To rectify this imbalance, improvements in engineering design and development technologies must be supported and accelerated, with a focus on component issues. This will require project managers to give increasing emphasis to component design needs in addition to their current focus on material development.

Introduction

Continuous fiber ceramic composites (CFCCs) are being considered for a number of commercial applications. These applications focus on a need for components that are lighter, stronger, more corrosion resistant, and capable of performing their design function at elevated temperatures for longer periods of time. To aid the implementation of components fabricated from CFCC materials, a number of research programs have been funded by the United States government. This national effort includes NASA's HITEMP and EPM Programs, DoE's CFCC Program, NIST's ATP Program, and DoD's IHPTET Program. With the exception of the NIST and DoE programs, the primary focus of these projects supports efforts that lead to demonstration and proof of concept. However, commercial viability of CFCCs (as well as other material systems) has recently become a paramount objective.

At this point in time the industrial sector that can benefit the most from federal programs focused on CFCC research are energy-related industries. In this sector of the economy there are numerous near-term applications. For example, high-temperature industrial furnaces often operate in an inefficient manner due to massive energy losses (over 75 percent for some applications) in the exhaust gas stream. Thus, for energy-intensive industries (e.g., aluminum casting, glass production, steel manufacturing, hazardous waste incineration) an improvement in furnace efficiency through the use of waste heat recovery systems can yield large cost savings. However, furnaces for these applications present a rigorous operating challenge to the materials that are exposed to the exhaust flue gas stream. For instance, airborne contaminants in the exhaust gases of aluminum casting processes contain severely corrosive fluxes. This results in a chemical attack that leads to premature failure of heat exchangers fabricated from metal alloys. For this type of application a heat exchanger fabricated from CFCCs could economically recover waste energy and return it to the manufacturing process as preheated air. However, to accomplish, this the component must survive temperatures above 1093°C (2000°F) in corrosive gas streams. Commercial viability would also require an ability to optimize a design, making the component amenable to retrofit applications in several types of industrial furnaces. The attending cost savings in retrofitting an existing process can make a marginal production facility profitable. This has a direct impact on jobs, since energy savings on a large scale can offset labor economics achieved by shutting down a mature manufacturing operation. This type of heat exchanger can also be used in advanced power generation cycles where the anticipated operating temperatures are well above the limits of metal alloys.

Other industries stand to benefit from incorporating CFCCs in high-temperature applications. These applications usually involve components utilized in technologically advanced applications where unit costs are not as critical as component performance. In aerospace applications CFCCs offer a significant potential for raising thrust/weight ratios, and reducing NO_x emissions of gas turbine engines. The NASA EPM initiative has identified CFCCs as candidate materials in the fabrication of segmented combustor liners. In this application increased combustion temperatures and the limited availability of cooling air increases the thermal stresses developed in the combustor liner. Combustor liners fabricated from CFCCs are particularly attractive, since combustor liner cooling can be substantially reduced. As Sorrell and Hoffman (1994) point out, increased liner temperatures also tend to reduce the production of carbon monoxide (CO) emissions that are produced as a result of reaction quenching. Even though in this application component costs play a diminished role relative to component performance, solving critical CFCC design-related issues in the EPM project can easily carry over to other applications that have more near-term commercial benefit. This includes land-based gas turbine engines in the power generation industry, auxiliary power units (APU) used in commercial aviation, and diesel engines.

Contributed by the International Gas Turbine Institute and presented at the 40th International Gas Turbine and Aeroengine Congress and Exhibition, Houston, Texas, June 5–8, 1995. Manuscript received by the International Gas Turbine Institute March 16, 1995. Paper No. 95-GT-405. Associate Technical Editor: C. J. Russo.

Parallel government funded programs have also been established in Japan. These programs focus on utilizing ceramic-based materials in cogeneration (Honjo et al., 1993) and automotive (Itoh and Kimura, 1993) applications. Undoubtedly a global awareness exists regarding the potential benefits that can be derived from the utilization of components fabricated from CFCC materials. Thus, American research engineers and materials scientists are obligated to work in tandem so that the full potential of the CFCC material system is realized. This teaming concept, which falls under the conceptual umbrella of concurrent engineering, can potentially shorten the time it takes to bring a material system to market. Concurrent engineering is the first of several design-related trends that will be discussed in this article. The other two trends that are discussed relate to the mechanical and thermal analysis of components. The reader will note that the latter two topics are presented in the context of time-independent analyses, i.e., life-limiting design approaches are not discussed here. Currently there is a general lack of agreement (but no lack of potential concepts) regarding an appropriate design-life methodology.

The teaming concept called for by concurrent engineering methods should not be restricted to bringing various technical disciplines together. Another type of advantageous partnering involves teaming research engineers from government labs and private industry. Development engineers at Babcock & Wilcox (B&W) have generally recognized the need to utilize current technology available in all sectors of the ceramics community. In order to expand the CFCC technology base at B&W the authors of this article affiliated with Cleveland State University (these individuals are also resident research associates at NASA Lewis Research Center) were invited to join a B&W project design team in an advisory capacity. Later in this article an overview is provided of a design analysis conducted by this team. The analysis focused on a critical component in a waste heat recovery system. This type of partnering allows for an immediate transfer of state-of-the-art technology from government to industry. It also permits federally sponsored researchers to gain valuable insight into key issues that foster the commercial application of research concepts. American industries benefit from this technology transfer, since they obtain a high level of technical insight from individual researchers who have spent years studying certain aspects of a research concept. In turn, the government receives valuable input regarding applications that either validate or redirect research efforts. Also, under certain limited conditions, performance data (some of which are proprietary) is made available to federal researchers who participate in the design project. This type of open interaction, where industry is protected by proprietary agreements, has the potential to shorten the research innovation cycle, and is essential in making the partnership a success.

Concurrent Engineering. Historically, most new materials have established viable markets and found commercial success through a linear product development cycle. In the past the materials scientist would develop a new material system, prototypical components were then fabricated and tested, data bases would be established, and design methodologies were developed in a sequential process. This linear product development approach was adequate during the cold-war era when large research and development budgets spawned a number of successful high-technology material systems (e.g., smart materials, the utilization of composite materials in the air frames of jet fighters, etc.). However, as American industry continues the struggle to reinvent itself constantly in the post-cold war era, artifacts such as the linear material development cycle are being discarded. The current political climate, reduced budgets, and the need to develop dual-use technology all demand that economic issues will dictate the direction of materials research and development. The materials community, which includes material scientists and product design engineers at the national research labs and within American industry, are beginning to form new integrated design teams that utilize an assortment of multidisciplinary skills. These integrated design teams are beginning to embrace the precepts of concurrent engineering. In addition, the teams are attempting to involve end users early in the development cycle to ensure economic viability. The primary goal of concurrent engineering in the materials industry is a reduction in the material development cycle. The competitiveness of American material suppliers and their product end users demands that the cycle for product development be shortened. If a reduction in time to market is achieved, the direct results are an improved economic position for American industries in today's global market and more American jobs.

However, to enable the team fully, an equitable balance must be struck between the materials scientist and the engineer. Balancing resources increases the probability that the design team will bring about a decrease in the product cycle. This is true for commercial projects supported by the material supplier, and materials development programs supported by the government. Specifically, project resources must be allocated so that a high-quality material is produced along with an appropriate data base of engineering properties. If the emerging material behaves outside the context of available design engineering methodologies, then development of new design technologies must also be supported early in the project. The historical perspective, which basically asserts that the lion's share of research and development funds must be committed to developing processing technology and coupon testing in the initial stages of the development cycle, must change. The current mindset apparently prevails in spite of innovations in engineering design that have been achieved through the use of computer technology. The development and implementation of computer-aided manufacturing (CAM), computer-aided engineering (CAE), and computer-aided design (CAD) tools have brought about gains in quality and productivity in a growing number of manufacturing applications. The personal computer and design software are becoming common tools on the production floor in many manufacturing facilities. In fact this genre of technology has already been implemented in CFCC production facilities through the use of computer controlled weaving operations. From the engineer's viewpoint design methods, requisite design data bases, and design software are critical in establishing the commercial success of a material. The availability of this information instills confidence in the end user that the behavior of a component fabricated from CFCCs can be accurately predicted. Without this ability, an end user will not utilize CFCCs. Ideally this need to predict component behavior should arise from a desire to achieve a certain level of product function. This also should continue through the product life cycle with design upgrades. However, design engineering is used primarily to mitigate costs in litigation concerning product liability. Product enhancements are considered as secondary gains since too often the primary industry motivation for executing design studies focuses on product liability.

Moreover, to establish a concurrent engineering infrastructure and coherent design methodologies for CFCCs, guidelines must be established early through codes and standards organizations such as ASTM and ASME. Unless there is a tremendous cost saving or system enhancement (e.g., the NO_x emission reduction in jet engines mentioned previously) product engineers will tend to ignore a new material until they are comfortable knowing that an appropriate design practice has been codified. The reader need only study the commercialization (or lack thereof) of polymer matrix composites and carbon–carbon composites to find the evidence to support this last statement. The authors have been active in ASTM Committee C-28 (Advanced Ceramics) and they are also committed to a nascent effort to generate a coherent design code applicable to CFCCs within ASME. The national ASTM committee was organized in 1986 when it became apparent that ceramics were being utilized in advanced

technology applications. Applications in the aerospace, biomedical, military, power generation, processing, and automotive industries were viewed as being particularly demanding in terms of property requirements. At that time an abundance of experimental data was required to guide emerging design and fabrication technologies that focused primarily on monolithic ceramics. It was also apparent that industry-oriented standards were needed for production, inspection, testing, data analysis, and probabilistic design of components fabricated from advanced ceramics. Past efforts of this committee in these areas has helped to utilize the attractive features of these emerging materials, as well as minimize any shortcomings. The committee has been organized into various subcommittees whose goals and objectives are reflected in the needs just mentioned. As an example, specific responsibilities of subcommittee C 28.02 (Design and Evaluation) include development of appropriate standards that address the topics of nondestructive evaluation, statistical analysis, and design of components fabricated from advanced ceramics. However, the structure of the overall committee is not static. Recently subcommittee C 28.07 (Ceramic Matrix Composites) was established to address the specific experimental issues related to CFCCs. The authors hope that the success of C 28 in harnessing the technology resources in government, industry, and academia can be duplicated in developing a pressure vessel design code specifically for CFCCs under the auspices of ASME.

Trends Relating to Mechanical Design and Analysis. The typical CFCC material system exhibits an increase in work of fracture in comparison to monolithic ceramics. This behavior allows for "graceful" rather than brittle catastrophic failure (the dominant failure mode of monolithic ceramics). When loaded in the fiber direction, these composites retain substantial strength capacity beyond the initiation of transverse matrix cracking. The failure behavior of this system is governed by large stress concentrations that occur at macroscopic as well as at microscopic flaws. These flaws are unavoidably present in the composite as a result of processing or in-service environmental degradation. The observed scatter in component strength is caused by the random occurrence of these flaws in either constituent and/or the interface. First matrix cracking stress in the composite consistently occurs at strains greater than that in the corresponding monolithic form of the matrix material. As additional load is applied beyond first matrix cracking, the matrix tends to break in a series of cracks bridged by the ceramic fibers. Thus any additional load is borne increasingly by the fibers until the ultimate strength of the composite is reached. For most applications the design failure stress will coincide with the first matrix cracking stress. Matrix cracking usually indicates a loss of component integrity since this phenomenon allows high-temperature oxidation of the interface, which leads to the embrittlement of current composites. The authors wish to point out that this failure mechanism may not be as large a concern in a CFCC material with an oxide matrix and an oxide fiber. Since first matrix cracking is the design point for most typical applications of CFCCs, then the behavior of the matrix material essentially controls component design. Focusing on the matrix behavior is counterintuitive to the concerns of the materials scientist where improving the properties of the fiber and the interface is paramount. This is an example where the design engineer and the materials scientist have different technical agendas that apparently conflict. This type of conflict impedes commercialization of CFCCs since project resources are withheld from the design engineer who "does not understand what is technically important." It would be far more beneficial to recognize the existence of the two agendas and deal with both simultaneously (and equitably).

The authors note that a number of deterministic fracture theories based on micromechanics concepts exist in the literature that predict first matrix cracking strength as a function of the constituents. Models have evolved as the architecture of CFCCs has grown in complexity. The deterministic modeling effort has been supported in the past by both the materials scientist and the design engineer. The materials scientist seeks models that can predict the observed behavior of the material system under development. If the model is conceptually correct then adjusting the parameters embedded in the model should aid in optimizing material properties. From an engineering standpoint, micromechanics help fulfill the need to develop predictive techniques that embody the "correct physics." If the focus of component design is on the matrix then recall that ceramics exhibit a decreasing bulk strength with increasing component volume (the so-called size effect) in their monolithic form. This physical behavior must be accounted for if first matrix cracking is the design point. Here is an example where a knowledge of the physical mechanisms active in the microstructure is essential in the development of coherent design strategies. However, currently available micromechanics methods are based on assumed idealistic microstructures, and the models are typically unable to predict the unavoidable strength variation in the current generation of composite materials.

It has been correctly argued that utilizing design practices based on micromechanics allows the engineer to design a component from the constituent level, specifically tailoring the composite microstructure to enhance component behavior. Although the engineering principles that support the micro-analysis approach are fundamentally sound, the concept of designing a component based on the properties of the ceramic constituents and tailoring the CFCC microstructure to a given application is well off in the future. Given the current difficulties associated with fabricating ceramic materials, industry is focusing attention on developing a single optimized material system. If an optimized material system can be reproduced faithfully and in bulk quantities, then it has an opportunity to become commercially viable. If a single optimized microstructure is brought to market it becomes unnecessary to design a component based on micromechanics. The design engineer can more easily utilize the concepts of macroscopic analysis based on the phenomenological behavior of a single optimized material system.

The phenomenological analysis and design of components fabricated from ceramic composite materials requires a departure from the usual deterministic design philosophy (i.e., the factor of safety approach) prevalent in the analysis of metallic structural components, which are more tolerant of flaws and material imperfections. Most quantities that are utilized in engineering designs have, to a greater or lesser extent, some level of uncertainty. Utilizing structural reliability methods provides a more general accounting of the entire spectrum of values that phenomenological strength parameters may exhibit. However, the reliability approach demands that the design engineer must tolerate a finite risk of unacceptable performance. This risk of unacceptable performance is identified as a component's probability of failure. The primary concern of the engineer is minimizing this risk in an economical manner. If reliability methods are utilized, appropriate analytical tools needed to quantify uncertainty must be readily available. A number of tools and design aids for dealing with uncertainty have been developed and tailored to specific ceramic composite material systems. These tools include reliability models and computer software. The reader is directed to the work by Duffy and Arnold (1990), Duffy and Manderscheid (1990), Thomas and Wetherhold (1991), and Duffy et al. (1993) regarding the development of reliability models and software.

The authors also recognize the potential for designing components beyond the first matrix cracking stress. This takes the component design point into the "graceful failure" regime of the stress–strain curve. Under certain limited circumstances the design point could even coincide with the ultimate strength of the CFCC material. When operating beyond the matrix cracking stress, the design engineer should be aware that the material

will not behave in a linear elastic fashion. As microcracking increases beyond the initial level at first matrix cracking the stiffness of the composite changes. In NASA's EPM project continuum damage mechanics is being utilized to capture the macroscopic changes in engineering properties at the component level. In the past, the principles of continuum damage mechanics have also been coupled with structural reliability analyses. The reader is directed to the work of Duffy and Gyekenyesi (1989) for monolithic material ceramics, and by Chuang and Duffy (1994) for CFCC application. However, these efforts are still maturing and this particular topic tends to transcend into design life issues since loss in stiffness can easily bring about component failure. As was indicated earlier, the authors wish to reserve a discussion regarding design life methodologies for a later date.

Trends Relating to Thermal Design and Analysis. Most near-term applications of CFCCs involve components in high-temperature applications that must transfer heat in some fashion. It was noted earlier that specific near-term applications involve heat exchangers and turbine combustors. Designing components for these applications demands a coherent thermal analysis. Traditionally, thermal analyses have been conducted by the structural engineer, whose efforts in this area have been facilitated by the availability of commercial finite element codes having thermal conduction algorithms. Most commercial algorithms are limited to simple thermal boundary conditions, but the majority of structural components fabricated from metal alloys can be analyzed by these simple schemes. The detailed thermal analyses required in the design of components utilizing CFCCs demand more sophisticated methods. The authors note that the importance of predicting the thermal and hydraulic performance of the system can be critical in the design of the overall system. Unfortunately, there has been little or no incentive to conduct refined thermal analyses in conjunction with advanced structural analyses. Yet the applications that demand the use of CFCCs involve high-temperature heat transfer mechanisms that interact with the combustion process. These combustion processes involve high-velocity convection and radiation transfer mechanisms, not only from the gases that participate in the process, but also from the structural elements that serve as subcomponents within the system and the interaction between subcomponents. These applications require advanced numerical heat transfer models that can predict the fluid flow, combustion, and heat transfer within the entire system. Outside of NASA's EPM project, very little effort has gone into synthesizing sophisticated heat transfer analyses with the structural analyses of critical components. Changing this lack of integration could further augment the commercialization of CFCCs.

Moreover, since CFCCs can have low thermal conductivities, large thermal stresses can be generated in a component. In many design applications (e.g., the segmented combustor liner under consideration in the EPM project) stresses produced by thermal gradients demand the attention of the design team early in a project. This requires an integrated approach where the heat transfer analysis is preformed interactively with the structural analysis in order to minimize thermal stress. Here the most advanced thermal analysis models should be utilized. The thermal analysis generates a temperature profile, which is subsequently used in the finite element analysis of the component. Software such as PATRAN is making the transfer of numerical data from the thermal analysis to the structural analysis easier, but further development is needed in this area.

With a limited amount of reflection, it becomes obvious that the thermal stress analysis of a component is only as good as the thermal properties used in the analysis. It has been a fairly straightforward task to apply traditional thermal design analyses to monolithic ceramics. As an example, a number of high-temperature ceramic components have been fabricated from monolithic silicon carbide. This material has a relatively high isotropic thermal conductivity, which can be measured using the same experimental techniques developed for metal alloys. In contrast, CFCCs exhibit orthotopic thermal behavior, and depending on the constituents the conductivity in the fiber direction can be much higher than the conductivity in the direction perpendicular to the fibers. At present, CFCC thermal conductivity data are very limited. Traditional thermal conductivity measurement techniques produce widely varying results when applied to CFCCs. Currently the laser flash technique is popular due to its ease of application. However, this technique was developed for isotropic materials. Although it is possible to obtain representative thermal conductivity data for CFCCs under highly controlled conditions with this method, it is far too easy to misinterpret the results in a composite material. New techniques are being developed (e.g., the Scanning Thermal Conductivity Microscope) but these techniques must be reliable and easily implemented by the practitioner. The authors strongly feel that the determination of thermal properties should be supported by a standing subcommittee within ASTM Committee C-28. With test methods in place and reliable data available, design engineers will have more confidence in their ability to predict the thermal/mechanical behavior of a CFCC component.

Design Application. In this section the authors review the efforts of a design team that analyzed various aspects of an innovative waste heat recovery system. As DeBellis and Kneidel (1987) point out, the critical component of this type of system is an advanced heat exchanger (AHX). In the application considered by the design team the AHX was placed in the exhaust path of an industrial furnace that produces hazardous and highly corrosive flue gases. Due to the corrosive environment, a ceramic composite was selected for the AHX. The heat exchanger is a prototype being developed by Babcock & Wilcox and partially funded by the Department of Energy (DoE). A schematic of the system and the tube are shown in Fig. 1. The AHX is an array of nine bayonet-type heat exchangers, where each bayonet consists of two concentric tubes. The outer tube was fabricated from a ceramic composite that consists of a zirconia matrix and an alumina–(20%)zirconia fiber. The inner tube, which is not exposed to process flue gases, is fabricated from a metal alloy. The metal tube connects to an upper plenum, which serves as the inlet for ambient air. The ambient air enters the upper plenum, proceeds down the inner tube, exits the base of the inner tube, reverses direction, and moves up the annulus between the metal alloy and ceramic composite tubes. As ambient air travels through the bayonet it is heated from the flue gas passing along the outside of the ceramic composite tube. The heated air col-

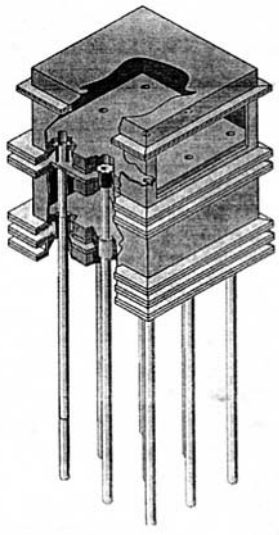

Fig. 1 Advanced heat exchanger (AHX)—full assembly

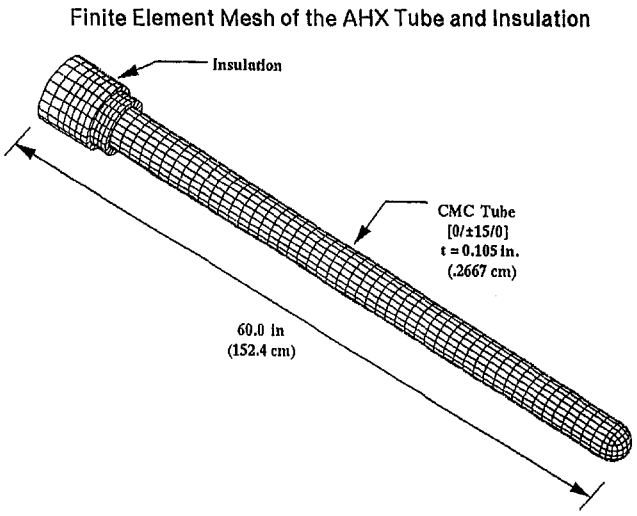

Fig. 2 Finite element mesh of the AHX tube and insulation

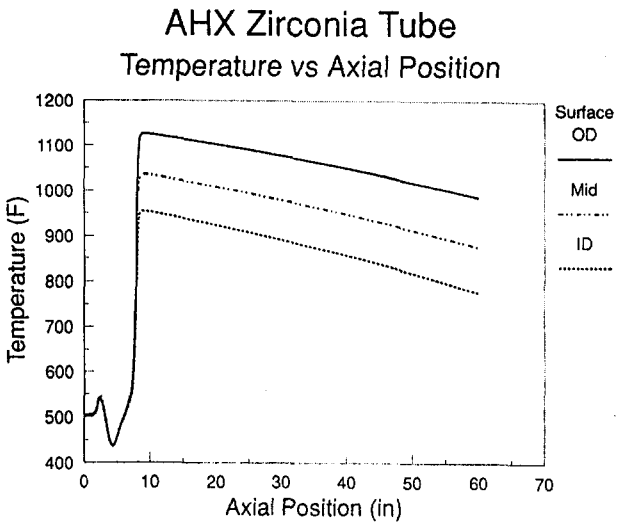

Fig. 3 Temperature as a function of axial position

lects at the lower plenum located at the top of the ceramic section of the bayonet. In a typical system this heated air is used in the combustion process thus reducing fuel requirements. Note that the clean air and the hazardous flue gases must be separated at all times.

During the feasibility study a thermal analysis and a stress analysis was conducted using the P/THERMAL finite element program for the thermal analysis and the ABAQUS finite element program for the stress analysis. In addition, PATRAN was used for pre- and postprocessing both finite element models. The C/CARES algorithm was utilized to conduct reliability analyses after the stress field throughout the AHX was determined. This reliability algorithm maintains an interface with PATRAN and ABAQUS. As Duffy et al. (1993) point out, the C/CARES algorithm is based on probabilistic design philosophies, and is developed specifically for laminated composites. A macroscopic approach is adopted in the algorithm whereby a material is treated as an homogenized continuum such that the individual properties of the constituents are not accounted for explicitly. A weakest link formulation is used at the ply level. The failure function currently used in C/CARES accounts for five failure modes in each ply. These include failure in the fiber direction due to tension and compression, failure due to tension and compression in the direction transverse to the fiber direction, and an in-plane shear failure. Each failure mode is characterized by a three-parameter Weibull distribution.

A schematic of the finite element mesh is depicted in Fig. 2. A total of 1656 elements were used to model the outer tube and the surrounding insulation. Of these 1656 elements 1296 QUAD/8 elements were used to model the laminated tube, and 360 HEX/20 elements were used to model the insulation surrounding the tube and the built up flange of the tube. The built-up flange was fabricated from several unidirectional plies where the fibers in each ply are wound in the hoop direction (0°). It was determined during preliminary design analyses that the flange section of the bayonet and the insulation were not critical subcomponents. The insulation, which is relatively more compliant, was modeled as an isotropic material.

The axial temperature distribution obtained from the thermal analysis is depicted in Fig. 3. The resulting thermal stresses were three orders of magnitude larger than any stresses resulting from internal pressure or dead load (0.13 MPa and 0.29 MPa, respectively). Hence mechanical loads were neglected during preliminary analyses. An initial design guideline suggested that stresses in the fiber direction would be maintained at or below 82.7 MPa. For this particular set of boundary conditions a maximum tensile stress of 82.2 MPa is present in the inner layer, and a maximum compressive stress of 85.7 MPa is present at the outer surface of the tube.

The reliability analysis of the four-ply laminate outer tube begins with the specification of the Weibull parameters. The parameters used in the analysis of the AHX are listed in Table 1. These parameters were chosen arbitrarily since failure data were not available at the time of the analysis. Note that a conservative assumption was made by taking the threshold parameter equal to zero for each failure mode. This implies that a finite probability of failure exists for each failure mode at all stress levels. The overall component reliability of the AHX was 99.97 percent. The least reliable ply was the inner ply with a reliability of 99.97 percent. The other plies had a reliability of 100 percent.

Summary and Conclusions. Based on past experience, the authors cannot overstate the point that the commercial success of CFCCs requires the early investment of project resources in engineering design and development technologies. Specifically, project resources must be allocated so that a high-quality mate-

Table 1 Weibull parameters used for the reliability analysis

	Failure Mode				
	σ_{11} (tensile)	σ_{22} (tensile)	τ_{12}	σ_{11} (comp.)	σ_{22} (comp.)
α	25.0	15.0	22.0	30.0	30.0
β	17,500	12,500	7,500	50,000	40,000
γ	0.0	0.0	0.0	0.0	0.0

rial is produced with an appropriate data base of engineering properties. It is clearly evident that recent progress in processing ceramic composites has not been matched by thermal or mechanical testing efforts. Design methods and data bases needed to characterize CFCCs have traditionally been treated as afterthoughts. This type of data supports the creation of a complete design data base for a given material. The overview of the AHX highlighted in the previous section presents an actual design application that emphasizes the need for design data bases. The analysis of the design team required far too many instances of estimating (guessing) values for design properties (e.g., stiffness properties, thermal properties, Weibull parameters, etc.). Even though the team approached the application with the intent of designing a component using concurrent engineering principles, the lack of design information made the task difficult. This lack of design data bases is not endemic to industrial projects. In a similar fashion many of the government projects cited within this article do not focus resources in this area.

Not only is there a shortage of design data bases, but too often current engineering design methods cannot capture the complex behavior of CFCCs at the component level. Technologies that focus on designing with the material (i.e., developing technology to design components fabricated from the new material) must be supported along with technologies that focus on designing the material (i.e., processing and fabrication technologies). There is a definite need for experiments that support the development of reliability models, continuum damage models, and sophisticated heat transfer models. Focusing on reliability analyses this effort could include experiments that test fundamental concepts, e.g., quantifying size effect in the fiber direction. Probing experiments could be conducted along various biaxial load paths to establish level surfaces of reliability in a particular two-dimensional stress space (similar to probing yield surfaces in metals). Concepts such as the maximum stress response, which is often assumed in reliability models, could be assessed. A data base for each failure mode would be assembled in order to uniquely characterize the material. After establishing a theoretical framework for a mechanical analysis, characterization tests should be conducted to provide the functional dependence of model parameters with respect to temperature.

Finally, data from structural tests that are multiaxial and nonisothermal could be used to challenge the predictive capabilities of models through comparison to benchmark response data. It can not be overemphasized that this kind of testing supports design and analysis of components. Currently the "make and break" (and/or "heat and beat") mind set usually produces uniaxial test data to demonstrate the benefits of embedding a continuous ceramic fiber in a ceramic matrix. Once this has been established, the project is too often regarded as successfully completed. This view tends to neglect the fact that CFCCs are subject to multi-axial states of stress in systems that must conduct heat in an efficient manner.

References

Chuang, T.-J., and Duffy, S. F., 1994, "A Methodology to Predict Creep Life for Advanced Ceramics Using Continuum Damage Mechanics Concepts," in: *Life Prediction Methodologies and Data for Ceramic Materials,* ASTM STP 1201, C. R. Brinkman and S. F. Duffy, eds., American Society for Testing and Materials, Philadelphia, pp. 207–227.

DeBellis, C. L., and Kneidel, K. E., 1987, "Thermal and Fluid Design of a High-Temperature Ceramic Fiber Composite Heat Exchanger," presented at the AIChE Sessions of the 24th National Heat Transfer Conference, Pittsburgh, PA.

Duffy, S. F., and Gyekenyesi, J. P., 1989, "Time Dependent Reliability Model Incorporating Continuum Damage Mechanics for High-Temperature Ceramics," NASA TM-102046.

Duffy, S. F., and Arnold, S. M., 1990, "Noninteractive Macroscopic Statistical Failure Theory for Whisker Reinforced Ceramic Composites," *Journal of Composite Materials,* Vol. 24, No. 3, pp. 293–308.

Duffy, S. F., and Manderscheid, J. M., 1990, "Noninteractive Macroscopic Reliability Model for Ceramic Matrix Composites With Orthotropic Material Symmetry," ASME JOURNAL OF ENGINEERING FOR GAS TURBINES AND POWER, Vol. 112, No. 4, pp. 507–511.

Duffy, S. F., Palko, J. L., and Gyekenyesi, J. P., 1993, "Structural Reliability Analysis of Laminated CMC Components," ASME JOURNAL OF ENGINEERING FOR GAS TURBINES AND POWER, Vol. 115, pp. 103–108.

Honjo, K., Hashimoto, R., and Oglyama, H., 1993, "Current Status of 300 kW Industrial Ceramic Gas Turbine R&D in Japan," ASME JOURNAL OF ENGINEERING FOR GAS TURBINES AND POWER, Vol. 115, pp. 51–57.

Itoh, T., and Kimura, H., 1993, "Status of the Automotive Ceramic Gas Turbine Development Program," ASME JOURNAL OF ENGINEERING FOR GAS TURBINES AND POWER, Vol. 115, pp. 42–50.

Sorrell, C. A., and Hoffman, P. A., 1994, "Innovative Composite Materials Research at the U.S. Department of Energy, Office of Energy Efficiency and Renewable Energy," *Composites Engineering,* Vol. 4, No. 8, pp. 857–882.

Thomas, D. J., and Wetherhold, R. C., 1991, "Reliability Analysis of Laminates With Load Sharing," *Journal of Composite Materials,* Vol. 25, pp. 1459–1475.

Fracture Toughness of Structural Ceramics Under Biaxial Stress State by Anticlastic Bending Test

T. Ono

M. Kaji

Central Research Laboratory,
Kyocera Corporation,
Kokubu, Kagoshima, Japan

Mixed-mode fracture of structural ceramics under a biaxial stress state was investigated by an anticlastic bending test using the controlled surface flaw technique. The stress state of the anticlastic bending specimen is biaxial. This test enables the study of fractures under pure mode I, pure mode II, or any combination of mode I and mode II loading. To discuss the experimental results, a parameter "T" was introduced to the modified maximum hoop stress criterion. This parameter represents frictional effects of crack interfaces on the mixed-mode fracture and can be obtained experimentally. Relative magnitudes of mode I and mode II stress intensity factors and the directions of non-coplanar crack extension angles were predicted using the parameter "T." Reasonable agreement with the experimental results was obtained.

Introduction

Ceramics have been applied to structural components such as gas turbine and reciprocal engines because of their advantages for light weight and stability compared with metals, particularly at high temperature. When ceramics are used for structural components in practical applications, they are often subjected to multiaxial stress states. In the case of a gas turbine rotor, for example, biaxial tensile stresses (tangential stress and radial stress) are generated by centrifugal force. This means that flaws in ceramics are under the mixed-mode fracture condition. Thus, it is important to find the mixed-mode fracture condition of structural ceramics under the multiaxial stress state.

A number of studies have been reported in both the mixed-mode fracture theories and the experimental techniques used to study the mixed-mode fracture of ceramics. Mixed-mode fracture theories can be grouped into three categories on the basis of the fracture criteria: (a) Maximum hoop stress theory (Erdogan and Sih, 1963), (b) minimum strain density theory (Sih, 1974), and (c) strain energy release rate theories (Hussain et al., 1974; Palaniswamy and Knauss, 1978; Chiang, 1977; Ichikawa and Tanaka, 1982). Predictions of these fracture criteria were compared to the mode I and mode II mixed-mode fracture tests and reasonable agreements have been reported. The majority of these mixed-mode fracture tests was conducted using a through crack as a precrack and under a uniaxial stress state. To approach the mixed-mode fracture condition of natural flaws in ceramics, it is important to conduct the mixed-mode fracture test using a small flaw as the precrack under a multiaxial stress state.

The mixed-mode fracture studies of ceramics using a small flaw as a precrack have mainly used a controlled surface flaw produced by Knoop hardness indentation (Petrovic and Mediratta, 1977; Marshall, 1984; Shetty et al., 1986; Hayashi et al., 1991; Ono et al., 1993). Applications of a Knoop surface flaw to the mixed-mode fracture test of ceramics are looked upon favorably because the size of the surface flaw is closer to that of natural flaws in addition to their experimental simplicity.

In the previous report (Ono et al., 1993), the authors performed mixed-mode fracture tests using silicon nitride flexure specimens having a Knoop surface flaw and tested in a four-point bending test. However, it appears that the four-point bending test using a Knoop surface flaw is not the most suitable test method from the viewpoint of the mixed-mode fracture. Firstly, even though ceramics are subjected to a multiaxial stress state when they are used in practical applications, the stress state of the four-point bending specimen is uniaxial. Secondly, this test does not permit the investigation of pure mode II fracture. This is evident from the results of the previous studies.

Thus, it is important to study the mixed-mode fracture under a multiaxial stress state and to find a fracture criterion that represents the mixed-mode fracture condition under multiaxial (uniaxial or biaxial) stress states.

In this study, mixed-mode fracture tests were performed using an anticlastic bending specimen that has a Knoop surface flaw. The stress state of the anticlastic bending specimen is biaxial. A silicon nitride, an alumina, and a silicon carbide were used and their mode I and mode II stress intensity factors and crack extension angles were measured. A modified maximum hoop stress theory was applied to the results and a parameter was added to the theory. The parameter expresses the shear tractions on the flaw surface due to grain interlocking and we obtained the value of the parameter for each material by comparing with experimental results. For the purpose of comparing mixed-mode fracture under a biaxial stress state with that under a uniaxial stress state, the mixed-mode fracture tests were also conducted using a flexure specimen that has a Knoop surface flaw. The result was compared with the prediction of the modified maximum hoop stress theory including the new parameter. The effect of the shear tractions on the flaw surface to the mixed-mode fracture is discussed in the light of microstructure of the materials.

Experimental Procedures

To find the mixed-mode fracture condition of the material, it is necessary to evaluate the crack extension angles or mixed-mode fracture toughness by a test. In this section, the mixed-mode fracture tests are explained.

Test Materials. Materials chosen for the present study were a silicon nitride, an alumina, and a silicon carbide. These ceramics are used mainly in structural components such as auto-

Contributed by the International Gas Turbine Institute and presented at the 40th International Gas Turbine and Aeroengine Congress and Exhibition, Houston, Texas, June 5–8, 1995. Manuscript received by the International Gas Turbine Institute February 27, 1995. Paper No. 95-GT-238. Associate Technical Editor: C. J. Russo.

Table 1 Material properties of the structural ceramics

	Silicon Nitride	Alumina	Silicon Carbide
Young's Modules (GPa)	301	373	410
Poisson's Ratio	0.28	0.24	0.17
Flexural Strength (MPa)	798±52.8	341±20.2	405±30.9

motive parts, industrial pumps, and mechanical seals. Mechanical properties of these materials are measured according to JIS R 1601 and 1602 and summarized in Table 1.

Mixed-Mode Fracture Test Under Biaxial Stress State. An anticlastic bending test was proposed by Ohji (1967). In the anticlastic bending test, a square specimen supported at two apexes on a diagonal line is loaded through two apexes on the other diagonal line of the specimen. Figure 1(*a*) shows the specimen and the loading geometry. The loading generates a biaxial stress state in the specimen with a tensile principal stress and a transverse compressive principal stress. These stresses are constant in the center of this square specimen. Their magnitudes are given by the relations:

$$\sigma_x = +\frac{3P}{2t^2}, \tag{1}$$

and

$$\sigma_y = -\frac{3P}{2t^2}, \tag{2}$$

where P is the applied load, t is the thickness of the square specimen, σ_x is the tensile principal stress, and σ_y is the compressive principal stress. The validity of the solutions for the principal stresses of Eq. (1) was verified by a direct measurement of stress using strain gages on an alumina specimen. Stress by the strain gage is compared with the stress according to Eq. (1) for the tensile principal stress on the surface of the square specimen in Fig. 2. As can be seen, the calibration agreement is good. This result indicates that Eq. (1) can be used to calculate principal stresses in the central area of the square specimen surface of the anticlastic bending test. In the present study, we have adopted an anticlastic bending specimen for the mixed-mode fracture test. Because of the tension-compression biaxial stress state with a ratio of -1 at the center area of the square specimen surface, mixed-mode fracture from the Knoop surface flaw can be examined ranging from pure mode I to pure mode II by proper orientation angles of the Knoop surface flaw relative to the principal stress direction. A single Knoop surface flaw was introduced on the surface of each square specimen. This flaw is inclined at an angle, α (a crack orientation angle) with respect to the direction of the tensile principal axis, as shown schematically in Fig. 1(*b*). On a plane of the inclined Knoop surface flaw, the normal stress, σ_n, and the shear stress, τ, are given by the relations:

$$\sigma_n = -\sigma \cdot \cos(2\alpha), \tag{3}$$

and

$$\tau = \sigma \cdot \sin(2\alpha), \tag{4}$$

where σ is the absolute value of the tensile or compressive principal stresses. The Knoop surface flaw has a semi-elliptical shape as shown in Fig. 1(*b*). For a semi-elliptical surface flaw in anticlastic bending, the maximum value of σ occurs at corners of the flaw surface (point A or A' shown in Fig. 1(*b*)) and the mode III stress intensity factor K_{III} is zero there. In the present study, we assume that fracture occurs from the corners in the mixed condition of mode I and mode II.

From an examination of Eqs. (3) and (4), it is evident that in the case of $\alpha = 90$ deg, a Knoop surface flaw is subjected only to tensile stress, and the surface flaw is in a condition of pure mode I. In the case of 45 deg $< \alpha <$ 90 deg, surface flaw is subjected to tensile and shear stresses, and the surface flaw is in the mixed-mode condition of mode I and mode II. In the case of $\alpha = 45$ deg, the surface flaw is subjected only to shear stress, and the surface flaw is in the condition of pure mode II.

The specimen size used in this study was 30 × 30 × 2 mm and its surface was mirror-polished. A Knoop surface flaw was introduced with an indentation load of 498 N on the surface of the square specimen at a proper angle ranging from $\alpha = 45$ to 90 deg.

When a Knoop surface flaw is introduced, a residual stress is caused around the flaw by plastic deformation. Following the indentation, the indented surface of specimens was removed to three or four times the indentation depth to eliminate the residual stress (Miyoshi et al., 1985). In the case of silicon carbide, the surface was removed to ten times the indentation depth because delamination of the surface occurred around the Knoop surface flaw. After the residual stress was removed, anticlastic bending tests were performed at room temperature. The dimensions a and b of the semi-elliptical surface crack (shown in Fig. 1(*b*)) were measured by observation of the fracture surface after the test was completed. The measurement error is within 30 μm and the influence on the value of stress intensity factor is less

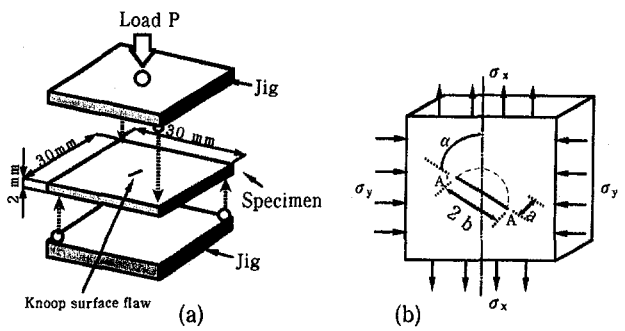

Fig. 1 Schematic view of an anticlastic bending test: (*a*) total view of an anticlastic bending test; (*b*) inclined Knoop surface flaw introduced on the surface

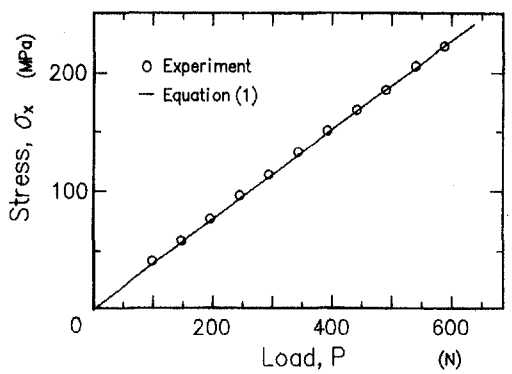

Fig. 2 Relationship between the applied load and the principal stress

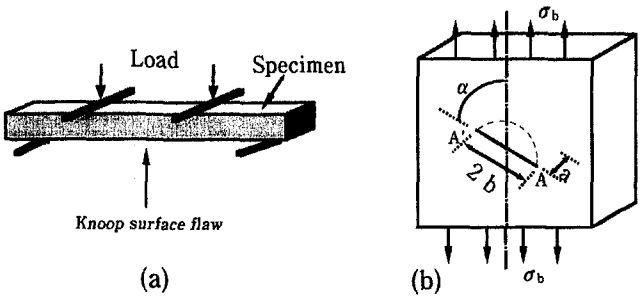

Fig. 3 Schematic view of a four-point bend test: (*a*) total view of a four-point bend test; (*b*) inclined Knoop surface flaw introduced on the surface

than 5 percent. Based on the results of this measurement, K_I and K_{II} were calculated using the equations of Raju–Newman and Smith–Sorensen for K_I and K_{II}, respectively. These equations are explained in the appendix.

Mixed-Mode Fracture Test Under Uniaxial Stress State. Several mixed-mode fracture tests of ceramics using flexure specimens containing a Knoop surface flaw (as shown in Fig. 3(*a*)) were reported due to the simplicity of the test. In the present study, flexure specimens with the dimensions of 3 × 4 × 40 mm were used. These specimens were chamfered at the edges, and their tensile surface was mirror-polished. A single Knoop surface flaw was introduced on the polished surface at an angle, α, from the direction of the tensile principal stress, as shown schematically in Fig. 3(*b*). On a plane of the inclined Knoop surface flaw, the normal stress, σ_n, and the shear stress, τ, are given by the relations:

$$\sigma_n = \sigma_b \cdot \sin^2 \alpha, \tag{5}$$

and

$$\tau = \sigma_b \cdot \sin \alpha \cdot \cos \alpha, \tag{6}$$

where σ_b is the bending stress on the tensile surface. The indentation produced a semi-elliptical surface crack as shown in Fig. 3(*b*). Similar to the anticlastic bending test, the maximum value of σ_b occurs at corners of the flaw surface in four point bending test (point A or A' shown in Fig. 3(*b*)) and the mode III stress intensity factor K_{III} is zero there. In this study, we again assume that fracture occurs in the mixed-mode condition of mode I and mode II.

From an examination of Eqs. (5) and (6), it is evident that a Knoop surface flaw is in the condition of pure mode I when α = 90 deg and in the mixed-mode condition of mode I and mode II when 0 deg < α < 90 deg. In this experiment, a Knoop surface flaw was introduced at a proper angle ranging from α = 45 deg to α = 90 deg. The Knoop indentation condition and the residual stress removal method were the same as those of the anticlastic bending test.

After the test was completed, the dimensions a and b of the semi-elliptical surface crack, as shown in Fig. 3(*b*), were measured by observation of the fracture surface. Based on the results of this measurement, K_I and K_{II} were calculated using the equations of Raju–Newman and Smith–Sorensen, respectively.

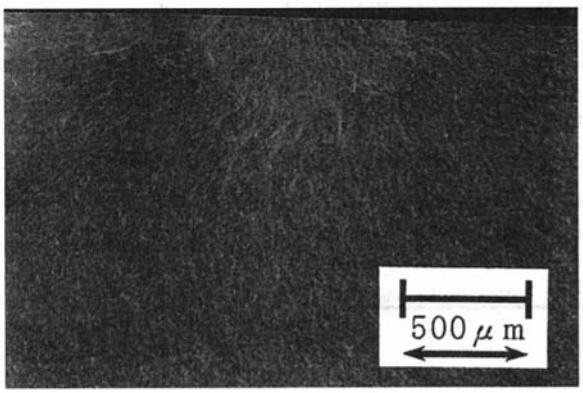

Fig. 4 Scanning electron micrograph of a Knoop surface flaw

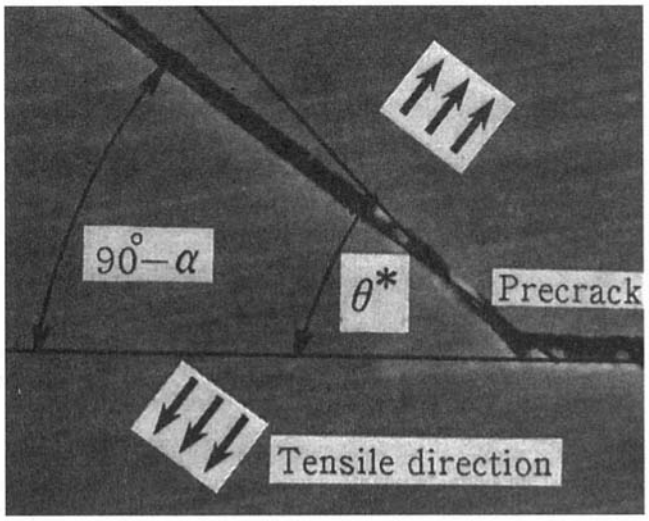

Fig. 5 Micrograph of a crack extension angle

Experimental Results

Figure 4 shows a typical scanning electron micrograph of the Knoop surface flaw oriented at α = 90 deg in a silicon nitride of the anticlastic bending test. As can be seen, a Knoop surface flaw has a semi-elliptical geometry. For all situations except the pure mode I condition, extending cracks were not straight. In the anticlastic bending test, crack extension angles, θ^* (the angle between the direction of crack extension and the Knoop surface flaw) were measured for each specimen by metallographic pictures taken around the Knoop surface flaw of the fractured specimen. Figure 5 shows a typical crack extension pattern near the initial flaw tip in a silicon nitride specimen

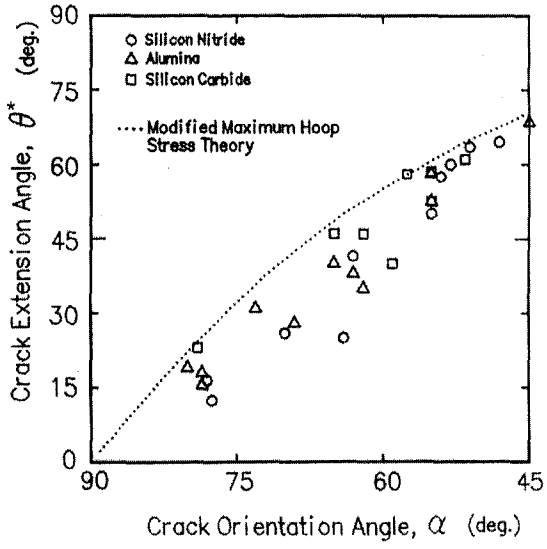

Fig. 6 Relationship between the crack orientation angle and the crack extension angle of the anticlastic bending test

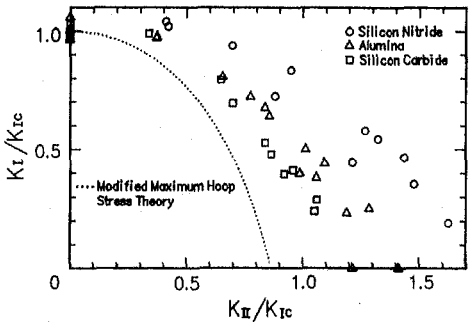

Fig. 7 Relationship between the normalized mode I stress-intensity factor and normalized mode II stress-intensity factor of the anticlastic bending test

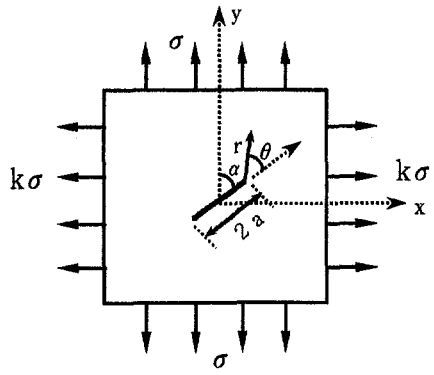

Fig. 8 Inclined crack in a general biaxial stress state

fractured under mixed-mode condition of $\alpha = 53$ deg in the anticlastic bending test. In most of the observed fracture patterns, crack extension angles, θ^*, decreased with crack extension until the crack finally extended in the direction perpendicular to the tensile principal stress direction, as shown in Fig. 5. In this case, the initial crack extension angles were measured as θ^*.

Figure 6 shows the crack extension angle, θ^*, as a function of their crack orientation angle, α for each material of the anticlastic bending test. It is obvious that the value of θ^* becomes larger as α decreases. Figure 7 shows the relationship between the mode I and mode II stress intensity factors normalized by K_{IC} of the anticlastic bending test for each material. It is obvious that the value of K_{II} becomes larger as K_I decreases. These experimental data indicate that the major mode of the fracture shifts from mode I to mode II as α decreases. In this study, experimental data were obtained ranging from $K_{II}/K_I = 0$ (pure mode I) to $K_{II}/K_I =$ infinity (pure mode II).

The average values of K_{IC} (the critical stress intensity factor of pure mode I) of the anticlastic bending test and the four-point bending test are summarized in Table 2. As shown in the table, K_{IC} values obtained by the two methods are in good agreement. This means that the compressive stress parallel to the direction of the Knoop surface flaw has little effect on K_{IC} significantly in the anticlastic bending test.

Discussion

To discuss and find the appropriate fracture criterion under biaxial or uniaxial stress state, experimental data obtained in this study are compared with the modified maximum hoop stress theory including a parameter, T. In this section, we introduce this fracture criterion to the mixed-mode fracture and discuss the effect of the shear tractions on the flaw surface.

Modified Maximum Hoop Stress Theory. In the case of an inclined crack in a plate subjected to a uniform biaxial stress state, Eftis and Subramonian (1978) modified the maximum hoop stress theory as a fracture criterion as briefly stated below.

According to the maximum hoop stress theory, a crack subjected to both mode I and mode II loading extends in a direction of crack extension angle, θ^*, along which the crack tip hoop stress, σ_θ, is the maximum with fracture occurring when the hoop stress attains a material characteristic critical value. Thus, the maximum hoop stress theory can be stated as follows:

$$\left.\frac{\partial \sigma_\theta}{\partial \theta}\right|_{\theta=\theta^*} = 0. \tag{7}$$

In the modified maximum hoop stress theory, the nonsingular second term in the expression for the hoop stress includes the effect of a biaxial stress component parallel to the crack (see Fig. 8). The crack-tip hoop stress for the inclined crack under a biaxial stress state is given as (Eftis and Subramonian, 1978)

$$\sigma_\theta = \frac{1}{4\sqrt{2\pi r}} \left\{ \begin{array}{l} K_{II}\left(-3\sin\dfrac{\theta}{2} - 3\sin\dfrac{3\theta}{2}\right) \\ \\ +K_I\left(3\cos\dfrac{\theta}{2} + \cos\dfrac{3\theta}{2}\right) \end{array} \right\} + \sigma(1-k)\cos 2\alpha \cdot \sin^2\theta, \tag{8}$$

where the mode I and mode II stress-intensity factors are given by the following equations:

$$K_I = \frac{\sigma\sqrt{\pi a}}{2}\{(1+k) - (1-k)\cdot\cos 2\alpha\}, \tag{9}$$

and

$$K_{II} = \frac{\sigma\sqrt{\pi a}}{2}(1-k)\cdot\sin 2\alpha. \tag{10}$$

Here α is the crack orientation angle, r and θ are the polar coordinates with a crack-tip as the origin, and a is the half length of the crack. A parameter, k, is the horizontal load parameter (Eftis and Subramonian, 1978) (or the stress state parameter (Shetty et al., 1987)), which expresses the stress ratio under biaxial or uniaxial stress states. For example, parameter k takes the value of 0 under the uniaxial stress state (i.e., the four-point bending test), and -1 under the tension-compression biaxial stress state (i.e., the anticlastic bending test).

Table 2 The values of K_{IC} for each test method

	Anticlastic bending test		4 point bending test	
	Number of specimens	K_{IC} (MPa $m^{1/2}$)	Number of specimens	K_{IC} (MPa $m^{1/2}$)
Silicon Nitride	2	6.5±0.20	5	6.7±0.25
Alumina	4	4.0±0.17	3	4.2±0.13
Silicon Carbide	2	2.7±0.10	8	3.0±0.06

By applying Eqs. (8), (9), and (10) to Eq. (7), the following equations are obtained:

$$4f_1 \cdot g_1 + 3f_2 \cdot g_2 - 16\sqrt{2} \times \sqrt{\frac{r}{a}}(1-k)\cos 2\alpha \cdot \sin 2\theta^* = 0 \quad (11)$$

and

$$K_I\left(g_3 - \frac{f_2 g_1}{f_1} + 2\sqrt{2}\,\frac{f_2}{f_1}\sqrt{\frac{r}{a}\frac{\sin^2\theta^*}{\tan 2\alpha}}\right) = K_{IC}, \quad (12)$$

where f_i $(i = 1, 2)$ and g_i $(i = 1, 2, 3)$ are defined as follows:

$$f_1(k, \alpha) = (1+k) - (1-k)\cdot\cos 2\alpha,$$

$$f_2(k, \alpha) = (1-k)\cdot\sin 2\alpha,$$

$$g_1(\theta^*) = \frac{3}{4}\left(\sin\frac{\theta^*}{2} + \sin\frac{3\theta^*}{2}\right),$$

$$g_2(\theta^*) = \left(\cos\frac{\theta^*}{2} + 3\cos\frac{3\theta^*}{2}\right),$$

$$g_3(\theta^*) = \frac{1}{4}\left(3\cos\frac{\theta^*}{2} + \cos\frac{3\theta^*}{2}\right). \quad (13)$$

The predicted values of the crack extension angle, θ^*, and the mode I and mode II fracture toughness can be obtained from Eqs. (11) and (12). The hoop stress is evaluated at a location with an infinitesimal distance from the crack tip. A location parameter, r/a, in Eqs. (11) and (12) should be chosen on the basis of physical considerations such as a characteristic microstructural dimension or the size of a process zone, but the value of the parameter for brittle materials such as ceramics is not clear (Shetty et al., 1987). In the present study, r/a = 0.01 was chosen similar to the previous studies by Eftis and Subramonian (1978) and Shetty et al. (1987).

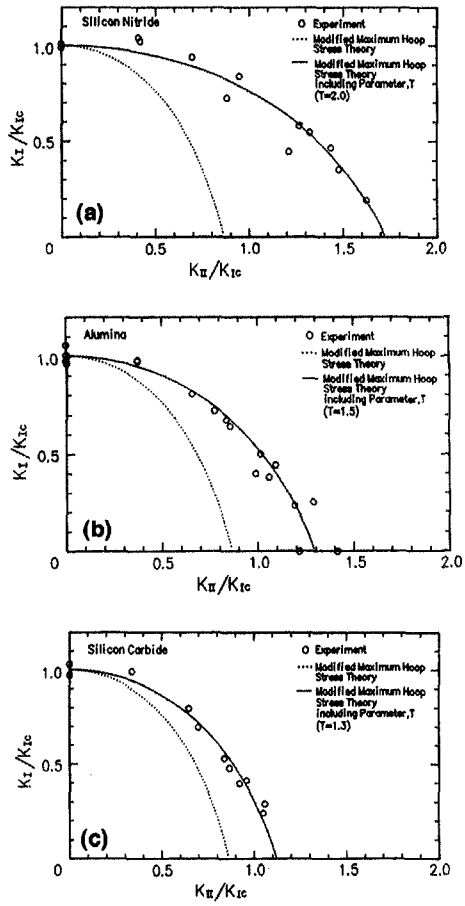

Fig. 10 Relationship between the normalized mode I stress-intensity factor and normalized mode II stress-intensity factor of the anticlastic bending test: (*a*) silicon nitride, (*b*) alumina, and (*c*) silicon carbide

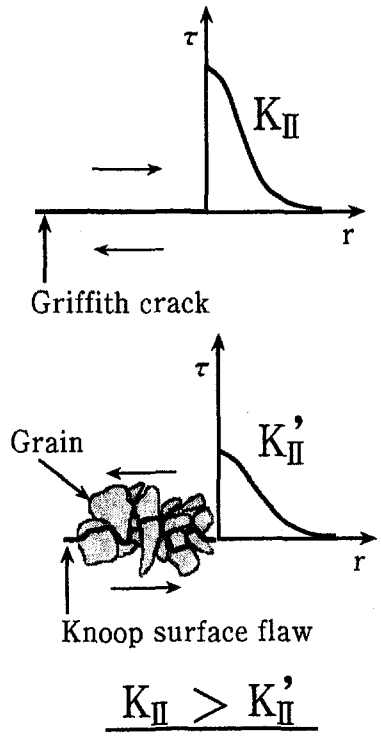

Fig. 9 A conceptional scheme of the shear traction on the crack surface due to grain interlocking effects

The dotted lines in Figs. 6 and 7 are predictions of the modified maximum hoop stress theory obtained from Eqs. (11) and (12) when $k = -1$. As shown in Fig. 6, the predicted values of the crack extension angles overestimate the measured values of θ^* for each material. It is clear, as shown in Fig. 7, that the predicted value overestimates the contribution of the shear stress to the mixed-mode fracture; i.e., the effect of K_{II} on the mixed-mode fracture.

Modified Maximum Hoop Stress Theory Including Parameter, *T*. It is considered that the reason the prediction of K_{II} obtained from the modified maximum hoop stress theory overestimates the effect of K_{II} is that there is a difference of crack configuration between a Griffith crack defined in the theory and the practical Knoop surface flaw produced on ceramics. The configuration of a Griffith crack is flat and it might be described by a level plane. On the other hand, the surface flaw extends with intergranular or intragranular fracture when the surface flaw is produced on polycrystalline ceramics by an indentor. Thus, tips of the Knoop surface flaw weave their way microstructurally.

It is believed that the shear tractions on the flaw surface due to grain interlocking between each flaw surface prevent shear displacement of such surface cracks. Thus, the K_{II} that governs the shear displacement of the surface flaw is less than that of the Griffith crack, as shown schematically in Fig. 9. An effect of the shear tractions must be taken into account in any linear elastic fracture mechanics analysis of the mixed-mode fracture of polycrystalline ceramics. Here, we attempt to take the effect

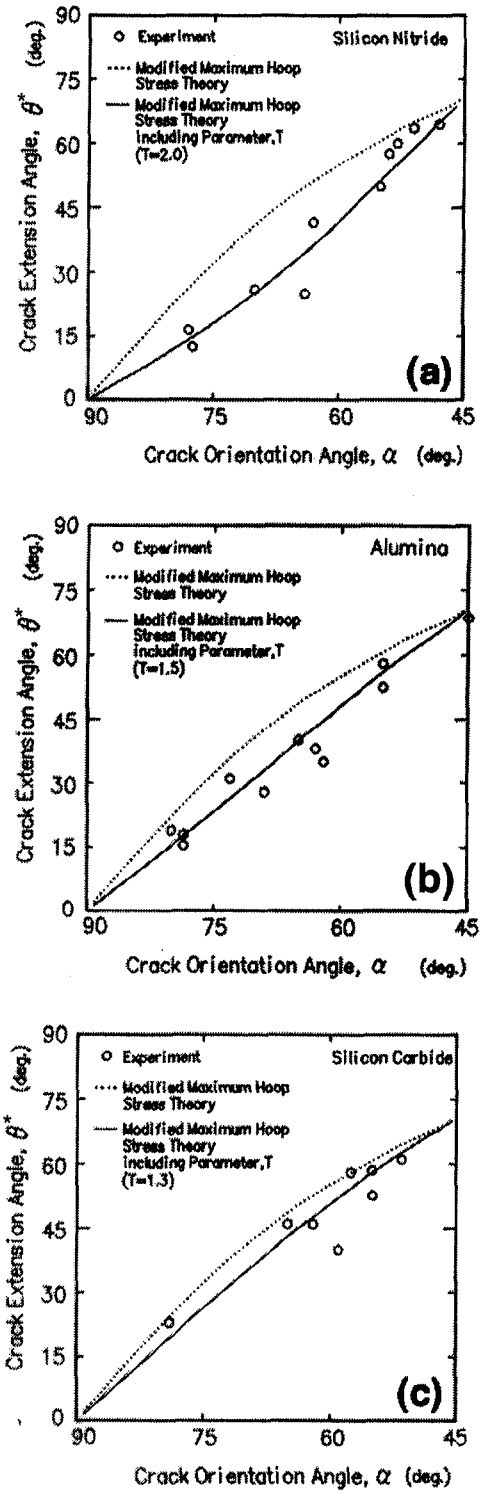

Fig. 11 Relationship between the crack orientation angle and the crack extension angle of the anticlastic bending test: (*a*) silicon nitride, (*b*) alumina, and (*c*) silicon carbide

of the shear tractions into consideration for the modified hoop stress theory, assuming that the magnitude of K_{II} of the Knoop surface flaw becomes $1/T$ of the K_{II} of the Griffith crack. The parameter T represents the decrease of K_{II} due to the grain interlocking on the flaw surface. It takes the value of 1 in the case that there is no effect of the grain interlocking (i.e., Griffith crack) and takes larger values as the effect of the grain interlocking becomes greater.

By substituting K_{II}/T for K_{II} in Eq. (8) and applying Eq. (7), the following equations are obtained:

$$4f_1 \cdot g_1 + \frac{1}{T} \cdot 3f_2 \cdot g_2 - 16\sqrt{2} \times \sqrt{\frac{r}{a}}(1-k)\cos 2\alpha \cdot \sin 2\theta^* = 0, \quad (14)$$

and

$$K_I\left(g_3 - \frac{1}{T} \cdot \frac{f_2 \cdot g_1}{f_1} + 2\sqrt{2} \cdot \frac{f_2}{f_1} \cdot \sqrt{\frac{r}{a}} \cdot \frac{\sin^2 \theta^*}{\tan 2\alpha}\right) = K_{IC}. \quad (15)$$

Figure 10 compares the normalized K_I–K_{II} fracture envelopes with the experimental results for each material. The dotted line in Fig. 10 is the prediction of Eq. (12) and the solid line is that of Eq. (15), which is fitted to the experimental results for each material. Equation (15) provides good fit to the results on a silicon nitride, an alumina and a silicon carbide with the parameter T = 2.0, 1.5, and 1.3, respectively.

Several fracture criteria for ceramics including an experimental parameter such as Shetty's empirical equation (Shetty et al.,

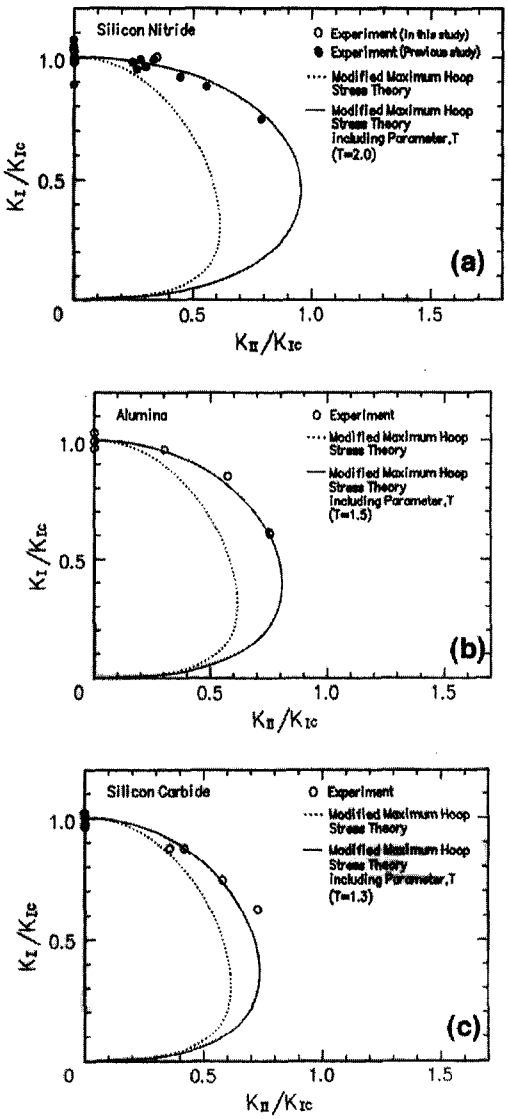

Fig. 12 Relationship between the normalized mode I stress-intensity factor and normalized mode II stress-intensity factor of the four-point bending test: (*a*) silicon nitride, (*b*) alumina, and (*c*) silicon carbide

Table 3 The measured value of grain size and aspect ratio for each material

	Grain Size, d (μm)	Aspect ratio, A
Siicon Nitride	5.3±2.09	2.8±1.02
Alumina	7.5±2.78	1.5±0.41
Silicon Carbide	2.2±0.48	1.5±0.38

1986) have been reported. These criteria can predict only the K_I–K_{II} fracture envelopes. Modified maximum hoop stress theory including a parameter, which was suggested here, can predict not only the K_I–K_{II} fracture envelopes but also the crack extension angles. Figure 11 shows the relationship between the crack orientation angle and the crack extension angle for each material in the anticlastic bending test. The dotted line in Fig. 11 is the prediction of Eq. (11), and the solid line is that of Eq. (14) including a parameter T, whose values for each material were obtained in Fig. 10. The agreement between the solid line and the experimental results is better than the dotted line for each material.

As mentioned above, this equation might be able to predict the mixed-mode fracture under both biaxial and uniaxial stress states because it includes the horizontal parameter, k, which expresses the stress ratio. We applied the modified maximum hoop stress theory including a parameter T, to the mixed-mode fracture results obtained by the four-point bending test (k = 0).

Figure 12 shows the relationship between the normalized mode I stress intensity factor and the normalized mode II stress intensity factor in the four-point bending test for each material. For the silicon nitride, we add the results obtained in the previous study (Ono et al., 1993). In that study, a Knoop surface flaw was introduced with an indented load of 98 N and the specimens were annealed for 2 hours at 1273 K in air to remove the residual stress produced by the indentation. The size of a Knoop surface flaw in that study was about one-fifth as large as that of the present study.

The dotted line in Fig. 12 is the prediction of Eq. (12) (k = 0), and the solid line is that of Eq. (15) (k = 0) including a parameter, T, whose value for each material was obtained in Fig. 10. In the mixed-mode fracture test under uniaxial stress state, the normal stress and the shear stress on a plane of the inclined Knoop surface flaw are zero when the direction of the surface flaw is parallel to the tensile direction, i.e., α = 0 deg in Eqs. (5) and (6). The solid and dotted line can explain the mixed-mode fracture envelopes under uniaxial stress state well because the predicted lines do not intersect the K_{II} axis and converge to the origin.

It is clear from Fig. 12 that the dotted line overestimates the effect of K_{II} on the mixed-mode fracture, and the agreement between the solid line and the experimental results is good. Especially, in the case of silicon nitride, the solid line agrees with the experimental results for different sizes of the Knoop surface flaws.

The mixed-mode fracture condition for the same material under uniaxial or biaxial stress states and with any surface flaw size can be stated by the modified maximum hoop stress theory including a parameter T. Thus, the parameter T denotes a characteristic value, which does not depend on either the mixed-mode fracture test method nor the flaw size and does depend only on the microstructure of the material.

The Relationship Between T and Microstructure. The modified maximum hoop stress theory including a parameter T agrees with the experimental results when T = 2.0 for the silicon nitride, T = 1.5 for the alumina, and T = 1.3 for the silicon carbide, respectively. In this section, we discuss the reason the effects of the shear traction on the mixed-mode fracture are different among the various materials.

In this study, we have assumed that the Knoop surface flaw extends with intergranular or intragranular fracture when the surface flaw is produced in ceramics by an indentor. As mentioned above, the tips of the surface flaw are not described by a level plane like the Griffith crack, but they weave their way from the microstructural point of view. Assume that the degree of the weave of the flaw tips depends on grain size, d, and the grain aspect ratio, A, of the material because the weave of the flaw tips depends on the degree of the intragranular fracture. Then the value of T depends on the degree of the weave of the flaw tips. Thus, the relationship between T, d, and A can be stated as: $T = (d \times A)$. It is clear that if the grain size is very small then the degree of the weave of the flaw tip is nearly equal to zero and we can treat the flaw as the Griffith crack in such a case. As mentioned above, the value of T is 1 in the case of the Griffith crack. Thus, the relationship between T, d, and A could assume the form of a simple equation:

$$T = C(d \times A) + 1, \tag{16}$$

where C is the correlation factor.

We measured the grain size, d, and the grain aspect ratio, A, of the material used in this study by an image analysis method to verify the assumption expressed in Eq. (16). Table 3 shows the measurement results (mean value and standard deviation) of d and A. The value of A for a silicon nitride is the biggest of the three materials because of its needlelike grains.

Figure 13 shows the relationship between $(d \times A)$ and T. The solid line is obtained from Eq. (16) (in this study, the correlation factor C = 0.058 was obtained). It is obvious that there is a correlation between $(d \times A)$ and the parameter T. Considering the scatter and the measurement errors of T, d, and A, the relationship between $(d \times A)$ and T cannot be determined quantitatively, but the effect of the overall qualitative correlation is expressed in Eq. (16).

Conclusions

Mixed-mode fracture under a biaxial stress state was studied by the anticlastic bending test. The measurement was conducted at room temperature using a silicon nitride, an alumina, and a silicon carbide specimen. The relative magnitudes of mode I

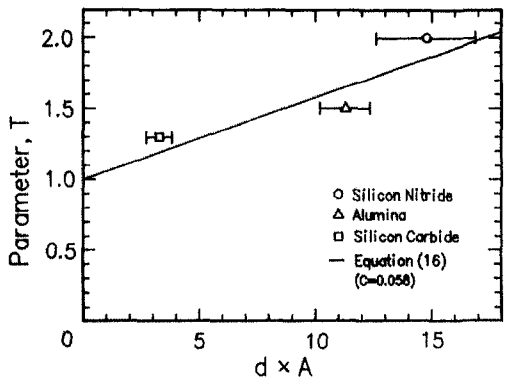

Fig. 13 Relationship between the value of $(D \times A)$ and the parameter T obtained in this study

and mode II stress intensity factors and the crack extension angles were measured.

To discuss the experimental results, we introduced a parameter T to the modified maximum hoop stress theory. This parameter represents the frictional effects of crack interfaces on the mixed-mode fracture. The modified maximum hoop stress theory including a parameter T provides good fit to the K_I–K_{II} fracture envelopes on a silicon nitride, an alumina, and a silicon carbide with the parameter $T = 2.0$, 1.5, and 1.3, respectively. The predictions of the crack extension angle were calculated for each material by the modified maximum hoop stress theory including a parameter T. The agreement between the predicted values of the crack extension angle was better than the modified maximum hoop stress theory. The predictions of the K_I–K_{II} fracture envelopes under uniaxial stress state were calculated for each material by the modified maximum hoop stress theory including a parameter, T. The predicted values of the K_I–K_{II} fracture envelopes are in good agreement with experimental results obtained from the four-point bending test. It was verified that the mixed-mode fracture condition for the same material under uniaxial or biaxial stress state can be stated by the modified maximum hoop stress theory including a parameter T.

The values of T were different for each material. It is suggested that the value of T depends on the microstructure of the material. To support this suggestion, the grain size, d, and the aspect ratio, A, of the materials used in this study were measured. As a result, it was shown that the value of T depends on that of $(d \times A)$, qualitatively.

Acknowledgments

The present study has been carried out under contract in a ceramic gas turbine program. The authors express deep appreciation to the Agency of Industrial Science and Technology, New Energy and Industrial Technology Development Organization, and to Professor M. Sakai for his valuable advice to this paper.

References

Chiang, W. T., 1977, "Fracture Criteria for Combined Mode Cracks," *Fracture 4*, pp. 135–154.

Eftis, J., and Subramonian, N., 1978, "The Inclined Crack Under Biaxial Load," *Eng. Fract. Mech.*, Vol. 10, pp. 43–67.

Erdogan, F., and Sih, G. C., 1963, "On the Crack Extension in Plates Under Plane Loading and Transverse Shear," ASME *Journal of Basic Engineering*, Vol. 85, pp. 519–527.

Hayashi, S., Suzuki, A., and Sugiyama, S., 1991, *Transactions of Japan Society of Mechanical Engineers*, Vol. 57, No. 534, pp. 298–302 [in Japanese].

Hussain, M. A., Pu, S. L., and Underwood, J., 1974, "Strain Energy Release Rate for a Crack Under Combined Mode I and Mode II," *Fracture Analyses*, ASTM STP 560, pp. 2–28.

Ichikawa, M., and Tanaka, S., 1982, "A Critical Analysis of the Relationship Between the Energy Release Rate and the Stress Intensity Factors for Non-coplanar Crack Extension Under Combined Mode Loading," *International Journal of Fracture*, Vol. 18, pp. 19–28.

Marshall, D. B., 1984, "Mechanics of Failure From Surface Flaws in Mixed-Mode Loading," *Journal Am. Ceram. Soc.*, Vol. 67, No. 2, pp. 110–116.

Miyoshi, T., Sagawa, N., and Sassa, T., 1985, *Transactions of Japan Society of Mechanical Engineers*, Vol. 51, No. 471 [in Japanese].

Newman, J. C., and Raju, I. S., 1979, "Analyses of Surface Cracks in Finite Plates Under Tension or Bending Loads," NASA Technical Paper 1578.

Ohji, K., 1967, *Journal of Material Science of Japan*, Vol. 16, pp. 213–21 [in Japanese].

Ono, T., Takenoshita, T., Uchimura, H., and Kaji, M., 1993, *Journal of Ceramics Society of Japan*, Vol. 101, No. 2, pp. 240–243 [in Japanese].

Palaniswamy, K., and Knauss, W. G., 1978, "On the Problem of Crack Extension in Brittle Solids Under General Loading," *Mechanics Today*, Vol. 4, pp. 87–148.

Petrovic, J. J., and Mediratta, M. G., 1977, "Correction of Mixed-Mode Fracture From Controlled Surface Flaws in Hot-Pressed Si3N4," *J. Am. Ceram. Soc.*, Vol. 60, No. 9.

Shetty, D. K., Rosenfield, A. R., and Duckworth, W. H., 1986, "Mixed-Mode Fracture of Ceramics in Diametral Compression," *J. Am. Ceram. Soc.*, Vol. 69, No. 6, pp. 437–443.

Shetty, D. K., Rosenfield, A. R., and Duckworth, W. H., 1987, "Mixed-Mode Fracture in Biaxial Stress State: Application of the Diametral-Compression (Brazilian Disk) Test," *Eng. Fract. Mech.*, Vol. 26, No. 6, pp. 825–840.

Shetty, D. K., 1987, "Mixed-Mode Fracture Criteria for Reliability Analysis and Design with Structural Ceramics," ASME JOURNAL OF ENGINEERING FOR GAS TURBINES AND POWER, Vol. 109, pp. 282–289.

Sih, G. C., 1974, "Strain-Energy-Density Factor Applied to Mixed-Mode Crack Problems," *International Journal of Fracture*, Vol. 10, pp. 305–321.

Smith, F. W., and Sorensen, D. R., 1974, "Mixed-Mode Stress Intensity Factors for Semielliptical Surface Cracks," NASA CR-134684.

APPENDIX

(A) Mode I Stress-Intensity Factor

The mode I stress intensity factor for a semi-elliptical crack was calculated from the following equations obtained by Newman and Raju (1979)

$$K_I = M_I \cdot \sigma_n \cdot \left(\frac{\pi a}{Q}\right)^{1/2}, \tag{A1}$$

where

$$Q = 1 + 1.464 \cdot y^{1.65},$$

$$M_I = \sqrt{y} \cdot (S_1 + S_2 \cdot x^2 + S_3 \cdot x^4) \cdot h \cdot g \cdot w,$$

$$S_1 = 1.13 - 0.09 \cdot y$$

$$S_2 = -0.54 + \left(\frac{0.89}{0.2 + y}\right) \cdot y,$$

$$S_3 = 0.5 - \left(\frac{1.0}{0.65 + y}\right) + 14(1 - y)^{24},$$

$$g = 1 + 0.1 + 0.35x^2,$$

$$w = \left\{\sec\left(\frac{\pi b}{2d}\sqrt{x}\right)\right\}^{1/2},$$

$$h = 1 - 0.34x - 0.11x \cdot y,$$

$$x = \frac{a}{t}, \quad y = \frac{a}{b} (y \leq 1). \tag{A2}$$

(B) Mode II Stress-Intensity Factor

The mode II stress intensity factor for a semi-elliptical crack was obtained from Smith and Sorensen (1974) as follows:

$$K_{II} = M_{II} \cdot \tau_n \cdot \left(\frac{\pi a}{Q}\right)^{1/2}, \tag{B1}$$

where M_{II} is calculated from the following equation (Ono et al., 1993)

$$M_{II} = 1.549 \cdot \left(\frac{y}{2}\right)^{0.42} + 0.027x. \tag{B2}$$

S. Yang

R. F. Gibson

Mechanical Engineering Department,
Advanced Composites Research Laboratory,
Wayne State University,
Detroit, MI 48202

G. M. Crosbie

R. L. Allor

Research Laboratory,
Ford Motor Company,
Dearborn, MI 48121

Dynamic Mechanical Properties of Ceramics and Ceramic Composites at Elevated Temperatures

This paper presents the preliminary results of our research on dynamic mechanical properties of silicon nitride based ceramics and ceramic composites at elevated temperatures. The temperature-dependent dynamic elastic modulus and internal damping of the cantilever beam samples were measured from room temperature up to 1100°C. The dynamic mechanical behavior is found to be rather stable up to 700°C, but damping peaks are found to occur at around 900°C, accompanied by a corresponding relaxation in elastic modulus for the tested samples. By simulating the thermal cycling environment of engines, the resulting changes in the dynamic mechanical properties of the samples are observed. The possible mechanisms affecting the dynamic mechanical properties of these ceramics and ceramic composites, with special emphasis on high-temperature behavior, are discussed.

Introduction

Ceramics include a wide variety of inorganic materials, which are generally nonmetallic and are processed at high temperatures. In view of the advances made in the last quarter of the 20th century, ceramic materials can be categorized into traditional or conventional ceramics and advanced or high-performance ceramics. The advanced ceramics represent a new and improved class of ceramics and ceramic composites designed with more precisely controlled microstructure and chemistry so as to enhance their particular material properties such as high-temperature stability, high strength and hardness, good wear and corrosion resistance, and low density. Due to their many salient features, ceramics and ceramic composites are strong candidates for many applications requiring new structural materials, especially for the high-temperature applications in advanced aircraft and automotive engines. Because of operating conditions such as high temperature and vibratory loading in advanced engines, the dynamic mechanical properties, damping and stiffness, at elevated temperatures are very important for the practical applications of ceramics and ceramic composites. However, research regarding the mechanical properties of ceramics and ceramic composites thus far has been largely concerned with the static strength, fracture toughness, and creep behavior, and little is known about the dynamic mechanical properties. This paper summarizes our recent research on the high-temperature dynamic mechanical behavior of silicon nitride ceramics and silicon carbide whisker reinforced silicon nitride composites. The internal damping and storage moduli of the materials were measured as a function of temperature up to 1100°C by using a specially designed impulse-frequency response apparatus. The thermal cycling environment of an engine was also simulated to assess its influences on these properties. Based on the experimental measurements, the possible mechanisms affecting the high-temperature dynamic mechanical properties of these ceramics and ceramic composites are investigated.

Contributed by the International Gas Turbine Institute for publication in the JOURNAL OF ENGINEERING FOR GAS TURBINES AND POWER. Manuscript received by the International Gas Turbine Institute July 4, 1995. Associate Technical Editor: H. L. Julien.

Calculation and Measurement

Dynamic mechanical properties herein refer to the internal damping and dynamic elastic modulus of materials. They are conveniently related by the so-called complex modulus notation as (Findley et al., 1989)

$$E^* = E' + iE'' \tag{1}$$

and

$$\eta = \frac{E''}{E'} \tag{2}$$

where E^* is the complex modulus, E' is the storage modulus, E'' is the loss modulus, $i = \sqrt{-1}$ is the imaginary operator, and η is the damping loss factor. Material damping can be defined and manifested by many different approaches. For example, the damping loss factor defined above can also be expressed by the half power band width method as (Gibson, 1992)

$$\eta = \frac{\Delta f}{f_n} \tag{3}$$

where f_n is the resonant frequency of nth vibration mode, Δf represents the half power band width of the nth mode resonant peak in the frequency response function. A schematic explanation of this definition is described in Fig. 1. The moduli defined in Eqs. (1) and (2) should be the corresponding flexural moduli in the flexural vibration tests used in this research. Thus, for a rectangular cantilever beam sample, its flexural storage modulus can be deduced from its resonant frequency and geometry by using the Bernoulli–Euler beam equation (Blevins, 1979)

$$E' = \frac{4\pi^2 \rho A L^4 f_n^2}{\lambda_n^4 I} \tag{4}$$

where ρ is the density of the material, A is the area of cross section, L is the length of beam sample, λ_n is the eigenvalue for the nth mode, and I is the area moment of inertia of the beam about its neutral axis. It should be clear that these equations only apply for isotropic materials, and that subscripts are required for anisotropic composites if multiple properties are involved. The composites tested here are assumed to be isotropic.

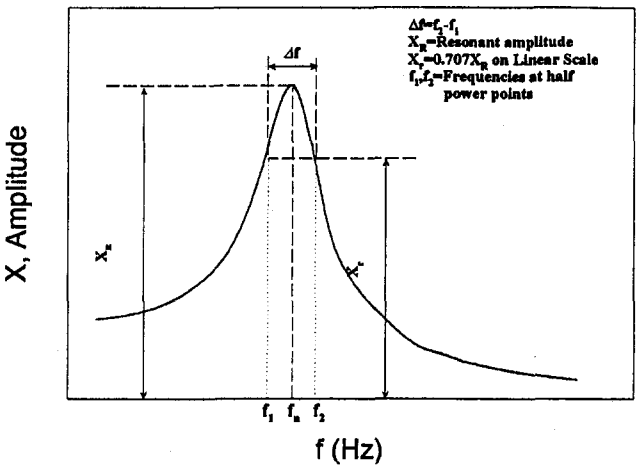

Fig. 1 Definition of parameters in Eq. (3) from frequency response spectrum

In the experiments, f_n, η, and E' are measured by the impulse frequency-response techniques (Suarez and Gibson, 1987). Figure 2 shows the schematic cutaway drawing of the experimental apparatus used for the high temperature experiments (Gibson et al., 1991). The cantilever beam sample is heated by the three-zone quartz lamp heater, and the required temperature is obtained by adjusting the controls for the zones independently. The specimen vibration is excited by the amplitude-controlled electric solenoid hammer, and the vibration signals are measured by a optron noncontacting electro-optical displacement follower. Analog signals from the displacement follower are transformed to generate the frequency domain response spectrum by the FFT (Fast Fourier Transform) spectrum analyzer, and finally, the desktop computer interrogates the FFT analyzer to find the resonant frequency and its half power band width, then calculates the flexural damping loss factor, the flexural storage modulus, and the flexural loss modulus according to Eqs. (3), (4), and (2), respectively.

Samples and Materials

Silicon nitride based ceramics exhibit excellent mechanical properties, good oxidation resistance, and thermal shock behavior at both room and high temperatures (Hoffmann and Petzow, 1993). The salient features of these ceramics are interesting for many applications, especially for high-temperature structural applications. So, silicon nitride based ceramics are often considered to represent the toughest of the high-temperature (above 1000°C) ceramics intended for advanced heat engine use (Crosbie et al., 1988). For this regard, damping behavior and the related research are of more practical significance for the optimum design of these materials in engine applications.

As a structural material, however, silicon nitride is naturally brittle, and cracks caused by impact loading can result in catastrophic failure. The impact damage resistance and fracture toughness of silicon nitride must be improved for its applications in engines, and this has led to the development of many toughening methods. Silicon carbide whisker reinforcement is one of these methods (Akimune, 1990). Ceramic whiskers are single ceramic crystals in the form of filaments; it has been known for many years that the mechanical properties of whiskers can approach those which are thought to be theoretically possible. This is because of the lack of defects that weaken other forms of matter. The requirement that the whiskers be free of defects usually means that they have to be extremely small with diameters less than about 1 μm and lengths usually not more than a few millimeters (Warren, 1992). Silicon carbide whiskers are chosen as high-temperature reinforcement due to the fact that silicon carbide is a very hard and abrasive material and has excellent resistance to high-temperature erosion and chemical attack.

From the materials science point of view, the superior properties of silicon nitride largely depend on its microstructure, particularly on the highly covalent nature of its chemical bonds, which makes densification of silicon nitride by solid-state diffusion impossible. When a liquid phase is introduced, however, high-density ceramics can be obtained. This liquid phase is produced by the addition of sintering additives, usually metal oxides, which form a low melting eutectic liquid with a surface layer of the silicon nitride powder. During sintering, the starting silicon nitride powder transforms from α-Si_3N_4 to β-Si_3N_4 by solution–precipitation. The newly formed β-Si_3N_4 grains have an elongated hexagonal rod morphology. These rod-shaped grains form an interlocking microstructure, which is responsible for the superior mechanical properties of these materials (Tien, 1993). Hot-press processing is one of the approaches used to obtain high-density silicon nitride (Chawla, 1993).

The microstructure of typical silicon nitride ceramics is shown in Fig. 3. The powder purity is important because a low solubility in silicon nitride for many impurities lead to high concentrations of those impurities in grain boundary phases, and the carbon residues (which are found in some high purity powders) are considered detrimental to second-phase oxynitride development, thermal stability, and mechanical properties

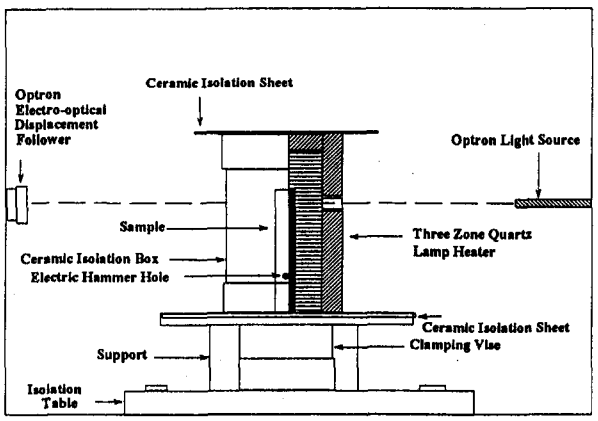

Fig. 2 Cutaway drawing of setup of cantilever beam test at elevated temperatures

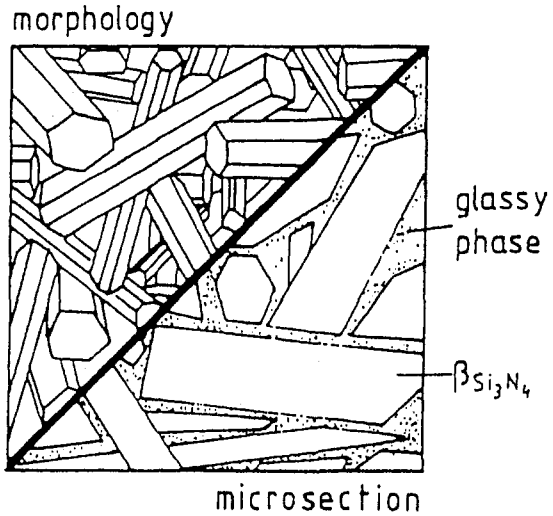

Fig. 3 Microstructure of dense silicon nitride (Woetting and Ziegler, 1986)

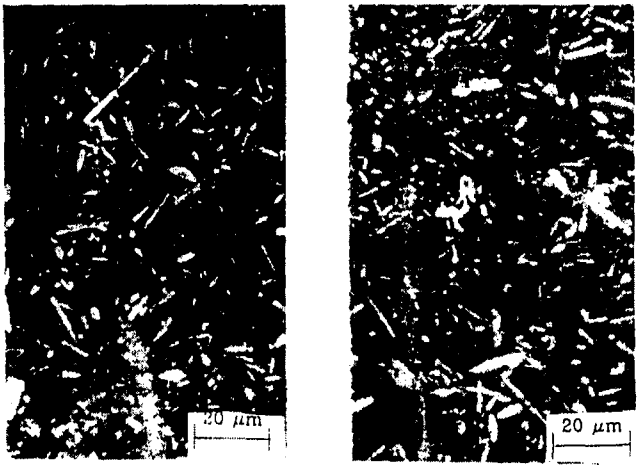

KNw/Sic UBEw/SiC

Fig. 4 Microstructure of silicon nitride with silicon carbide whiskers (Allor et al., 1990)

(Crosbie et al., 1988; Woetting and Ziegler, 1986). The microstructures of silicon nitride composites reinforced with silicon carbide whiskers are shown in two optical micrographs in Fig. 4, where it is seen that the whiskers are rather uniformly distributed in the matrix, for both moderate purity KN powder and high purity UBE powder. For both purity levels, β-Si_3N_4 and a minor amount of β-SiC were determined present by x-ray diffraction (XRD). The initially high α-Si_3N_4 powder was converted to β-phase as is desired for needlelike grain growth; since no other crystalline Si-N-Y-O phases were determined, the nitride matrix grain boundary phase is assumed to have remained glassy (Allor et al., 1990).

Rectangular beam samples, with lengths of about 156 mm, width of 12.7 mm, but three different thicknesses of 1.524, 3.048, and 6.350 mm, respectively, of four different silicon nitride based ceramic materials were provided by Ford Motor Company. Table 1 summarizes the identification, structural compositions, and processing techniques for these samples.

Experimental Results and Discussions

Experiments thus far have been conducted on 1.524 and 3.048-mm-thick samples in the following sequence: (1) measurement of the dynamic mechanical properties at room temperature, (2) measurement of the dynamic mechanical properties at elevated temperatures up to 1100°C, and (3) investigation of thermal cycling effects on the dynamic mechanical properties under the simulated conditions to 1100°C. All the measurements were carried out in first mode flexural vibrations.

Table 1 Identification, composition and processing of samples

Sample[1]	Matrix	Whisker	Additive	Processing
KNw/SiC	Si_3N_4	SiC (5)[2]	Y_2O_3/Al_2O_3 (6/3)	Hot-pressed
KNw/oSiC	Si_3N_4	--	Y_2O_3/Al_2O_3 (6/3)	Hot-pressed
UBEw/SiC	Si_3N_4	SiC (5)	Y_2O_3/Al_2O_3 (6/3)	Hot-pressed
UBEw/oSiC	Si_3N_4	--	Y_2O_3/Al_2O_3 (6/3)	Hot-pressed

[1] KNw/SiC = Kemanord moderate purity Si_3N_4 powder matrix with SiC whiskers,
KNw/oSiC = Kemanord moderate purity Si_3N_4 powder matrix without SiC whiskers;
UBEw/SiC = High purity Si_3N_4 powder matrix with SiC whiskers,
UBEw/oSiC = High purity Si_3N_4 powder matrix without SiC whiskers.
[2] Numbers in parentheses represent volume percentage for whisker and weight percentage for additive, respectively.

Table 2 Test results of 1.524-mm-thick samples at room temperature[3]

Sample	E' (Gpa) Mean	f_n (Hz) Mean	η Max (10^{-3})	η Min (10^{-3})	η Mean (10^{-3})	η Std. Dev (10^{-3})
KNw/SiC	295.65	119.69	0.67	0.34	0.49	0.109
KNw/oSiC	278.76	116.22	0.57	0.42	0.51	0.057
UBEw/SiC	288.41	118.21	0.58	0.36	0.49	0.060
UBEw/oSiC	285.17	117.56	0.63	0.40	0.52	0.075

[3] Tabulated values are based on 32 tests on each sample

Room Temperature Tests. The results of the dynamic mechanical property measurements at room temperature are shown in Tables 2 and 3 for two different thickness samples, respectively. The measurements indicate that the room temperature damping is very small, with the loss factor in the middle of the range 10^{-4} to 10^{-3} for all four materials with two different thicknesses. By comparison, these values are in the same range as the damping values for metallic materials such as steel or aluminum, but are roughly ten times less than the damping values for polymer composites. This small damping made the experiments difficult to conduct because it is almost in the same range as the air damping or other background damping (Wren and Kinra, 1989). Hence, the statistical information for the damping measurements is given in this paper. It should be emphasized here that damping, no matter large or small, is a property that is difficult to either experimentally measure or to theoretically predict due to the fact that it usually involves a variety of energy-dissipation mechanisms, and these mechanisms are dependent on vibration parameters such as frequency and amplitude and are greatly influenced by material conditions such as impurities and cracks in specimen, as well as environmental conditions such as temperature and humidity. Hence, the minimum measured damping is sought and is considered to be the best indication of the real damping.

It is believed that the room temperature damping in the ceramics and ceramic composites is strongly influenced by the initial defects or microcracks in the materials, but that the elastic behavior mainly depends on the elastic properties of the constituent materials. Tables 2 and 3 show that the reinforced composites (KNw/SiC and UBEw/SiC) seem to have similar damping than the corresponding ceramics (KNw/oSiC and UBEw/oSiC), but the T-test shows no significant difference between them at 95 percent confidence level. the same tables also show that the reinforced composites have higher natural frequencies and moduli than the unreinforced ceramics, which is because of the presence of higher stiffness SiC whiskers in the ceramic composites. This difference is verified by the T-test at 95 percent confidence level. Natural frequency is proportional to square root of the modulus of the material, as seen in Eq. (4). The slight reduction in the measured storage modulus of the thicker samples is believed to be caused by the transverse shear and rotary inertia effects, which always become larger for thicker beams in flexural vibrations.

High-Temperature Tests. The curves of measured damping loss factors and storage moduli as a function of temperature up to 1100°C for the four materials are shown in Fig. 5, and the numerical values corresponding to the damping peak tem-

Table 3 Test results of 3.048-mm-thick samples at room temperature[3]

Sample	E' (Gpa) Mean	f_n (Hz) Mean	η Max (10^{-3})	η Min (10^{-3})	η Mean (10^{-3})	η Std. Dev (10^{-3})
KNw/SiC	286.41	235.62	0.60	0.39	0.52	0.066
KNw/oSiC	273.59	230.00	0.60	0.42	0.52	0.059
UBEw/SiC	280.07	233.00	0.60	0.35	0.49	0.067
UBEw/oSiC	275.31	231.01	0.59	0.42	0.51	0.053

[3] Tabulated values are based on 32 tests on each sample

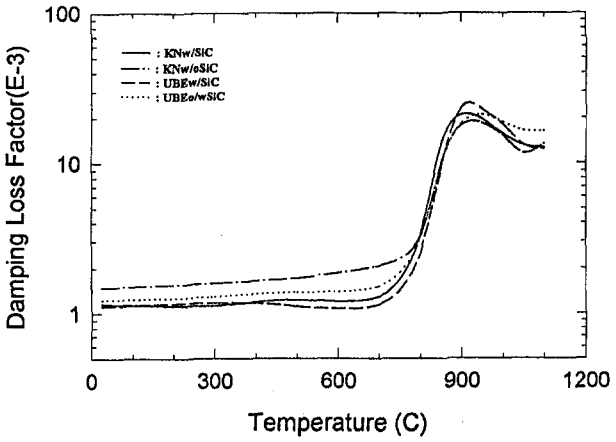

a. Damping loss factor

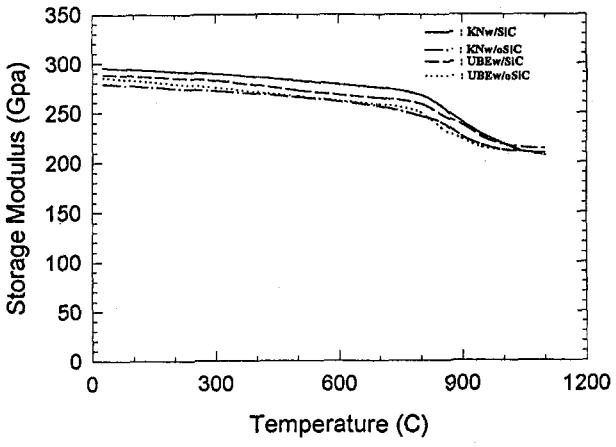

b. Storage modulus

Fig. 5 Damping and storage modulus of 1.524 mm thick samples versus temperature: (*a*) damping loss factor; (*b*) storage modulus

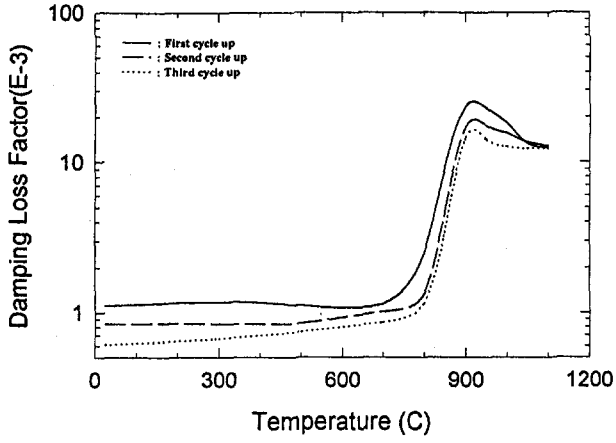

a. Damping loss factor

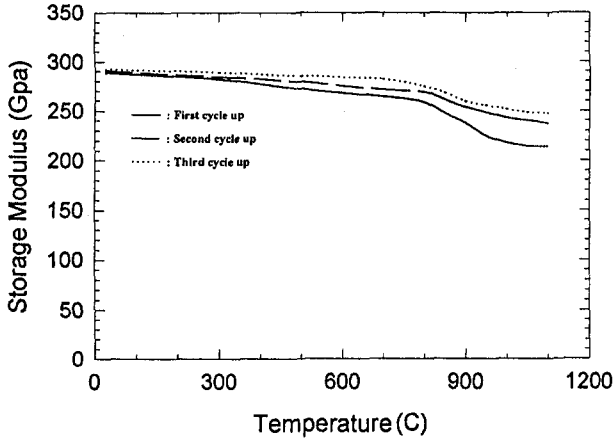

b. Storage modulus

Fig. 6 Effect of thermal cycling on damping and storage modulus of 1.524-mm-thick UBEw/SiC samples: (*a*) damping loss factor, (*b*) storage modulus

perature are listed in Table 4. Only the results for the 1.524-mm-thick samples under the first thermal cycle are presented here. Figure 5 shows that the dynamic mechanical properties are rather stable up to about 700°C, with only slight increases in damping and decreases in modulus, then the damping abruptly rises up to a peak value at about 900°C. The peak loss factor values for the four materials are located in the range of 10^{-2}, which is much greater than that of the room-temperature damping and far beyond that of the possible air damping or background damping. Contrary to the room temperature results, ceramic composites (KNw/SiC and UBEw/SiC), at elevated temperatures, have slightly larger damping than ceramics (KNw/oSiC and UBEw/oSiC), and the *T*-test confirms this difference at the 95 percent confidence level. This seems to imply that the mechanical behavior of the materials under the environments of room temperature and high temperature is dominated by different mechanisms. Most likely, the initial defects or microcracks in the materials no longer dominate the damping behavior at high temperatures.

More importantly, the damping peak accompanies the relaxation of the elastic modulus, which more or less exposes the mechanisms principally dominating the dynamic mechanical behavior of the materials at high temperatures. As shown in the figures, the materials present typical viscoelastic behavior (Nashif et al., 1985), and the glassy grain boundary phase in the Si_3N_4 matrix is believed to be the dominant factor in this behavior.

Thermal Cycling Effects. As mentioned above, the dynamic mechanical properties of the four materials have been found to be affected by simulated thermal cycling. Figure 6 and Table 5 show such effects for the 1.524-mm-thick UBEw/SiC samples with three cycles of thermal loading. These effects were observed by repeated heating of the sample to 1100°C, then cooling it down to room temperature. Experiments were

Table 4 Test results of 1.524-mm-thick samples at 900°C[4]

Sample	E' (Gpa) Mean	f_n (Hz) Mean	η Max (10^{-3})	η Min (10^{-3})	η Mean (10^{-3})	η Std. Dev (10^{-3})
KNw/SiC	240.60	108.02	21.95	20.38	21.10	0.545
KNw/oSiC	225.88	104.67	20.35	17.42	18.44	0.723
UBEw/SiC	239.54	107.79	24.01	22.72	23.51	0.448
UBEw/oSiC	223.18	104.04	21.97	20.33	20.93	0.500

[4] Tabulated values are based on 16 tests on each sample.

Table 5 Properties of 1.524-mm-thick UBEw/SiC samples versus thermal cycles to 900°C[4]

Cycle Number	E' (Gpa) Mean	f_n (Hz) Mean	η Max (10^{-3})	η Min (10^{-3})	η Mean (10^{-3})	η Std. Dev (10^{-3})
1	239.54	107.79	24.01	22.72	23.51	0.448
2	253.65	110.91	17.62	16.58	17.31	0.260
3	259.18	112.12	14.78	13.96	14.46	0.294

[4] Tabulated values are based on 16 tests on each sample.

only conducted during the heating part of the thermal cycle, not during the cooling part. The results show that the materials seem to be stiffened, with larger storage moduli, higher natural frequencies, and smaller damping loss factors, following each thermal cycle. This observation is quite consistent with the results of the research conducted by Grady and Lerch (1992) regarding the effect of heat treatment on the dynamic mechanical behavior of SiC/Ti-15-3, which is a ceramic fiber–metal matrix composite. Their research shows that heat treatment changed the microstructure, stiffened the matrix, and reduced the damping capacity of the tested material. The difference in our research is that the materials are ceramics and ceramic matrix composites, and they are being tested under a simulated engine working environment.

Among the possible explanations for the influence of thermal cycling on the dynamic mechanical properties are that microcracks within the Si_3N_4 matrix may be partially "healed" as a result of the viscoelastic flow at high temperatures, and hence the Coulomb friction damping due to crack interfaces rubbing together is reduced. From the materials science point of view, changes in chemical composition and/or phase transformations may be responsible for the stiffening of the materials, and among these changes, the most likely ones are the crystallization and nucleation of the glass phase and the grain boundary glassy phase in the materials.

Concluding Remarks

The dynamic mechanical behavior of hot-pressed silicon nitride ceramics and silicon nitride composites reinforced with silicon carbide whiskers has been studied from room temperature to 1100°C. Both the elastic and damping properties are found to be relatively stable below 700°C, with only small changes in the properties occurring as temperature increases. Above 700°C, the damping rapidly rises up until it reaches its maximum value, accompanied by the relaxation in elastic modulus, at about 900°C. The damping and storage modulus curves in the temperature domain prove that the materials exhibit typical viscoelastic behavior at elevated temperatures. Even though the room temperature damping is small, the high-temperature damping of these silicon nitride ceramics and ceramic composites is quite comparable with the damping of polymer matrix materials, which have been considered to have good damping capacities but which usually fail at such high temperatures. Hence, these silicon nitride based ceramics should be able to play important roles as structural materials in manufacturing advanced heat engines because of their contributions to reduce noise and vibration levels at high temperatures. These are rather unfamiliar virtues compared with their other well-known salient features such as light weight, high strength, good heat and environment resistance.

The dynamic mechanical behavior of the tested materials has also been found to be affected by repeated thermal cycling. Although the inherent changes in the materials should be further confirmed and investigated microstructurally, it is also of interest to ask, "Can the dynamic mechanical behavior, or more specifically, the damping behavior (because it is more sensitive), be used to nondestructively detect the microstructural changes caused by practical environmental conditions?"

The elevated temperature dynamic mechanical properties of ceramics and ceramic composites should become increasingly important for their structural applications in high-temperature, vibratory environments.

Acknowledgments

The authors acknowledge the support of the Ford Motor Company through an unrestricted grant. Whisker dispersion and hot pressing were carried out at Cercom, Inc., Vista, California, under the direction of A. Ezis.

References

Akimune, Y., 1990, "Impact Damage and Strength Degradation in a Silicon Carbide Reinforced Silicon Nitride Composite," *Journal of American Ceramics Society,* Vol. 73(10), pp. 3019–3025.

Allor, R. L., Crosbie, C. M., Cartwright, E. L., and Govila, R. K., 1990, "Silicon Nitride Based Ceramic Composites," *Structural Composites: Design and Processing Technologies,* ASM International, Materials Park, OH, pp. 555–641.

Blevins, R. D., 1979, *Formulas for Natural Frequency and Mode Shape,* Van Nostrand Reinhold.

Chawla, K. K., 1993, *Ceramic Matrix Composites,* Chapman & Hall.

Crosbie, G. M., Nicholson, J. M., Predmesky, R. L., and Stiles, E. D., 1988, "Silicon Nitride Power Synthesis Program," *Proc. 25th Automotive Technology Development Contractors' Coordination Meeting,* Society of Automotive Engineers, Warrendale, PA, pp. 127–135.

Findley, W. N., Lai, J. S., and Onaran, K., 1989, *Creep and Relaxation of Nonlinear Viscoelastic Materials,* Dover Publications, Inc.

Gibson, R. F., Thirumalai, R., and Pant, R., 1991, "Development of an Apparatus to Measure Dynamic Modulus and Damping of Reinforcing Fibers at Elevated Temperature," *Proc. Society for Experimental Mechanics 1991 Spring Conference,* Milwaukee, WI, June 9–12, pp. 860–869.

Gibson, R. F., 1992, "Damping Characteristics of Composite Materials and Structures," *Journal of Materials Engineering and Performance,* Vol. 1(1), pp. 11–20.

Grady, J. E., and Lerch, B. A., 1992, "Effect of Heat Treatment on Stiffness and Damping of SiC/Ti-15-3," *Sample Quarterly—Society for the Advancement of Material and Processing Engineering,* Vol. 23, No. 2, pp. 11–16.

Hoffmann, M. J., and Petzow, G., 1993, "Microstructural Design of Si_3N_4 Based Ceramics," *Silicon Nitride Ceramics—Scientific and Technological Advances,* Materials Research Society Symposium Proceedings, Vol. 287, pp. 3–14.

Nashif, A. D., Jones, D. I. G., and Henderson, J. P., 1985, *Vibration Damping,* Wiley, New York.

Suarez, S. A., and Gibson, R. F., 1987, "Improved Impulse-Frequency Response Techniques for Measurement of Dynamic Mechanical Properties of Composite Materials," *Journal of Testing and Evaluation,* Vol. 15(2), pp. 114–121.

Tien, T., 1993, "Silicon Nitride Ceramics—Alloy Design," *Silicon Nitride Ceramics—Scientific and Technological Advances,* Materials Research Society Symposium Proceedings, Vol. 287, pp. 51–63.

Warren, R., 1992, *Ceramic-Matrix Composites,* Chapman and Hall, New York.

Woetting, G., and Ziegler, G., 1986, "Powder Characteristics and Sintering Behavior of Si_3N_4 Powders," *Powder Metall. Intl.,* Vol. 18(1), pp. 25–32.

Wren, G. G., and Kinra, V. K., 1989, "On the Effect of an End-Mass on Beam Damping," *Experimental Mechanics,* Vol. 29, pp. 336–341.

Air Extraction in a Gas Turbine for Integrated Gasification Combined Cycle (IGCC): Experiments and Analysis[1]

J. S. Kapat
Department of Mechanical Engineering,
University of South Alabama,
Mobile, AL 36688

A. K. Agrawal
School of Aerospace and
Mechanical Engineering,
University of Oklahoma,
Norman, OK 73019

T. Yang
Department of Mechanical Engineering,
Clemson University,
Clemson, SC 29634

This paper presents an investigation of extracting air from the compressor discharge of a heavy-frame gas turbine. The study aimed to verify results of an approximate analysis: whether extracting air from the turbine wrapper would create unacceptable nonuniformity in the flow field inside the compressor discharge casing. A combined experimental and computational approach was undertaken. Cold flow experiments were conducted in an approximately one-third scale model of a heavy-frame gas turbine; a closely approximated three-dimensional computational fluid dynamic analysis was also performed. This study substantiated the earlier prediction that extracting air from the turbine wrapper would be undesirable, although this method of air extraction is simple to retrofit. Prediffuser inlet is suggested as an alternate location for extracting air. The results show that not only was the problem of flow nonuniformity alleviated with this alternate scheme, but the frictional power loss in the compressor discharge casing was also reduced by a factor of two.

Introduction

Air-blown, simplified Integrated Gasification Combined Cycle (IGCC) power plants with hot gas cleanup offer superior environmental performance and high thermal efficiency for generating electricity using coal. This concept, shown schematically in Fig. 1, utilizes a portion of the gas turbine compressor discharge air to oxidize coal in a gasifier for producing the low-Btu coal gas. Particulate and sulfur-bearing gases are removed in the hot gas cleanup system before the coal gas is burned in the gas turbine combustor(s). IGCC systems are becoming commercially attractive partly because of system simplification by integration and recent advances in hot gas cleanup (Notestein, 1990; Todd and Allen, 1991; Becker and Schetter, 1992; Todd, 1993).

Several options are available to configure an IGCC system (Corman and Todd, 1993). In many of these options the gas turbine is integrated with the coal gasifier, which requires a scheme to extract the compressor discharge air. Figure 2 shows the compressor discharge region of a heavy-frame gas turbine. The major subcomponents and the airflow path of such a turbine are highlighted in Fig. 3. It is seen that the air exiting the compressor is decelerated in an annular prediffuser before it is discharged into a dump diffuser. The dump diffuser houses several combustor casing/impingement sleeve assemblies, each surrounding a respective combustor can/transition piece unit, equally spaced in the circumferential direction. A portion of the compressed air from the dump diffuser flows through the cooling holes in the impingement sleeve into the space between the impingement sleeve and the transition piece, thereby cooling the outer surface of the transition piece. The air then flows through this annular space toward the combustor casing/combustor can where it mixes with the balance of the air entering through the bypass air holes on the combustor casing. Finally, the air enters the combustor can through primary, secondary, dilution and cooling holes.

In selecting an air extraction scheme, one must consider how the scheme affects the air supply to hot sections of the gas turbine and the frictional loss in the flow region. A proper distribution of air to the combustors is necessary to prevent burnout and to maintain effective air/fuel mixing, hence the combustor exit pattern factor. Minimizing pressure losses associated with air extraction could also minimize the overall thermal efficiency of the power plant. Thus, investigating airflow in the compressor discharge casing with and without air extraction would enhance our understanding of the flow behavior and thus ensure integrity and high performance of the gas turbine.

Air extraction from the turbine wrapper (or the compressor discharge casing) might be the simplest design from manufacturing and retrofitting considerations. An approximate analysis indicated adverse effects of this scheme on the impingement cooling of the transition pieces. Agrawal and Yang (1991) suggested replacing the straight wall prediffuser by a curved wall diffuser with a suction slot (Griffith diffuser), and extracting air at the inlet of the modified diffuser. These two sites for extracting air are depicted in Fig. 2. The present investigation experimentally reaffirms the analytically identified problems in the impingement cooling with air extraction at the turbine wrapper and substantiates the benefits of extracting air at the prediffuser inlet.

Technical Approach

A scale model of a heavy-frame gas turbine to simulate airflow between the compressor discharge and the turbine expander was fabricated and instrumented to investigate the aerodynamic performance and flow uniformity around combustor casing/impingement sleeve assemblies. A closely approximated three-dimensional computational fluid dynamic (CFD) analysis was also performed to construct a comprehensive description of the flow field in the diffusers. This study was conducted for the two air extraction sites depicted in Fig. 2. In the first scheme, the air was extracted at the turbine wrapper. In the second scheme, the air was extracted from a suction slot at the inlet of the prediffuser with a redesigned outer wall (see Fig. 4 for details). Brief descriptions of the experimental facility, the ex-

[1] This work was conducted at Clemson University, Clemson, SC.

Contributed by the International Gas Turbine Institute and based on a paper presented at the 39th International Gas Turbine and Aeroengine Congress and Exposition, The Hague, The Netherlands, June 13–16, 1994. Manuscript received by the International Gas Turbine Institute September 1993. Paper No. 94-GT-193. Associate Technical Editor: E. M. Greitzer.

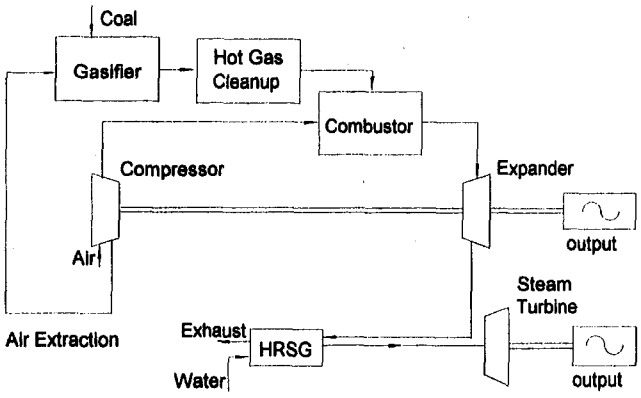

Fig. 1 Schematic diagram of a air-blown, simplified IGCC system

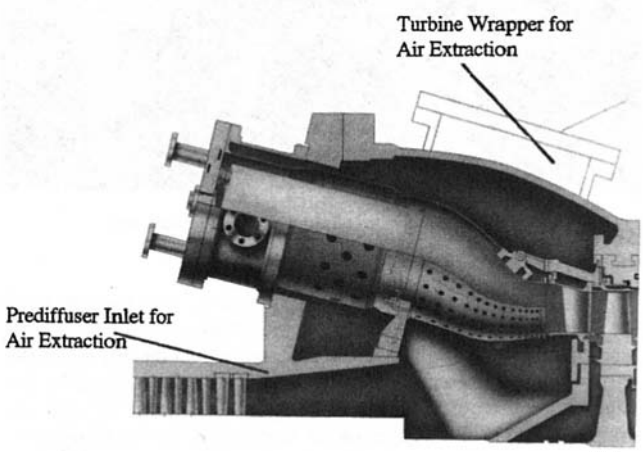

Fig. 2 Compressor discharge region of a heavy frame gas turbine

perimental procedure, and the computational procedure are given in the following sections.

Experimental Facility. Figure 5 shows a bird's eye view of the experimental facility. This facility includes (1) a gas turbine test model and a system to induce airflow through it, (2) the collection manifold, and (3) a system to extract airflow from the test model.

Test Model and the Throughflow System. The one-third scale test model was 360 deg in circumference with 14 combustor casing/impingement sleeve assemblies. Cross-sectional views of the test models are shown in Figs. 3 and 4. The test

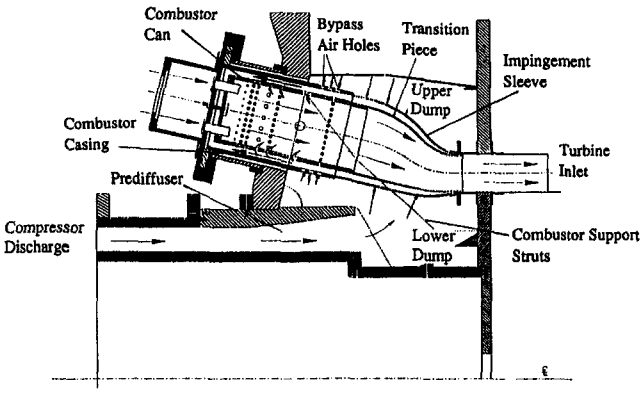

Fig. 3 Airflow path in a scale model of the heavy frame gas turbine (turbine wrapper air extraction design is shown)

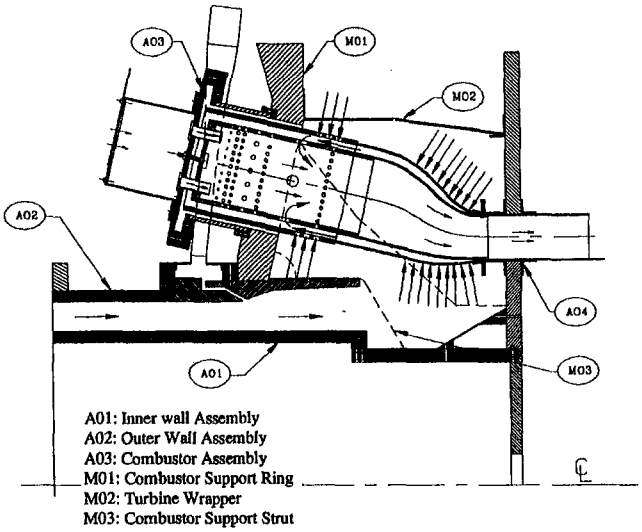

Fig. 4 Cross-sectional view of the test model (prediffuser air extraction design is shown)

model does not simulate the combustion or the heat transfer processes. However, geometric details of the hot sections were included to simulate the cold flow accurately in the compressor discharge region. Because the focus of this study was on fluid flow prior to the combustion, simulating heat transfer in the test model was not necessary. The test model was constructed such that the prediffuser and other components could be replaced with similar yet different designs. Design of the configuration in Fig. 4 for extracting air at the prediffuser inlet was based on the analysis by Agrawal and Yang (1991).

Figure 6 shows the layout of the flow system with the test model. The flow system was approximately 9.5 m long while the test model was 0.76 m long. The centerline of the flow tunnel was 1.0 m above the floor. The ambient air entering this suction type wind tunnel went through an inlet lip, filters, a 90-deg bend, a honeycomb, and transition pieces that guided the air to an annular flow developing section. The exit of the flow developing section then attached to the test section. The airflow exiting the test section discharged into a plenum box, which isolated the test section from vibrations or oscillations of the suction fan located downstream of the plenum box. The suction fan was an industrial fan (IAP PHB31) operating at a constant rpm by a 150 kW, three-phase electric motor. The flow rate through the test section was regulated by a set of louvers at the

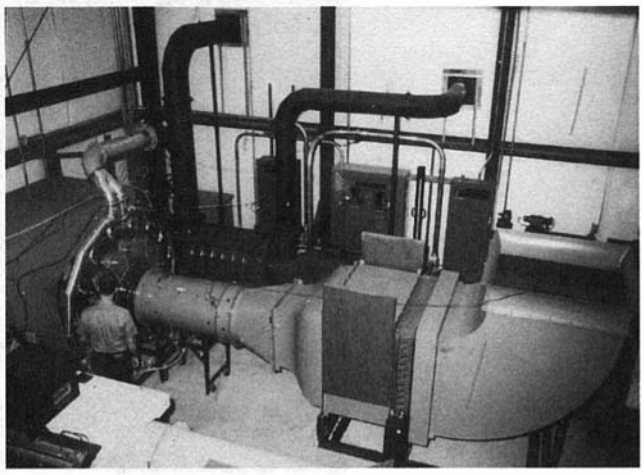

Fig. 5 Bird's-eye view of the experimental setup

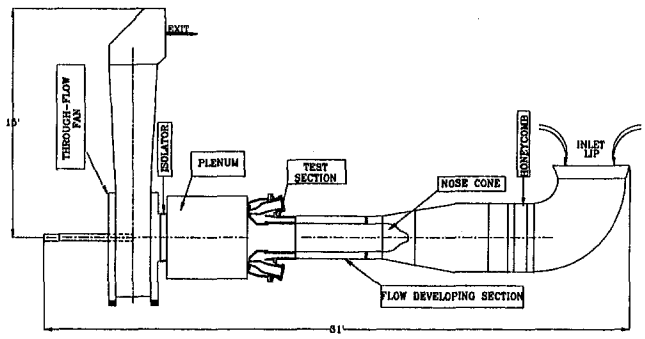

Fig. 6 Layout of the throughflow system with the test model

fan inlet. These louvers were operated by a computer controlled stepper motor.

Collection Manifold. The air collection system consisted of two manifolds, a left-sided and a right-sided, each with seven arms, which attached to the collection ports on the test model. An inverted Y-section then combined the two manifolds and attached them to the air extraction fan. The main guiding rule used to design the manifold dictated that the mainstream flow area increase while maintaining a constant mean flow velocity. This resulted in the manifold arms entering the mainstream at an angle of 30 deg. Butterfly control valves were provided on all branches of the manifold to equalize flow rate through the branches.

Figures 7 and 8 show the extraction manifold at the turbine wrapper and the prediffuser inlet, respectively. The two manifold systems were similar except that the manifold to extract air at the prediffuser inlet was larger in diameter. This manifold, shown schematically in Fig. 9, was connected to ports around the prediffuser outer wall using conical tubes attached to the manifold arms. These conical tubes passed between adjacent combustor casing/impingement sleeve assemblies.

The manifold was calibrated independently prior to installation to equalize the airflow rates through all of its branches. First, the manifold system was attached to the air extraction system (discussed in the next section) to provide the desired

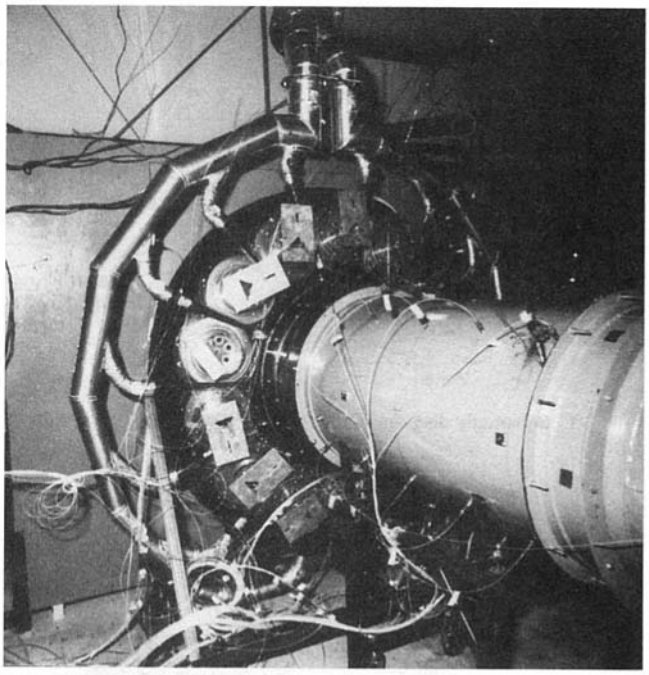

Fig. 8 Extraction manifold at the prediffuser inlet

extraction airflow rate. Then, a venturimeter was used to gage the airflow rate through each of the manifold arms. Venturimeter readings from all the branches were equalized by adjusting the corresponding butterfly valves. The flow rate measured by the venturimeter would not be the actual flow rate through the branch because the venturimeter itself adds to the flow resistance. However, the resistance added by the venturimeter will be the same if the airflow rate through the venturimeter were the same. Matching the venturimeter readings of all the branches, therefore, signifies equal flow through the manifold arms. The flow rate through a branch was sensitive to flow resistances in the neighboring branches. Therefore, the butterfly valves were adjusted strategically to equalize the airflow while minimizing

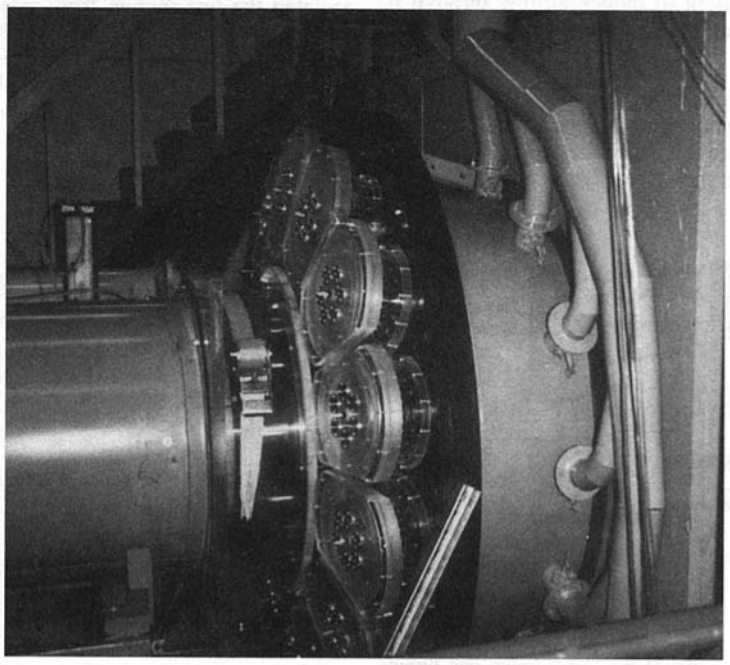

Fig. 7 Extraction manifold at the turbine wrapper

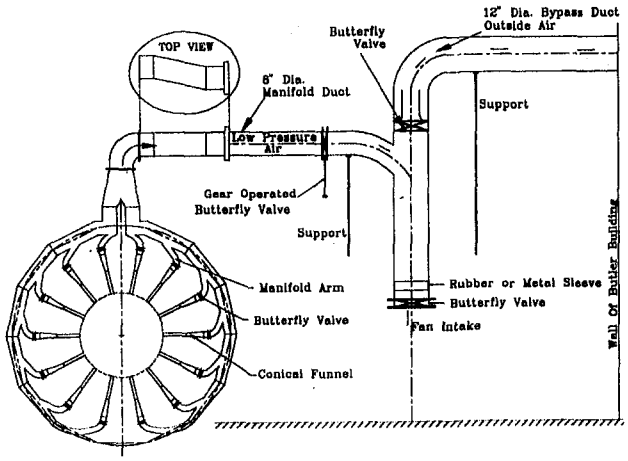

Fig. 9 A schematic of the air extraction system

the overall flow resistance. Once adjustments were made, the venturimeter readings were repeated at all the branches. Equalizing flow through all branches of the manifold system typically required several iterations of this process.

Air Extraction Flow System. The downstream ends of the manifolds connect to the flow system, which extracts air from the test model. Figure 9 shows a schematic of the air extraction flow system connected to the collection manifold. The air was extracted by a Hoffman Model 76106A, two-stage centrifugal blower driven by a 150 kW, three-phase constant-speed motor. The fan intake draws air from a 0.20-m-dia manifold duct and a 0.30-m-dia bypass air duct. The manifold duct extracts low-pressure air from the test model while the bypass duct draws air from the ambient. Each of these two ducts has a butterfly valve to regulate their respective airflow rates. These two ducts join into a 0.3-m-dia duct connected to the blower inlet. The total airflow rate through the blower could also be regulated by a butterfly valve at the blower inlet. The air exiting this fan was discharged outside the laboratory area by a 0.25-m-dia duct passage. By discharging air to the outside, the temperature in the laboratory area could be regulated or kept close to the ambient temperature. In the prototype, the extracted air is supplied to the coal gasifier.

The extraction airflow rate could vary from no flow to the maximum required flow rate by adjusting the butterfly valve on the manifold duct. The bypass airflow rate decreased when more air was extracted through the manifold. When no air was extracted and the fan was operating, only the outside air was drawn into the blower. Thus, the bypass duct ensured that the airflow rate through the blower remained within design limits.

Instrumentation and Data Acquisition

Mass Flow. The airflow rate through the test model was monitored upstream of the prediffuser by a pitot-static probe. Only a single point measurement determined this airflow rate because the wind tunnel was calibrated prior to the tests using measured profile of axial velocity at the prediffuser inlet. The maximum flow rate through the test model was 3.8 m^3/s (8000 scfm), which corresponded to a dynamic head of 0.13 m (5.2 in.) of water at the monitoring location.

The extraction airflow was also monitored at a single point by a pitot-static probe mounted on the manifold duct. Prior to the tests, the axial velocity profile was measured at the probe location, which subsequently provided the relation between the dynamic head and the extraction airflow rate. At full load, the maximum extraction airflow rate was 0.76 m^3/s (1600 cfm), which corresponded to a dynamic head of 0.03 m (1.2 in.) of water at the monitoring location. The extraction airflow rate was regulated manually by a gear-operated butterfly valve on the manifold duct. In a simplified, air-blown IGCC, the extracted air returns to the gas turbine as a constituent of the low-Btu gasified coal. Thus, the room air was inducted into the combustor cans to simulate the fuel flow. This airflow rate was metered and equalized with the extraction airflow rate using calibrated fuel nozzles in the test model.

An experiment was performed to check the accuracy of the overall mass balance in the test model and the air extraction system. The data showed that the net mass flow rates of air into and out of the test model were within 7 percent of each other. The mass flow rates of air into and out of the extraction fan were within 2 percent of each other.

Pressure Measurements. A computer-controlled pressure measurement system, Scanivalve MSS-48C, was used to measure (1) wall pressures given by the wall pressure taps, (2) total pressure given by the Kiel and impact probes, and (3) total and static pressures given by the pitot-static probes. This system had two pressure sensors with maximum pressure inputs of ± 0.34 bar (5 psig) and ± 0.17 bar (2.5 psig), respectively. Each of the two sensors could accept a maximum of 48 pressure inputs. To avoid the measurement error because of the zero shift, one of the 48 pressure input lines to each sensor always measured the ambient pressure, which was then subtracted from the other pressure readings. For each pressure measurement, 20 readings were taken in 6 seconds.

Automated Velocity Measurements. A single-wire, hot-film probe was used to measure the two components of velocity at different locations in the flow. These measurements were made at longitudinal planes with axisymmetry where the circumferential velocity would be zero. This was the key condition behind the applicability of the single-wire, hot-film probe in measuring the other two components: radial and axial. The voltage outputs from the hot-film probe were measured for two different orientations at each measurement location. The hot-film probe was calibrated using a blowing type wind tunnel fitted with a 9:1 area ratio nozzle which provided a uniform (within 1 percent) velocity profile over the central 75 percent portion of the 0.15-m-dia exit.

Surface Flow Visualization. Qualitative observations were made over the outer surface of the transition piece to determine the impingement cooling flow pattern. One of the 14 transition pieces was coated with lampblack. The air entered through the cooling holes in the impingement sleeve and formed jets, which impinged over the outer surface of the transition piece. These air jets removed the lampblack coating, which, in turn, provided traces of flow at the outer surface of the transition piece. These traces were lifted off the surface by a transparent tape.

Computational Procedure. The flow description was supplemented by a closely approximated three-dimensional computational fluid dynamic analysis. In this analysis, the airflow path was divided into two computational domains. These two domains shared an interface region that communicated and updated the boundary condition data between the two domains. The body-fitted, curvilinear coordinate system was used to incorporate the geometric details in the computational analysis. Internal solid objects, such as the support struts and the surface of the impingement sleeve, were simulated by blocking flow through grids representing these areas. The computations were done with a total of 125,856 grids; 62,208 in the lower domain and 63,648 in the upper domain. Further details of the computational procedure are given by Agrawal and Yang (1993).

Results and Discussions

At the prediffuser inlet, the Reynolds number based on the prediffuser inlet height was 1.5×10^5. The corresponding Reynolds number in the prototype would be 2.5×10^6. The flow at

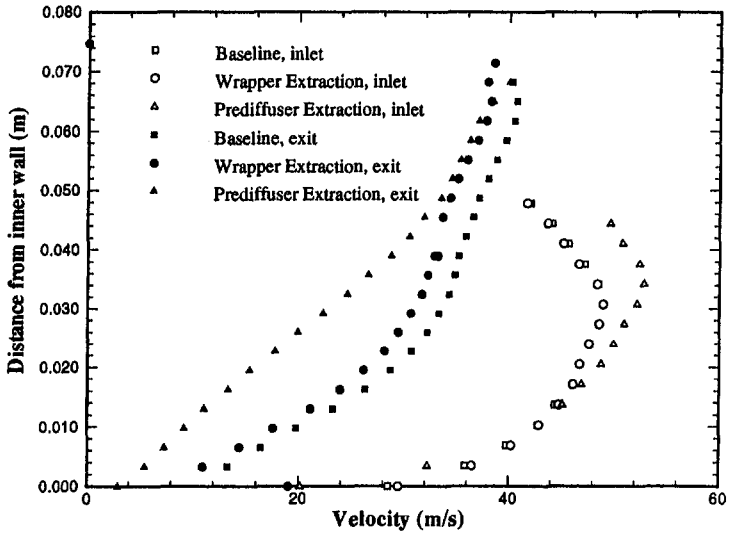

Fig. 10 Axial velocity profiles in the prediffuser

the prediffuser inlet was characterized as fully turbulent in both the prototype and test model. Thus, the difference in the flow behavior between those Reynolds numbers would be second order in nature. However, the percentage of the total pressure loss derived from the model test is expected to be higher than that in the prototype. In the following section, selected results are presented for three test cases: (1) straight wall prediffuser without air extraction (baseline configuration), (2) straight wall prediffuser with 20 percent air extraction at the turbine wrapper, and (3) modified prediffuser with 20 percent air extraction at the prediffuser inlet.

Aerodynamic Performance

Prediffuser Flow Field. Figures 10 and 11 show, respectively, the measured axial and radial velocity profiles in the prediffuser. Figure 10 shows that for all test cases, the axial velocity near the outer wall is higher at prediffuser exit than that at the prediffuser inlet. The air in the prediffuser's outer region accelerated because of the downstream sink effect of the combustor bypass holes. Such flow acceleration is detrimental to the prediffuser's performance because the primary function of a diffuser is to decelerate the flow. The air extraction at the turbine wrapper has only a marginal influence on the flow field in the prediffuser. The prediffuser flow field changes when the redesigned prediffuser or the Griffith diffuser is used. A finite radial velocity at the inlet of the Griffith diffuser (see Fig. 11) reflects the slot suction influencing the upstream. The axial velocity profiles at the prediffuser exit peak closer to the outer wall when the air is extracted at the prediffuser inlet.

Prediffuser Wall Static Pressure Recovery. The prediffuser performance was evaluated by the wall static pressure recovery coefficient given by $C_p = [p - \bar{p}_a]/h_D$ where p is the wall static pressure, $\bar{p}_a$ is the mass-averaged static pressure at the prediffuser inlet (Plane A), and h_D is the prediffuser inlet dynamic head $[=\bar{P}_a - \bar{p}_a]$ with $\bar{P}_a$ as the total pressure at the prediffuser inlet. Figures 12 and 13 show the static pressure recovery coefficients along the inner and outer walls of the prediffuser. The axial distance from the prediffuser inlet in Figs. 12 and 13 was nondimensionalized by the prediffuser inlet height. The pressure increases linearly along the inner wall of the prediffuser. However, the pressure at the outer wall decreases toward the exit of the prediffuser. The outer wall pressure decreases as the flow accelerates at the prediffuser exit because of the sink effect of the bypass holes on the combustor casing as discussed earlier. The air extraction at the turbine wrapper has only a marginal effect on the flow field in the prediffuser. With air extraction at the prediffuser inlet, the outer wall pressure recovery coefficient reaches a high value of 0.5. The overall static pressure recovery coefficients in the prediffuser are comparable for the two extraction schemes.

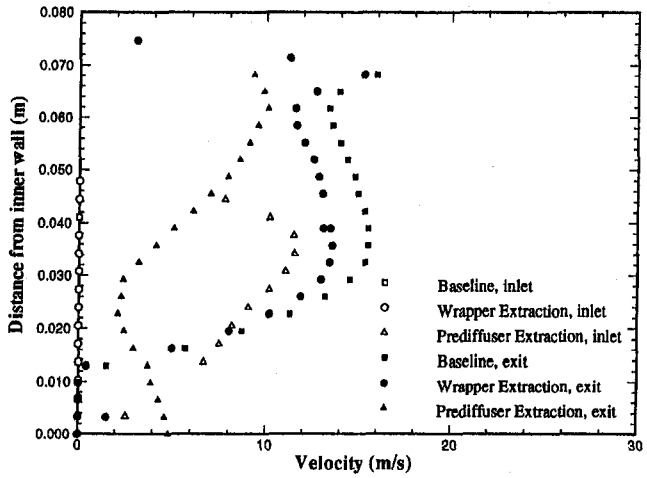

Fig. 11 Radial velocity profiles in the prediffuser

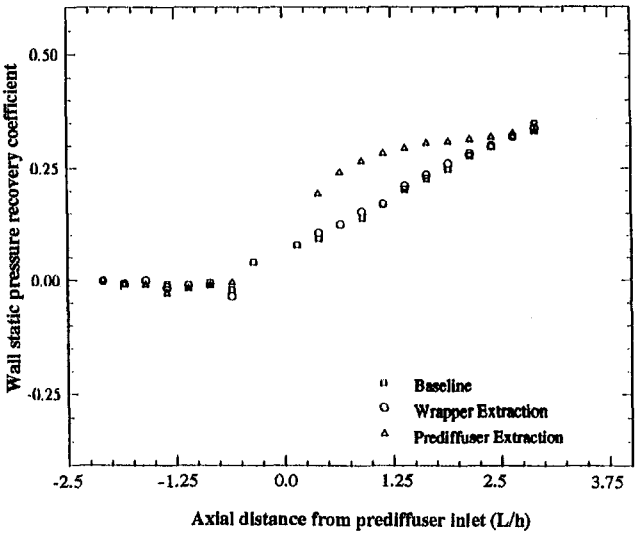

Fig. 12 Static pressure recovery coefficient at the prediffuser inner wall

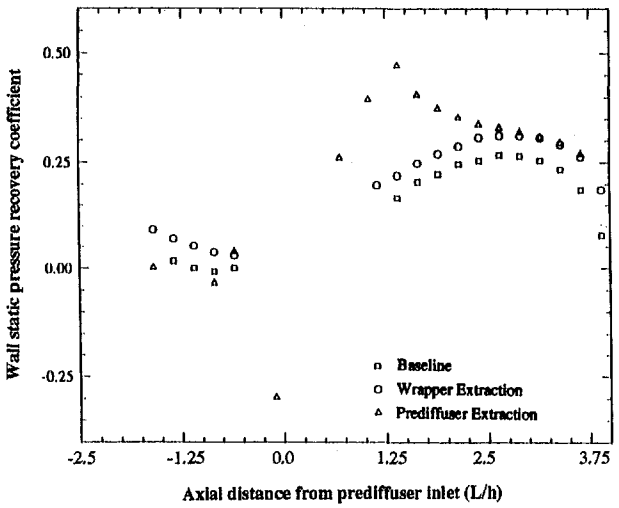

Fig. 13 Static pressure recovery coefficient at the prediffuser outer wall

Table 2 Test results applied to the prototype

	Base Case No Extraction	Turbine Wrapper Extraction	Prediffuser Inlet Extraction
Total Pressure Loss Coefficient	1.2	1.0	0.7
Total Pressure Loss (%)	2.2	1.8	1.3
Power Loss, MW	3.2	2.7	1.5
Thermal Efficiency (%)	35.0*	35.23	35.75
Change in Thermal Efficiency (% point)	0	0.23	0.75

* based on GE MS7001F specifications

Total Pressure Loss. The mass-averaged total pressure loss coefficient $\lambda_{a-b} = [\bar{P}_a - \bar{P}_b]/h_D$ between planes A and B was calculated using the total pressure profiles measured by the Kiel probe, the axial velocity profiles measured by the hot-film probe, and the static pressure profile measured by the pitot-static probe. Table 1 summarizes the measured and computed total pressure loss coefficients in the diffusers. The dump diffuser losses were divided into the lower part directly facing the prediffuser exit and the upper part comprising the remaining portion of the dump. Both the measurements and computations for the baseline configuration indicate that more than one dynamic head at the prediffuser inlet is lost in the diffusers. Approximately 80 percent of this loss occurs in the upper dump where the fluid must pass through the narrow gaps and pathways between adjacent combustor casing/impingement sleeve assemblies. The total pressure loss in the prediffuser is relatively small: only 4 percent of the total pressure loss in the diffusers.

Because the air extraction at the turbine wrapper does not affect flow field in the prediffuser and lower dump diffuser, the pressure loss coefficients in these parts are essentially the same as those for the baseline configuration. A decrease in the total pressure loss coefficient in the upper dump diffuser (from 0.93 to 0.72) occurs because only 80 percent of the air passes through the impingement sleeve and the remaining 20 percent is extracted at the turbine wrapper. The total pressure loss coefficients are lower when the air is extracted at the prediffuser inlet because only 80 percent of the compressed air enters the dump diffuser. The loss coefficients in the dump diffuser were 0.94 and 0.66, respectively, with the turbine wrapper extraction and the prediffuser inlet extraction.

The total pressure loss coefficients thus obtained are related to the total pressure losses and the power losses in the prototype. Table 2 summarizes the results and shows that when the air is extracted at the prediffuser inlet, the power loss in the diffusers is nearly half of that when the air is extracted at the turbine wrapper. This difference in the power loss translates to an increase of 0.5 percentage point in the gas turbine thermal efficiency.

Flow Uniformity

Lamp Black Traces. A significant test result includes the lampblack traces over the outer surface of the transition piece. Figure 14 shows the lampblack traces over the surface of the transition piece facing the turbine wrapper. The top panel was recorded at the baseline conditions. Without extraction, the air jets impinged on the transition piece, providing the necessary cooling airflow. The bottom panel was recorded when the air was extracted at the turbine wrapper. This panel indicates virtually no air impingement on the transition piece surface facing the turbine wrapper.

Pressure Measurements. Tables 3(*a*)–(*c*) show wall static pressures, along with the measurement locations, in the impingement sleeve and the combustor casing. The data are given in both meters and inches of water head, the latter in parentheses. The wall static pressures on the inside surface of the impingement sleeve at section BB (Table 3(*a*)) are nearly the same in the circumferential direction. However, the wall static pressures on the outer surfaces of the impingement sleeve at section BB (Table 3(*b*)) as well as on the combustor casing at section AA (Table 3(*c*)) vary in the circumferential direction. The circumferential variation is small on the combustor casing where the bypass holes are located, but is significant

Table 1 Mass-averaged total pressure loss coefficient with air extraction

	Measurements			Computations		
	Baseline No Extraction	Turbine Wrapper	Prediffuser Inlet	Baseline No Extraction	Turbine Wrapper	Prediffuser Inlet
Prediffuser	0.02-0.11	0.02-0.11	0.01-0.10	0.04 (4%)	0.04 (4%)	0.04 (6%)
Dump Diffuser						
Lower part	0.08	0.08	no data	0.22 (19%)	0.22 (22%)	0.06 (9%)
Upper part	<1.0	<0.95	<0.8	0.93 (77%)	0.72 (74%)	0.60 (85%)
Total				1.19 (100%)	0.98 (100%)	0.70 (100%)
Mass Flow through the diffusers (% of base line)	100%	100%	80%	100%	100%	80%

around the impingement sleeve. The wall static pressure is lowest at the 3 o'clock position and highest at the 6 o'clock position. The pressure is low at the 3 o'clock position because of the venturi effect of the crossflow between adjacent combustor casing/impingement sleeve assemblies. The venturi effect is more pronounced at section BB where the crossflow area or the space between adjacent impingement sleeves is small. The nonuniform pressure distribution would cause air to enter nonuniformly through the impingement cooling holes, thereby, resulting in nonuniform cooling of the transition piece.

Table 3 also points to an increase in the circumferential nonuniformity of the wall pressure when the air is extracted at the turbine wrapper. Extracting air at the turbine wrapper increases the crossflow and hence, the venturi effect on the side panels (i.e., the 3 o'clock position) where the wall static pressure decreases. This may accentuate nonuniform cooling of the transition piece leading to the hot spots and possibly the burnout. Extracting air at the prediffuser inlet, however, does not adversely affect the flow around the combustor casing/impingement sleeve assemblies.

Concluding Remarks

From an aerodynamic point of view, air extraction at the prediffuser inlet would be beneficial. Lower pressure losses associated with air extraction at the prediffuser could increase the gas turbine efficiency by 0.5 percentage point. Unlike air extraction at the turbine wrapper, prediffuser air extraction does not accentuate flow nonuniformities around the combustor casing/impingement sleeve, which is necessary to avoid hot spots on the transition piece. In the test model, the number of extraction ports was the same as the number of the combustor casing/transition piece assemblies. Such an idealized scheme allowing uniform air extraction around the periphery would not be structurally suitable in the prototype. A decrease in the number of extraction ports at the turbine wrapper would disturb the circumferential periodicity in the dump diffuser and distort the flow field even more, thereby requiring deflectors or guide vanes to redistribute flow around the impingement sleeve. These modifications to the flow region when the air is extracted at the turbine wrapper would incur additional pressure losses and, therefore, render the prediffuser air extraction even more beneficial.

Fig. 14(*a*) No air extraction (baseline configuration)

Fig. 14(*b*) Air extraction at the turbine wrapper

Fig. 14 Lampblack traces on the surface of the transition piece

Table 3 Wall pressure measurements, meters (inches) of water

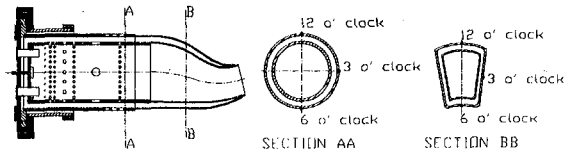

Table 3(a) Impingement Sleeve, Section BB (Inner Surface)

	Base Case No Extraction	Turbine Wrapper Extraction	Prediffuser Inlet Extraction
12 o'clock	-0.577 (-22.7)	-0.513 (-20.2)	-0.483 (-19.0)
6 o'clock	-0.574 (-22.6)	-0.513 (-20.2)	-0.480 (-18.9)
3 o'clock	-0.587 (-23.1)	-0.523 (-20.6)	-0.488 (-19.2)

Table 3(b) Impingement Sleeve, Section BB (Outer Surface)

	Base Case No Extraction	Turbine Wrapper Extraction	Prediffuser Inlet Extraction
12 o'clock	-0.366 (-14.4)	-0.371 (-14.6)	-0.343 (-13.5)
6 o'clock	-0.399 (-15.7)	-0.411 (-16.2)	-0.368 (-14.5)
3 o'clock	-0.244 (-9.6)	-0.241 (-9.5)	-0.259 (-10.2)

Table 3(c) Combustor Casing, Section AA (Outer Surface)

	Base Case No Extraction	Turbine Wrapper Extraction	Prediffuser Inlet Extraction
12 o'clock	-0.378 (-14.9)	-0.366 (-14.4)	-0.358 (-14.1)
6 o'clock	-0.368 (-14.5)	-0.368 (-14.5)	-0.338 (-13.3)
3 o'clock	-0.348 (-13.7)	-0.332 (-13.1)	-0.332 (-13.1)

Acknowledgments

This work was performed at Clemson University under the aegis of the Morgantown Energy Technology Center, Department of Energy contract number DE-AC21-89MC26041 and with assistance from Mr. Thomas Ekstrom at the General Electric Gas Turbine Technology Department, Schenectady, New York. Mr. Leland E. Paulson was the METC project manager. We wish to express gratitude to Jim Roache, Ziqin Hu, and Girish Srinivas for their assistance during experiments and data processing.

References

Agrawal, A. K., and Yang, T.-T., 1991, "Viscous Flow Computations for Compressor/Combustor Diffuser Design to Allow Air Extraction for IGCC Systems," ASME Paper No. 91-GT-62.

Agrawal, A. K., and Yang, T.-T., 1993, "3D Numerical Study of Airflow in the Compressor/Combustor Prediffuser and Dump Diffuser of an Industrial Gas Turbine," *Proc. 5th Annual Thermal Analysis Workshop,* NASA CP 10122, pp. 395–409.

Becker, B., and Schetter, B., 1992, "Gas Turbine Above 150 MW for Integrated Coal Gasification Combined Cycles (IGCC)," ASME JOURNAL OF ENGINEERING FOR GAS TURBINES AND POWER, Vol. 114, pp. 660–664.

Corman, J. C., and Todd, D. M., 1993, "Technology Considerations for Optimizing IGCC Plant Performance," ASME Paper No. 93-GT-358.

Notestein, J. E., 1990, "Commercial Gasifier for IGCC Applications Study Report," DOE/METC-91/6118.

Todd, D. M., and Allen, R. P., 1991, "Commercialization of Gas Turbines for IGCC," in: *Proc. 8th Annual Coal-Fueled Heat Engines and Gas Stream Cleanup System Contractors Review Meeting,* DOE/METC-91/6122, pp. 35–63.

Todd, D. M., 1993, "Clean Coal Technologies for Gas Turbines," *Turbomachinery International,* Mar.–Apr., pp. 20–27.

Topping Combustor Status for Second-Generation Pressurized Fluidized Bed Cycle Application

W. F. Domeracki

T. E. Dowdy

Westinghouse Electric Corporation,
Power Generation Business Unit,
Orlando, FL 32826-2399

D. M. Bachovchin

Westinghouse Electric Corporation,
Science & Technology Center,
Pittsburgh, PA 15235

Second-generation Pressurized Fluidized Bed (PFB) combined cycles employ topping combustion to raise the turbine inlet temperature for enhanced cycle efficiency. This concept creates special combustion system requirements that are very different from requirements of conventional gas turbine systems. The topping combustor provides the means for achieving state-of-the-art turbine inlet temperatures and is the main contributor to enhanced plant performance. The objective of this program is to develop a topping combustor that provides low emissions, and is a durable, efficient device exhibiting stable combustion and manageable wall temperature. The combustor will be required to burn a low-Btu syngas under normal "coal-fired" conditions. However, for start-up and/or carbonizer outage, it may be necessary to fire a clean fuel, such as oil or natural gas. Prior testing has shown the Westinghouse Multi-Annular Swirl Burner (MASB) to have excellent potential for this application. Metal wall temperatures can be maintained at acceptable levels, even though most "cooling" is done by 1600°F vitiated air. Good pattern factors and combustion efficiencies have been obtained. Additionally, low conversion rates of fuel bound nitrogen to NO_x have been demonstrated. This paper presents an update of the status of an ongoing topping combustor development and test program for application to "Second-Generation Pressurized Fluidized Bed Combined Cycles (PFBCC)." The program is sponsored by the Department of Energy's Morgantown Energy Technology Center (DOE/METC) and will first be applied commercially into the Clean Coal Technology Round V Four Rivers Energy Modernization Project. Phase 1 of the program involved a conceptual and economic study (Robertson et al., 1988); Phase 2 addresses design and subscale testing of components; and Phase 3 will cover pilot plant testing of components integrated into one system.

Introduction

A project team consisting of Foster Wheeler Development Corporation, Westinghouse Electric Corporation, Gilbert/Commonwealth, and the Institute of Gas Technology, are developing a Second-Generation Pressurized Fluidized Bed System. Foster Wheeler is developing a carbonizer (a partial gasifier) and a pressurized fluidized bed combustor. Both these units operate at a nominal 1600°F (870°C) for optimal sulfur capture. Since this temperature is well below the current combustion turbine combustor outlet operating temperature of 2350°F (1290°C) to reach commercialization, a topping combustor and hot gas cleanup (HGCU) equipment must be developed.

Westinghouse's efforts are focused on the development of the high-temperature gas cleanup equipment and the topping combustor. This paper concentrates on the design and test of the topping combustor, which must use a low heating value syngas from the carbonizer at approximately 1600°F (870°C) and 150 to 210 psi (1.0 to 1.4 MPa). The syngas entering the topping combustor has been previously cleaned of particulates and alkali by the hot gas cleanup (HGCU) system. It also contains significant fuel bound nitrogen present as ammonia and other compounds. The fuel-bound nitrogen is significant because it will selectively convert to NO_x if the fuel is burned under the highly oxidizing conditions of standard combustion turbine combustors.

Contributed by the International Gas Turbine Institute and presented at the 40th International Gas Turbine and Aeroengine Congress and Exhibition, Houston, Texas, June 5–8, 1995. Manuscript received by the International Gas Turbine Institute February 10, 1995. Paper No. 95-GT-106. Associate Technical Editor: C. J. Russo.

The fuel must be burned with the vitiated air produced by the pressurized fluidized bed combustor (PFBC). The vitiated air has been cleaned of particulates and alkali by the HGCU system, and has also been partially depleted of oxygen. The 1600°F (870°C) vitiated air must also be used to cool the combustor as much as possible, though a small amount of compressor discharge air at a lower temperature 700°F (about 370°C) may be used.

The application requirements indicate that a rich-quench-lean (RQL) combustor is necessary and the multi-annular swirl burner (MASB) was selected for further development. This paper provides an update on the development and testing of this MASB combustor. Additionally, Westinghouse has been conducting computational fluid dynamic (CFD) and chemical kinetic studies to assist in the design and to help optimize the operation of the combustor. Results of these models are presented and compared to the test results.

Cycle Description. In a second-generation PFB combined cycle, coal is fed to a pyrolyzer/carbonizer unit that operates at 1600°F (871°C) to produce a low heating value fuel gas and combustible char. The char is burned in the PFB, and the 1600°F (871°C) product gases, after filtration, are piped back to the combustion turbine as illustrated in Figs. 1 and 2.

Before entering the gas turbine, the 1600°F (871°C) gas, still rich in oxygen, is raised to 2100°F (1149°C) or higher by burning the filtered, pyrolyzer-produced low heating value fuel gas in a topping combustion system. Since turbine inlet temperature is at least 500°F higher than the PFB air temperature, plant efficiency is 5 to 7 percentage points higher than similar first-generation PFB plants.

The Combustion Turbine. The use of a Circulating Pressurized Fluidized Bed Combustor (CPFBC) as the primary combustion system for a combustion turbine requires trans-

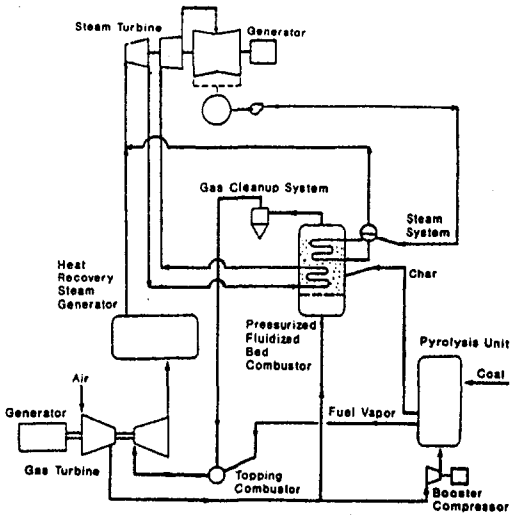

Fig. 1 Schematic representation of a second-generation PFB combined cycle

porting compressor air to the CPFBC and vitiated air/fuel gas back to the turbine. In addition, the topping combustion system must be located in the returning vitiated airflow path. The conventional fuel system and turbine center section require major changes for the applications.

The combustion zone of the Westinghouse 501 and 251 combustion turbines currently in production cannot contain a topping combustion system within the main structural pressure shell. Although the pressure casing can be enlarged both radially and longitudinally to accommodate the topping combustor system, the integrity and rigidity of the main shell would be significantly affected, possibly impacting rotor dynamics and precluding shipping the unit assembled.

One alternative configuration, which uses one or two topping combustor assemblies, on the side of the unit, is shown in Fig. 2. The vitiated air from the CPFBC enters each of the internal plenum chambers in which the topping combustors are mounted. Fuel gas enters the assembly via the fuel nozzles at the head end of the combustor. Combustion occurs, and the products of combustion are ducted into the main shell for distribution to the first-stage turbine vanes.

Compressor discharge air leaves the main shell, flowing around the annular duct into adjacent combustion shells. The air flows around the vitiated air plenums and leaves each combustion assembly via nozzles and is ducted to the CPFBC and carbonizer (see Fig. 2).

Combustor Design. Because the air entering the combustor is at 1600°F rather than the 700°F usual for gas turbines, the conventional type of combustor is not suitable. Both emissions and wall cooling problems preclude the use of the conventional design. Therefore, a combustor that will meet the requirements of utilizing the higher temperature air for both wall cooling and combustion is required.

In selecting a combustor design that will withstand the conditions expected in the topping application, the effective utilization of the 1600°F air mentioned above could satisfy the wall cooling challenge by maintaining a cooling air layer of substantial thickness. The creation of thick layers of cooling air at the leading edge of each inlet section is easily achieved if the combustor is made up of concentric annular passages. In addition to wall cooling considerations, the burner must inhibit the formation of NO_x from syngas that contains fuel-bound nitrogen, have high combustion efficiency, produce an acceptable exhaust temperature pattern, exhibit good stability, and be able to light off at cold plant conditions. The Multi-Annular Swirl Burner (MASB) was chosen as the candidate to meet these requirements.

The MASB as shown in Fig. 3 is designed to operate in a staged combustion mode to inhibit the formation of NO_x. The details of the NO_x-inhibiting process were described in a previous paper (Garland and Pillsbury, 1992). Figure 4 shows the half-scale 14 in. MASB.

Test Facility

The topping combustor tests are being conducted at the University of Tennessee Space Institute (UTSI), Tullahoma, Tennessee in the DOE Coal, Oil, or Gas-Fired Flow Facility (CFFF). This facility was designed to accommodate a variety of coal-, oil-, or gas-fired energy conversion equipment.

UTSI modified the existing facility to accommodate the topping combustor and provided all necessary ancillary systems

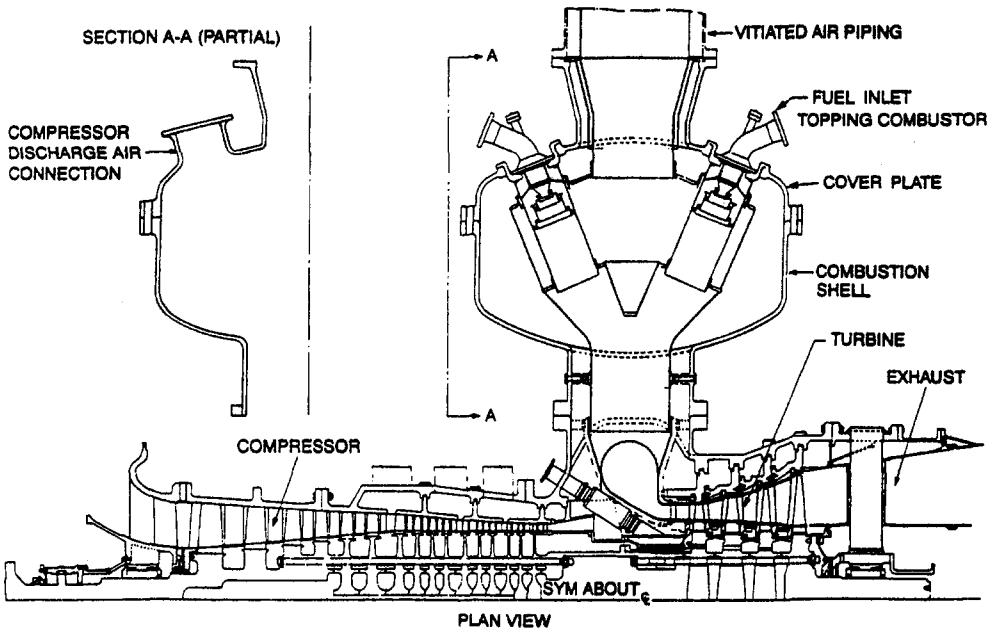

Fig. 2 Combustion turbine conceptual design

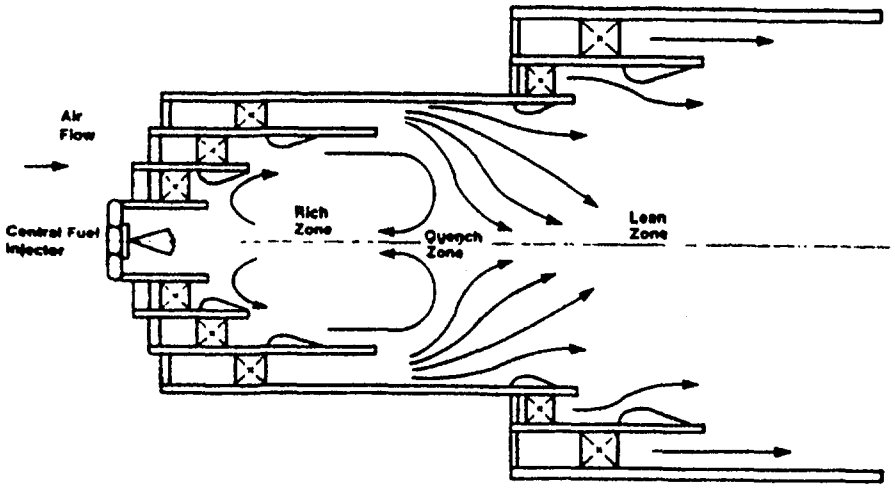

Fig. 3 Conceptual arrangement of the multi-annular swirl

required to conduct the test and obtain data for evaluation. Modifications included the installation of the syngas fuel system with heater, which delivers fuel from tube trailers to the combustor at 1200°F (650°C), establishing required pressure, and perform fuel blending. The fuel gas is a six-component mixture of N_2, H_2, CH_4, CO, H_2O, and NH_3, which simulates the heating value and flammability limits of carbonizer gas.

Test Rig

The Westinghouse advanced combustor test rig was adapted for use at the UTSI test site. Figure 5 is a longitudinal view of the rig as configured for use in the topping combustor tests.

To simulate actual operating conditions, several modifications and auxiliary systems were required. These items provided: the supply of hot vitiated air; the supply of hot, synthesized fuel gas and/or natural gas and/or fuel oil; and, the ability to dope the fuel with ammonia when firing syngas. The ammonia allowed investigating the effects of fuel bound nitrogen on emissions.

The test facility at UTSI is capable of delivering 20 lb/s (9.1 kg/s) of air at 200 psia (1.4 MPa) and 120°F (50°C). To raise this air to the required 1600°F (870°C) temperature, a distillate oil-fired combustor, referred to as the preheater or the preburner, is placed upstream of the MASB. Directly heating the air through combustion partially depletes the oxygen in the air while adding carbon dioxide, water vapor, and NO_x. The vitiated air, still high in oxygen content, produced by the preheater simulates the PFB exhaust gases and makes the test conditions more realistic. The high oxygen content is important as it relates to obtaining high plant efficiency (Robertson et al., 1988).

Note on Fig. 5 that the MASB is held within a series of flanged containment cylinders. In this way, the entering 120°F (50°C) air comes forward to the preheater, where it burns the distillate oil, and is raised to 1600°F (870°C).

Instrumentation and Control

Approximately 200 temperature measurements, over 50 pressure measurements, and measurements relating to flow and emissions were taken during testing.

Summary of Pre-1993 MASB Tests. The MASB has the desired characteristics for a topping combustor for this application. Three syngas tests and one fuel oil/natural gas test were conducted in 1990–1991 with 12 in. (30.5 cm) and 14 in. (35.6 cm) diameter MASBs at The University of Tennessee Space Institute (UTSI). These tests have confirmed that the MASB can be successfully cooled with 1600°F (870°C) vitiated air (supplemented with a small amount (5 to 10 percent of total air flow) of additional cooling air at the hottest locations). The 12 in. (30.5 cm) combustor demonstrated that good temperature patterns could be obtained at 2100°F (1150°C) firing temperature, and the 14 in. (35.6 cm) test showed that a uniform 2350°F (1290°C) combustor outlet temperature could be obtained without overheating the materials of construction.

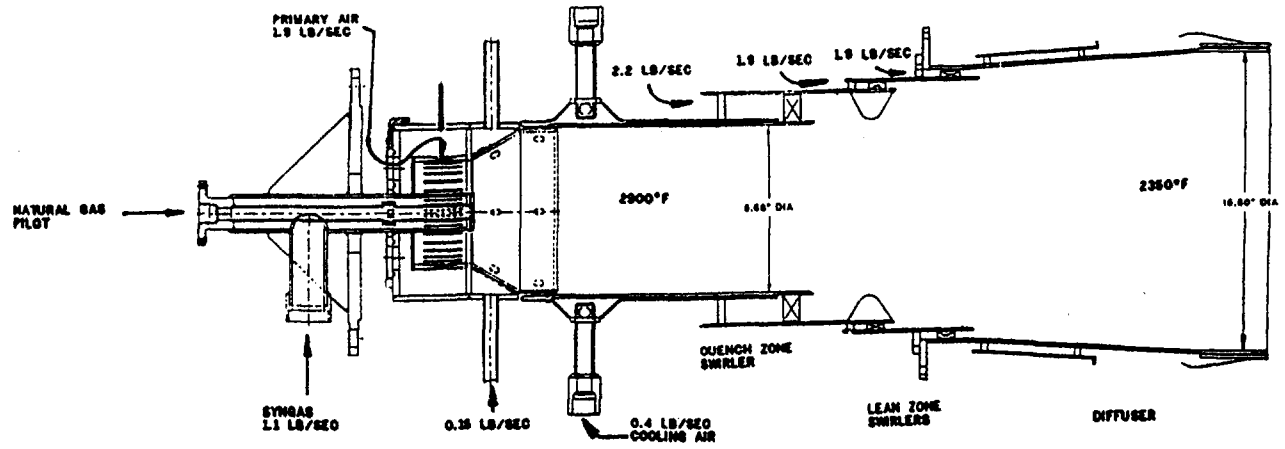

Fig. 4 Recent 14 in. MASB design

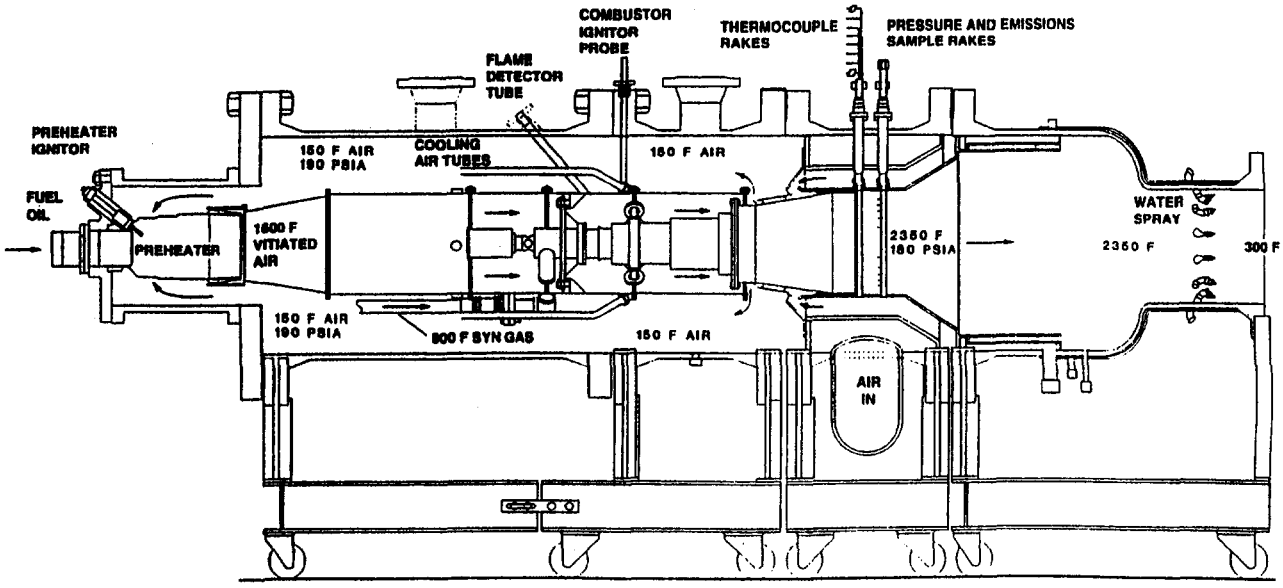

Fig. 5 Topping combustor test rig configuration

Emissions from the 12 in. (30.5 cm) and 14 in. (35.6 cm) MASB tests have shown low CO, and no soot or unburned hydrocarbons have been detected. In a "conventional" oil or natural gas fired combustion turbine combustor, Westinghouse would predict that as much as 85 percent of the fuel-bound nitrogen would be selectively converted to NO_x. The 1990–1991 tests with the 12 in. (30.3 cm) and 14 in. (35.6 cm) MASBs have shown 20 to 30 percent conversion of the NH_3 added to the syngas to simulate fuel bound nitrogen to NO_x. This is obviously a significant improvement over conventional combustors, but further improvements on the NH_3 conversion appear possible.

Recent MASB Design Development. The MASB has been designed as a combustor specifically for low-Btu, coal-derived fuel gases containing significant fuel bound nitrogen, primarily in the form of NH_3. Standard Dry Low-NO_x combustors have focused on minimization of thermal NO_x generation. The MASB must minimize thermal NO_x and also must convert NH_3 to molecular nitrogen.

The MASB approach is to:

- employ a high-residence-time, fuel-rich zone at an optimized temperature such that NH_3 is converted to N_2 rather than to NO_x.
- establish strong swirl and strong recirculation in the rich zone for flame stabilization, and to ensure that the entire rich zone is used for this purpose.
- achieve a rapid quench to fuel lean conditions to minimize the formation of thermal NO_x after the rich zone.

Westinghouse, together with UTSI, has completed significant computer models of the system, both with computational fluid dynamic (CFD) codes and with chemical kinetics codes. Output from this analysis has been factored into the latest designs of the MASB, particularly with respect to the primary (fuel-rich) zone. CFD modeling of the redesigned configuration shown in Fig. 4 shows that this new design will have significant recirculation in the primary zone.

A half-scale cold flow model with similar Reynolds number and velocity profiles as the hot 18 in. MASB was tested to verify the flow characteristics required and expected. Axial and radial velocity measurements were made across the diameter of the unit at each of seven axial positions.

Figure 6 is a map of the resulting axial velocities. A strong donut-shaped recirculation region was confirmed in the wake of the bluff body end of the fuel swirler. This extends about one third of the way down the rich zone cylinder. Additionally, there is an absolute boundary (location C to C2) between the rich and quench zones through which no reverse flow occurs, thereby guaranteeing the existence of fuel rich combustion. Swirl was very strong (100 to 200 ft/sec tangential velocity), especially near the wall, for good stabilization, and wall cooling.

These results verified CFD modeling efforts and confirmed that no additional design changes were needed prior to full-size MASB testing.

Westinghouse has performed chemical kinetic studies under conditions as close as possible to those planned for the next series of tests. Basically, the equivalent of 5 ms of backmixing followed by 40 ms of plug flow could yield NO_x levels below 20 ppm when corrected to 15 percent O_2. The CFD model and the cold flow work indicate that significant recirculation (backmixing) should occur with the redesigned fuel-rich zone.

Recently, significant MASB design improvements have been made with the objective of improving the flame pattern in the combustor, and thereby achieving improved low NO_x performance. The effectiveness of these improvements is to be demonstrated in a two-stage test.

The first test was conducted in June 1993 with the 14 in. configuration shown in Fig. 4. These tests confirmed that the redesigned fuel nozzle achieved the rich zone environmental control, flame stability, and oxidant distribution required. The redesigned rich zone also improved upon the fuel bound nitrogen to NO_x conversion rates. Results of the tests showed a conversion rate of only 9 to 10 percent at the 0.27 percent ammonia levels, surpassing our goal of 10 to 12 percent conversion. The detailed results of these tests were reported in a previous paper (Domeracki et al., 1994).

In the next stage, a full-scale 18 in. (45.7 cm) MASB was tested. Lessons learned in the 14 in. (35.6) MASB tests were incorporated into a full-scale 18 in. (45.7 cm) MASB. In addition, the 18 in. (45.7 cm) design will have a greater rich zone residence time for improvement of low-NO_x performance, higher pressure drop downstream swirlers, and on-line oxidant flow control.

Full-Scale 18 in. MASB Test Results

During the summer of 1994, the 18 in. MASB was successfully tested, meeting all of the following objectives:

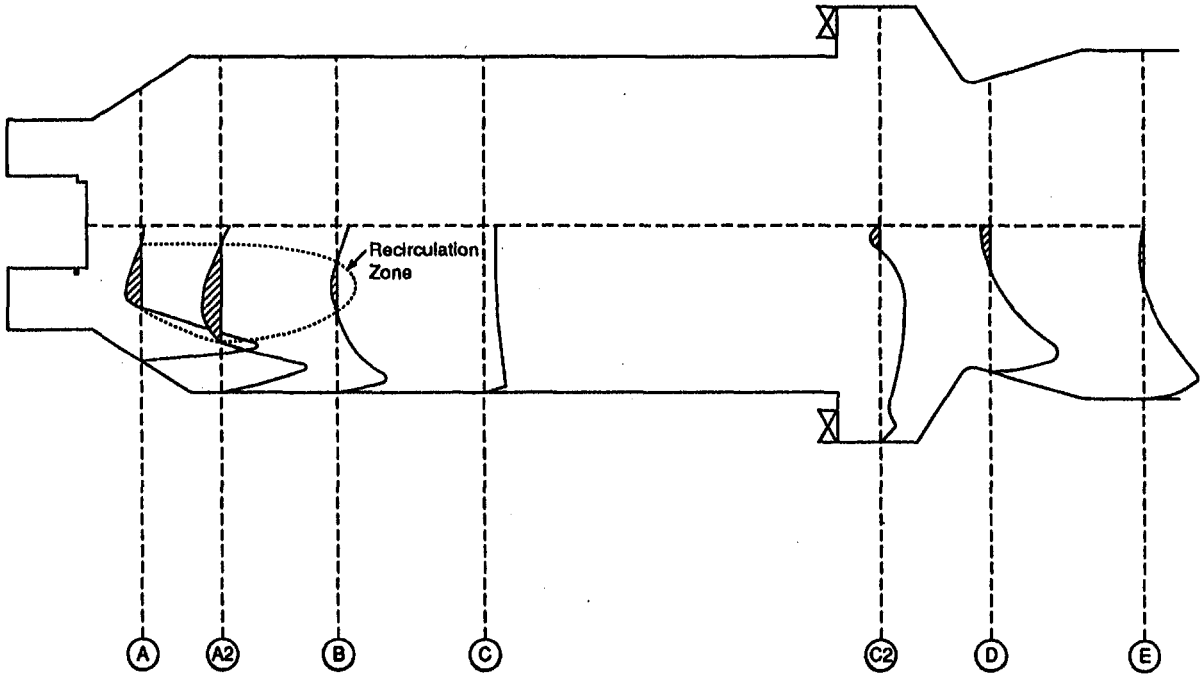

Fig. 6 Cold flow model axial velocities

1 Demonstrate successful scale up to full commercial size single-basket design.
2 Optimize rich zone performance for lower (12 percent target) conversion of fuel nitrogen (as NH_3) to NO_x, by increasing residence time and tighter and control of equivalence ratio in the 1.2 to 1.4 range.
3 Demonstrate effectiveness and durability of mechanical design improvements, particularly as related to the quench flow deflector, swirlers, ignitor, and cooling designs.
4 Operate on-line adjustable control of the variable orifice mechanism for rich zone fuel/air ratio control.
5 Operate firing with syngas in vitiated air, and with natural gas in vitiated air.
6 Explore affects of variable operating parameters: fuel NH_3 content, rich zone temperature, part load, vitiated air temperature, vitiated air oxygen level.

Remaining future test objectives include demonstration of operation firing natural gas in compressor (700°F) air, and on-line fuel switching.

Natural gas firing in vitiated air was successfully demonstrated over a range of operating conditions. A stable flame was easily achieved, with no ignitor firing required. The burner proved mechanically durable, with no metal distress and wall (Haynes 230) temperatures maintained at less than 1500°F at all conditions. Generally, the rich zone was operated at higher temperatures and lower equivalence ratio than planned, because of difficulties in operating the fuel/air ratio control mechanism (caused by pretest preburner excessive discharge temperature). MASB exhaust temperature rakes revealed the flame to be somewhat stretched out.

The emission results in terms of NO_x and CO are summarized in Table 1. Note that the burner functions as a very low NO_x

Table 1 Natural gas test results—emissions

Conditions:

- Vitiated air oxygen level: 12 to 18 vol% (dry)
- Vitiated air temperature: 1575 to 1700°F
- Background NOx in vitiated air: 26 to 200 ppm (dry, unnormalized)
- Pressure: 7.3 and 10 atm
- Calculated Rich zone temperature: 2300 to 3460°F

NOx (dry, normalized to 15% O2):

7.3 atm results (rich zone equivalence ratio 1.05 to 1.3)

- 2 ppm MASB-generated NOx @ 12.2 vol% O2 in vitiated air
- 5 to 15 ppm MASB-generated NOx @ 14.7 vol% O2 in vitiated air
- 50 to 75% reduction compared to earlier 14-inch MASB testing

10 atm results (rich zone equivalence ratio 0.85 to 1.05)

- 46 to 74 ppm MASB-generated NOx

CO (dry):

- 0 to 20 ppm exit CO when vitiated air CO < 100 ppm CO
- CO reduced by 50 to 75% when vitiated air CO > 150 ppm

Table 2 Syngas test results—emissions

Conditions:

- Vitiated air oxygen level: 10 to 17 vol% (dry)
- Vitiated air temperature: 1400 to 1630°F
- Background NOx in vitiated air: 20 to 130 ppm (dry, unnormalized)
- Pressure: 7.3 atm
- NH3 in syngas: 0 to 0.41 vol%, 0.17 for most set points
- Calculated Rich zone temperature: 2650 to 3160°F
- Calculated Rich zone equivalence ratio: 0.9 to 1.5, 1.2 to 1.4 for most set points

NOx (dry, normalized to 15% O2):

- 8.3 ppm MASB-generated NOx, averaged over entire test matrix
- 5.8% conversion of NH3 to NOx, averaged over entire test matrix
- Insensitive to NH3 level
- Low Sensitivity to rich zone equivalence ratio or temperature
- 50% reduction from 14" MASB results

CO (dry):

- CO reduced by 50%. (Vitiated air CO always > 150 ppm)

combustor for natural gas when the rich zone is operated rich, and then NO_x results are not excessive even when operated lean. The MASB completely burns out CO in vitiated air at the levels expected in actual PFBC plant operation.

Following natural gas testing, the two identified issues were solved by minor hardware modifications: (1) The fuel/air ratio control mechanism was rebuilt with more forgiving tolerances to differential thermal expansion; (2) several backwall holes were drilled to admit a fraction of the primary air without swirl, thereby reducing flame stretch.

Note that rich zone temperatures are calculated using flow distributions and assuming uniformity without backflow from subsequent zones, and so are approximations ONLY.

Syngas testing was then successfully executed. Again a stable flame was easily achieved and controlled, without the need for ignitor firing. Apart from one thin weld crack, without test performance consequence, there was no burner damage. The fuel/air ratio control functioned properly. Rich zone equivalence ratio was controlled in the proper range. There was no flame stretch apparent.

Emissions results for the syngas tests are shown in Table 2. The MASB has now been demonstrated to generate negligible NO_x additional to the PFBC background levels. This is a result of engineering the rich zone to achieve needed residence time and good recirculation. Figure 7 shows theoretical curves of NO_x generation, as well as data for the 14 in. MASB and the current 18 in. MASB. Note in Fig. 7 and in Table 2 that "MASB-generated NO_x" is defined as the difference between the measured exit NO_x, and the expected NO_x exit level if 100 percent of the vitiated air NO_x survived and no additional NO_x were generated. The theoretical curves in Fig. 7 were calculated using the Chemkin model with a Westinghouse data base, with the "no recirculation" line being plug flow, and the "good recirculation" line being 5 msec well mixed plus balance of residence time plug flow. (There is scatter because of the wide range of other variables in the actual testing.) The progress made is clear.

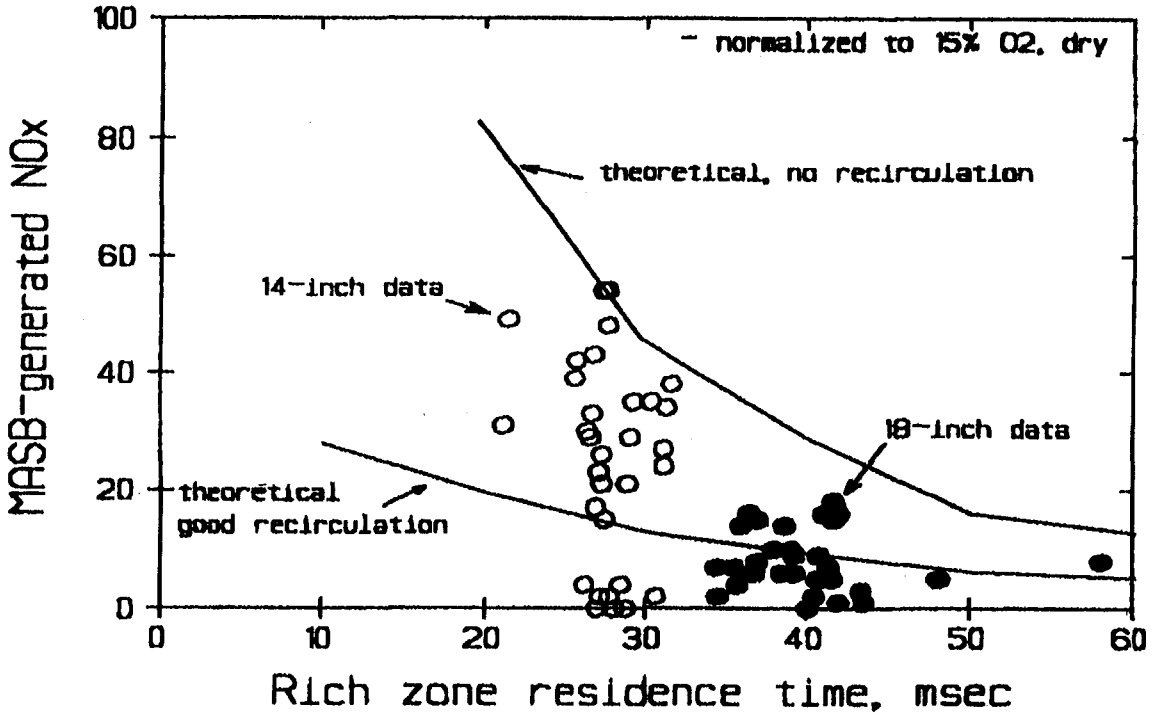

Fig. 7 MASB performance and design basis

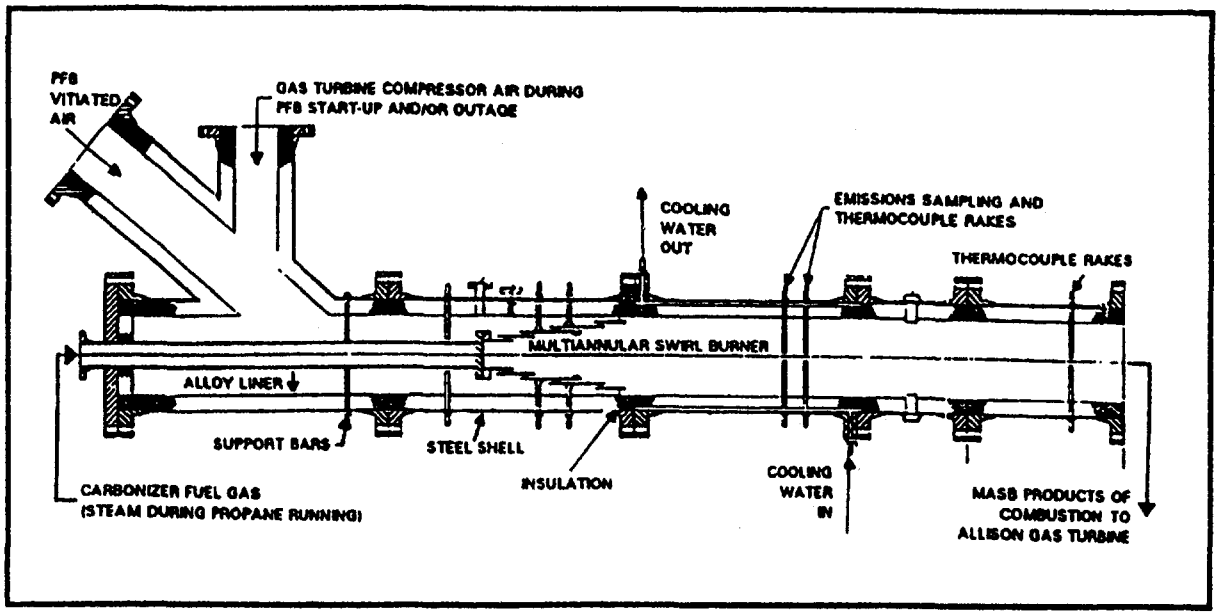

Fig. 8 Topping combustor assembly

Applications

The MASB design described in this paper will be used at the Power Systems Development Facility (PSDF) in Wilsonville, Alabama, which is a DOE/Industry cost-shared facility operated by Southern Company Services.

This facility is designed to provide long-term hot gas cleanup and process testing for an advanced design Pressurized Fluidized Bed Combustion (PFBC) and Gasification system. It incorporates carbonization with a circulating fluidized bed and topping combustion developed at Foster Wheeler. The nominal 7-MW plant is being designed by Foster Wheeler and is scheduled to go into operation in 1996.

Figure 8 shows the topping combustor assembly for the PSDF. Each of the carbon steel spools is a pressure vessel. A concentric stainless steel cylinder inside each piece serves as the high temperature boundary. A layer of insulation fills the void between the concentric cylinders. The exhaust diffuser is a double-wall steel piece designed to accommodate cooling water for this region of the MASB. The inner liner of this piece is a Hastelloy alloy. The topping combustor itself is an Inconel or Hastelloy-type alloy with a diameter of about 457 mm (18 in.), which is commercial scale. Multiple combustors will be used in a utility-size plant incorporating Westinghouse 501 or 251 combustion turbines.

About 9.58 kg/s (76,000 lb/h) vitiated air enters the combustor at 1.03 MPa-a/760°C (150 psia/1400°F). About 1.46 kg/s (11,600 lb/h) carbonizer fuel gas, at about 899°C (1650°F), is burned in the MASB, producing an exhaust gas temperature of 1288°C (2350°F)—the optimum firing temperature for a utility-size plant. In a commercial plant, the 1288°C (2350°F) gas from the MASB is fed at full temperature to the gas turbine expander. For Wilsonville, the gas will be cooled to about 1080°C (1975°F) with compressor bypass air since the combustion turbine is limited to this temperature level. This advanced CPFBC facility at Wilsonville Alabama was described in detail by McClung et al. (1994).

In addition to the Wilsonville facility mentioned above, the MASB configuration will be applied at Air Products and Chemicals Four Rivers Energy Modernization Project (FREMP). This application will be the first commercial power plant using second-generation pressurized fluidized bed (CPFBC) combustion technology. Air Products has been selected in the DOE Clean Coal Technology Round V to build, own and operate this combined cycle facility, which will produce 66 MWe, export up to 400,000 lb/hr of steam, and be located at their chemical manufacturing facility in Calvert City, KY. The gas turbine will be a Westinghouse model 251B12 that will be modified to accommodate full air extraction and an external topping combustor with a cluster of MASBs as shown in Fig. 2. This project was described in detail by J. J. Lewnard et al. (1993).

Acknowledgments

The topping combustor development work is being performed by Westinghouse through DOE/METC. Mr. Don Bonk is the Project Manager. The original design work for the combustor was performed in consultation with Dr. János Beér, Professor of Chemical Fuel Engineering, at MIT.

References

Domeracki, W. F., Dowdy, T. E., and Bachovchin, D. M., 1994, "Topping Combustor Development for Second-Generation Pressurized Fluidized Bed Combined Cycles," ASME Paper No. 94-GT-176.

Garland, R. V., and Pillsbury, P. W., 1992, "Status of Topping Combustor Development for Second-Generation Fluidized Bed Combined Cycles," ASME JOURNAL OF ENGINEERING FOR GAS TURBINES AND POWER, Vol. 114, pp. 126–131.

Lewnard, J. J., et al., 1993, "Commercialization of Second Generation Pressurized Circulating Fluid Bed Combustion Process," *Proc. Power Gen. Americas Conference,* Dallas, TX.

McClung, J. D., Quandt, M. T., and Frochlich, R. D., 1994, "The Advanced CPFBC Facility at Wilsonville, AL, USA." *Proc. First International Conference on Combined Cycle Power Generation,* Calcutta, India.

Robertson, A., Garland, R., Newby, R., Patel, J., and Rubow, L., 1988, "Second-Generation PFB Combustion Plant Performance and Economics," EPRI Seminar on Fluidized Bed Combustion Technology for Utility Applications.

Modeling of Gas Turbine Fuel Nozzle Spray

N. K. Rizk

J. S. Chin

M. K. Razdan

Allison Engine Company,
Indianapolis, IN 46206

Satisfactory performance of the gas turbine combustor relies on the careful design of various components, particularly the fuel injector. It is, therefore, essential to establish a fundamental basis for fuel injection modeling that involves various atomization processes. A two-dimensional fuel injection model has been formulated to simulate the airflow within and downstream of the atomizer and address the formation and breakup of the liquid sheet formed at the atomizer exit. The sheet breakup under the effects of airblast, fuel pressure, or the combined atomization mode of the air-assist type is considered in the calculation. The model accounts for secondary breakup of drops and the stochastic Lagrangian treatment of spray. The calculation of spray evaporation addresses both droplet heat-up and steady-state mechanisms, and fuel vapor concentration is based on the partial pressure concept. An enhanced evaporation model has been developed that accounts for multicomponent, finite mass diffusivity and conductivity effects, and addresses near-critical evaporation. The present investigation involved predictions of flow and spray characteristics of two distinctively different fuel atomizers under both nonreacting and reacting conditions. The predictions of the continuous phase velocity components and the spray mean drop sizes agree well with the detailed measurements obtained for the two atomizers, which indicates the model accounts for key aspects of atomization. The model also provides insight into ligament formation and breakup at the atomizer exit and the initial drop sizes formed in the atomizer near field region where measurements are difficult to obtain. The calculations of the reacting spray show the fuel-rich region occupied most of the spray volume with two-peak radial gas temperature profiles. The results also provided local concentrations of unburned hydrocarbon (UHC) and carbon monoxide (CO) in atomizer flowfield, information that could support the effort to reduce emission levels of gas turbine combustors.

Introduction

In recent years, significant effort has been made to develop advanced combustor concepts to meet the future needs of improved performance and reduced emission levels in gas turbine engines. The success of such concepts relies significantly on achieving optimum fuel atomization and rapid and uniform mixing with the combustor air. By this means, conditions that may have adverse effects on combustor performance and emissions and engine durability are avoided. Although the atomization of fuel, either by using airblast forces or injecting the fuel under high pressure, is relatively easy to achieve, it is difficult to obtain satisfactory spray quality over the entire range of engine operation. As a means of overcoming this deficiency, it is a common practice to utilize both atomization concepts in a single hybrid atomizer design. Efficient combustion at starting and low power conditions is achieved by utilizing a pilot pressure nozzle in airblast atomizer. Improved atomization and fuel/air mixing of pressure injection systems are effected by the employment of available pressure drop to provide the airblast needed to assist the atomization process.

To guide the design and development of the combustor, it is important to acquire sufficient details of the atomizer performance. Calculation of the evaporation and reaction of spray in the combustor involves the evaluation of such parameters as spray mean diameter, range of drop sizes in the spray, and drop trajectory. To render these details useful to the combustor component designer, empirical expressions have been derived to provide a global picture of the whole spray in terms of operating parameters, fuel properties, and atomizer dimensions (Lefebvre, 1989; Jasuja, 1979; Simmons, 1979). However, an expression derived for a certain application may not be suitable for use with other types of applications because of the different nature of the fuel preparation and air utilization in each concept (Rizk and Lefebvre, 1983). Analytical models, on the other hand, have shown promising results by matching the details of the spray characteristics with reasonable accuracy. These models, however, require either the estimation of the initial conditions at the atomizer exit or the utilization as initial values of data measured at some downstream distance (Sturgess et al., 1984; Mostafa and Mongia, 1987); this is due to the difficulties involved in carrying out reliable measurements in the near region of the atomizer.

To improve combustor performance predictions significantly requires not only accurate analytical models for sprays, but also an accurate representation of the fuel evaporation processes. In the last few years, an effort has been made to develop a model to address the formation and breakup of fuel sheets, secondary atomization, and droplet dispersion in the combustor flowfield (Rizk and Mongia, 1991; Rizk, 1994; Rizk and Chin, 1994). A fundamental basis for a fuel injection calculation method involving various atomization processes has been developed, and the present investigation involves the application of the fuel injection model to predict the performance of two distinctively different atomizers. Modeling activities have also included consideration of the effects of real fuel properties, finite diffusivity within the fuel droplet, and near-critical evaporation. These activities are particularly important due to the significant increase of the pressures and temperatures of the next generation gas turbine combustor.

Modeling of Fuel Injection Processes

Fuel atomization concepts rely on either injecting the fuel under high pressure into a relatively slow moving gas or utiliz-

Contributed by the International Gas Turbine Institute and presented at the 40th International Gas Turbine and Aeroengine Congress and Exhibition, Houston, Texas, June 5–8, 1995. Manuscript received by the International Gas Turbine Institute February 27, 1995. Paper No. 95-GT-225. Associate Technical Editor: C. J. Russo.

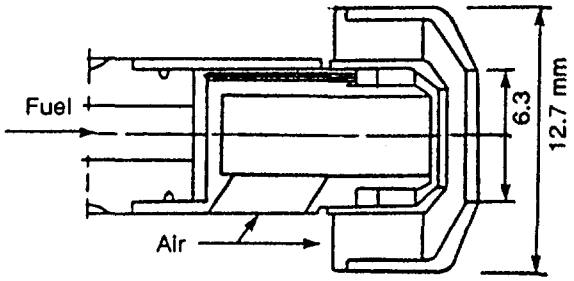

Fig. 1 Airblast atomizer used in the study

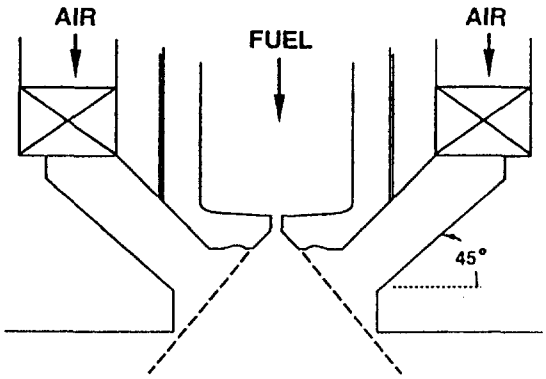

Fig. 2 Research air-assist atomizer

ing high-speed airblast to disintegrate the liquid sheet or jet prepared inside the atomizer. The fine sprays produced by these methods are attributed to the existence of high relative motion between the fuel stream and surrounding gases. It is, however, observed that good atomization quality could still be achieved under conditions of high-velocity air and high fuel pressure where the relative velocity may actually be low. This mode of operation is encountered in the pressure air-assist atomizers as well as in the hybrid airblast type. It is, therefore, realized that the liquid sheet or jet may disintegrate through mechanisms that vary according to the levels of air/fuel injection velocities.

Rizk and Mongia (1992) observed that in atomizers utilizing both pressure and airblast atomization concepts in one design, the atomizer acts more or less as a pressure type when air pressure drop across the atomizer is low. At high levels of air pressure differential and low fuel pressures, though, the performance of the atomizer is similar to that of the airblast kind. When both air pressure drop and fuel pressure are high, the effect of fuel injection pressure dominates the liquid sheet breakup and offsets the adverse effects of the reduced relative velocity under this condition. Based on these observations, a fuel injector calculation approach has been formulated to address liquid breakup mechanisms under different modes of operation. A description of the model is given in the following subsections.

Fuel Injection Concepts. Two fuel atomizers of different concepts were selected for the present investigation to illustrate the atomization modes involved and to evaluate model capabilities to match spray characteristics. Figure 1 shows a pure airblast atomizer where fuel is injected through six tangential ports into a swirl chamber to form a sheet that is immediately exposed to air on both sides. The outer air flows through a swirler, while the inner air passes through a number of tangential slots to the central passage. Figure 2 shows a research atomizer that operates as a simplex pressure type or as an air-assist atomizer, with either swirling or nonswirling air. The liquid is fed into the swirl chamber through three equally spaced slots, and the air swirler surrounding the fuel injector has six vanes. The details of the experimental effort are giving in next section.

Fuel Atomization Processes. The formation of liquid film in airblast atomizers may be achieved by spreading the liquid onto a prefilmer under the effect of high-velocity air. The prefilmer geometry, fuel and air properties, and operating parameters are the main factors controlling the film thickness, as shown by Rizk and Lefebvre (1980). In some other designs, the filming surface is made so short that the actual film leaving the atomizer is controlled by the swirl chamber and atomizer lip geometry. The mechanism of film formation in this case is more or less similar to the one associated with pressure swirl atomization (Rizk and Lefebvre, 1985). The film thickness is given by

$$T = 3.66(FN \cdot \mu_L \cdot d_c/(\rho_L \cdot \Delta P_L)^{0.5})^{0.25} \quad (1)$$

where FN is atomizer flow number, d_c is the characteristic dimension of fuel passage, ΔP_L is the fuel pressure drop, and μ_L and ρ_L are the viscosity and density of liquid.

In pressure atomizers, liquid is fed into a swirl chamber through a number of tangential ports to form a rotating film that exits the final orifice as an expanding conical sheet. The sheet is normally disturbed by ambient effects, causing fragments of liquid to break off the edge of the wavy sheet (Fraser et al., 1962; Dombrowski and Hooper, 1962). The balance with surface tension forces causes the formation of unstable waves with exponentially increasing amplitude. The most rapid growth rate of wave amplitude (β_{max}) is governed by sheet thickness (T) and liquid and air properties as given by

$$\beta_{max} = (\rho_a/\rho_L)(U_o/T)\mathrm{We}^{0.5} \quad (2)$$

where ρ_a is air density, U_o is sheet velocity, and We is the Weber number.

It has been shown by Fraser et al. (1962) that, in the investigation of jet disintegration by symmetric oscillations, a universally constant value of the ratio of wave amplitude to initial wave amplitude at orifice is reached at breakup. A similar criterion was assumed to apply to the disintegration of a liquid sheet. Using this concept, the breakup of the sheet is considered to occur as the total growth of the wave (E), which is given by the natural logarithm of the ratio of wave amplitudes, approaches a constant value of 12 (Dombrowski and Jones, 1963). The time needed to complete sheet breakup is, thus, calculated from

$$t = E/\beta_{max} \quad (3)$$

The sheet breakup distance is then determined from the breakup time and average sheet velocity. At breakup, a segment

Nomenclature

C_D = drag coefficient
d = drop diameter, m
d_c = characteristic dimension of atomizer, m
FN = atomizer flow number, m^2
g = gravitational acceleration, m/s^2
P = pressure, Pa
T = film thickness, m
t = time, s
U = velocity of carrier phase, m/s
u = fluctuating velocity of carrier phase, m/s
V = velocity of droplet, m/s
$\mathrm{W_e}$ = Weber number
X = molar fraction
β_{max} = growth rate of wave amplitude, s^{-1}
ΔP = pressure drop, Pa
μ = dynamic viscosity, kg/m-s
ρ = density, kg/m^3
σ = surface tension, N/m

of the sheet is assumed to separate with a width equivalent to half wavelength. The segment immediately contracts into a ligament with a diameter calculated by equating volumes of the segment and the formed ligament (Rizk, 1994).

The breakup mechanism associated with fuel pressure atomization is considered to dominate in the absence of air-assist or at low air pressure drop. At higher air pressure drop, the atomizer acts as an airblast type and the liquid sheet disintegrates under the effect of the aerodynamic forces. The balance of forces caused by gas pressure, surface tension, liquid inertia, and viscosity yields the following governing equation:

$$2\rho a U_r^2 - 2\sigma n^2 - \rho_L T(\partial f/\partial t)^2 - \mu_L T n^2(\partial f/\partial t) = 0 \quad (4)$$

where U_r is relative velocity, σ is surface tension, f is total growth of wave, and n is wave number of the disturbance imposed on the liquid stream and is given by

$$n = F^2\rho_a U_r/2\sigma \quad (5)$$

and F is the ratio of wave growth of liquid to that of inviscid liquid (Rizk and Chin, 1994). Breakup of the liquid stream due to wave growth concept occurs as the total growth of the wave approaches a constant value of 12. In the present calculation approach, it is assumed that the airblast atomization mode becomes effective when the relative velocity between the air and liquid sheet at the atomizer exit exceeds the initial injection velocity of the liquid.

The disintegrating parts of the ligaments instantly form spherical drops in the calculation, and these drops are assumed to move in the domain at the velocity of the sheet at the breakup point. The drops formed at breakup are allowed to deform according to the Weber number level experienced by each drop. The deformation of the drops is modeled considering a change of sphericity of drops with time toward circular disk shapes. The deformed drops may undergo secondary atomization, if the Weber number exceeds a critical value. A typical value of 13 is reported by Pilch and Erdman (1987). Secondary atomization due to the stripping breakup concept, described by Jenkins and Brooker (1965), becomes important when sufficient relative velocity exists between air and droplet.

The concept of the breakup of a liquid film of a uniform thickness into ligaments and drops leads to the formation of a single-size drop spray. Actual spray, however, contains droplets that vary over a wide range of sizes. This is mainly because of the nonuniformity in the ligament formation and the breakup resulting from the turbulent nature of the atomizing air and the local variation in film thickness. To account for this nonuniformity, the liquid film thickness at breakup is considered to vary around the mean value, with a probability distribution following a Gaussian curve. To account for the effects of the turbulent airstreams in ligament formation and breakup, similar approaches are followed to define the distributions of the ligament exit angle and disintegrated length around the nominal values.

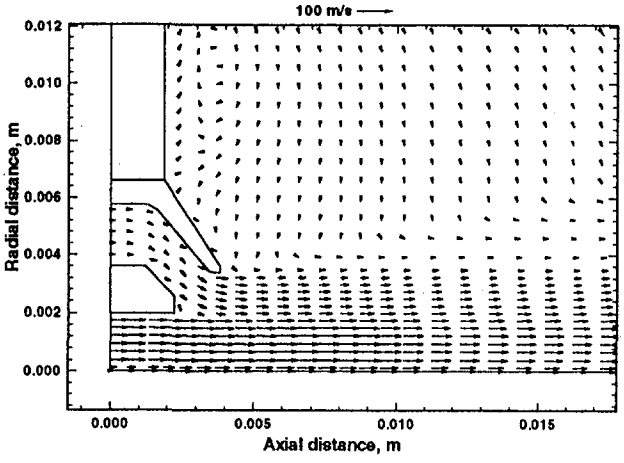

Fig. 3 Air velocity profiles inside and in the near region of the airblast atomizer

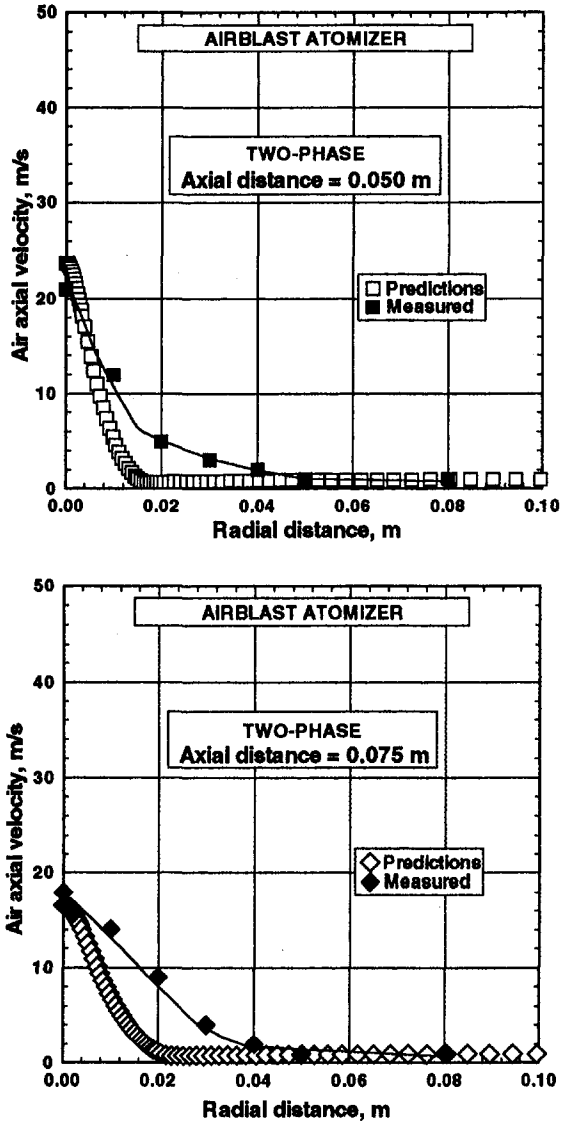

Fig. 4 Axial velocity profiles of air for airblast type

Spray Dynamics. Elliptic two-dimensional transport equations of continuity, momentum, and the standard $k-\epsilon$ turbulence model for an incompressible flow are used to establish the flowfield within and downstream of the atomizer. A boundary-fitted, curvilinear grid system is utilized to simulate the internal passages of the fuel nozzle. The momentum equation is given by

$$\partial/\partial x_j(\rho U_j U_i) = -\partial P/\partial x_i + \partial/\partial x_j(\mu\partial U_i/\partial x_j - \rho\overline{u_i u_j}) \quad (6)$$

where U_i is local instantaneous velocity component in the i direction and $-\rho\overline{u_i u_j}$ are the Reynolds stresses. Similar equations for the transport of turbulent kinetic energy and its dissipation rate are used in the calculation. The presence of the spray droplets within the gas phase is accounted for by the inclusion of the appropriate source terms that consider the effects of droplet mass and the interphase friction.

The two-phase flow model used in the present approach considers the effects of the instantaneous gas droplet relative veloc-

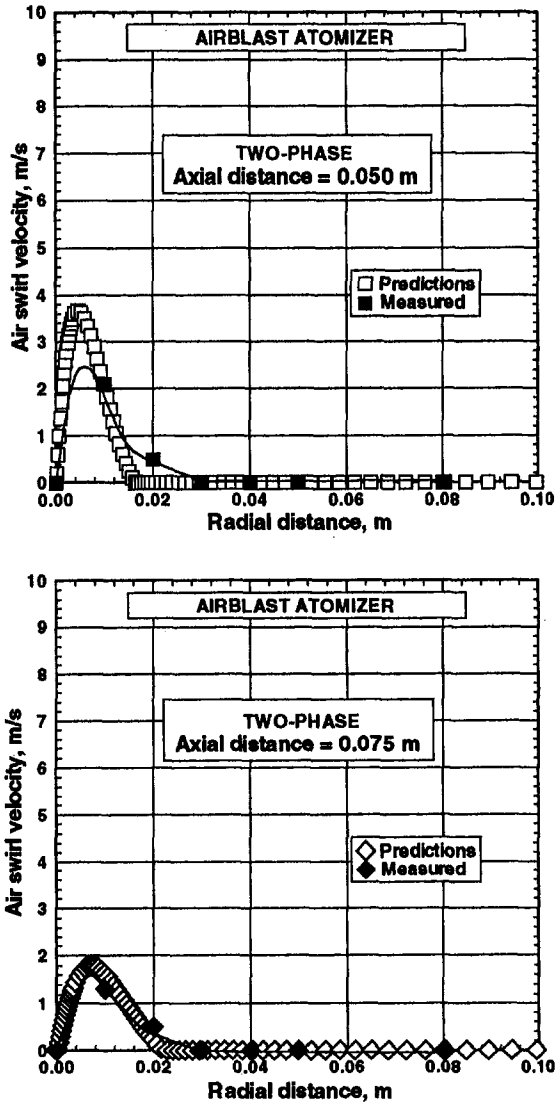

Fig. 5 Air swirl velocity profiles of airblast atomizer

ity on the transfer quantities and the interaction of the mean and fluctuating motion between the two phases. The model consists of a fully coupled combination of Lagrangian droplet and Eulerian fluid calculations. The equation of motion of each computation droplet in the i direction is given by

$$dV/dt = (Ui - Vi)/\tau_d + g_i \tag{7}$$

where

$$\tau_d = 4d\rho_L/(3C_D\rho a|U - V|) \tag{8}$$

The drag coefficient C_D is calculated from the standard experimental drag curve of solid sphere, and d and V are the instantaneous diameter and velocity of the droplet. U_i is the sum of the mean velocity of the carrier phase and the fluctuating velocity u_i that is chosen randomly from an isotropic Gaussian distribution. For each droplet, after a turbulent correlation time (τ), a new value for u_i is chosen. The τ is the minimum of the two scales: One is a typical turbulent eddy lifetime and the other is the residence time of the droplet in the eddy.

Spray Evaporation and Reaction. The calculation of the spray evaporation considers both the droplet heat-up period, where most of the heat transferred to the droplet from the surroundings is employed to raise the droplet temperature, and the steady-state evaporation. The heat available for heating up the droplet is obtained as the difference between the heat transferred from the gas to the drop and the heat used in vaporizing the fuel. The properties of the gas surrounding the drop are calculated at reference concentration and temperature based on the $\frac{1}{3}$ rule (Faeth, 1977). The mass transfer number used in the calculation depends on the partial pressure of the fuel vapor and the ratio of the molecular weights of fuel and air. The correction for forced convection effects is based on Reynolds and Prandtl numbers.

The evaporation calculation method described above considers the fuel drop to consist of a single component with a normal boiling temperature equal to the temperature corresponding to the 50 percent distillation point of the fuel. The drop temperature distribution is considered uniform with the thermal conductivity of infinity. Under the high pressure and temperature environment of future energy efficient gas turbine combustors, the droplet surface temperature can be close to critical values. Consequently, the liquid surface tension can approach zero with an attendant increase in the secondary breakup process. The usual assumptions of ideal gas law and absence of air solubility in the liquid fuel may be inaccurate, In addition, droplet-to-droplet interaction coupled with droplet breakup in high-pressure combustors may be significant.

To enhance the capability of the fuel injection model to simulate the evaporation process of real turbine fuels, a practical approach has recently been developed accounting for multicomponent, finite mass diffusivity and conductivity effects (Chin, 1994). The extension of the model to address near critical evaporation under high pressure and temperature conditions is illustrated by Chin (1995). In this detailed evaporation model, the fuel vapor pressure (P) is given by

$$P_{pe} = P_{pe=\infty} + (P_{pe=o} - P_{pe=\infty}) \exp(-C \cdot \mathrm{Pe}) \tag{9}$$

where Peclet number (Pe) is used as a controlling parameter to represent the diffusion resistance. It is given by

$$\mathrm{Pe} = m/2\pi d\rho_L D_F \tag{10}$$

where m is the evaporation rate and D_F is the diffusion coefficient. Equation (9) indicates the vapor pressure at any level of diffusivity is calculated from the estimate of vapor pressure at both zero and infinite diffusivity cases. The parameter (C) appearing in Eq. (10) depends on the fraction of fuel evaporated (E_v)

$$C = a_1E_v + a_2E_v^2 + a_3E_v^3 \tag{11}$$

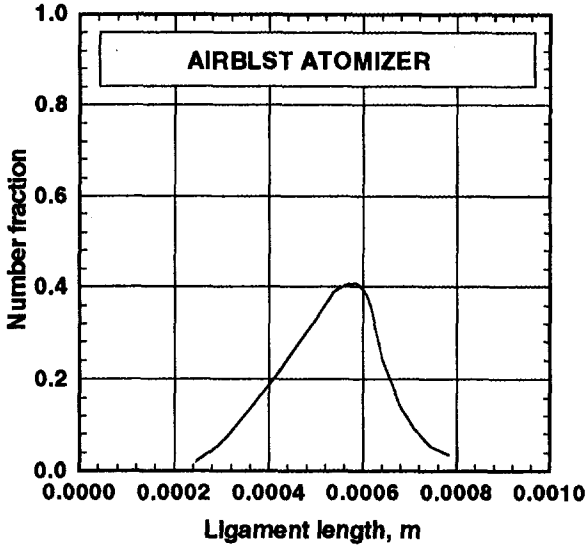

Fig. 6 Predicted ligament length distribution of airblast atomization

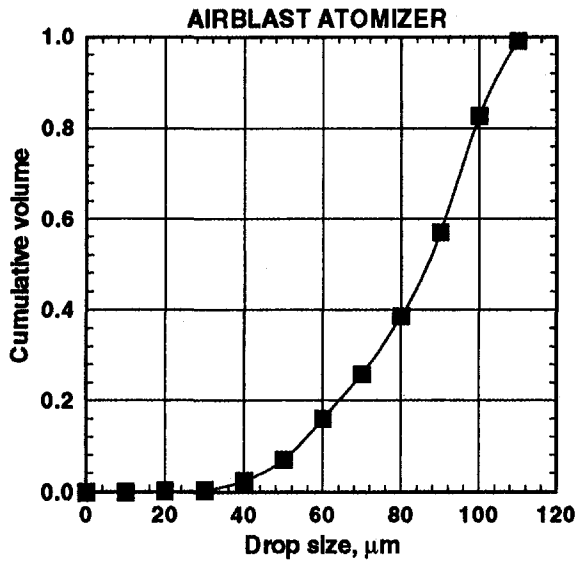

Fig. 7 Initial drop size distribution at ligament breakup of airblast atomizer

where the constants a_1, a_2, and a_3 have the values of 0.305, −0.35, and 0.14, respectively. The vapor pressures at the two extreme ends of the diffusivity scale are calculated using an expression of the following form:

$$P = f_1 \exp(-f_2/T_s) \tag{12}$$

The parameters f_1 and f_2 vary with the fraction of fuel evaporated and fuel types, and T_s is the drop surface temperature. The vapor pressure is then used to calculate the fuel vapor concentration and mass transfer number needed to estimate the fuel evaporation rate.

Under high-pressure critical conditions, the fuel vapor molar fraction (Xg) calculation needs to be modified to account for real gas effects and air solubility in liquid phase

$$X_g = X_f P_g / P_\infty \psi \tag{13}$$

where X_f is liquid concentration in droplet considering air solubility, P_∞ is ambient pressure, P_g is vapor pressure, and ψ is the vapor–liquid equilibrium coefficient representing real gas effects that can be significant under high pressure and temperature conditions.

Combustion modeling in multidimensional analysis is usually simplified by using a global approach that can provide fuel consumption and heat release rates. In the present fuel nozzle model, a two-step reaction mechanism is used (Srinivasan et al., 1983). The reaction rates of fuel and CO are evaluated by calculating the minimum of the rates given by the Arrhenius expression and the eddy breakup model to account for turbulence effects on combustion. The fuel reactions, as given by both methods, are

$$S_{fu1} = F_1 \rho^{1.5} m_{fu}^{0.5} m_{ox} \exp(-E_1/RT) \tag{14}$$

$$S_{fu2} = C_{R1} m_{fu} \epsilon / k \tag{15}$$

The constants F_1, E_1/R, C_{R1} are 3.3×10^{14}, 27,000, and 3.0, respectively, and m_{fu} and m_{ox} are mass fractions of fuel and oxygen. A similar approach is used to calculate the CO reaction rate.

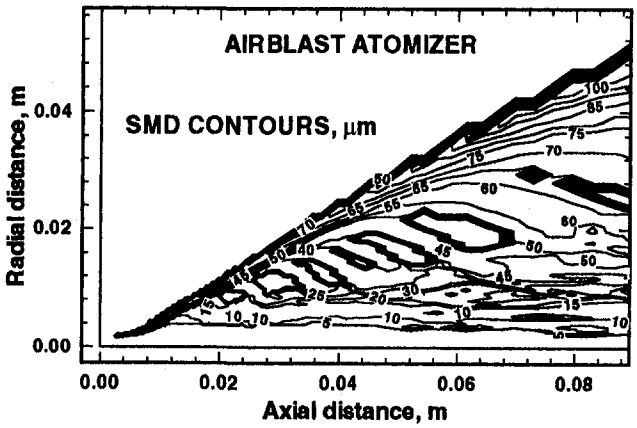

Fig. 8 Sauter mean diameter contours in airblast spray

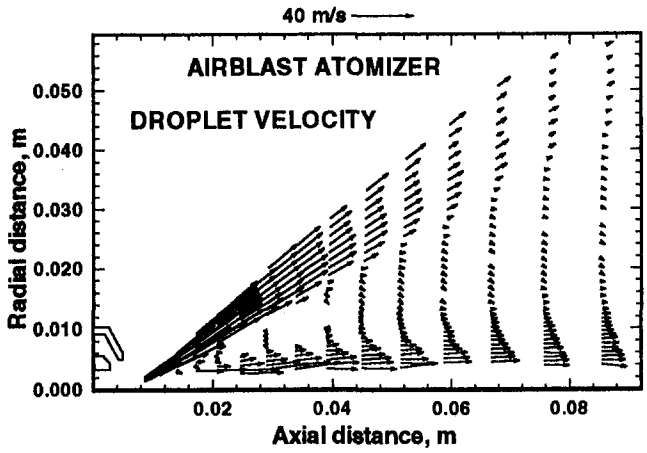

Fig. 9 Droplet velocity vectors for airblast atomizer

Fuel Injection Model Validation

Experimental. The fuel injection model was used in the present investigation to calculate the flow and spray characteristics of the pure airblast atomizer (Fig. 1) and the research air-assist atomizer (Fig. 2). The details of the experiment and test facility are given by McDonell and Samuelsen (1991a, b). Only a brief description of the test conditions and measurement technique is given here. For the airblast atomizer, the measured airflow effective area, airflow rate, and fuel/air ratio were 19.5 mm^2, 0.0021 kg/s, and 1.0, respectively. The research air-assist atomizer exit orifice diameter and air swirler angle are 0.4 mm and 52 deg. The selected airflow rate through the atomizer is 0.00129 kg/s, and the atomizer injects fuel at a rate of 0.00126 kg/s corresponding to fuel pressure differential of 400 kPa. In both atomizers, the fuel used was methanol.

The atomizers sprayed the methanol downward into a square duct and were mounted on a traverse system that provided three degrees of transitional freedom. A screen air-bulk velocity of 1 m/s was provided to avoid the recirculation of fine droplets to the measurement control volume. Two-component, phase Doppler interferometry was used for the simultaneous measurement of droplet size and velocity. The velocity of the gas phase was measured by seeding the airflow with alumina oxide particles of the nominal size of 1μ. In two-phase flows the gas velocity within the spray was deduced by measuring the velocity of the particles small enough to track the flow. Measurements were carried out in both nonreacting and reacting flowfield under normal atmospheric conditions.

Evaluation of Spray Characteristics. The calculations were performed on a work station using grid networks that simulate the internal passages and the flowfield of the atomizers

with a total number of grid points of 101 and 87 in the axial and radial directions, respectively. Provisions were made to block zones in the calculation domain to simulate the details of the atomizer geometry. A typical case would need approximately 3 hours of CPU time to converge, with about equal split between the flow and fuel injection calculations.

Airblast Atomizer. The predictions of the gas velocity vectors within the airblast atomizer and in the near region of the flowfield are plotted in Fig. 3. The results show the interaction between the two airstreams of the atomizer and the development of air velocity profiles with peaks moving towards the atomizer centerline. It should be noted that the outer swirler turns the airflow 52 deg with respect to the atomizer centerline, while the inlet air slots to the inner passage impart a modest degree of swirl to the central air stream.

Comparisons between the measured air velocity profiles and the calculations are illustrated in Figs. 4 and 5. Figure 4 shows the air axial velocity distributions under the two-phase flow conditions at two locations of 0.05 and 0.075 m from the nozzle exit; no measurements were taken closer than 0.05 m from the nozzle. The results indicate satisfactory agreement between the predictions and data, in particular near the atomizer centerline. At far downstream distance, the predicted axial velocity is somewhat lower than the measured velocity. The air swirl velocity profiles at the two axial locations are presented in Fig. 5, and although the model overpredicts the swirl component of the continuous phase near the atomizer, very good agreement with the data is obtained at locations farther away from the atomizer. The inlet conditions were based on inlet airflow rate and area and assumed uniform velocity distribution. More accurate simulation of the inlet boundary conditions and internal passages of the atomizer may further improve the predictions of the model.

The results of the ligament breakup are plotted in Fig. 6 in terms of a ligament length distribution. The figure shows that most of the ligaments break up within 1 mm of the atomizing edge. Although detailed measurements in this critical region are needed to verify the results, the range of ligament length observed in the figure is in reasonable agreement with the data reported by Rizk (1977). The initial drop size distribution at

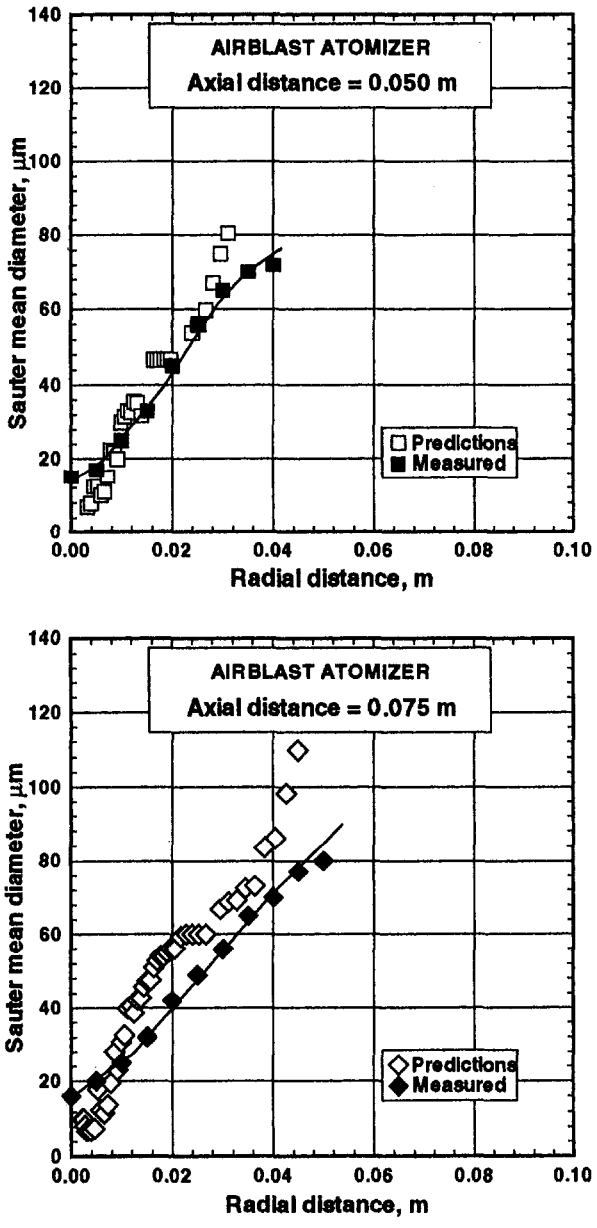

Fig. 10 Predicted and measured Sauter mean diameter profiles for airblast atomizer

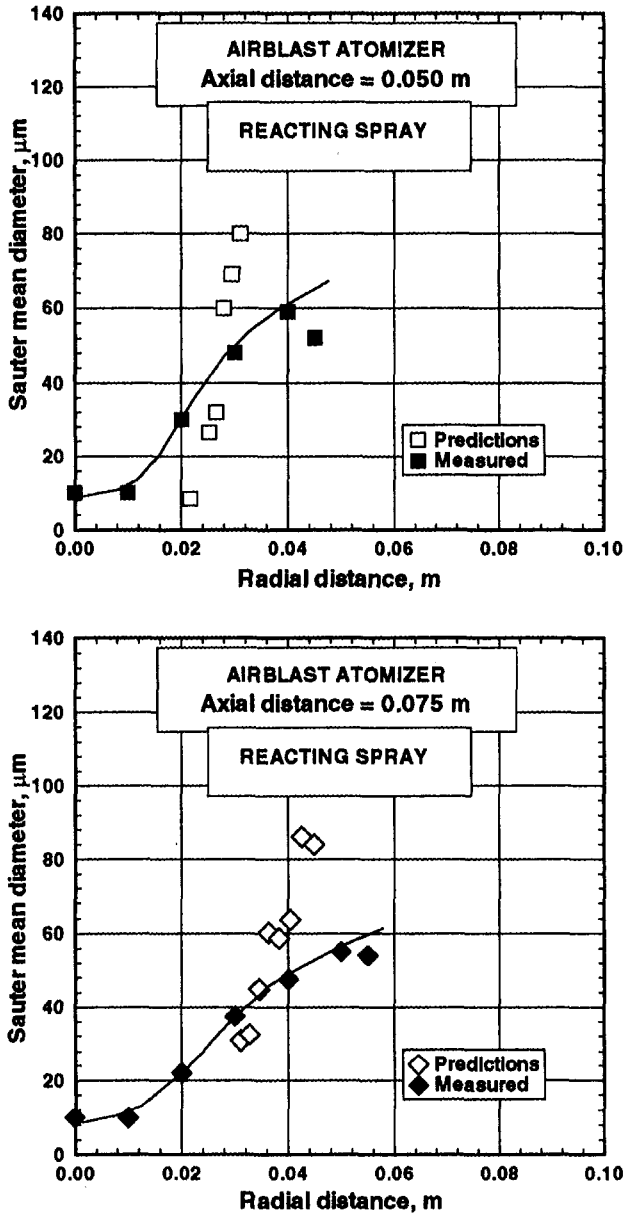

Fig. 11 Sauter mean diameter profiles in reacting spray of airblast type

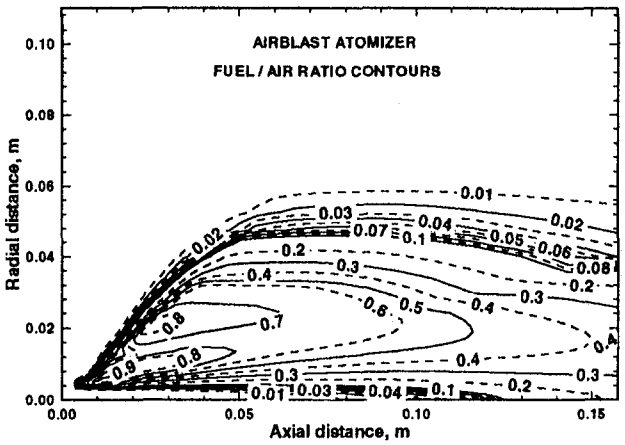

Fig. 12 Contours of fuel/air ratio in airblast atomizer flowfield

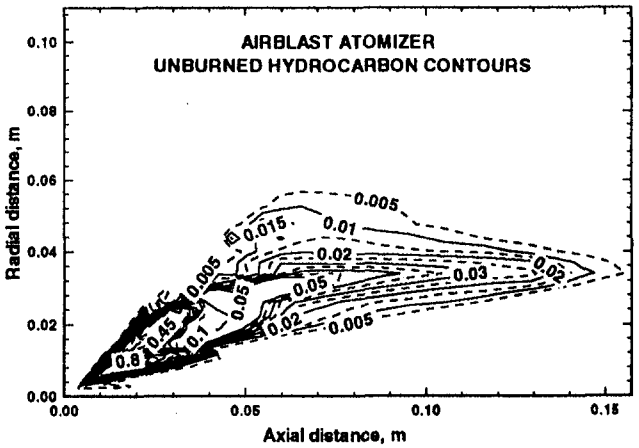

Fig. 14 Unburned hydrocarbon contours in airblast atomizer spray

the ligament breakup is shown in Fig. 7. The results indicate the initial spray formed downstream of the atomizer contains drops varying in sizes from 5 μm up to about 100 μm. Reduction in drop sizes occurs in the spray farther away from the atomizer due to droplet secondary breakup and evaporation.

An overall picture of the spray predicted under nonreacting conditions is shown in Figs. 8 and 9. Figure 8 illustrates the spray Sauter mean diameter (SMD) contours in the atomizer flowfield. The figure indicates the presence of the fine droplets near the atomizer centerline, while most of the larger drops tend to follow their original trajectories and stay toward the spray edge. It should be noted that the consideration of turbulence effects on droplet motion causes the fine droplets to spread toward the spray centerline, simulating the features found in real sprays. Figure 9 shows the corresponding droplet velocity vectors at various locations in the spray, as predicted by the model. The results indicate that large drops tend to lose their initial velocities as they stay in the outer region of the spray, while the smaller droplets gradually approach the relatively high air velocities that exist in the inner region of the spray.

Comparison between the predicted and measured SMD profiles at the two axial locations for the nonreacting case is illustrated in Figure 10. The agreement between the predictions and measurements of the SMD is very satisfactory in regards to the levels and radial spread. The model, however, predicts the presence of few large drops near the outer envelope of the spray and finer droplets near the atomizer centerline.

The results obtained for the reacting spray of the airblast atomizer (Fig. 1) are plotted in Figs. 11–15. The predictions of SMD radial distributions are given in Fig. 11 along with the measured data. The results show the agreement between the predictions and data is satisfactory near the atomizer; however,

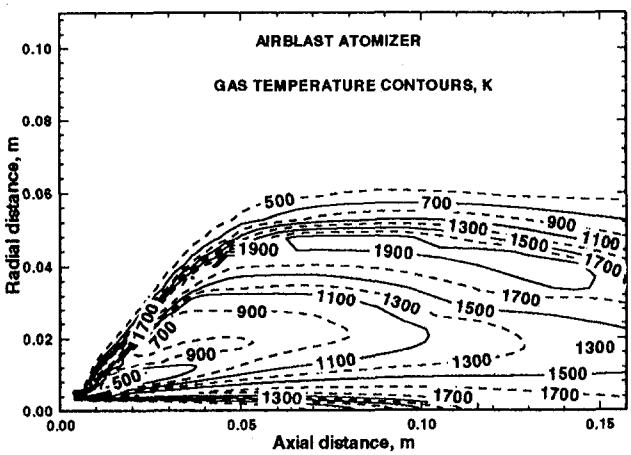

Fig. 13 Gas temperatures in airblast atomizer flowfield

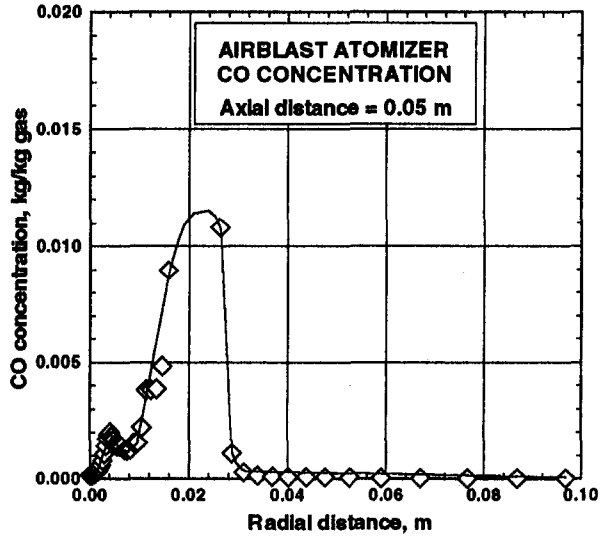

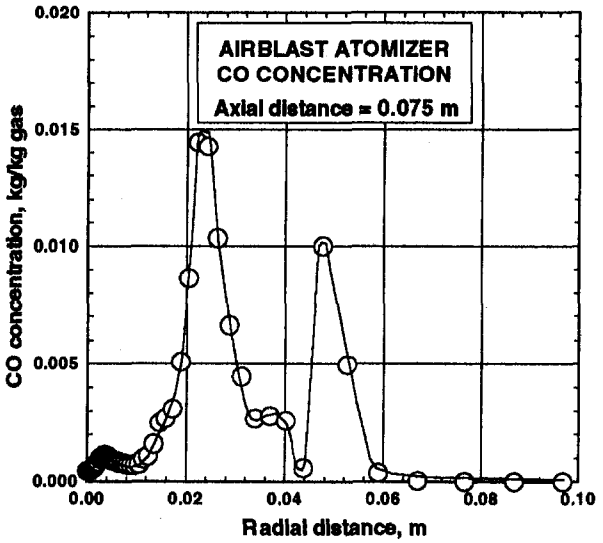

Fig. 15 Carbon monoxide concentrations in airblast atomizer reacting spray

it is noted that most of the fine droplets near the atomizer centerline are completely evaporated according to the calculations. The figure also shows the presence of few large drops toward the outer envelope of the spray that are not detected in the measurements. This is attributed to the differences in the gas velocity profiles between the measurements and calculation, overprediction of the evaporation rates, and the calculated reaction envelope features. It has been shown by Rizk and Chin (1994) that the higher evaporation rate is obtained with the conventional evaporation models as compared to those of the real evaporation model that accounts for multicomponent, finite mass diffusivity, and thermal conductivity effects. The difference is more pronounced under low temperature and pressure conditions. By using the enhanced evaporation calculation approach described in the previous section, it is anticipated that the complete evaporation of the fine droplets may be delayed enough to bring the predicted drop sizes near the centerline closer to the measured ones.

The contours of the fuel/air ratio in the atomizer flowfield are plotted in Fig. 12. The figure clearly shows a fuel-rich region occupies most of the spray volume with a significant reduction in fuel/air ratio occurring near the edges of the spray and toward the atomizer centerline. The fuel concentration is spread over a wider radial distance, with lower peaks, as the droplets travel farther downstream. The corresponding gas temperature contours in the atomizer flowfield are given in Fig. 13. Lower gas temperatures are observed in the fuel-rich region of the spray, surrounded by higher temperature regions in locations where the fuel/air ratio drops to more favorable levels. Although no detailed measurement of the gas temperature profiles was made,

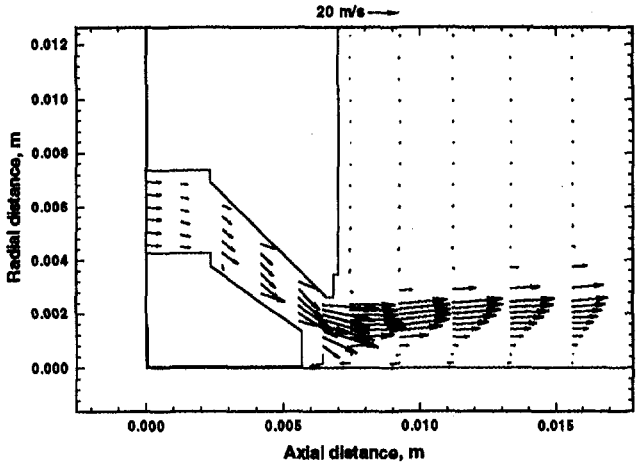

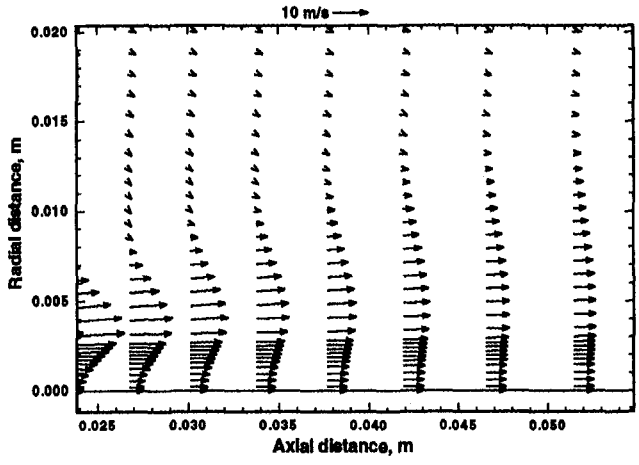

Fig. 16 Air velocity vectors within and downstream of air-assist atomizer

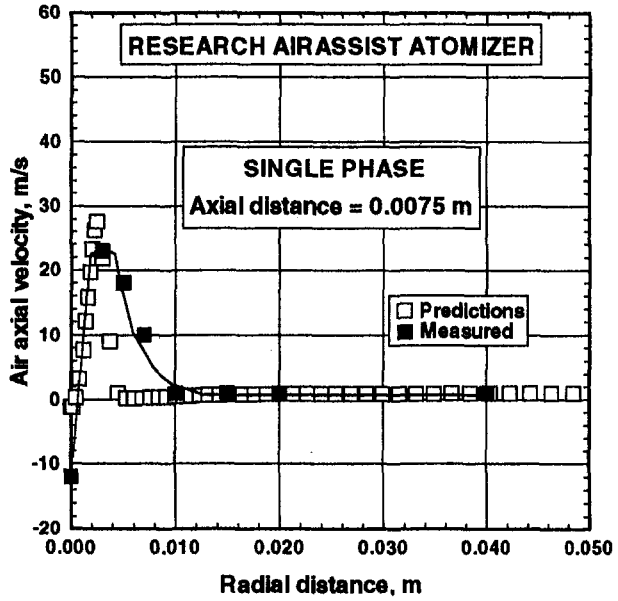

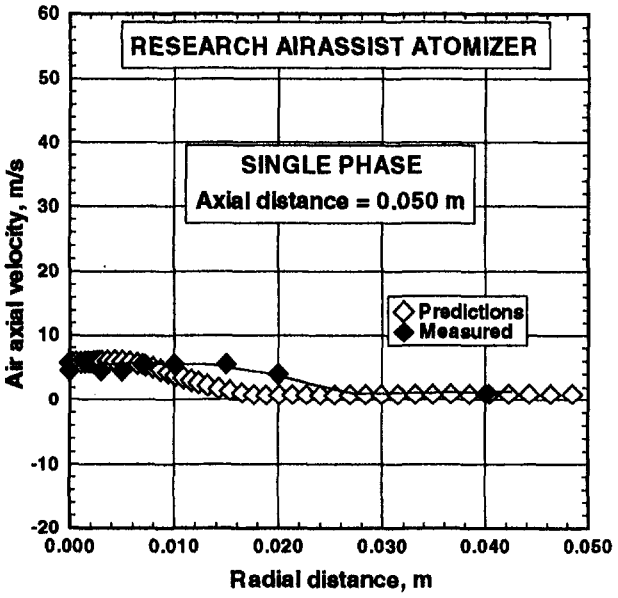

Fig. 17 Single-phase air axial velocity profiles for air-assist atomizer

the overall picture of the reaction envelope given by McDonell and Samuelsen (1991a) agrees with the calculations.

Figure 14 shows the contours of the unburned hydrocarbons in the airblast atomizer spray. The results reflect the balance between the consumption of the fuel and the supply of fresh fuel vapor at each location. The presence of a large concentration of unburned fuel is evident even at distances exceeding 0.10 m from the atomizer. It is also noticed that most of the fuel in the spray core is consumed early in the flowfield, leaving a larger concentration of fuel near the edge of the spray.

The CO profiles are plotted in Fig. 15. The figure shows that the CO is formed in larger quantities, exceeding the amount of CO conversion to carbon dioxide (CO_2) over a large portion of the flowfield. Not until a distance over 0.075 m, a reduction of CO concentration is observed in the flame. Once again, the absence of CO is noticed in the spray core and toward the outside of the flame region. Although the calculations of pollutant species are not supported by detailed measurements, they provide insight into the reacting sprays produced by a typical

gas turbine airblast atomizer. The effort needed to reduce emission levels produced by the combustor could significantly benefit from such analysis.

Research Air-Assist Atomizer. The general features of the air flowfield within and in the near region of the air-assist atomizer given by the model are illustrated in Fig. 16. It is observed that the velocity profile peaks are located away from the atomizer centerline due to the air swirler effect. The profiles become more uniform as the downstream distance increases. The calculated air velocity profiles are compared with the measurements at a number of axial locations in Fig. 17. The figure shows the air axial velocity is well predicted in regard to peak values. The results, however, indicate that the measured velocity profile has more spread radially outward than the calculated one. These calculations show that the swirling airflow within the atomizer passage maintains its radially inward motion even after leaving the atomizer.

A summary of the results obtained for the atomizer flowfield under two-phase flow conditions is plotted in Fig. 18, and shows the measured and predicted velocity components at an axial distance of 0.0075 m. Satisfactory agreement with the data is observed in the figure, in particular the location and the peaks of the velocity profiles. Once again, narrower profiles are predicted than the measured ones.

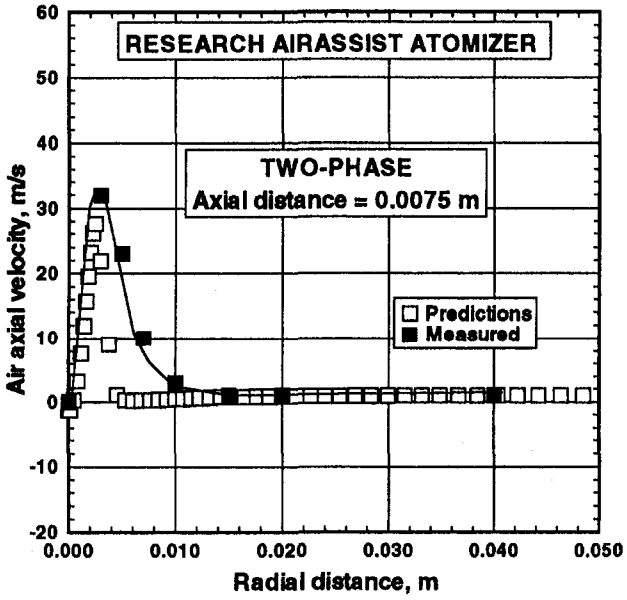

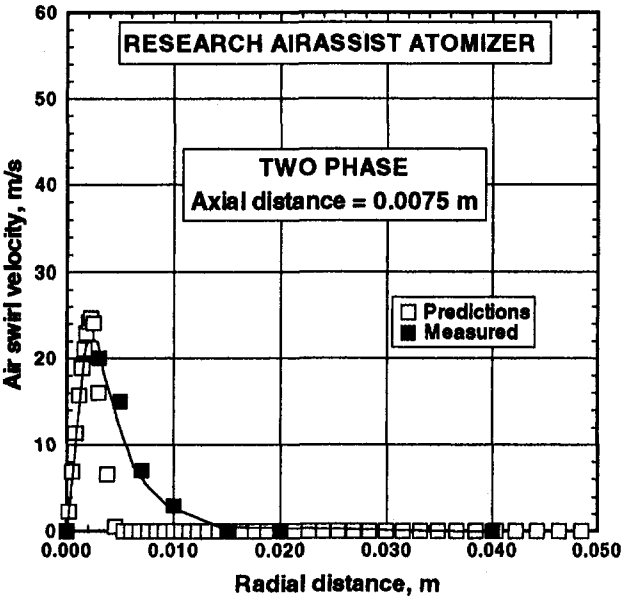

Fig. 18 Air velocities in two-phase flow of air-assist atomizer

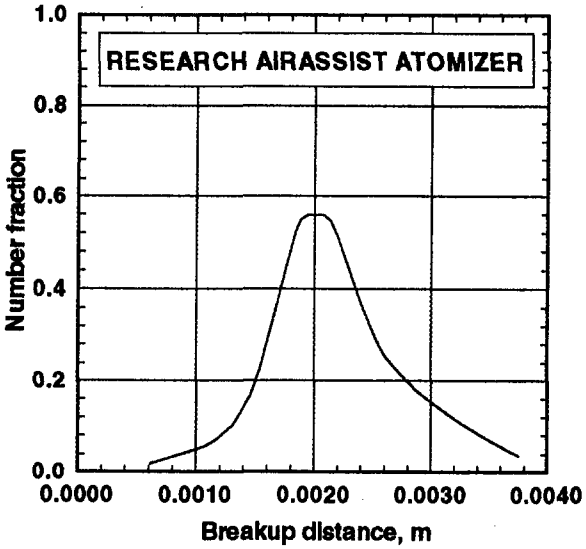

Fig. 19 Air-assist sheet breakup distance

As described in the previous section, the liquid film formed inside the simplex pressure injector of the air-assist atomizer exits the final orifice as an expanding conical sheet. The breakup of the sheet under the combined effects of fuel pressure and airblast is considered in the fuel injection model. The results of the sheet breakup are plotted in Fig. 19 as a breakup distance distribution. It can be seen that the liquid sheet disintegrates over a range of distance from 0.001 to 0.004 m from the atomizer fuel orifice. The disintegrated segments of the sheet immediately contract into ligaments that subsequently break up into drops. The distribution of these initial drops formed at ligament breakup is plotted in Fig. 20. The figure shows the initial spray formed downstream of the atomizer contains a wide variety of drop sizes covering a range from 5 to over 90 μm. These drops may undergo further reduction in size due to secondary atomiza-

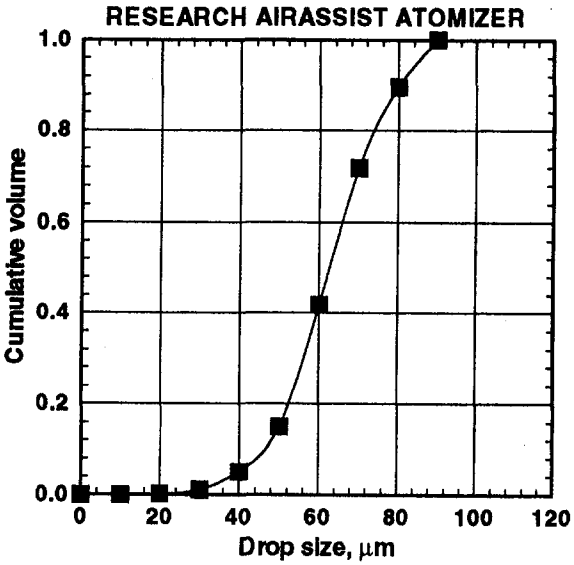

Fig. 20 Initial drop size distribution of air-assist atomization

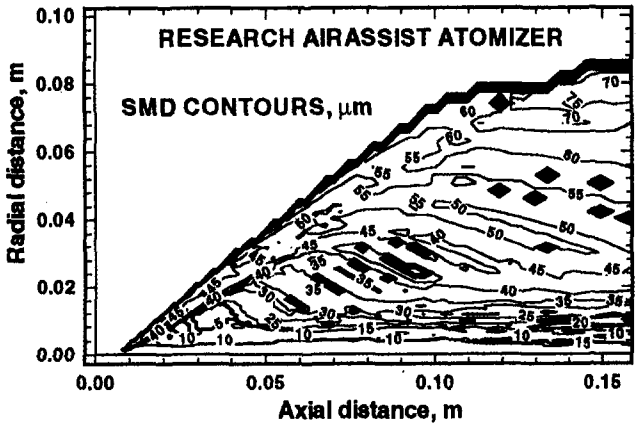

Fig. 21 Predicted Sauter mean diameter distribution in air-assist spray

tion that is governed by the relative velocity with respect to the surrounding air.

An overall view of the predicted SMD distribution in the spray is given in Fig. 21. The figure demonstrates similar trends, in regard to drop sizes and trajectories produced under air-assist atomization, to those obtained with the airblast atomizer. The stochastic treatment of the spray dynamics brings fine droplets to the core of the spray. The corresponding droplet velocity vectors in the atomizer flowfield are plotted in Fig. 22. It is observed that most of the droplets move toward the outer envelope of the spray and rapidly lose their momentum, but the fine droplets near the atomizer centerline tend to follow the air velocity pattern closely in this region.

The calculated SMD profiles at various axial locations are compared to the measurements in Fig. 23. It is obvious that at locations near the atomizer, the predicted air flowfield with less radial outward spread causes the formed droplets in the spray to stay closer to the centerline. Better agreement between the calculations and the measured data is observed at larger axial distances, which indicates that the developed model accounts for the key processes involved in the fuel atomization.

Summary and Conclusions

The present investigation involved the predictions of the flow and spray characteristics of two different fuel atomizers representing the airblast and air-assist atomization concepts. In the first type, fuel film disintegration relies solely on the impact of the high velocity air on both sides of the film. In the air-assist

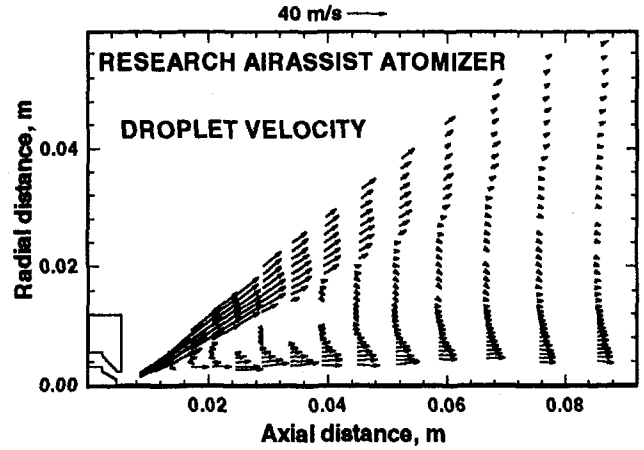

Fig. 22 Droplet velocities in air-assist atomizer spray

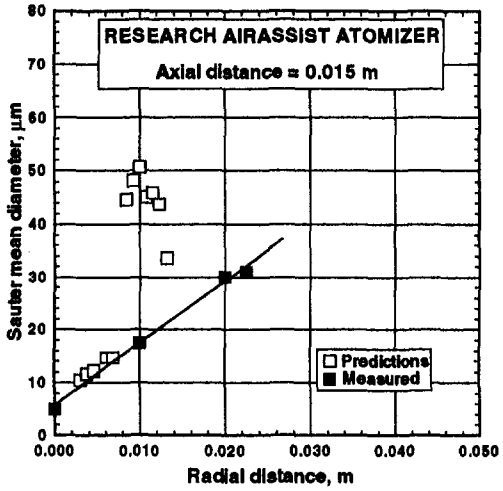

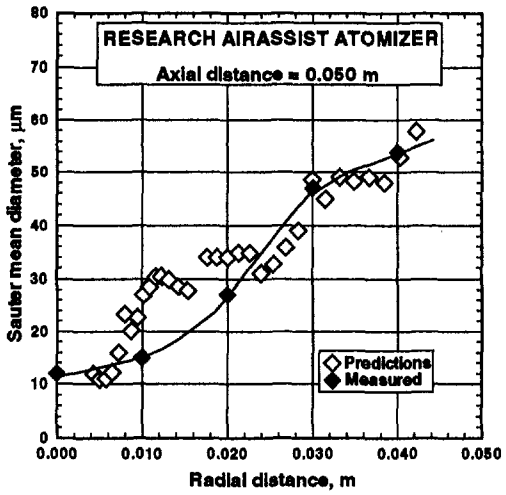

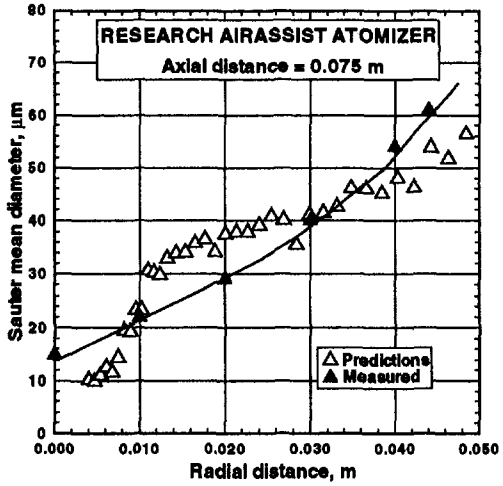

Fig. 23 Comparison between predictions and Sauter mean diameter data of air-assist atomizer

atomizer, both fuel pressure and airblast forces are utilized to atomize the fuel.

A fuel injection model has been formulated involving the two-dimensional simulation of airflow through and downstream of the atomizer and addressing the formation and breakup of liquid films into ligaments and drops. The model includes provisions for secondary atomization in addition to a stochastic Lagrangian treatment of spray dynamics. The calculation of

spray evaporation considers both a droplet heat-up period and steady-state evaporation. The fuel vapor concentration is based on partial pressure concept, and the properties of the gas surrounding the droplet are evaluated at reference conditions using the $\frac{1}{3}$ rule. An enhanced model has been formulated that accounts for real turbine fuel characteristics of multicomponent finite mass diffusivity and conductivity and addresses near critical evaporation, droplet breakup process, and droplet–droplet interaction. A two-step reaction mechanism with reaction rates evaluated using the minimum of the rates given by Arrhenius expression and eddy breakup model is utilized in the present model.

The results obtained for the airblast atomizer indicates satisfactory agreement between model predictions of air velocity components and data under nonreacting and reacting conditions, in particular near the atomizer centerline. Although the model overpredicts the swirl component of air near the atomizer, very good agreement with the data is obtained farther away from the atomizer. Ligament formation and breakup modeling shows most of the ligaments formed at the atomizing lip breakup within 1 mm distance. These results agree qualitatively with the data reported in the literature, which emphasizes the need for accurate measurements in the near region of the atomizer. The predictions of the SMD distributions agree well with the measurements and demonstrate the importance of the accurate simulation of the turbulence effects on droplet dispersion.

The calculation also shows that the fuel-rich region occupies most of the spray volume with significant reduction in fuel/air ratio near the edges of the spray and toward the atomizer centerline. The gas temperature calculations demonstrate two-peak profiles indicating the locations of the highest reaction rates in the atomizer flowfield. The calculations also indicate the presence of significant amounts of UHC and CO at large axial locations downstream of the atomizer.

The predictions of the air velocity profiles in the research air-assist atomizer flowfield are in good agreement with the measured data obtained for both single- and two-phase flow cases. The results, however, indicate the measured velocity profile has more spread radially outward than the calculated profile. The calculation of the sheet breakup under the combined effects of fuel pressure and airblast typical in this type of atomizer shows the expanding conical sheet disintegrates over a range of distances from 0.001 to 0.004 m from the atomizer fuel orifice. The subsequent formation of ligaments from disintegrated sheet segments and their breakup yield a wide variety of drop sizes in the initial spray.

Near the atomizer exit, the predicted air flowfield with less radial spread causes the droplets to stay closer to the centerline than the measured profile. At larger axial distances, better agreement with the data is observed. The stochastic treatment of the droplets in the present model well captures the presence of fine droplets in the spray core.

References

Chin, J. S., 1994, "An Engineering Calculation Method for Multi-Component Stagnant Droplet Evaporation With Finite Diffusivity," ASME Paper No. 94-GT-440.

Chin, J. S., 1995, "An Engineering Calculation Method for Turbine Fuel Droplet Evaporation at Critical Conditions With Finite Liquid Diffusivity," AIAA Paper No. 95-0494.

Dombrowski, N., and Hooper, P. C., 1962, "The Effect of Ambient Density on Drop Formation in Sprays," *Chem. Eng. Science,* Vol. 17, pp. 291–305.

Dombrowski, N., and Johns, W. R., 1963, "The Aerodynamic Instability and Disintegration of Viscous Liquid Sheets," *Chem. Eng. Science,* Vol. 18, pp. 203–214.

Faeth, G. M., 1977, "Current Status of Droplet and Liquid Combustion," *Prog. in Energy and Combustion Science,* Vol. 3, pp. 191–224.

Fraser, R. P., Eisenklam, P., Dombrowski, N., and Hasson, D., 1962, "Drop Formation From Rapidly Moving Liquid Sheets," *AIChE Journal,* Vol. 8, No. 5, pp. 672–680.

Jasuja, A. K., 1979, "Atomization of Crude and Residual Fuel Oils," ASME JOURNAL OF ENGINEERING FOR POWER, Vol. 101, pp. 250–258.

Jenkins, D. C., and Booker, J. D., 1965, *The Time Required for High Speed Air Streams to Disintegrate Water Drops,* Ministry of Aviation, Aeronautical Research Council, London, CP827.

Lefebvre, A. H., 1989, *Atomization and Spray,* Hemisphere Publishing Corporation.

McDonell, V. G., and Samuelsen, G. S., 1991a, "Gas and Drop Behavior in Reacting and Non-reacting Airblast Atomizer Sprays," AIAA *J. Propulsion and Power,* Vol. 7, No. 5, pp. 684–691.

McDonell, V. G., and Samuelsen, G. S., 1991b, "Structure of Vaporizing Pressure Atomized Sprays," University of California, Irvine, Internal Report.

Mostafa, A. A., and Mongia, H. C., 1987, "On the Modeling of Turbulent Evaporating Sprays: Eulerian Versus Lagrangian Approach," *Int. J. Heat Mass Transfer,* Vol. 30, No. 12, pp. 2583–2593.

Pilch, M., and Erdman, C. A., 1987, "Use of Breakup Time Data and Velocity History Data to Predict the Maximum Size of Stable Fragments for Acceleration Induced Breakup of Liquid Drop," *Multiphase Flow J.,* Vol. 13, No. 6, pp. 741–757.

Rizk, N. K., 1977, "Studies on Liquid Sheet Disintegration in Airblast Atomizers," Ph.D. Dissertation, Cranfield Institute of Technology, England.

Rizk, N. K., and Lefebvre, A. H., 1980, "Influence of Liquid Film Thickness on Airblast Atomization," ASME JOURNAL OF ENGINEERING FOR POWER, Vol. 102, pp. 706–710.

Rizk, N. K., and Lefebvre, A. H., 1983, "Influence of Atomizer Design Features on Mean Drop Size," *AIAA J.,* Vol. 21, No. 8, pp. 1139–1142.

Rizk, N. K., and Lefebvre, A. H., 1985, "Internal Flow Characteristics of Simplex Swirl Atomizers," AIAA *J. of Propulsion and Power,* Vol. 1, No. 3, pp. 193–199.

Rizk, N. K., and Mongia, H. C., 1991, "Model for Airblast Atomization," AIAA *J. Propulsion and Power,* Vol. 7, No. 3, pp. 305–311.

Rizk, N. K., and Mongia, H. C., 1992, "Performance of Hybrid Airblast Atomizes Under Low Power Conditions," AIAA Paper No. 92-0463.

Rizk, N. K., 1994, "Model for Research Swirl Atomizers," AIAA Paper No. 94-2777.

Rizk, N. K., and Chin, J. S., 1994, "Comprehensive Fuel Nozzle Model," AIAA Paper No. 94-3278.

Simmons, H. C., 1979, "The Predictions of Sauter Mean Diameter for Gas Turbine Fuel Nozzles of Different Types," ASME Paper No. 79-WA/GT-5.

Srinivasan, R., Reynolds, R., Ball, I., Berry, R., Johnson, K., and Mongia, H., 1983, *Aerothermal Modeling Program, Phase I Final Report,* NASA CR-168243.

Sturgess, S. A., Syed, S. A., and McMannus, K. R., 1984, "Calculation of a Hollow-Cone Spray in a Uniform Air Stream," AIAA *J. Propulsion and Power,* Vol. 1, No. 5, pp. 360–368.

Effects of Cycle Operating Conditions on Combustor Performance

N. T. Davis

V. G. McDonell

G. S. Samuelsen

UCI Combustion Laboratory,
University of California,
Irvine, CA 92697-3550

To mitigate the environmental impact of next-generation gas turbine combustors, the emission performance at each condition throughout the load duty cycle must be optimized. Achieving this with a single combustor geometry may not be possible. Rather, the mixing processes and air flow splits must likely be modified as a function of load in order to (1) abate the emission of oxides of nitrogen, (2) maintain combustion efficiency, and (3) preclude lean blow-out over the entire duty cycle. The present study employs a model combustor to evaluate combustor performance as a function of load and explore the application of variable geometry to optimize performance at each condition. A parametric variation of flow splits is conducted at each load condition by independently adjusting the primary jet area and swirler choke area. The resultant impact on combustor performance is measured and quantified in terms of a cost function. The cost function is defined to increase with improving combustor performance (e.g., improving combustion efficiency and/or declining NO_x emissions). Cycle operating conditions are found to alter the response mappings of efficiency and NO_x. As a result, the optimal configuration of the combustor changes as the load is varied over the duty cycle. The results provide guidance on the application of active control.

Introduction

The environmental impact of aero and stationary gas turbines is the focus of major research initiatives in both the United States and abroad. In particular, attention is directed to the reduction of oxides of nitrogen (NO_x) while maintaining high efficiency and broad stability limits.

This challenge is exacerbated by a trend toward higher pressure ratios and increased combustor inlet temperatures. It is an inevitable requirement that emissions must be minimized not at just one load, but over the complete duty cycle of a given engine.

As a result, the optimum design must minimize both NO and CO at each load condition and preclude blow-out. As the load changes, the combustor must adapt to attain the optimal emission signature. A fixed geometric configuration is, at the moment, the approach employed. An "adaptive" control approach, such as that employed by Brouwer et al. (1990) and Padmanabhan et al. (1994), will eventually be required to optimize combustor performance over the conflicting demands of the duty cycle.

This paper addresses the potential application of geometric control to a duty cycle. A duty cycle is simulated with the goal of identifying the issues that must be considered in the development of practical systems. To evaluate an adaptive system, (1) geometric variation that can produce the desired combustor performance must first be identified, and (2) actuators that are amenable to implementation must be selected. In the present case, the technique selected to control combustor performance is the partitioning of the combustor air between the swirl generator, the primary jets, and the secondary jets. As a result, the local fuel–air ratios as well as the aerodynamic properties of the dome region are manipulated as a function of load. The combustor adopted has a "variable geometry" design, an approach that (for some time) has been identified to mitigate pollutant emission (e.g., Henderson and Blazowski, 1973, and Bahr, 1973). This paper addresses the combustor mapping and not the active control aspect. In particular, the objectives of the current study are to (1) develop a combustor amenable to electronic articulation, (2) evaluate the response of the combustor to articulation, and (3) determine the potential and/or shortfalls of the design before implementing active control.

Contributed by the International Gas Turbine Institute and presented at the 40th International Gas Turbine and Aeroengine Congress and Exhibition, Houston, Texas, June 5–8, 1995. Manuscript received by the International Gas Turbine Institute March 2, 1995. Paper No. 95-GT-221. Associate Technical Editor: C. J. Russo.

Experiment

Combustor. To examine the response of combustor performance to duty-cycle variation and geometric manipulation, a variable geometry model combustor was designed and constructed. A schematic is shown in Fig. 1. The variable geometry combustor retains the 80 mm inner diameter (D_c) of previous experiments (e.g., Cameron et al., 1988), while incorporating modularity for future studies. The total length of the combustion chamber is $3D_c$. The spacing between the quarl and the primary jets' centerline is D_c, as is the distance between the primary jets' and secondary jets' centerline. The overall layout was selected to be representative of gas turbine combustor aerodynamics, provide relatively "clean" boundary conditions, be amenable to active control, and exhibit flexibility for future modifications.

The unit has two articulators: (1) swirl air choke and (2) primary jet choke. Figure 2 shows the primary jet choke in more detail. Essentially, this device consists of two matched donuts. By rotating the outer "donut," the air distribution is apportioned by the level of overlap in the respective slots. The swirl choke operates in a similar manner in that air flow to the swirl cup is articulated by restricting the air flow. Control of the airflow distribution within the combustor allows tuning the operation of the combustor as cycle conditions vary.

The primary jets consist of six slots nominally 8 mm tall and, when fully open, 21 mm wide. The swirl choke consists of two plates drilled with matching sets of three 19-mm-dia holes. Secondary jets consist of six 10.75-mm-dia holes. The articulated area or each choke's range spans the range from fully

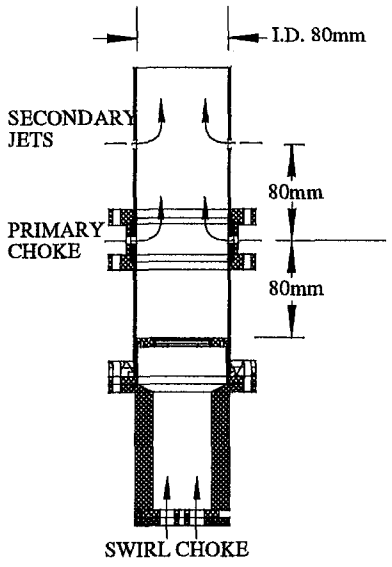

Fig. 1 Combustor, partial assembly

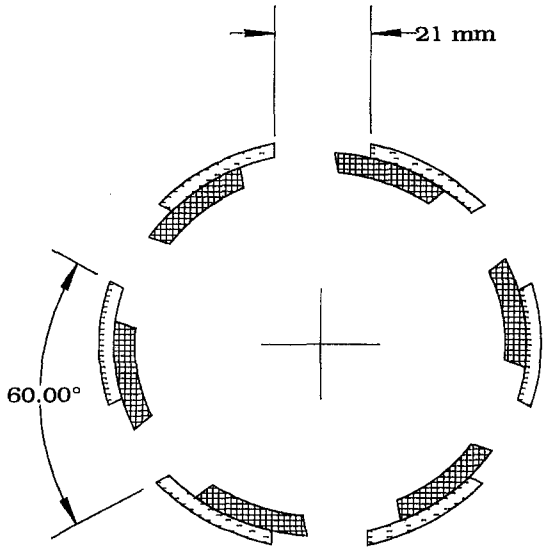

Fig. 2 Primary choke, top view

closed to the maximum area of the holes. Note, over-restriction of the swirl air produces a negative effect upon the combustor stability and was therefore avoided.

It was assumed that flow splits were distributed in relation to the effective area. Six jet flow settings and four swirl flow settings were established. The primary jets have an effective area of 0, 92, 184, 367, 550, and 733 $\times 10^{-6}$ m^2, the swirl 98, 132, 148, and 162 $\times 10^{-6}$ m^2, and the secondary jets 487 $\times 10^{-6}$ m^2 (fixed). Calculated air flow distributions of 0 to 56 percent, 7 to 28 percent, and 35 to 85 percent for the primary, swirl, and secondary air flows, respectively. Pressure drops across the liner were 0.7 to 2.4 percent, 1.4 to 6.3 percent, 1.1 to 5.0 percent, and 1.4 to 6.3 percent, respectively, for the four load conditions (after correction for losses across the mixing section).

The current study employed a swirl cup from a GE/SNECMA CFM-56-3 gas turbine as the swirler. The selection of this component was predicated by (1) operating experience within the laboratory (e.g., Wang et al., 1994a, b), and (2) the advantage of using practical hardware as an integral component of the model combustor. The nozzle selected was a Delevan 80 deg simplex with a flow number of 1.50.

Air Preheat. The plenum air was preheated with a 25 kW Watlow circulation heater Model 9335 with a Series 965 digital controller. For the cycle conditions examined, air was preheated to a temperature of either 93°C (200°F) or 204°C (400°F) before entering the plenum.

Duty Cycle. The duty cycle selected for this study is presented in Table 1. The conditions were selected to be representative of a typical operational unit with the exception of pressure which, for the present experiment, was maintained at one atmosphere. The fuel used in this study was commercially available Jet A.

The reference velocity is defined as:

$$U_{\text{ref}} = \frac{\dot{m}}{\rho_3 A_{\text{ref}}} \tag{1}$$

where:

ρ_3 = density of air entering combustor
A_{ref} = cross-sectional area of combustor

Emissions Sampling. For this series of experiments, an extractive probe fed a sample to a bank of analyzers. Instead of traversing the apparatus, a mixing section commingled the exhaust gas to allow for one spatial data point to represent the entire reaction. The mixing section consisted of a 0.13-m-dia pipe 0.6 m long with four baffles to promote mixing. The sample was taken at the centerline of the mixer, 0.16 m upstream of the mixing section exit.

Five analyzers were used in the open loop tests conducted: O_2, CO_2, CO, NO_x, and UHC. Information regarding the analyzers is presented in Table 2. Uniformly, the sensors have an accuracy of ±1 percent full scale, with the lowest possible range used in each case (e.g., NO_x at 100 ppm full scale for giving an accuracy of ±1 ppm).

Cost Function. Since improving combustion performance in one area (e.g., NO reduction) can degrade performance in another (e.g., combustion efficiency), a means of quantitatively measuring the trade-off is required. In addition, when a multivariable system is evaluated, a quantitative means of weighting the emphasis of each performance criterion is a prerequisite. In optimal control this is accomplished by establishing a mathematical representation of the "value" of the state of the system.

Table 1 Duty cycle

Condition	Description	Equivalence Ratio ϕ	Inlet Temperature °C	Reference Velocity m/sec	Air kg/s	Fuel kg/s*10-3
1	Low Power	0.20	93	10	0.049	0.64
2	Med. Power I	0.25	93	12.5	0.061	0.98
3	Med. Power II	0.25	204	12.5	0.047	0.64
4	High Power	0.30	93	15	0.073	1.40

Table 2 Sensor description

Sensor	Model #	Type	Effluent	Max. Range
Horiba	PIR-2000	NDIR	CO	7500ppm
Horiba	PIR-2000	NDIR	CO_2	5l%
Horiba	CLA-120	Chemiluminescent	NO_x	100ppm
Horiba	MEXA-1120TFI-F	H, Flame Ionization	HC	500ppm
Beckman Industries	755	Paramagnetic	O_2	25%

In the present study, this is accomplished by the use of the following cost function:

$$J = \omega^*_{(\text{eff})} J_{(\text{eff})} + \omega^*_{(\text{NO}_x)} J_{(\text{NO}_x)} \quad (2)$$

For this series of experiments, combustion efficiency and NO_x were weighted by: $\omega_{(\text{eff})} = 0.667$ and $\omega_{(\text{NO}_x)} = 0.333$. The cost functions for efficiency ($J_{(\text{eff})}$) and NO_x ($J_{(\text{NO}_x)}$), presented in Figs. 3 and 4, respectively, are designed such that maximizing J optimizes performance.

For the determination of a representative efficiency cost function, the following criteria must be satisfied: (1) a significant sensitivity in the desired operating range, (2) little reward for poor efficiency, and (3) a monotonically increasing value as the efficiency improves. A hyperbola was found to suit the requirements. However, in order to achieve sensitivity to efficiency changes in poor efficiency regimes and maintain a steep gradient in the operating range, a composite function was formed. As a result, from 99.8 to 100 percent combustion efficiency the hyperbola is superseded by a linear function (Fig. 3).

For the NO_x cost function, a proportionally heavier penalty at high emissions is appropriate. At low NO_x levels, changes in the NO_x concentration should incur a small penalty and have a minor gradient. To meet these two criteria, a parabolic function was selected to represent the NO_x cost function (Fig. 4).

Other factors besides efficiency and emissions could be utilized in a cost function (e.g., pressure drop, pressure fluctuations, heat release rate, flame stability). In this study the two-variable formula was selected for the purpose of demonstration.

Due to the specific form of the cost functions selected for this study, equal weighting of each would sacrifice efficiency disproportionately. Hence, efficiency is weighted twice as heavily as NO_x (i.e., $\omega_{(\text{eff})}$ is double $\omega_{(\text{NO}_x)}$).

Results and Discussion

Overview. The effects of a variable-geometry approach are complex, as this is not a single-input, single-output system. Altering the state of either of the two control mechanisms (swirl or primary choke) affects several parameters: swirl intensity, pressure drop across the liner, residence time within the primary and/or secondary regions of the combustor, local stoichiometries, and the fuel spray-aerodynamic field pairing.

A representative result is presented in Fig. 5 for the Medium Power I condition (Condition 2). Note the effect of the flow splits on both the combustor efficiency (η_c) (Fig. 5(a)) and the emission of NO_x (Fig. 5(b)). This case is particularly interesting as combustion efficiency gains are achieved with concomitant reductions in NO_x emission.

The overall combustor performance for this condition is revealed in the cost function of Fig. 5(c). The region of optimal performance corresponds to the peak of the cost function. Hence, for Condition 2, the combustor operates optimally at a primary opening of 0 to approximately 0.25, and a swirl opening in excess of 0.5.

Note that the difference plot (Fig. 5(d)) is horizontal. The difference plot represents a subtraction of the cost function for a given condition relative to the Condition 2 results (e.g., each condition cost function is subtracted from the Condition 2 cost function). Therefore, Fig. 5(d) is a flat plane at a Subtraction Quotient value of zero (0) since Condition 2 is subtracted from itself. The subsequent plots reveal, as a result, the relative performance for a given condition, referenced to the Medium Power I condition.

Effect of Duty Cycle. Changing cycle operating conditions notably affect combustor performance. As evidence for this, the resulting surface plots of η_c, [NO_x], and the calculated cost function value vary markedly depending on cycle operating condition. For example, Fig. 6 shows the η_c and [NO_x] profiles for the four cycle conditions evaluated in this paper. Each row represents a cycle operating condition: Low Power (Condition 1), Medium Power I (Condition 2), a "high-temperature" medium power, Medium Power II (Condition 3), and High Power (Condition 4). Condition 3 was operated at an identical reference velocity and stoichiometry to Condition 2, but with a enhanced inlet air temperature (Table 1). The graphs in the left column present a surface plot regression of η_c, while those in the right column present [NO_x] corrected to 15 percent O_2.

It is of interest to note the contrasting response among the various cycle conditions. For example, note that the combustion

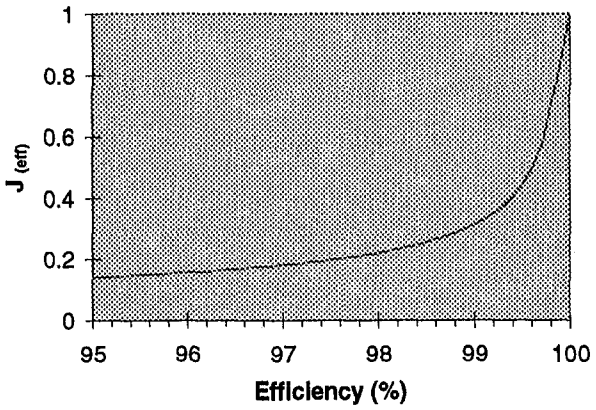

Fig. 3 Cost function for efficiency

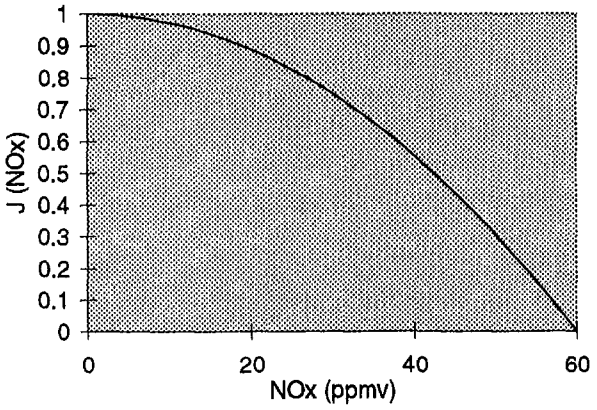

Fig. 4 Cost function for NO_x

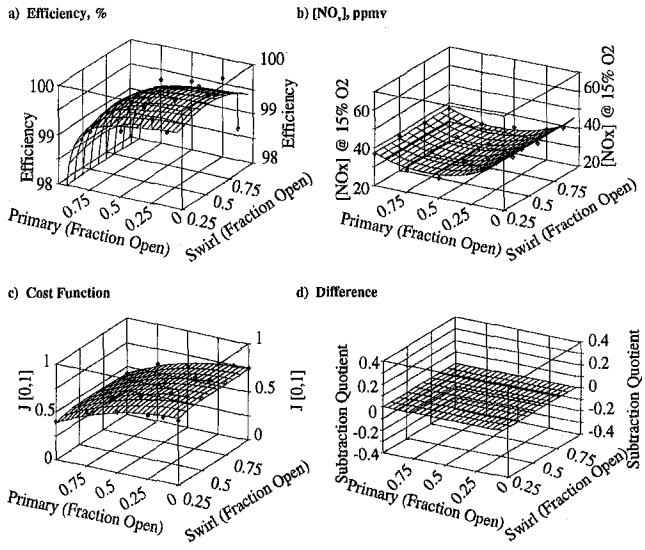

Fig. 5 Results at Medium Power I (Condition 2) (Phi 0.25, velocity 12.5 m/s, preheat to 200°F)

efficiency of Condition 1 plunges in a region where the other three loading maintain more acceptable performance, especially Conditions 3 and 4.

The surfaces in Fig. 7 show how the compromise between η_c and NO_x production evolves. The graphs in the left column are the cost function mappings for each cycle loading. The graphs in the right column are difference plots (relative to Condition 2). Positive values of the Subtraction Quotient reveal

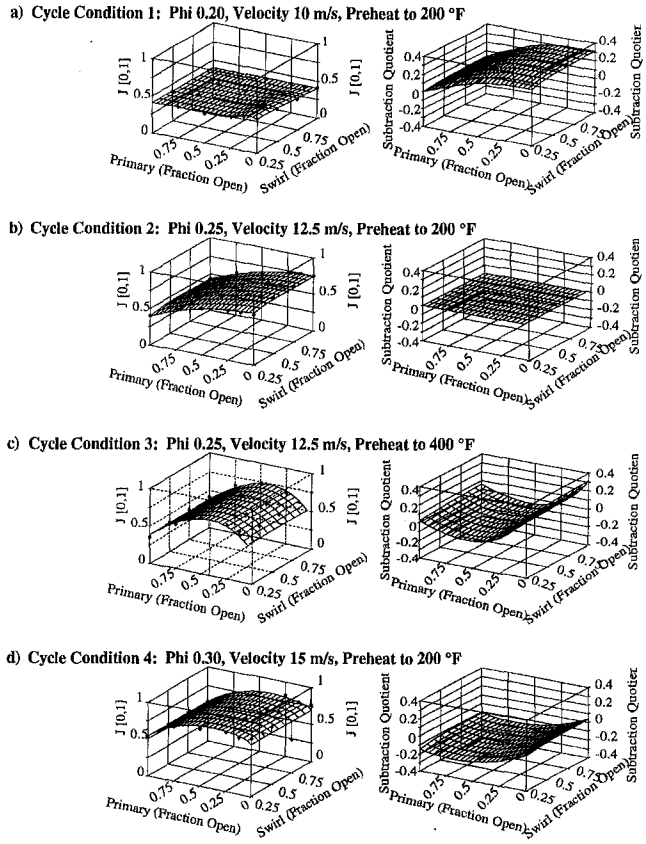

Fig. 7 Surface plots of the cost function and difference plots

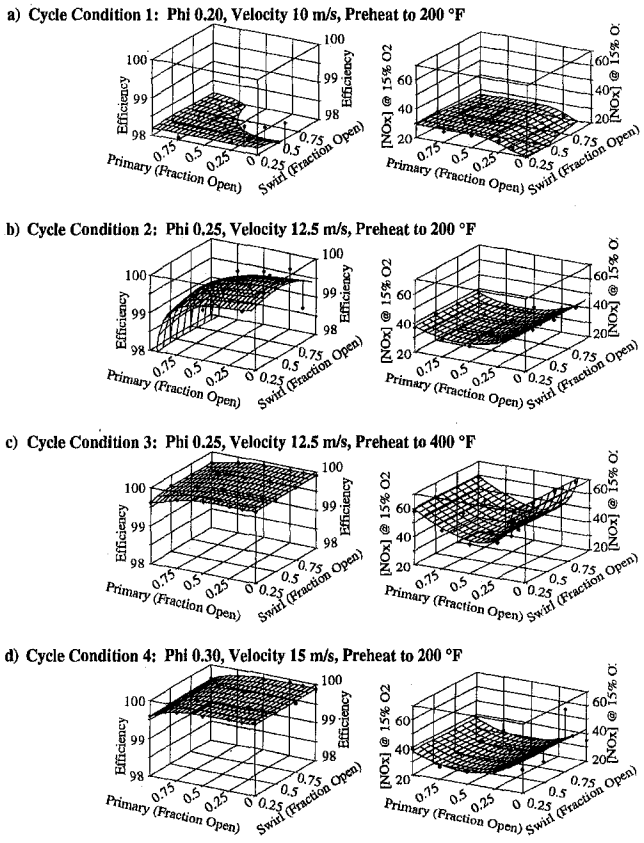

Fig. 6 Surface plots of efficiency and [NO_x] (corrected to 15 percent O_2)

degraded performance relative to Condition 2. Negative values correspond to improved performance.

Each operating condition demands different approaches to maximizing performance. Condition 1 has lower NO_x emissions than the other cases (Fig. 6), but at the expense of degraded efficiency. The conditions display a similar, concave response with regard to NO_x production, except for Condition 1, which develops a flat plane until the primary jet orifice area is reduced below 25 percent of the maximum area.

Examination of the graphs in Fig. 7 shows that the optimal geometry shifts as the operating load is varied. Optimal performance occurs when the primary jet area is approximately 10, 25, 40, and 30 percent of the maximum orifice for Conditions 1, 2, 3, and 4, respectively. For the present experiment, the performance is relatively insensitive to swirl opening.

To emphasize the penalty for operating at a fixed geometry, the geometry was fixed at the best measured performance for Condition 2 at other conditions. At this geometry (primary choke fully closed and swirler choke 75 percent open), performance at other conditions is suboptimal (as compared to their peak measured cost function). Condition 1, for example, would yield 1 ppm higher NO_x and notably worse efficiency (0.6 percent). Condition 3 would suffer a 1.2 ppm increment in NO_x production (efficiency unchanged). The most striking difference would be the performance hit at Condition 4. By fixing the combustor geometry instead of having an adapting configuration, NO_x production doubles and efficiency decreases dramatically (almost 0.9 percent).

Conditions 2 and 4 produce nearly identical NO_x response graphs. Higher NO_x production would be expected for Condition 4 due to the higher heat loading. However, the reduced residence time for Condition 4 impacts the pollutant formation along with other factors, such as an increased pressure drop across the atomizer. It is noteworthy that the increased reference

velocity of Condition 4 will result in a higher overall mass emission rate.

When the inlet temperature is raised relative to other fixed parameters (e.g., Condition 3 relative to Condition 2), NO_x production increases and the NO_x response curve reveals a higher sensitivity to the flow splits. The accommodation to articulation, as indicated by the cost function, is relatively high.

Each condition has a unique optimum operating condition in order to attain the best performance for that condition. In addition, the subtraction plots reveal the differing optimization requirements of each loading. No two cycle conditions produce identical combustor performance responses.

Cost Function Sensitivity. Careful examination of the cost function plot Fig. 7(*a*) and efficiency plot in Fig. 6(*a*) shows that the performance peak occurs for Condition 1 in an area of declining efficiency. Hence, variations in $J_{(NO_x)}$, which is improving due to declining NO_x levels, dominates the cost function J (Fig. 7). Combustion efficiency for this load is down to where $J_{(eff)}$ has a relatively gradual slope (Fig. 3) whereas the $J_{(NO_x)}$ derivative is proportionately much larger (Fig. 3). This results in an artificial leveling of J. Accordingly, $J_{(eff)}$ does not adequately quantify the performance changes at low efficiencies.

A modified efficiency cost function (Fig. 8) was devised for conditions with low combustion efficiency. This new efficiency cost function, $J_{(eff2)}$, is substituted into Eq. (1) in place of $J_{(eff)}$. The resulting surface plot for Condition 1 is shown in Fig. 9. [NO_x] still impacts the cost function, but a more reasonable curve results for this condition where efficiency plays a major role. The optimal configuration thereby shifts markedly, from a ridge where the primary choke was 12.5 percent open and the swirler choke is 50 percent open to a plane with the primary choke mostly open. This example also illustrates the care required in the specification of a cost function.

Selection of an appropriate cost function with sufficient resolution and appropriate sensitivity is required for proper combustor optimization. If this new efficiency cost function were to be employed at higher efficiency cases, insufficient sensitivity to NO_x emissions would be the result.

Conclusions

Varying the cycle operating condition markedly shifts the optimal geometry and is required to optimize combustor performance. Plots of the combustor performance revealed differing responses at each load. Overall:

1 *The geometry to achieve optimal performance depends on the cycle condition.* The combustor flow splits that optimize performance shift as load varies over a duty cycle. A fixed geometry that optimizes for one condition or a compromise between several conditions was found to compromise other conditions. In the example presented, a fixed geometry optimized for Condition 2 resulted in markedly higher emissions for Condition 4. No one geometry proved ideal for all loadings.

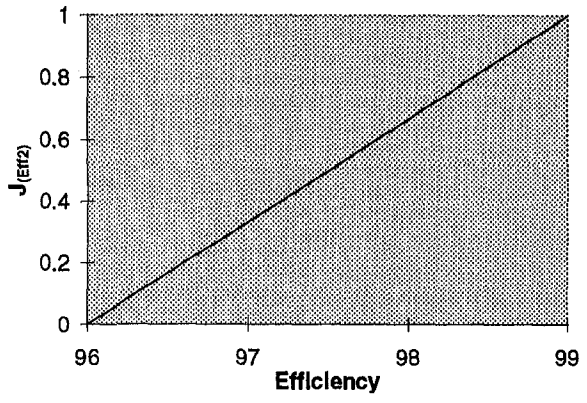

Fig. 8 Modified cost function, low-efficiency case

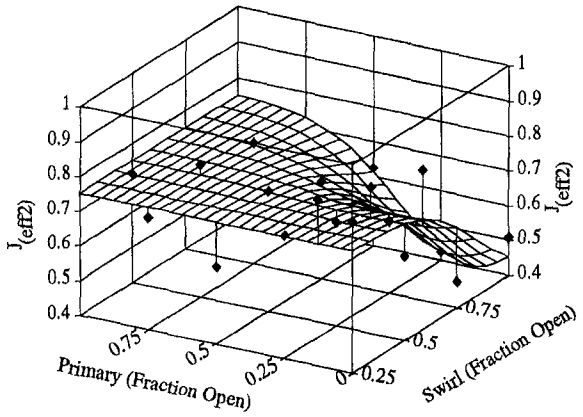

Fig. 9 Surface plot for the low efficiency case, modified cost function

2 *A variable geometry combustor is an approach to attaining optimal performance over the duty cycle.* Depending on the regulatory scenario, a form of combustor articulation may be required in order to minimize the environmental impact over a duty cycle. In this manner, emissions are kept to a minimum for each load condition.

3 *To attain and maintain optimal gas turbine combustor performance over a duty cycle, an adaptive control strategy may be required.* Closed-loop feedback control would, for example, provide the required tuning throughout the duty cycle. Not only must the optimal performance be established for a given load, active control is needed to assure maintenance of the optimal state.

4 *Specification of the cost function requires care.* In an adaptive control scheme, the selection of the cost function quantifies the quality of the combustor operation and therefore determines the nature of the "optimal" operating regime. As a result, the specification of the cost function requires care in combining the requirements imposed by the regulatory process with the various operating characteristics of the combustor. Simply stated, the cost function will be system specific and application dependent.

References

Bahr, D. W., 1973, "Technology for the Reduction of Aircraft Turbine Engine Exhaust Emissions," AGARD-CP-125, Paper No. 29.

Brouwer, J., Ault, B. A., Bobrow, J. E., and Samuelsen, G. S., 1990, "Active Control for Gas Turbine Combustors," *Twenty-Third Symposium (International) on Combustion,* The Combustion Institute, pp. 1087–1092, 1990.

Cameron, C. D., Brouwer, J., and Samuelson, G. S., 1988, "A Model Gas Turbine Combustor With Wall Jets and Optical Access for Turbulent Mixing, Fuel Effects, and Spray Studies," *Twenty-Second Symposium (International) on Combustion,* The Combustion Institute, pp. 465–474.

Henderson, R. E., and Blazowski, W. S., 1973, "Aircraft Gas Turbine Pollutant Limitations Oriented Toward Minimum Effect on Engine Performance," AGARD-CP-125, Paper No. 33.

Padmanabhan, K. T., Bowman, C. T., and Powell, J. D., 1994, "An Adaptive Optimal Combustion Control Strategy," *Twenty-Fifth Symposium (International) on Combustion,* The Combustion Institute.

Wang, H. Y., McDonell, V. G., Sowa, W. A., and Samuelsen, G. S., 1994a, "Experimental Study of a Model Gas Turbine Combustor Swirl Cup, Part I: Two-Phase Characterization." AIAA *Journal of Propulsion and Power,* Vol. 10, No. 4, pp. 441–445.

Wang, H. Y., McDonell, V. G., Sowa, W. A., and Samuelsen, G. S., 1994b, "Experimental Study of a Model Gas Turbine Combustor Swirl Cup, Part II: Droplet Dynamics." AIAA *Journal of Propulsion and Power,* Vol. 10, No. 4, pp. 446–452.

Field Test Results of a Dry Low NO_x Combustion System for the MS3002J Regenerative Cycle Gas Turbine

J. R. Maughan
GE Corporate Research and Development, Schenectady, NY 12301

K. M. Elward
GE Power Generation, Greenville, SC 29602

S. M. De Pietro
European Gas Turbines, Lincoln, England

P. J. Bautista
Gas Research Institute, Chicago, IL 60631

A dry low NO_x combustion system for the MS3002J regenerative cycle gas turbine has been developed and successfully installed at two pipeline compressor stations. Preparation for the DLN retrofits began with initial field testing of the conventional system intended to characterize some of the unique features of the two-shaft, regenerative cycle machine that might affect the proposed premixed combustor design. Combustor transition pieces were instrumented with gas sampling probes for CO_2 analysis. Fuel flow to each combustor was measured and controlled. Consequently, the fuel/air ratio, exit temperature, and air flow for each combustor could be determined over the operating range. The dry low NO_x combustion system for the MS3002J R/C is based on an existing system for the MS6001B gas turbine. A description of the hardware and system operation is given. Because of the relatively high inlet temperature of the MS3002J R/C (950°F), some portions of the liner required highly efficient effusion cooling. A new transition piece seal was developed to reduce leakage and ensure uniform air flow throughout the machine. A control strategy was developed to guide the machine through diffusion modes of operation at low load to premixed combustion at higher loads. Results showed acceptable component temperatures throughout. Emissions measurements were consistent with previous laboratory measurements and met design targets of 33 ppm NO_x and 25 ppm CO (at 15 percent O_2) over the required range. The fuel split between the two premixed flame zones was controlled over the load range of the turbine to optimize CO, NO_x, and liner temperatures. Because of the high inlet temperature and low overall temperature rise, dynamic pressure activity was low. Following a successful inspection after 6000 hours of operation, the hardware inspection interval has been set at 12,000 h.

Introduction

As the advantages of reducing emissions from power sources become more apparent, the availability of low emissions combustion systems is increasing worldwide. The latest product in the GE family of gas turbines to receive low emissions combustors is the MS3002J regenerative cycle (R/C) gas turbine. This work follows the earlier development of dry low NO_x systems for the Frame 6, 7, and 9 machines.

The MS3002J R/C machine is one of the smaller frame gas turbines, with a firing temperature of approximately 1750°F and a rated output of 14,000 hp (10 MW). A majority of the more than 900 MS3002 machines throughout the world are used as mechanical drives for compressors in natural gas pipeline stations.

The Frame 3 is a two-shaft gas turbine. As shown in the schematic of Fig. 1, the high-pressure shaft powers the 15 stage axial flow compressor with fixed inlet guide vanes. As a regenerative cycle machine, air is extracted from the compressor discharge for heat exchange with the exhaust gases in the regenerator, and is reintroduced through two return headers, one on each side of the machine and each containing three combustors.

The MS3002J R/C combustion system includes the header, combustion liner (or can), elbow, and transition piece. A sketch of the system is shown in Fig. 2 with the new dry low NO_x liner in place. Because the combustion liners pass through the header, only a portion of the total air moves toward the head end of the combustor and enters the flame zone. The remainder is directed to the aft end of the liner and elbow, enters a flow sleeve, and provides counterflow cooling for the elbow before entering the hot gas path as dilution air. The transition pieces are not actively cooled, but are bathed in relatively low-temperature compressor discharge air. A seal prevents airflow between the compressor discharge wrapper and the combustion header.

The film-cooled first-stage nozzle directs combustion products through the single-stage high-pressure turbine, which, again, is connected to the axial flow compressor. A characteristic feature of the MS3002 is the variable second-stage nozzle, which can be opened or closed to vary the air flow rate through the turbine and control the pressure ahead of the low-pressure turbine. The second shaft connects the low-pressure set to the load compressor.

Frame 3 machines are typically gas only and operate without steam or water injection for NO_x abatement. The remote location and unattended operation of these gas turbines make them unlikely candidates for these emissions reduction techniques. A Dry Low NO_x system (DLN) is likely the best option for reduced emissions in most applications.

Such a system was recently requested by the El Paso Natural Gas Company for two sites on an expanding pipeline passing through the states of Arizona and New Mexico, USA. Accordingly, a program was initiated with General Electric and their business associate European Gas Turbines to develop such a combustor. The Gas Research Institute also supported underlying research and testing.

Contributed by the International Gas Turbine Institute and presented at the 40th International Gas Turbine and Aeroengine Congress and Exhibition, Houston, Texas, June 5–8, 1995. Manuscript received by the International Gas Turbine Institute February 8, 1995. Paper No. 95-GT-47. Associate Technical Editor: C. J. Russo.

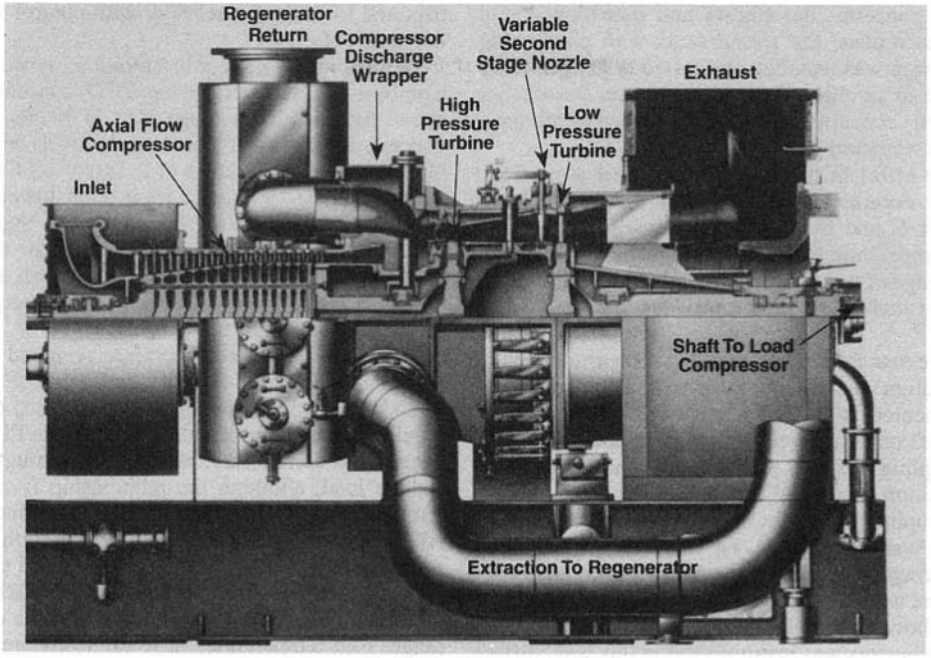

Fig. 1 The MS3002J R/C gas turbine

The design approach was to adapt GE's DLN technology from existing MS6001B gas turbine combustors to the MS3002J machine. However, it was apparent that there were several issues involved in such a modification. The MS3002J fires at a lower temperature than the MS6001B (1750°F versus 2020°F), and has a higher inlet temperature than the MS6001B (950°F versus 650°F) due to the regenerative cycle. In addition, the unique features of the two-shaft machine with combustion headers and elbows presented mechanical design, aerothermal, and control concerns. These issues were addressed through early machine characterization tests, laboratory tests, full pressure development tests, and a final DLN installation and evaluation.

Initial Machine Characterization

An initial characterization test was performed at the El Paso Natural Gas Company's Dilkon, AZ, pipeline compressor station to gain information critical to the successful development of the DLN hardware. Objectives included noting the machine startup sequence, determining regenerator effectiveness, measuring combustor inlet temperature and exit fuel/air ratio, assessing the flow distribution between combustion chambers, and evaluating a new elbow and transition piece seal design.

The new seals were designed to reduce nonuniformities in fuel/air ratio around the machine. As is well known, the NO_x produced in a lean, premixed flame is exponentially sensitive to reaction zone temperature. Similarly, CO emissions from a premixed combustor are also highly nonlinear with temperature. Consequently, variations in fuel/air ratio or temperature between combustion chambers can result in an overall degradation in emissions performance. Chambers that are hotter than average will produce a disproportionate amount of NO_x. Those which are cooler will result in excess CO.

These considerations are reduced in a standard diffusion flame, and the original spring-type seals in the MS3002 were not intended to ensure tight control of leakage paths. However, as discussed, leakage here will dilute the hot regenerator return air entering the combustor with cooler air directly from the compressor discharge. This not only reduces efficiency, but also lowers the fuel/air ratio of the combustion chamber. Variability in this leakage path will result in nonuniformities around the machine. Given the tolerances of the original design, it was estimated that variations in air flow of as much as ±4 percent could result from this seal alone. When coupled with other potential sources of nonuniformity, a significant emissions penalty results.

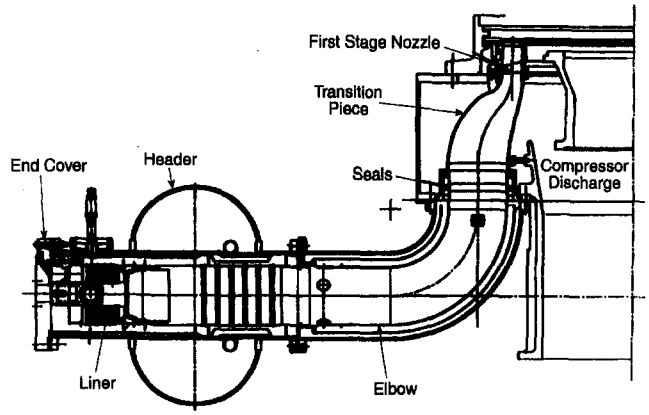

Fig. 2 Top view schematic of DLN combustion system

To avoid these concerns, the elbows and transition pieces were redesigned to replace the spring seals with piston ring seals. The new design was installed and tested at the pre-DLN test and was found to significantly reduce leakage. Posttest inspection showed no concerns and the new components have become part of the standard DLN retrofit.

The bulk of the effort in this test was centered around the need to determine accurately the combustor exit temperature of the MS3002J R/C and to verify algorithms for predicting combustor exit temperature and performance in the Frame 3 machines. Knowledge of this temperature is critical to designing a premixed system that meets tight emissions and operability targets.

This temperature was inferred from a direct measurement of the CO_2 concentration at the combustor exit. Each transition piece was instrumented at its exit plane with eight uncooled gas sampling probes manufactured from high-temperature alloy MA956. The sampling location was just upstream of the seal between the transition piece and the first stage nozzle. Each probe had five sampling ports. An aggregate gas sample from these eight probes was conditioned and analyzed for CO_2 concentration, and, through calculation, the fuel/air ratio and average exit temperature were determined. In addition, measurement of the fuel flow allowed for calculation of the air flow. Since each of the six combustors was instrumented in this way, differences in parameters between individual combustors and the machine average could be determined.

Typical data for fuel flow, CO_2 concentration, calculated exit temperature, and airflow are shown in Fig. 3. The average for each parameter is shown along with the deviation from the average for each can, arranged according to their position around the machine. The cans are numbered 1–6 counterclockwise from the upper left. A similar schematic is used for the 12 exhaust thermocouples.

As seen, the average fuel flow for this condition is 0.171 lbm/s for each combustor. The deviations from this value are all less than 0.5 percent, as the machine was intentionally

Parameter	Deviation from average for:	
average	can 1	can 6
	can 2	can 5
	can 3	can 4
fuel flow:	+0.06 %	-0.20
0.171 lbm/s	+0.08	+0.30
	-0.16	-0.09
CO2:	+1.51 %	+3.35
2.39 vol%	-2.86	+2.70
	-3.39	-1.30
calc exit T:	+12.8 F	+27.8
1864 F	-23.8	+22.4
	-28.3	-11.0
air flow:	-1.48 %	-3.46
13.1 lbm/s	+2.93	-2.38
	+3.24	+1.15
exhaust T:	+15.9 F	+21.6
1010 F	+7.4	+15.2
	+1.3	+10.4
	-8.5	-16.8
	-7.1	-10.4
	-10.6	-18.5

Fig. 3 Typical data from pre-DLN test showing average value and deviation from average for each of the six combustors

trimmed to uniform fuel flow with control valves installed for this purpose.

Deviations in CO_2 concentration, however, are apparent. Combustor 6, for example, has a CO_2 concentration 3.35 percent above the machine average of 2.38 vol%. (The absolute CO_2 concentration for chamber 6 is 2.46 vol%, or 3.35 percent above the average concentration of 2.38 vol%.) Combustor 3, on the other hand, has a CO_2 concentration lower than the average. The exit temperatures calculated from these results are also shown, based on a measured regenerator exit temperature of 947°F. The average value is 1864°F, with a range of approximately ± 30°F. These differences also propagate through to the 12 thermocouples in the exhaust.

The calculated exit temperature averaged for all six combustors is shown in Fig. 4 for low-pressure (LP) shaft speeds from 70 to 97 percent of maximum design speed (6500 rpm) for one pipeline and ambient condition. Since the LP shaft is connected to the load compressor, its speed is a rough indication of gas turbine load, although the relationship is not linear. The exit temperature at maximum LP speed is approximately 1900°F. Although the exit temperature will vary with pipeline and ambient conditions, these results could be used to verify the performance prediction routines for the MS3002J, ensuring that the DLN combustor would be designed for the correct temperature range. Exit temperatures at lower loads are also shown in the figure.

A second curve in Fig. 4 shows the effect of changing the high-pressure shaft speed control curve to reduce the allowable minimum speed. As seen, a lower HP speed restricts air flow and increases the exit temperature for the same load. Because holding the combustor temperature as high as possible during turndown will reduce CO emissions, it is important to determine and maintain the minimum HP speed accurately over the lower portion of the load range.

Since Fig. 3 showed variations in CO_2 concentrations but uniform fuel flow, the differences in fuel/air ratios must be attributed to differences in air flow. These calculated values are also shown in Fig. 3 for a single condition and in Fig. 5 for a range of LP speeds. Note that the differences remain consistent with changes in speed.

These variations can be accounted for by considering the geometry of the headers. The header for combustors 1, 2, and 3 and the header for combustors 4, 5, and 6 are fed from the top by independent lines from the regenerator. Static pressure recovery within the header forces slightly greater flow into the combustors at the bottom of the header. Combustors 3 and 4 have more flow than those above them. The left side of the machine also has consistently more air than the right.

Since variations in temperature from combustor to combustor may result in higher emissions, provisions were made to explore the possibility of fuel tuning, or intentionally varying the fuel flow to match air flow. Figure 6 illustrates a 15 minute period of time where this was demonstrated. Initially, the machine was set to uniform fuel flow, resulting in different CO_2 concentrations in each of the six combustors. Using the fuel control valves in each fuel line, the machine was manually trimmed to uniform fuel/air ratio, but different fuel flows. If necessary, such a technique can be used to optimize emissions. Based on this information, a design was also prepared to provide an additional, controlled pressure drop at the entrance of each combustor to create more uniform flow. As will be seen, however, it was not required to meet performance and emissions goals.

NO_x emissions data for the standard diffusion combustor are shown in Fig. 7 as a function of shaft speed. The high inlet temperature of the regenerative cycle contributes to elevated NO_x emissions by increasing the flame temperature at the stoichiometric interface between the fuel and air.

Development Program

The testing just described served to identify the operating envelope of the MS3002J R/C combustor and laid a foundation

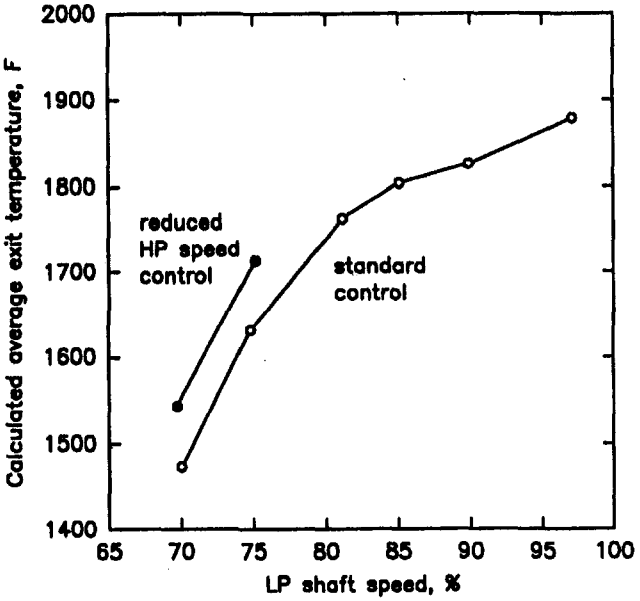

Fig. 4 Average combustor exit temperature calculated from measured CO_2 concentrations

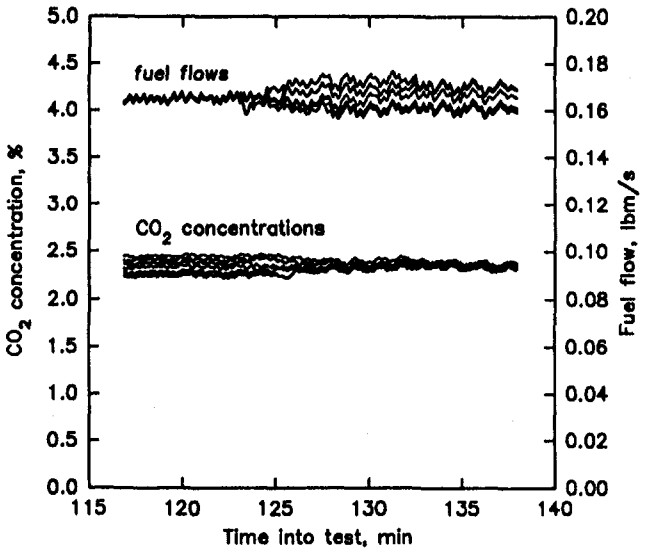

Fig. 6 Illustration of tuning the gas turbine from uniform fuel flow to *uniform exit temperature*

for the subsequent development program. The starting point for the new combustion system was the MS6001B Dry Low NO_x combustor (DLN), which is shown conceptually in Fig. 8. The fundamental issues associated with adapting the existing technology to the higher inlet temperature of the MS3002J regenerative cycle were addressed through technology screening tests at the GE Corporate Research and Development Center (Maughan et al., 1994).

These results confirmed that increasing the inlet temperature raises NO_x emissions in a diffusion flame. However, an increasing inlet temperature resulted in a net drop in NO_x levels when the combustor was operated with a premixed flame and a constant combustor exit temperature. As a relatively low firing temperature gas turbine, the MS3002J has a significant amount of dilution air entering the combustor downstream of the flame. With an increase in the inlet temperature, the temperature of the dilution air also increases, requiring a drop in the head end or burning zone temperature if the overall combustor exit temperature is to be held constant. For a premixed reaction zone, the drop in temperature lowers the NO_x production rate, and emissions decrease. In addition, the fuel flow and overall temperature rise of the combustor are reduced, weakening dynamic pressure activity.

Following the initial screening tests, a complete development program was undertaken at European Gas Turbine's engineering and testing laboratory in Lincoln, England. The development was centered around the main issues of tuning the reaction zone temperature to optimize NO_x and CO emissions over the expected operating range, and providing adequate cooling to the liner and components.

After optimizing fuel distribution and mixing for near perfectly premixed NO_x performance, dilution and mixing jet hole sizes were adjusted to control air flow (and consequently temperature) in the reaction zone to hold NO_x emissions at baseload below the 33 ppm design goal. Further leaning of the reaction

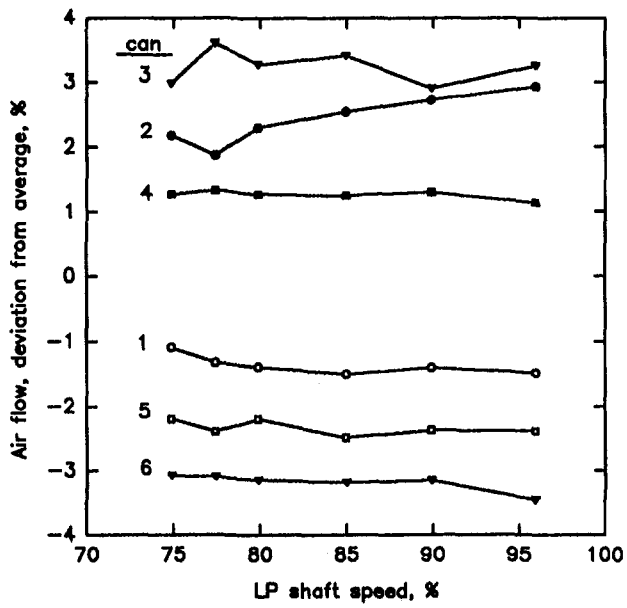

Fig. 5 Variation in airflow nonuniformities with LP shaft speed

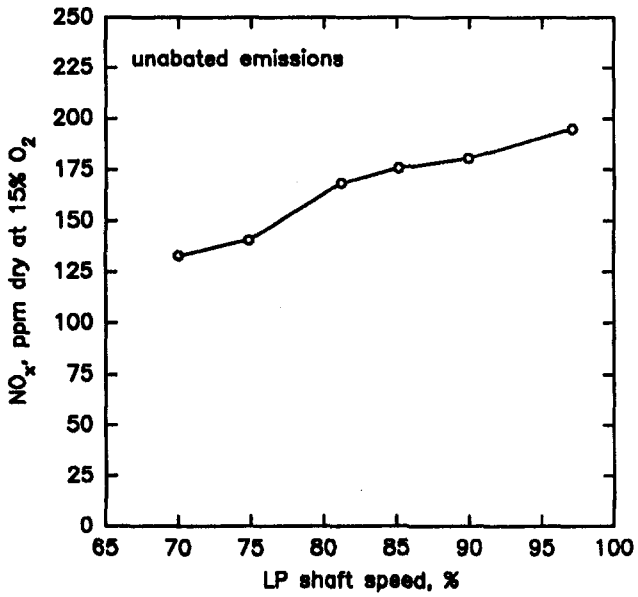

Fig. 7 Unabated NO_x emissions from pre-DLN test. Ambient conditions are 79°F, 11.9 psia, and 57 percent relative humidity.

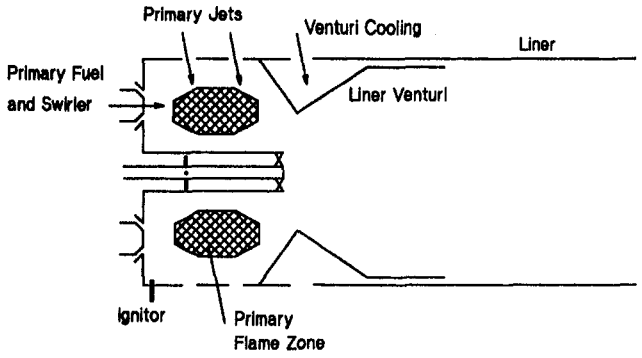

Fig. 8(*a*) Schematic of the DLN combustor in primary mode of operation. During ignition and low loads, diffusion flame burning occurs upstream of liner venturi.

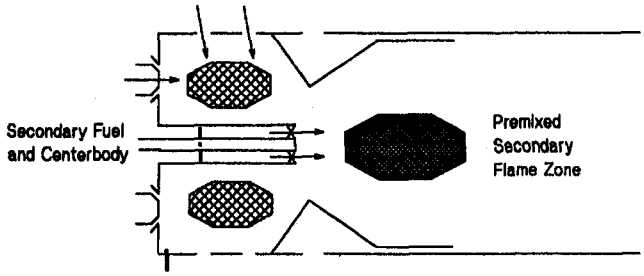

Fig. 8(*b*) Lean-lean mode of operation. At higher loads, a premixed secondary flame is ignited along the combustor centerline.

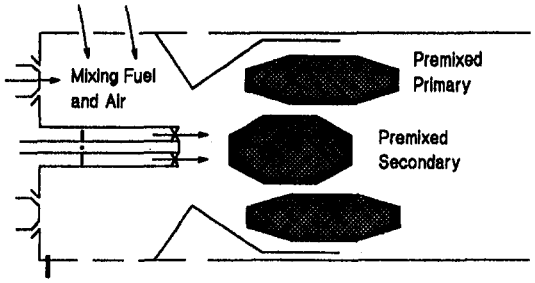

Fig. 8(*c*) Premixed mode of operation. Momentarily interrupting the primary fuel causes the primary zone to be extinguished and then reignited as a premixed flame behind the liner venturi.

zone can result in lower NO_x emissions, but at the expense of operability and CO emissions at part load. The CO emissions target was less than 25 ppm at 70 percent load.

In the course of the development program, additional cooling was required on both the liner venturi and the centerbody. The centerbody is a particularly difficult component to cool since during primary and lean-lean modes of operation, a high inlet temperature diffusion flame impinges on its outer surface with relatively hot cooling air on the inner surface. Highly efficient multihole or effusion cooling was used over a portion of the surface to maintain acceptable metal temperatures.

DLN Installation

The first installation of the new low emissions combustion system was at the El Paso Natural Gas Company's Dilkon Station in northeastern Arizona. Site altitude is 5885 ft and ambient temperatures range from subzero to over 100°F with relatively low humidity. The turbine is used by the El Paso Natural Gas Company (EPNG) to pump gas from fields in New Mexico and Colorado to consumers in California and the Southwest U.S. The turbine was refurbished and installed by EPNG in April 1992 and retrofitted with dry low emissions combustors in August 1993. The DLN installation required disassembly of the combustion system for replacement of the transition pieces with the newly designed seals, header modification to accommodate the DLN end covers, and replacement of the liners themselves. Additional piping was also required for the secondary fuel system and primary/secondary splitter valve. New flame detectors and spark plugs are also required.

Overall unit control was retained by the EPNG programmable logic controller. However, an additional programmable logic controller was installed by GE to handle control functions specific to the DLN system, such as secondary flame detection and fuel split control. Based on inputs such as exhaust temperature and shaft speeds, the DLN controller determines the correct operating mode for the combustor and schedules primary and secondary fuel accordingly. Such functions are totally transparent to the unit. As part of the first installation, a diagnostic monitor was also installed to record machine performance and provide remote access to operating conditions. Installation was followed by an approximately three-week field test to optimize performance, ensure the commercial viability of the machine, and explore off-design conditions.

DLN Test Results

Typical data showing several machine parameters during a 15 minute startup period are shown in Fig. 9. The start sequence begins with the expansion gas starting turbine bringing the high-pressure set to approximately 20 percent speed. Following a 2 minute purge, the spark plugs are fired and the starting turbine begins to accelerate the unit. As seen, the fuel split at ignition is approximately 100 percent, indicating primary only mode. When the HP shaft reaches a preset speed, the starting turbine breaks away, occurring here 5.5 minutes into the start. During a cold start, the HP shaft may momentarily lose speed before resuming acceleration under its own power.

At breakaway, the fuel split is reprogrammed to approximately 70/30 in lean-lean mode. Total fuel flow to the machine, however, remains essentially constant. Entering lean–lean mode immediately reduces the metal temperature on the liner venturi. As the high-pressure turbine accelerates toward its minimum set point, the fuel split is gradually ramped to a final

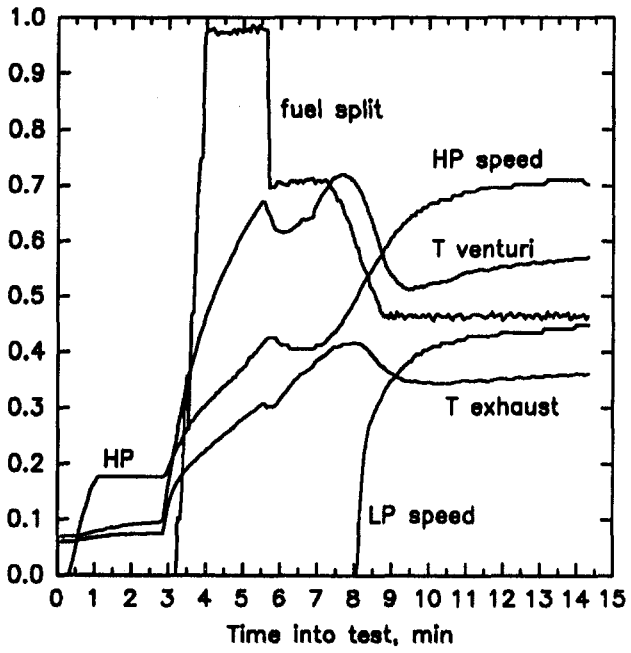

Fig. 9 Typical start of the MS3002J R/C turbine. Variable scaling is as follows: high and low-pressure shaft speeds 0–10,000 rpm, fuel split 0–100 percent, exhaust and venturi temperatures 0–2000°F.

lean–lean value of 50/50. This fuel split schedule optimizes ignition, part-load emissions, and component temperatures during startup.

Approximately 8 minutes into this start, the low-pressure turbine breaks away and accelerates rapidly toward its minimum setpoint. As this energy is extracted from the flow, the exhaust temperature decreases. A complete start sequence is achieved when the low-pressure shaft reaches its minimum set point, usually at 70 or 75 percent speed.

Initially, the second-stage nozzles are held open to aid in accelerating the high-pressure turbine to its setpoint. However, since the greatest efficiency is obtained in a regenerative cycle machine by maximizing the exhaust temperature, any further increase in load and fuel flow causes the nozzles to close. This keeps the HP speed at its minimum setpoint, restricts air flow, and increases exhaust temperature. Once the exhaust temperature reaches its maximum limit, however, the nozzles will begin to open, accelerating the high-pressure set. Maximum load is achieved when the HP shaft reaches 100 percent speed at 7100 rpm. The low-pressure turbine speed and output power at this point can vary significantly with ambient conditions and the pipeline pressure and flow rate.

After reaching maximum exhaust temperature, further loading of the gas turbine initiates transfer from lean–lean combustion mode to premix mode. One initial transfer is shown in Fig. 10. Within a 30 second period, the fuel split is changed from approximately 50/50 lean–lean mode to 0/100, indicating 100 percent of the fuel is burning in the secondary zone. This extinguishes the primary zone so that when the fuel split is ramped back to 82/18 the primary fuel burns in a premixed flame downstream of the venturi. The drop in NO_x emissions is immediately evident (allowing for sample delay time to the exhaust analyzers). The 0/100 fuel split occurring during transfer to premix mode causes a momentary spike in CO emissions. Dynamic pressure activity also peaks somewhat during transfer, but thereafter resumes levels only slightly higher than for the diffusion modes of operation. Because premix transfer occurs at constant fuel flow, the gas turbine output and performance are unaffected by the transfer to premixed combustion. Only emissions change.

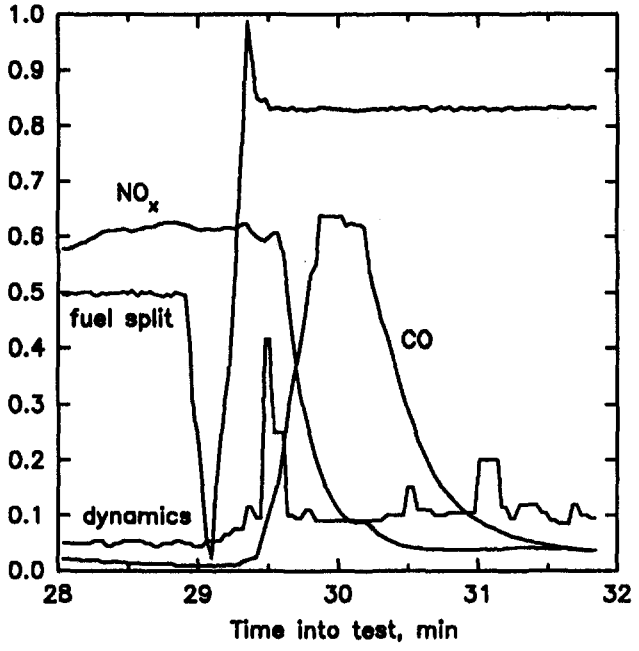

Fig. 10 Typical transfer from lean–lean to premix combustion. Variable scaling is as follows: NO_x and CO emissions 0–200 ppm at 15 percent O_2, fuel split 0–100 percent, dynamic pressure of peak discrete 0–2 psi.

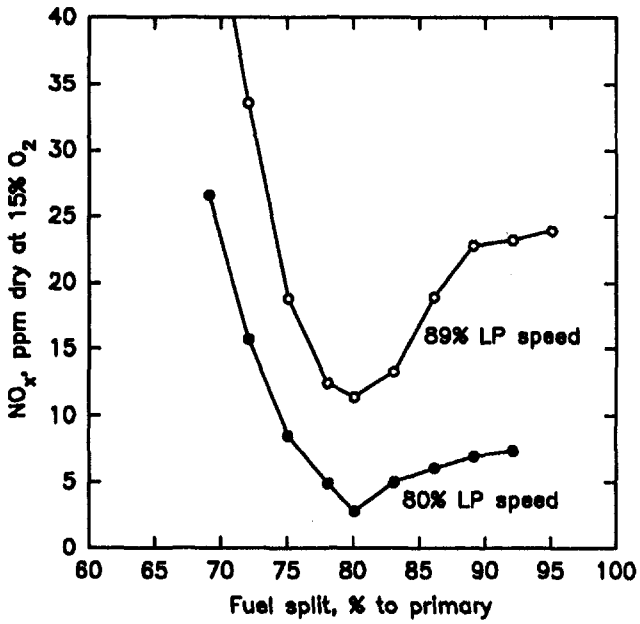

Fig. 11 Effect of fuel split on NO_x emissions. Ambient conditions are 84°F, 12.1 psia, and 35 percent relative humidity.

Because of the extremely low dynamic pressure levels in the MS3002J R/C combustor, premix transfer occurs without the transfer fuel circuit used to provide operability margin in the Frame 6, 7, and 9 machines. This simplifies the piping and controls required for the DLN retrofit.

Data in Figs. 11–13 illustrate how premix fuel split affects NO_x emissions, CO emissions, and the liner venturi temperature. Data are shown for LP speeds of 80 and 89 percent, which was the maximum speed possible for the pipeline condition on this particular day of testing. The NO_x data clearly show a fuel split where NO_x emissions are minimized by balancing the reaction zone temperatures in the primary and secondary zones. NO_x emissions increase with load or LP shaft speed. CO emissions exhibit the opposite trend and are higher at lower loads and, unlike the NO_x data, continue to decrease as the split is increased

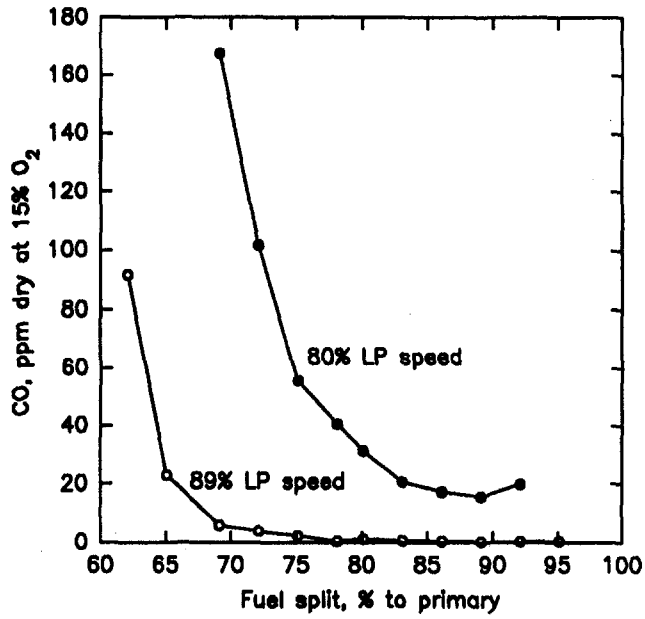

Fig. 12 Effect of fuel split on CO emissions. Ambient conditions are 84°F, 12.1 psia, and 35 percent relative humidity.

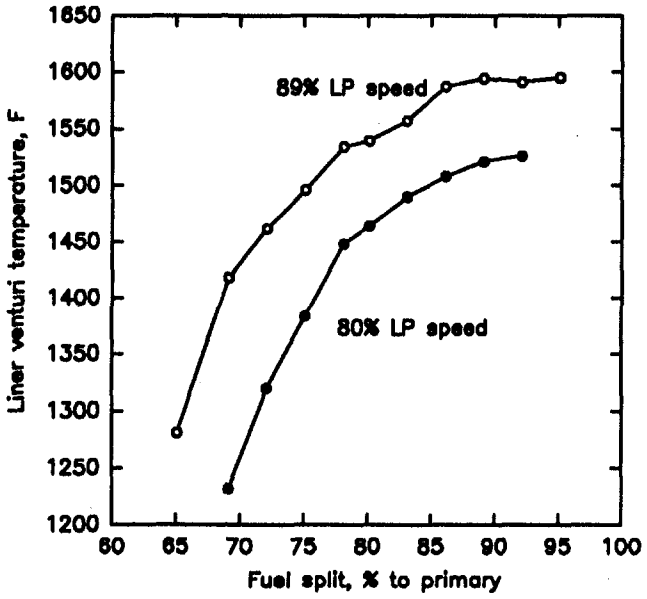

Fig. 13 Effect of fuel split on liner venturi temperatures

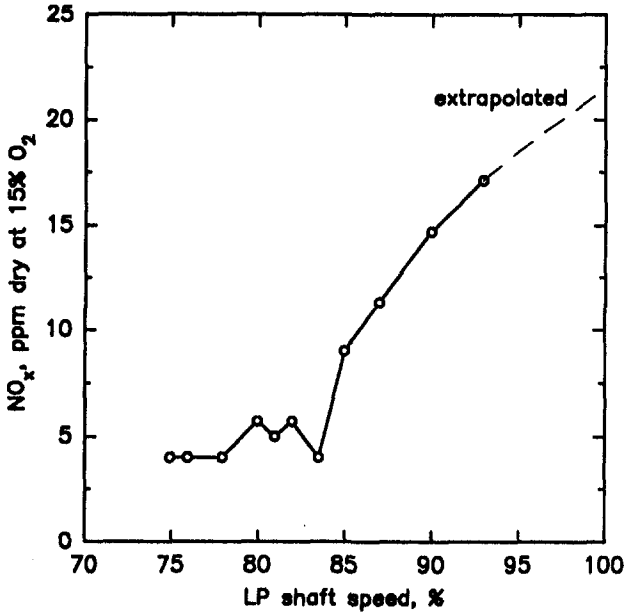

Fig. 15 Effect of LP shaft speed on NO_x emissions. Ambient conditions are 58°F, 11.8 psia, and 75 percent relative humidity.

toward 100/0. Venturi temperatures are decreased at lower fuel splits, as expected, since this removes fuel from the premixed flame zone behind the venturi and shifts it toward the secondary zone along the combustor centerline. The venturi temperatures shown occur near the extreme downstream edge of the component, where stresses are very low. The higher-stress sections closer to the throat are considerably cooler.

Operation of a low emissions combustor requires optimizing NO_x emissions, CO emissions, and liner temperatures, yet the data of the preceding three figures suggest that the optimum operating point may vary depending on gas turbine load or ambient conditions. The flexibility of the two-stage premixed combustor used here allows the fuel split to be scheduled with LP speed to improve overall performance. One possible method applicable to the Dilkon site is shown in Fig. 14, where the premix fuel split near maximum load (high LP speed) is reduced to 75/25 to lower component temperatures and at part loads (low LP speeds) is increased to minimize CO emissions. Although NO_x emissions are only optimized in a fairly narrow operating range when the premix fuel split is programmed to approximately 80/20 at 83 percent LP speed, this control algorithm provides the best overall performance.

NO_x emissions over the load range on one day of testing are shown in Fig. 15, where the dip in NO_x emissions near an LP speed of 83 percent is evident. As discussed, the pipeline pressure during testing allowed turbine operation up to only 92 percent speed. Emissions levels at 100 percent speed are extrapolated in the figure, but are expected to meet the 33 ppm design goal, with some margin to allow for variations in ambient and pipeline conditions. Further information on how these conditions and turbine shaft speeds affect emissions is now being

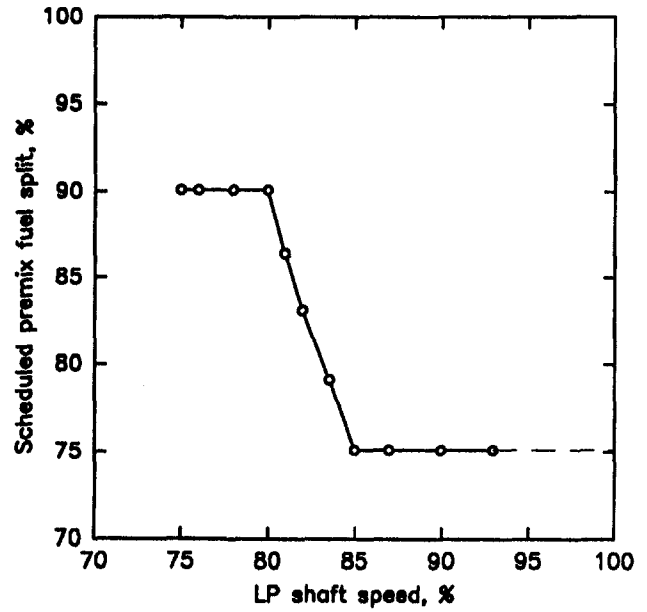

Fig. 14 Schedule of fuel split with shaft speed to reduce venturi temperatures and CO emissions

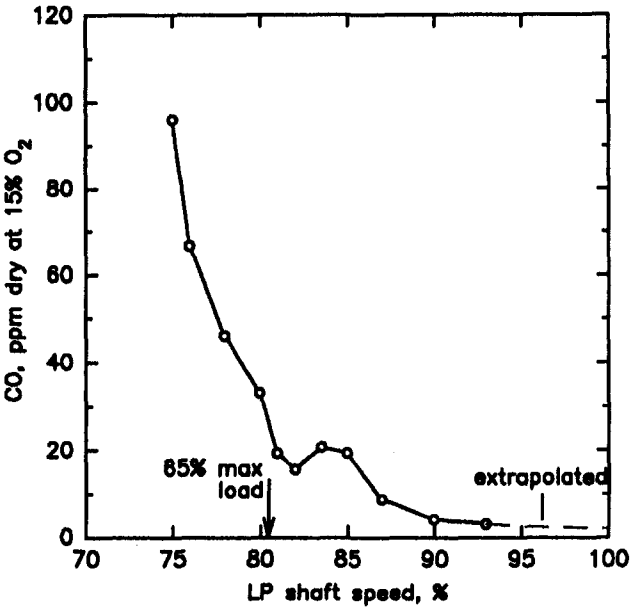

Fig. 16 Effect of LP shaft speed on CO emissions. Ambient conditions are 58°F, 11.8 psia, and 75 percent relative humidity.

gathered through remote access to the continuous emissions monitor (CEM) and unit and DLN controllers on site.

The corresponding CO emissions are shown in Fig. 16. Note the shift in the curve between 80 and 85 percent speed where the fuel split is adjusted to minimize CO production rates. The design goal of 25 ppm is exceeded below an LP speed of approximately 80 percent, which in Fig. 16 corresponds to 6500 hp. Maximum load for the MS3002J R/C under ISO conditions at the Dilkon site is 10,700 hp.

Further Developments and Plans

Further refinements and simplifications to the control strategy were developed and implemented in two brief additional tests, each coinciding with a combustion hardware inspection. A 500 hour inspection showed only minor wear related to the igniter insertion depth. A 6000 hour inspection at the Dilkon site revealed no hardware concerns and the recommended combustion inspection interval has been established at 12,000 hours.

A second dry low NO_x combustion system was installed on an EPNG MS3002J R/C gas turbine at the White Rock pumping station near Farmington, New Mexico, in June 1994. The hardware retrofit, additional controls installation, and startup were competed within 10 days. Subsequent performance and emissions testing confirmed the earlier results from the Dilkon station. DLN combustion systems are also planned for additional EPNG units.

A similar program for the MS3002J simple cycle gas turbine is now nearing completion, following a joint GE/EGT development effort and a successful installation test at a pumping station in Germany in September 1994. A combustor for the MS5001 gas turbine will shortly be tested in the field and development programs for the MS3002F regenerative cycle and MS5002C regenerative cycle are now under way in the laboratory.

Acknowledgments

This work would not have been possible without the assistance of A. Luts, J. Benoit, D. Tegel, J. Beckett, and J. F. Dalpe from GE and C. Derome, H. J. Groschopp, and R. Noden from EGT, among many others. Funding from the Gas Research Institute is gratefully acknowledged for the pre-DLN testing, screening tests at GE-CRD, and further developments in the field. GRI also contributed funding for emissions testing during the DLN installation. The full cooperation and participation of the El Paso Natural Gas Company are also acknowledged and greatly appreciated.

References

Maughan, J. R., Luts, A., and Bautista, P. J., 1994, "A Dry Low NO_x Combustor for the MS3002 Regenerative Gas Turbine," ASME Paper No. 94-GT-252.

Dual-Use Conversion of a High-Mach-Number Jet Engine Test Cell for Industrial Gas Turbine Low-Emission Combustor Development

P. W. Pillsbury

W. R. Ryan

Combustion Turbine Engineering,
Westinghouse Electric Corporation,
Orlando, FL 32826

J. R. Moore

AEDC Group,
Sverdrup Technology, Inc.,
Arnold Air Force Base, TN 37389

With the recent trend of reducing U.S. military expenditures, it has become desirable to develop dual use of certain Department of Defense facilities. These efforts have a commercial purpose, while still retaining a military benefit. The goals of these efforts are to make U.S. business more competitive in world markets, to develop the technology to solve pressing national problems, and to maintain intact the necessary talent pool and equipment for possible military needs. In a recent initiative described in this paper, test cell equipment at the Arnold Engineering Development Center, Arnold AFB, Tennessee, was modified and expanded to allow development by the Westinghouse Electric Corporation of low-emission combustors for heavy-duty gas turbines for commercial power generation.

Introduction

The Power Generation Business Unit of Westinghouse had been evaluating various sites where combustors for the new generation of large stationary gas turbines could be developed, at full pressure, temperature, and flow. A full-scale, high-pressure combustor test facility is costly to operate, so combustor development at Westinghouse is split into at least four steps, as shown in Table 1. Step 4 testing will be performed only on those combustors that have successfully come through the lower cost screening of Steps 1–3.

The combustors to be developed represent such a state-of-the-art change in form and function (in order to meet ultralow NO_x emission goals), that it is considered necessary to test them at full conditions in a single-combustor test rig before undertaking a field test in an operating power plant. What was needed was a site having a supply of 660 K (725°F) air at 14.2 atm, in a quantity of 22 kg/s (48 lb/s), and free of any combustion products (i.e., unvitiated), together with access to a high-pressure pipeline capable of furnishing 3800 Nm^3/h (2350 scfm) of natural gas (Table 2). After considering many possibilities, both domestic and overseas in 1992–93, it was determined that a cooperative facility development with AEDC best met all criteria.

There is a test cell at AEDC, designated T-3, which is designed for testing small jet engines at simulated high flight Mach numbers. It is equipped with an unvitiated air supply having well in excess of the airflow, pressure, and temperature needed for one heavy-duty gas turbine combustor. Test time is available at this cell, there is a large state-of-the-art control room, and extensive data acquisition hardware is in place. Furthermore, arrangements could be made to utilize the existing experienced technical staff to support much of the effort. Difficulties were encountered in attempting to adapt a jet engine test cell to combustor development, as described below, but the facility is now fully operational.

Contributed by the International Gas Turbine Institute and presented at the 40th International Gas Turbine and Aeroengine Congress and Exhibition, Houston, Texas, June 5–8, 1995. Manuscript received by the International Gas Turbine Institute February 8, 1995. Paper No. 95-GT-46. Associate Technical Editor: C. J. Russo.

Installation Considerations

The large Westinghouse combustor test rig had to be installed without compromising the capability of the test cell to test jet engines. Figure 1 shows a conceptual view of test cell T-3 before installation of the Westinghouse combustor test rig. As built, the test cell contained a heavy thrust stand capable of retaining an operating jet engine, and recording its thrust using load cells. Surrounding the thrust stand was a heavy pressure-tight chamber, designed to be pressurized to simulate high Mach number, low altitude flight, or evacuated to simulate lower speeds and high altitudes. A heavy, air-tight cover opens at the top, to allow installing or removing jet engines. This feature is indicated in Fig. 1.

Also indicated in Fig. 1 is one of the two large air preheaters. It is a tube-type, indirect-fired heat exchanger. On its cold side, high-pressure air from another building (not shown) is received. On the hot side, the heating medium is combustion products at approximately one atmosphere. This comes from natural gas burners. The burner-blower is indicated on the figure. Shown between the preheater and the test chamber is a blending section where air from the preheaters, and air direct from the compressors is mixed to achieve the desired temperature. An air heater of the flow rate and pressure capability to supply a jet engine is extremely rare in combustor test facilities and it forms a very valuable part of the test apparatus. Figure 2 is included to show its scale.

A *small* jet engine on a thrust frame is depicted in Fig. 1. Unfortunately the combustor test rig more nearly resembles a *large* jet engine in size. The test rig is approximately 4 m (13 ft) long by 2.6 m (8.5 ft) at its widest point.

The initial plan was to place the combustor test rig inside the test cell on the thrust frame. Figure 3 shows this arrangement drawn to scale. In some respects it appears desirable, in that the ability of the test cell to receive jet engines is in no way disturbed. However, as is shown later in Fig. 7, changing combustors for testing through the port in the forward bulkhead of the combustor test rig, would be impossible in this arrangement, because the port would be so close to the head end of the altitude chamber.

Figure 1 makes it appear that the altitude test cell is surrounded on both sides by ample space, but in actuality there

Table 1 Steps in full-size combustor development testing

Step 1	Step 2	Step 3	Step 4
ATMOSPHERIC, COLD FLOW	ATMOSPHERIC, COMBUSTION	MID-PRESSURE, COMBUSTION	FULL PRESSURE, COMBUSTION
Flow Visualization	Ignition	Emissions trends	Definitive emissions
Flow Distribution	Stability Trends	Stability Limits	Combustion Efficiency
Pressure Loss	Pressure Loss	Pressure Loss	Pressure Loss
Internal Velocities	NOx Propensity	Part Power Combustion Efficiency	Wall Hot Spots
Fuel-Air Mixing Trends	Flashback Propensity	Wall Hot Spot Early Warning	Turbine Inlet Pattern Factor
Verify CFD Cold Flow Modeling	Access for Laser Diagnostics	Gross Flashback Screening	Combustion-Driven Oscillations
	View Flame	Possibly View Flame	Define Flashback

was inadequate space in the T-3 test cell building to locate the combustor test rig. The decision was made to locate it in the area between the building housing T-3 and the adjoining larger building on the south. The addition of a new concrete foundation underneath, and a sturdy rain/sun shield and steel support frame above, together with the existing building walls on two sides provides all the shelter that is needed.

Figure 4 shows the final arrangement of the hot-air/cold-air mixer, the original T-3 altitude chamber, and the combustor test rig. When combustor tests are to be conducted, a blank-off plate is placed in the large flange at the inlet end of the altitude test chamber. This diverts air out the side of the hot/cold air mixer through the two small flanges shown in Fig. 4, and then through a tee into approximately 20 m (65 ft) of 25.2 cm (10 in.) diameter pipe. Valves provide controllability over a wide range of airflows. When jet engine tests are run, blank-off plates are installed at the mixing plenum flange and the large blank-off plate is removed from the head end of the altitude chamber. Downstream of the Westinghouse test rig, there is a deluge section, consisting of approximately 2.75 m (9 ft) of 50.8 cm (20 in.) pipe, fitted with 15 water spray nozzles. This section has been very effective in reducing stack noise to an acceptable level, and eliminating any hot spots (in excess of 477 K [400°F]) in the pipe or the back-pressure valve.

Controlling the Heated Combustion Air Supply

Large air heaters, such as the one used here, resist rapid temperature changes needed for testing. For example, proper evaluation of an industrial gas turbine combustor in a test rig requires moving expeditiously through a series of conditions such as those shown in Table 3.

Rapid setting of test conditions is accomplished in this facility by a system of air-blending valves (Fig. 5), rather than adjusting the gas burners. Air for the combustor comes to the heater from a large air compression system located in an adjacent test facility, labeled "VKF." After filtering and pressure regulation by valves, it enters the cold side of the heater through a 25.4 cm (10 in.) pipe, and leaves in a 30.5 cm (12 in.) line. Process air for turbine engines in T-3 or in this case the Westinghouse combustor, passes through flow control valves, with excess hot air vented to atmosphere through alternate valves. Large and small valves are installed in pairs to cover a wide range of airflows. Fortunately this was done when T-3 was originally developed for turbojet testing, for this permits it to supply the proper airflow for the Westinghouse rig, which requires only a third of that for which the cell was designed. Similarly, the provision to vent hot air is vital, because at many of the combustor test rig conditions, there would not be enough throughflow in the air heater to prevent its tubes from overheating. Downstream of the hot valves, FV9 and FV10, the hot air enters a cylindrical mixing chamber, just upstream of the original T-3 altitude cell. Cold air bypasses the heater, and goes directly through flow control valves FV3 and FV4 to the mixer. Excellent mixing is achieved by routing the cold air into a ring manifold surrounding the mixing cylinder, and then feeding the cold stream into the hot, in 34 equally spaced jets. Combustion air temperature, pressure, and airflow rate to the combustor test rig can be rapidly set or changed by simultaneously opening or

Table 2 Facilities capabilities required for combustor testing

Parameter	Required Value, SI Units	Req'd. Value, US Customary
Combustor Inlet Pressure	1.2 atm to 14.3 atm.	18.0 to 210 psia
Combustor Inlet Air Temp.	310 K to 660 K	100°F. to 725°F.
Combustor Airflow	1.6 kg/s to 22 kg/s	3.6 lb/sec to 48 lb/sec
Combustor Outlet Temp.	310 K to 1811 K	100°F. to 2800°F.
Fuel Flow, No.2 Distillate Oil	3.2 l/m to 69.1 l/m	0.7 gpm to 15.2 gpm
Fuel Flow, Natural Gas	170 Nm^3/h to 3800 Nm^3/h	105 SCFM to 2350 SCFM
Steam Flow, (for injection)	0 to 5443 kg/h	0 to 12,000 lb/h
Gaseous Nitrogen (coolant)	0.6 kg/s	1.4 lb/s
Cooling Water	0 to 9200 l/m	0 to 2000 GPM

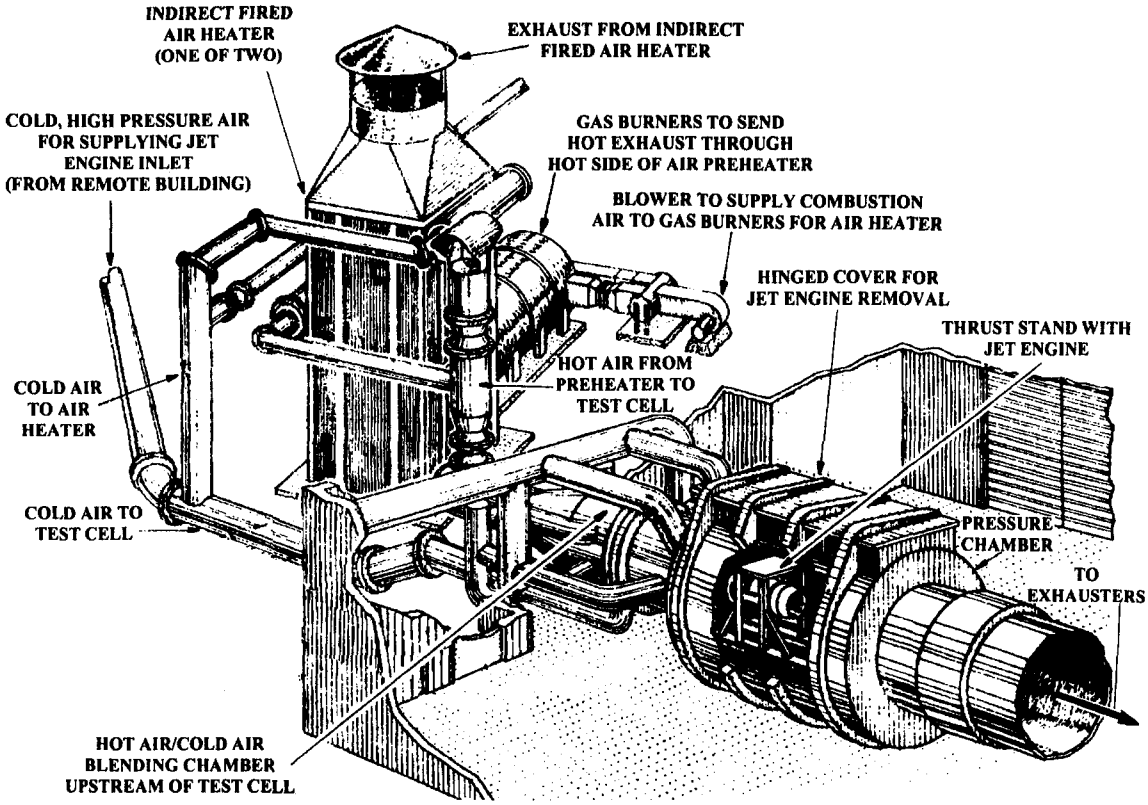

Fig. 1 Artist's concept of T-3 test cell before installation of Westinghouse rig

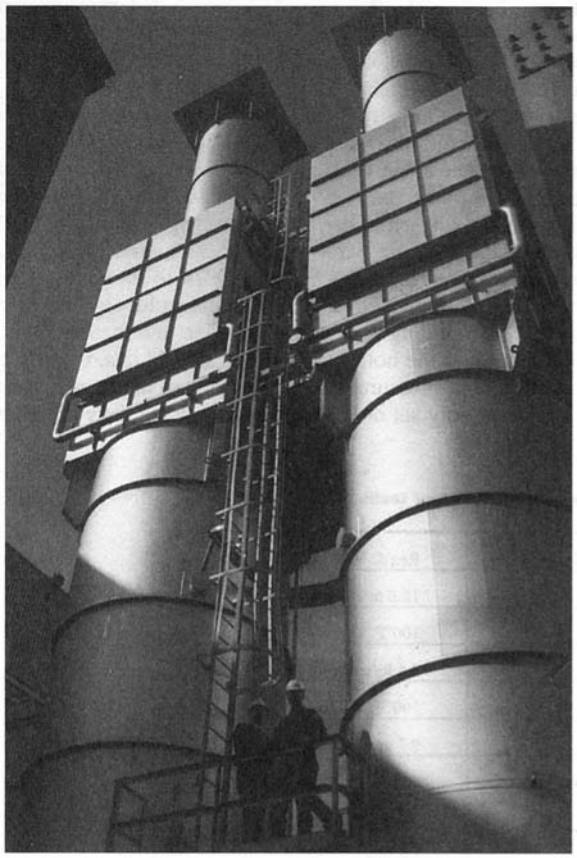

Fig. 2 Photo of preheater for T-3 test cell combustion air

closing of the hot and cold flow control valves. All control valves are automatically controlled by a computer system called the Test Environmental Controller (TEC) in order to provide both stable operation and rapid response in changing test conditions.

Combustor Test Rig and Instrumentation

The test rig, as installed, is shown in Fig. 6. This test rig was used in the 1970s and 1980s by Westinghouse for full-size combustor development (Hendry and Pillsbury, 1987), and was reactivated and overhauled for this program. Prominent in the foreground are four hoses. These hoses carry natural gas to each of four zones in an experimental dry low NO_x combustor, and are rated well in excess of the 2069 kPa (300 psi) needed for this application. Below the fuel hoses is the rig combustion air inlet. The flange for this inlet is heavily insulated for personnel protection, since the inlet air averages 658 K (725°F). The test rig itself, being completely water-jacketed, remains cool to the touch during all phases of combustion. The combustor to be tested is installed and removed via the cover just above the air inlet.

A better idea of how the test rig works can be seen from Fig. 7. A conventional, rather than a staged dry low NO_x combustor, is shown. Note that the combustion air enters at the bottom, passes through a simulated diffuser, turns 180 deg, and flows back to the head end of the combustor. This airflow pattern duplicates the reverse flow of the heavy-duty machines designed in the U.S. (Scalzo et al., 1996). A curving transition piece receives hot combustion gases from the burner, and conveys them to the simulated turbine plane. Instead of a turbine cascade, however, the hot gases pass through an array of 14 cooled probes: 7 temperature probes, followed by 7 pressure/emission probes. At today's firing temperatures, these probes must be cooled by a very substantial flow of 0.63 kg/s (1.4 lb/s) of gaseous nitrogen (GN_2). AEDC has a high-capacity GN_2 supply, another illustration of the advantages of dual-use conver-

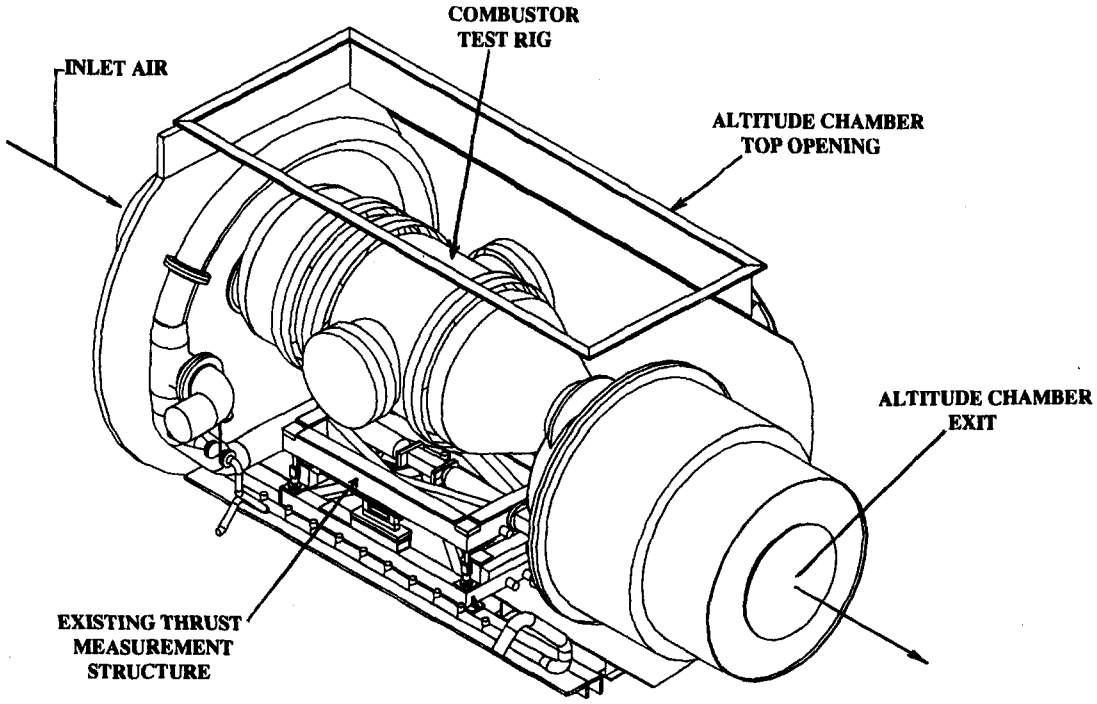

Fig. 3 Conceptual layout of Westinghouse test rig installed in T-3 altitude chamber

sion projects at a facility such as this. The 14 probes range in diameter from 1.9 to 2.5 cm (0.75 to 1.0 in.) and create a substantial pressure drop, which works together with the back-pressure valve farther downstream, to hold the maximum required pressure of 14 atm in the test chamber.

Figure 8 displays the system that protects the probe rakes from elevated burner outlet temperatures, and cools the emission sample on its way to the emission measurement instruments. The first row of probes, the three supervisory thermocouples, are located in the boundary layer, and this location,

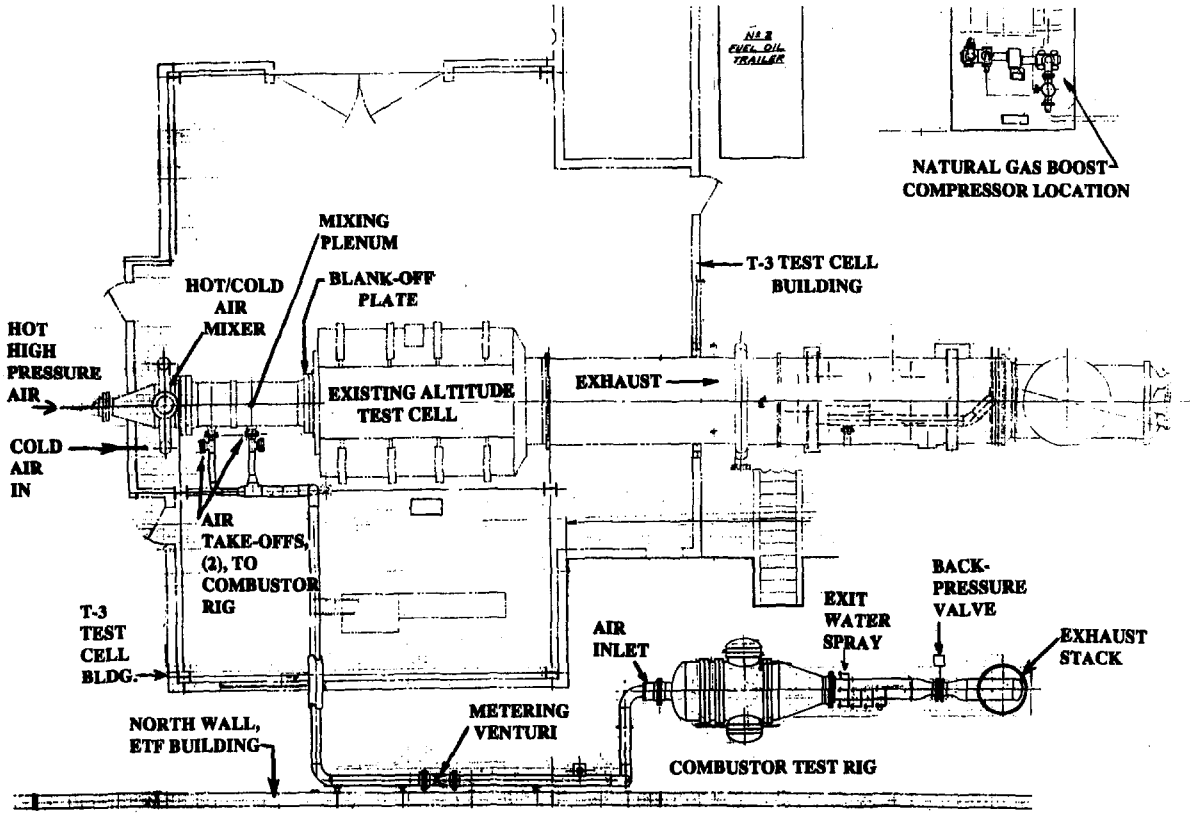

Fig. 4 Layout of T-3 area showing final position of Westinghouse test rig

Table 3 Conditions a single-combustor rig must produce in order to duplicate an engine

	Cold Flow	Ignition	0% Load	25% Load	50% Load	75% Load	100% Load
Inlet Press.,kPa (psia)	124 (18)	124 (18)	1034 (150)	1138 (165)	1241 (180)	1345 (195)	1448 (210)
Inlet Temp.,K (°F.)	311 (100)	311 (100)	611 (640)	622 (660)	633 (680)	644 (700)	658 (725)
Combustion Airflow, kg/s (lb/s)	1.6 (3.6)	1.6 (3.6)	21.8 (48)	21.8 (48)	21.8 (48)	21.8 (48)	21.8 (48)
Fuel Flow, kg/s (lb/s)	----	0.04 (0.08)	0.18 (0.40)	0.30 (0.66)	0.40 (0.88)	0.54 (1.20)	0.68 (1.50)
Steam Flow; kg/h* (lb/h)	----	----	----	907 (2000)	1451 (3200)	3175 (7000)	4535 (10,000)

* Non-dry low NOx combustors, only

together with heavy-duty construction, preserves them. These thermocouples provide a full-time, but somewhat slow and approximate indication of combustion temperature. The next row contains 7 equally spaced thermocouple probes, which span the entire transition exit height, and being fixed in position, must withstand the full total temperature of the burner discharge gases. These are continuously purged with GN_2 except for intervals of approximately 15 seconds when a reading is desired. The readings are extrapolated in real time by the AEDC data system to give a steady-state burner outlet temperature value, using the *pulsed thermocouple* method (Gabriel et al., 1982). During the brief interval when the thermocouple probes are taking a reading, hot gases flow into the probe bodies, over the thermocouple junctions, and then out to the stack. The cycling on and off of the purge and the aspiration of hot gas is controlled by solenoid valves as shown in Fig. 8. To protect the valve to the stack, TCCV2, the hot gases go through a cooler, as shown.

The final row contains 7 pressure/emissions probes, which also are fixed in position, and span the entire height of the passage. They are designed with three concentric passages. The outermost passage is continuously purged with GN_2, which is discharged downstream into the combustor exhaust. The second passage is purged until an emission reading is desired. Then, the solenoid valves depicted cycle, cutting off the purge, sending the sample to the three coolers shown and then to the emissions measurement line. Transport times in the emissions probes and associated lines are kept low by dumping most of the sample to the stack downstream of valve PTCV3. Only the sample actually needed for the instruments is tapped off through the hand valve shown, and sent through the final cooler to the instruments. The innermost passage in the pressure/emissions probes is for total pressure measurement, and since it is a nonflow passage, leading to a transducer, it is not purged.

All instrumentation systems, measurement lines, and probes used for measurement during this testing comply with SAE ARP 1256. Smoke measurements during testing with fuel oil comply with SAE ARP 1179. Currently, the emissions measurement instruments used include the following: 2 Thermo Electron Model 10AR chemiluminescent analyzers, for NO and NO_x; 3 Beckman Model 865 NDIR analyzers; 2 for CO, and one for CO_2; one Beckman Model 404 flame ionization detector for total hydrocarbons; and one Beckman Model 755 paramagnetic oxygen analyzer.

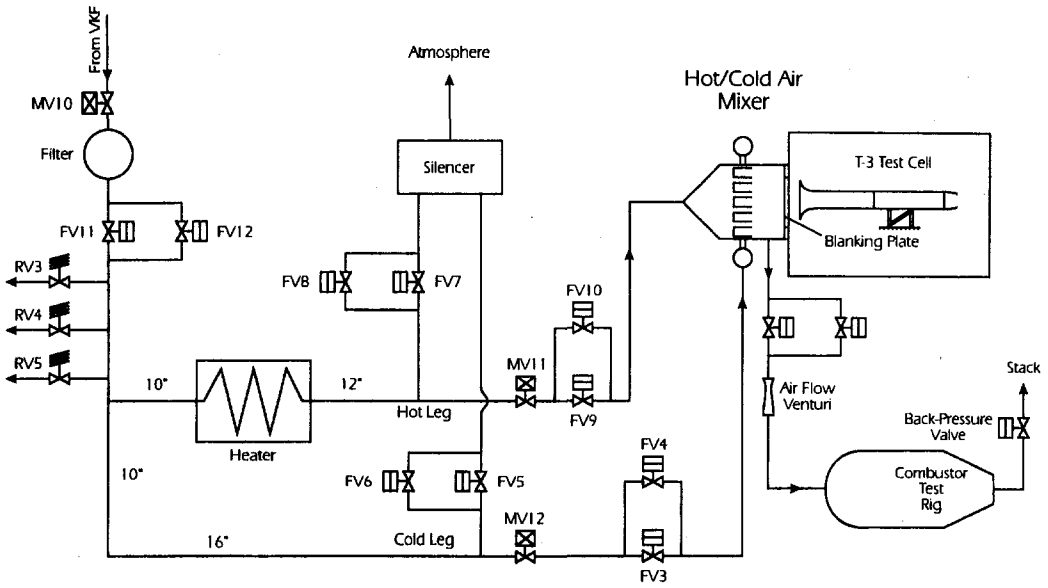

Fig. 5 Schematic of valving for quick-response changes of combustion air temperature

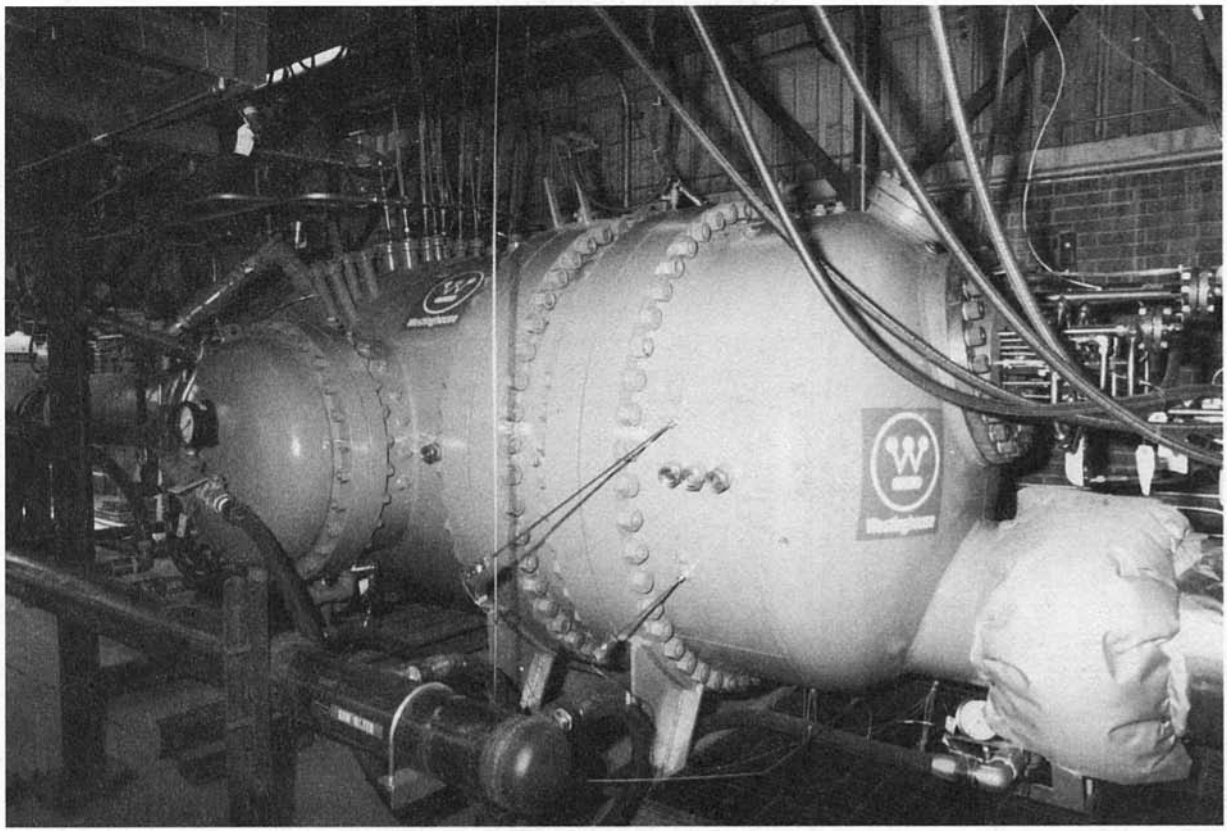

Fig. 6 Photo of test rig

Fuel Supply Considerations

As an aeropropulsion test facility, AEDC is primarily equipped to supply volatile liquid hydrocarbon fuels to the test cells. However, current industrial gas turbines are predominantly fueled on natural gas; most are sold with back-up distillate oil operating capability also. Natural gas in sufficient quantities for the 63 Nm^3/min (2350 scfm) flow rate required for the test rig was available in the vicinity of test cell T-3. However, the available line pressure of 621 kPa (90 psi) was lower than the required test rig operating pressure of 2758 kPa (400 psi). To meet this requirement, a Dresser-Rand Model 2KOA-1 compressor, packaged with a 198 kW (265 hp) Caterpillar Model G342TA natural gas-fueled drive engine was supplied by Westinghouse, and installed near the test cell. It draws its fuel from the same pipeline that supplies the gas it compresses, and represented one of the largest items purchased for the test stand conversion. It is an example of how dual-use conversion enhances the capability of a facility.

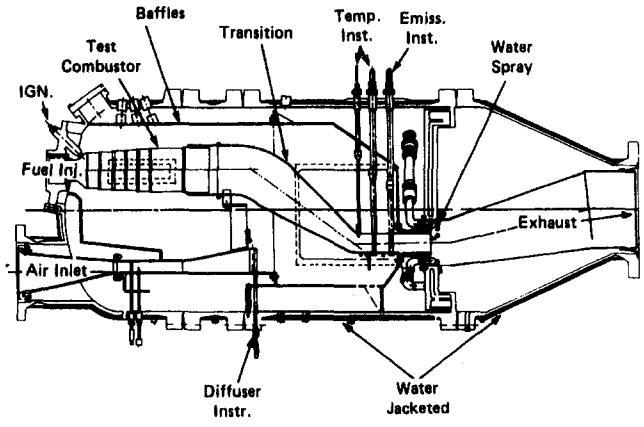

Fig. 7 Cutaway view of test rig

Dry low NO_x combustors for developmental industrial gas turbines often must be fuel-staged in order to meet stringent low emissions requirements or standards. T-3 was therefore equipped with five-zone fuel supply systems for both natural gas and distillate oil fuel. Figure 9 shows a schematic of the natural gas portion of the fuel system; the distillate oil system is similar. Downstream of the natural gas compressor the line splits into five branches, each with its own turbine-type flowmeter and throttle valve. Zones 1A and 1B are shown connected together, since it was contemplated that they would feed a conventional diffusion-flame pilot in an otherwise premixing-type combustor. Such diffusion flame pilots may have to go from very low to very high fuel flows, and so two parallel flowmeters and valves were specified to cover the range. Zones 1A and 1B can also be operated as separate zones by removing the tee. Control of the fuel systems was programmed in the Westinghouse Distributed Processing Unit available in the T-3 control room and used for control of all test cell functions.

Initial Operating Experience

Conversion of T-3 cell was sufficiently complete by late April, 1994, so that combustion testing could begin. Initial test experience immediately showed areas where improvements were needed, and several modifications have been made. For example:

- Local pneumatic accumulators were added to speed up operation of the back-pressure valve.
- A readout of the natural gas compressor rpm was added to a control room screen so that gas pressure could be controlled more precisely.

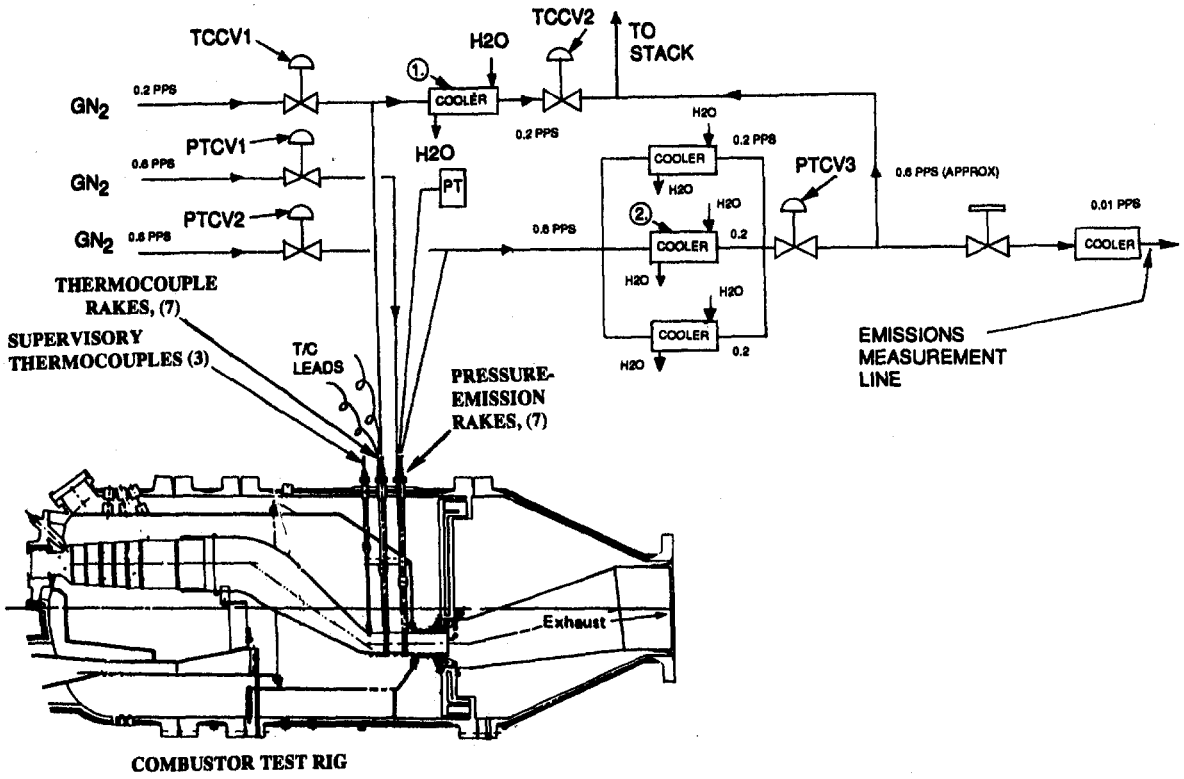

Fig. 8 Probe rake purge/read system

- An analog display of supervisory thermocouple temperature outputs was added to the control panel (this was found much quicker to follow than digital numerals on screens, especially during lighting attempts).
- Six water spray nozzles were added to the original nine in the duct downstream of the rig to eliminate duct wall and back-pressure valve hot spots.

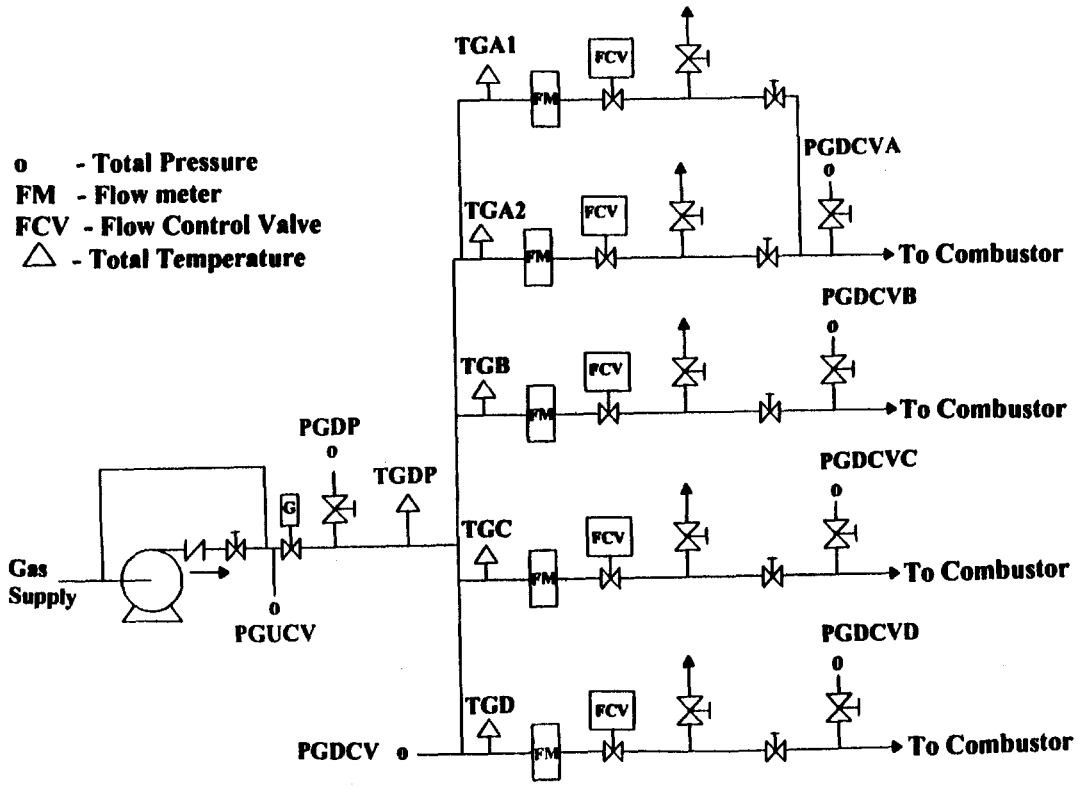

Fig. 9 Schematic of fuel system

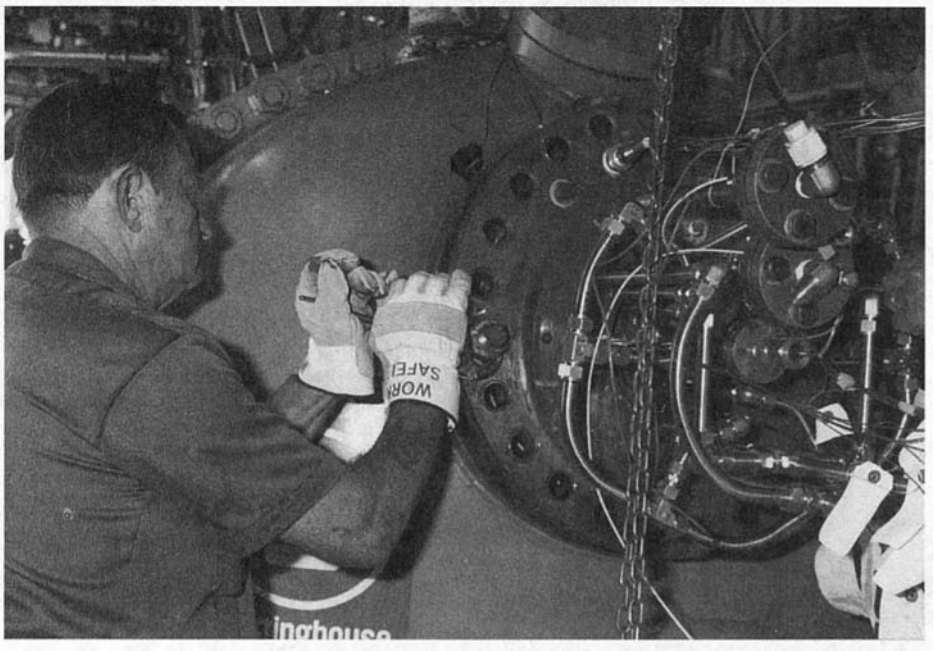

Fig. 10 Typical staged combustor being installed in test rig

- Combustion air temperature and mass flow rate control were made automatic, rather than manual.
- Air–fuel ratios in the five zones of premix type combustors were taken out of the large data displays, and put on a dedicated, rapidly updating screen, to assist operator control.

Figure 10 is a close-up photo of a full-size experimental combustor being installed in the test rig. Here the combustor itself is already inside the rig, and the cover plate is being tightened. In Westinghouse practice, the experimental combustors are mounted to cover plates, the fuel injectors installed, and the whole assembly instrumented with sealed leads, before they are brought to the test area. The combustor shown has five zones, each with its own fuel connection, which, together with the instrumentation leads, explains the complexity of the cover plate in the photo.

Conclusions

A dual-use modification of jet engine test cell T-3 at Arnold Engineering Development Center has been completed, and it is now in use as part of the ongoing development testing of new type dry low NO_x combustors for industrial gas turbines.

Relative to engine testing, use of the facility is saving time and expense. Other positive results for the industrial participant, and for the Air Force are summarized below:

- Development of a successful cooperative effort with benefits for both Westinghouse and AEDC.
- Reduced uncertainty for Westinghouse when new design combustors are first introduced into power plant gas turbines.
- An opportunity for staff at an Air Force facility to gain skills in component development in addition to turbine engine testing.
- A ground power plant development capability at AEDC to supplement the existing aeropropulsion capabilities.
- Assistance in keeping the AEDC technical team together by supplementing the military workload.
- A center where U.S. manufacturers can hone their skills in the areas of emissions reduction and energy efficiency to compete better in world markets.

Acknowledgments

The authors wish to acknowledge the very significant help of Mr. T. D. Garretson of the U.S. Air Force in bringing about the development of a high-pressure combustor test facility at Arnold Engineering Development Center, as well as the efforts of Sverdrup Technology, Inc. personnel at Arnold, especially L. R. Bahor, W. C. Gobbell, C. A. Leach III, J. E. Reavis, D. G. Gardner, C. L. Walters, W. L. Bonson, and many others; and, from L. P. G. Industries, Mr. F. K. Gabriel.

References

Gabriel, F. K., DeZubay, E. A., and Mitchell, R. W., 1982, "Fluid Pulsed Thermocouple Rake System for Automated High Gas Temperature Measurements," ASME Paper No. 82-GT-107.

Hendry, R. L., and Pillsbury, P. W., 1987, "Commercial Demonstration of the Dow Gasification Process in an Integrated Combined Cycle Cogeneration Application," *Proc. American Power Conference,* Vol. 49, pp. 149–153.

Scalzo, A. J., Bannister, R. L., De Corso, M., and Howard, G. S., 1996, "Evolution of Westinghouse Heavy-Duty Power Generation and Industrial Combustion Turbines," ASME JOURNAL OF ENGINEERING FOR GAS TURBINES AND POWER, Vol. 118, pp. 316–330.

On-Engine Evaluation of Emissions Characteristics of a Variable Geometry Lean-Premixed Combustor

H. Yamada

K. Shimodaira

S. Hayashi

Thermofluid Dynamics Division,
National Aerospace Laboratory,
Chofu, Tokyo 182, Japan

The design and on-engine testing of a lean-premixed, low-NO_x combustor for a simple-cycle, single-shaft, 250-kW gas turbine engine of a pressure ratio of eight are described. A variable-geometry system composed of butterfly air valves was used to control the combustor air split between combustion and dilution. Fuel was staged to a direct-injection pilot burner, and a lean-premixed main burner was fitted to the combustor liner. The NO_x emissions with natural gas fueling were found to be less than 20 ppm (at 15 percent O_2) at and near full-load conditions with combustion efficiencies greater than 99.8 percent. Emissions data from early high-pressure rig tests of the combustor hardware are also presented.

Introduction

Control methods for NO_x (oxides of nitrogen) emissions from stationary gas turbine engines are necessary to meet the increasingly stringent emissions standards imposed by regulatory agencies worldwide. Current practices involve injection of water or steam and use of selective catalytic reduction. These abatement methods have specific limitations and problems including high installation and operating costs, large installation space, and fuel consumption penalty. Development programs of "dry" low-NO_x combustors using lean-premixed combustion concepts are being actively conducted by several gas turbine manufacturers (Solt and Tuzson, 1993). For natural gas-fueled gas turbines of medium and large outputs, reductions of NO_x emissions to the 25-ppm level have recently been achieved. Several concepts for combustion-zone equivalence ratio control are used for the lean-premixed combustors to prevent excessive increase in CO and unburned hydrocarbon (HC) emissions: combustion staging by using multiple, innovative premixed burners (Aigner and Muller, 1993), inlet guide vane modulation (Smith, 1992), air bleed (Etheridge, 1994), and swirler inlet air control (Smith, 1992; Smith et al., 1991). For gas turbines of smaller outputs, however, such a strategy is impractical. A problem inherent to the application of the lean-premixed combustion concept to combustors of small gas turbines of lower operation temperatures is an increase in CO emission or a decrease in combustion efficiency. Oxidation reactions of CO and unburned hydrocarbons are likely to be quenched on the liner wall because of the lower combustor inlet temperatures. Additionally, CO oxidation is not appreciable downstream of the combustion region since the turbine inlet gas temperatures are on the 900–1000°C level. Thus, achieving both low-NO_x emissions and high combustion efficiencies at the same time is much more difficult for small gas turbines than for medium to large scale gas turbines of higher operating temperatures.

The use of a variable-geometry system that can modulate air distribution over a wide range is necessary for the successful application of the lean-premixed combustion concept to NO_x emissions control for small gas turbines. In the present low-NO_x combustor development program, a single can combustor using butterfly valves as a variable-geometry system for the air split control was designed and evaluated by on-engine testing.

Combustor Design

The low-NO_x combustor of the final configuration is illustrated in Fig. 1. The combustor liner, main and pilot burners, and variable geometry system are described below.

Combustor Liner. The lean-premixed combustor liner is generally similar to the original combustor liner in terms of geometry and dimensions. The diameter and length of the combustor liner are 136 mm and 360 mm, respectively. Though an increase in combustor liner volume favors complete combustion, the casing configuration of the present test engine constrains the radial dimensions of the combustor casing and therefore those of the combustor liner.

The most significant feature of the combustor liner is the use of the hot-wall construction for the primary combustion zone. Cooling air, which impinges on the back side of the wall, flows through the channels to form a cooling film on the liner wall. Hot-wall combustion liners were found to be very effective in reducing CO and HC emissions, especially in lean-premixed combustion at relatively lower combustor inlet air temperatures (Hayashi, 1983; Razdan et al., 1994).

The liner has four dilution air ports of fixed geometry (11 mm in diameter) 265 mm downstream of the burner head, and four connected to the air-flow control valves with ducts. The axial position of the variable-geometry air ports are shifted upstream as compared with that of the dilution holes in the original combustor liner due to the combustor casing's configuration constraints.

Pilot Burner. Engine lightoff is made by fueling the pilot burner alone, which is composed of a 12-vane, axial swirler/fuel injector module. A multi-orifice fuel injector is used to inject natural gas directly into the swirling air jet. The orifices are 4.4 mm in diameter, and the full-cone angle of the fuel jets is 60 deg. The passage of air is contracted to 20 mm in diameter at a distance from the end of the fuel injector to promote quick mixing of fuel and air in the combustion zone and to prevent flash back into the passage.

Main Burner. The main burner is used when the combustor is operated in the low-NO_x emission mode. Combustion air is fed through four tangential ports to a swirl chamber in the

Contributed by the International Gas Turbine Institute and presented at the 40th International Gas Turbine and Aeroengine Congress and Exhibition, Houston, Texas, June 5–8, 1995. Manuscript received by the International Gas Turbine Institute February 10, 1995. Paper No. 95-GT-48. Associate Technical Editor: C. J. Russo.

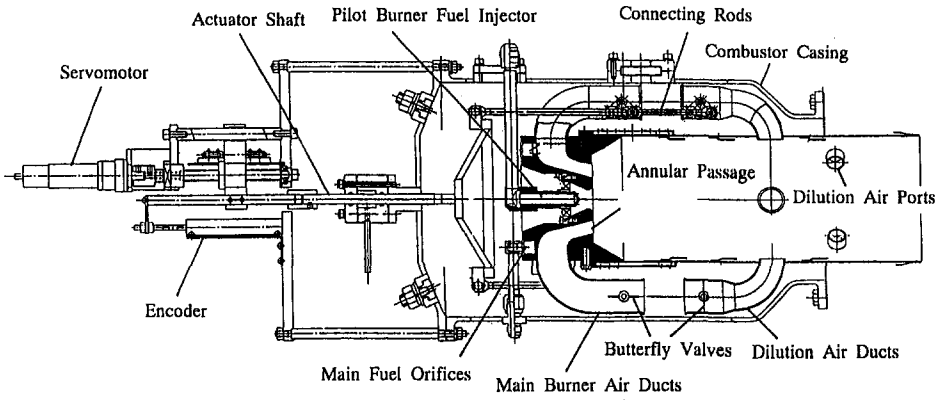

Fig. 1 Variable geometry, lean-premixed combustor (final configuration)

burner head, where natural gas is injected through 45 orifices drilled on the chamber wall. The premixed mixture flows through the annular passage surrounding the pilot burner to issue into the primary combustion zone. The inner and outer diameters of the annular passage are 44 and 70 mm, respectively. The swirl chamber/tangential port system imparts a rotation to the mixture jet for better flame stabilization.

Variable-Geometry System. In lean-premixed combustion, both low-NO_x emissions and high combustion efficiencies are achieved only in a very narrow operating range. To broaden the favorable operating range for a gas turbine, variable geometry for controlling the combustor air split between combustion and dilution, and fuel staging to multiple combustion zones can be employed. Air flow control by inlet guide vane modulation is applicable to gas turbines with variable inlet guide vanes.

In the present lean-premixed combustor design, a variable-geometry system using butterfly valves is employed for controlling the combustor air split between main burner and dilution. These valves are of the same size and are attached to the inlets of the main-burner air ducts and dilution air ducts. The shaft of each main-burner air valve is linked to that of the corresponding dilution air valve by a connecting rod. The valve position of the former is 90 deg out of phase with that of the latter: The main-burner air valves are fully open when the dilution air valves are closed. Four sets of air valve units are actuated in phase by a single servomotor. At engine lightoff, fuel is injected into the pilot burner with the main-burner air valves closed or partially opened.

According to the combustor design, the air flow in the combustor is divided roughly into 30 percent for liner cooling, 9 percent for pilot-burner combustion, and 61 percent for main-burner combustion and dilution. At full opening of the main-burner valves (100 percent valve position), 50 percent of the air flow is for main burner combustion and 11 percent is for dilution.

Engine

In engine testing of the lean-premixed combustor of the final configurations, a gas turbine engine, AT360C (Yammer Diesel Engine Co. Ltd.), was used. The engine was a simple-cycle, single-shaft gas turbine of a nominal pressure ratio of eight. The design-point operating conditions of the engine are summarized in Table 1. Engine load was controlled using a water dynamometer (Frude Co. Ltd). The rotational speed of the gas turbine rotor was kept at 46,000 rpm by a mechanical governor.

Experimental Combustor Rig-Test and Engine-Test Procedures

Rig Tests. Prior to engine tests, the combustor was evaluated at medium to high pressures using combustor test rigs to investigate ignitability, flame-stability range, and combustion and emission characteristics. Equivalence ratios were varied over a range of 0.12–0.24, covering the combustor operating conditions of the actual engine.

Electrically preheated combustion air entered the test section after being measured with an orifice. The air flow was in a reverse-flow direction around the outside of the combustor liner. This reverse-flow configuration simulated the flow pattern in the combustion liner installed in the test engine. Combustor pressure and air flow rate were controlled using a pressure-regulating valve upstream of the test section and a back-pressure valve downstream of the test section. Main and pilot-burner fuel flow rates were measured using calibrated orifices.

Combustor exhaust gas entered a ceramic lined water-cooled instrumentation section and a water spray before exiting to the atmosphere. Combustor exit gas temperatures were measured using three radial thermocouple rakes. Emissions sampling was conducted using a set of two water-cooled, diametral, gas sampling probes mounted downstream of the combustor. Each equal-area sampling probe contained a total of 12 holes. The samples from the two probes were combined and analyzed by the standard gas analysis procedure to determine exhaust gas compositions (CO, CO_2, NO, NO_x, O_2, HC). The overall equivalence ratios were calculated not only from measured fuel and air flow rates but also from measured exhaust gas compositions. These two values were agreed in an accuracy of 1 percent: The equivalence ratio used in this paper is based on the measured gas compositions.

Engine Tests. Following rig testing, the lean-premixed combustor was installed in the engine, as is shown in Fig. 2. The production-fuel control valve was used in the usual manner to maintain rated engine speed by means of a mechanical linkage to the engine governor. Total fuel flow rate was thus established by the engine control system in response to the imposed load. The fuel flow to the pilot burner was controlled manually by the engine operator to adjust the division of the fuel flow between the pilot and main burners.

The engine was started and brought to part-load operation by fueling the pilot burner. Then, the main-burner air valves were opened to a position, followed by main-burner fueling. With increasing fuel flow to the main burner, the fuel flow to the pilot burner was decreasing since the governor closes the pilot-

Table 1 Nominal design point operating conditions of the test engine (at 15°C)

Output	257 kW
Combustor pressure	0.79 MPa
Combustor inlet air temperature	600 K
Turbine inlet temperature	1143 K
Air flow	1.82 kg

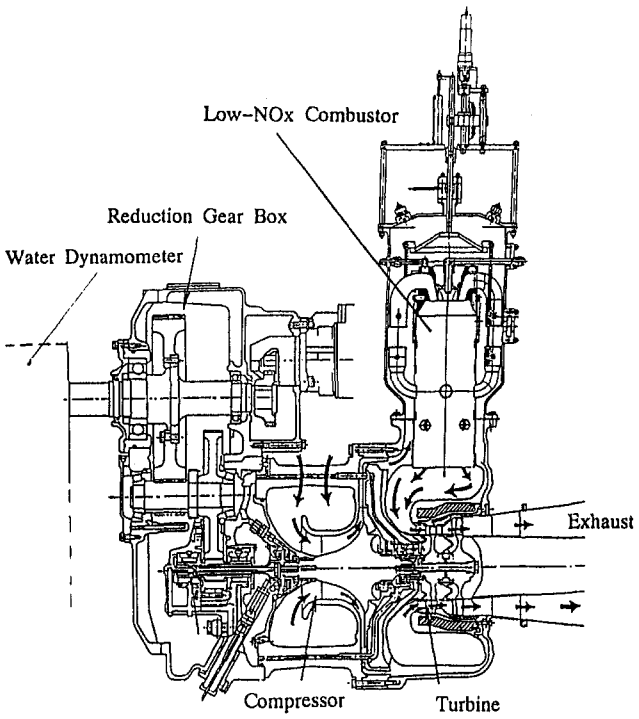

Fig. 2 Cross-sectional view of test engine equipped with variable geometry combustor

fuel metering valve to keep the engine speed. An increase in engine load increased not only main-burner fuel flow but also pilot burner fuel flow at first, but the fuel flow to the pilot burner was soon decreased to a minimum as the main-burner fuel flow was increased manually. This process was repeated until full power was reached. The maximum load to the engine was limited by the turbine inlet temperature restriction, decreasing with increasing ambient air temperature.

Gas sampling was made at the exit of the exhaust pipe by using water-cooled gas sampling probe rakes. Gas compositions were determined. The emission and combustion characteristics were varied significantly depending upon the scheduling of valve position and fuel staging.

Rig Test Results

Minor modifications were made for the combustor during the rig tests: Flow guides were added to the fixed dilution ports to modify the exit gas temperature patterns, the fuel orifice diameter of the main burner was decreased from 2 mm to 1 mm to improve the penetration and uniformity of fuel jets, and the main-burner annular exit area was increased by 60 percent to admit more air for leaner mixtures.

Figure 3 shows the results measured for the final model of the lean-premixed combustor. The NO_x emissions and combustion efficiencies are shown as functions of overall equivalence ratio for different schedules of fuel staging and air valve positions. The numerical values preceded by the symbol "VP" represent the main-burner air valve positions expressed in percentages. The combustor inlet conditions were typical of those at the engine full-load operation.

For the single operation of the pilot burner, the NO_x emission level increased steeply to a maximum and then decreased with increasing equivalence ratio. This trend in NO_x emissions suggests that the injected fuel mixed with air very quickly before combustion in the burner, though they were supplied separately. This direct-injection burner showed a similar NO_x emissions trend for kerosine fuel (Hayashi, 1982). The flow pattern downstream of the swirler is quite different from that with a conventional swirler, which forms a recirculation zone downstream of the fuel nozzle. Intense swirl and high jet velocity promote mixing of the injected fuel jets with air in the region very close to the swirler exit. The combustion efficiency was very high (> 99.9 percent) over the whole range of equivalence ratios as long as the main-burner air valves were closed (VP0). Introduction of main-burner air led to an appreciable decrease in combustion efficiency due to quenching of pilot-burner combustion by the annular air jet of lower temperatures.

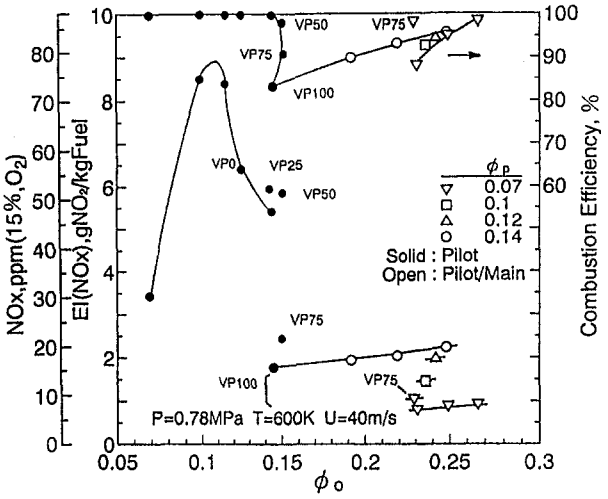

Fig. 3 NO_x emissions and combustion efficiencies for using fuel and air split

In the premixed combustion mode, combustion efficiency increased with increasing main fuel, while the corrected NO_x concentration in the exhaust gas or emission index was almost independent of overall equivalence ratio. At reduced main air flow (VP75) combustion efficiency was improved appreciably, followed by a very small increase of the NO_x emissions. The NO_x emission levels were decreased at reduced pilot-burner fuel flow rates. The operating conditions of the pilot burner are expressed by using the apparent equivalence ratio, ϕ_p, which is defined based on the ratio of pilot fuel to total air flow rates. The minimum NO_x emission levels less than 10 ppm (at 15 percent O_2) were measured at VP100. Thus, the combination of fine control of main-burner air flow rate and minimizing pilot-burner equivalence ratio leads to ultra-low NO_x emissions and high combustion efficiencies.

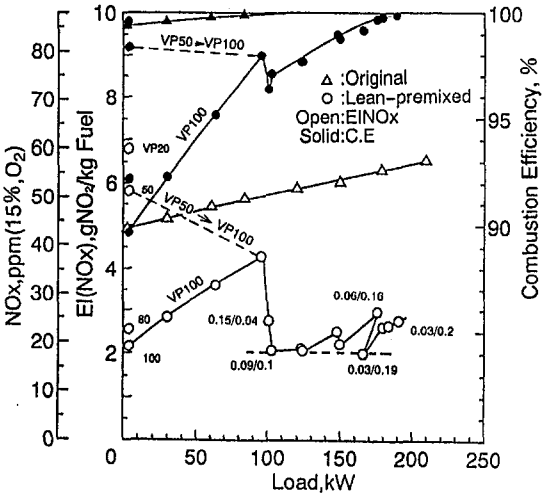

Fig. 4 Variations of NO_x emissions and combustion efficiencies with engine load

Engine Test Results

Emissions Data. Figure 4 shows typical results of NO_x emissions and combustion efficiencies as functions of engine load for the lean-premixed and conventional combustors. For the lean-premixed combustor, the air valve position and fuel staging were varied in the following manner: The main-burner air valves were gradually opened to a position at idling, and then the pilot-burner fuel flow was increased till a load of 100 kW was reached. Once at the load, fuel supply to the main burner was started with the main burner air valves fully opened.

In the premixed operation, a step increase in engine load caused a transient increase in the pilot fuel flow. This resulted in a jagged variation of the measured NO_x emissions level with engine load. A pair of numerical values, separated by a slash, attached to some data points for NO_x emissions in Fig. 4 are used to represent the fuel split to the main and pilot burners. The indicated numerical value before a slash represents the apparent equivalence for the pilot burner, which is based on the measured pilot-fuel flow rate and the total air flow calculated from the measured overall equivalence ratio. The numerical value after the slash is for the main burner.

Combustor Liner Temperatures. Combustor liner temperatures were monitored with a series of eight thermocouples mounted on the inner surface of the liner, six of which were in a single axial row circumferentially positioned at 45 deg from the air duct row and the other two were off the axial row. Figure 5 shows typical liner temperature data of the premixed combustor during engine testing at no and full-load conditions. The temperature profiles with varying operation conditions are very similar. Test data with the conventional diffusion-flame combustor are presented in the same figure for comparison. The data show that liner wall temperature was lower for the premixed combustor than for the conventional combustor, except for temperatures of the impingement-cooled wall where higher liner temperatures were measured. The data show liner temperatures well below the 800°C level generally specified for good liner durability. Additional liner temperature data with thermally sensitive paint substantiated the data with thermocouple. A considerable margin for reducing the amount of liner cooling air exists. The reduction in cool air can decrease CO emissions by minimizing the quenching of oxidation reactions along the liner inner wall by low-temperature liner cooling flow.

Conclusions

A variable-geometry combustor with a lean-premixed main burner and a non-premixed pilot burner successfully demonstrated ultra-low NO_x emissions in combustor rig testing and on-engine testing. Major results are summarized as follows:

1 NO_x emissions less than 20 ppm (at 15 percent O_2) or 2.8 EI (g/kg fuel) were measured at a combustion efficiency of 99.8 percent at and near full load when the fuel split was optimally controlled.
2 NO_x emissions of the 10 ppm level were measured at simulated full-power operations in the combustor rig test.
3 Fine control of main-burner air by the variable-geometry system actuated by the governor would result in the 20-ppm NO_x emissions level over a load range from half to full-power operations.

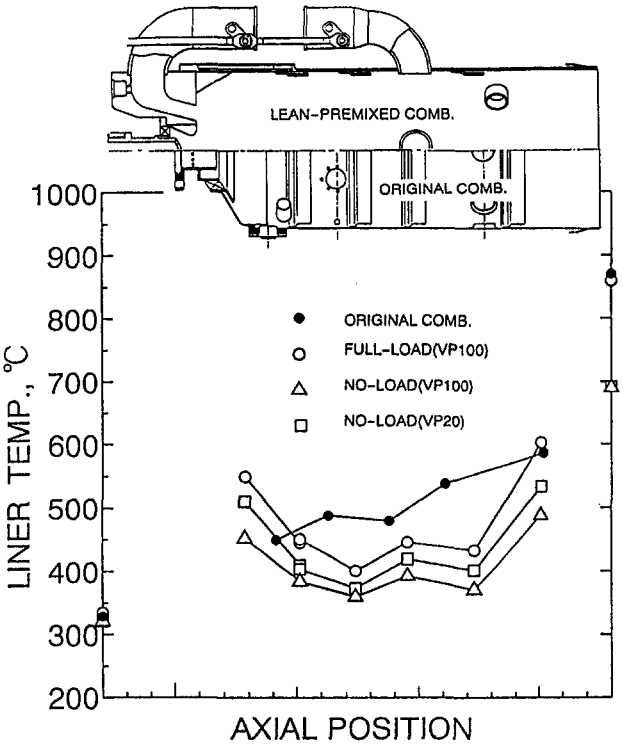

Fig. 5 Combustor liner wall temperatures

Acknowledgments

The work presented in this paper was made as a research program sponsored by the Environmental Agency of Japan for the period 1989 to 1993.

References

Aigner, M., and Muller, G., 1993, "Second-Generation Low-Emission Combustors for ABB Gas Turbines: Field Measurements With GT11N-EV," ASME JOURNAL OF ENGINEERING FOR GAS TURBINE AND POWER, Vol. 115, pp. 533–536.

Etherdge, C. J., 1994, "Mars SoLoNO$_x$-Lean Premix Combustion Technology in Production," ASME Paper No. 94-GT-255.

Hayashi, S., 1982, "Research on NO_x Emissions Reduction for Gas Turbine Combustors (I), Reduction by Fuel–Air Premixing," National Aerospace Laboratory Technical Report TM-470.

Hayashi, S., 1983, "Reduction of NO_x Emissions From Gas Turbine Combustors by Lean Premixed and Prevaporized Combustion," Paper No. B-7, *Proc. 11th Gas Turbine Conference,* Gas Turbine Soc. Japan.

Razdan, M. K., McLeroy, J. T., and Weaver, W. E., 1994, "Retrofittable Dry Low Emissions Combustor for 501-K Industrial Gas Turbine Engines," ASME Paper No. 94-GT-439.

Smith, K. O., Holsapple, A. C., Mak, H. K., and Watkins, L., 1991, "Development of a Natural Gas Fired, Ultra-Low NO_x Can Combustor for 800 kW Gas Turbine," ASME Paper No. 92-GT-303.

Smith, K. D., 1992, "Engine Testing of a Prototype Low NO_x Gas Turbine Combustor," ASME Paper No. 92-GT-116.

Solt, J. C., and Tuzson, J., 1993, "Status of Low NO_x Combustor Development," ASME Paper No. 93-GT-270.

Combustor Stability and Emissions Research Using a Well-Stirred Reactor

J. Zelina

D. R. Ballal
Fellow ASME

Department of Mechanical and Aerospace Engineering, University of Dayton, Dayton, OH 45469

The design and development of low-emissions, lean premixed aero or industrial gas turbine combustors is very challenging because it entails many compromises. To satisfy the projected CO and NO_x emissions regulations without relaxing the conflicting requirements of combustion stability, efficiency, pattern factor, relight (for aero combustor), or off-peak loading (for industrial combustor) capability demands great design ingenuity. The well-stirred reactor (WSR) provides a laboratory idealization of an efficient and highly compact advanced combustion system of the future that is capable of yielding global kinetics of value to the combustor designers. In this paper, we have studied the combustion performance and emissions using a toroidal WSR. It was found that the toroidal WSR was capable of peak loading almost twice as high as that for a spherical WSR and also yielded a better fuel-lean performance. A simple analysis based upon WSR theory provided good predictions of the WSR lean blowout limits. The WSR combustion efficiency was 99 percent over a wide range of mixture ratios and reactor loading. CO emissions reached a minimum at a flame temperature of 1600 K and NO_x increased rapidly with an increase in flame temperature, moderately with increasing residence time, and peaked at or slightly on the fuel-lean side of the stoichiometric equivalence ratio. Finally, emissions maps of different combustors were plotted and showed that the WSR has the characteristics of an idealized high-efficiency, low-emissions combustor of the future.

Introduction

The design and development of low-emissions, lean premixed aero or industrial gas turbine combustors is very challenging because it entails many compromises. Emissions of CO and NO_x in the upper stratosphere and pollutant exhaust from coal-fired and/or the combined steam-gas turbine cycle power plants are a major contributor to atmospheric pollution, acid rain, and ozone depletion. The Clean-Air Act of 1991 is forcing the burning of natural gas fuel and the application of sophisticated aerospace-derived technology to improve ground-based industrial gas turbine combustion systems. To satisfy the projected CO and NO_x emissions regulations without relaxing the conflicting requirements of combustion stability, efficiency, pattern factor, relight (for aero combustor) or off-peak loading (for industrial combustor) capability demands great design ingenuity. Also, in the design of future high-output combustors, minimizing combustor volume and maximizing combustor heat release are invariably the major goals. To meet these challenges, the designer has to search for basic concepts that provide a global, yet quantitative description of the combustion process in a gas turbine combustor. One such concept is to approximate the practical combustion zone as a WSR into which premixed fuel and air are fed and the overall kinetics of chemical reactions is controlling. The WSR provides a laboratory idealization of an efficient and highly compact advanced combustion system of the future that is capable of yielding global kinetics of value to the combustor designers.

In this paper, we describe the design of a WSR and measure combustion efficiency, combustion stability (lean blowout), and emissions of CO, unburned hydrocarbon (UHC), and NO_x. These data were obtained for propane and an HC fuel blend (a mixture of methane, ethane, and ethylene, which represents the products of thermal degradation of advanced endothermic jet fuels that are being developed for the high-speed flight). Finally, the combustion and emissions performance of the WSR are compared with a theoretical analysis and with measurements of pollutant emissions from gas turbine combustors, and implications to practical combustor design are discussed.

Contributed by the International Gas Turbine Institute and presented at the 40th International Gas Turbine and Aeroengine Congress and Exhibition, Houston, Texas, June 5–8, 1995. Manuscript received by the International Gas Turbine Institute February 10, 1995. Paper No. 95-GT-109. Associate Technical Editor: C. J. Russo.

WSR Design

WSR Test Facility. The first WSR was developed by Longwell and Weiss (1955) at Exxon Corporation, Linden, NJ. Subsequently, other researchers designed reactors of various geometries (see Table 1); this past work is summarized by Zelina and Ballal (1994). We capitalized on the findings of previous researchers, weighted the pros and cons of different designs, and constructed a 250-ml toroidal WSR designed by Nenniger et al. (1984). A schematic of this WSR design is shown in Fig. 1. The WSR volume is about 50 percent of the volume of a single swirl cup primary zone typically used in a modern aero-engine combustor. The design details of this toroidal WSR are given by Zelina and Ballal (1994).

The WSR is cast in two halves (each 125 ml) out of alumina ceramic cement. The lower half of the reactor has three holes on the centerline of the toroid for the thermocouple, gas sampling probe, and the ignitor. Notches are cast along the outside circumference of the reactor to accommodate the fuel jet ring, which is constructed of 304 stainless steel. Premixed fuel and air enter the ring through a 0.5 inch o.d. feed tube. Thirty-two tapped holes are placed on the ring and accommodate 1.2-mm-dia sonic jets, 20 deg off the radius. Finally, the top half of the reactor houses a flow straightener, which turns the flow 90 deg into a plug flow reactor (PFR).

Figure 2 illustrates the WSR test facility and its associated instrumentation: thermocouples, gas sampling probes, emissions analyzers, gas chromatography–mass spectrometry (GC-MS) system, and a Fourier transform infrared spectroscopy

Table 1 Comparison of WSR designs

	Longwell and Weiss (1955)	Blazowski (1980a, b)	Thornton et al. (1987)	Nenniger et. al (1984)	Zelina and Ballal (1994)	GT Combustor
τ	0.1-5 ms	0.6-4 ms	0.5-6 ms	1-6 ms	2-12 ms	2-12 ms
T_o	475K	290K	300-600 K	473K	300-500K	400-700K
P	0.13-1 atm	1.05 atm	1 atm	1 atm	1-5 atm	5-35 atm
V	240 mL	35 mL	15.8 mL	250 mL	250 mL	500 mL

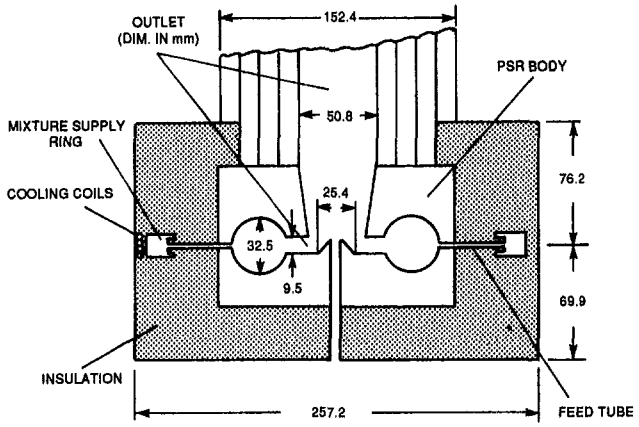

Fig. 1 Schematic of the toroidal WSR (all dimensions in mm)

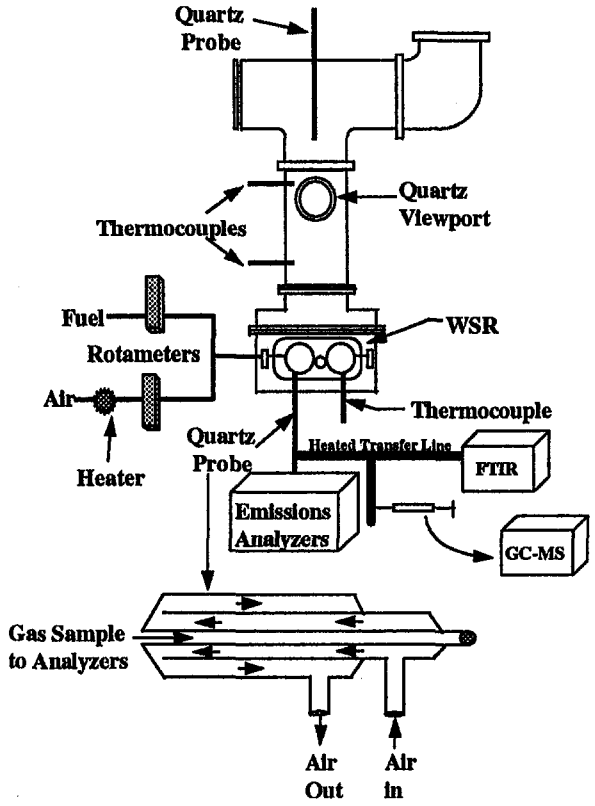

Fig. 2 Toroidal WSR test facility showing associated emissions and control instrumentation

(FTIR) equipment. Two Type B Pt-Rh thermocouples (0.01″ dia bare wire) rated at 2100 K and two Type K, Cr–Al thermocouples rated at 1660 K were installed in the WSR and PFR, respectively. The Pt–Rh thermocouples were coated with an yttrium chloride/beryllium oxide substance as described by Kent (1970) to eliminate catalytic effects on the thermocouple surface. Air-cooled quartz gas-sampling probes were used to withdraw pollutant samples from the WSR. These gas samples pass through a water trap and a dehumidifier, then are fed into various emissions analyzers.

The Horiba emissions analyzers comprise the following units: model MPA-510 oxygen analyzer (0 to 50 percent), model FIA-510 total hydrocarbon analyzer (0 to 5000 ppm carbon), model VIA-510 CO (0 to 5000 ppmV), model VIA-510 CO (0 to 2 percent) and CO_2 (0 to 25 percent) analyzer, and model CLA-510 SS NO and NO_x analyzer (0 to 200 ppmV). A gas sample of 500 ml/min is drawn in by each Horiba unit and analyzed for various pollutant species.

Test Conditions. The WSR test facility was operated slightly above atmospheric pressure and at room temperature (300 K). In this facility, the air rotameter was rated at 0 to 25 g/s and fuel supply was in the 0 to 5 g/s range. These flow conditions permitted the operation of the reactor over a broad range of loading parameter (LP) and equivalence ratios ϕ = 0.4 to 2.5, residence time τ_c = 2.5 to 12 ms, a cold mixture velocity in the toroid $\cong$ 100 m/s, mixing time $\tau_m \cong$ 0.1 ms, and reactor temperature T_f = 1200 to 2050 K. In this study, focus was on fuel-lean combustion ($\phi < 1$), at mean residence times of 2.5 ms and 12 ms.

The WSR was operated so that it does not suffer thermal shock and its wall temperature does not exceed 2300 K. Accordingly, the WSR was lightly loaded during the ignition sequence, allowed to reach over 1000 K and only then the lean blowout tests were performed. Propane and HC blend fuel (composition of 15 percent methane, 25 percent ethane, and 60 percent ethylene) were burned in the WSR. The HC blend fuel composition represents the products of thermal degradation of advanced endothermic jet fuels that are being developed for the high-speed civil transport (HSCT) and the Hypersonic System Technology Program (HySTP). A vaporizer chamber has been fabricated

Nomenclature

C_f = reaction rate constant
E = activation energy, cal/g-mol
EI = emissions index, g/kg fuel
LP = loading parameter, g-mol/s-L-atm^n
m = fuel concentration exponent
$\dot{m}$ = air mass flow rate, kg/s
n = global reaction rate
P = pressure, kPa
T_a = adiabatic flame temperature, K
T_f = reactor temperature, K
T_o = inlet temperature, K
R = universal gas constant
V = reaction volume, m^3
x_f, x_o = volume fraction in combustion gases of fuel and oxygen, respectively
Z = exponent of equivalence ratio
β = fraction of fuel burned
η = combustion efficiency
ρ = density, kg/m^3
τ = residence time, ms
ϕ = equivalence ratio

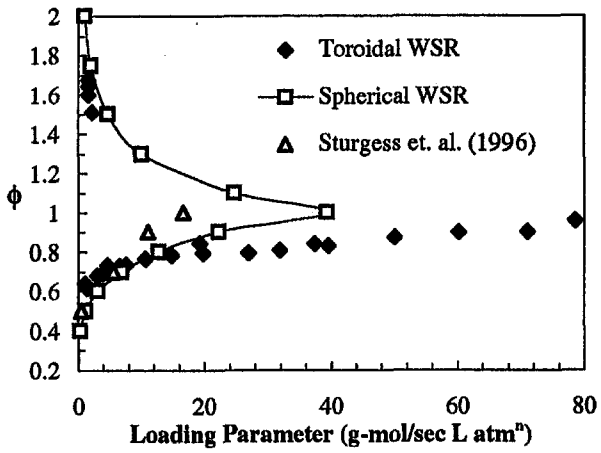

Fig. 3 Measured stability loops for propane/air mixtures at atmospheric pressure and 300 K inlet temperature

for future studies of the combustion of liquid fuels such as benzene, heptane, toluene, methyl cyclohexane, NORPAR, JP-4, JP-5, and JP-8.

Error Analysis. Both the fuel flow and airflow were monitored to within 2 percent. The combined error produced a maximum uncertainty of 5 percent in the value of equivalence ratio. The thermocouple temperature measurements, after correcting for radiation and conduction heat loss, were accurate to within 40 K. The Horiba emissions analyzers and the HP GC-MS system quote an accuracy to within 1 percent of full scale.

Results and Discussion

Combustion Stability and Lean Blowout. Figure 3 shows a typical measured WSR stability loop for propane–air mixtures at 300 K inlet temperature. Also plotted on this figure is the stability loop for the spherical WSR (Kretschmer and Odgers, 1972) and stability curves for a mixing-controlled research step combustor (Sturgess et al., 1996). At light loading ($LP < 20$), both the spherical WSR and the step combustor exhibit wide stability limits and better lean blowout performance. In contrast, the toroidal WSR is capable of better fuel-lean performance and peak loading (almost twice as high as that for the spherical design and step combustor) at medium to high loading ($LP > 20$). The differences in stability limits for these combustor configurations can be attributed to the combined effects of imperfect mixing and heat losses in earlier reactors, and recirculation.

Lean Blowout Theory. In a WSR, the rate of reaction between fuel and air may be expressed by the material balance equation:

$$\beta\phi\dot{m} = C_f V T_f^{0.5} \exp\left(\frac{-E}{RT_f}\right)\rho^n x_f^m x_o^{(n-m)} \qquad (1)$$

For fuel-lean propane–air mixtures ($\phi < 1$):

$$\phi C_3H_8 + 5O_2 + 18.8N_2 = 3\beta\phi CO_2 + 4\beta\phi H_2O + (1-\beta)\phi C_3H_8 + 5(1-\beta\phi)O_2 + 18.8N_2 \qquad (2)$$

From this equation, values of x_f and x_o can be calculated. Substituting these values into Eq. (1) gives

$$\frac{\dot{m}}{VP^n} = \frac{C_F}{R^n T^{n-0.5}\exp\left(\frac{E}{RT}\right)} \frac{1}{\phi^{1-m}} \frac{(1-\beta)^m(1-\beta\phi)^{n-m}}{\beta(23.8+\phi+\beta\phi)} \qquad (3)$$

The work of Kretschmer and Odgers (1972) suggests that the value n depends upon the equivalence ratio at lean blowout. Ballal and Lefebvre (1979) used $n = 1.25$, $m = n/2 = 0.625$, and $E = 54$ kcal/mol. Using corresponding values of P, T_f, β, and ϕ in the equation, it is possible to plot LP versus β for different equivalence ratios. Maximum loading occurs on the peaks of these curves, corresponding to the highest possible heat release rate at a stipulated values of T_o and ϕ. By plotting log (LP) versus log (ϕ) for different values of T_o, Ballal and Lefebvre (1979) found that

$$\left(\frac{\dot{m}}{VP^n}\right)_{\max} = 1.93 \exp\left(\frac{T_o}{150}\right)\phi^z \qquad (4)$$

As shown in Fig. 4, Eq. (4) provides a satisfactory prediction of the WSR lean blowout limits when $z = 7$ and n varies in a linear fashion from 1 to 1.25, depending upon the equivalence ratio.

Combustion Efficiency. As Lefebvre (1983) has stated, in a continuous-burn combustion system, the main factors affecting the level of combustion efficiency are evaporation or vaporization rate, mixing rate, and reaction rate. In practical combustors, the maximum heat release is rarely controlled by all three rates. Rather, *one* of the three key rates participates in determining overall combustion efficiency. In this investigation, the WSR combustion efficiency is reaction-rate controlled and may be calculated on an enthalpy basis by simply subtracting the inefficiencies due to incomplete burning in the form of CO and UHC. This method was developed to determine combustion efficiency based on emissions measurements from aircraft gas turbine engines (SAE ARP 1533, 1994). This method can be readily applied to a variety of practical and laboratory combustors and emissions measurements and the WSR results are shown in Figs. 5 and 6.

Figure 5 shows combustion efficiency as a function of the reactor temperature (equivalence ratio) and indicates that for a low value of the residence time ($\tau = 2.5$ ms), the combustion efficiency of the propane–air mixture is above 99 percent over a wide range of mixture ratios ranging from near-lean blowout to stoichiometric ratio. The combustion efficiency decreases above 1800 K for longer residence times ($\tau = 12$ ms) primarily due to the dissociation of CO_2 in these high-temperature regions. As residence time is decreased, combustion gases do not remain in the high-temperature region long enough for dissociation reactions to take place and high values of combustion efficiency are obtained.

Figure 6 shows the variation in WSR combustion efficiency as a function of LP (for $\phi = 0.8$), this latter parameter is

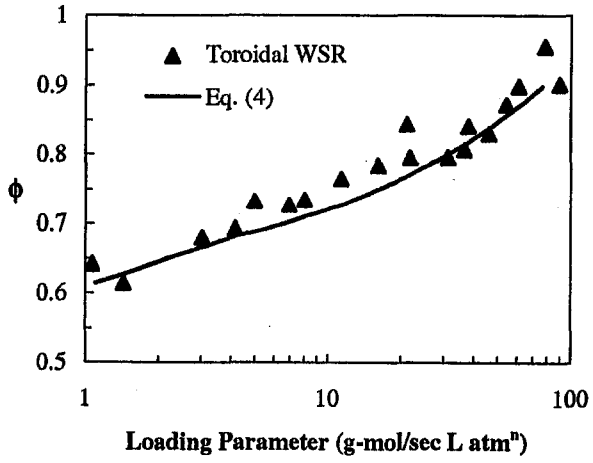

Fig. 4 Comparison between measured values of WSR lean blowout and predictions

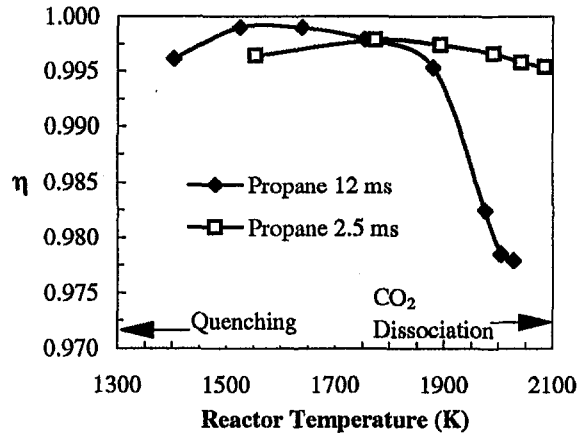

Fig. 5 Combustion efficiency as a function of reactor temperature for propane/air mixtures at two different residence times

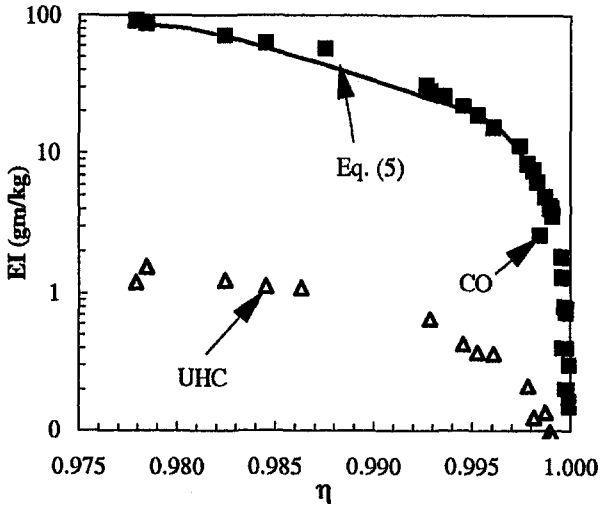

Fig. 7 Relationship between combustion efficiency and emissions of CO and UHC in a WSR

inversely related to the residence time τ. These data also confirm the generally high level of combustion efficiency of the WSR. Thus, it may be concluded that the WSR data represent the upper range of efficiency values that advanced gas turbine combustor designs should approach given adequate pressure drop (rapid mixing), reduced wall quenching, and good fuel atomization leading to rapid fuel evaporation.

CO and UHC Emissions. CO and UHC emissions represent a direct manifestation of combustion *inefficiency*. If the primary zone of a combustor operates fuel-rich, has inadequate mixing, or is prematurely quenched by cold air, large quantities of CO (which is relatively resistant to oxidation) will be formed due to the lack of oxygen needed to complete the reaction to CO_2. UHC emissions include fuel that emerges at the combustor exit in the form of droplets or vapor, and the products of the thermal degradation of the parent fuel into species of lower molecular weight such as methane and acetylene. UHC emissions are associated with poor atomization, inadequate burning rates, and premature quenching. In general, UHC emissions parallel those of CO. Any combustor design modification that decreases CO emissions will also decrease UHC emissions.

Figure 7 shows a measured combustion efficiency plotted versus emissions of CO and UHC. Also plotted is an efficiency versus emissions relationship developed by Bahr (1972) for gas turbine combustors:

$$\eta = 1 - \left(\frac{EI_{\mathrm{UHC}} + 0.232 EI_{\mathrm{CO}}}{1000} \right). \qquad (5)$$

A good agreement is obtained between WSR measurements and predictions of CO emissions using Eq. (5). This provides further evidence that the combustion performance of the primary zone of a gas turbine combustor is very similar to that of a WSR.

Figure 8 shows the emissions of CO from the toroidal WSR over a range of equivalence ratios. Also plotted are typical CO emissions from a practical gas turbine combustor burning jet fuel (Rizk and Mongia, 1993). Although trends are similar (i.e., CO emissions reach a minimum around $\phi = 0.6$ corresponding to the combustion zone temperature of 1600 K), the CO emissions index for the practical gas turbine combustor are two to three times higher than those for the WSR. Two key factors influence CO emissions in practical systems: (*i*) for $\phi < 0.6$ cold gas quenching and combustion temperatures are usually too low for CO to burn to CO_2 and (*ii*) for $\phi > 0.6$, CO quickly reaches the equilibrium value, which is higher than the acceptable emission level. In such a situation, special care is required in practice to dilute hot combustion products to turbine entry temperatures. Other factors such as poor fuel atom-

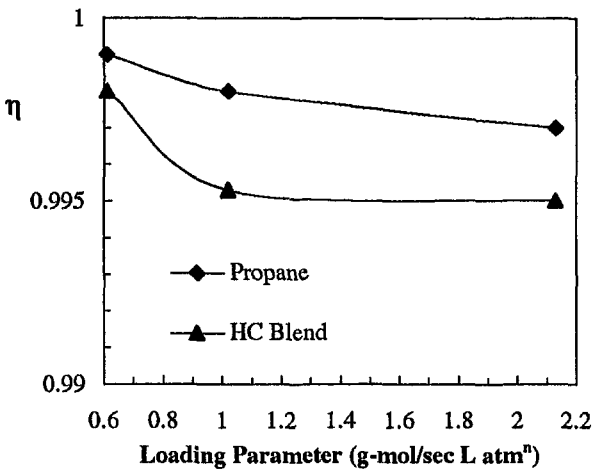

Fig. 6 WSR combustion efficiency versus loading parameter for two fuels

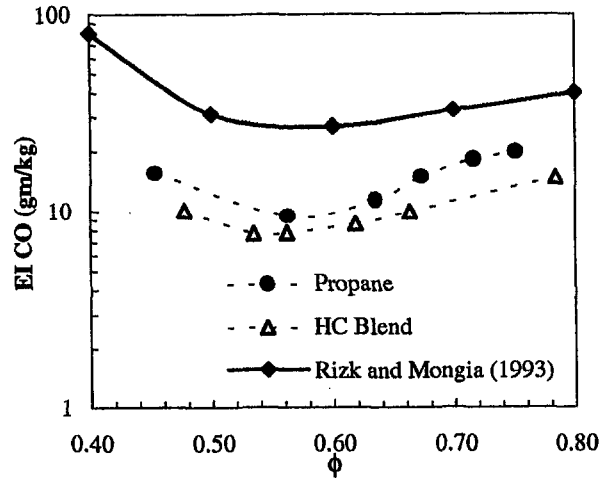

Fig. 8 Emissions of CO from the WSR compared to a practical gas turbine combustor

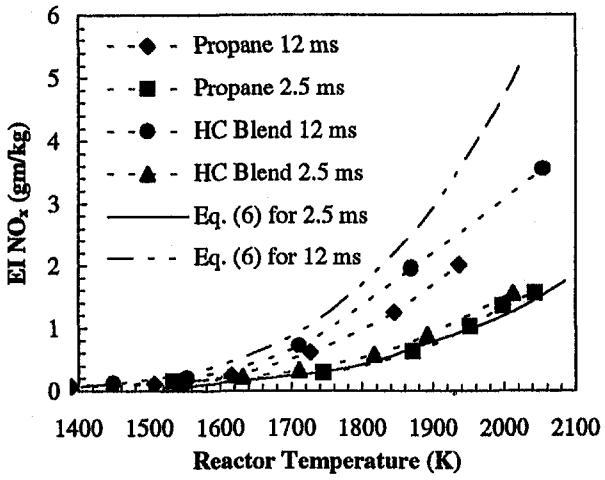

Fig. 9 Emissions of NO_x as a function of reactor temperature for two different residence times and different fuel/air mixtures

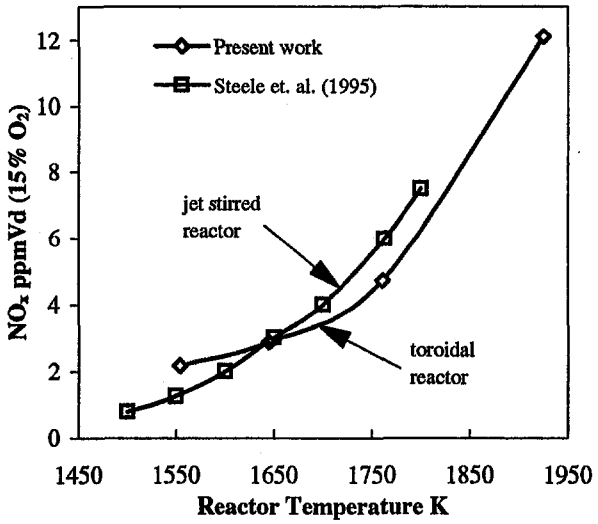

Fig. 10 Comparison of NO_x emissions from the toroidal WSR and the jet-stirred reactor at 3.5 ms residence time

ization leading to inadequate fuel vaporization, improper fuel–air mixing, and premature quenching of combustion products due to film cooling air can also increase CO emissions levels in practical systems.

NO_x Emissions. Variables affecting the production of NO_x have been extensively studied by Nicol et al. (1995) and Steele et al. (1997). Advanced combustor designs employing intense reactant mixing and high-temperature stoichiometric combustion produce a large quantity of NO_x. In fact, NO_x emissions rise moderately with high pressure and residence time, and exponentially with flame temperature. The WSR offers a unique opportunity to investigate the chemistry of NO_x emissions because of the absence of interaction between chemical reactions and the fluid dynamics processes of turbulent mixing and fuel evaporation.

NO_x emissions comprise thermal NO produced by the oxidation of atmospheric nitrogen in the postflame gases, prompt NO produced by the high-speed reactions at the flame front, and fuel NO produced by the oxidation of fuel-bound nitrogen. For propane–air combustion systems, Roffe and Venkataramani (1978) have found that:

$$\ln\left(\frac{EI_{NO_x}}{\tau}\right) = -72.28 + 2.8\sqrt{T_a} - \frac{T_a}{38}. \qquad (6)$$

Figure 9 shows the measured effect of flame temperature on NO_x emissions for propane and HC blend fuels and for two different values of residence time. Although residence time certainly increases NO_x (for example, for propane–air combustion at 1900 K, 0.75 g/kg and 1.75 g/kg of NO_x are formed corresponding to residence times of 2.5 ms and 12 ms, respectively), it is the flame temperature that causes a major increase in NO_x emissions. As seen in Fig. 9, Eq. (6) provides a satisfactory prediction of NO_x when τ = 2.5 ms. Also, as seen in Fig. 10, our measured values of NO_x emissions were in close agreement with propane–air data of Steele et al. (1997) taken in a jet-stirred reactor. To decrease NO_x emissions from practical combustion systems, the primary goal must be to lower the reaction temperature (by using water or steam injection) and/or the elimination of hot spots inside the combustor.

Figure 11 shows emissions index of NO_x for four different combustors: (*i*) a research step swirl combustor of Durbin and Ballal (1994), (*ii*) an advanced axially staged combustor (ASC) of Segalman et al. (1993), (*iii*) a conventional gas turbine combustor design of Rizk and Mongia (1993), and (*iv*) the present WSR. As shown, data were obtained for the combustion of different fuels in the WSR. It is observed that the emissions indices of the various combustors burning different fuels were in fairly good qualitative agreement with the WSR data. These results again attest to the importance of WSR studies to practical combustor design. In Fig. 10, it should be noted that NO_x emissions index for the production gas turbine combustors are generally higher by a factor of two to three as compared to the WSR data. These higher values of NO_x emissions are presumably due to the unmixedness (see Fric, 1993) present in practical gas turbine combustor as compared to the near-perfectly mixed WSR.

Emissions Map. A basic feature of many methods of emissions abatement is that they represent trade-offs between CO/UHC and NO_x emissions. This led Verkamp et al. (1973) to advocate the idea of presenting the relation between CO and NO_x in the form of an emissions map, which distinguishes between true advances in emissions technology and mere emissions trade-offs. Figure 12 shows an emissions map. Included in this figure are published data from two practical combustors and the WSR data obtained in our experiments. It shows that the emissions characteristics of the WSR fall within the bandwidth that could be proposed for the low-emissions advanced combustor design of the future.

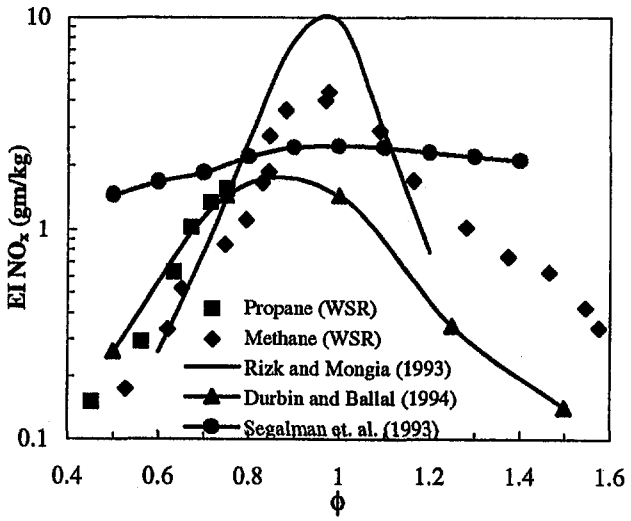

Fig. 11 Emissions of NO_x from the WSR compared to three different combustor configurations

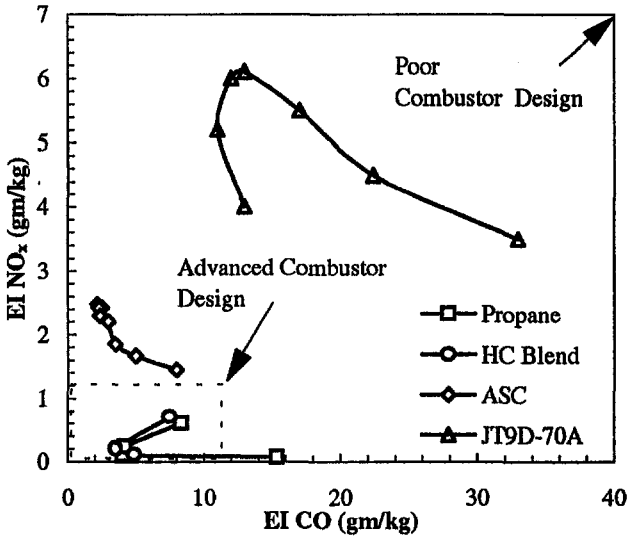

Fig. 12 Emissions map illustrating the status of emissions control technology for practical combustion systems

Conclusions

A study of combustion stability and pollutant emissions was completed using a toroidal WSR burning propane and HC blend fuels. The WSR represents a laboratory idealization of an efficient, low-emissions advanced combustor of the future. The following conclusions emerged:

1 The toroidal WSR was capable of peak loading almost twice as high as that for a spherical WSR and also yielded a better fuel-lean performance at medium to high loading. A simple analysis based upon WSR theory (Eq. (4)) provided good predictions of the WSR lean blowout limits.

2 The WSR combustion efficiency was above 99 percent over a wide range of mixture ratios and reactor loading. Thus, the WSR provides an upper range of efficiency values that advanced gas turbine combustor designs should approach given good fuel atomization (and evaporation), adequate pressure drop, and reduced wall quenching.

3 CO emissions reached a minimum at $\phi = 0.6$, corresponding to flame temperatures of 1600 K. The predictions of CO emissions using a quantitative relationship developed for gas turbine combustors (Eq. (5)) showed a good agreement with WSR measurements. Of course, in a practical gas turbine combustor, absolute CO emissions were found to be higher presumably because of incomplete combustion arising due to insufficient residence time at high loading, inadequate mixing, or quenching of postflame combustion products.

4 Production of NO_x depends upon two main parameters: combustion temperature and residence time. As expected, NO_x increased rapidly with an increase in flame temperature, moderately with increasing residence time, and peaked at or slightly on the fuel-lean side of the stoichiometric equivalence ratio. Equation (6), developed for propane–air combustion systems, yields good agreement with WSR data. Also, the NO_x emissions index for the production gas turbine combustor was higher, presumably due to the unmixedness present in practical gas turbine combustors.

5 Finally, emissions maps of different combustors were plotted and show that the WSR has the characteristics of an idealized high-efficiency, low-emissions combustor of the future.

Acknowledgments

This work was supported by the Air Force Wright Laboratory, Aeropropulsion and Power Directorate, Wright-Patterson Air Force Base, OH, under contract F33615-92-C-2207 with Mr. Charles W. Frayne serving as the Technical Monitor. The authors are grateful to Professor J. P. Longwell of MIT and to Dr. R. C. Steele and Professor P. C. Malte of the University of Washington, Seattle, WA, for making available their WSR design, WSR data, and for useful discussions.

References

Bahr, D. W., 1972, "Control and Reduction of Aircraft Turbine Engine Exhaust Emissions," *in*: W. Cornelius and W. G. Agnew, *eds., Emissions From Continuous Combustion Systems,* Plenum, New York, pp. 345–372.

Ballal, D. R., and Lefebvre, A. H., 1979, "Weak Extinction Limits of Turbulent Flowing Mixtures," ASME JOURNAL OF ENGINEERING FOR POWER, Vol. 101, pp. 343–348.

Blazowski, W. S., 1980a, "Dependence of Soot Production on Fuel Structure in Backmixed Combustion," *Combustion Science and Technology,* Vol. 21, pp. 87–96.

Blazowski, W. S., 1980b, "Dependence of Soot Production on Fuel Blend Characteristics and Combustion Conditions," ASME JOURNAL OF ENGINEERING FOR POWER, Vol. 102, pp. 403–408.

Durbin, M. D., and Ballal, D. R., 1994, "Characteristics of Swirl Flames in a Step Combustor," AIAA Paper No. 94-3272.

Fric, T., 1993, "The Effects of Fuel–Air Unmixedness on NO_x Emissions," *Journal of Propulsion and Power,* Vol. 9, pp. 708–713.

Kent, J. H., 1970, "A Noncatalytic Coating for Platinum–Rhodium Thermocouples," *Combustion and Flame,* Vol. 14, pp. 279–282.

Kretschmer, D., and Odgers, J., 1972, "Modeling of Gas Turbine Combustors—A Convenient Reaction Rate Equation," ASME JOURNAL OF ENGINEERING FOR POWER, pp. 173–180.

Lefebvre, A. H., 1983, *Gas Turbine Combustion,* Hemisphere Publishing Corporation, New York.

Longwell, J. P., and Weiss, M. A., 1955, "High Temperature Reaction Rates in Hydrocarbon Combustion," *Industrial and Engineering Chemistry,* Vol. 47, pp. 1634–1642.

Nenniger, J. E., Kridiotis, A., Chomiak, J., Longwell, J. P., and Sarofim, A. F., 1984, "Characterization of a Toroidal Well Stirred Reactor," *Twentieth Symposium (International) on Combustion,* The Combustion Institute, pp. 473–479.

Nicol, D. G., Steele, R. C., Marinov, N. M., and Malte, P. C., 1995, "The Importance of the Nitrous Oxide Pathway to NO_x in Lean-Premixed Combustion," ASME JOURNAL OF ENGINEERING FOR GAS TURBINES AND POWER, Vol. 117, pp. 100–111.

Odgers, J., and Carrier, C., 1973, "Modeling of Gas Turbine Combustors; Consideration of Combustion Efficiency and Stability," ASME JOURNAL OF ENGINEERING FOR POWER, Vol. 95, pp. 105–113.

Rizk, N. K., and Mongia, H. C., 1993, "Semianalytical Correlations for NO_x, CO and UHC Emissions," ASME JOURNAL OF ENGINEERING FOR GAS TURBINES AND POWER, Vol. 115, pp. 612–619.

Roffe, G., and Venkataramani, K. S., 1978, "Emissions Measurements for Lean Premixed Propane/Air System at Pressures up to 30 Atmospheres," NASA CR-159421.

Segalman, I., McKinney, R. G., Sturgess, G. J., and Huang, L. M., 1993, "Reduction of NO_x by Fuel-Staging in Gas Turbine Engines—A Commitment to the Future," AGARD-CP-536, Paris.

Society of Automotive Engineers, 1994, "Procedure for the Calculation of Basic Emission Parameters for Aircraft Turbine Engines," AIR 1533.

Steele, R. C., Jarrett, A. C., Malte, P. C., Tonouchi, J. H., and Nicol, D. G., 1997, "Variables Affecting NO_x Formation in Lean-Premixed Combustion," ASME JOURNAL OF ENGINEERING FOR GAS TURBINES AND POWER, Vol. 119, this issue, pp. 102–107.

Sturgess, G. J., Heneghen, S. P., Vangsness, M. D., Ballal, D. R., and Lesmerises, A. L., 1996, "Lean Blowout in a Research Combustor at Simulated Low Pressures," ASME JOURNAL OF ENGINEERING FOR GAS TURBINES AND POWER, Vol. 118, pp. 773–781.

Thornton, M. M., Malte, P. C., and Crittenden, A. L., 1987, "A Well-Stirred Reactor for the Study of Pyrolysis and Oxidation Kinetics—Carbon Monoxide and n-Pentane Oxidation," *Combustion Science and Technology,* Vol. 54, pp. 275–297.

Verkamp, F. J., Verdouw, A. J., and Tomlinson, J. G., 1973, "Impact of Emission Regulations on Future Gas Turbine Engine Combustors," AIAA Paper No. 73-1277.

Zelina, J., and Ballal, D. R., 1994, "Combustion Studies in a Well Stirred Reactor," AIAA Paper No. 94-0114.

A Computational Study of Pressure Effects on Pollutant Generation in Gas Turbine Combustors

E. M. Amin

G. E. Andrews

M. Pourkashnian

A. Williams

Department of Fuel and Energy,
The University of Leeds,
Leeds, LS2 9JT, United Kingdom

R. A. Yetter
Department of Mechanical
and Aerospace Engineering,
Princeton University,
Princeton, NJ 08544

A numerical study of the effect of pressure on the formation of NO_x and soot in an axisymmetric 30 deg counterrotating axial swirler lean low-NO_x gas turbine combustor has been conducted. This has previously been studied experimentally and this CFD investigation was undertaken to explain the higher than expected NO_x emissions. The combustion conditions selected for the present study were 300 K inlet air, 0.4 overall equivalence ratio, and pressures of 1 and 10 bar. The numerical model used here involved the solution of time-averaged governing equations using an elliptic flowfield solver. The turbulence was modeled using algebraic stress modeling (ASM). The thermochemical model was based on the laminar flamelet formulation. The conserved scalar/assumed pdf approach was used to model the turbulence chemistry interaction. The study was for two pressure cases at 1 and 10 bar. The turbulence–chemistry interaction is closed by assumption of a clipped Gaussian function form for the fluctuations in the mixture fraction. The kinetic calculations were done separately from the flowfield solver using an opposed laminar diffusion flame code of SANDIA. The temperature and species profiles were made available to the computations through look-up tables. The pollutants studied in this work were soot and NO for which three more additional transport equations are required, namely: averaged soot mass fraction, averaged soot particle number density, and finally averaged NO mass fraction. Soot oxidation was modeled using molecular oxygen only and a strong influence of pressure was predicted. Pressure was shown to have a major effect on soot formation.

Introduction

There is presently an increased interest in using CFD as a reliable design tool in gas turbine engines (Rizk and Mongia, 1992), because of the increase in costs associated with experimental studies. In addition, the recent advances in computational techniques have motivated a considerable number of research efforts in combustor flowfield modeling.

Because of the lack of understanding of the physical processes such as pollutant formation and flame extinction, the CFD modeling still cannot be considered quantitatively accurate. On the other hand, the technique of semi-empirical correlation has been successfully used for scale-up and data correlations (Lefebvre, 1985). The development of alternative approaches to combine the three-dimensional finite volume calculations with macro volume expressions to yield the quantities of interest has been demonstrated to give satisfactory agreements (Rizk and Mongia, 1992).

In gas turbine applications, the effect of different operating conditions on the performance is important. The interest in the pressure effects is due to the requirement for a high thermal efficiency and an increase in power/weight ratio is strongly dependent on the pressure ratio.

The effect of the elevated pressure operation on the formation of thermal NO and particulate soot is studied in this paper. In the present investigation the study of the pressure effects is limited to 10 bar because of two reasons. The first is that data on rate constants at higher pressures are not reliably known. Second, the 10 bar pressure is considered to be high enough to observe the influence of pressure on soot formation (Wagner, 1987).

Although the present approach can be applied to any combustor configuration, the computation time is large and for use on workstations two-dimensional computations were undertaken. However, some swirl flows are predominantly two-dimensional and there is considerable interest at present in the use of high flow swirlers for lean low NO_x combustion applications. One low-NO_x design that has been investigated (Valachovic, 1993; Andrews et al., 1991) is that of axisymmetric counterrotating double axial swirlers. This is still amenable to a two-dimensional treatment if blade wake effects are not a dominant influence. In the present work a counterrotating swirler with fuel injection between the two swirlers has been studied; this geometry is also under experimental investigation using a 76 mm outer swirler diameter and a dump expansion into a 140 mm diameter combustor (Andrews et al., 1991). No film or primary zone wall jets are used, as all the primary zone air is required to pass through the swirler to achieve the leanest possible combustion. This simplifies the CFD as these aerodynamic features would immediately make the problem highly three-dimensional. Techniques to cool primary zones externally are also under investigation for this application. This cylindrical combustor geometry has been used in the present two-dimensional CFD predictions. The major approximation in the two-dimensional study was that it essentially assumes an annular fuel injector, whereas in practice the fuel was injected through a series of eight uniformly spaced holes. In the two-dimensional CFD study the fuel was modeled with the same momentum as well as the air/fuel mass flow ratio required for a 0.4 equivalence ratio. The fuel used in the present modeling is pure methane.

Contributed by the International Gas Turbine Institute and presented at the 40th International Gas Turbine and Aeroengine Congress and Exhibition, Houston, Texas, June 5–8, 1995. Manuscript received by the International Gas Turbine Institute March 18, 1995. Paper No. 95-GT-304. Associate Technical Editor: C. J. Russo.

Previous Studies

In the case of NO formation, Shaw (1974) developed a semi-empirical calculation model to compute the NO concentration based on the equilibrium concentration. This technique has been used and developed further by other investigators (Nicol et al., 1992; Corr et al., 1992). In this correlation the NO concentration is shown to be proportional to the square root of the pressure. This pressure relationship comes directly from the dominant kinetic equation (Eq. (9)) in the thermal formation of NO (Shaw, 1974).

However, although there have been several investigations of the pressure effect on NO that agree with this exponent of 0.5, there is a wide variation in the literature and some indication of an equivalence ratio effect (Lefebvre, 1983).

This simple 0.5 NO pressure exponent ignores the more complex full chemistry of thermal NO formation and also ignores the influence of pressure on the peak stoichiometric flame temperatures due to the reduction in dissociation at elevated pressures. Thus combustors with near-stoichiometric primary zones may exhibit pressure exponents higher than 0.5. For lean mixtures, dissociation is negligible and pressure has little effect on the flame temperatures. Thus there can be a variation in the exponent with combustor design. In the present work lean combustion is studied and local stochiometric regions only occur due to poor fuel/air mixing. Thus the adequate prediction of mixing is an essential feature of any study of NO_x formation.

The strong influence of pressure on the generation of soot in gas turbines is well known (Lefebvre, 1983), but a prediction of this effect in CFD programs is difficult without the use of correlations of soot formation as a function of predicted local temperature and equivalence ratio. In the present work a kinetic reaction approach to soot formation and oxidation is attempted. Miller (1978) and Maans et al. (1980) reported an increase in soot volume fraction in CH_4–air diffusion flame for pressures up to 50 bar. The soot yield increased with pressure according to p^n ($n \approx 1.7$).

Flower (1986, 1988) and Flower and Bowman (1985, 1987) performed an experimental study on laminar and turbulent ethylene air diffusion flame. For a range of pressures up to 10 bar, they have found a similar value for the pressure exponent ($n \approx 1.2$–1.4). Their measurements showed that the increase of the soot emissions at higher pressures was mainly due to the lower oxidation levels. They concluded that net soot formation was increased due to the decreased role played by soot oxidation as a result of increased radiation levels at pressure. However, in a gas turbine combustor, the radiation to the wall is increased by the film cooling air. This results in changes in temperature profile, which will affect NO_x but with no net reduction in mean temperature. In the present work it will be shown that part of the pressure effect on soot emissions is due to the increase in the rate of soot growth with pressure. Also, with no radiation heat losses, oxidation of soot increases due to the increased peak flame temperature with pressure.

Flowfield Equations and Turbulence Modeling

For the present numerical investigation a modified form of the FLUENT V3.03 CFD is used as a framework for applying the present turbulence–chemistry interaction as well as soot and NO_x formation models. The modeling approach follows that of Bilger et al., commonly known as conserved scalar/assumed pdf approach. To apply this model the original solver structure of FLUENT has been modified to contain a transport equation for the Favre-averaged concentration fluctuations (g) (Spalding, 1976). The set of steady-state transport equations for an axisymmetric reacting flow has the following general form:

$$\frac{\partial}{\partial x}(\rho u \phi) + \frac{\partial}{r\partial r}(\rho r v \phi) = \frac{\partial}{\partial x}\left(\Gamma_\phi \frac{\partial \phi}{\partial x}\right) + \frac{\partial}{r\partial r}\left(r\Gamma_\phi \frac{\partial \phi}{\partial r}\right) + S_\phi \quad (1)$$

where ϕ stands for the mean values of u, v, w, p, k, ϵ, ξ, and g. The expressions for the exchange coefficient Γ_ϕ and source term S_ϕ are given in Table 1.

The mixture fraction is considered to be the main parameter required to characterize the mixing field in diffusion flames (Bilger, 1976). The local mixture fraction in the present model is defined as (Bilger, 1989):

$$\xi = \frac{\beta - \beta_{ox}}{\beta_{fu} - \beta_{ox}} \quad (2)$$

with

$$\beta = 2 \cdot \frac{Y_C}{M_C} + \frac{1}{2} \cdot \frac{Y_H}{M_H} - \frac{Y_O}{M_O} \quad (3)$$

where $Y_{c,j}$ is the mass fraction of the carbon element in the fuel stream. The subscripts *fu* and *ox* refer to the fuel and oxidant streams. The mixture fraction is a conserved scalar defined so that it equals 0 in the air stream and 1 in the fuel stream. The state of mixing in the diffusion flame is bounded by these two values as the mixture fraction is neither created nor destroyed (i.e., conserved scalar) (Bilger, 1976).

The counterswirl flowfield features anisotropic turbulence due to the existence of strong streamline curvature. It is known that the commonly used k–ϵ two-equation model of turbulence is only valid for isotropic turbulence in simple shear flows. Algebraic stress modeling (ASM), which is driven under the assumption of local equilibrium between the convection and diffusion of Reynolds stresses, is considered to be more computationally affordable in comparison to full Reynolds stress modeling (RSM) in turbulent reacting flows (Nikjooy et al., 1988). The ASM is able to capture better flow physics (e.g., stress anisotropy, streamline curvature, and body forces) in comparison to the k–ϵ model.

Nomenclature

α = strain rate
C_a = soot agglomeration constant
C_{min} = soot agglomeration constant
f_v = soot volume fraction
g = square of fluctuations in mixture fraction (variance)
k_j = reaction rate constant for step j
M = molecular weight
N = particle number density, particles/kg
n = pressure exponent
p = pressure
P = probability density function (pdf)
r = radial distance
S = source term
T = temperature
v = radial velocity component
w_i = rate of formation of species i
Y = mass fraction
λ = underrelaxation factor
μ_{eff} = effective viscosity
ξ = mixture fraction
ρ = mixture density
ρ_c = soot density = 2000 kg/m^3

Subscripts

c = carbon, coagulation
g = growth
i = inception
n = nucleation
ox = oxidation
st = stoichiometric
th = thermophoresis

Table 1 Exchange coefficients and source terms

ϕ	Γ_ϕ	S_ϕ
1	0	0
u	μ_{eff}	$-\frac{\partial p}{\partial x}+\frac{\partial}{\partial x}(\mu_{eff}\frac{\partial u}{\partial x})+\frac{1}{r}\frac{\partial}{\partial r}(r\mu_{eff}\frac{\partial v}{\partial x})$
v	μ_{eff}	$-\frac{\partial p}{\partial r}+\frac{\partial}{\partial x}(\mu_{eff}\frac{\partial u}{\partial r})+\frac{1}{r}\frac{\partial}{\partial r}(r\mu_{eff}\frac{\partial v}{\partial r})-2\mu_{eff}\frac{v}{r}+\rho\frac{W^2}{r}$
w	μ_{eff}	$-\frac{w}{r^2}\frac{\partial}{\partial r}[r(\mu_t+\mu_l)]-\rho\frac{vw}{r}$
k	μ_{eff}/σ_k	$G_k-\rho\varepsilon$
ε	$\mu_{eff}/\sigma_\varepsilon$	$C_1\varepsilon G_k/k-C_2\rho\varepsilon^2/k$
ξ	μ_{eff}/σ_f	0
g	μ_{eff}/σ_f	$C_g-C_{g2}\rho\varepsilon g/k$

where

$$C_g=C_{g1}\mu_{eff}\left[\left(\frac{\partial\xi}{\partial x}\right)^2+\left(\frac{\partial\xi}{\partial r}\right)^2\right]$$

$$G_k=\mu_{eff}\left[2\left\{\left(\frac{\partial u}{\partial x}\right)^2+\left(\frac{\partial v}{\partial r}\right)^2+\left(\frac{v}{r}\right)^2\right\}+\left(\frac{\partial u}{\partial r}+\frac{\partial v}{\partial x}\right)^2+\left(r\frac{\partial}{\partial r}\left(\frac{w}{r}\right)^2\right)+\left(\frac{\partial w}{\partial x}\right)^2\right]$$

In the present work, which involves modeling of turbulent reacting counterswirling flow, the ASM is used to calculate the turbulent viscosity. The kinetic energy of turbulence (K) and its dissipation rate (ϵ) equations are also solved in conjunction with the flowfield, mean mixture fraction, and mean mixture fraction fluctuations. The constants for the flowfield and turbulence model are shown in Table 2.

Calculation of pdf and Mean Mixture Density

From the value of the two moments, mean mixture fraction and its variance, the pdf of the mixture fraction is determined. The mean mixture density is calculated by the pdf convolution integral in the mixture fraction space. The instantaneous values of the density used in the calculations are supplied to the code through look-up tables. During each iteration the mean density is entered into the flowfield equations in addition to the transport of mixture fraction and variance fluxes.

Different shapes for the pdf have been used in modeling a turbulent diffusion flame (Abou-Ellail et al., 1978). Clipped Gaussian pdf without intermittency (Lockwood and Naguib, 1975), with intermittency based on empirical relations (Kent and Bilger, 1976), three Dirac delta function pdf (Bockhorn and Lutz, 1984), and beta function pdf with and without intermittency (Jancika and Kollman, 1980; Correa et al. 1984) are some examples.

In the present model a composite pdf function is used. The pdf $P(\xi)$ consists of a turbulent part, $P_t(\xi)$, represented by a Gaussian distribution and a nonturbulent part represented by a delta function. The use of the composite pdf in this manner alleviates most of the problems associated with numerical singularities, which result from unphysical combinations of the mean and variance values. The first part is the original continuous probability distribution (clipped Gaussian), which is assumed to hold inside the turbulent jet boundary. Outside this boundary the continuous distribution is replaced by a delta function evaluated at the undistributed conditions ($\xi = 0$). The location of the turbulent jet boundary is then determined by the intermittency factor. Therefore the composite pdf may be written as

$$P(\xi) = (1 - \tilde{\gamma})\delta(0) + \tilde{\gamma}P_t(\xi) \tag{4}$$

where γ is the intermittency factor ($1 > \gamma > 0$),

$$\tilde{\gamma} = \begin{cases} 1.0 & \text{for } g < 0.25\tilde{\xi}^2 \\ 1.25/(g/\tilde{\xi}^2 + 1) & \text{for } g \geq 0.25\tilde{\xi}^2 \end{cases} \tag{5}$$

and $P_t(\xi)$ is given by

$$P_t(\xi) = \frac{1}{\sqrt{2\pi\tilde{g}}}\exp\left\{\frac{-1}{2\tilde{g}}(\tilde{\xi} - \xi)^2\right\} \tag{6}$$

for a clipped Gaussian distribution.

The mean value of any thermochemical value (e.g., temperature, species mass fraction, or rate of formation) $\phi(\xi)$, is thus given by

$$\tilde{\phi}(\xi) = (1 - \gamma)\phi(0) + \gamma\int_0^1 \phi(\xi)\tilde{P}_t(\xi)d\xi \tag{7}$$

Combustion Modeling

The calculation of the main reacting flowfield is done after a converged solution of the mixing field above is achieved. The products of combustion are assumed to be in reactive-diffusive balance, which admits the relation of the type

$$Y_i = Y_i(\xi) \tag{8}$$

where the subscript i stands for any of the major chemical species. These functions are precomputed and tabulated in the lookup table. The average value of the Y_i is calculated in a similar way to mean mixture density. For the trace species like NO and soot, the formation rates instead of the concentrations are tabulated in the lookup table.

NO_x and Soot Formation Submodels. Many investigators has attempted modeling of NO_x and soot formation in laminar and turbulent diffusion flames. The majority of those workers have agreed that the laminar flamelet concept cannot be applied to the concentration of these trace species but can be applied to their rate of formation.

Leung et al. (1991) and Fairweather et al. (1991) used a two-equation model to predict soot in a laminar ethylene diffusion flame. This model has also been used by Fairweather et al. (1992) in predicting soot formation in propane–air turbulent and large-scale buoyant methane–air diffusion flames. From these studies it has been shown that the different processes involved in soot formation can be related to the gas phase combustion through an indicative species (acetylene).

In the present work these submodels are used to predict the formation of thermal NO and soot volume fraction in a gas turbine configuration operating at the two different pressures of 1 and 10 bar.

Table 2 Constants in the turbulence model

C_D	C_1	C_2	C_μ	C_{g1}	C_{g2}	σ_k	σ_ε	σ_ξ	σ_g
0.55	1.5	1.9	0.09	1.8	2.0	1.0	1.3	0.6	0.6

Thermal NO_x Formation. The transport equation for mean NO mass fraction is given by the substitution of mass fraction of NO (Y_{NO}) for general variable ϕ in Eq. (1). The source of NO formation dealt with in the current model is that of Zeldovich (1946):

$$N_2 + O \overset{k_1}{\rightarrow} NO + N \tag{9}$$

$$N + O_2 \overset{k_1}{\rightarrow} NO + O \tag{10}$$

As the second step is fast the molar production rate of thermal NO may be written as

$$\dot{W}_{NO} = 2k_1[N_2][O] \tag{11}$$

where k_1 is the specific reaction rate constant for the first step ($k_1 = 1.36 \times 10^{11} \exp(-37{,}750/T)$ m^3/kmol/s). The laminar rate of NO formation, computed from the previous equation, is precomputed in the lookup table as a function of the mixture fraction (ξ).

Soot Formation. For soot formation the Favre-averaged soot mass fraction source term in kg soot/m^3/s can be written as (Fairweather et al., 1992),

$$\tilde{\rho}\tilde{S}(Y_c) = \tilde{r}_n M_c + \tilde{r}_g \tilde{\rho} M_c^{1/3} \tilde{Y}_c^{2/3} \tilde{N}_c^{1/3} - \tilde{r}_{oxi} \tilde{\rho} M_c^{1/3} \tilde{Y}_c^{2/3} \tilde{N}_c^{1/3} - \tilde{S}_{Yth} \tag{12}$$

For averaged soot particle number density the source term in particles/m^3/s is

$$\tilde{\rho}\tilde{S}(N) = \tilde{r}_i - \tilde{r}_c \tilde{\rho}^2 M_c^{-1/6} \tilde{Y}_c^{1/6} \tilde{N}_c^{11/16} - \tilde{S}_{Nth} \tag{13}$$

In these equations r_n is the rate of nucleation, r_g is the rate of surface growth, and r_{oxi} is the rate of soot oxidation. The rate constants for these equations can be found from Fairweather et al. (1992) and will not be repeated here. The oxidation process dealt with in this work is due to molecular oxygen (O_2). However, it has been shown by many previous investigations that other radical species (e.g., O and OH) play an important role in soot oxidation process near the reaction zone (Fenimore and Jones, 1967; Garo et al., 1990).

S_{Yth} is the source term due to the thermophoretic effect of soot particles. In the present work the thermophoresis is considered only in the radial direction, although the temperature gradient in the other directions might have a similar effect to that in radial direction especially in highly swirling gas turbine combustor flowfield. The expression for the source terms due to thermophoresis effect in soot mass fraction and particle number density equations could be written as

$$S_{Yth} = \frac{1}{r}\frac{\partial}{\partial r}(r\rho v_{th} Y_c) \tag{14}$$

$$S_{Nth} = \frac{1}{r}\frac{\partial}{\partial r}(r\rho v_{th} N) \tag{15}$$

where the thermophoretic velocity component in the radial direction can be written as

$$v_{th} = -0.55\frac{\mu}{\rho T}\frac{\partial T}{\partial r} \tag{16}$$

The source terms in both the soot mass fraction and particle number density equation were averaged by the pdf in a similar way to the mean density.

Laminar Flame Calculations and Lookup Tables. The laminar flame calculations were done for two operating conditions using the one-dimensional opposed diffusion flame code of SANDIA. The reaction scheme is that of the GRI (Gas Research Institute) for the two conditions the inlet temperature for the fuel and oxidizer were kept at 300 K. The inlet pressure for the oxidizer was changed from 1 bar to 10 bar. The kinetic data required for this computation were only available at these conditions and work is in progress to compute the required kinetic data at other inlet conditions. The strain rate (α) was kept the same value for the two conditions (≈ 150 s^{-1}). The detailed temperature and composition profiles are transformed into the mixture fraction space in ordered to obtain the flamelet relationships required for the CFD modeling. The value of the strain rate chosen to represent an intermediate value in the combustor. The variation of strain rate because of the local turbulent conditions is expected to affect appreciably the state relationships shown in Fig. 1. For example, the oxygen radical is expected to shoot up with the increase in the strain rate, while the temperature is expected to decrease. To account for this variation in the computations we have to create three-dimensional lookup tables with subsequent increase in CPU time. To reduce the computational burden, we have chosen a constant value of the strain rate in order to represent the thermochemical state in the combustor.

For the present case of the gas turbine high-intensity combustion, the heat loss by radiation was neglected in comparison to the main heat release due to hydrocarbon combustion. Any heat transferred by convection or radiation to the combustor walls is recycled as preheated air and gas turbine combustion overall operates close to adiabatic conditions. This allows the use of the adiabatic flamelet relationships safely in the present computations, without introducing significant errors.

The lookup tables that are linked to the computations contain specific volume, temperature, and all the major species concentrations. In addition the source terms for calculating soot and NO concentrations are also tabulated.

The results of these laminar flamelet computations in the mixture fraction space are presented in Fig. 1. The flamelet temperature profiles show that the increase from 1 bar to 10 bar results in an increase in the peak adiabatic temperature of 300 K, due to the reduction in dissociation at high pressure, with an associated reduction in OH radicals. The effect of pressure rise on the reaction zone can be examined from the OH radical profile, which is considered to be a good marker for the reaction zone. Generally there are two effects that have occurred. First, the location of the peak OH concentration has moved toward the rich side by approximately 5 percent, indicating a thinner flame. And second, the width of the OH curve base in the mixture fraction space has decreased, indicating a smaller reaction zone thickness.

The increase in pressure is accompanied by a decrease in O, OH, and CH concentrations, which indicates faster recombination of the radicals to form stable species. This is an expected behavior since the effect of pressure rise is to decrease major species dissociation and hence cause the adiabatic flame temperature to increase.

Regarding the thermal NO formation rate, although the decrease in the peak value of the O radical was almost 74 percent, the formation rate of thermal NO increased by more than two orders of magnitude in the vicinity of stoichiometric mixture fraction of methane ($\xi_{st} = 0.055$). This indicates, as expected, the strong role played by the increased temperature at higher pressure in the formation of thermal NO.

For soot formation, increasing the pressure results in the indicative species concentration (acetylene) increasing in its peak concentration by almost 11 percent. This increase in acetylene concentration affects the soot formation processes as follows: The peak rate of soot nucleation has increased more than two orders of magnitude, while the soot surface growth rate increased by an order of magnitude and moved closer to the stoichiometric mixture fraction. The oxidation rate shows a similar behavior, but the peaks at the two pressures, in contrast to the surface growth and nucleation rates, are located on the other side of stoichiometric (i.e., the lean side). The rate of soot coagulation is almost the same at the two pressures (the peak

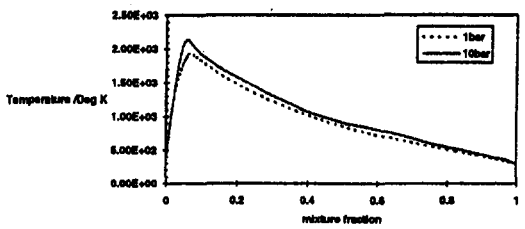

Fig. 1(*a*) Temperature as a function of the mixture fraction for the two pressure cases

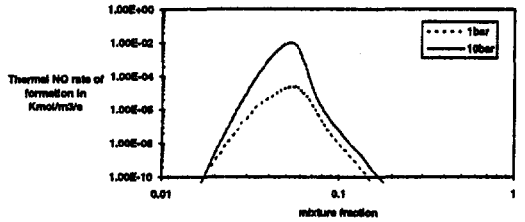

Fig. 1(*b*) Thermal NO formation rate as a function of the mixture fraction for the two pressure cases

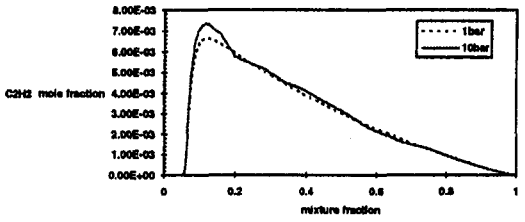

Fig. 1(*c*) C_2H_2 as a function of the mixture fraction for the two pressure cases

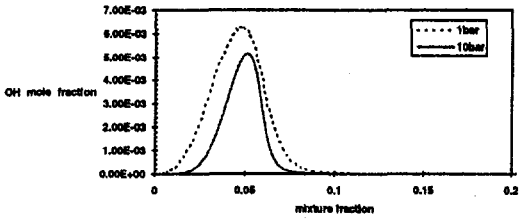

Fig. 1(*d*) OH mole fraction as a function of the mixture fraction for the two pressure cases

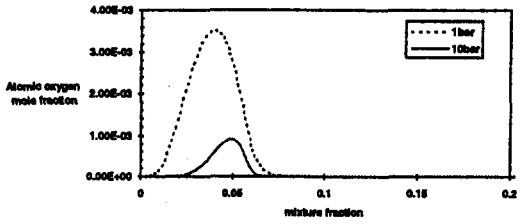

Fig. 1(*e*) O mole fraction as a function of the mixture fraction for the two pressure cases

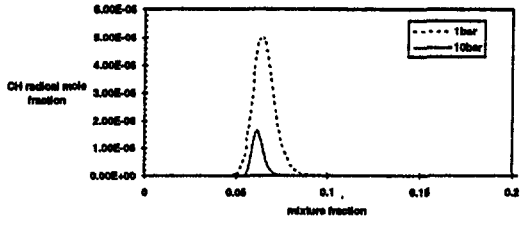

Fig. 1(*f*) CH mole fraction as a function of the mixture fraction for the two pressure cases

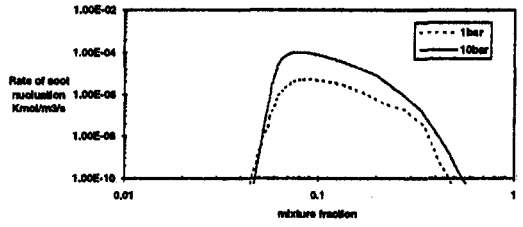

Fig. 1(*g*) Rate of soot nucleation as a function of the mixture fraction for the two pressure cases

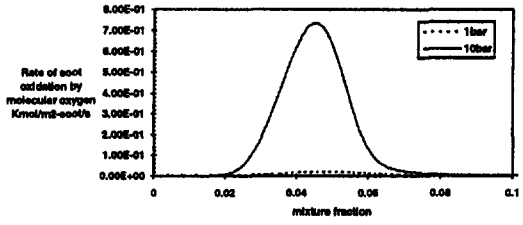

Fig. 1(*h*) Rate of soot oxidation by O_2 as a function of the mixture fraction for the two pressure cases

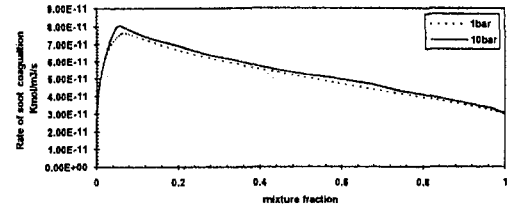

Fig. 1(*i*) Rate of soot mass growth as a function of the mixture fraction for the two pressure cases

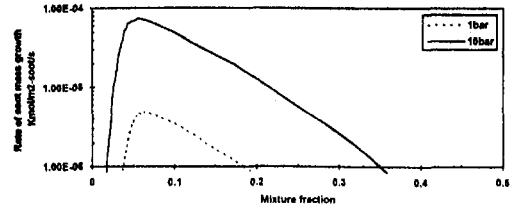

Fig. 1(*j*) Rate of soot particle coagulation as a function of the mixture fraction for the two pressure cases

is 5 percent higher at 10 bar), and similarly the growth and nucleation rates have moved toward the stoichiometric surface from the fuel rich side.

Numerical Simulation and Results

The combustor configuration for which the current modeling has been made is shown in Fig. 2. It is a single can dump expansion type with 140 mm internal diameter. A 30 deg flat bladed axial counterrotating swirler is providing the inlet combustion air with the fuel injector located in the middistance between the inner and outer swirlers. The overall equivalence ratio in the primary zone is 0.4.

Preliminary calculations have been made to determine a suitable grid-independent solution for the variable density mixing

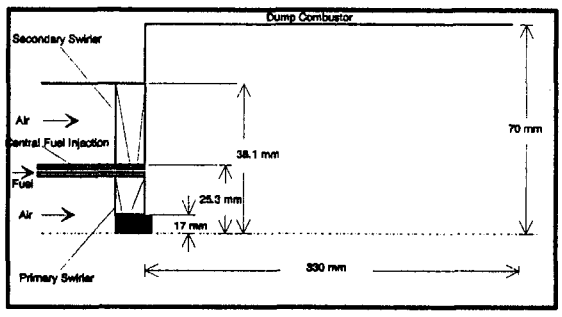

Fig. 2 Dump combustor configuration with counterrotating axial swirler

flow. The final computations were made for 81 × 44 nodes in the x and r directions, respectively.

As the present work is mainly concerned with investigating the pressure effects, an accurate representation of the inlet velocity profiles is unnecessary at this stage. Work is in progress on the three-dimensional computation of the flow through the swirler to give a more complete CFD solution to this combustion situation. The inlet profiles of the axial and tangential velocities were assumed to be flat before the inlet to the combustor. The fuel jet velocity was 178 m/s and the inlet air velocity for the two cases corresponded to a 0.023 Mach number at 300 K. This represents approximately 50 percent of the combustor airflow through the swirler. The air jet velocities were set to correspond to those required for a typical 3 percent pressure loss. The magnitude of the axial and tangential velocities was 82 m/s. The inner and outer tangential velocities were opposite in sign to represent the counterswirl.

The calculations are initiated upstream of the combustor to allow for the velocity profiles to be more realistically represented at the inlet to the combustor. At the exit, zero gradient is assumed for all the variables and similarly at the axis of symmetry. At the combustor wall, adiabatic conditions are assumed with zero gradient for the mean mixture fraction and variance values.

In the present implementation of the conserved scalar assumed pdf approach it is found necessary to underrelax the density slightly to enable the flowfield convergence thus:

$$\rho = \lambda\rho^{\text{new}} + (1 - \lambda)\rho^{\text{old}} \tag{17}$$

where the superscripts "new" and "old" represent the current iteration and previous iteration values. The value of λ is kept small ($\approx$0.2) to ensure a stable converged solution.

The comparison between the mixing characteristics for the two pressure ranges in terms of equivalence ratio at the centerline is shown in Fig. 3. As could be seen, the mixing field did not change appreciably as a result of the pressure increase. The peak value of the equivalence ration is around 0.6 at $X/D \approx$ 2–2.5. This poor mixing condition, which is confirmed experimentally at one bar and with propane fuel, resulted in an inefficiency as high as 6 percent at the 0.4 mean equivalence ratio (Amin, 1991). The present CFD model shows that the inadequate mixing is due to inability of the fuel to diffuse into the central recirculation and corner recirculation zones and not to the richness of the center core as previously postulated (Andrews et al., 1991).

The detailed property maps are shown in Fig. 4. From the mean equivalence ratio contours it can be seen that the fuel is not able to diffuse and mix properly with either the central recirculation or the corner recirculation zone, even though the overall mixture is lean. Comparison of the mixture fraction predictions with those for the turbulent kinetic energy shows that the axial fuel injection results in the fuel being placed on the outer part of the zone of peak turbulence. To improve the performance of this type of combustion, this CFD study indicates that better fuel placement is required, resulting in the fuel being directed at the zone of maximum turbulence. Improved fuel injection systems have been investigated experimentally and much improved performance with lower NO_x emissions has been achieved.

The increase in thermal NO concentration by almost one order of magnitude is shown as a result of the pressure increase. The increase is not proportional to the square root of pressure; the peak NO_x scales as pressure to the 1.5 exponent. The increase in NO is also accompanied by the movement of the thermal NO concentration farther upstream. The mean NO_x emissions also increased by a similar exponent. This high pressure exponent was dominated by the influence of pressure on the maximum adiabatic flame temperature. Preliminary work on the inclusion of prompt NO into these computations shows that this strongly reduces the NO pressure exponent as there is no significant pressure dependence of prompt NO and it forms a large fraction of the NO at 1 bar. Prompt NO is related to the concentration of CH radicals, which are predicted to be reduced by a factor of 4 at 10 bar; thus it is possible that prompt NO will have a negative pressure dependence, and this will drastically reduce the total NO pressure exponent. Some evidence for this was provided in the computations of Dupont et al. (1993) for a simple partially premixed flame with the full kinetic predictions of prompt NO.

The predicted pressure exponent for the peak soot concentration was 1.8, similar to the predicted exponents discussed above with a range 1.2–1.7. The soot formation and oxidation was mainly concentrated in the interjet shear layer, where the local mixtures were richer than stoichiometric. The particle number density levels (not shown here) didn't change appreciably with pressure, which is in agreement with previous observation by Wagner (1987).

Yoshihara et al. (1994) have shown that on average the rate of oxidation of soot by molecular oxygen is of the order of 100 times slower than by OH and soot emissions are dominated by the OH oxidation. Thus the pressure effect on soot might be dominated by the influence of pressure on OH oxidation of soot. The OH maps show that the pressure decreases the reaction zone thickness and depresses the radical overshoot. Although OH oxidation of soot has not been included in this work, the decreased levels of OH at pressure would indicate that OH oxidation of soot could be reduced at pressure if the peak flame temperature was constant. However, the strong influence of the increased peak temperature at high pressure could be more important than the decreased oxidation rate.

The peak soot volume fraction was predicted to increase by about three orders of magnitude at 10 bar compared with 1 bar and also moved nearer to the swirler. The dominant cause of this effect is difficult to determine, but the very large increase in the rate of soot nucleation and soot mass growth rate with pressure, shown in Fig. 1, indicates that the pressure effect may have a strong contribution from increased soot formation and may not be predominantly due to reduced oxidation, as postulated by Flower and Bowman (1985, 1987). The present calculations of molecular oxygen soot oxidation show that oxidation rates were increased by an order of magnitude at high pressure, mainly due to the increased peak flame temperature, and the absence of the radiation heat losses that occur in most experimental investigations.

Alizadeh and Moss (1993) have also attempted to predict the influence of pressure in a gas turbine combustor configuration. They used experimentally based flamelet relations for soot formation and nucleation, whereas the present work is based on kinetic computations of these parameters, using acetylene as the key soot precursor.

Summary and Conclusions

The design of a counterrotating axial swirler has been investigated numerically with comprehensive CFD modeling of the

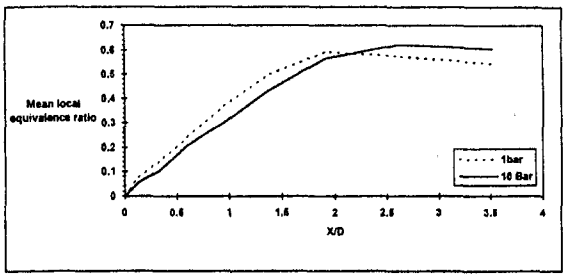

Fig. 3 The variation of the local mean equivalence ratio on the centerline for the two pressure cases

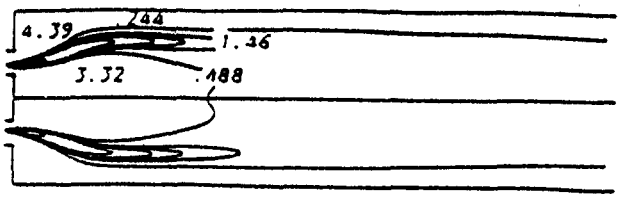

Fig. 4(*a*) Predicted CO mole fraction contours at 1 bar

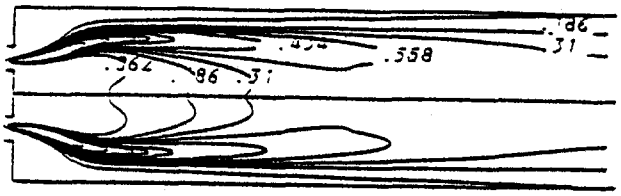

Fig. 4(*b*) Predicted OH mole fraction contours at 1 bar

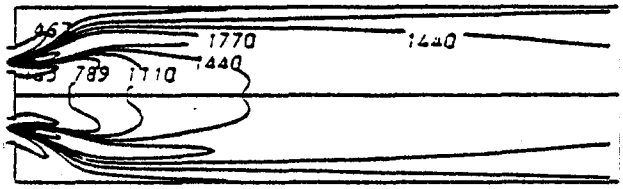

Fig. 4(c) Predicted temperature contours at 1 bar

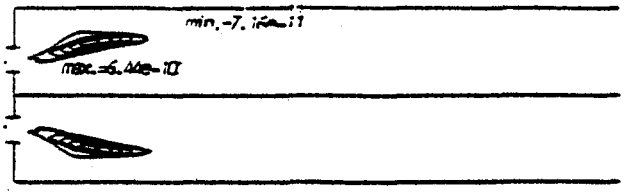

Fig. 4(*d*) Predicted soot volume fraction contours at 1 bar

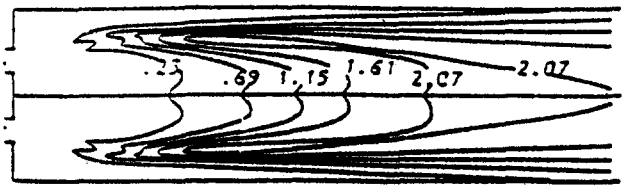

Fig. 4(*e*) Predicted thermal NO concentration in ppm contours at 1 bar

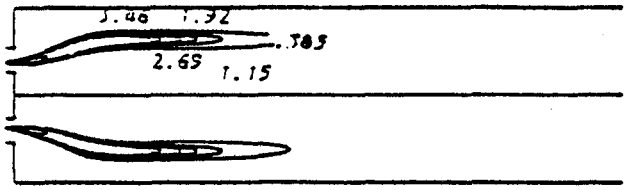

Fig. 4(*f*) Predicted CO mole fraction contours at 10 bar

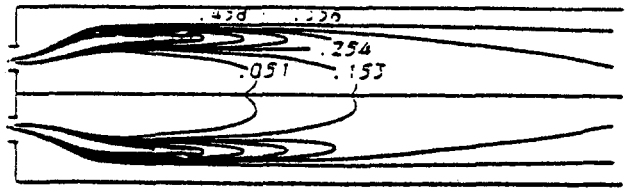

Fig. 4(*g*) Predicted OH mole fraction contours at 10 bar

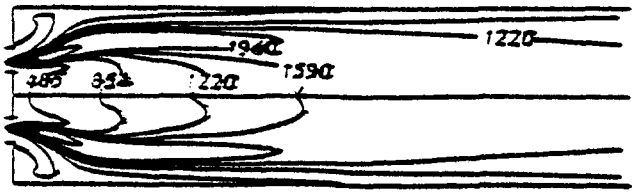

Fig. 4(*h*) Predicted temperature contours at 10 bar

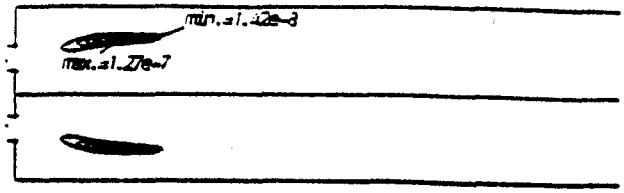

Fig. 4(*i*) Predicted soot volume fraction contours at 10 bar

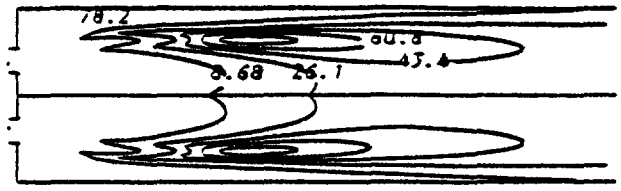

Fig. 4(*j*) Predicted thermal NO concentration in ppm at 10 bar

flowfield, soot, and thermal NO formation. The model depends on the laminar flame formulation for the description of the thermochemistry and conserved scalar/assumed pdf approach for turbulence–chemistry interaction. The conserved scalar approximation assume that enthalpy and species are diffusing at the same rate. This reduces the description of the combustion process to a single scalar transport and simplifies the calculation considerably. However, to account for the strong coupling between the radiative heat transfer and soot formation, this model has to be modified to account for the effect of heat transfer by radiation on the flow and temperature field and hence on the trace species production (Amin, 1994).

The pressure effect showed that the flame region gets thinner and the formation of pollutants increases. The peak thermal NO was predicted to have a 1.5 pressure exponent, mainly due to the increase in the peak flame temperature with pressure. However, this exponent is purely for thermal NO and it is anticipated that the inclusion of prompt NO will considerably reduce this exponent as it has a small influence of pressure.

The pressure exponent for the peak soot concentration was predicted to be 1.8, close to that for experimental measurements. The main influence of pressure on soot emissions is considered to be dominated by the increase in peak temperature with pressure, which strongly increases the soot growth rate and is the principle reason for the predicted increased soot oxidation. Thus the pressure effect on soot may be mainly due to increased soot growth rate in adiabatic combustion systems such as gas turbines.

The present design of direct fuel injection in the interjet shear layer of a counterrotating axial swirler results in high soot and NO emissions. The predictions of the fuel distribution show that this was mainly due to poor fuel and air mixing as the fuel injection was not directed at the peak turbulence region. The fuel injection needs to be modified to redistribute the fuel in a more homogeneous manner in the combustor, possibly by redesigning the fuel injection location to achieve better air/fuel mixing in the primary zone. Such improved designs are currently under experimental investigation and CFD modeling, and large reductions in NO_x and soot emissions have been achieved. Future improvements in the present CFD model that are in progress include the prediction of prompt NO, NO_2 formation, and three-dimensional effects.

Acknowledgments

We would like to thank the UK EPSRC for a research grant (GR/J07976) in support of this work. The authors wish to thank BOC G.T.C., USA, for the computational facilities. The

University of Leeds scholarship to E. M. Amin is gratefully acknowledged.

References

Alizadeh, S., and Moss, J. B., 1993, "Flowfield Prediction of NO_x and Smoke Production in Aircraft Engines," AGARD-CP-536.

Amin, E. M., 1991, "Influence of Counter-rotating Swirl on Combustion and Emissions," M.Sc. thesis, University of Leeds.

Amin, E. M., 1994, "CFD Modelling of Turbulent Diffusion Flames," PhD Thesis, University of Leeds.

Andrews, G. E., Amin, E. A., Ahmed, N. T., and Kowkabi, M., 1991, "Counter Rotating Double Axial Swirlers With Fuel Injection in the Counter Swirl Shear Layer," presented at the Japanese International Gas Turbine Congress, Yokohama.

Bilger, R. W., 1976, "Turbulent Jet Diffusion Flames," *Prog. Energy Combust. Sci.,* Vol. 1, pp. 87–109.

Bilger, R. W., 1989, "Turbulent Diffusion Flames," *Ann. Rev. Fluid Mech.,* Vol. 21, p. 101.

Bradley, D., Dixon-Lewis, G., El-Din Habik, E., and Mushi, E. M. J., 1985, *Twentieth Symposium (International) on Combustion,* The Combustion Institute, Pittsburgh, p. 931.

Corr, R. A., Malte, P. C., and Marinov, N. M., 1992, "Evaluation of NO_x Mechanisms for Lean, Premixed Combustion," ASME JOURNAL OF ENGINEERING FOR GAS TURBINES AND POWER, Vol. 114, p. 425.

Dupont, V., Pourkashanian, M., and Williams, A., 1993, "Predictions of Prompt NO_x in Hydrocarbon Air Flames," AGARD Conf. Proc. CP 536, p. 3-1–3-13.

Fairweather, M., Jones, W. P., and Lindstedt, R. P., 1992, *Twenty Fourth Symposium (International) on Combustion,* The Combustion Institute, Pittsburgh, PA.

Fairweather, M., Jones, W. P., and Lindstedt, R. P., 1991, *Combust. Flame,* Vol. 87, pp. 289–305.

Fairweather, M., Jones, W. P., and Lindstedt, R. P., 1992, *Combust. Flame,* Vol. 89, pp. 45–63.

Fenimore, C. P., and Jones, G. W., 1967, *J. of Phys. Chem.,* Vol. 71, p. 593.

Flower, W. L., and Bowman, C. T., 1985, *Twentieth Symposium (International) on Combustion,* The Combustion Institute, Pittsburgh, p. 1035.

Flower, W. L., and Bowman, C. T., 1987, "Soot Production in Axisymmetric Laminar Diffusion Flames at Pressures From One to Ten Atmosphere," *Twenty-First Symposium (International) on Combustion,* The Combustion Institute, Pittsburgh, p. 1115.

Garo, A., Lahaye, J., and Prado, G., 1990, *Combust. Flame,* Vol. 76, pp. 226–233.

Lefebvre, A. H., 1983, *Gas Turbine Combustion,* Hemisphere Publishing Corp., Washington, DC.

Lefebvre, A. H., 1985, ASME JOURNAL OF ENGINEERING FOR GAS TURBINES AND POWER, Vol. 107, p. 24.

Leung, K. M., Lindstedt, R. P., and Jones, W. P., 1991, *Combust. Flame,* Vol. 87, pp. 289–305.

Maans, H. G., and Miller, I. M., 1980, NASA T.P. 1673.

Miller, I. M., 1978, NASA T.P. 1318.

Moss, J. B., Stewart, C. D., and Syed, K. J., 1988, "Flowfield Modelling of Soot Formation at Elevated Pressures," *Twenty-Second Symposium (International) on Combustion,* The Combustion Institute, Pittsburgh, p. 413.

Nicol, D., Malte, P. C., Lai, J., Marinov, N. N., Pratt, D. T., and Corr, R. A., 1992, "NO_x Sensitivities for Gas Turbine Engines Operated on Lean-Premixed Combustion and Conventional Diffusion Flames," ASME Paper No. 92-GT-115.

Nikjooy, M., So, R. M., and Peck, R. E., 1988, "Modelling of Jet and Swirl-Stabilised Reacting Flows in Axisymmetric Combustors," *Combust. Sci. and Tech.,* Vol. 58, pp. 135–153.

Rizk, N. K., and Mongia, H. C., 1986, AIAA Paper No. 86-1531.

Rizk, N. K., and Mongia, H. C., 1992, *Twenty-Fourth Symposium (International) on Combustion,* The Combustion Institute, Pittsburgh, p. 1063.

Rodi, W., 1976, "A New Algebraic Relation for Calculating the Reynolds Stresses," *ZAMM,* Vol. 56, p. 219.

Shaw, H., 1974, "The Effects of Water, Pressure, and Equivalence Ratio on Nitric Oxide Production in Gas Turbines," ASME JOURNAL OF ENGINEERING FOR POWER, Vol. 96, pp. 240–246.

Valachovic, T. G., 1993, "Numerical Predictions of Idle-Power Emissions From Gas Turbine Combustors," ASME Paper No. 93-GT-175.

Wagner, H. Gg., 1987, "The Influence of Pressure on Soot Formation," AGARD-CP-422.

Yoshihara, Y., Kazakov, A., Wang, H., and Franklach, M., 1994, *Twenty-Fifth Symposium (International) on Combustion,* The Combustion Institute, Pittsburgh.

Zel'dovich, Ya. B., 1946, *Acta Physicochim. (USSR),* Vol. 21, p. 577.

A Coal-Fueled Combustion Turbine Cogeneration System With Topping Combustion

J. M. Beér
Massachusetts Institute of Technology, Cambridge, MA 02139

R. V. Garland
Westinghouse Electric Corporation, Orlando, FL

Cogeneration systems fired with coal or other solid fuels and containing conventional extracting-condensing or back pressure steam turbines can be found throughout the world. A potentially more economical plant of higher output per unit thermal energy is presented that employs a pressurized fluidized bed (PFB) and coal carbonizer. The carbonizer produces a char that is fed to the PFB and a low heating value fuel gas that is utilized in a topping combustion system. The topping combustor provides the means for achieving state-of-the-art turbine inlet temperatures and is the main contributor to enhancing the plant performance. An alternative to this fully coal-fired system is the partially coal, partially natural gas-fired air heater topping combustion cycle. In this cycle compressed air is preheated in an atmospheric pressure coal-fired boiler and its temperature raised further by burning natural gas in a topping gas turbine combustor. The coal fired boiler also generates steam for use in a cogeneration combined cycle. The conceptual design of the combustion turbine is presented with special emphasis on the low-emissions multiannular swirl burner topping combustion system and its special requirements and features.

1 Introduction

Coal combustion in direct-fired gas turbine cycles, in which the combustion products pass through the gas turbine, presents limitations not only on the maximum temperature at entry to the gas turbine, but also on the peak temperature to which the coal mineral matter has been exposed during combustion. A small fraction of the coal ash, increasing with increasing temperature, is vaporized and forms a submicron aerosol upon condensation as the gas cools down, which deposits on turbine blades. Fluidized combustion is the choice of combustion mode for this task because of the much lower combustion temperature (about 1600°F or 1144 K) compared to that in pulverized coal combustion (about 3100°F or 1977 K).

The lower temperature range in fluidized combustion is also favorable for in-bed sulfur capture by calcium oxide particles. At temperatures above 2400°F (1589 K) the product of sulfation, $CaSO_4$, becomes increasingly unstable and decomposes to CaO and SO_2, but it remains stable at fluidized combustion conditions.

One disadvantage of the low gas temperature in pressurized fluidized bed combustion (PFBC) is, however, that it limits the gas turbine cycle efficiency. Another disadvantage is the emission of N_2O, a greenhouse gas that also depletes stratospheric ozone. By applying a topping combustion, the gas temperature can be raised at entry to the gas turbine. The N_2O decomposes and the gas turbine efficiency increases at the elevated temperature. The fuel in the topping combustor can be a coal fuel, produced in a carbonizer, or natural gas. When the coal is devolatilized in a carbonizer, the residual char is fed into the PFBC. The char combustion products and the carbonizer volatiles have to undergo hot gas cleanup for the removal of particulates. The sulfur is removed from the carbonizer by calcareous sorbent.

In indirectly fired gas turbine cycles the coal combustion products do not enter the gas turbine; instead, air is preheated by coal to high temperatures, say 1500°F (1089 K), and a clean fuel such as natural gas is burned in the topping combustor. When natural gas is injected into preheated air in the topping combustor, there is an opportunity for the cycle efficiency to be further improved because the maximum gas temperature at gas turbine entry is now limited only by the state-of-the-art gas turbine development for a clean medium, but not by impurities such as alkali or particulates in the gas.

The topping combustion system in both cases described above permits raising the temperature of the gas before entry to the gas turbine. The combustion problems for these two cases, however, are somewhat different. For the PFBC with carbonizer, the fuel gas burned in the topping combustor is of low heating value, and contains nitrogenous compounds (amines, cyanides), which require staged, fuel-rich-fast-quench-lean combustion mode for low NO_x emission. When, on the other hand, natural gas with a high heating value fuel is burned in preheated air, the main problem is "thermal" NO formation and ultralean premixed combustion may present the effective technical response for achieving low NO_x emission.

Both the above-mentioned topping combustion cycles provide potent and versatile systems that enhance three important goals of any cogeneration venture:

- Economic benefit
- Increased coal use to reduce dependence on oil
- Environmental acceptability

The two candidate systems and their topping combustors are discussed in the following.

2 The Second-Generation PFB Cogeneration System

Over the past several years, Westinghouse has been part of a U.S. Department of Energy-sponsored project on a second generation PFB. Led by Foster Wheeler Development Corp., a team of contractors is developing the second-generation PFB technology (Robertson et al., 1989). Westinghouse's participation relates to gas cleanup, the use of the ceramic crossflow filter, the turbomachinery, steam, and gas turbines. A schematic representation of the second-generation PFB system adapted to cogeneration is shown in Fig. 1.

Fundamentally, the plant operates as follows: Coal slurry is fed to a pressurized carbonizer that produces a low-calorific

Contributed by the International Gas Turbine Institute and presented at Cogen-Turbo, Budapest, Hungary, September 3–5, 1991. Manuscript received by the International Gas Turbine Institute January 1994. Associate Technical Editor: S. Samuelsen.

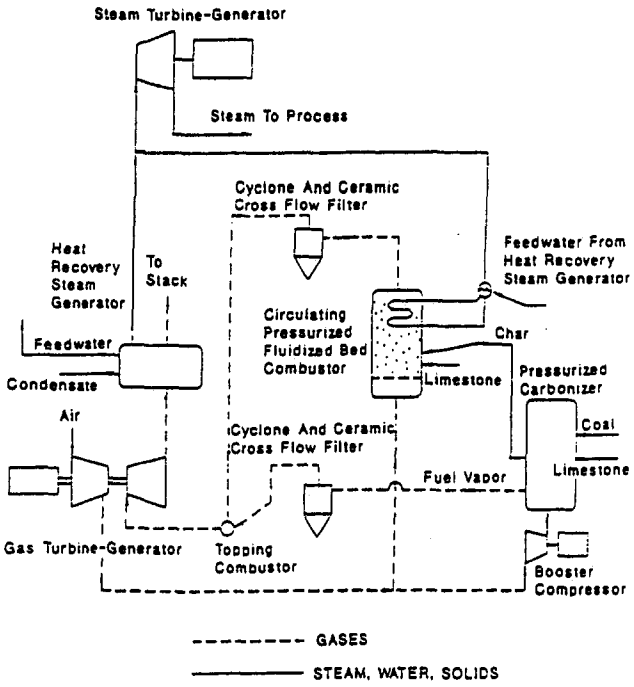

Fig. 1 Second generation PFBC cogeneration cycle

value fuel gas and char. After passing through a cyclone and crossflow filter to remove gas-entrained particulates, the fuel gas is burned in a topping combustor to produce the energy required to drive a gas turbine. The gas turbine drives a generator and a compressor that feeds air to the cabonizer, PFB, and fluidized bed heat exchanger (FBHE). The PFB and the FBHE are basic components of a circulating fluidized combustor (CPFBC). The carbonizer char is burned in the PFB with high excess air, and the vitiated air from the PFB is used to support combustion of the fuel gas in the topping combustor. Steam generated in a heat-recovery steam generator (HRSG) downstream of the gas turbine and in the FBHE associated with the PFB drive the steam turbine generator that furnishes the balance of electric power delivered by the plant and the steam for process.

The low-calorific value gas is produced in the carbonizer by pyrolysis/mild devolatilization of coal in a fluidized bed reactor. Because this unit operates at temperatures much lower than gasifiers currently under development, char residue is also produced. Left untreated, the fuel gas will contain hydrogen sulfide and sulfur-containing tar/light oil vapors; therefore, lime-based sorbents are injected into the carbonizer to catalytically enhance tar cracking and to capture sulfur as calcium sulfide. Sulfur is captured in situ and the raw fuel gas is fired hot. Thus the expensive, complex fuel gas heat exchangers and chemical or sulfur-capturing bed cleanup systems in coal gasification combined-cycle plants now being developed, are eliminated.

The char and calcium sulfide produced in the carbonizer, and contained in the fuel gas as elutriated particles, are captured by high-temperature filters, rendering the fuel gas essentially particulate free and meeting the New Source Performance Standard (NSPS of the US EPA). The captured material, together with carbonizer bed drains, is collected in a central hopper and injected into the PFB through a nitrogen-aerated nonmechanical valve. The high excess air in the combustor transforms the calcium sulfide to sulfate, allowing its disposal with the normal PFB spent sorbent.

Atmospheric fluidized bed experience has shown that circulating-bed performance can be superior to bubbling-bed performance (i.e., higher combustion efficiencies and heat-transfer coefficients along with lower SO_2 and NO_x emissions). Because

Table 1 Second generation PFB cogeneration performance

Gas Turbine Power	21,211 kW	
Steam Turbine Power	20,266 kW	
Auxiliary Power	(1,835) kW	
Net Electric Power	39,641 kW	
Process Steam Flow	353,394 b/h	(160,298 Kg/h)
Process Steam Pressure	150 psig	(1.14 Mpa)
Process Stream Temp.	386 F	(470K) (Sat.)
Coal Feed Rate	53,980 lb/h	(24,485 Kg/h)
Thermal Efficiency	82.85%	

of this superior performance and because second-generation plants may have to meet more stringent NSPS in the future and ideally should be capable of operating effectively with low-reactivity sorbents, a Circulating Pressurized Fluidized Bed Combustor (CPFBC) has been chosen. In the CPFBC, the burning char heats the high-excess-air flue gas to 1600°F (1144 K); any surplus heat is transferred to the external FBHE by the recirculation of sorbent between the two units. Controlled recirculation is accomplished with cyclone separators and nonmechanical valves. The CPFBC configuration selected is a vertical, refractory-lined pressure vessel, with all cooling tube surfaces

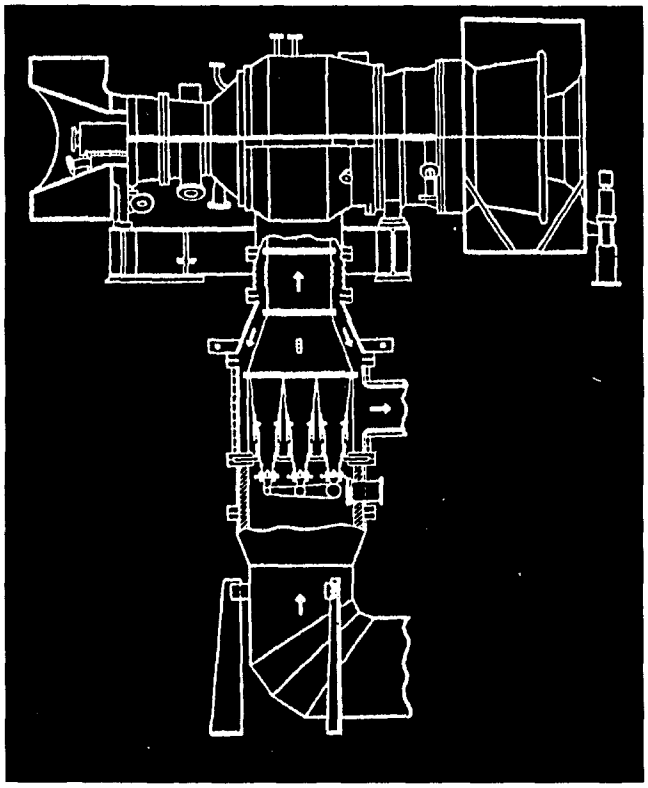

Fig. 2 The W151 gas turbine adapted to second-generation PFBC with topping combustor

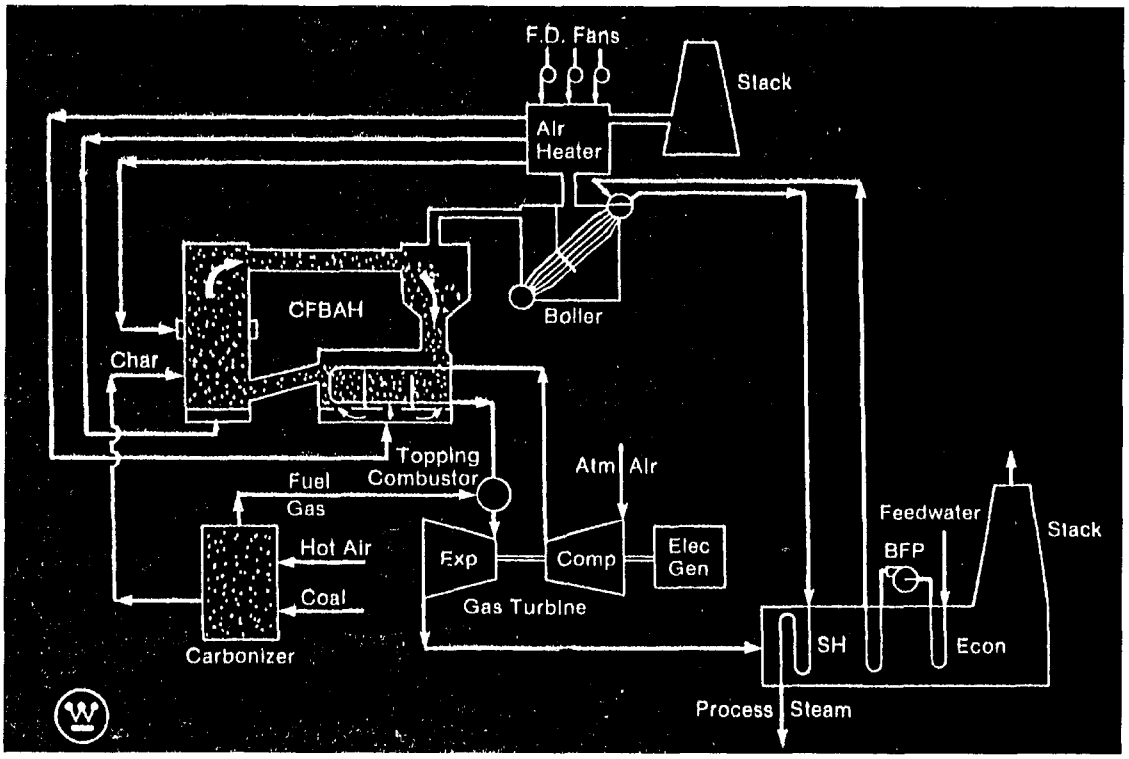

Fig. 3 Atmospheric circulating fluidized bed air heater cycle with syngas-fired topping combustor

placed in the FBHE. Because of the low fluidizing velocity in the FBHE ($\leq$0.15 m/s ($\leq\frac{1}{2}$ ft/s), the risk of tube erosion is virtually eliminated. Also, since no combustion is taking place in the FBHE, there is no gas side corrosion risk.

The exhaust gases leaving the carbonizer and the CPFBC contain particles of char, sorbent, and fly ash—all of which can erode and foul downstream equipment. To prevent erosion and fouling, a hot gas cleanup (HGCU) system, consisting of ceramic crossflow filters preceded by cyclone separators, cleans these gases to <20 ppm solids loading before they enter the fuel gas topping combustor and the gas turbine. Ceramic candle filters, hot electrostatic precipitators (ESPs), screenless granular-bed filters, etc., are also candidate alternatives for the crossflow filter should their performance and economics be found superior. All these devices are currently under development for first-generation PFB combustion cycles. They should also be applicable to the second-generation plant.

The topping combustor consists of metallic-wall multiannular swirl burners (MASBs), which are currently under development (Garland and Pillsbury, 1990). Each MASB contains a

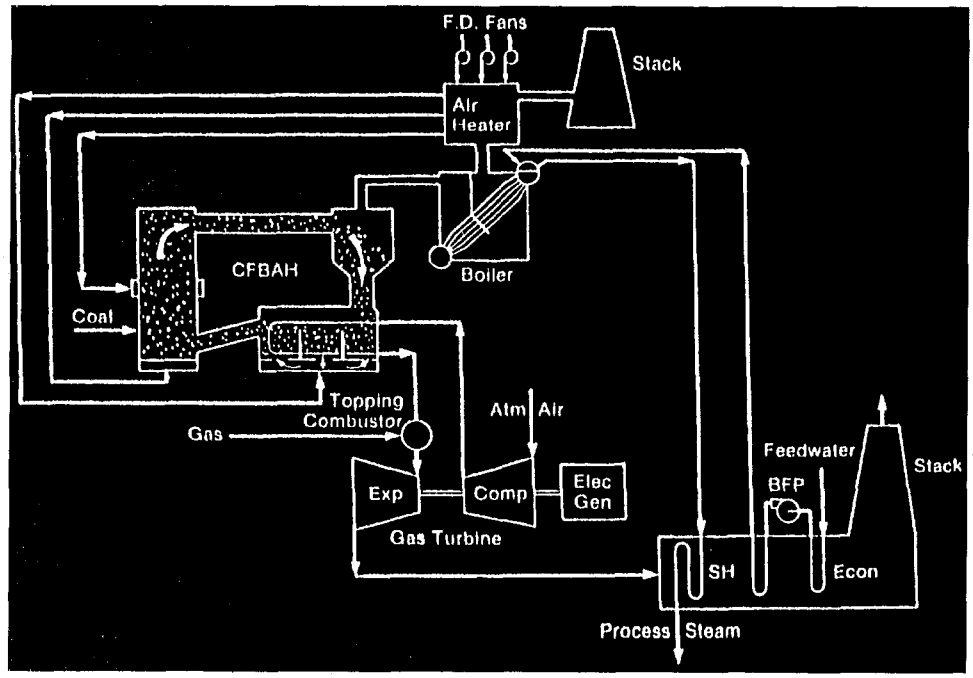

Fig. 4 Atmospheric circulating fluidized bed air heater cycle with natural gas-fired topping combustor

Table 2 Effect of topping combustion

DESCRIPTION	NO TOPPING COMBUSTOR	NATURAL GAS-FIRED TOPPING COMBUSTOR
Net Kw Output	19152	37880
Auxiliary	4453	3650
Gross Kw Output	23605	41530
Bed Temp~°F (°C)	1600.(871)	1600.(871)
Turbine Inlet~°F (°C)	1500.(816)	**2000/(1093)
Bed Stack~°F (°C)	296.(147)	300.(149)
HRSG Stack~°F (°C)	150.(66)	300.(149)
Turbine Press Ratio	6.7	13.7
Coal Flow~Lb/Hr. (Kg/Hr)	48100.(21818)	*36212/12060.(16425/5470)
Process Steam~Lb/Hr. (Kg/Hr)	210000.(95255)	210000.(95255)
Process Air~Lb/Hr. (Kg/Hr)	717468.(325441)	724248.(328516)
Energy Efficiency, %	82.3	78.0
Effective Generation Efficiency %	51.8	53.7
Power to Heat (E/T) %	16	31

*Coal/Natural Gas Flow

Coal HHV = 12235 Btu/Lb

Natural Gas HHV = 21690 Btu/Lb

**Air Temperature Out of Bed, Before Topping Combustor is 1400°F (760°C)

series of swirlers and aerodynamically creates fuel-rich, quick-quench, and fuel-lean zones to minimize NO_x formation during the topping combustion process. The swirlers also provide a thick layer of air at the wall boundary to control the temperature of the metallic walls.

Table 1 lists the performance of this second-generation PFB cogeneration system.

2.1 The Combustion Turbine. The combustion turbine proposed for this PFB cogeneration is basically a modified version of the well-known Westinghouse W-251 combustion turbine that has been in service for more than twenty years.

One of the latest versions of the model 251 combustion turbine is rated at about 48 MWe. To fill the need for a smaller capacity machine, the 251 was scaled down by a factor of 0.76, and, consequently, its output was scaled down by a similar amount. Thus, the ISO rating for the oil-fired Model 151 Base Load is about 21 Mwe. The machine retained the 18-stage compressor and 3-stage turbine of the W251B, although they were scaled down as mentioned above. It is this model that is adapted to the Second-Generation PFBC cogeneration concept.

Adapting the Model 151 to the Second-Generation PFBC concept does not involve a totally new combustion turbine design. While the compressor and turbine blading require some degree of blade reorientation to effect a suitable match, the changes do not involve major redesign or analysis. The center section, however, is redesigned to bring the majority of the compressor air out of the machine so that it can be delivered to the coal carbonizer and PFB. In addition, the conventional combustors, eight of them in the conventional machine, are eliminated; an external combustion system is added that also channels the hot gases back into the turbine casing.

The redesign of the combustion turbine center section is patterned after a similar application involving the combustion of blast furnace gas. That installation at the Kamaishi Works of Nippon Steel Corporation in Japan employed a modified W151 combustion turbine (Muyama et al., 1984). A single external can-type combustor was designed to burn the low heating value gaseous fuel.

The 1600°F (1144 K) vitiated air is too hot to provide combustor wall cooling for the conventional combustor construction (employed in Japanese steel works application). In addition, the fuel-bound nitrogen in the fuel gas must be converted to N_2 through specific pyrolysis-combustion processes that will preclude the formation of NO_x. Thus, in place of the large can-type combustor with multifuel nozzles, the patented multi-annular swirl burner (MASB) is used (Beér, 1989).

A group of seven MASBs is accommodated within the external combustor housing as shown in Fig. 2. The compressor air leaves the main casing in an annular duct that surrounds the combustor housing and is piped to the PFB and carbonizer. Figure 2 shows that air leaves about halfway down the combustor housing. The vitiated air returning from the PFB system enters the combustor housing at the bottom and provides the cooling and combustion air for the seven MASBs.

3 Air Heater Topping Cycles

Using an atmospheric pressure circulating fluidized coal combustor (ACFBC) the air heater topping cycle can be applied in either a semidirect or indirect coal-fired mode.

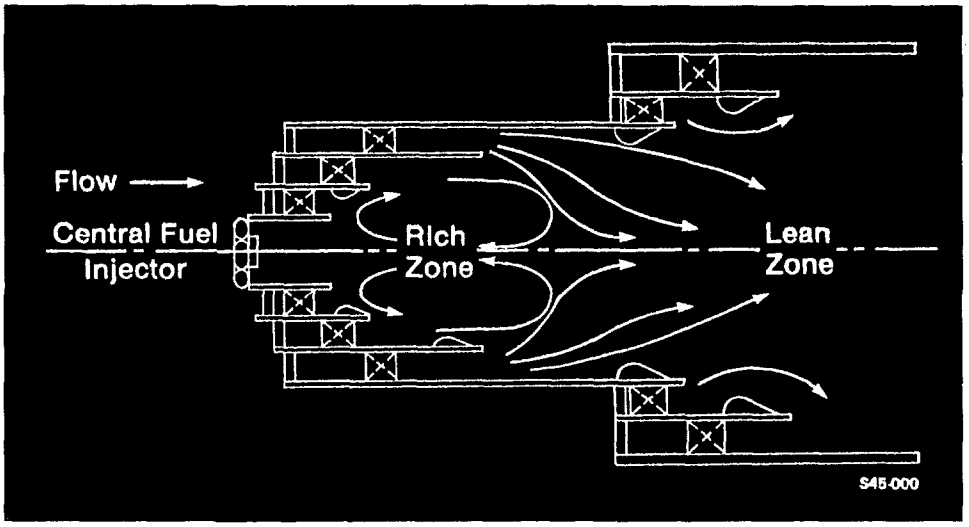

Fig. 5 Conceptual design of rich-lean multi-annular swirl burner (Beér, 1989)

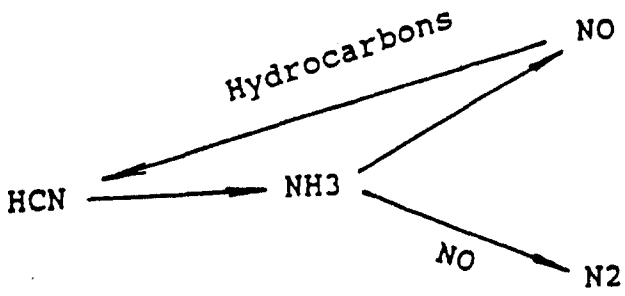

Fig. 6 Interaction between ammonia, NO, and hydrocarbons in fuel-rich hydrocarbon flames (Haynes, 1977)

3.1 Semidirect Mode. In the semidirect mode, a pressurized carbonizer provides the feedstock of char to the atmospheric pressure fluidized combustor (AFBC), and fuel gas (mainly coal volatiles) is injected into the topping combustor (Fig. 3). Compressed air is preheated in the external FBHE to 1400°F (1033 K) before entry to the topping combustor where the coal gas is burned to raise its temperature to 2000°F (1367 K). In this cycle only the coal gas needs to be cleaned; the rest of the gas turbine medium is clean air. The topping combustor R&D challenges are similar to those of the PFBC-carbonizer cycle: application of fuel-rich, fast-quench, fuel-lean mode of combustion to reduce NO_x emission, and adequate cooling of the combustor by means of high-temperature preheated air.

3.2 Indirect Coal-Fired Mode. In the indirect coal-fired air-heater topping cycle, compressed air is preheated in a coal-fired atmospheric pressure boiler (AFBC), and natural gas is burned in the topping combustor (Fig. 4). The gas turbine cycle works with a clean medium, the lean products of combustion of natural gas in air. The effects of the topping combustion upon the performance characteristics of a cogeneration combined cycle computed as an example in a study (Berman and Eustis, 1986) are illustrated in Table 2. The significant increase in the power-to-heat ratio and the high effective power generation efficiency are noteworthy.

3.3 Pulverized Coal-Fired High-Temperature Air Furnace (HITAF). An alternative to the AFBC is a High-Temperature Air Heater Furnace (HITAF) fired by pulverized coal. Such a system is under development by a consortium led by United Technologies Research Center (Robson and Seery, 1994) under the "Combustion 2000" Program of the DOE Pittsburgh Energy Technology Center. The target is a higher air preheat temperature, 1700°F (1150 K), which, in turn, would reduce the contribution of natural gas to 36 percent from about 50 percent for the 1400°F (1033 K) air preheat in the AFBC. The higher air preheat, however, requires a ceramic heat exchanger that will stand up to the corrosive attack of molten slag on the fire side in addition to the high mechanical and thermal stresses due to the high air pressure and temperature. Because of this, the ceramic heat exchanger for 1700°F air preheat is expected to be available in the longer term, compared with the metallic heat exchanger capable of 1400°F air preheat that is presently available.

3.4 Technical Risks. There are two areas of technical risk associated with the application of air heater topping cycles: the high-temperature high-pressure air preheater and the topping combustor. A material designated X5 NiCrCeNb3227 manufactured by Mannesmann, A. G. (1989) has been developed for a duty similar to that of the air preheater tubes. Material specifications and results of long-term testing seem to be favorable for preheat temperatures of 1400°F to be maintained and probably even exceeded. The challenges of the topping combustor development and the technical responses are discussed in the following.

4 Topping Combustor Design

The technical tasks that have to be solved in the course of the development of a topping combustor include:

(*a*) Adequate cooling of combustor walls to ensure structural integrity of the combustor
(*b*) Low fuel-nitrogen conversion when using nitrogen bearing fuels in the topping combustor
(*c*) Low "thermal" NO_x emission from natural gas fired topping combustors operated with high air preheat
(*d*) Complete burn-out of hydrocarbons and CO over the operating ranges of the combustor.

4.1 Combustor Wall Cooling. Because the air entering the combustor is at 1600°F (1144 K) rather than the usual 700°F (644 K) for gas turbines, the conventional type of combustor is not suitable. Both emissions and wall cooling problems preclude the use of the conventional design.

In selecting a combustor design that will withstand the conditions expected in the topping application, the effective utiliza-

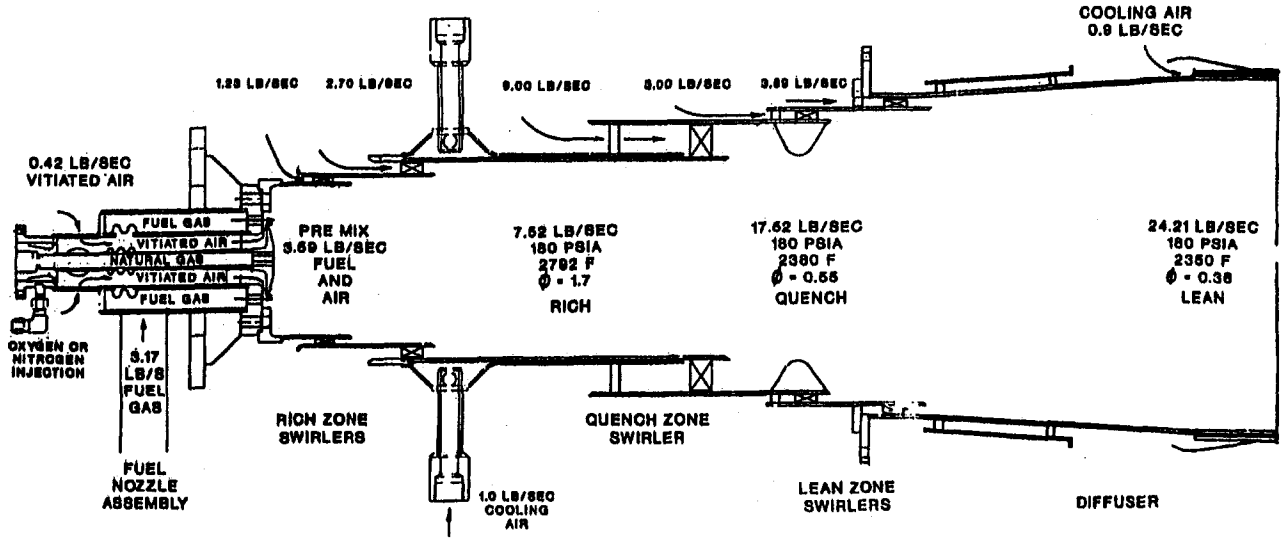

Fig. 7 Schematic design of the MASB and operating conditions of syngas-fired MASB tests at UTSI

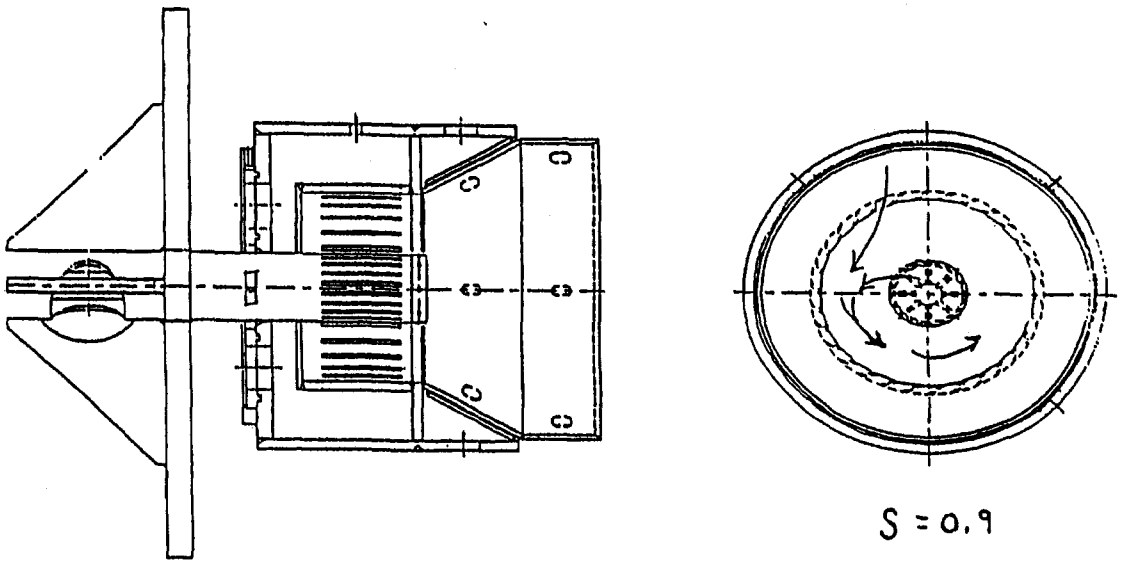

Fig. 8 Redesigned fuel injection system for the MASB (Domeracki et al., 1994): fuel gas and vitiated air mix in an annular space between two coaxial tangential arrays of jets

tion of the high-temperature air mentioned above could satisfy the wall cooling challenge by maintaining a cooling air layer of substantial thickness. The creation of thick layers of cooling air at the leading edge of each inlet section is easily achieved if the combustor is made up of concentric annular passages. In the Multi-Annular Swirl Burner (MASB), Fig. 5, the entire combustion air quantity is introduced into the combustor by means of annuli of substantial radial thickness. The MASB is constructed of high-alloy metals avoiding refractory construction so that refractory spalling will not result in turbine damage.

A previous DOE-sponsored topping combustor test program tested a 10-inch MASB fired with methane (Garland et al., 1986). The engineering design and combustor development were carried out by a team at Westinghouse in Corcordville, PA. In that program wall temperatures were the major concern just as they are in the present applications. To thoroughly investigate the potential problem of excessive wall temperature, a two-phase test program was conducted. The first phase of the program fired the test MASB with methane using 850°F (728 K) combustion air. Radiometers were placed in the rich zone of the MASB to measure flame radiation. Data from this first test confirmed the analysis performed during the design phase. The measured wall temperatures were actually somewhat lower than those predicted before the test. Assumptions were adjusted accordingly, and wall temperature predictions were made for the second test that would fire methane with 1400°F (1033 K) combustion air.

The test utilizing 1400°F (1033 K) combustion air yielded encouraging results and corroborated the wall temperature predictions. The measured wall temperatures were less than 100°F (56 K) higher than the combustion air temperature. The condition of the combustor after test was excellent even though the calculated adiabatic flame temperature in the rich zone was 3964°F (2458 K).

A DOE-sponsored MASB test program is under way to develop the MASB to burn the low heating value NH_3 bearing fuel gas produced by the carbonizer in the second-generation PFB cycle. The design of the combustor has been presented by Garland and Pillsbury (1990) and the results of the first tests by Garland et al. (1991).

Tests have been conducted at the University of Tennessee Space Institute (UTSI) in their DOE Coal-Fired Flow Facility. The facility accommodates the MASB fired by a 1200°F (650°C) temperature six-component fuel gas (H_2, CO, CH_4, NH_3, N_2, H_2O), the ammonia representing the fuel N. A distillate fuel oil fired combustor is used to provide 1600°F (870°C) vitiated air simulating the high excess air containing flue gas of the PCB entering the topping combustor. The flames pro-

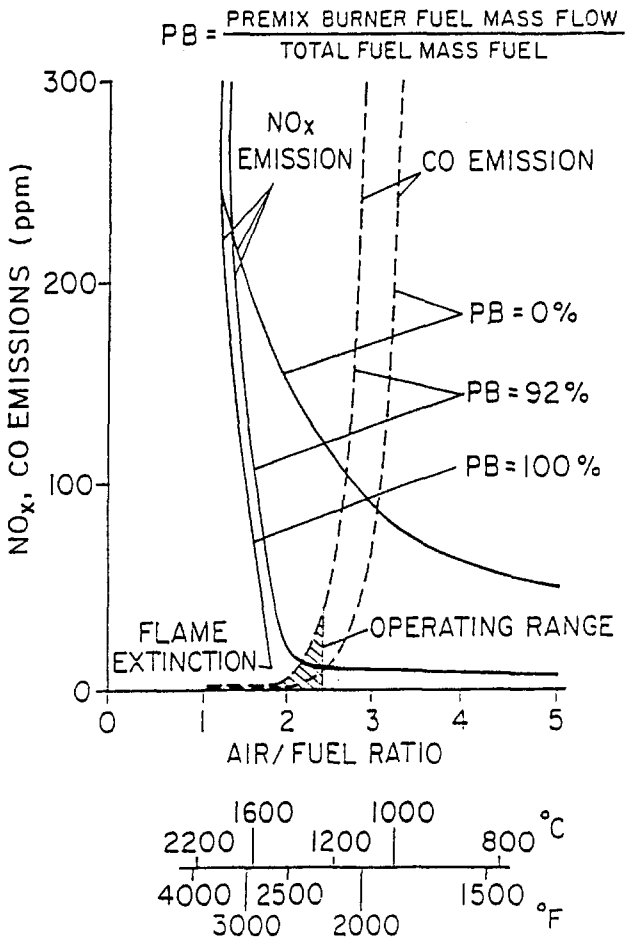

Fig. 9 Dry NO_x and CO emissions measured in premixed natural gas-air combustion (Maghon et al., 1988)

Table 3 Topping combustion characteristics (calculated for premixed combustion conditions)

	Ta = 1073 K (1472·F)			Ta = 1173 K (1652·F)			Ta = 1273 K (1832·F)		
O	Tad	t_i ms	t_c ms	Tad	t_i ms	t_c ms	Tad	t_i ms	t_c ms
0.1	1314	15	25	1412	5	10	**1510**	**5**	**5**
0.2	**1539**	**10**	**10**	1634	5	5	1730	5	5
0.3	1749	10	10	1842	5	5	1936	5	5
0.4	1945	10	10						

O : Fuel Equivalence Ratio

Ta : Air Preheat
Pressure: 13 atm.
Miller Chemkin

duced by this high-temperature air and the synthetic gas are assumed to have ignition and combustion characteristics similar to those in the topping combustor of the PFB. Three syngas tests and one fuel oil/natural gas test were carried out during 1990–91 at scales of 12 in. (0.305 m) and 14 in. (0.356 m) diameter. The MASB was successfully cooled with 1600°F vitiated air supplemented with 5 to 10 percent of cooling air used at the hottest locations. Favorably uniform temperature patterns were obtained with both the 12 in. and 14 in. combustors at 2100°F (1150°C and 2350°C) combustor outlet temperatures, respectively.

Additionally to the wall cooling requirement, the MASB design has to satisfy conditions for low NO_x emission, and a high degree of oxidative destruction of CO and hydrocarbons in the combustion process. Also, it is desirable for the combustor to be operable without the air having been preheated; otherwise the turbine could not be operated without the fluidized bed (''black plant start''). To meet this requirement, the design of choice has to have a recirculation zone where hot gases will support and maintain combustion even in the absence of high air inlet temperature.

4.2 NO_x Emissions Control. Design protocols for the reduction of NO_x for a practical plant are based on the improved understanding of the chemistry of nitrogen species and their interaction with hydrocarbon species in flames. The main routes for formation of NO are:

- Fixation of atmospheric nitrogen in oxidizing atmospheres at temperatures of 2800°F and above (''thermal NO'')
- Fixation of atmospheric nitrogen by hydrocarbon fragments (CH, CH_2) in fuel-rich flames close to the fuel nozzle (''prompt NO'')
- Oxidation of organically bound nitrogen compounds present in the fuel (''fuel NO'').

''Thermal NO'' formation can be mitigated by avoiding high peak temperatures and long residence times of combustion products at elevated temperatures, while fuel-bound nitrogen conversion to NO can be reduced by air or fuel staging in the combustion process. There is experimental evidence to show that fuel-bound nitrogen in fuel-rich high-temperature pyrolysis rapidly forms HCN, which is then converted via radicals, NCO, HNCO, to other nitrogenous products such as amines, NH, NH_2, with these latter species reducing to molecular nitrogen, N_2. A schematic reaction path in Fig. 6 shows the interaction between the ammonia species, NO, and hydrocarbons. Once the fuel-bound nitrogen has been converted to molecular nitrogen, the rest of the combustion air can be added to burn the fuel completely without the risk of oxidizing the fuel bound nitrogen to NO. At this point, however, care has to be taken to avoid ''thermal NO'' formation in the fuel lean combustion zone of the flame.

In the practical realization of staged combustion, the problem is to prevent premature mixing between fuel and air in the fuel-rich pyrolysis zone, but then promote mixing in the fast quench and fuel lean burn-out zones. In the MASB, the fuel is concentrated in the central region of the fuel rich zone followed by vigorous mixing in the fast quench and lean burn-out zones of the combustor (Beér, 1974, 1989).

The operating conditions of the syngas-fired MASB tests are shown in Fig. 7. Initial results of the Westinghouse–UTSI experiments showed low rates of thermal NO formation, and acceptable levels of CO emissions. A few data from the 1990–91 tests are given below to illustrate the general levels of emissions.

- NO formed incrementally in the MASB at 2100°F (1422 K) was 8 ppm (NO_x in 1600°F or 1144 K vitiated air was 48 ppm)

Table 4 Topping combustion characteristics nitric oxide concentrations (ppm) (calculated for premixed combustion conditions)

	Ta = 1073 K (1472·F)					Ta = 1173 K (1652·F)					Ta = 1273 K (1832·F)				
O	5 ms	10	20	30	40	5 ms	10	20	30	40	5 ms	10	20	30	40
0.1	0.0	0.0	0.03	0.04	0.04	0.09	0.11	0.12	0.12	0.12	**0.3**	**0.31**	**0.31**	**0.31**	**0.32**
0.2	**0.0**	**0.03**	**0.3**	**0.3**	**0.31**	0.68	0.71	0.8	0.86	0.93	1.6	1.95	2.6	3.2	3.8
0.3	0.0	1.56	2.4	3.2	4	4.2	6.8	12	17.2	22.4	17.4	31.6	60	88	116
0.4	0.0	16.8	47	77	107	54.2	121	253	383	510	250	505	993	1450	1880

O : Fuel Equivalence Ratio

Ta : Air Preheat
Pressure: 13 atm.
Miller Chemkin

- Combustion efficiency was better than 99.9 percent
- Combustor pressure drop was about $\frac{1}{2}$ percent

The conversion to NO_x of the additive NH_3 in the fuel gas varied over the range of 20 to 30 percent. While this was significantly lower than in conventional combustors, examination of the experimental temperature distribution close to the fuel nozzle and computational modeling by the Westinghouse and UTSI teams (Garland et al., 1991) showed that further improvements to the design of the fuel injector and the front end of the MASB could be made. One of the key requirements of the MASB design is to ensure rapid temperature rise close to the fuel nozzle to take full advantage of extended residence time in the high-temperature fuel-rich stage of the combustor. In order to achieve this the MASB fuel injection system was redesigned as shown in Fig. 8 (Domeracki et al., 1994). In the new design fuel gas and vitiated air mix in an annular space between two coaxial tangential arrays of jets. This well-stirred annulus opens to the full diameter of the fuel-rich stage of the combustor by a wide angle divergence, which, in combination with the high swirl flow, produces vortex breakdown and a strong central recirculation on the combustor axis. Subsequent experiments corroborated the results of chemical kinetic and fluid flow modeling: The conversion of fuel N to NO_x dropped from 20 percent to below 10 percent due to the faster temperature rise near the fuel nozzle and hence increased residence time of the fuel-rich mixture at the target temperature of 2900°F (1866 K).

4.3 High Air Preheat—Natural Gas Fired Topping Combustion. When natural gas is burned in the topping combustor, the high air preheat ($T > 1050$ K) and the high heating value of the gas will produce very high adiabatic flame temperatures leading to excessive NO_x emission by the "thermal" NO_x formation route.

Because of the nature of "thermal" NO formation, the usual diffusion flame combustion process in which fuel and oxidant mix concurrently with the progress of combustion is not favorable. Diffusion flames lead to locally stoichiometric, or close to stoichiometric mixture ratios concomitant with high NO_x formation rates; premixed ultralean combustion instead is favored. It is argued that, because air is used as a dilutant in gas turbine combustors, the fuel/air ratio in the gas turbine combustor exit is determined by the maximum gas temperature permitted to enter the gas turbine. If fuel and oxidant can be premixed to this fuel lean mixture ratio prior to ignition, and combustion proceeds close to isothermally at a temperature $T < 1800$ K, there will be very little thermal NO formation. A number of practical developments of lean, premixed combustors have been reported in recent years by manufacturers and operators of gas turbines (Becker et al., 1986; Davies, 1988; Marnet et al., 1985; Smith et al., 1986).

The problem presented in the design of such ultralean premixed combustors is illustrated by Maghon et al. (1988) in Fig. 9. There is but a narrow fuel/air mixture ratio or temperature range in which both NO_x emission requirements and those for combustion stability and CO burn-out can be satisfied. The flame is stabilized in their combustor by a pilot diffusion flame burning 8 percent of the total fuel input. The rest of the fuel, 92 percent, is premixed with the combustion air.

The situation, however, becomes more favorable for topping combustors because of the highly preheated combustion air. In Table 3, calculated adiabatic flame temperatures are presented for ultralean premixed combustion and for different air preheat temperatures and fuel/air ratios. Also in Table 3, the computed residence times required for methane decomposition, t_1, and for CO burn-out to below 50 ppmv, t_2, are given. Calculated NO_x emissions for the same conditions are shown in Table 4. The NO_x emission is low for ultralean mixture ratios but rises rapidly with increasing fuel equivalence ratio.

The results of these chemical kinetic calculations show that for practical conditions of topping combustors operation, e.g., air preheat: 1472°F (1073 K); combustor outlet temperature: 2310°F (1539 K) and fuel equivalence ratio $\Phi = 0.2$, 10 ms is required for methane decomposition and 10 ms residence time in the combustor for CO burn-out.

The R&D challenges of the ultralean-premixed topping combustor will be the mode of fuel/air premixing without flashback of the flame into the mixing zone, and combustor wall cooling. The conceptual design of a MASB capable of operating in the ultralean premixed topping combustion mode is shown in Fig. 10.

Conclusions

Two systems of coal-fueled steam–gas turbine combined cycle cogeneration with topping combustion are discussed: pressurized fluidized combustion with syngas fired topping combustor, and atmospheric pressure boiler air heater cycles with either a syngas or a natural gas fired topping combustor. Adaptation of an existing combustion turbine (Model W-151) to the pressurized fluidized combustion system requires no major redesign except for the ducting of the compressor air out of the machine so that it can be delivered to the carbonizer and the PFB, and the application of an external combustion system with a group of multiannular topping combustors.

In the area of topping combustor development, the major challenges are the adequate cooling of the combustor walls and

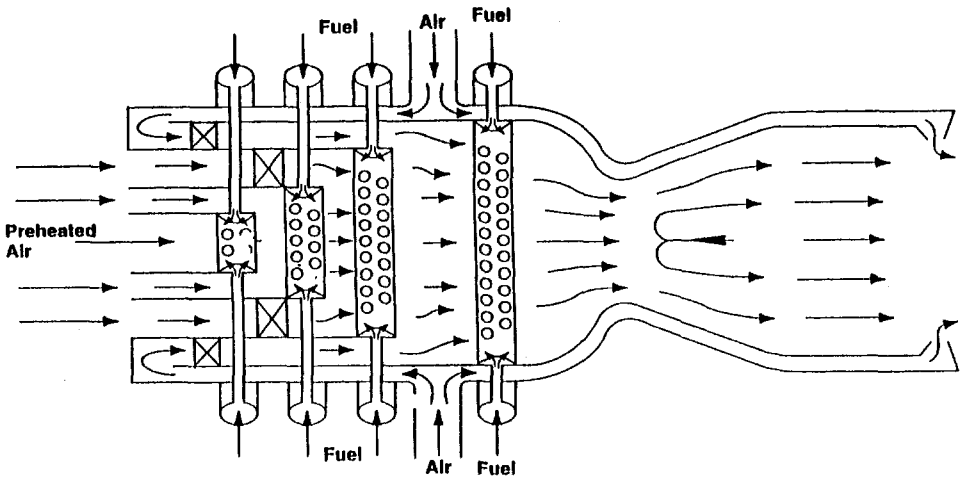

Fig. 10 Ultralean-premixed MASB conceptual design (Beér, 1990)

NO_x emission control. Experimental results show that in the Multiannular Combustor (MASB) design the subdivision of the total air into concentric annular passages with rotating flow ensures satisfactory response to the wall cooling challenge ($T_{wall} - T_{air}$) < 100°F (56 K).

For the coal gas-fired topping combustor, where the fuel contains nitrogen compounds (NH_i), staged combustion is necessary to suppress the conversion of NH_i to NO_x. Tests with the full-size MASB during 1994 gave very low emissions of MASB generated NO_x (8.3 ppm) and fuel-N conversion to NO_x (5.8 percent) with less than 100 ppm CO and no HC and soot in the combustion products.

When natural gas is burned in highly preheated air and the NO_x emission limits are low, ultralean premixed combustion is the preferred mode of MASB operation. Theoretical calculations of hydrocarbon and CO burn-out, and NO_x emission levels show that there is a practical range of operating variables within which high efficiency-low emission operation with good flame stability is possible.

Acknowledgments

The topping combustor development work being performed by Westinghouse through the Department of Energy's Morgantown Energy Technology Center is managed by Mr. Don Bonk, Project Manager, Office of Technical Management.

This DOE/METC project is being carried out through the efforts of several contractors. The prime contractor is Foster Wheeler Development Corporation and four subcontractors are working in conjunction. The five companies and their prime contract personnel are listed below:

- Foster Wheeler Development Corporation
  Archie Robertson, Program Manager
- Gilbert/Commonwealth, Inc.
  Lynn Rubow, Project Manager
- Institute of Gas Technology
  Amir Rehmat, Project Leader
- Westinghouse Power Generation Business Unit
  Richard Garland, Project Manager
- Westinghouse Science and Technology Center
  Richard Newby, Project Manager

Co-author Beér also wants to acknowledge the valuable assistance of Mr. Angelo Testa (Eniricerche) with the chemical kinetic calculations of ultralean topping combustors, and Dr. Majed Toqan (MIT-CRF) for many stimulating discussions on NO_x emissions reduction.

References

Becker, B., Berenbrink, P., and Brandther, H., 1986, "Premixing Gas and Air to Reduce NO_x Emission With Existing Proven Gas Turbine Combustion Chambers," ASME Paper No. 86-GT-157.

Beér, J. M., 1974, *Combustion Aerodynamics in Combustion Technology, Some Modern Developments,* H. B. Palmer and J. M. Beér, eds., Academic Press, New York, Chap. III.

Beér, J. M., 1989, U.S. Patent No. 4845940; 1965, British Patent 45652/65.

Beér, J. M., 1990, unpublished data.

Berman, P. A., and Eustis, J. N., 1982, "Atmospheric Fluid Bed Air Heater Systems for Cogeneration Coal-Fired Gas Turbine Cogeneration," report to US DOE Contract No. 7819, prepared by Westinghouse Electric Corp. for Oak Ridge National Lab, Dec.

Davies, L. B., 1988, "Gas Turbine Combustion and Emissions," GE Turbine Reference Library No. 3568.

Domeracki, W. F., Dowdy, T. E., and Bachovchin, D. M., 1994, "Topping Combustor Development for Second-Generation Pressurized Fluidized Bed Combined Cycle," ASME Paper No. 94-GT-176.

Garland, R. V., Pillsbury, P. W., and Vermes, G., 1986, "Generic Studies of Advanced Fluidized Bed Air Heater Technology," DOE/DE/40543-5, Westinghouse Electric Corp.

Garland, R. V., and Pillsbury, P. W., 1992, "Status of Topping Combustor Development for Second-Generation Fluidized Bed Combined Cycles," ASME JOURNAL OF ENGINEERING FOR GAS TURBINES AND POWER, Vol. 114, pp. 126–131.

Garland, R. V., Pillsbury, P. W., and Dowdy, T. E., 1991, "Design and Test of Candidate Topping Combustor for Second Generation PFB Applications," ASME Paper No. 91-GT-113.

Haynes, B. S., 1977, "Reactions of Ammonia and Nitric Oxide in the Burned Gases of Fuel Rich Hydrocarbon Air Flames," *Combustion and Flame,* Vol. 28, No. 2, pp. 113–121.

Maghon, H., Kreutzer, A., and Termuehlen, H., 1988, "The V84 Gas Turbine Designed for Base-Load and Peaking Duty," *Proc. 1988 American Power Conference,* Vol. 60.

Mannesmann Edelstahlrohr GmbH, 1989, "A High Temperature Corrosion Resistant Material of Construction AC 66 (X 5 NiCrNb 3227)," report of public presentation, Duisberg-Huckingen, Germany, Mar. 7.

Marnet, C., Kassebohm, B., Koch, H., and Sponholz, H. J., 1985, "No_x Minderung in Kombinierten Gas/Dampf Kraftwerk Lausward," *Brower Boveri Technik,* Vol. 72, No. 3, pp. 120–124.

Muyama, A., Hiura, H., and Morimoto, K., 1984, "Repowering in Steel Works by Introducing a Blast-Furnace, Gas-Firing Gas Turbine," ASME JOURNAL OF ENGINEERING FOR GAS TURBINES AND POWER, Vol. 106, pp. 806–811.

Robertson, A., Garland, R., Newby, R., Rehmat, A., and Rebow, L., 1989, "Second-Generation Pressurized Fluidized Bed Combustion Plant: Conceptual Design and Optimization of a Second-Generation PFB Combustion Plant," Foster Wheeler Development Corporation Phase 1, Task 1 Report, FWC/FWDC-TR-89/11 (3 volumes) to the U.S. DOE under Contract DE-AC21-86MC21023.

Robson, F. L., and Seery, D. J., 1994, "High Efficiency Gas Turbine Power Systems Using Coal Fired High Temperature Air Furnace," ASME Paper No. 94-JPGC-GT-6.

Smith, K. O., Angello, L. C., and Kurzynske, F. R., 1986, "Design and Testing of an Ultra Low NO_x Gas Turbine Combustor," ASME Paper No. 86-GT-264.

Dry Ultralow NO_x "Green Thumb" Combustor for Allison's 501-K Series Industrial Engines

R. Puri

D. M. Stansel

D. A. Smith

M. K. Razdan

Allison Engine Company, Inc., Indianapolis, IN

This paper describes the progress made in developing an external ultralow oxides of nitrogen (NO_x) "Green Thumb" combustor for the Allison Engine Company's 501-K series engines. A lean premixed approach is being pursued to meet the emissions goals of 9 ppm NO_x, 50 ppm carbon monoxide (CO), and 10 ppm unburned hydrocarbon (UHC). Several lean premixed (LPM) module configurations were identified computationally for the best NO_x–CO trade-off by varying the location of fuel injection and the swirl angle of the module. These configurations were fabricated and screened under atmospheric conditions by direct visualization through a quartz liner; measurement of the stoichiometry at lean blow out (LBO); measurement of the fuel–air mixing efficiency at the module exit; and emissions measurements at the combustor exit, as well as velocity measurements. The influence of linear residence time on emissions was also examined. An LPM module featuring a radial inflow swirler demonstrated efficient fuel–air mixing and subsequent low NO_x and CO production in extensive atmospheric bench and simulated engine testing. Measurements show the fuel concentration distribution at the module exit impacts the tradeoff between NO_x and CO emissions. The effect of varying the swirl angle of the module also has a similar effect with the gains in NO_x emissions reduction being traded for increased CO emissions. A uniform fuel–air mixture (±2.5 percent azimuthal variation) at the exit of the module yields low NO_x (5–10 ppm) at inlet conditions of 1 MPa (~10 atm) and temperatures as high as 616 K (650°F). The combustion efficiency at these conditions was also good (>99.9 percent) with CO and UHC emissions below 76 ppm and 39 ppm, respectively. This LPM module was resistant to flashback, and stability was good as LBO was observed below $\phi = 0.50$. Tests with multiple modules in a single liner indicate a strong intermodule interaction and show lower NO_x and CO emissions. The close proximity of adjacent modules and lower confinement in the liner most likely reduces the size of the recirculation zone associated with each module, thereby reducing the NO_x formed therein. The CO emissions are probably lowered due to the reduced cool liner surface area per module resulting when several modules feed into the same liner.

Introduction

Recently, Allison developed an in-line dry low emissions combustor with 25 ppm NO_x levels for its 501-K series gas turbine engines (Razdan et al., 1994; McLeroy et al., 1995). Allison is continuing the development of dry low emissions (NO_x, CO, and UHC) combustors with increasingly lower emissions goals to address current and future stringent regulations. The approach adopted in these programs involves premixing the fuel and the air prior to introduction into the combustor. This approach has been widely used (Bauermeister et al., 1993; Kajita et al., 1993; Leonard and Stegmaier, 1994; Willis et al., 1993; Döbbeling et al., 1996; Etheridge, 1994; Snyder et al., 1996) and is the most promising means to single digit NO_x (ppm) in gas turbine engines (Correa, 1992). This approach represents a fundamental departure from the traditional diffusion flame combustor in which fuel/air mixing and combustion occur simultaneously.

In the traditional combustor, regions exist in the primary combustion zone that have stoichiometric mixtures with attendant high gas temperatures enhancing stability and combustion efficiency at the expense of NO_x production. Although NO_x emissions from these combustors can be lowered by selective catalytic reduction of the exhaust and/or by diluent (water or steam) injection, these methods are expensive and impose durability limits. The latter control technology of diluent injection also incurs a fuel consumption penalty with increased CO and UHC emissions. By premixing the fuel and the air, stoichiometric fuel–air mixtures yielding the highest temperatures are avoided and the NO_x formation rate, which is exponentially dependent on temperature, is lowered. With lower primary zone temperatures, however, hydrocarbon chemistry is also slower and additional considerations are needed to ensure minimal CO and UHC emissions.

Under the current program a retrofittable off-centerline silo combustor is being developed. This combustor is also referred to as the Green Thumb combustor, reflecting its aggressive emissions goals and orientation with respect to the rest of the engine (Fig. 1). Like its predecessor developed to meet 25 ppm NO_x (Razdan et al., 1994; McLeroy et al., 1995), the Green Thumb combustor will be retrofittable on existing Allison 501-K series engines in service. The most significant departure from the earlier low NO_x system is the orientation of the combustor. The integration of an external combustion system has already been successfully demonstrated by Allison for its 501-KB5 engine. As part of Allison's coal-fired gas turbine development work, a production 501-KB5 engine was modified to accept an external combustion system (Wilkes et al., 1989, 1990). The modified engine (now designated as the Allison 501-KM) incor-

Contributed by the International Gas Turbine Institute and presented at the 40th International Gas Turbine and Aeroengine Congress and Exhibition, Houston, Texas, June 5–8, 1995. Manuscript received by the International Gas Turbine Institute March 16, 1995. Paper No. 95-GT-406. Associate Technical Editor: C. J. Russo.

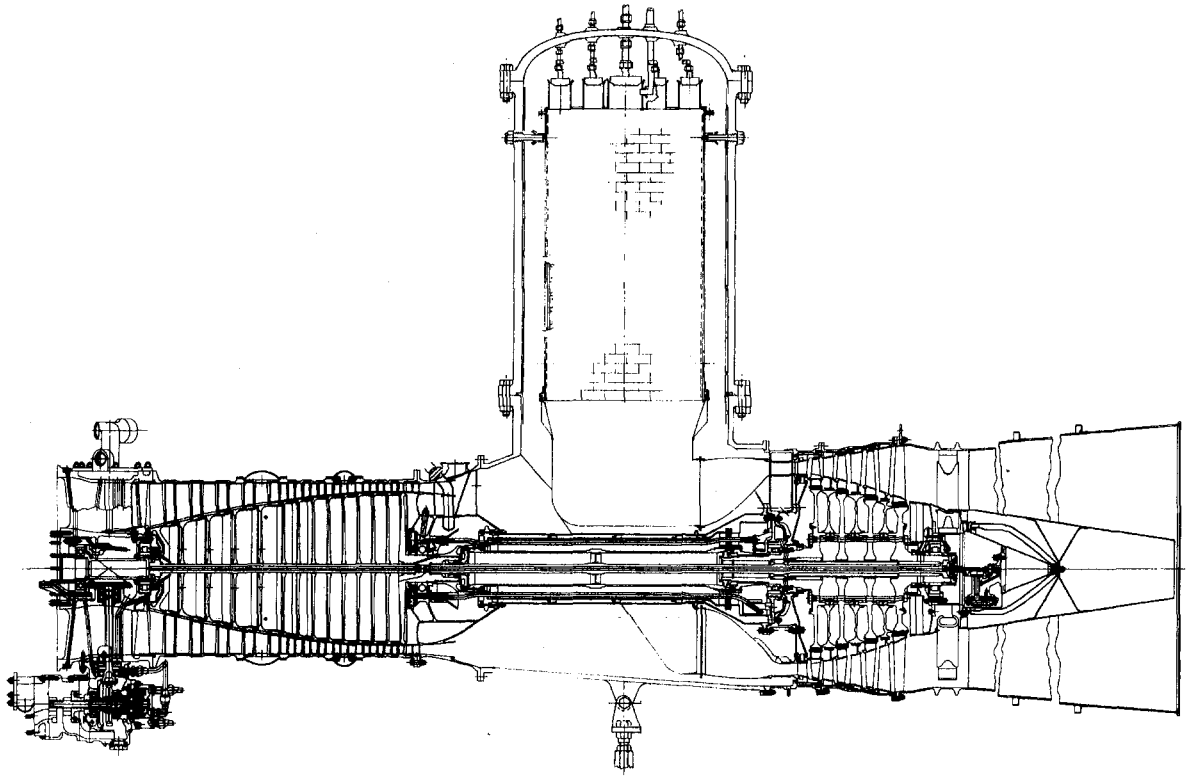

Fig. 1 Schematic of the Green Thumb external combustion system

porates a new engine center case and a transition duct to allow for extraction of compressor discharge air and re-entry of hot combustion products into the turbine.

In the Green Thumb silo combustor, the air from the compressor will be discharged between the combustion liner and the combustor case. The flow will turn up to a maximum of 180 deg before entering the combustor through several LPM modules arranged in either a parallel or series stage. The off-centerline combustion system has several advantages over the current in-line combustion system. The size or volume of the combustor is no longer constrained to be within the space between the compressor and the turbine. Additional combustor volume is essential for reducing CO and UHC emissions in premixed combustor systems operating at lower temperatures. An off-centerline combustor has greater potential for being a universal combustor for use with several engine models (either as is or as a scaled version) and is also easier to access. Various fuel staging concepts can be considered while the residence time and velocity within the combustor can be tailored by changing the combustor's cross-sectional area and length. This flexibility is essential for meeting the extremely stringent NO_x, CO, and UHC emissions goals for the LPM system being considered herein. Finally, an off-centerline combustion system also has the advantage of being able to incorporate a catalytic stage that may be needed to meet the increasingly stringent emissions goals of the future.

Approach

Allison's second generation combustor design codes, including two-dimensional and three-dimensional combustor flow models and one-dimensional and two-dimensional heat transfer models, have been used to design candidate LPM modules and combustion systems. Several LPM configurations were identified computationally by varying the location of fuel injection, swirl angle, and the length of the module. The desirable characteristics being sought are optimal recirculation patterns, residence time in the primary zone, and fuel/air distribution. These characteristics influence stability, efficiency, flashback propensity, and emissions performance.

Various LPM arrangements representing series and parallel staging of modules (to cover the entire engine turndown operation) within the combustor were also evaluated computationally. The arrangement of the modules inside the combustor has a significant impact on emissions as well as liner wall temperatures. In addition, a feasibility study of various other stoichiometry control techniques, including overboard bleed and variable geometry, was carried out.

The promising LPM module configurations obtained from the computational exercise were fabricated and screened under atmospheric conditions. The screening tests included direct visualization through a quartz liner, measurement of the stoichiometry at LBO, measurement of the fuel–air mixing efficiency at the module exit, emissions measurements at the combustor exit, as well as velocity measurements using laser-Doppler velocimetry (LDV). Multiple module tests were also carried out to study the influence of adjacent combusting or cold modules on stability and emissions.

A high-pressure sector rig was designed, fabricated, and assembled for this project with the flexibility to test both single and multiple modules. Single module high-pressure rig tests have been carried out at simulated engine operating conditions. Sector rig tests of the parallel staging scheme with the most promising LPM candidate have been initiated. Following the evaluation of the parallel staging scheme, sector rig tests of the series staging scheme will be carried out.

Lean Premixed Module Design

The most promising candidate for the off-centerline silo combustor incorporates a radial swirler and is designated the Radial Swirler Plus Nozzle (RSPN). The nozzle refers to the converging–diverging section of the module shown schematically in Fig. 2. The throat of the nozzle separates the premixing section

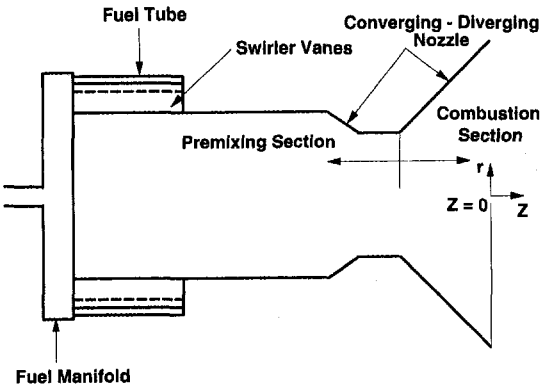

Fig. 2 Schematic of the lean premixed module RSPN

from the combustion section. In this module, the fuel is introduced through fuel tubes located between the vanes of the swirler. The flow is stabilized at the exit of the module by expanding the flow and inducing a recirculation zone.

Flame Stability. One of the primary design criteria for an LPM module is an optimal recirculation zone size. The recirculation zone stabilizes the LPM flame by mixing the fresh combustible mixture with hot combustion products. In this region of the combustor, the flow velocities are lower and can be matched with the flame speed (Gupta et al., 1984). Thus, the size and shape of the recirculation zone are critical to flame stability, combustion intensity, and performance. While a large recirculation zone may be desirable to enhance combustor stability, the increased residence time promotes the production of NO_x and is therefore detrimental (Micklow and Shivaraman, 1994). Consequently, the size of the recirculation zone has to be optimized.

Figure 3 illustrates a single central recirculation zone established at the exit of the RSPN module as predicted by Allison's two-dimensional computational model. The bottom of the figure corresponds to the centerline of the module. The recirculation zone shape and size of RSPN is sensitive to the swirler vane angle, the swirler length, the entry to the swirler, as well as the rate and degree of expansion at the exit of the module. These attributes have been varied both computationally and experimentally in achieving the current design. It should also be noted that the location of the recirculation zone away from the combustor walls is desirable to minimize the quenching of CO and UHC burnout that will occur with any combustor wall cooling scheme.

Mixing Performance. Perhaps the most important criterion for the design of low-NO_x LPM modules is the efficiency with which the fuel and air are mixed prior to combustion. Due to its exponential dependence on temperature, the NO_x production rate is enhanced more in relatively fuel-rich pockets than it is retarded in fuel-lean pockets. Thus, for a given aerodynamic design, a perfect mixture of fuel and air will yield the lowest NO_x.

Since the fuel is introduced between the vanes of the RSPN module and the flow through it is highly three dimensional, a three-dimensional computational model is appropriate for mixing predictions. A detailed model was set up to study the mixing processes within the swirler. Figure 4 presents part of a plane (perpendicular to the axis of the swirler) illustrating the fuel–air (F/A) ratio contours for an overall F/A ratio of 0.03. The location of the vanes and fuel tubes is apparent from the silhouette created by the flow vectors. With the fuel tubes placed between the vanes, a wake is created downstream of the tubes. The fuel jets lack sufficient momentum to penetrate the cross-flow of air and are entrained into the wake of the fuel tubes where rapid mixing with air occurs. The efficient mixing performance of this design becomes apparent when the F/A ratio at the exit of the swirler vanes is examined. The F/A ratio here is close to the overall F/A ratio of 0.03 used in this calculation; thus, most of the fuel/air mixing occurs before the mixture leaves the swirler vanes.

The location of fuel holes along the length of the tubes is chosen to yield the desired F/A ratio profile at the exit of the premixing section. While a uniform F/A ratio profile will give the lowest NO_x emissions, flashback considerations dictate the practically usable mixing profile as will be discussed later.

Module Test Results

Various RSPN modules were tested extensively under atmospheric conditions. The current RSPN design was also tested in a parallel stage consisting of three RSPN modules under atmospheric conditions. The current RSPN design has been tested as a single module and in a parallel stage under simulated engine conditions. Additional parallel as well as series staging tests of the same are planned for the near future. The results of the tests completed to date are presented in this section. All testing was conducted using natural gas as fuel. In the following sections, the single/multiple module atmospheric test results and the single/multiple module high-pressure/temperature test results are described.

Single Module Atmospheric Bench Tests. The RSPN modules were tested at atmospheric conditions (T_{in} = 308–373 K, P = 0.1 MPa) to determine flow areas, flashback propensity, F/A ratios at LBO, fuel concentration profiles at the exit of the premixing section, emissions at the exit of a quartz liner, and velocity measurements at a few planes inside the quartz liner. A three-axis traverse made it possible to make detailed measurements when warranted. Details of the bench test setup have been published earlier (Razdan et al., 1994). In these tests, the flow factor was identical to that in the engine at 100 percent power. The natural gas used for these tests was analyzed as having the following composition by volume: CH_4—95.3 percent; C_2H_6—1.8 percent; C_3H_8—0.4 percent; CO_2—1.9 percent; and N_2—0.6 percent.

Stability. The lean stability limit of the modules was determined by continuously reducing fuel flow to the module and noting the fuel flow at which the flame blew out. The air flow was maintained fixed at the desired rate and sufficient warm-up time was allowed to ensure steady-state operation of the combustor. The F/A ratios reported here for LBO correspond to complete extinguishment of the flame.

The RSPN modules have remarkable stability as indicated by their low F/A ratios at LBO. Under atmospheric conditions, these modules typically experienced lean extinction at F/A ratios between 0.033 and 0.035. These values of LBO translate to equivalence ratios (ϕ) of 0.534 to 0.567 for the fuel used. No definite trends were observed with the variation of the mix-

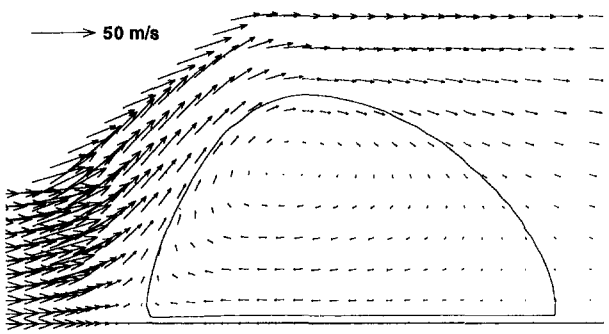

Fig. 3 Modeling results showing a single central recirculation zone created by expanding the flow

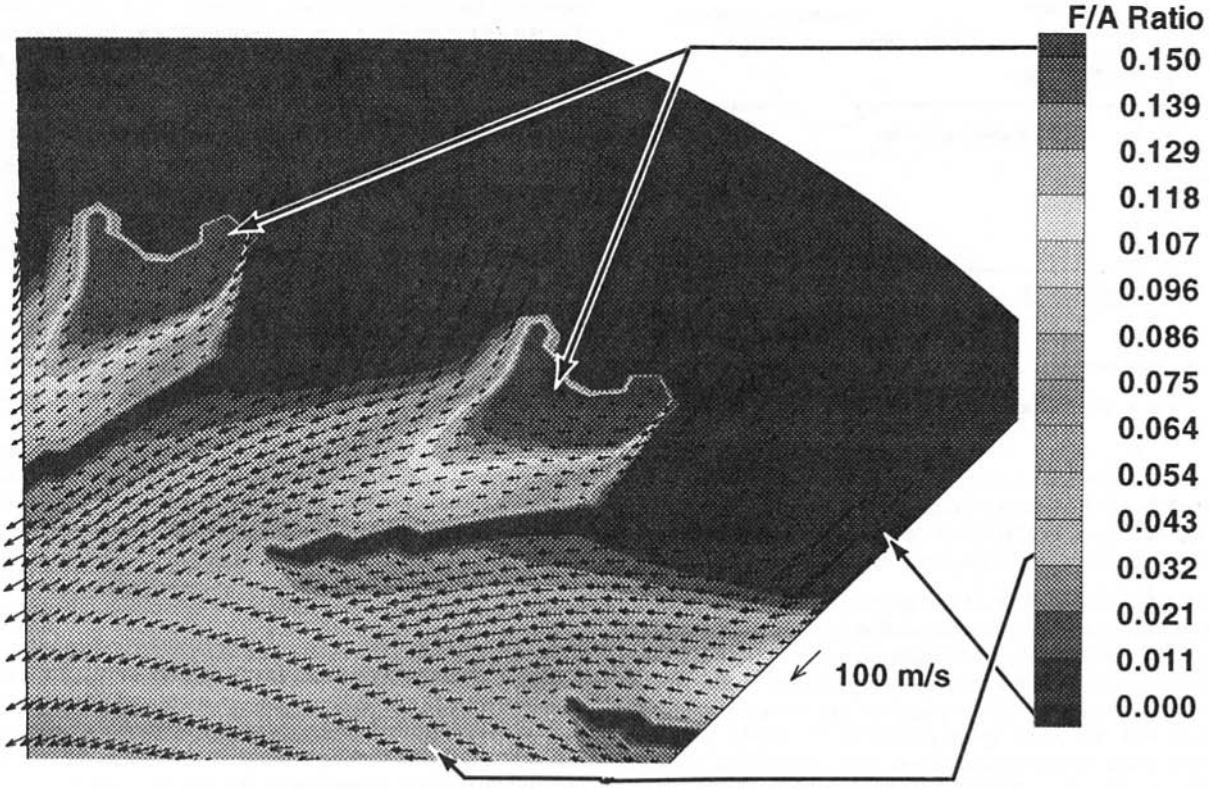

Fig. 4 Modeling results illustrating the rapid mixing that occurs in the wake of the fuel tubes of RSPN

ing profile at the module exit, the variation of the swirler flow angle, or the divergence angle of the nozzle. At atmospheric conditions, the lean flammability limit of the three hydrocarbons in the natural gas used is $\phi = 0.53$ (Glassman, 1987). These results suggest lean extinction or LBO with the RSPN design is not hardware limited and is limited only by the lean flammability of the fuel. These results also reconfirm the excellent mixing performance of this design, since fuel-rich pockets can result in flame stability at overall F/A ratios lower than the lean flammability limit.

Mixing and Flashback Propensity. The fuel concentration profiles at the mixing cup exit were obtained under cold conditions by sampling through a ~3 mm (0.125 in.) diameter uncooled probe. The modules were tested for flashback propensity by inserting a hydrogen torch into the mixing cup to see if a flame is sustained after the torch is removed. The module was considered prone to flashback if the flow could not purge the flame out of the mixing cup. These tests were carried out at several pressure drops through the module and at a few different F/A ratios.

As indicated earlier, the fuel concentration profile at the exit of the mixing cup is easily changed by relocating the fuel holes on the fuel tubes. The fuel concentration profile at the mixing cup exit is also affected by the swirler vane angle and the entry to the swirler. Figure 5(*a–c*) illustrates three profiles obtained with the RSPN modules. Figure 5(*a*, *b*) presents profiles obtained with the same swirler but with different fuel hole patterns, while Fig. 5(*b*, *c*) shows mixing profiles with the same fuel hole pattern but different swirlers. The module with the profile shown in Fig. 5(*c*) had the most resistance to flashback. A flame was sustained in the mixing cup only when the F/A ratio was raised above stoichiometric ($\phi > 1$) and the pressure drop through the module was lowered below 0.25 percent of the inlet pressure. These conditions are obviously far from the steady operating conditions that will be seen in the engine. The module with the profile shown in Fig. 5(*a*) is somewhat more prone to flashback but offers the best NO_x performance, as will be discussed later. In the current design, a middle ground has been sought with the mixing profile shown in Fig. 5(*b*), where mixing processes continue beyond the exit of the mixing cup and yield a uniform profile at the end of the diverging section. Note the rig data reported later are with the mixing profile shown in Fig. 5(*b*) and the tangential variation in the mixing is small (±2.5 percent). Some of this variation (±0.7 percent) is due to measurement uncertainty as determined from consecutive repeat measurements. Most of this uncertainty is related to positioning the sampling probe in a swirling flow with a concentration gradient.

The mixing profile at the exit of the premixing section, and hence flashback propensity, is also affected by the direction of flow prior to its entry into the swirler. With a silo combustor as shown in Fig. 1, the modules located close to the combustor casing will see the flow turn 180 deg through the swirler. For modules away from the combustor casing, the flow will have already turned 180 deg before entry into the swirler. The effect of flow direction on the mixing profile at the mixing cup exit was studied, and Fig. 6 presents the fractional change in the fuel concentration, as a function of radius at the mixing cup exit, when the flow reverses direction through the swirler. Based on these results, modules close to the combustor case can see 8–9 percent higher fuel concentrations at their centerlines. With the safety margin incorporated into the current design's mixing profile (Fig. 5(*b*)), modules close to the combustor case will have a flat mixing profile similar to that shown in Fig. 5(*a*). From flashback considerations, it is important not to have a richer than average module centerline since this region has the lowest velocities due to a centrally located recirculation zone.

Emissions. The concentrations of CO, UHC, NO_x, CO_2, and O_2 were measured at the exit of a quartz liner only slightly larger in diameter than the module and approximately 300 mm long. A traversable water-cooled probe was used to quench the reactions and heated sample lines prevented moisture condensation prior to the moisture trap. The combustion products were

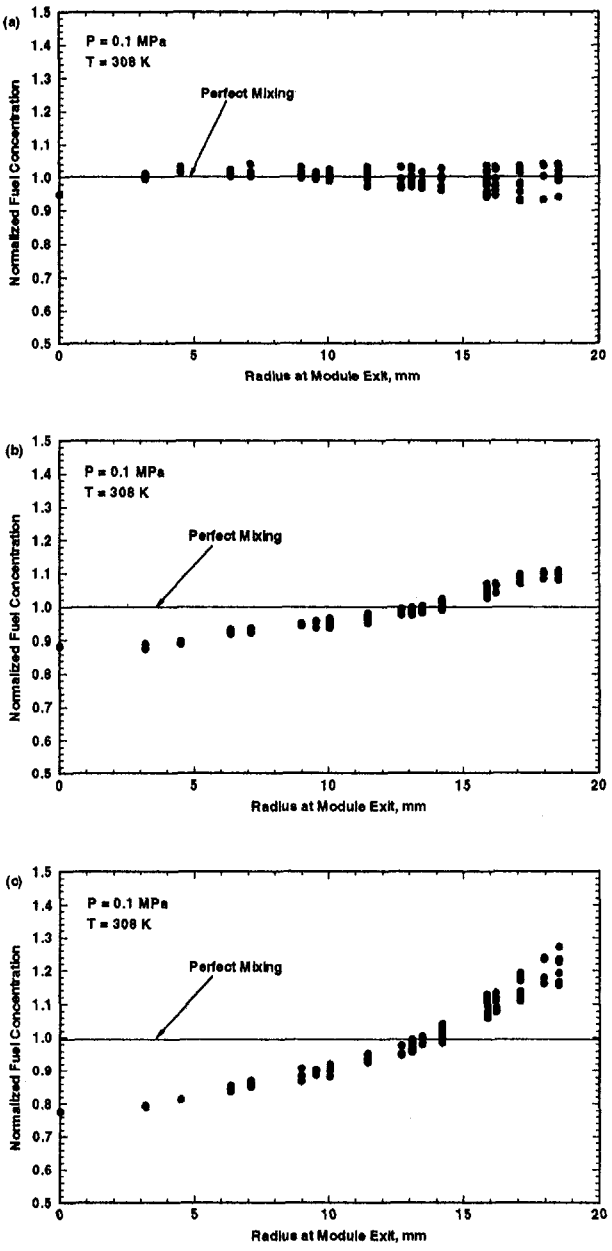

Fig. 5 Effect of fuel hole pattern and swirler cup on fuel–air mixing

sampled at radial locations representing equal annular areas, so area-averaged emissions could be obtained. The emissions measurements were made with conventional on-line gas analyzers: NDIR analyzers for CO and CO_2, a flame ionization detector for UHC, a chemiluminescent detector for NO_x, and a paramagnetic analyzer for O_2. The analyzers were calibrated with span gases that typically corresponded to 80 percent of the range used for the measurements. For the measurement of NO_x, loss of NO_2 in the condensate was minimized by using an additional converter upstream of the moisture trap. Repeatability tests were carried out in which the humidity of the combustion air was controlled. The averaged emissions measurements were repeatable to within 2 percent of the measured values for the various species.

Figure 7 presents the averaged dry uncorrected NO_x and CO emissions for several RSPN modules in which the stoichiometry and the fuel concentration profile at the module exit was varied. During these tests, air preheated to 373 K was used, and fuel concentration modifications impacted the trade-off between the averaged NO_x and CO emissions. With a uniform fuel concentration profile at the mixing cup exit, the lowest NO_x emissions were obtained. However, improvements in the NO_x emissions were offset by deterioration in the rate at which CO was oxidized. Also presented in the figure are emissions results utilizing a parallel stage, which will be discussed later.

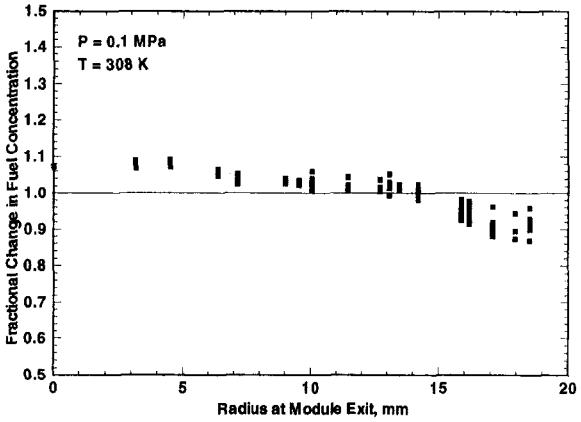

Fig. 6 The flow direction prior to entry into the swirler influences the fuel concentration profile at the module exit

A study to determine the optimum swirl angle for the RSPN module was also carried out. Since the fuel concentration profile at the mixing cup exit impacted the NO_x and CO emissions, the fuel and air were premixed in this study to isolate the effect of the modified swirl. The air was not preheated because the fuel was introduced upstream of the heaters to give close to a perfect mixture of fuel and air at the exit of the premixing section. Figure 8 presents the averaged dry uncorrected NO_x and CO emissions results obtained from the tests. Emissions measurements were made at F/A ratios of 0.04 and 0.042 for all the configurations investigated. Again it is quite obvious that the degree of swirl impacts the NO_x–CO tradeoff. The current RSPN design (solid circles) has the most superior NO_x–CO tradeoff curve of the designs tested. For comparison, the fit to the data presented in Fig. 7 is also presented in Fig. 8 and shows that preheat improves combustion efficiency, yielding lower CO emissions. Also presented in Fig. 8 are data (solid squares) obtained with a longer (~450 mm) quartz liner. Note that an increase in the liner length greatly enhances CO burnout with only a small NO_x penalty. This is consistent with our understanding that NO_x formation takes place primarily in the recirculation zone, while CO burnout continues throughout the combustor and is only impeded by liner length and cooler wall temperatures.

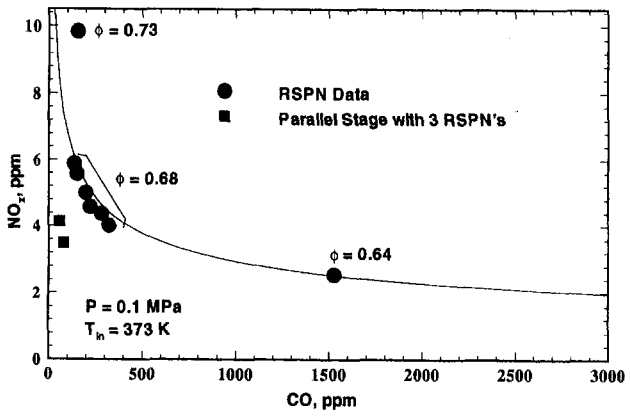

Fig. 7 Bench test data showing the NO_x–CO tradeoff for RSPN modules

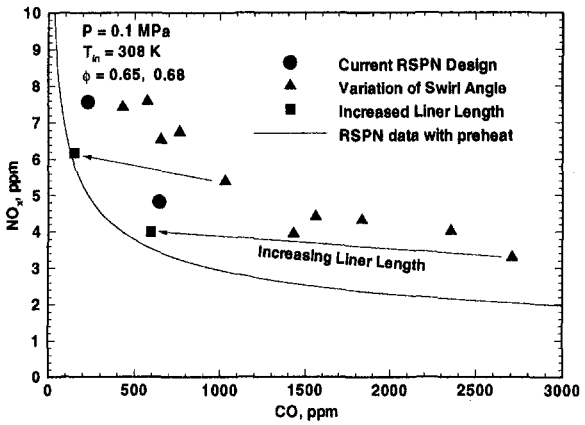

Fig. 8 Data showing the current swirler design as having the best NO_x–CO tradeoff

Velocity. The axial and tangential components of velocity were measured inside the quartz combustor using a two-component LDV system. Data were obtained for both cold and combusting flows. Figure 9 presents plots of the axial component of velocity at four planes in the combustor. The farthest downstream plane shown corresponds to a location 118 mm from the nozzle exit and is the approximate axial location where the recirculation zone ends. The results confirm our modeling predictions of a single central recirculation zone without any flow separation at the diverging exit of the module. This large recirculation zone is responsible for the excellent stability of the RSPN design.

Multiple Module Atmospheric Bench Tests. A parallel stage, consisting of three current RSPN design modules (with their centers forming an equilateral triangle), was also tested at atmospheric conditions (T_{in} = 308–373 K; P = 0.1 MPa). A quartz liner was used for these tests as well. The composition of the natural gas used for these tests was the same as that used for the single module atmospheric tests described earlier.

Stability. The stability tests on the parallel stage were performed at various values of F/A by first lighting all three modules, and then the fuel flow to a single module was lowered continuously and the stability of the stage was observed. After the fuel to this module was completely cut off, fuel supply to the second module was lowered in a similar fashion.

The LBO performance of each module in this parallel stage was strongly affected by the amount of fuel supplied to the adjacent modules. LBO of a given module also depended on whether one or both of the adjacent modules was lighted.

With two hot modules operating at $\phi \geq 0.7$, the third module experienced blow out around $\phi = 0.41$. Thus the hot adjacent modules served as a continuous source of ignition and maintained a flame on the third module even below its flammability limit. With one hot module ($\phi \geq 0.7$) and one cold adjacent module, the LBO of the third module was around $\phi = 0.56$. This value of LBO is similar to that observed in the single module tests. With two adjacent cold modules, however, the flame blew out at a much higher ϕ of 0.79. This value was lower if a small amount of fuel was supplied to one of the adjacent modules. For example, with one of the cold modules delivering a mixture at a ϕ of 0.20, the flame blew out at a ϕ of 0.73. These stability studies have helped define the fuel staging strategies discussed later in this paper.

Mixing. The fuel concentration profiles at the exit of the three modules in the parallel stage were similar to what is shown in Fig. 5(*b*). The distribution of fuel to the various modules was equitable with a common fuel manifold with no significant impact on the fuel concentration profiles.

Emissions. The strong interaction between the modules is also apparent in the emissions results presented in Fig. 7. The multiple RSPN module operation with all modules lighted and operating at a similar stoichiometry had both lower CO and NO_x than the single RSPN. The lower NO_x numbers suggest the central recirculation zones on the individual RSPNs in the parallel stage were smaller. Gupta et al. (1984) present evidence supporting this interpretation. These workers reviewed the effect of confinement, which increases the size of the central recirculation zone. Since the quartz liner diameter for the multiple module tests is larger than that used in the single module tests, the individual RSPNs in the parallel stage are less confined, and hence, have smaller central recirculation zones. It is also likely that the strong swirling flows from the adjacent modules affects the size of the central recirculation zone. The lower CO emissions can be attributed to reduced liner surface area per unit volume as well as increased residence time due to the bigger volume per unit length of the parallel stage liner.

Emissions measurements were also made to investigate the impact of adjacent cold fueled/unfueled modules such as may be seen at different power points of the engine cycle. As one may expect, for the same overall stoichiometry, operating two modules at a higher ϕ adjacent to either a cold or combusting module resulted in much higher NO_x emissions. If the adjacent module was cold, then even the CO and UHC emissions were higher. By staging some fuel to the cold module and simultaneously reducing the operating ϕ of the hot modules, the NO_x emissions were significantly reduced, although CO and UHC emissions were higher. Some heat release was obtained from the cold fueled module since the fuel is easily entrained into the hot swirling flow of the combustor.

Single Module High-Pressure Rig Tests. The RSPN module has been tested in the Green Thumb sector rig under simulated engine conditions for the 501-KB5 and 501-KB7 cycles. The latter cycle has higher combustor inlet temperature, pressure, and engine air flow rates than the 501-KB5 cycle (Table 1).

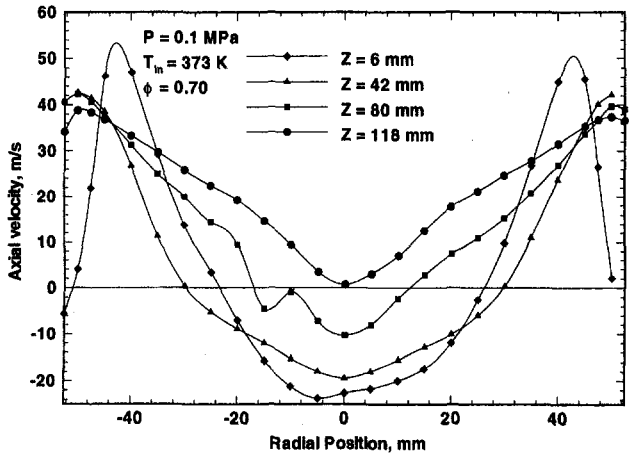

Fig. 9 Plots of the axial component of velocity at several liner locations *Z* (see Fig. 2), showing the extent of the recirculation zone

Table 1 Nominal—100 percent power specifications for the 501-KB5 and 501-KB7 industrial engines

	KB5	KB7
Airflow, kg/s	15	20
Overall fuel/air ratio	0.020	0.019
Pressure ratio	10	13.4
Burner inlet temperature, K	615	665
Burner outlet temperature, K	1380	1380

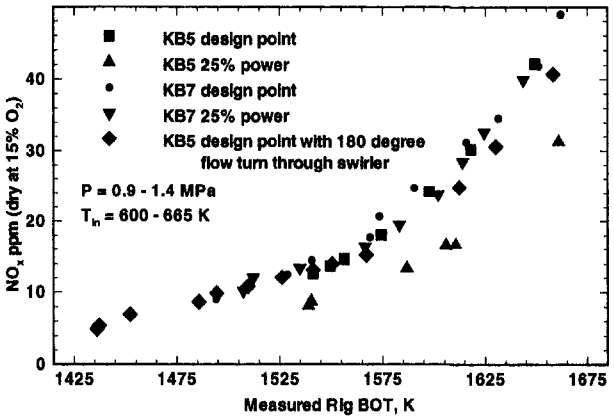

Fig. 10 Rig test data showing NO_x (dry 15 percent O_2 corrected) as a function of measured rig BOT

The module has been tested to determine flow areas, flashback propensity, F/A ratios at LBO, and emissions. Tests were run at conditions corresponding to several power levels of the 501-KB5 and 501-KB7 cycles. The natural gas composition by volume for these tests was: CH_4—93.6 percent; C_2H_6—3.0 percent; C_3H_8—0.4 percent; CO_2—0.6 percent; and N_2—2.4 percent.

Stability. The RSPN module showed higher stability at the simulated engine conditions of the 501-KB5 and 501-KB7 cycles. LBO was observed below a primary zone ϕ of 0.50 for these cycle conditions. The higher stability (than observed under atmospheric conditions) is expected since the higher inlet temperatures enhance the lean flammability limit (Glassman, 1987).

Flashback Propensity. In the Green Thumb rig, flashback propensity was studied by varying combustor pressure while maintaining the mass flow through the combustor. This essentially changed the pressure drop through the module, affecting flashback performance. Thermocouples were mounted on the walls of the module to detect propagation of the flame upstream of the module exit. With the current RSPN design operating at ϕ of 0.65, no flashbacks were observed over the typical gas turbine combustor operating pressure drops of 1–4 percent of the inlet pressure. The targeted operating conditions for the maximum power point are a pressure drop of 3–4 percent and a ϕ close to 0.50. Therefore, the RSPN design gives a good safety margin for operation of the engine at full load. Flashback propensity at partial loads will depend on the stoichiometric control strategy adopted and will be discussed later.

Emissions. Emissions measurements were made per SAE Aerospace Recommended Practices (ARP) called out in ARP 1256A. The gas sampling probe was located approximately 250 mm downstream of the module exit and was equipped with several sampling orifices so area-averaged emissions could be obtained efficiently. To verify the integrity of the average obtained with this probe, area-averaged emissions were also obtained with a traversable single orifice probe. Since the agreement in the emissions obtained with these probes was good, only the multiple orifice probe was used for most of the data acquired and reported here.

Figure 10 presents the dry corrected NO_x rig data as a function of the measured burner outlet temperature (BOT). The data correlate well with temperature for all the cycle conditions investigated. The lower numbers for the 501-KB5 25 percent power point are perhaps due to increased liner cooling which may have lowered the primary zone temperatures. Also presented in Fig. 10 are the emissions results obtained by turning the flow 180 deg through the swirler of the current RSPN module design. Based on the mixing results presented in Figs. 5(*b*) and 6, the fuel concentration profile for this test should have been like the one presented in Fig. 5(*a*). With all the NO_x data collapsing onto a single curve as a function of measured BOT, it seems that changing the fuel concentration profile at the mixing cup exit does not impact the NO_x emissions. In the atmospheric tests we did see an impact on the NO_x–CO tradeoff, which may be due to the reduced combustion efficiencies with a flatter profile.

For the rig test data reported here, the combustion efficiencies were always greater than 99.9 percent. The CO and UHC emissions were very low even with operation close to LBO. The highest measured CO and UHC emissions with the current design were 35 ppm and 3 ppm, respectively. With the flatter fuel concentration profile these emissions increased slightly. The maximum values measured were still fairly low: 76 ppm CO and 39 ppm UHC. Figure 11 presents some of the NO_x, CO, and UHC data as a function of the measured rig BOT for 501-KB5 operating conditions. Also presented on this figure are equilibrium concentrations of CO. The lowest CO emissions were obtained at temperatures around 1530 K (~2300°F). Above this temperature, the CO emissions increase and essentially follow the shape of the equilibrium curve. The CO emissions are very close to being equilibrated in this temperature regime. At temperatures lower than 1530 K, the measurements rapidly increase and depart from equilibrium predictions, suggesting CO burnout is kinetically controlled in this region. Figure 11 also shows that the emissions goals of 9 ppm NO_x, 50 ppm CO, and 10 ppm UHC have been simultaneously met by the current RSPN design. With the ultralean operation possible from the highly stable RSPN design, NO_x emissions as low as 5 ppm were measured on the rig.

Multiple Module High-Pressure Rig Tests. Testing of a parallel stage consisting of seven current RSPN design modules has been initiated. These modules are arranged with the centers of six modules forming a hexagon and the seventh module in the center of the stage. Due to current rig limitations and higher flow requirements with seven modules, the stage was only operated up to a pressure of 0.6 MPa. The natural gas composition for these tests was the same as that used for the single module high pressure rig tests.

Figure 12 presents the preliminary results obtained from the tests done so far. All modules were connected to a common fuel manifold so that the combustion stage was operated with all modules having similar stoichiometries. Single module rig data obtained at 0.6 MPa and 1 MPa are also presented in this figure for comparison and show that NO_x formation is independent of pressure between 0.6 and 1 MPa. As expected from the bench testing experience, staging of multiple modules yields lower NO_x emissions for similar burner outlet temperatures. For

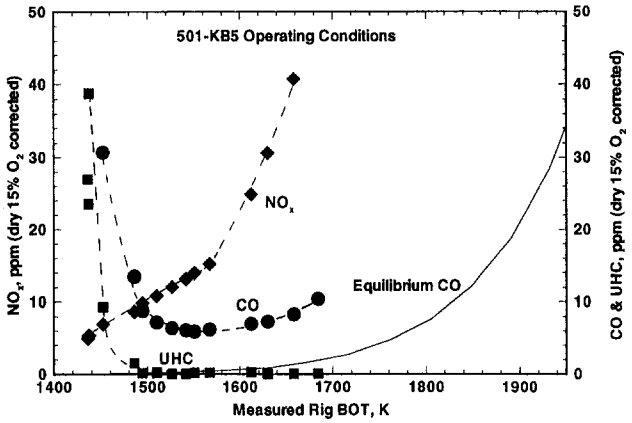

Fig. 11 The CO emissions approach equilibrium values, except in the neighborhood of LBO

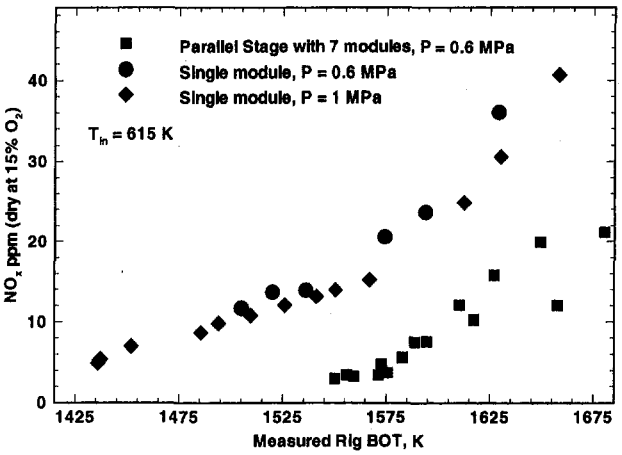

Fig. 12 Rig test data showing improvements in NO_x (dry 15 percent O_2 corrected) emissions with staging of multiple modules

the parallel stage NO_x data shown, the corrected CO and UHC emissions were less than 25 ppm and 3 ppm, respectively. This should give sufficient operation margin away from LBO to meet the maximum power emissions goals of this program.

Combustor Arrangement

Although the schematic in Fig. 1 shows a parallel fuel staging approach, a series staging option is also being evaluated. The best staging approach will be selected only after rig tests with parallel and series staging of the RSPN modules are completed. In addition to fuel staging, modulation of the air to the modules is also being evaluated.

Parallel and Series Fuel Staging. Parallel staging of several LPM modules represents the simplest combustor arrangement. In this design, the modules are closely packed in the dome of the combustor. All modules receive similar amounts of air, while the number of modules supplied with fuel will be governed by the power requirements. To maintain manifolding and valving costs within reasonable limits, the modules are supplied with fuel in stages comprising several modules each. Figure 13 presents an example of the combustor equivalence ratio along with variations in the primary zone equivalence ratio as a function of power with a 19-module combustor for the 501-KB5 cycle. The modules are arranged in six stages with four modules in the first stage and three modules in the subsequent stages. The numbers labeled on the primary zone equivalence ratio graph represent the total number of operational modules. The variations in the primary zone ϕ are significant and will negatively impact emissions at partial loads.

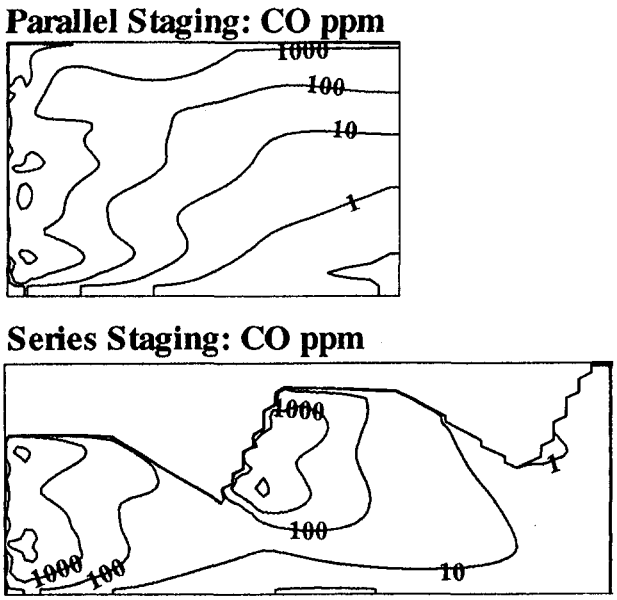

Fig. 14 Modeling results comparing CO emissions between parallel and series staging of modules

Series staging has some advantages over parallel staging, at the expense of increased complexity. Rather than having all the stages in the dome of the combustor, the stages could be spread out axially along the length of the combustor. Obviously, the number of stages would have to be reduced to constrain the length of the combustor. A series staged system offers reduced CO emissions when compared to a parallel staged system at partial loads (Willis et al., 1993). Parallel and series staging at 60 percent load were compared computationally using a three-dimensional model. Figure 14 presents predicted CO contour plots obtained from this exercise. Note the series staged combustor is longer than the parallel staged combustor. Since several complexities are involved in setting up and modeling the flow through the liner, the presented predictions are only indicative of trends that can be expected and should not be interpreted in terms of absolute numbers. With parallel staging, the cold air from adjacent modules partially quenches the reacting flow of the adjacent module, resulting in enhanced CO emissions.

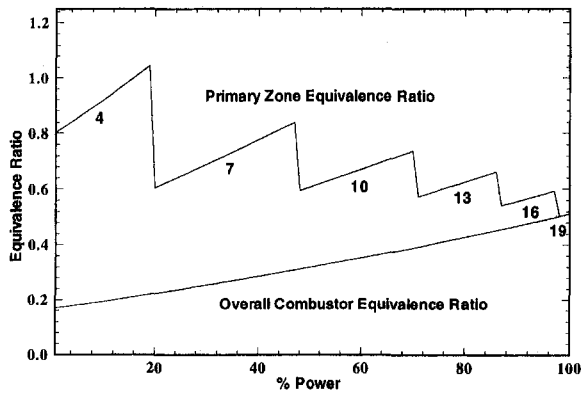

Fig. 13 Variations in the primary zone and overall combustor equivalence ratio as a function of power with a six-stage stoichiometric control strategy

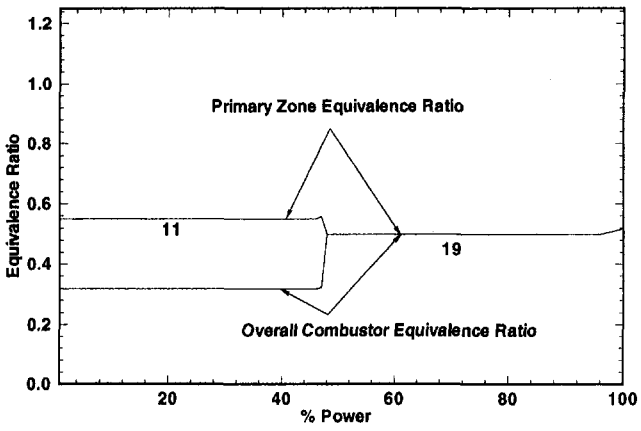

Fig. 15 Minimal variations in the primary zone and overall combustor equivalence ratio with power using a combination of series staging and variable geometry

Modulation of Air. Although series staging alleviates the CO burnout problem seen with parallel staging, modulation of the air can provide additional stoichiometric control to minimize CO emissions further.

The air supplied to some or all of the modules can be modulated by either dumping air overboard or through variable geometry. All the variable geometry options being considered vary the split of air supplied to the primary zone and the dilution zone of the combustor. Thus modulation of the air permits operation of all modules throughout the power range. By maintaining all the modules at the stoichiometry where best results are obtained, low NO_x and CO emissions become possible regardless of the power point. As an example, Fig. 15 presents the minimal variations in the equivalence ratio that will be observed with the use of two series stages with 11 and 8 modules each in conjunction with variable geometry.

By diverting the air away from the primary zone of the combustor, the velocities of the flow through the modules are lowered, hence, the pressure drop across the modules is lower and the safety margin for flashback is lowered. Since this approach minimizes stoichiometry variations, however, operation at lean conditions should be safe with the RSPN design for which the fuel concentration profile is easily controlled.

Summary and Future Work

The RSPN module design is the primary candidate for the Green Thumb 9 ppm NO_x combustor. It has excellent stability, is resistant to flashback, and has yielded lower than 5 ppm NO_x in simulated engine tests. The combustion efficiencies are very high even while operating close to the lean extinction limit. Stoichiometric control strategies including axial staging with possibly variable geometry are being considered to improve combustion efficiencies.

Sector rig testing will continue to evaluate the best configurations for the combustion liner. Further refinements to the RSPN module may be carried out as warranted. The overall engine system design will proceed concurrently, adapting to the evolving combustor design. The overall engine design includes the design of the turbine transition passage; the engine support; the outer combustion case, combustion liner, and dome; and the fuel manifolds. The engine control design will also be adapted to the needs of the combustor to maintain stoichiometric control allowing the emissions goals to be realized.

Acknowledgments

Allison would like to thank the Department of Energy (DoE), Southern California Gas (SoCal Gas), and the Santa Barbara Air Pollution Control District (SBAPCD) for their support of this development effort. Discussions with Mr. Stephen Waslo (DoE, Program Manager), Mr. Cherif Youssef (SoCal Gas), and Mr. Mahesh Talwar (SBAPCD) on various aspects of this program have been very useful and are appreciated. The authors would also like to acknowledge Mr. Christopher Brown at the Energy Research Consultants (ERC) for conducting the bench tests for this program.

References

Bauermeister, K. J., Schetter, B., and Mohr, K. D., 1993, "A 9.25 MW Industrial Gas Turbine With Extreme Low Dry NO_x and CO Emissions," ASME Paper No. 93-GT-307.

Correa, S. M., 1992, "A Review of NO_x Formation Under Gas-Turbine Combustion Conditions," *Combustion Science and Technology*, Vol. 87, pp. 329–362.

Döbbeling, K., Knöpfel, H. P., Polifke, W., Winkler, D., Steinbach, C., and Sattelmayer, T., 1996, "Low NO_x Premixed Combustion of MBtu Fuels Using the ABB Double Cone Burner (EV Burner)," ASME JOURNAL OF ENGINEERING FOR GAS TURBINES AND POWER, Vol. 118, pp. 46–53.

Etheridge, C. J., 1994, "MARS SoLoNO$_x$—Lean Premix Combustion Technology in Production," ASME Paper No. 94-GT-255.

Glassman, I., 1987, *Combustion*, Academic Press, Orlando.

Gupta, A. K., Lilley, D. G., and Syred, N., 1984, *Swirl Flows*, Abacus Press, Kent.

Kajita, S., Ohga, S., Kitajima, J., Kimura, T., and Sasaki, T., 1993, "Development of a Dry Low NO_x Combustor for 1.5 MW Gas Turbines," ASME Paper No. 93-GT-393.

Leonard, G., and Stegmaier, J., 1994, "Development of an Aeroderivative Gas Turbine Dry Low Emissions Combustion System," ASME JOURNAL OF ENGINEERING FOR GAS TURBINES AND POWER, Vol. 116, pp. 542–546.

McLeroy, J. T., Smith, D. A., and Razdan, M. K., 1995, "Development and Engine Testing of a Dry Low Emissions Combustor for Allison 501-K Industrial Gas Turbine Engines," ASME Paper No. 95-GT-335.

Micklow, G. J., and Shivaraman, K., 1994, "Effect of Swirl and Wall Geometry on the Emissions of Advanced Gas Turbine Combustors," ASME Paper No. 94-GT-259.

Razdan, M. K., McLeroy, J. T., and Weaver, W. E., 1994, "Retrofittable Dry Low Emissions Combustor for 501-K Industrial Gas Turbine Engines," ASME Paper No. 94-GT-439.

Snyder, T. S., Rosfjord, T. J., McVey, J. B., Hu, A. S., and Schlein, B. C., 1996, "Emission and Performance of a Lean-Premixed Gas Fuel Injection System for Aeroderivative Gas Turbine Engines," ASME JOURNAL OF ENGINEERING FOR GAS TURBINES AND POWER, Vol. 118, pp. 38–45.

Wilkes, C., Razdan, M. K., and Santanam, C. B., 1989, "A Water Quenched Low NO_x Coal Slurry Combustor for Industrial Gas Turbines," ASME Paper No. 89-GT-106.

Wilkes, C., Mongia, H. C., and Santanam, C. B., 1990, "An Ultra-Low NO_x Combustion System for a 3.5 MW Industrial Gas Turbine," ASME Paper No. 90-GT-83.

Willis, J. D., Toon, I. J., Schweiger, T., and Owen, D. A., 1993, "Industrial RB211 Dry Low Emission Combustion," ASME Paper No. 93-GT-391.

Variables Affecting NO_x Formation in Lean-Premixed Combustion

R. C. Steele

A. C. Jarrett

P. C. Malte

J. H. Tonouchi

D. G. Nicol

University of Washington,
Dept. of Mechanical Engineering,
Seattle, WA 98195

The formation of NO_x in lean-premixed, high-intensity combustion is examined as a function of several of the relevant variables. The variables are the combustion temperature and pressure, fuel type, combustion zone residence time, mixture inlet temperature, reactor surface-to-volume ratio, and inlet jet size. The effects of these variables are examined by using jet-stirred reactors and chemical reactor modeling. The atmospheric pressure experiments have been completed and are fully reported. The results cover the combustion temperature range (measured) of 1500 to 1850 K, and include the following four fuels: methane, ethylene, propane, and carbon monoxide/hydrogen mixtures. The reactor residence time is varied from 1.7 to 7.4 ms, with most of the work done at 3.5 ms. The mixture inlet temperature is taken as 300 and 600 K, and two inlet jet sizes are used. Elevated pressure experiments are reported for pressures up to 7.1 atm for methane combustion at 4.0 ms with a mixture inlet temperature of 300 K. Experimental results are compared to chemical reactor modeling. This is accomplished by using a detailed chemical kinetic mechanism in a chemical reactor model, consisting of a perfectly stirred reactor (PSR) followed by a plug flow reactor (PFR). The methane results are also compared to several laboratory-scale and industrial-scale burners operated at simulated gas turbine engine conditions.

Introduction

Recently, experimental studies of NO_x formation in lean-premixed combustion have appeared in the literature for a range of natural gas-fired laboratory and developmental gas turbine combustors. The combustion temperature range covered is 1600 to 2000 K and the pressure range is 1 to 30 atm. These studies are in agreement on one essential point: The overall activation energy of the NO_x formation is low (40 to 70 kcal/gmol) compared to that for thermal NO_x formation (134 kcal/gmol). All of these values include the energy required to form the O atom. Throughout this paper, unless stated otherwise, the NO_x emission is expressed in terms of ppmvd (15 percent O_2), that is, as parts per million by volume, adjusted to a 15 percent O_2, dry basis.

In some cases it is possible to present the NO_x data solely in terms of a single variable: the adiabatic equilibrium flame temperature. Leonard and Stegmaier (1994) were able to accomplish this for laboratory burner data, for which the NO_x concentration was less than 10 ppmvd (15 percent O_2). There was little dependency of the NO_x on the other variables they examined: pressure, 1 to 30 atm; air inlet temperature, 300 to 800 K; and overall burner residence time, 2 to 100 ms. However, the lack of dependency on inlet temperature is not observed in the data of Maughan et al. (1994), for a developmental gas turbine combustor. These investigators observed that the NO_x decreased as the inlet temperature increased relative to a fixed combustor exit temperature. Also, the lack of significant dependency of the NO_x on pressure is not observed for some of the developmental combustors. Positive pressure dependency is seen in the results of Snyder et al. (1996), and in the combined results of Aigner et al. (1990) and Sattelmayer et al. (1992). With respect to the dependency of NO_x on the residence time, one has to be careful in the interpretation of results. Whereas the NO_x may not vary significantly with overall flame-zone/burn-out zone residence time (as reported by Leonard and Stegmaier, 1994), it is known from modeling (including that of this study) that the NO_x increases with increasing combustion zone residence time.

Because of these differences and apparent uncertainties, careful, systematic measurements of NO_x as a function of the relevant independent variables are presented. It is suspected that some of the uncertainties in the NO_x behavior are due to uncertainties in the flame temperature. Although NO_x measurements need to be obtained in both fundamental and practical burners, an advantage possessed by the fundamental burners (such as the jet-stirred reactors used herein) is that the combustion temperature can be measured relatively accurately. It is also suspected that differences in the degree of fuel–air premixing between the various experiments are responsible for differences in the reported NO_x. This needs to be explored also, with the degree of premixing measured, though in this study only essentially perfectly premixed reactants are examined.

Experimental Approach

The formation of NO_x in lean-premixed combustors occurs principally in the flame zone, rather than in the postflame zone, as in traditional combustors. Because of this, the NO_x formation is strongly influenced by super-equilibrium free-radical concentrations, and occurs significantly by pathways other than the thermal NO_x route. At elevated pressures NO_x forms significantly by the N_2O intermediate pathway. Further, if the flame zone residence time is extremely short, there is evidence that the prompt NO_x pathway (involving CH attack on N_2 leading to HCN and N, which oxidizes to NO) contributes. As shown in our previous work (e.g., see Nicol et al., 1994, 1995, and Steele et al., 1994), the jet-stirred reactor provides a combustion environment high in superequilibrium free-radical concentrations. The reactor is well suited for establishing the pathways by which NO_x forms, and for establishing the underlying dependencies of the NO_x chemistry on the primary independent variables of the combustion process.

Contributed by the International Gas Turbine Institute and presented at the 40th International Gas Turbine and Aeroengine Congress and Exhibition, Houston, Texas, June 5–8, 1995. Manuscript received by the International Gas Turbine Institute February 10, 1995. Paper No. 95-GT-107. Associate Technical Editor: C. J. Russo.

The atmospheric pressure jet-stirred reactor is shown schematically in Fig. 1. The internal volume is 16 cc, although for comparison, a 2 cc reactor is also used. The 2 cc reactor is also used at elevated pressures by housing the system in a pressure vessel designed to 15 atm. Pressurized, premixed, electrically heated air and fuel are injected through the Inconel nozzle block. Two nozzle blocks are used: One provides a single, centered jet, while the other provides eight, diverging jets. The overall nozzle area is the same in each case. The recirculation zone accounts for the bulk of the reactor, and is a region of uniform temperature and composition in which the probe measurements are taken.

The atmospheric pressure test matrix has been conducted with the fuels methane, ethylene, and propane, and mixtures of carbon monoxide and hydrogen. Some of the methane and carbon monoxide/hydrogen data have been reported and analyzed previously (Steele et al., 1994). The data set involves combustion temperatures (measured) of 1500 to 1850 K, inlet mixture temperatures of 300 and 600 K, fuel–air equivalence ratios of 0.45 to 0.7, and reactor mean residence times of 1.7 to 7.4 ms, with most of the work done at 3.5 ms. The elevated pressure experiments have been completed for methane in the range of 1 to 7.1 atm, similar combustion temperatures to those stated above, inlet mixture temperature of 300 K, and a reactor residence time of 4.0 ms (nominal). Essential parts of the database obtained in this study are listed in the appendix.

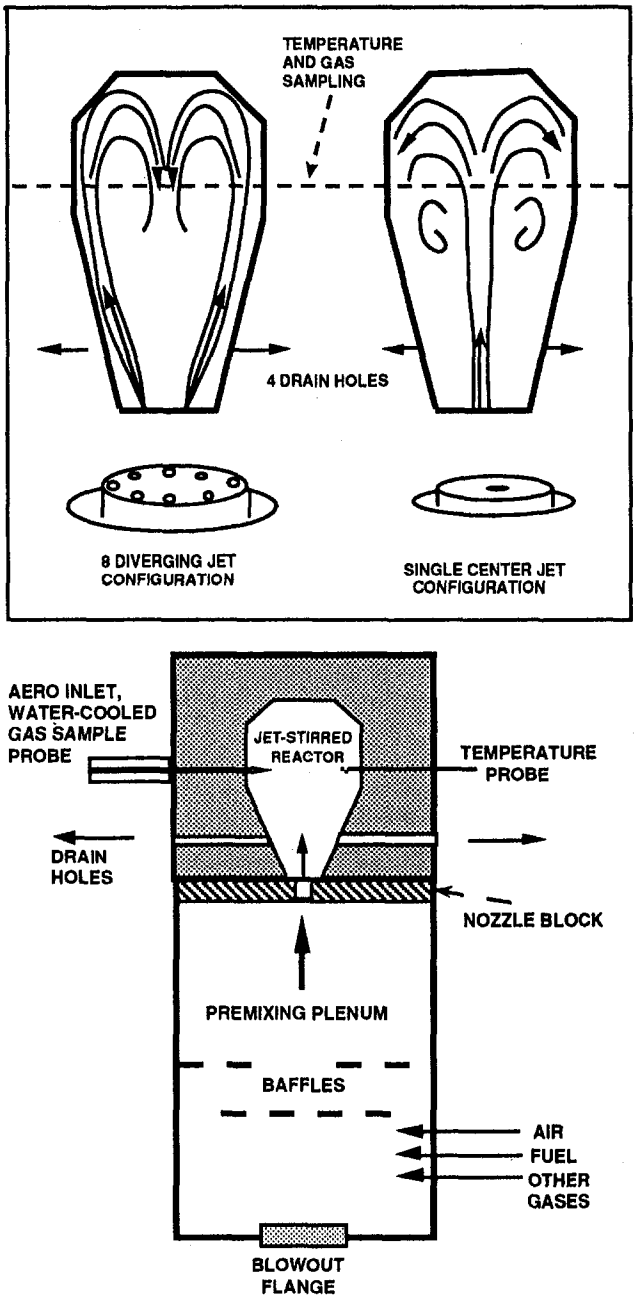

Fig. 1 Schematic of the 2 cc or the 16 cc jet-stirred reactor. The two inlet jet configurations are included showing the flow recirculation patterns and the temperature/gas sampling locations.

The temperature is measured with a Pt/Rh thermocouple, coated to prevent catalytic surface reaction, and corrected by calculation for radiation heat loss. For the highest combustion loadings (i.e., the shortest residence times) the reactor operates nearly adiabatically, within 20 to 30 K of the adiabatic temperature. Gas sampling from the jet-stirred reactor is accomplished with a quartz probe, which utilizes both aerodynamic quench and wall water cooling. Gas samples are analyzed for NO, NO_x, N_2O, CO, CO_2, O_2, and C_1-C_3 hydrocarbons. See Steele et al. (1994) for details.

Atmospheric Experimental Results

Methane. The atmospheric pressure NO_x data for methane are shown in Fig. 2. These data depend primarily on the combustion temperature and residence time. For the case of 600 K inlet mixture temperature (nominal) the curve fit to these data is:

$$NO_x \text{ (ppmv, 15 percent } O_2 \text{ dry)}/\tau \text{ (ms)} = 4.22 \times 10^5 \exp(-22115/T(K))$$

where τ is the residence time. The apparent activation energy of NO_x formation of 44 kcal/gmol given by the expression is significantly lower than the 134 kcal/gmol thermal NO_x activation energy.

The data in Fig. 2 show some sensitivity to inlet mixture temperature. This is seen by comparing the 300 and 600 K inlet mixture temperature cases for the 3.4/3.5 ms data. Given identical combustion temperature, the NO_x yields for the 300 K cases are somewhat lower than those for the 600 K cases. Also, the apparent activation energy of the NO_x formation is somewhat lower (than 44 kcal/gmol) for the 300 K cases.

Insensitivity to nozzle type and reactor size is evident in the Fig. 2 data. The insensitivity to reactor size is important, because prior to these experiments, there was concern that the small (2 cc) reactor, because of its high surface-to-volume ratio, would suffer from surface reaction effects. The fact that NO_x data from reactors of 2 and 16 cc give essentially identical results gives little evidence to this possibility.

Steele et al. (1994) compared chemical reactor modeling to the atmospheric NO_x data plotted in Fig. 2. The model consists of a PSR (perfectly stirred reactor) followed by a PFR (plug flow reactor). The C_1–C_2 hydrocarbon oxidation/NO_x formation mechanism of Miller and Bowman (1989) was used in these computations. The PFR component comprised no more than 20 percent of the total reactor. The PFR component had little effect on the NO_x; that is, the experimental NO_x could be matched by treating the whole reactor as a PSR. However, the PFR component was required to match the experimental temperature (for the short residence time, nearly adiabatic cases) and the CO concentration. That is, the PFR component permitted the gas to relax toward equilibrium. The CO relaxation in the probe was modeled using a second PFR.

Close agreement of the modeled NO_x to that measured was obtained for the 1.7 ms and 3.4/3.5 ms cases (of Fig. 2). The 1.7 ms model assumed an adiabatic reactor. The 3.4/3.5 ms models were assigned the measured temperature. For the 6.0/6.9 ms cases, the model (based on the measured temperature) underpredicted the NO_x by 20 to 30 percent. This is thought to be due to small temperature and concentration gradients within

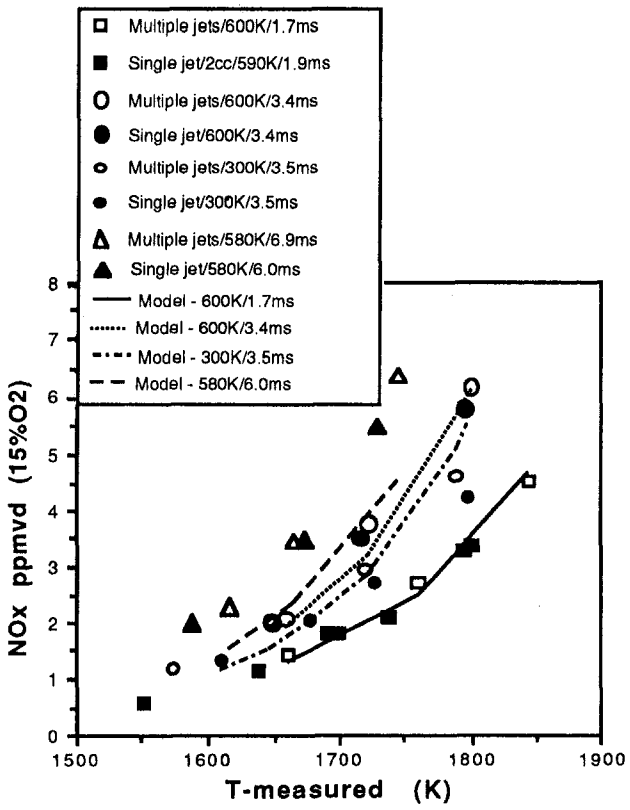

Fig. 2 NO_x data for atmospheric jet-stirred reactors of 2 and 16 cc volume, and chemical reactor modeling at the experimental conditions. The fuel is methane.

the reactor, which are not treated by the model, and which increase as the residence time is increased, and the mixing rate is diminished.

Ethylene and Propane. The NO_x results for ethylene are shown in Fig. 3. Shown are results for: (1) 300 K and 600 K inlet temperatures, (2) single jet and diverging jet nozzles, (3) chemical reactor modeling applied to experimental conditions, and (4) the 250 cc toroidal jet-stirred reactor data of Zelina and Ballal (1994).

The data show that the NO_x depends primarily on the combustion temperature. Similar to the results for methane, there is a small sensitivity to the mixture inlet temperature. The modeling (same C_1–C_2 mechanism as for methane) also shows a slight sensitivity to inlet temperature. Insensitivity to reactor inlet nozzle type and reactor size is evident in the experimental data. The 250 cc toroidal reactor operated by Zelina and Ballal (1994) has a surface-to-volume ratio of 1.0 cm^{-1}. The 16 cc reactor used for this study has a surface-to-volume ratio of 2.0 cm^{-1}. The excellent comparison of these datasets supports the hypothesis that surface-to-volume effects are negligible.

The NO_x experimental results and chemical reactor modeling for propane are shown in Fig. 4. The predictions are based on the C_1–C_2 mechanism used for methane and ethylene with three reactions added for the conversion of the propane to ethane (Nguyen et al., 1989). The data show close agreement with the chemical reactor model. The results for methane, ethylene, and propane indicate a nonnegligible dependency of the NO_x on the hydrocarbon fuel type. The NO_x formed by the methane combustion is overall about 30–50 percent less than the NO_x formed by the ethylene and propane combustion, given the same combustion temperature. Modeling indicates that this difference in NO_x occurs because of greater O-atom levels formed with the C_2–C_3 hydrocarbon combustion compared to the methane combustion.

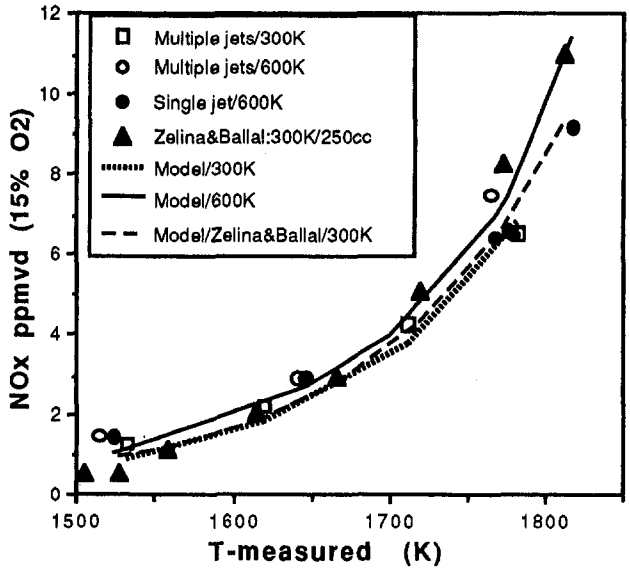

Fig. 3 NO_x data and chemical reactor modeling for ethylene combustion for the 16 cc jet-stirred reactor at 3.5 ms, and for the 250 cc toroidal jet-stirred reactor (Zelina and Ballal, 1994) at 4.5 ms

Carbon Monoxide/Hydrogen. The NO_x results for three mixtures of carbon monoxide and hydrogen are shown in Fig. 5. The molar composition of the fuel mixtures are: H_2/CO = 0.5, 1.0, and 2.0. The first mixture of 33 percent H_2/67 percent CO represents a typical coal gasification fuel from oxygen-blown processes (Döbbeling et al., 1996). The second mixture of 50 percent H_2/50 percent CO represents a typical residual oil gasification fuel. The third mixture of 67 percent H_2/33 percent CO was chosen to simulate methane fuel (i.e., one carbon atom to four hydrogen atoms).

The data plotted in Fig. 5 show that the NO_x depends on the combustion temperature and the H_2/CO ratio. The lower the H_2/CO ratio, the higher the NO_x. This trend is a result of an increase in O atom formed from the increase in the fraction of carbon monoxide in the fuel.

In order to compare the H_2/CO mixtures with the methane, ethylene, and propane, the measured NO_x for the same residence time and reactor size is plotted in Fig. 6. The data clearly show

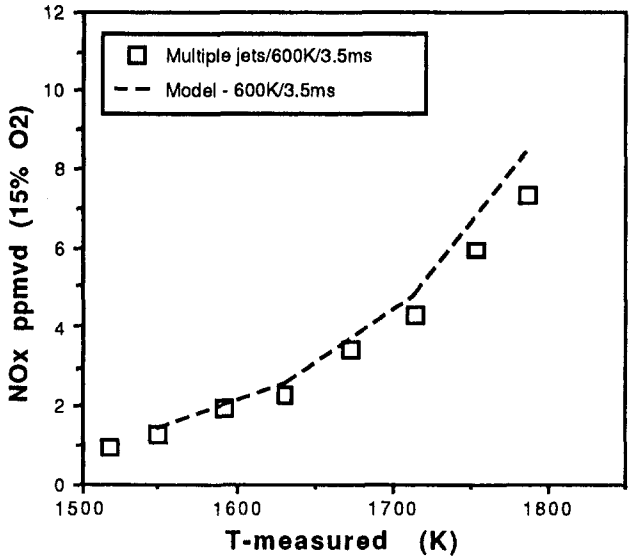

Fig. 4 NO_x data and chemical reactor modeling for propane combustion for the 16 cc jet-stirred reactor

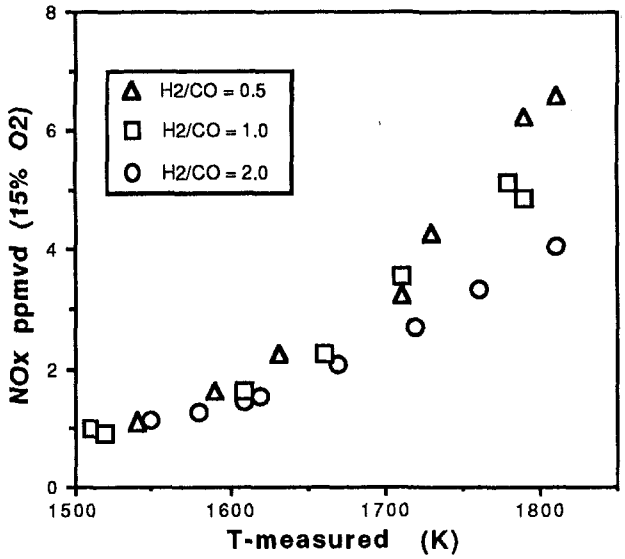

Fig. 5 NO_x data for three molar mixtures of hydrogen/carbon monoxide combustion for the 16 cc, single-jet nozzle, at 300 K inlet temperature and 3.5 ms

a sensitivity of NO_x to the fuel type. The results for H_2/CO = 2.0 agree closely with the methane results. The results for H_2/CO = 0.5 and 1.0 fall between the ethylene/propane data and the methane data. The agreement obtained between the hydrocarbon fuels and the counterpart H_2/CO fuels (especially for methane and H_2/CO = 2.0) supports the hypothesis that the NO_x is formed mainly through O atom attack on the nitrogen, rather than through significant attack of hydrocarbon fragments on the nitrogen (the prompt pathway).

Pressure Effects on NO_x Formation

In order to examine the effect of pressure on the formation of NO_x, a 2 cc jet-stirred reactor is operated in the range of 1 to 7.1 atm. The NO_x data for methane combustion are shown in Fig. 7 for a mixture inlet temperature of 300 K and a residence time of 4 ms (nominal). The data show that the NO_x depends primarily on the combustion temperature, with a neutral or slightly negative pressure effect. A similar NO_x dependency on pressure is reported by Joshi et al. (1994) for the 5 to 30 atm range.

In order to model the experimental data, the PSR-followed-by-PFR model (Nicol et al., 1994) is used. The results are shown in Fig. 8 for the case of 1750 K combustion temperature. The independent variable is the residence time of the PSR component of the model, which is varied from the blowout value (at the far left) to the 4 ms residence time of the experimental reactor. The difference between 4 ms and the PSR residence time is the PFR residence time.

The modeling results indicate two trends: (1) an increase in the flame zone residence time (which is simulated by the PSR component) causes an increase in the NO_x, and (2) an increase in pressure for fixed PSR component also causes an increase in NO_x over the pressure range studied.

The results suggest that significant reductions in NO_x occur when the size of the free-radical rich, NO_x producing flame zone is decreased. This explains the apparent neutral or slightly negative pressure effect shown in the NO_x data of Fig. 7.

Profiling of the experimental reactor for temperature and the CO, N_2O, and NO_x concentrations (see Fig. 1 for the location) confirms a decrease in the size of the free-radical rich zone with increasing pressure. At 1 atm, the CO and N_2O concentrations are relatively uniform in the reactor, whereas at high pressure, these concentrations (especially the CO) fall markedly between the jet zone and the recirculation zone of the reactor. Since the CO and N_2O are indicative of the free radical chemistry (especially the O atom; see Nicol et al., 1994), the profiling indicates a decrease in the radical rich zone size with increasing pressure.

Figure 8 is based on the Miller–Bowman (1989) mechanism. However, modeling has been conducted also with the GRI mechanism, version 1.2, with the Miller–Bowman nitrogen chemistry added. Because of the large amount of CH radical predicted by the GRI mechanism, leading to enhanced prompt NO_x formation, the NO_x is overpredicted by this model. The overprediction at 1750 K, 1 atm is a factor two.

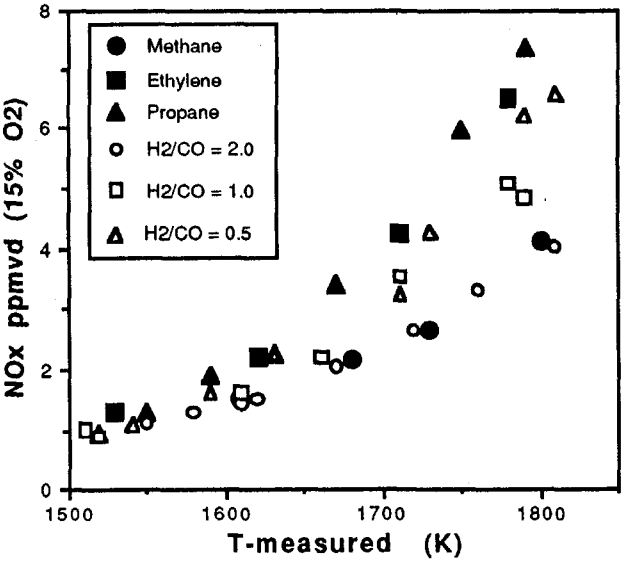

Fig. 6 NO_x data for methane, ethylene, propane, and hydrogen/carbon monoxide combustion for the 16 cc, single-jet nozzle, at 300 K inlet temperature and 3.5 ms (multiple-jet nozzle for ethylene and propane, 600 K inlet temperature for propane)

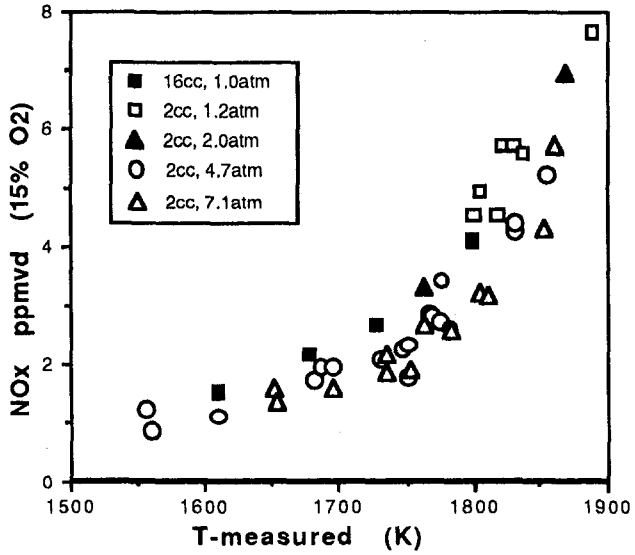

Fig. 7 NO_x data for methane showing pressure effect for the 2 cc reactor, single-jet nozzle, 300 K inlet temperature and 3.5 to 4 ms residence time

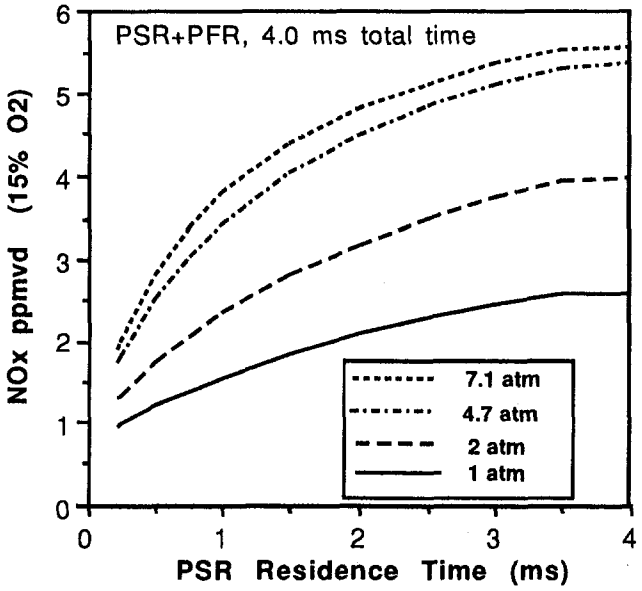

Fig. 8 Chemical reactor modeling results showing the pressure and PSR residence time effects for methane combustion for an inlet temperature of 300 K, combustion temperature of 1750 K, and total residence time of 4.0 ms

Comparison of NO_x for Different Burners

It is informative to compare the NO_x measurements of a wide range of lean-premixed burners for which data are found in the recent literature. For all cases the fuel is either natural gas or methane. The flame temperature is the measured temperature in the case of the stirred reactor data; and in the case of the other studies, it is either stated or assumed to be the adiabatic equilibrium flame temperature.

In Fig. 9, the jet-stirred reactor results for 1 atm, 300 to 600 K mixture inlet temperatures, and nominal residence times of 1.7 to 6.9 ms are compared to the data from the literature. The jet-stirred reactor results for 7.1 atm, 300 K mixture inlet temperature, and nominal residence time of 4.0 ms are also included.

The data of Sattelmayer et al. (1992) are for the ABB double-cone burner run at atmospheric pressure. In this case the adiabatic equilibrium flame temperature was computed assuming methane and using the fuel–air equivalence ratios given in the paper. The curve fit of Leonard and Stegmaier (1994) pertains to laboratory burner results obtained with a nearly perfect premixer and a variety of flame holders. A wide range of conditions was tested, including: pressures of 1 to 30 atm, inlet air temperatures of 300 to 800 K, and residence times of 2 to 100 ms. The NO_x depended almost exclusively on the flame temperature, which is assumed to be the adiabatic equilibrium temperature. Visser and Levinsky (1993) examined NO_x data from a number of lean-premixed gas burners and developed a curve fit (based on 0 percent O_2). Over the temperature range plotted in Fig. 9 Visser and Levinsky's curve fit (adjusted to 15 percent O_2) is shown.

The results of Altemark and Knauber (1987) are for the SINOX prototype burner. The pressure range covered in these experiments was 4 to 10 atm; over this range the NO_x showed no sensitivity to pressure. The measurements did show a sensitivity to inlet temperature, which is not reflected in our overall fit of the data. The change from 673 to 473 K inlet temperature reduced the NO_x by about 20 percent. The flame temperature is that computed by Altemark and Knauber (1987). We adjusted the NO_x data from dry, actual O_2 basis to dry, 15 percent O_2 basis.

Results of Aigner et al. (1990) for the ABB double cone burner operated at engine conditions are also shown in Fig. 9. The adiabatic equilibrium flame temperature was computed assuming methane and using the fuel-air equivalence ratios given in the paper. On average, these NO_x data show about the same flame temperature sensitivity as the Sattelmayer et al. (1992) data.

The data shown in Fig. 9 suggest the following:

1 For the most part, the jet-stirred reactor data (from 1.7/1.9 ms to 6.0/6.9 ms nominal residence time) bracket the other atmospheric pressure data and the data for which the pressure effect appears to be weak to negligible (i.e., the data of Leonard and Stegmaier, 1994; Visser and Levinsky, 1993; and Altemark and Knauber, 1987). The jet-stirred reactor data of 7.1 atm compare well with the data of Leonard and Stegmaier (1994) and Visser and Levinsky (1993).
2 The exponential curve fits of the cited data give apparent activation energies of NO_x formation in the range of 32 to 57 kcal/gmol. The average apparent activation energy of 44.5 kcal/gmol is nearly identical to that of the 590/600 K jet-stirred reactor data, i.e., 44 kcal/gmol (for 15 percent O_2, dry).

Conclusions

The formation of NO_x in lean-premixed, high-intensity combustion has been examined as a function of the relevant variables. The primary conclusions from this study are as follows:

- The jet-stirred reactor is a useful laboratory tool for studying the formation of NO_x.
- The combustion temperature has the most significant effect on the NO_x.
- The combustion pressure has a neutral or slightly negative effect on the NO_x. Chemical reactor modeling indicates

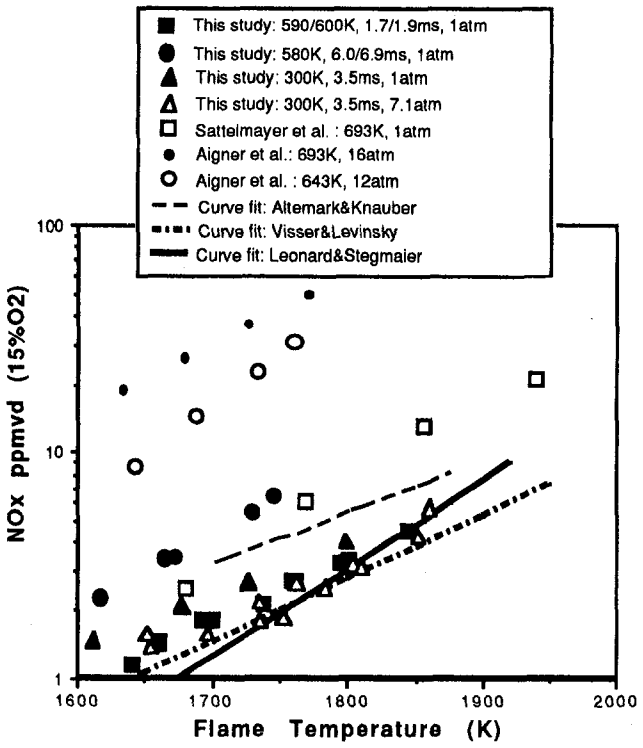

Fig. 9 Comparison of jet-stirred reactor NO_x data to that of various published studies. All data are for natural gas or methane fuel burned at lean-premixed conditions.

that this effect is the result of the decreasing size of the free-radical rich zone.

- The fuel type has an effect on the NO_x, especially at temperatures greater than 1700 K.
- The residence time of the combustion zone (i.e., region of high free-radical concentrations) significantly influences the NO_x.
- An increase in the inlet temperature from 300 to 600 K causes only a slight increase in the NO_x.
- The reactor surface-to-volume ratio and the inlet jet configurations have negligible effects on the NO_x.

Acknowledgments

The authors wish to thank Professor D. R. Ballal and Mr. J. Zelina of the University of Dayton for their cooperation in the comparison of jet-stirred reactor databases. Asea Brown Boveri Ltd. is thanked for the Fellowship to the University of Washington, which has supported graduate student research in the combustion area.

References

Aigner, M., Mayer, A., Schiessel, P., and Strittmatter, W., 1990, "Second-Generation Low-Emission Combustors for ABB Gas Turbines: Test Under Full-Engine Conditions," ASME Paper No. 90-GT-308.

Altemark, D., and Knauber, R., 1987, "Ergebnisse von Untersuchungen an einem Vormischbrenner unter Druck mit extrem neidriger NO_x-Emission," *VDI Berichte No. 645*, pp. 299–311.

Döbbeling, K., Knöpfel, H. P., Polifke, W., Winkler, D., Steinbach, C., and Sattelmayer, T., 1996, "Low-NO_x Premixed Combustion of MBtu Fuels Using the ABB Double Cone Burner (EV Burner)," ASME JOURNAL OF ENGINEERING FOR GAS TURBINES AND POWER, Vol. 118, pp. 46–53.

Joshi, N. D., Epstein, M. J., Durlak, S., Marakovits, S., and Sabla, P. E., 1994, "Development of a Fuel Air Premixer for Aero-Derivative Dry Low Emissions Combustors," ASME Paper No. 94-GT-253.

Leonard, G., and Stegmaier, J., 1994, "Development of an Aeroderivative Gas Turbine Dry Low Emissions Combustion System," ASME JOURNAL OF ENGINEERING FOR GAS TURBINES AND POWER, Vol. 116, pp. 542–546.

Maughan, J. R., Luts, A., and Bautista, P. J., 1994, "A Dry Low NO_x Combustor for the MS3002 Regenerative Gas Turbine," ASME Paper No. 94-GT-252.

Miller, J. D., and Bowman, C. T., 1989, "Mechanism and Modeling of Nitrogen Chemistry in Combustion," *Prog. in Energy and Combust. Science*, Vol. 15, pp. 287–338.

Nguyen, H. L., Bittker, D. A., and Niedzwiecki, R. W., 1989, "Investigation of Low NO_x Staged Combustor Concept in High-Speed Civil Transport Engines," NASA-TM-101977.

Nicol, D. G., Steele, R. C., Marinov, N. M., and Malte, P. C., 1995, "The Importance of the Nitrous Oxide Pathway to NO_x in Lean-Premixed Combustion," ASME JOURNAL OF ENGINEERING FOR GAS TURBINES AND POWER, Vol. 117, pp. 100–111.

Nicol, D. G., Malte, P. C., and Steele, R. C., 1994, "Simplified Models for NO_x Production Rates in Lean-Premixed Combustion," ASME Paper No. 94-GT-432.

Sattelmayer, T., Felchlin, M. P., Haumann, J., Hellat, J., Styner, D., 1992, "Second-Generation Combustors for ABB Gas Turbines: Burner Development and Tests at Atmospheric Pressure," ASME JOURNAL OF ENGINEERING FOR GAS TURBINES AND POWER, Vol. 114, pp. 118–125.

Snyder, T. S., Rosfjord, T. J., McVey, J. B., Hu, A. S., and Schlein, B. C., 1996, "Emission and Performance of a Lean-Premixed Gas Fuel Injection System for Aeroderivative Gas Turbine Engines," ASME JOURNAL OF ENGINEERING FOR GAS TURBINES AND POWER, Vol. 118, pp. 38–45.

Steele, R. C., Malte, P. C., Nicol, D. G., and Kramlich, J. C., 1994, "NO_x and N_2O in Lean-Premixed Jet-Stirred Flames," presented at the 25th Symposium (International) on Combustion, Irvine, CA (to appear in *Combustion and Flame*).

Visser, M. B. M., and Levinsky, H. B., 1993, "Premixed Combustion in Gas Fired Equipment," *VDI Berichte No. 1090*, pp. 139–146.

Zelina, J., and Ballal, D. R., 1994, "Combustion Studies in a Well-Stirred Reactor," AIAA Paper No. 94-0114.

APPENDIX

Table 1 Jet-stirred reactor experimental data

Fuel/Volume(cc)/Nozzle/T-inlet(K)/Pres.(atm)						
				Wet Basis		
τ (ms)	ϕ	Temp. (K)	O2 (%)	CO (%)	NOx (ppmv)	N2O (ppmv)
CH4/16cc/Single/310K/1atm						
3.3	0.68	1798	5.9	0.549	8.5	0.4
3.5	0.67	1727	6.6	0.252	5.2	0.47
3.6	0.63	1677	7.6	0.304	3.9	0.59
3.7	0.62	1611	8.7	0.388	2.4	0.63
CH4/2cc/Single/297K/4.7atm						
3.8	0.71	1855	6.2	0.032	10.5	1.3
3.6	0.67	1831	6.7	0.02	8.5	1.2
4	0.66	1768	7.1	0.087	5.3	1.5
4.2	0.61	1682	8.3	0.151	2.9	1.9
4.1	0.56	1611	9.5	0.224	1.7	2.1
CH4/2cc/Single/298K/7.1atm						
3.9	0.7	1860	6.2	0.013	11.5	0.64
4.2	0.68	1810	6.7	0.02	6.2	1.2
4.1	0.66	1783	7.1	0.07	4.8	1.6
4.3	0.61	1696	8.1	0.04	2.7	1.7
4.4	0.6	1654	8.4	0.149	2.4	2.5
C2H4/16cc/Single/603K/1atm						
3.5	0.56	1818	10	0.231	14.5	0.66
3.5	0.54	1779	9.6	0.246	10.7	0.67
3.7	0.47	1646	11.5	0.221	4	1
4.1	0.4	1523	13	0.316	1.7	1.1
C2H4/16cc/Multiple/310K/1atm						
3.4	0.61	1783	8	0.108	12.3	0.85
3.6	0.57	1712	9	0.069	7.4	1
3.8	0.52	1620	10	0.058	3.5	1.1
4	0.49	1532	10.9	0.061	1.8	1.2
C3H8/16cc/Multiple/612K/1atm						
3.4	0.6	1786	8.4	0.054	13.1	0.82
3.5	0.58	1714	9.6	0.035	6.9	0.99
3.7	0.48	1631	10.7	0.028	3.3	1.17
3.9	0.44	1549	11.8	0.036	1.7	1.28
CO:H2/16cc/Single/312K/1atm						
3.9	0.63	1778	8.3	0.317	8.9	0.52
4	0.58	1712	9.3	0.313	5.7	0.64
4.2	0.52	1605	10.7	0.331	2.3	0.76
4.3	0.46	1519	11.6	0.443	1.1	0.91
CO:2H2/16cc/Single/312K/1atm						
3.8	0.64	1808	7.3	0.141	7	0.62
4	0.57	1724	8.4	0.125	4.2	0.74
4.2	0.5	1618	9.7	0.12	2.1	0.9
4.4	0.46	1553	10.4	0.152	1.5	0.93
2CO:H2/16cc/Single/312K/1atm						
3.7	0.62	1806	7.5	0.475	13.2	0.56
3.9	0.58	1733	8.7	0.385	7.7	0.67
4	0.53	1632	10	0.332	3.6	0.83
4.2	0.47	1543	11.1	0.415	1.6	0.92

Lean Blowout Research in a Generic Gas Turbine Combustor With High Optical Access

G. J. Sturgess[1]
Pratt & Whitney,
East Hartford, CT 06108

D. Shouse
Wright Laboratories,
Wright-Patterson Air Force Base,
Dayton, OH 45433

The U.S. Air Force is conducting a comprehensive research program aimed at improving the design and analysis capabilities for flame stability and lean blowout in the combustors of aircraft gas turbine engines. As part of this program, a simplified version of a generic gas turbine combustor is used. The intent is to provide an experimental data base against which lean blowout modeling might be evaluated and calibrated. The design features of the combustor and its instrumentation are highlighted, and the test facility is described. Lean blowout results for gaseous propane fuel are presented over a range of operating conditions at three different dome flow splits. Comparison of results with those of a simplified research combustor is also made. Lean blowout behavior is complex, so that simple phenomenological correlations of experimental data will not be general enough for use as design tools.

Introduction

Combustion stability is extremely important in gas turbine engines for aircraft use. It is becoming increasingly more difficult to ensure that adequate stability margins can be maintained in the future because of current design trends toward improved atomization of liquid fuel, high temperature rise, and low-emissions combustors, and their associated technologies.

In 1987 the U.S. Air Force established the Combustor Design Model Evaluation (CDME) program, with the goal of improving physical modeling to facilitate design work. Under the CDME effort, a joint industry/Government laboratory/university research program was initiated to address stability (Sturgess et al., 1991).

The intent of the stability research program is to investigate, understand, and model lean blowouts in the context of combustors for aircraft gas turbines. The experimental portion of the program utilizes three combustors as test vehicles. These consist of a research combustor, a technology-development combustor, and a generic gas turbine combustor. The research combustor underwent extensive development (Sturgess et al., 1992a; Heneghan et al., 1990) and is providing basic information on lean blowout (LBO) for a combustor that is simple in configuration but, nevertheless, contains the essential primary zone flow features of a practical gas turbine combustor (Roquemore et al., 1991; Sturgess et al., 1992b, 1992c, 1993). A preliminary description of the generic gas turbine combustor is given by Sturgess et al. (1991).

The majority of the published work on flame stability is for bluff-body flame-holders of various types, or for well-stirred reactors, as reviewed by Lefebvre (1983). The amount of experimental data published in the open literature for practical gas turbine combustors is much less extensive. Given the large number of possible geometric variables that govern flow pattern, systematic investigations are largely lacking, although some basic studies are reported by Jeffs (1962) and Stewart (1956). However, the commonly used form of practical combustor in these studies is the can-type; almost all information on the annular-type of combustor currently used in aircraft applications is confined to relatively inaccessible company reports. The intent of this paper is to describe the lean stability behavior of an annular combustor, with an aim of eventually modeling this behavior.

Design of Generic Combustor

The purpose of the generic gas turbine combustor (known as the Task 200 combustor) is to provide an experimental data base against which lean blowout modeling of various types might be evaluated and calibrated. This purpose places three major requirements on the design of the Task 200 combustor: First, that it be as close to a real aircraft gas turbine combustor as possible in terms of LBO characteristics and flow field. Second, that it be flexible enough to allow sufficient variation in relevant geometry and flow distribution to afford some investigation of the important primary zone design parameters, such as equivalence ratio and residence time. Third, that sufficient optical access be provided so that laser diagnostics might yield details of important flow features and their role in providing stability. Finally, it was decided to approach the LBO problem in two distinct stages—initially, with gaseous fuels (propane and methane), and last, with liquid fuels (ethanol). By this means the effects of liquid fuel atomization and spray evaporation can be separated from the aerothermochemical effects.

The aerothermodynamic design of the annular combustor was based on present Pratt & Whitney design practice, and it utilized airblast-atomizing fuel injectors and "inside-out" recirculation (Sturgess et al., 1991, 1992a). The configuration adopted for the Task 200 combustor is a four-injector, planar-section, simplified geometry version of this annular combustor design. The fundamental rig design to accommodate this combustor was carried out by United Technologies Research Center (UTRC), with subsequent modifications made by Wright Laboratories to improve handling, access and window durability. The distance between fuel injector centerlines is 7.62 cm (3.0 in.), and the height between liners is 9.91 cm (3.9 in.), while the length of the combustor is 20.83 cm (8.2 in.) from the fuel injector face to the exit nozzle entrance.

The fuel injectors are actual engine hardware, with sets modified, calibrated and individually balanced with Lee-jets to flow gaseous or liquid fuels. Low and high swirl versions of the injector were provided. The fuel injector/combustor dome interfaces simulated engine practice. The major dimensions of combustor dome height, length, and injector spacing are based on those of the engine from which the fuel injectors were taken.

[1] Current address: Innovative Scientific Solutions, Inc., Beavercreek, OH 45430-1658.

Contributed by the International Gas Turbine Institute and presented at the 38th International Gas Turbine and Aeroengine Congress and Exposition, Cincinnati, Ohio, May 24–27, 1993. Manuscript received at ASME Headquarters March 17, 1993. Paper No. 93-GT-332. Associate Technical Editor: H. Lukas.

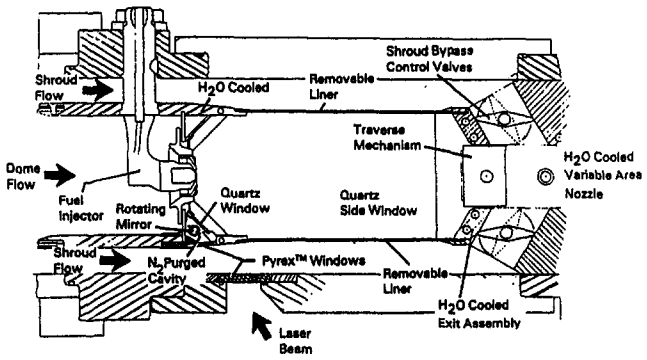

Fig. 1 Cross section of the Task 200 generic combustor, showing optical access and flexibility features of the design

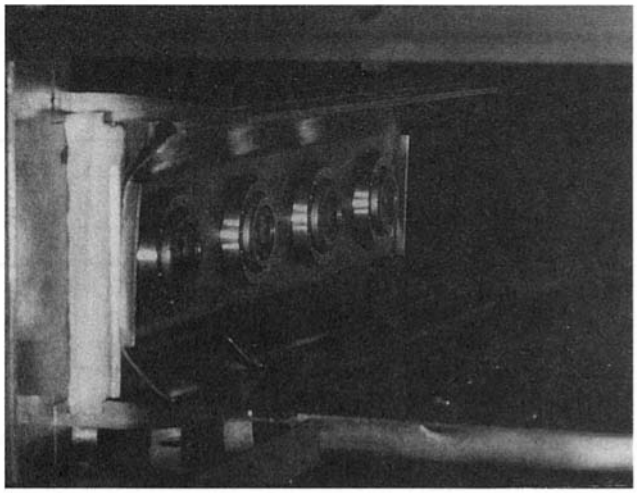

Fig. 2 Partially assembled combustor, showing dome, fuel injector/dome interfaces, and one liner

Cooling air is introduced as a surface film at the dome/liner interfaces. The liners, upper and lower, are removable and may contain any desired pattern of air ports. Metal liners do not have any specific internal film cooling, but are provided with a thermal barrier coating and are convectively cooled by the shroud flows.

The diameters of the ports in the three rows of air addition are 0.635, 1.303, and 0.897 cm (0.250, 0.513, and 0.353 in.), respectively, with a lateral spacing between ports in each row of 3.81 cm (1.5 in.). Ports in a given row are staggered half a port pitch relative to adjacent rows, while the ports in each row in upper and lower liners are directly opposed. The ports in the first row are positioned with a port directly in-line with a fuel injector. The spacings between rows of ports are as follows: first to second—4.267 cm (1.68 in.), and second to third—3.962 cm (1.56 in.); the centerline of the first row of ports is positioned 4.902 cm (1.93 in.) downstream from the fuel injector faces.

The current pattern of circular air ports in the liners is one successfully developed at Pratt & Whitney for an in-service engine. Careful in situ measurements were made of the discharge coefficients for the dome, liner ports, and fuel injectors.

Two domes are available; one a plain bulkhead (also provided with thermal barrier coating) and the other a vertically symmetric configuration having filleted upper and lower corners (Fig. 1). Dome cooling is provided by means of impingement jets, with spent dome cooling air being discharged at the dome/liner interfaces as a liner film. Ignition is by means of a hydrogen torch-ignitor mounted in the dome.

Air is supplied to the dome and upper and lower shrouds by individually metered supplies that are always isolated from each other by means of an upstream array of sonic venturis. At the exits from the combustor and shrouds are independent water-cooled valves that control the bypass flows.

Figure 2 shows the partially assembled rig; the combustor dome, the fuel injectors, and one liner can be seen.

Optical Access

Direct optical access to the combustor for visualization and laser diagnostics is provided primarily by the side-walls enclosing the four-injector section. These side-walls are of fused quartz and are contained in water-cooled housings. Two thicknesses of sidewall are available—1.905 cm (0.75 in.) for operation at internal pressures up to 448.2 kN/m^2 (65 psia), and 0.318 cm (0.125 in.) for operation at atmospheric pressure.

A further optical path is provided by windows in the base of the rig (Fig. 1) that allow laser beam access to a high-speed rotating mirror contained by the dome lower fillet-piece (this dome configuration only). Through selectively opened slits up the height of the dome, the rotating mirror can scan the combustor with vertical, planar sheets of laser light for imaging purposes. For thermal protection, the mirror cavity is purged with a small, pressure-balanced flow of gaseous nitrogen.

A set of liners, containing the current air port hole pattern, is available in fused quartz for direct vertical access to the reacting flow.

Rig and Facility

The rig is mounted horizontally in a test cell (Room 20) of Wright Laboratories, Wright-Patterson Air Force Base, Dayton, Ohio. It provides flow, metering and control of air, fuel, nitrogen and cooling water to the Task 200 combustor. A schematic flow path for the rig is given in Fig. 3.

Compressor air is supplied to the facility via a delivery system and isolating valve. The rig divides this air into three separate streams that respectively feed the upper shroud, dome, and lower shroud. The passage flow splits are set by means of con-

Nomenclature

$B.Z.$ = burning zone
F = temperature correction factor
LBO = lean blowout
$L.P.$ = reactor loading parameter
$l_{B.Z.}$ = burning zone length
$\dot{m}_a$ = air mass flow rate in reactor
$\dot{m}_f$ = fuel mass flow rate
$\dot{m}_{N2}$ = excess nitrogen mass flow rate in reactor
$\dot{m}_{\mathrm{Tot}}$ = reactor total gaseous mass flow rate
n = apparent global reaction order
P = pressure in reactor
$P.Z.$ = primary zone
T = inlet temperature of reactants
V = reactor volume
W_{ab} = combustor total (cold) airflow
W_{cooling} = dome cooling air, entering as film at dome/liner interface
W_{dome} = total (cold) airflow entering combustor through dome (including fuel injectors)
$W_{\mathrm{insertjets}}$ = smoke-control airflow, as jets around fuel injectors
$W_{\mathrm{jets,1}}$ = airflow for first row of transverse air jets (upper and lower liners)
$W_{P.Z.}$ = primary zone airflow
W.S.R. = well-stirred reactor
ϕ = fuel/air equivalence ratio by mass

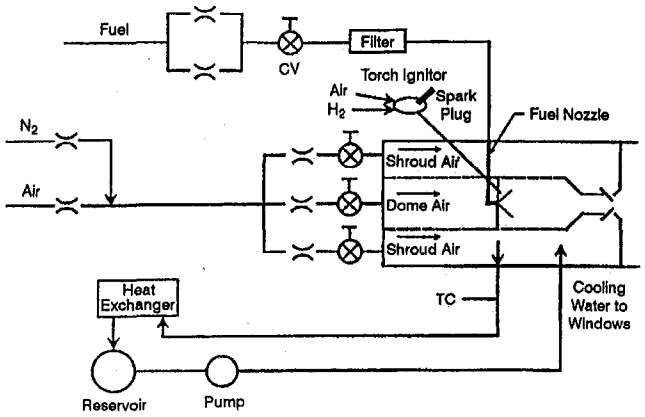

Fig. 3 Schematic of facility, showing air, fuel, excess nitrogen, and cooling water circuits

trol valves, and each stream is pressure-isolated from its companions on the valve upstream side by means of appropriately sized sonic venturis. Individual stream flows are then measured by calibrated orifice plates downstream of the control valves. For simulation of low pressures, gaseous nitrogen from a bottled supply is introduced into the main air line far upstream from the three-way split, so that it is thoroughly mixed with the incoming air prior to the sonic venturis.

Gaseous propane from a tank farm is metered by low-range and high-range turbine flow meters, and the filtered supply is delivered to a manifold feeding the four fuel injectors.

The torch ignitor is mounted on the rig and discharges directly into the dome. It is supplied separately with air and gaseous hydrogen; ignition is by spark plug. After a successful light of the main combustor, the torch ignitor is turned off.

Cooling water for the window frames is pumped from a reservoir to the frames where it flows upstream (counterflow heat exchanger). As the heated water leaves the rig, its temperature is monitored by a thermocouple. Before being returned to the reservoir, the heated water is first passed through a heat exchanger.

The discharge from the rig enters an atmospheric-pressure exhaust ejector and exits the facility to ambient conditions.

Figure 4 shows the rig mounted in the facility. Flow is from left to right, and the rig exhausts from the facility via the circular duct on the right. Mounted under and on either side of the test section may be seen the hardened LDA and CARS system

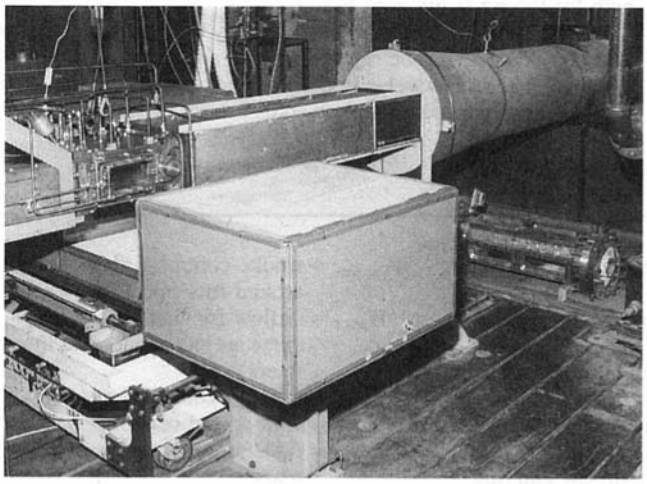

Fig. 4 Rig mounted in the facility, showing exhaust arrangement and hardened LDA/CARS instruments

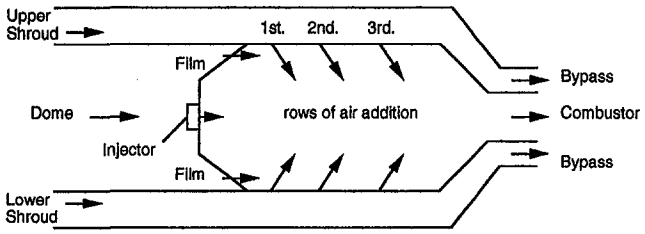

Fig. 5 Diagrammatic representation of combustor flow splits

currently being used to map the combustor velocity and temperature fields.

The facility in which the rig is installed is capable of supplying up to 13.61 kg/s (30.0 lbm/sec) of air at ambient temperature, and up to 10.433 kg/s (23 lbm/sec) at temperatures up to 922 K (1200 F) (nonvitiated); the air can be delivered at pressures up to 5171 kN/m^2 (750 psia). The fuel supplies in the facility are, for propane, up to 0.227 kg/min (0.5 lbm/min) at 689.5 kN/m^2 (100 psig); for methane, up to 0.181 kg/min (0.4 lbm/min) at 1034.2 kN/m^2 (150 psig); and for liquid fuels, up to 6.804 kg/h (15 lbm/hr) at 1379 kN/m^2 (200 psig). The bottled nitrogen supply is capable of delivering up to 9.072 kg/min (20 lbm/min) at 3447.4 kN/m^2 (500 psig) for a limited period of time.

Combustor Flow Splits

Figure 5 shows diagrammatically the flow distribution in the combustor rig. The minimum levels of bypass flows were always set for convective cooling of the liners. The combustor total airflow was defined as the sum of the metered dome flow and the calculated jet flows based on measured pressure drops and pre-established hole effective areas, i.e.,

$$W_{ab} = W_{\text{dome}} + W_{\text{jets}} \tag{1}$$

The dome flow was made up of the injector, insert jets (around the individual injectors), and dome cooling airflows, i.e.,

$$W_{\text{dome}} = W_{\text{injectors}} + W_{\text{insertjets}} + W_{\text{cooling}} \tag{2}$$

The primary zone airflow consisted of the dome flow plus 27.9 percent of the first row jet air. This value of primary zone-active jet air has been established separately (Sturgess et al., 1993b) for the particular primary zone aerodynamic flow pattern used. Thus,

$$W_{P.Z.} = W_{\text{dome}} + 0.279 W_{\text{1st.jets}} \tag{3}$$

For a particular run, flow split information was established at the set point without combustion, prior to each blowout test point.

The measured effective areas for the liner air ports, top and bottom, respectively, are as follows: first row—1.516 and 1.632 cm^2 (0.235 and 0.253 in.^{2}); second row—4.968 and 5.394 cm^2 (0.77 and 0.836 in.^{2}); and third row—2.845 and 2.852 cm^2 (0.441 and 0.442 in.^{2}). The total effective area of the dome is 8.652 cm^2 (1.341 in.^{2}), and that of the fuel injector air passages is 5.929 cm^2 (0.919 in.^{2}) (total of four injectors).

Blowouts With Propane

Testing with gaseous propane has been completed for three values of dome flow, consisting of 10, 15, and 20 percent of the total airflow entering the combustor. For each flow split, lean blowouts were taken for a series of total airflows, and for a range of excess nitrogen flows at each airflow. Flame characteristics during the blowouts were recorded on videotape with viewing through the side windows. The liner hole patterns

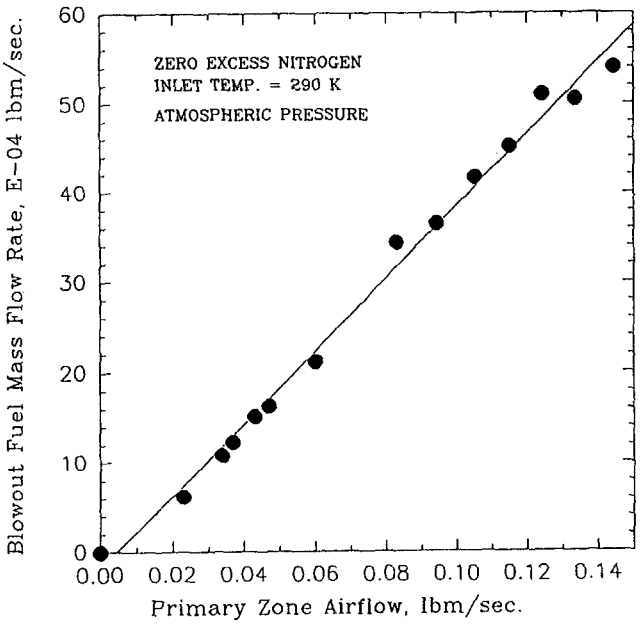

Fig. 6 Dependence of blowout fuel mass flow rate on primary zone airflow for the 15 percent dome flow combustor at atmospheric pressure

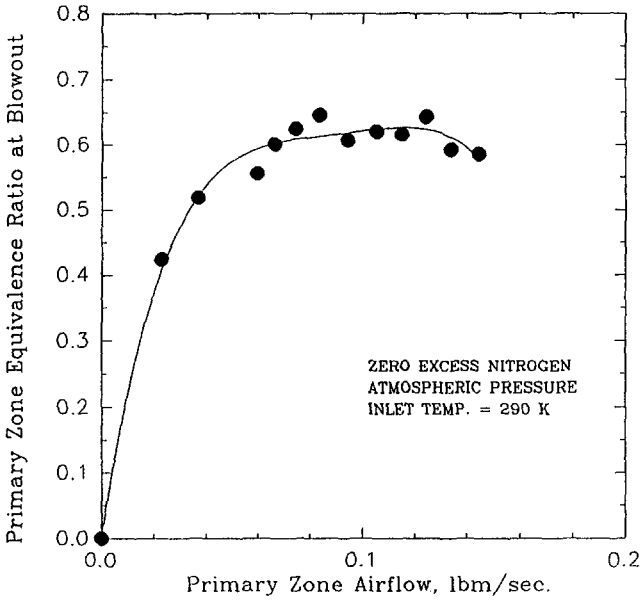

Fig. 8 Relation between primary zone equivalence ratio at blowout and primary zone airflow at atmospheric pressure in the 15 percent dome flow combustor

remained fixed for all tests reported. The low-swirl fuel injectors were used for all the data presently reported.

Without combustion, the required airflow rate and dome/shroud bypass flow splits were established. The combustor was lit and the torch ignitor turned off. Once thermal stability was established, the flow rates and flow splits were again taken. Fuel flow was then reduced in a series of progressively smaller steps, with allowance for thermal stabilization at each fuel decrement. Blowout was detected visually through the side windows. Instrumentation was automatically scanned both before and immediately after the ultimate fuel decrement.

Shown in Fig. 6 is the atmospheric pressure LBO fuel mass flow rate (all four injectors) with increase in primary zone airflow for zero excess nitrogen flow at 15 percent dome flow. The effect of nitrogen addition is given in Fig. 7 over a series of primary zone airflows. Both flow relationships are linear for the ranges covered, with LBO fuel flow increasing with both airflow and nitrogen flow. For the range of air and excess nitrogen flows covered at 15 percent dome flow, the primary zone equivalence ratio remains less than unity, as Fig. 8 indicates for zero excess nitrogen.

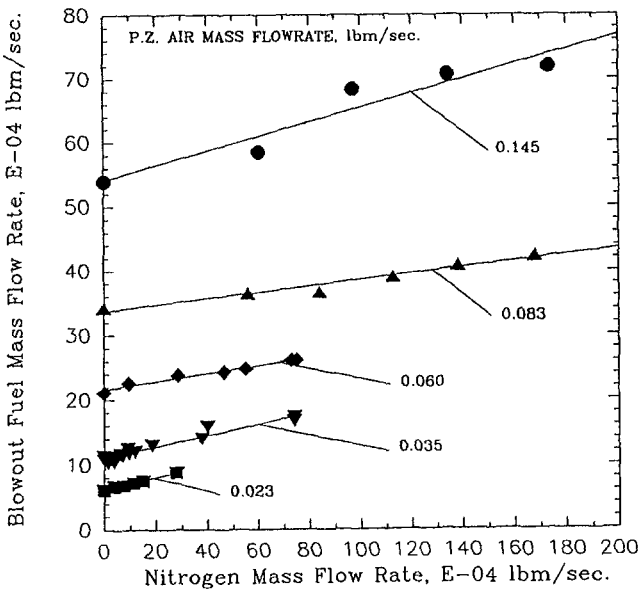

Fig. 7 Dependence of blowout fuel mass flow rate on excess nitrogen mass flow rate at several primary zone airflows in the 15 percent dome flow combustor

For 10 percent dome flow, the primary zone equivalence ratio can exceed unity when the combustor airflow is low and/or the nitrogen flow rate is high. Under these circumstances, the burning zone is greater in length than the primary zone, and extends to encompass sufficient air to burn all the fuel. When this happens, the flame extends around the first row of transverse air jets. Eventually, the local equivalence ratio can again exceed a value of unity, and the second row of air jets becomes involved in the combustion process. The result of this behavior is that as combustor loading is increased, a quasi-fuel-staging process (Sturgess et al., 1993b) develops. Quasi-fuel-staging for the Task 200 combustor at 10 percent dome flow is illustrated in Fig. 9, with the corresponding changes in burning zone length being shown in Fig. 10. When quasi fuel staging occurs, it is more realistic to refer to "burning zone" rather than primary zone. The burning zone length is determined by adding to the primary zone downstream air in bulk fashion until a local equivalence ratio of unity is reached or exceeded.

The inert gas, excess nitrogen dilution technique (Sturgess et al., 1992c) simulates low pressures through slowing chemical reaction rates by lowering the concentration of reactants, and through reduction in reaction temperature by virtue of the nitrogen heat capacity. If the mass flow rate of nitrogen is high relative to that of the air, it will also result in a reduction of residence time in the reaction zone. The viability of the technique depends on the assumption that combustion is not residence time limited. Fortunately, for LBOs the flame does not fill the complete combustor, even with quasi-fuel-staging. The presence of the excess nitrogen must be accounted for if constant residence time/reference velocity comparisons are to be made. It must be remembered that although the inert diluent can slow chemical reaction rates in a similar fashion to true low pressures, the actual pressure in the reactor is not reduced. Thus, reference velocity and residence time are conveniently independent of simulated pressure.

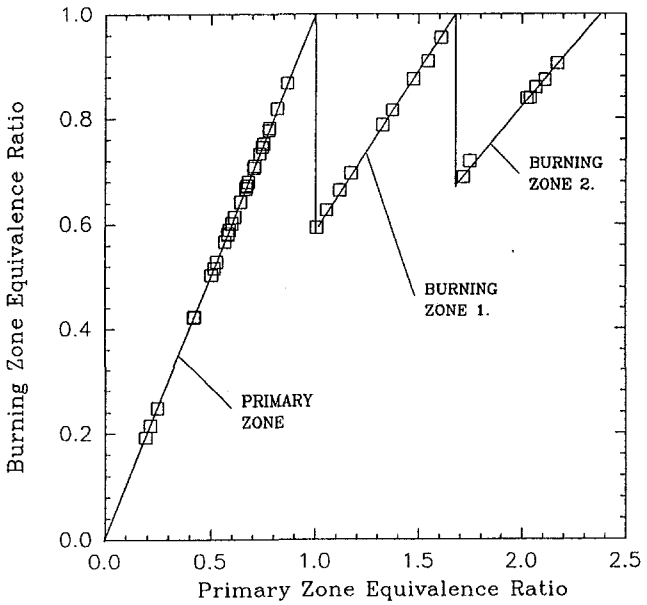

Fig. 9 Relationship between burning zone and primary zone equivalence ratios in the 10 percent dome flow combustor to illustrate quasi-staging of fuel

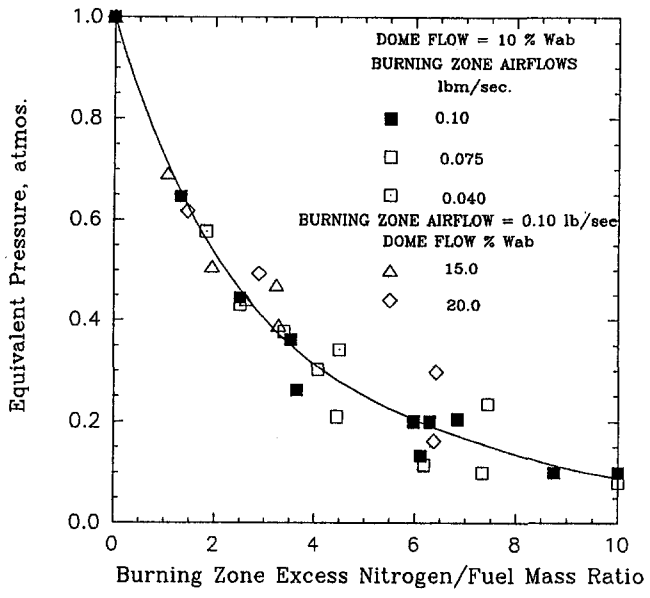

Fig. 11 Effect of equivalent pressure due to excess nitrogen on blowout characteristic for Task 200 combustor

The calibration of excess nitrogen as an inert diluent for simulation of low pressures is presented graphically by Sturgess et al. (1992c). Using the calibration of the inert diluent, an equivalent pressure for the LBOs can be obtained. The relation between equivalent pressure and burning zone excess nitrogen to fuel mass ratio is shown in Fig. 11 for burning zone airflows of 0.018 to 0.045 kg/s (0.040 to 0.100 lbm/sec) at 10 percent dome flow, and for 10, 15, and 20 percent dome flows at 0.045 kg/s (0.100 lbm/sec) burning zone airflow. Extremely low values of equivalent pressure can be achieved, although the technique does reach saturation for excess nitrogen to fuel mass ratios greater than 8.0.

The effect of equivalent pressure on blowout primary zone equivalence ratio with increasing primary zone airflow can be seen by comparing Fig. 12 (0.4 atm) against Fig. 8 (1.0 atm). Figure 12 is corrected to the same residence times as for Fig. 8. The correction is to multiply the observed blowout equivalence ratio at fixed inlet airflow by the ratio of total mass flows entering the primary zone without and with excess nitrogen. The equivalence ratio plateau observed at atmospheric pressure is reduced in presence at the lower pressure. This decrease appears to be due to the changing slope of the overall blowout curve (see Fig. 20 for example) at the higher combustor loadings associated with the lower pressure.

For 10 percent dome flow, the effect of equivalent pressure is complicated by the change in burning zone that takes place as combustor loading is increased. Figure 13 shows the variation in LBO burning zone equivalence ratio with equivalent pressure for burning zone airflows of 0.018 to 0.045 kg/s (0.040 to 0.100 lbm/sec), where the data have been linearly corrected to

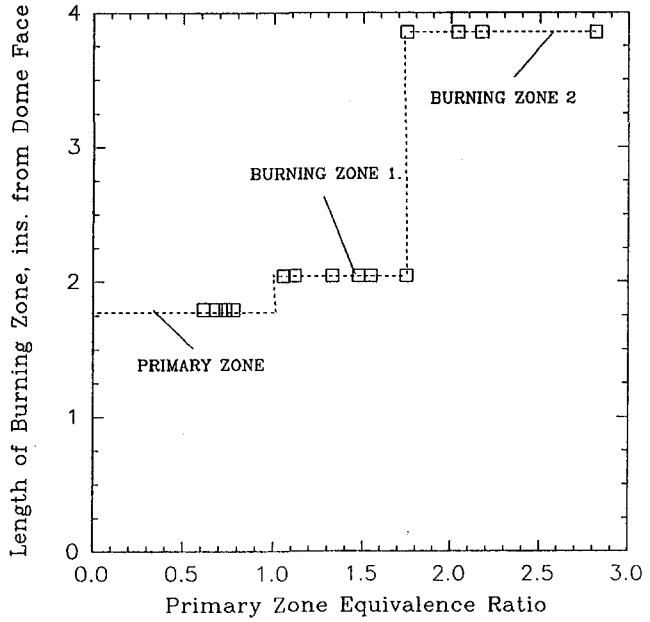

Fig. 10 Variation of burning zone length with primary zone equivalence ratio in the 10 percent dome flow combustor as a result of quasi-staging of fuel

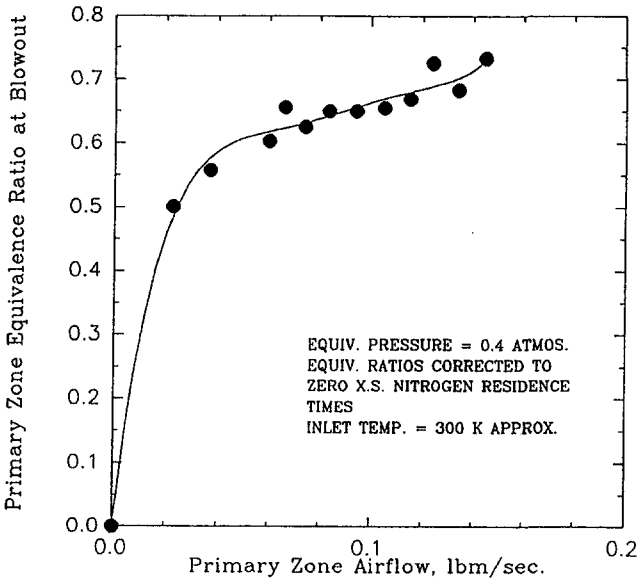

Fig. 12 Dependence of primary zone blowout equivalence ratio on primary zone airflow in the 15 percent dome flow combustor at 0.4 atm equivalent pressure

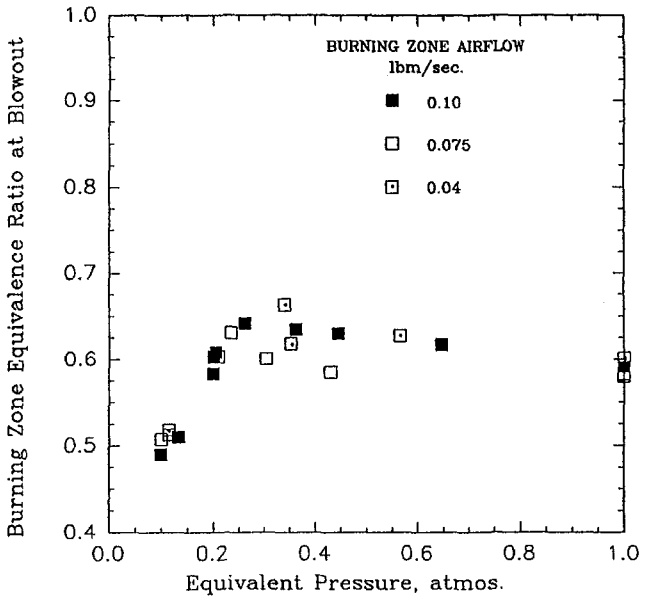

Fig. 13 Effect of equivalent pressure on burning zone equivalence ratio at blowout in the 10 percent dome flow combustor for several constant values of burning zone airflow

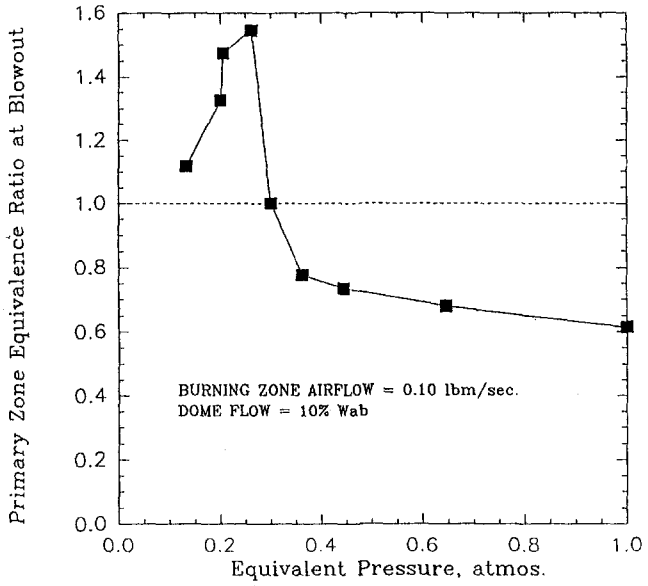

Fig. 14 Variation of primary zone equivalence ratio at blowout with decreasing equivalent pressure in the 10 percent dome flow combustor at a fixed burning zone airflow

zero excess nitrogen residence times. The three burning zone airflows correspond to constant (cold) reference velocities of 1.372, 1.036, and 0.549 m/s (4.5, 3.4, and 1.8 ft/sec), respectively. The blowout data for the three reference velocities collapse within the scatter of an individual reference velocity.

It can be seen that as the equivalent pressure is reduced the burning zone equivalence ratio at blowout increases slightly from the value at atmospheric pressure (loss of stability) to a maximum value of about 0.65 at 0.3 atm. Thereafter, it decreases sharply with further decrease in effective pressure (gain of stability). The peak in blowout occurs at an equivalent pressure that corresponds to a condition at which the primary zone reaches unity (uncorrected) equivalence ratio. (The peak blowout equivalence ratio is at a value less than unity due to the residence time correction necessary because of the excess nitrogen.) Thus, for equivalent pressures greater than 0.3 atm, the flame at blowout is stabilized in the primary zone; for equivalent pressures less than 0.3 atm, the flame is stabilized in a burning zone that includes and extends beyond the primary zone. Flame holding in this condition is provided by the first row of air jets supplementing the regular primary zone.

The discrete character of the air addition to the combustor and the burning zone (*B.Z.*) definition together allow the possibility that the uncorrected equivalence ratio could be below unity at quasi-staging, and that as the burning zone extends itself, the corrected equivalence ratio would fall as the equivalent pressure falls. The residence time correction then applied to the equivalence ratio will also increase as the equivalent pressure falls, due to the growing quantities of excess nitrogen introduced.

Figure 14 shows the variation of the uncorrected primary zone equivalence ratio at blowout with equivalent pressure for a constant *B.Z.* airflow of 0.045 kg/s (0.100 lbm/sec) [constant cold reference velocity of 1.372 m/s (4.5 ft/sec)] in the 10 percent dome flow combustor. The behavior is similar to that shown in Fig. 13 for the *B.Z.*'s, and shows unity equivalence ratio is reached at an equivalent pressure of 0.3 atmosphere. This confirms the interpretation of the minimum stability point in Fig. 13.

Figure 15 gives the combined *B.Z.* blowout behavior with different dome flows at constant *B.Z.* airflow, as the equivalent pressure is reduced. There is more scatter but the characteristics are again very similar to those of Fig. 13. The 20 percent dome flow combustor has a *P.Z.* that reaches an uncorrected unity equivalence ratio at 0.4 atm (from a plot similar to Fig. 14). The peak corrected *B.Z.* equivalence ratios at blowout depend on the dome flow, and increase with increasing dome flow. The peak corrected *B.Z.* equivalence ratio at LBO occurs at higher equivalent pressures for higher dome flow splits. Although Fig. 15 is for a constant cold reference velocity of 1.372 m/s (4.5 ft/sec), the higher dome flow combustor has a shorter *P.Z.* residence time than does the lower dome flow combustor. Note that the *B.Z.* stability for both dome flow splits is independent

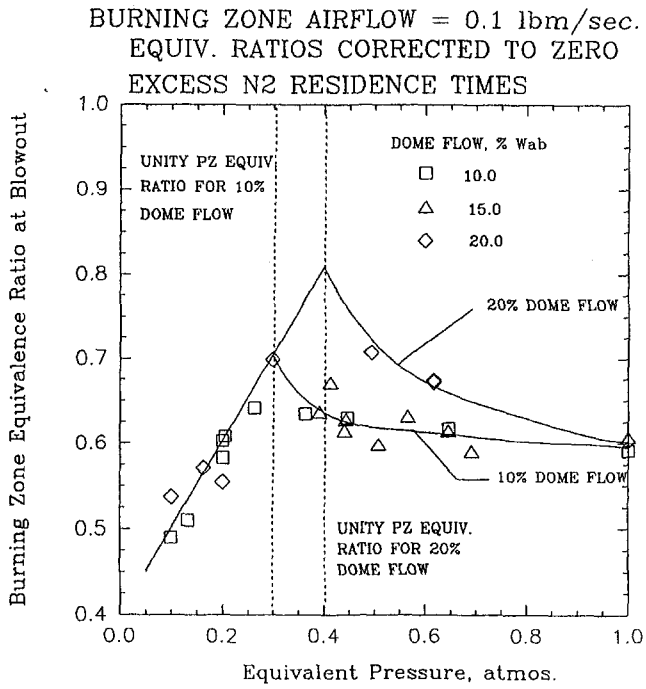

Fig. 15 Variation of burning zone equivalence ratio at blowout with equivalent pressure at fixed burning zone airflow, showing the dependence on dome flow for primary zone burning and the independence of dome flow for downstream burning

of dome flow when the flame holding also depends on jet stabilization as well as on the dome.

The lines shown on the figure for 10 and 20 percent dome flows are curve fits to the data that are forced to intersect the combined (linear) line at the respective value of equivalent pressure for which the *P.Z.* equivalence ratio reaches unity.

Flame Pattern Changes

For the 15 percent dome flow split, it was observed for high values of primary zone airflow that a marked change in primary zone flame shape took place, and this was also accompanied by a marked reduction in combustion noise. The two flame patterns have been denoted as a "lifted flame" (normal condition) and an "attached flame" (occurring at the higher flows). Figure 16 displays photographs of the two flames. Figure 17 is a repeat of Fig. 8 but with delineation of the flame type and some additional (no blowout) points to illustrate this effect. Comparison of Figs. 8 and 17 suggests that the attached flame

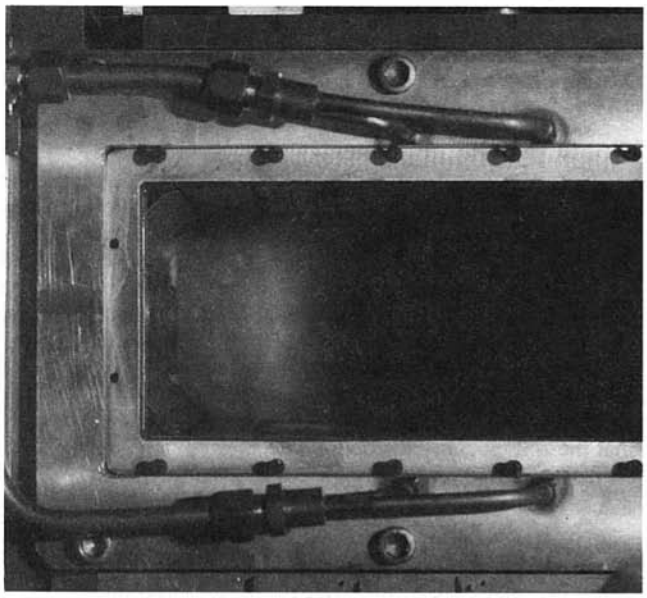

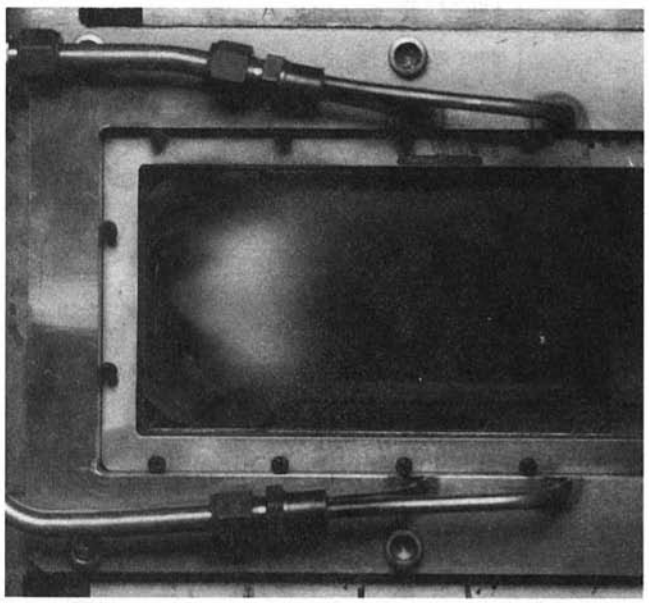

Fig. 16 Attached and lifted flames in the Task 200 combustor

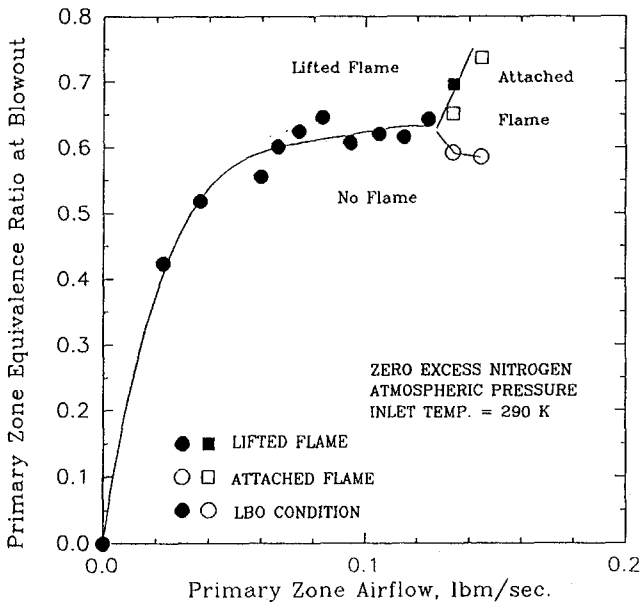

Fig. 17 Demonstration of different flame conditions at atmospheric pressure in the 15 percent dome flow combustor with primary zone burning

condition might represent a more stable combustion situation. The reduction in combustion noise also suggests this.

The blowout data presented up to Fig. 17 are all of a single flame type—the lifted flame. This is believed to be the more usual burning mode in combustors of the present type at these operating conditions. The attached flame was only encountered for extremely high values of airflow at the lower primary zone airflow splits. It was almost never encountered at the 20 percent dome flow. Since a significant proportion of the flow through the dome is air passing through the (airblast) fuel injectors, the injectors at these conditions are being operated "off-design." There is evidence from the technology combustor (Hedman et al., 1994) that the local flame characteristics immediately adjacent to the injector discharge are dictated by local stoichiometry distributions associated with the injector, i.e., a local flammability window is opened between the rich and lean limits that permits combustion close to the injector.

A definitive explanation of the circumstances of the attached flame/lifted flame phenomenon is not yet available, and it is being further explored in the (Task 150) technology-development combustor, which is a single Task 200 fuel injector element mounted in a version of the (Task 100) research combustor. The phenomenon has been reproduced in the Task 150 combustor and so, is clearly associated with the design of the fuel injectors. The behavior appears to be analogous to the attached/lifted flame behavior observed in the (Task 100) research combustor (Sturgess et al., 1992c, 1993a).

Correlated Data

Some of the blowout modeling being developed as part of this research effort is based on well-stirred reactor networks. Because of this, the collected blowout data have been correlated on the basis of well-stirred reactor theory. LBO data from the research combustor were successfully correlated (Sturgess et al., 1992c) by the combustor loading parameter, defined as,

$$L.P. = \frac{\dot{m}_{\mathrm{Tot}}}{VP^n F}$$

where

$\dot{m}_{\mathrm{Tot}} = \dot{m}_f + \dot{m}_a + \dot{m}_{N2}$, lbm/sec

V = reactor volume, ft^3
P = pressure, atm
n = $2\phi_{LBO}/(1 + \dot{m}_{N2}/\dot{m}_a)$, apparent global reaction order
F = $10^{0.00143T}/3.72$ (to correct to 400 K)
T = inlet temperature, K

Correction of the data to a constant inlet temperature of 400 K represents tribute to the pioneering well-stirred reactor work of Longwell, since 400 K was the inlet temperature used in his original experiments (Longwell et al., 1953).

The general form of the W.S.R. loading parameter correlation group follows Kretschmer and Odgers (1972), and has been in common use for many years; here, it has been modified to account for the use of excess nitrogen as a diluent, as described in Sturgess et al. (1992c). The intended use of the group is as a correlating parameter for experimental data. In general, the equivalence ratio of a combustor primary zone will be established at a specific design point by considerations other than flame stability. It will, therefore, be known at off-design point operating conditions where stability becomes important. The design engineer then desires to check whether or not the combustor as designed remains alight at these off-design conditions. This is done by determining if the operating line for the combustor falls within the previously determined appropriate stability loop for the type of combustor under consideration (see Sturgess et al., 1992a, for an example).

Well-stirred reactor modeling is a convenient and inexpensive method to introduce a (reasonably) full chemical reaction mechanism into consideration for calculations of lean blowout. A difficulty is in defining a suitable network to represent a practical combustor. One of the procedures being developed under this research effort is network definition via computational fluid dynamics (CFD) modeling (Sturgess et al., 1992a). For this reason, it is presently convenient to use the well-stirred reactor approach for the purposes of experimental data comparison.

Shown in Fig. 18 are the correlated blowout data for lifted flames only, in the 10 percent dome flow combustor. The blowout equivalence ratio is for the complete combustor, as is the reactor volume used in the loading parameter. The complete combustor airflow is the sum of (Fig. 5) dome and first, second, and third rows of transverse jet airflows, and this is used to calculate the overall equivalence ratio. The correlation achieved is quite satisfactory.

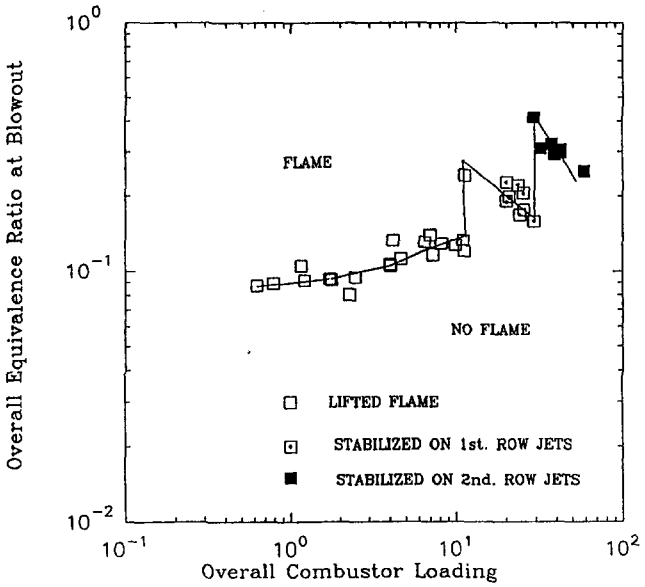

Fig. 18 Correlated LBO data, demonstrating quasi-staging in the 10 percent dome flow combustor for lifted primary zone and jet-stabilized flames

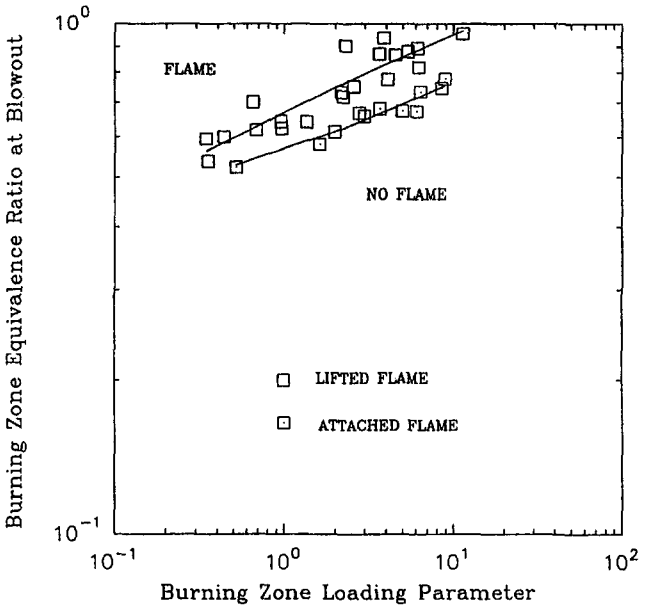

Fig. 19 Correlated LBO data in the 10 percent dome flow combustor, prior to quasi-staging (i.e., primary zone burning) for lifted and attached flames, showing improved stability with attached flames

It can be seen that the behavior up to a loading of 10 lbm/sec (ft^3 atm^n) follows the traditional lean-side stability loop characteristic form. The flame is stabilized only in the primary zone for these loadings. For loadings greater than 10, quasi-staging comes into effect as the flame grows first around the first row of transverse air jets in the combustor, and then, eventually extends to involve the second row of jets. The behavior can be easily related to Fig. 9. It is interesting to note that the staging behavior observed in the Task 200 generic combustor might also explain the LBO characteristic of another practical combustor presented in Sturgess et al. (1992a).

The correlated data for the 15 percent dome flow combustor do not exhibit quasi-staging up to a loading parameter of 15 lbm/sec (ft^3 atmos^n), and the 20 percent dome flow combustor does not evidence it up to loadings of 20 lbm/sec (ft^3 atmos^n). This is because of the higher primary zone airflows of these combustors.

In Fig. 19 the correlated LBO data for the attached and lifted flames up to the first quasi-staging point for the 10 percent dome flow combustor are compared. The loading parameters are based on the actual burning zones containing the flame. It can be seen that either flame can exist at a given loading parameter, and that the attached flame does indeed have improved stability over the lifted flame, as was suggested by Fig. 17. Again, there is, as yet, no definitive explanation for the circumstances that result in an attached or lifted flame condition.

The effect of dome flow for primary zone burning only is shown in Fig. 20 by comparing the correlated data for the 10 and 20 percent dome flow combustors. For the 10 percent case, both attached and lifted flame data are shown, and the flame effect is almost as strong an influence on stability as is the percent dome flow. Only two data points for attached flames in the 20 percent dome were available at the time of writing, and these fall in with the lifted flame data for this dome. The lifted flame data for the 15 percent dome flow combustor fall between the data for the 10 and 20 percent domes. Note that the higher primary zone loading for the 20 percent dome results in an increased sensitivity of LBO equivalence ratio to loading when overall loading exceeds

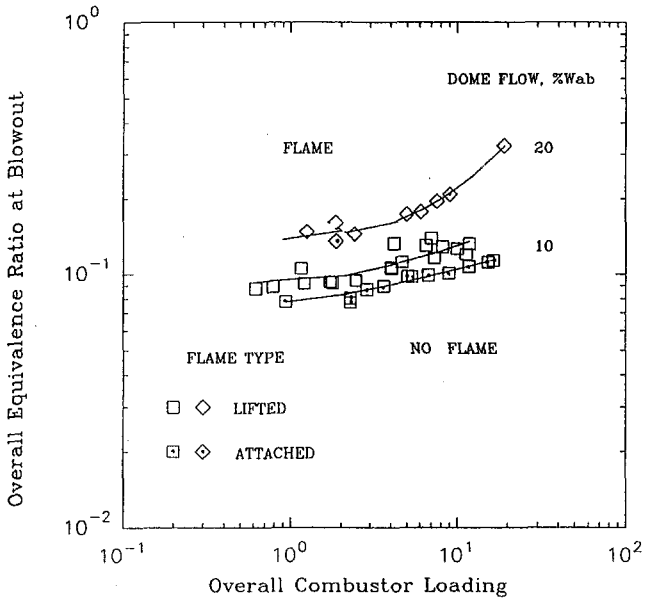

Fig. 20 Effect of dome flow for primary zone burning in the Task 200 combustor, for lifted and attached flames

10 lbm/sec (ft^3 atmos″). The effect of increased dome flow is to reduce the combustor stability.

Comparison With Well-Stirred Reactor

The stability performance of a combustor can be usefully compared with that of a well-stirred reactor (W.S.R.), which achieves its peak heat release rate (unity equivalence ratio) at very high values of loading parameter and whose lean blowout tends to the lean flammability limit of the reactants at very low values of loading parameter.

In order to make this comparison for practical gas turbine combustors, it is necessary to account for the (combustion) redundancy of the dilution zone of such combustors. This is because the dilution zone is generally not involved in the combustion process. In the case of the Task 200 generic combustor, the burning zone definition is used to describe the effective reactor portion of the total combustor.

Sturgess et al. (1991c) established that the Task 100 research combustor, operating on propane at near-blowout, was behaving as a well-stirred reactor. Therefore, well-stirred reactor performance is represented by the lean blowout results obtained (also using the excess nitrogen dilution technique for low pressures) in the Task 100 combustor.

Figure 21 compares the Task 100 research combustor stability characteristic with the collected burning zone equivalence ratios at lean blowout for the 10, 15, and 20 percent dome flow Task 200 generic combustors, on a basis of burning zone loading parameter.

For the generic combustor data presented, the burning zone is confined to the conventional primary zone. Furthermore, only lifted-flame data are shown. Thus, quasi-staging data have been excluded so that consistent types of flame-holding behavior in the generic combustor are compared with the W.S.R. Since the flames near blowout in the research combustor were all lifted, the partial-premixing character of the lifted flames in both combustors should be similar.

The figure shows that the generic combustor data, although not well correlated, show no systematic variation with dome flow, as they do for example in Fig. 20. For the range of loading parameters covered, the stability of the generic gas turbine combustor is less than that of the research combustor (W.S.R.). The W.S.R. reaches its peak heat release rate at a loading of about 50 lbm/sec (ft^3 atmos″) at 400 K inlet temperature, while the primary zone of the generic combustor appears to reach its peak heat release rate at a loading of roughly 8 to 10 lbm/sec (ft^3 atmos″). The W.S.R. is asymptotically tending to a blowout equivalence ratio of about 0.5 at low values of loading, less than 1.0 lbm/sec (ft^3 atmos″). The lean flammability limit for propane in air is about 0.5 at atmospheric pressure and temperature (Lewis and von Elbe, 1987). Although the data do not extend to sufficiently low values of loading parameter for either combustor, it appears from the respective slopes that the two stability curves might cross at values of loading parameter less than 0.1 lbm/sec (ft^3 atmos″). Such a crossing would imply better stability on a bulk equivalence ratio basis for the generic combustor than the flammability limits for the reactants. This can only arise because of imperfect mixing of fuel and air in the generic combustor, so that local burning takes place at other than bulk equivalence ratios.

On the evidence of this comparison, it would appear that the primary zone of the generic combustor is behaving relative to the W.S.R., exactly as might be expected from theory.

Figure 22 is a repeat of Fig. 21, except that only attached flame data for the generic combustor are presented. Attached flame data for the 20 percent dome flow combustor case are not extensive enough to be worth including.

The attached flame data are correlated extremely well and give a stability characteristic for the primary zone that is quite close to that for the W.S.R. over the range of loadings covered. The Task 200 attached flame data do not cover a sufficient range of loading parameter to permit observations concerning peak heat release rates, etc. It is not clear from consideration of Figs. 21 and 22 of the respective roles of mixing and combustion noise in the stability of lifted and attached flames.

Discussion

The Task 200 generic combustor rig has achieved its major design objectives of geometric flexibility and good optical access. The separately metered and controlled air supplies, interchangeable dome configurations, removable combustor liners, and alternative fuel injectors, allow a large number of combinations of major design variables to be explored. Aerothermochemical and liquid fuel atomization/vaporization aspects can be addressed through use of different gaseous and liquid fuels. The optical access permits superb direct viewing of the flame.

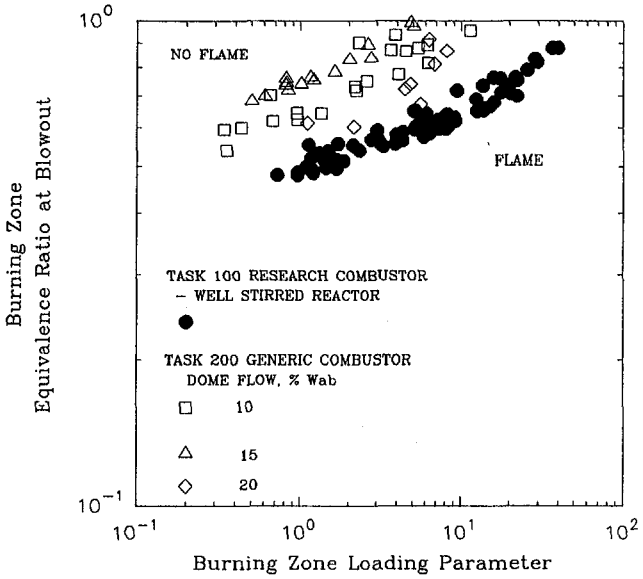

Fig. 21 Comparison of the generic combustor primary zone stability with lifted flames against well-stirred reactor stability

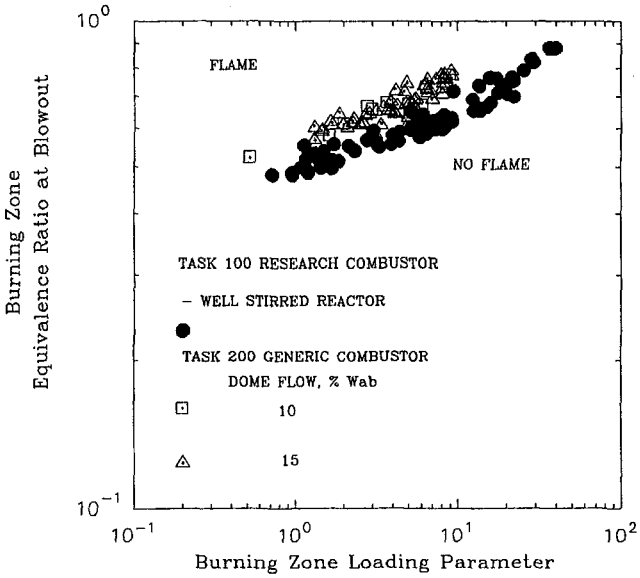

Fig. 22 Comparison of the generic combustor primary zone stability with attached flames against well-stirred reactor stability

The complex lean blowout behavior observed could not have been untangled to the extent that it has without reference to flame visuals. The "instant-replay" capability provided by the monitoring color videotapes formed valuable records and were particularly important in this. Three-dimensional temperature fields within the operating combustor are being mapped (Switzer et al., 1994) with CARS via the windows, and reasonably successful penetration deep across the combustor is being obtained. The planar imaging capability provided by the rig has not yet been used, however.

The simulation of low pressures by means of an inert diluent (nitrogen) and developed in the research combustor, has been successfully carried over to the generic combustor. Lean blowout data obtained in the generic combustor are consistent, repeatable, and reliable.

The combustion behavior as lean blowout is approached at simulated low pressures is extremely complicated. It contains quasi-staging of the fuel as loading in the combustor is increased. When quasi-staging takes place, the flame becomes stabilized by the combustion air jets, as well as in the primary zone. When jet stabilization exists, the lean blowouts are insensitive to dome airflow; without it, blowouts are sensitive to dome airflow. Flame changes from lifted to attached flames can occur, and at given loading either flame can exist, depending on how the loading is achieved.

Common flow features and behavior can be seen in the Task 100 research combustor, the Task 150 technology combustor, and the Task 200 generic combustor. However, there is much still to be understood in the generic combustor behavior. This complicated behavior will serve as a serious challenge when testing the efficacy of lean blowout modeling.

The blowout data can, in general, be successfully correlated by the combustor loading parameter based on the well-stirred reactor approach. However, as a result of the various flow aspects, a universal correlation did not result. This was not unexpected. Given the strong effects of the combustor geometric variables on burning zone flow patterns, a simple phenomenological correlation of experimental data is most unlikely ever to be general enough to form a unique design curve for lean blowout stability margin. The behavior of the correlated data in Fig. 18 confirms that for modeling purposes, the classical representation (Bragg, 1953) of a practical combustor as a single W.S.R. followed by a single plug-flow reactor, does not result in an adequate description of the combustion behavior during lean blowout. For this reason, it is essential to develop successful modeling techniques for lean blowout.

Lean blowout is a process that is dominated by chemical reaction effects. The use of well-stirred reactor modeling does allow a convenient introduction of full chemistry, whereas the cost of this is prohibitive with a CFD code. The efficacy of the W.S.R. approach depends on how well the chosen reactor network that must replace the classical description of a single W.S.R., represents the real combustor under consideration. The CFD calculation itself (with rudimentary chemistry at best) can be used to establish this network (Sturgess et al., 1992a). The influences of turbulence on chemical reaction rates are still unaccounted for, even with this procedure. Although it is possible in principle to extend the method to allow for unmixedness, using stochastic methods, this has not yet been done.

Conclusions

1 Experimental LBO data have been provided for a generic gas turbine combustor over wide ranges of operating conditions and can serve to test modeling of the lean blowout process.

2 The lean blowout behavior of the generic gas turbine combustor is much more complicated than had been suspected and would not have been understood without direct visual access to the flame structure. According to operating conditions, quasi-staging and flame structure changes were exhibited.

3 A universal correlation of LBO data, using a well-stirred reactor loading group, was not obtained when the major variables were confined to total air mass flow rate, primary zone air flow split, and operating pressure. Simple phenomenological correlations of experimental blowout data are not likely to be good enough to serve as design tools for stability margin in a gas turbine combustor. Some form of blowout modeling will be necessary for this purpose.

4 The classic representation of a gas turbine combustor, as consisting of a single well-stirred reactor followed by a plug-flow reactor, is not sufficient to represent LBO behavior. If stirred reactor modeling of LBO is to be used, it must consist of a reactor network capable of adequately representing the flow field and fuel distributions, and their changes with operating conditions.

Acknowledgments

The authors wish to acknowledge the contributions to this work from their colleagues at Wright-Patterson Air Force Base and Pratt & Whitney. The enthusiasm, encouragement, and support of Dr. W. M. Roquemore of Wright Laboratories has been particularly appreciated. Thanks also to Mr. Brian Knight of United Technologies Research Center who did the basic design work on the rig and who provided much help with operating procedures, and to Dr. David G. Sloan, formerly of Pratt & Whitney (current address: ABB, Windsor Locks, CT) who conducted the fuel injector and combustor effective area measurements. Mr. Irwin Segalman of Pratt & Whitney kindly arranged for engine hardware for this program. The work was supported by the U.S. Air Force Wright Laboratories, under Contract No. F33615-87-C-2822 to Pratt & Whitney, East Hartford, Connecticut. The authors thank Pratt & Whitney Engineering for permission to publish these results, and ISSI for additional funding.

References

Bragg, S. L., 1953, "Application of Reaction Rate Theory to Combustion Chamber Analysis," Aeronautical Research Council Pub. ARC 16170, London.

Heneghan, S. P., Vangsness, M. D., Ballal, D. R., Lesmerises, A. L., and Sturgess, G. J., 1990, "Acoustic Characteristics of a Research Step Combustor," AIAA Paper No. AIAA-90-1851 (to appear in the *Journal of Propulsion*).

Jeffs, R. A., 1962, "The Flame Stability and Heat Release Rates of Some Can-Type Combustion Chambers," *Proc. Eighth Symposium (International) on Combustion,* Williams and Wilkins, Baltimore, pp. 1014–1027.

Kretschmer, D., and Odgers, J., 1972, "Modeling of Gas Turbine Combustors—A Convenient Reaction Rate Expression," ASME JOURNAL OF ENGINEERING FOR POWER, Vol. 94, pp. 173–180.

Hedman, P. O., Sturgess, G. J., Warren, D. L., Goss, L. P., and Shouse, D. T., 1994, "Observations of Flame Behavior From a Practical Fuel Injector Using Gaseous Fuel in a Technology Combustor," ASME JOURNAL OF ENGINEERING FOR GAS TURBINES AND POWER, Vol. 117, pp. 441–452.

Lefebvre, A. H., 1983, *Gas Turbine Combustion,* Hemisphere Publishing Co., McGraw-Hill.

Lewis, B., and von Elbe, G., 1987, *Combustion, Flames and Explosion of Gases,* 3rd ed., Academic Press.

Longwell, J. P., Frost, E. E., and Weiss, M. A., 1953, "Flame Stability in Bluff-Body Recirculation Zones," *Ind. Eng. Chem.,* Vol. 45, No. 8, pp. 1629–1633.

Roquemore, W. M., Reddy, V. K., Hedman, P. O., Post, M. E., Chen, T. H., Goss, L. P., Trump, D., Vilimpoc, V., and Sturgess, G. J., 1991, "Experimental and Theoretical Studies in a Gas-Fueled Research Combustor," AIAA Paper No. AIAA-91-0639.

Stewart, D. G., 1956, *Selected Combustion Problems II,* AGARD/NATO, Butterworths, London, pp. 384–413.

Sturgess, G. J., Sloan, D. G., Roquemore, W. M., Reddy, V. K., Shouse, D., Lesmerises, A. L., Ballal, D. R., Heneghan, S. P., Vangsness, M. D., and Hedman, P. O., 1991, "Flame Stability and Lean Blowout—A Research Program Progress Report," *Proc. 10th ISABE,* Nottingham, England, pp. 372–384.

Sturgess, G. J., Sloan, D. G., Lesmerises, A. L., Heneghan, S. P., and Ballal, D. R., 1992a, "Design and Development of a Research Combustor for Lean Blowout Studies," ASME JOURNAL OF ENGINEERING FOR GAS TURBINES AND POWER, Vol. 114, pp. 13–19.

Sturgess, G. J., Heneghan, S. P., Vangsness, M. D., Ballal, D. R., and Lesmerises, A. L., 1992b, "Isothermal Flow Fields in a Research Combustor for Lean Blowout Studies," ASME JOURNAL OF ENGINEERING FOR GAS TURBINES AND POWER, Vol. 114, pp. 435–444.

Sturgess, G. J., Heneghan, S. P., Vangsness, M. D., Ballal, D. R., and Lesmerises, A. L., 1992c, "Lean Blowout in a Research Combustor at Simulated Low Pressures," ASME JOURNAL OF ENGINEERING FOR GAS TURBINES AND POWER, Vol. 118, pp. 773–781.

Sturgess, G. J., Heneghan, S. P., Vangsness, M. D., Ballal, D. R., Lesmerises, A. L., and Shouse, D., 1993a, "Effects of Back-Pressure in a Lean Blowout Research Combustor," ASME JOURNAL OF ENGINEERING FOR GAS TURBINES AND POWER, Vol. 115, pp. 486–498.

Sturgess, G. J., McKinney, R., and Morford, S., 1993b, "Modification of Combustor Stoichiometry Distribution for Reduced NO_x Emission From Aircraft Engines," ASME JOURNAL OF ENGINEERING FOR GAS TURBINES AND POWER, Vol. 115, pp. 570–580.

Switzer, G., Sturgess, G. J., Sloan, D., and Shouse, D., 1994, "Relation of CARS Temperature Fields to Lean Blowout Performance in an Aircraft Gas Turbine Generic Combustor," AIAA Paper No. 94-3271.

Aero-Engine Derivative Gas Turbines for Power Generation: Thermodynamic and Economic Perspectives

J. H. Horlock
Whittle Laboratory,
Cambridge, United Kingdom

Both the direct use of aero-engine hardware, in gas turbines for power generation, and the indirect influence of aero-engine technology, in the design of more conventional heavy-duty plants (including combined cycle gas turbines, CCGTs), are reviewed.

1 Introduction

Aero-engine technology has played a major part in the development of both the industrial gas turbine and, more recently, the combined cycle gas turbine (CCGT) plant. A distinction may be drawn between the direct use of developed aero-engine hardware in power generation (and in marine applications), and the more indirect influence of aero-engine technology, particularly in design of heavy-duty gas turbines. Here these two roles are reviewed, together with how they affect the thermodynamics and economics of power plant development.

The choice of the form of power generator depends partly on the thermodynamic cycle, but overall on economics—principally the levelized (long-term) price for electricity ($P\hat{E}$) but also plant reliability. Williams (1978) derived a simple expression for unit electricity price:

$$Y\hat{E} = P\hat{E}/WH = \beta C_0/WH + \zeta/\eta + [OM]/WH$$
$$= \beta C_0/WH + \zeta[HR] + [OM]/WH \quad (1)$$

The dominant factors are the capital cost per kilowatt ($C\hat{O}/W$), which generally decreases inversely as the square root of the power (i.e., as $W^{1/2}$), the fuel price ζ, the thermal efficiency η (or its inverse, the heat rate [HR]), the utilization (H hours per year), and to a lesser extent the operational and maintenance costs (OM). β(i,N) is the discount factor, dependent on the interest or discount rate (i) and the life of the plant (N years).

Figure 1 shows simply how $Y\hat{E}$, less the (OM/WH) component, varies with ($C\hat{O}/W$) and (HR) (or η), for H = 4000 hours and ζ = 1 c/kWh. The location of a particular plant on this graph is critical to its marketability and this will be discussed in detail later. But for the present it may be noted that a change in efficiency, say from 40 percent to 41 percent would be worthwhile if it cost less than 25-30 $/kW in capital cost to implement.

2 History

The history of aero-engine influence on the development of the industrial gas turbine is a long one. It was the war-time development of the jet engine that emphasized the potential of the gas turbine for use in power generation, mechanical drive applications, and marine propulsion. Following the early work by aeronautical engineers like A. A. Griffith of the R.A.E. and of course Sir Frank Whittle and his colleagues, many industrial steam turbine designers (such as D. M. Smith, of Metrovick in the UK, R. P. Kroon of Westinghouse in the USA) became involved in development of the gas turbine. Later, some members of these teams remained in the aero-engine field while others moved into the power generation industry.

For example, one of Whittle's engineers, G. B. R. Feilden, joined Ruston and Hornsby of Lincoln and designed a most successful new industrial gas turbine. The key to Feilden's success was in the application of sound logical design, using his aero-engine experience, to a simple gas turbine cycle, producing a rugged and reliable engine (see Feilden et al., 1956).

Industrial gas turbine design proceeded steadily in the sixties and seventies, but has moved much more rapidly in recent years, particularly with the advent of the combined cycle gas turbine/steam turbine (or CCGT) plant (Horlock, 1992).

The "traditional" approach to the use of aero-engine derivatives has been to use the aero-engine as a gas generator (see the perceptive early review by Williams and Larson, 1988). The earliest direct use of developed aero-engines essentially involved the simple replacement of the final nozzle by a power turbine, for example the Rolls-Royce Avon (Holmes Fletcher, 1963, and GEC Rolls-Royce, 1985) and the GE LM 2500 gas generator (derived from the TF39/CF6-6, pressure ratio 18.8). Both were examples of single-shaft units with power turbines added.

This traditional approach was extended to the use of two-shaft engines (see Fig. 2, taken from Haaser and Casper, 1991). The fans were removed and separate power turbines added (e.g., the GE LM 1600 based on the F404 turbofan aircraft engine, with a pressure ratio of 22, and the LM 5000, based on the CF 6-50 engine, with a pressure ratio of 26). The LP compressors were modified (essentially to absorb the compression provided by the original fan root), new LP turbines were designed to drive the (modified) LP compressors, and new power turbines were provided on separate shafts. The modification of the Rolls-Royce three-shaft RB211 followed essentially the same principle; the fan was eliminated, together with its turbine, to form a two-shaft gas generator and the power turbine was added (GEC Rolls-Royce, 1985).

Subsequently industrialization of the big turbofan aero-engine gas turbines has followed another route (see Fig. 3, also from Haaser and Casper). In this approach, following the design of the GE LM 6000 gas turbine, the HP core has been used, the LP compressor redesigned (essentially taking the place of the fan root and the original LP compressor but employing a degree of commonality in that design), and a new LP turbine designed to act as a drive for the new LP compressor and as a power turbine. The three-shaft Rolls-Royce industrial Trent has involved similar modification. The two-shaft IP and HP core has been retained but the fan turbine replaced by a power turbine

Contributed by the International Gas Turbine Institute for publication in the JOURNAL OF ENGINEERING FOR GAS TURBINES AND POWER. Manuscript received by the International Gas Turbine Institute September 15, 1996. Associate Technical Editor: L. A. Riekert.

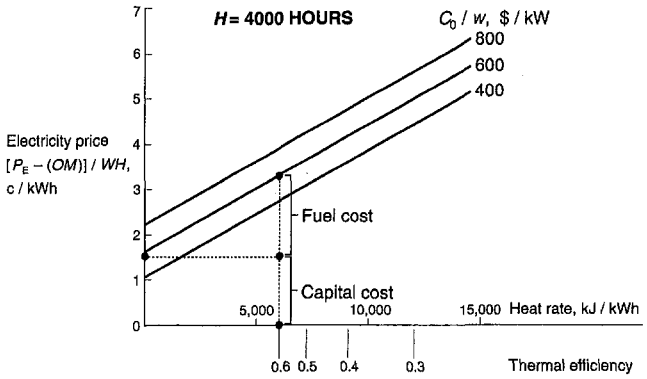

Fig. 1 Unit electricity price (less operational and maintenance costs) as a function of specific capital cost (C0/W) and heat rate (or thermal efficiency)

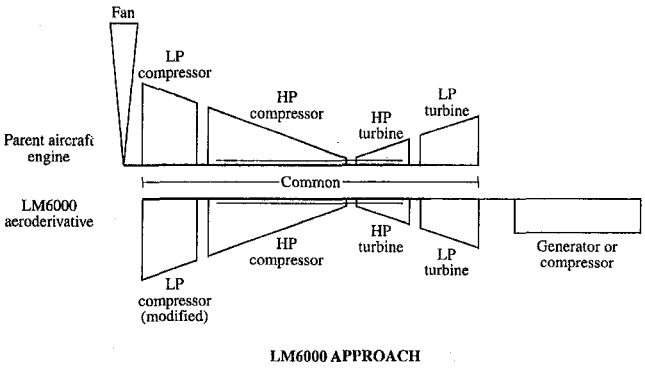

Fig. 3 LM 6000 approach to the use of aero-engine derivatives (after Haaser and Casper)

also driving a modified LP compressor, all on the third shaft (Rolls- Royce Industrial Power Group, 1995).

The use of components from various previous engines is well illustrated by Haaser and Casper (Table 1); the LM 6000 has relied on components from earlier engines, not only two aircraft engines but the earlier LM 5000. The derivation of the whole LM series from aircraft engines is shown in Table 2, which also illustrates the continual advance in turbine entry temperatures, and the corresponding increases in compressor pressure ratio.

In these direct applications of aero-engine derivatives, an objective has been to minimize the modification of the gas generator (except for necessary modification of the combustor to cater for a different fuel and to reduce emissions). Where a fan is removed, the pressure ratio of the redesigned LP compressor is increased, so that the nondimensional flow and rotational speed functions remain little changed at entry to the HP compressor, and hence through the gas generator.

Aero-engine derivatives have gained a substantial part of the market in offshore and pipeline applications and in marine propulsion. They have gained a relatively small share of the power generation market for gas turbines—perhaps 7–10 percent. This has been dominated by the heavy industrial gas turbine, which has benefited from the indirect influence of aero-engine design (see Section 4).

3 Thermodynamics of Simple Cycle and CCGT Plants

First a different thermodynamic philosophy can be discerned in the design of the aero-engine derivatives and the heavy-duty gas turbines. In spite of modifications, such as removing the fan and modifying the LP compressor and turbine, the former

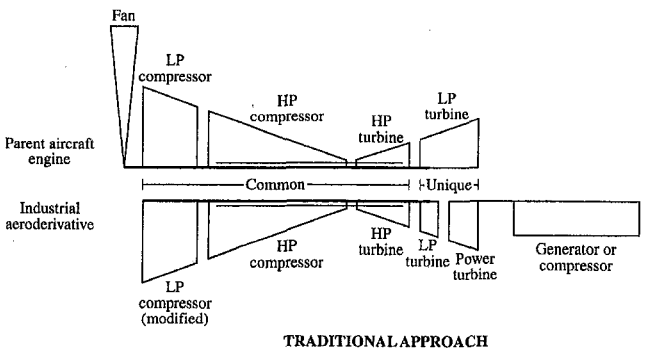

Fig. 2 Traditional approach to the use of aero-engine derivatives (after Haaser and Casper)

are essentially higher pressure ratio engines than the latter. This has meant that the derivatives have been little used in CCGT applications because of the relatively low gas turbine exhaust temperatures.

The efficiency of the simple gas turbine cycle peaks at a high pressure ratio, increasing with maximum turbine entry temperature (T_{max}), as is illustrated in Fig. 4, after Davidson and Keeley (1991). The aero-engine derivatives (now usually two or three-shaft) have pressure ratios close to the optimum, e.g., 30 to 1 for the LM 6000 with a T_{max} of 1270°C.

In contrast, the heavy industrial gas turbines (in simple cycle and usually single-shaft) historically have had a lower maximum temperature (T_{max}) and have also been of lower pressure ratio, even less than that for maximum efficiency at the lower T_{max}. But the loss of efficiency resulting from operation below the optimum is small because the efficiency-pressure ratio curves are flat.

However, with the advent of the CCGT plant, a high pressure ratio is no longer required anyway, even on efficiency grounds. When the lower steam cycle is added, taking its heat supply from the gas turbine exhaust and generating extra work, the optimum pressure ratio of the gas turbine part of the combined cycle plant drops considerably, down to the level with which the heavy plant can cope on its single shaft.

This point on optimum pressure ratio was emphasized in the Calvin Rice lecture (Horlock, 1995). The efficiency of a CCGT plant (η_{CP}) may be simply expressed in terms of the thermal efficiency of the higher (gas turbine) plant (η_H), and the overall efficiency ($[\eta_O]_L$) of the steam plant (the product of its thermal efficiency, η_L, and the boiler efficiency of the HRSG, η_B, which increases as the stack temperature comes down with the use of sulfur-free fuels). Thus

$$\eta_{CP} = \eta_H + \eta_B\eta_L - \eta_B\eta_H\eta_L = \eta_H + [\eta_O]_L - \eta_H[\eta_O]_L \quad (2)$$

Differentiation of this expression with respect to pressure ratio, with all other parameters held constant, to determine the maximum η_{CP}, leads to the approximate result

$$\partial\eta_H/\partial r = -[1 - \eta_H]/[1 - [\eta_O]_L]\ \partial[\eta_O]_L/\partial r$$
$$\approx -[\eta_O]_L/\partial r \quad (3)$$

Thus the optimum efficiency of a CCGT plant occurs when the gas turbine efficiency is still increasing with pressure ratio, but the steam turbine plant efficiency is dropping with gas turbine pressure ratio (turbine exhaust temperature dropping and steam turbine maximum temperature and thermal efficiency dropping with it). This has been well illustrated by Briesch and his colleagues at Westinghouse (1994). The efficiency pressure ratio curve is very flat (Fig. 5) and little combined plant thermal efficiency is lost by designing below or above the optimum; however specific power begins to drop with increasing the pressure ratio above that for optimum efficiency.

Table 1 LM 6000 design heritage

Module	Production Source
Low pressure compressor	LM 5000
High pressure compressor	CF6-80C2
Combustion system	CF6-80C2, LM 5000
High pressure turbine	CF6-80C2
VIGV, front and rear frames	New

Thus the requirement for a much lower optimum pressure ratio in the CCGT plant tends to negate the case for using the aero-engine derivative (with its high pressure ratio) in a CCGT application.

4 The Indirect Use of Aero-engine Technology in Design of Heavy-Duty Plants

As opposed to the direct importation of hardware described in Section 2, aero-engine technology has had a major indirect influence on heavy-duty industrial plant development, through the use of design techniques. The large manufacturers have improved performance in this way, mainly by increasing component efficiency and turbine entry temperature (using new materials and blade cooling), with the compressor pressure ratio increasing as maximum temperature has been raised.

An illustration of this indirect effect is the increase in thermal efficiency achieved by the Westinghouse/RR alliance, which has utilized aero-engine technology in the 501G gas turbine. A gain of about 3 percent - from 55 percent to 58 percent on combined cycle thermal efficiency - is expected from increases in T_{max} and turbine and compressor efficiency.

Jansen et al. (1995) have described the progress made by Siemens, in collaboration with Pratt and Whitney, on their V84.3 heavy-duty gas turbine, by increasing compressor and turbine efficiency, refining the cycle and increasing turbine inlet temperature. In the compressor, use of controlled diffusion aerofoils and custom tailored blading near the end walls have provided both increased efficiency and surge margin. In the turbine, CFD design has reduced profile and secondary losses, and aero-engine cooling configurations and single crystal materials have been introduced. Back to back tests with the original engine have shown a 5 percent improvement in heat rate.

The GE F family of gas turbines have also benefited from similar applications of aero-engine technology.

Table 2 GE use of aero-engine derivatives

ENGINE	TYPE	A/E DERIV	INDUSTRIAL VERSION PRESSURE RATIO [NOMINAL]	TET °C [NOMINAL]
LM 1600	2 SHAFT GAS GEN.+ POWER TURBINE	F404	22.0	1240
LM 2500	1 SHAFT GAS GEN.+ POWER TURBINE	TF39/ CF6-6	18.8	1230
LM 5000	2 SHAFT GAS GEN.+ POWER TURBINE	CF6-50	26.0	1175
LM 6000	2 SHAFT WITH INTEGRATED POWER TURBINE	CF6-80C2	30.0	1270

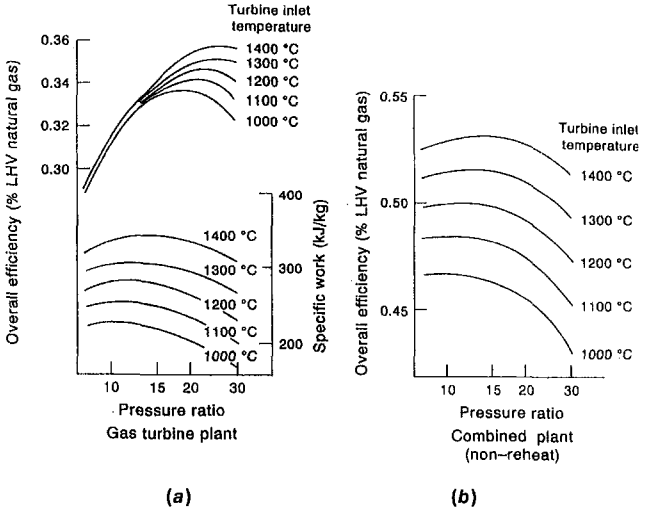

Fig. 4 (a) Efficiency and specific work—simple gas turbine plant; (b) efficiency of CCGT plant (nonreheat) (after Davidson and Keeley)

5 Some Recent Developments in Heavy-Duty Industrial Plants

A recent major development in heavy-duty industrial plants has been the introduction of closed-loop steam cooling of the gas turbine in the new H combined cycle system (Corman and Paul, 1995). "Chargeable" compressor air for cooling (which subsequently enters the main gas stream with a performance penalty) has been replaced by steam drawn from the exit from the HP steam turbine. This steam cools the first and second stages of the gas turbine, but is itself reheated in the process, and rejoins reheated steam from the HRSG before entry to the LP steam turbine. This "closed-loop" cooling enables the turbine (first rotor) inlet temperature to be increased while the combustion (firing) temperature is held approximately constant, maintaining reduced emissions.

A separate and distinct line of development for heavy-duty plants has been introduced by ABB (1993). After their steady development of the relatively low-pressure simple cycle, ABB have recently produced the GT 24 and 26 CCGT plants with a much higher pressure ratio (30 to 1), splitting the gas turbine expansion and introducing sequential combustion (or reheat). The optimum pressure ratio for this type of cycle is indeed higher (well over 30). ABB have achieved such high pressure ratios on a single shaft (by use of variable stators).

6 A Future Development—the ICAD Proposal for Intercooling in the Gas Turbine Cycle

A recent stimulus toward the further introduction of aero-engine technology into power generation has come from the

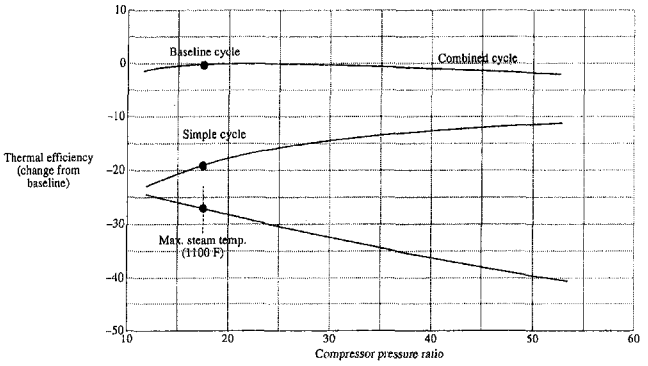

Fig. 5 Change in efficiency of CCGT plant with pressure ratio, for simple cycle and combined cycle (after Briesch et al.)

Collaborative Advanced Gas Turbine program, initiated first by Pacific Gas and Electric, but subsequently sponsored by EPRI and many other utilities. One proposal within this program is ICAD (the intercooled aero-engine derivative, using intercooling within the compression process), described by Hay (1994).

This choice of cycle is of particular thermodynamic interest. Intercooling alone in a simple gas turbine cycle increases the specific work but lowers the thermal efficiency; similarly the introduction of reheat alone (within the expansion process) increases the specific work at the expense of lower efficiency. But the addition of intercooling and/or reheat to a recuperative gas turbine cycle not only raises the specific work but also the thermal efficiency.

However, this is a simplistic and somewhat academic approach. In practice, the introduction of intercooling in the simple cycle allows the lower temperature delivered by the HP compressor (for a given pressure ratio) to be used either (i) to give an increased turbine entry temperature with the same quantity of cooling air or (ii) to reduce the cooling air quantity and maintain the same turbine entry temperature. In either case it may be possible to maintain the thermal efficiency of the simple cycle while introducing the intercooler, as well as gain on specific work.

This point is again illustrated by Briesch et al. (1994). Their calculation of gas turbine (simple cycle) efficiency (η_H) with and without intercooling shows little change in thermal efficiency, because of this effect - the turbine cooling air taken from the compressor exit being at a lower temperature when intercooling is used between LP and HP compressors.

But another point of interest from Briesch's calculations relates to the use of the intercooled gas turbine in a CCGT plant. Although both the higher and lower cycle efficiencies η_H and $(\eta_O)_L$ are virtually unchanged, the overall CCGT plant efficiency falls (Fig. 6). This drop is related to an additional term that must be added to the expression for CCGT efficiency (Eq. (2)) because of the heat rejection in the intercooler Q_{IC}. The equation then becomes

$$\eta_{CP} = \eta_H + [\eta_O]_L - \eta_H[\eta_O]_L - \nu_{IC}[\eta_O]_L \qquad (4)$$

where ν_{IC} is the ratio of Q_{IC} to the heat supplied. If this ratio is, say, 0.1, and the steam plant overall efficiency is, say, 30 percent, then we may expect a drop in CCGT thermal efficiency of 3 percent, of the order encountered by Briesch et al. in their calculations.

7 Discussion

So at least four lines of development in gas turbine power generation may be discerned:

(i) The heavy-duty simple cycle gas turbine, benefiting indirectly from aero-engine experience. This plant has moderate capital cost, and has a relatively low pressure ratio.

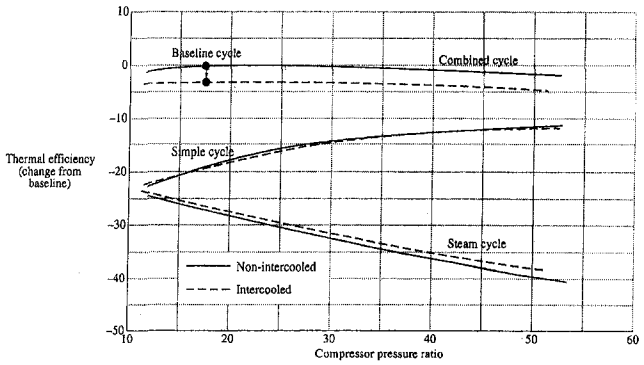

Fig. 6 Effect of intercooling on simple cycle and combined cycle efficiencies (after Briesch et al.)

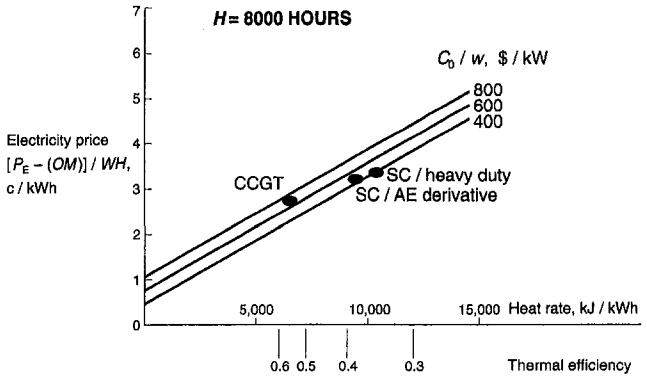

Fig. 7 Unit electricity price—simple cycle (heavy-duty), simple cycle (aero-engine derivative), and CCGT plants compared for high utilization (H = 8000 hours)

(ii) The aero-engine derivative simple cycle gas turbine, now usually two-shaft and of high pressure ratio. The capital cost per kilowatt of this plant is surprisingly little different from (i) (indeed perhaps slightly higher), in spite of its being derived from developed aero-engines.

(iii) The heavy-duty CCGT plant, based on (i), which has a high thermal efficiency but increased capital cost. This type of plant has generally been unreheated and of relatively low pressure ratio but a recently developed reheated plant has involved a much higher pressure ratio.

(iv) The ICAD aero-engine derivative gas turbine plant, which will have high specific power, moderately high efficiency, high pressure ratio. Capital cost is as yet uncertain, but probably less than the heavy-duty CCGT plant.

Type (ii)—the high-pressure-ratio aero-engine derivative—has not often been used in "conventional" CCGT plant application, but has been developed for steam injection or STIG (see Tuzson's excellent review (1992) and Williams and Larson (1988)), for cogeneration[1] (e.g., in the provision of industrial process steam), sometimes for both (Kolp and Moeller, 1989). Supplementary (exhaust duct) firing is frequently used in cogeneration to control steam production or process temperature, which eliminates the disadvantage of the low gas turbine exhaust temperature in aero-engine derivatives.

The key to the choice between these options lies in economics—the levelized price for electricity. The balance is often a fine one and comparisons between prices are dependent on several assumptions, most of them subject to criticism and argument. Rough locations for types (i), (ii), and (iii) are given on the electricity price charts of Figs. 7 and 8, for 8000 hours and 4000 hours utilization, respectively. For 8000 hours the CCGT plant type (iii) has a clear advantage in spite of increased capital cost. At 4000 hours the CCGT plant loses this advantage over the aero-engine derivatives because of the increase in the capital cost element (H has been decreased).

However, more direct comparisons should include factors of operational and maintenance, the cost of which have been omitted in the presentations of Figs. 7 and 8. The characteristics of modular "quick build" and relatively light handling have made the aero-engine derivatives popular in such applications as offshore rigs. They can be replaced quickly and their compact design makes them easier to site (or to repower existing plants).

8 Conclusions and Future Developments

Some conclusions on the aero-engine's role in industrial power generation may be drawn from this review.

[1]In Europe, cogeneration is usually referred to as combined heat and power or CHP (see Horlock, 1987, 1996).

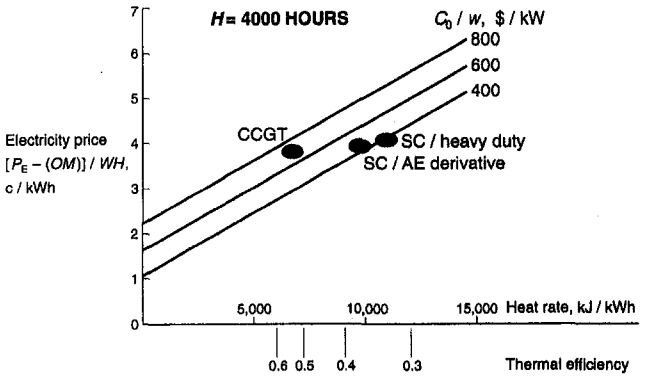

Fig. 8 Unit electricity price—simple cycle (heavy-duty),simple cycle (aero-engine derivative), and CCGT plants compared for low utilization (H = 4000 hours)

First, it would appear that at the largest sizes (200 MW and above), and for high utilization, the heavy-duty CCGT plant is the most attractive (either with the low pressure ratio simple gas turbine or the higher pressure ratio reheated gas turbine). The effect of high thermal efficiency in reducing the fuel cost term in the unit electricity price is dominant (high utilization has reduced the size of the capital cost term). Indirect use of aero-engine technology has shown, and is still showing, major benefit in this respect.

Second, in the lower power range (say 12–40 MW), the aero-engine derivative simple cycle plant has been a good competitor. Its high pressure ratio gives it an efficiency edge over the low pressure ratio machine, even if its capital costs are slightly higher (perhaps 10 percent or so) but its maintenance costs may be high.

Third, at very low power level (say up to about 15 MW), increased capital cost (perhaps 30 percent) counts against the aero-derivative, but it has found a strong market in off-shore and pipeline applications. Its major success in the marine field should be recognized, an area not covered in this paper on industrial power generation.

Fourth, the ICAD machine should increase the upper limit for the aero-engine derivative beyond 40-50 MW (particularly if its efficiency can be held quite high). There may then be little difference between the heavy-duty simple cycle plant and the ICAD on electricity price, but it may again be the question of higher maintenance costs for the latter that decides the issue.

Use of aero-engine technology will continue to raise component efficiency and T_{max}, but limits may be approaching. It appears that the introduction of more complication in the gas turbine cycle (e.g., recuperation in addition to intercooling and reheat) would give relatively little gain in thermal efficiency compared with the latest CCGT plants.

A better route to follow is likely to be the further integration of the gas and steam cycles in CCGT plants (e.g., steam cooling of gas turbine plant combustion transition sections and turbines, as in recent plants announced). The humid air turbine plant (e.g., El-Masri, 1988) is another "integrated" proposal; it has the STIG type advantage of increased power output, coupled with the promise of high efficiency, but of course it also has the penalty of a make-up water requirement.

Acknowledgments

The author is grateful to colleagues in the Whittle Laboratory for their comments, and to many friends in industry: European Gas Turbines (Kelvin Bray particularly) and GE, Rolls Royce, and Westinghouse.

References

ABB Power Generation, 1993, GT24, "Advanced Cycle System, the Innovative Answer to Lower the Cost of Electricity," ABB Brochure PGT 2103 93.

Briesch, M.S., Bannister, R.L., Diakunchak, I.S., and Huber, D.J., 1994, "A Combined Cycle Designed to Achieve Greater Than 60 Percent Efficiency," presented at ASME COGEN-TURBO 1994.

Corman, J.C., and Paul, T.C., 1995, "Power Systems for the 21st Century—"H" Gas Turbine Combined Cycles," GE Power Systems, Report No. GER-3935.

Davidson, B.J., and Keeley, K.R., 1991, "The Thermodynamics of Practical Combined Cycles," *Proc. IMechE Conference on Combined Cycle Gas Turbines,* pp. 28-50.

El-Masri, M.A., 1988, "A Modified High-Efficiency Recuperated Gas Turbine Cycle," ASME JOURNAL OF ENGINEERING FOR GAS TURBINES AND POWER, Vol. 110, p. 233.

Feilden, G.B.R., Thorn, J.D., and Kemper, M.J., 1956, "A Standard Gas Turbine to Burn a Variety of Fuels," *Proc. IMechE,* Vol. 170, No. 20, p. 664.

GEC Rolls-Royce (Power Generation Limited), 1985, "Gas Turbine Power Generation Systems," Brochure GR1015.

Haaser, F.G., and Casper, R.L., 1991, "Development of the LM 6000: the World's Most Efficient Simple Cycle Industrial Gas Turbine," *Proc. ASME COGEN 1991*, pp. 177-188.

Hay, G., 1994, "Intercooled Aero-derivative (ICAD) Gas Turbines," *ASME IGTI Global Gas Turbine News*, Fall.

Holmes Fletcher, A., 1963, "The Avon Aircraft Engine and Its Industrial Power Applications," *Proc. IMechE*, Vol. 177, No. 38, p. 1068.

Horlock, J.H., 1987, *Co-generation: Combined Heat and Power,* Pergamon Press, Oxford (see also Krieger, Melbourne, FL, 1996).

Horlock, J.H., 1992, *Combined Power Plants*, Pergamon Press, Oxford.

Horlock, J.H., 1995, "Combined Power Plants: Past, Present and Future (the Calvin Rice Lecture)," ASME JOURNAL OF ENGINEERING FOR GAS TURBINES AND POWER, Vol. 117, p. 4.

Jansen, M., Zimmerman, H., Kopper, F., and Richardson, J., 1995, "Application of Aero-Engine Technology to Heavy Duty Gas Turbines," ASME Paper 95-GT-133.

Kolp, D.A., and Moeller, D.J., 1989, "World's First Full STIG LM 5000 Installed at Simpson Paper Company," ASME JOURNAL OF ENGINEERING FOR GAS TURBINES AND POWER, Vol. 111, pp. 200-210.

Rolls-Royce Industrial Power Group, 1995, "Rolls-Royce Industrial Trent," Rolls-Royce and Westinghouse Brochure WEC050934.

Tuzson, J., 1992, "Status of Steam Injection Gas Turbines," ASME JOURNAL OF ENGINEERING FOR GAS TURBINES AND POWER, Vol. 114, pp. 682-687.

Williams, R.H., 1978, "Industrial Cogeneration," *Ann. Review Energy*, Vol. 3, pp. 313-356.

Williams, R.H., and Larson, E.D., 1988, "Aeroderivative Turbines for Stationary Power," *Ann. Review Energy*, Vol. 13, pp. 429-489.

Optimum Power Boosting of Gas Turbine Cycles With Compressor Inlet Air Refrigeration

M. A. Ait-Ali
Ecole Nationale Polytechnique,
B.P. 182 Hassen-Badi,
Alger 16100, Algeria;
Professeur Invité,
Laboratoire EM.2.C.-Ecole Centrale-Paris,
92295, Chatenay-Malabry-Cedex, France

A conceptual gas turbine cycle with refrigerated air supplied to the compressor inlet is proposed to increase the cycle specific net power significantly and render it practically insensitive to seasonal temperature fluctuations. It is optimized for maximum power per m^3/s and maximum power per kg/s of induced air. These cycle performances are evaluated in a numerical example for two refrigeration cycle efficiencies, based on state-of-the-art isentropic efficiency coefficients of the compressor and turbine. The specific heats of air and products of combustion are treated as temperature-dependent parameters to be determined as integrated mean averages.

I Introduction

Unlike steam turbine cycles, which require a very small compressor to turbine (back) work ratio, gas turbine cycles may require back work ratios up to 40 or even 50 percent, depending essentially on the compressor air inlet temperature and the extent of compressor intercooling. An alternate way of looking at the expression of compressor power is to replace for the air mass flow rate from the perfect gas equation and observe that power is no longer a function of inlet temperature, but rather a function of volumetric flow rate and compression ratio; it is the air mass flow rate that decreases with increasing inlet temperature. Hence, for a given compression ratio and volumetric flow rate, the compressor power is constant while the turbine power decreases with increasing inlet temperature. Therefore, maximizing the net power of a gas turbine cycle requires the largest feasible value of the turbine to compressor inlet temperature ratio.

Modern gas turbine technology has extensively used compressor intercooling and high turbine inlet temperatures in order to achieve higher net power and thermal efficiency requirements. Both of these solutions lead to additional investment costs; but higher turbine inlet temperatures are also limited by turbine blade cooling requirements and metallurgical improvements. These technologically sophisticated solutions, which are used mostly in advanced propulsion systems, are less affordable in power plants and other propulsion systems for which the maximum turbine inlet temperature is limited to less than 1200 K without blade cooling (Spurrier, 1979).

It is known that the maximum power pressure ratio increases with the ratio of turbine and compressor inlet temperatures, and the product of compressor and turbine isentropic efficiencies (Wu and Kiang, 1991); it has been shown (Ait-Ali, 1979) that it also increases with increasing pressure losses as charged to the compressor and turbine components.

It has been reported in a recent paper on optimum power cycles using finite time thermodynamics concepts (Ibrahim et al., 1991), that for both finite and infinite thermal capacitance of the working fluid, the maximum power of a Brayton–Joule cycle approaches that of a Carnot-like cycle asymptotically, whereas the cycle efficiency is the same as that achieved by the Curzon–Ahlborn (1975) maximum power solution.

While the quest for higher gas turbine inlet temperatures and compressor intercooling has been the panacea for higher net power outputs, not as much effort has been devoted to decreasing the compressor inlet air temperature, except for those modest reductions allowed by adiabatic air cooling of dry and warm ambient air in arid climates. One possible explanation for this bias is that gas turbine developments have been largely determined by the solutions adopted for aircraft engines, for which the warm temperature handicap is encountered only during take-off.

Feasible potential gains to be achieved by lowering the compressor inlet temperature can be shown to be proportional to the square root of the turbine-to-compressor inlet temperature ratio for a net power comparison, and proportional to the same full ratio for a thermal efficiency comparison. These estimates do not include the gains from increasing the air density; therefore, the larger this temperature ratio, the larger the potential power and efficiency gains, that is, if we discount the refrigeration power required by inlet air cooling.

Gas turbine power augmentation in a cogeneration plant using inlet air chilling has been investigated (Ondryas et al., 1993); but air cooling temperatures have been recommended not to reach values below 7.2°C to safeguard against potential ice build-up in the compressor suction line from the adiabatically saturated air. Based on 35°C and 20 percent relative humidity for the ambient air, the power boost has been estimated at 15.5 percent. However, the recommended solution does not embrace the full inlet air refrigeration conceptual problem in which specific air humidity of saturated air drops well below 0.001 g of water vapor per kg of dry air for refrigeration temperatures below −20°C. Existing industrial solutions to prevent ice formation with low-temperature refrigeration are expected to be relatively inexpensive compared to the potential power gains to be achieved. Such solutions are used, for instance, in the drying of natural gas before liquefaction.

More recently, output power gains of some 20 percent have been reported (De Lucia et al., 1994) for a 26 MW cogeneration gas turbine power plant, in which the inlet air is cooled with an absorption refrigeration cycle only to 10°C, based on maximum efficiency considerations of the refrigeration unit used; the authors also recommend not to cool the air below 4.4°C to prevent ice formation at the compressor suction. The authors have not indicated whether the installed refrigeration capacity is optimum, given the parameters of the gas turbine cogeneration power plant.

The overall optimization problem of such a system could be solved first without any constraints, in order to determine the global optimum, then in a second stage, compare the cost of induced loss of power against the cost of removing the constraints, here the cost of preventing any ice formation. Such an

Contributed by the International Gas Turbine Institute for publication in the JOURNAL OF ENGINEERING FOR GAS TURBINES AND POWER. Manuscript received by the International Gas Turbine Institute January 2, 1995. Associate Technical Editor: L. A. Riekert.

approach has been used recently by the author in a similar work, in which the overall specific energy of compressing and dehumidifying air for glass bottle manufacturing is minimized. It has been found that the overall specific energy decreases with mild air refrigeration, then decreases with low-temperature refrigeration, as the coefficient of performance deteriorates very rapidly. These results suggest that the net power of a gas turbine cycle with refrigerated air inlet would first increase with refrigeration, then decrease after a certain refrigeration temperature is exceeded for which the refrigeration power exceeds the power gain from refrigeration.

Such a conceptual Brayton–Joule gas turbine cycle is investigated in this paper, where air and products of combustion specific heats are considered as temperature-dependent parameters. The overall net power per m^3/s and specific net power per kg/s of induced air are maximized as unconstrained two-degree-of-freedom problems, first with respect to the pressure ratio, then with respect to the refrigeration inlet air temperature.

The endoreversible refrigeration cycle model used is optimized for maximum refrigeration duty given an overall heat transfer conductance specification (Ait-Ali, 1995). In this model, the optimum heat rejection temperature is obtained as an explicit function of the refrigeration temperature when using arithmetic mean temperature differences in the condenser and evaporator.

The performances of this optimum gas turbine cycle with inlet refrigeration are discussed in relation to a numerical example evaluated using two efficiency values for the refrigeration cycle COP, then compared with the performances reported in the literature for potentially similar gas turbine applications.

II Optimum Gas Turbine Cycle With Inlet Air Refrigeration

(a) Maximum Overall Net Power per Unit Volumetric Air Flow Rate. The overall net power delivered by a conceptual gas turbine cycle with refrigerated air supplied to the compressor is equal to the net power delivered by the gas turbine cycle minus the power supplied to the refrigeration cycle; the least favorable case, in terms of power, would be a vapor compression refrigeration cycle with a Joule–Thompson expansion valve rather than a turbo-expander. The schematic diagram of such a cycle is represented in Fig. 1 and the corresponding T–s diagram in Fig. 2.

The overall net power delivered by this cycle is expressed by the difference between the gas turbine net power given by the following equation:

$$W_{net}/V_1 = (P_1/R)\{(1+f)C_{pt}\cdot\eta_t\cdot T_3/T_1[1-(\eta_{pt}P_r)^{-\alpha t}] - C_{pc}[(\eta_{pc}P_r)^{\alpha c}-1]/\eta_c\} \quad (1)$$

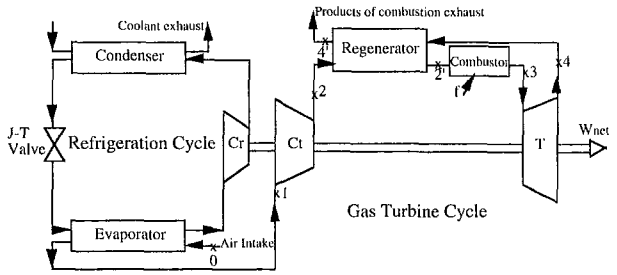

Fig. 1 Schematic diagram of a gas turbine cycle with refrigerated air to the compressor inlet

and the refrigeration cycle required power for the same air mass flow rate, expressed by:

$$W_r/V_1 = (P_1/R)C_{pa}\eta_r^{-1}(T_0/T_1-1)[T_{hc}(\exp(XT_1)-1)/(T_1\exp(XT_1)-T_0)-1] \quad (2)$$

where X is defined as:

$$X = R\cdot UA/C_{pa}V_1P_1 \quad (3)$$

The parameter X represents the ratio of the heat transfer conductance of the refrigeration cycle evaporator per degree of T_1 to the thermal capacitance of the inlet air being refrigerated; ideal gas behavior has been assumed in the related energy balance. The detailed derivations of the refrigeration power expression are given in Appendix 1.

Note: If an absorption refrigeration cycle is considered instead of the vapor compression refrigeration cycle, another expression would have to be written for the required mechanical and thermal power with an equivalence coefficient less than unity to multiply the refrigeration thermal power term. As a consequence, lower refrigeration temperatures could thus be powerwise optimum; but then, the capital cost could also be higher than for mechanical refrigeration.

Going back to Eqs. (1) and (2), the overall net power is seen to be a function of two independent variables:

(a) the pressure ratio P_r, which does not affect the refrigeration power.
(b) the compressor inlet air temperature T_1, which affects the turbine net power as well as the refrigeration power.

The unconstrained optimization procedure is carried out in two steps. First the gas turbine cycle power as expressed by Eq. (1) is maximized with respect to the pressure ratio P_r, then the overall cycle net power is maximized with respect to the temperature T_1, which is the only linking variable between the gas turbine cycle and the refrigeration cycle. For any value of T_1, the optimality of the refrigeration cycle is enforced by

Nomenclature

C_{pa} = average specific heat of ambient air
C_{pc} = average specific heat of compressed air
C_{pt} = average specific heat of products of combustion
f = fuel-to-air mass ratio
m^* = nondimensional air mass flow rate
P_1 = inlet pressure to the compressor
P_r = compressor pressure ratio
Q_h = combustor thermal power
Q_r = regenerator thermal power
R = ideal gas constant
T_{ce} = refrigerant lower isotherm
T_{hc} = refrigerant higher isotherm
T_0 = ambient air temperature
T_1 = compressor inlet temperature
T_2 = compressor exit temperature
T_3 = turbine inlet temperature
T_4 = turbine exit temperature
UA = evaporator heat conductance
V_1 = volumetric air flow rate
W^* = specific power
W_c = compressor power
W_{net} = overall cycle net power
W_r = refrigeration power
W_t = turbine power
$\alpha_c = R/C_{pc}$ ratio
$\alpha_t = R/C_{pt}$ ratio
ϵ_r = regenerator effectiveness
η_c = compressor isentropic efficiency
η_{pc} = compressor pressure effectiveness
η_{pt} = turbine pressure effectiveness
η_r = refriger. cycle isentropic efficiency
η_c = turbine isentropic efficiency

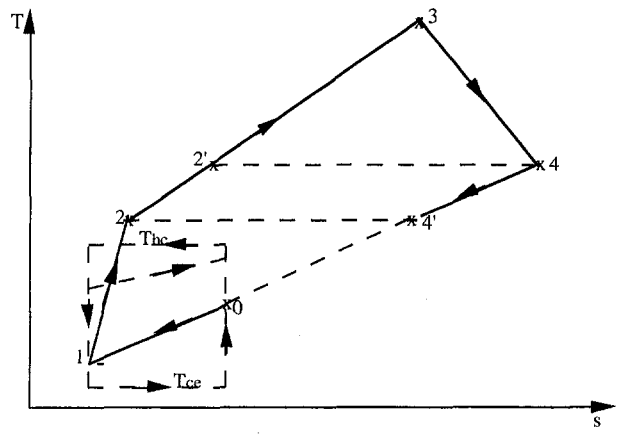

Fig. 2 *T–s* diagram of a regenerative gas turbine cycle with refrigerated air to the compressor inlet

applying the optimality rule, which sets the corresponding heat rejection temperature T_{hc}.

Setting the first derivative of the objective function as expressed by Eq. (1) with respect to P_r equal to zero, gives the following optimum value of the pressure ratio:

$$P_r^* = [\eta_t\eta_c(1+f)(T_3/T_1)/(\eta_{pc}^{\alpha c}\eta_{pt}^{\alpha t})]^{1/(\alpha c+\alpha t)} \quad (4)$$

where $\alpha_c = R/C_{pc}$ and $\alpha_t = R/C_{pt}$.

Note: This general result takes into account the temperature effects on the specific heats C_{pc} and C_{pt}, where their values are taken as mean integrated averages, as well as the compressor and turbine pressure effectivenesses η_{pc} and η_{pt}; values of unity for these parameters mean that pressure losses charged to the compressor and turbine are negligibly small; the smaller these values, the larger the optimum pressure ratio.

The corresponding compressor and turbine exit temperatures and their difference are then obtained to express the temperature potential for regeneration, the thermal power supplied to the combustor, and the cycle thermal efficiency. These expressions are derived in Appendix 2.

The overall net power is now written as the following objective function to be minimized with respect to the compressor inlet temperature T_1:

$$\begin{aligned}(W_{net}/V_1) = (P_1/R)\{&(C_{pt}/\eta_c)\\ &\times F(T_1)[1 - F(T_1)^{-\alpha t/(\alpha c+\alpha t)}(\eta_{pc}/\eta_{pt})^{\alpha c\cdot\alpha t/(\alpha c+\alpha t)}]\\ &- (C_{pc}/\eta_c)[F(T_1)^{\alpha c/(\alpha c+\alpha t)}(\eta_{pc}/\eta_{pt})^{\alpha c\cdot\alpha t/(\alpha c+\alpha t)} - 1]\\ &- (C_{pa}/\eta_r)(T_0/T_1 - 1)[T_{hc}(\exp(XT_1) - 1)/\\ &\qquad (T_1\exp(XT_1) - T_0) - 1)]\} \quad (5)\end{aligned}$$

where:

$$F(T_1) = (1+f)\eta_c\eta_tT_3/T_1 \quad (6)$$

The first term of Eq. (5) represents the turbine power, the second term represents the compressor power, and the third term, the refrigeration power. This last term needs to be simplified to translate the endoreversibile optimality rule existing between T_{hc} and T_1.

Taking the first derivative of the overall net power with respect to T_1 in Eq. (5) and setting it equal to zero does not yield an analytical solution for T_1. This would have been a most useful result to show the influence of the cycle parameters. A one-dimensional search in T_1 will be used instead in connection with a numerical example.

(*b*) Maximum Specific Net Power. The specific net power is defined as the overall net power delivered by the cycle per kg of compressed air. Its expression is given by the following function to be maximized with respect to T_1:

$$\begin{aligned}W_{net1}^* = &(1+f)C_{pt}\eta_tT_3[1 - (\eta_{pt}P_r)^{-\alpha t}]\\ &- C_{pc}T_1[(P_r\eta_{pc})^{\alpha c} - 1]/\eta_c - C_{pa}/\eta_r(T_0 - T_1)\\ &\times [T_{hc}(\exp(XT_1) - 1)/(T_1\exp(XT_1) - T_0) - 1] \quad (7)\end{aligned}$$

The specific power maximum with respect to the pressure ratio occurs, as expected, for the same optimum value of the pressure ratio given by Eq. (4). Replacing for P_r in Eq. (7), gives the following function of T_1:

$$\begin{aligned}W_{net}^* = &(1+f)C_{pt}\eta_tT_3\\ &\times [1 - (F(T_1)^{-\alpha t/(\alpha c+\alpha t)}(\eta_{pc}/\eta_{pt})^{\alpha c\cdot\alpha t/(\alpha c+\alpha t)}]\\ &- C_{pc}T_1/\eta_c[F(T_1)^{\alpha c/(\alpha c+\alpha t)}(\eta_{pc}/\eta_{pt})^{\alpha c\cdot\alpha t/(\alpha c+\alpha t)} - 1]\\ &- C_{pa}/\eta_r(T_0 - T_1)[T_{hc}(\exp(XT_1) - 1)/\\ &\qquad (T_1\exp(XT_1) - T_0) - 1] \quad (8)\end{aligned}$$

Taking the first derivative of this expression with respect to T_1 and setting it equal to zero does not yield an analytical solution, just as for the overall net power problem considered above.

The maxima of the overall net power and specific net power with respect to T_1 are shown more simply with the following numerical example, evaluated for two values of the refrigeration cycle isentropic efficiency, defined here as the ratio of the cycle COP to the corresponding Carnot refrigeration cycle COP.

In order to simplify the expression of the refrigeration power, and since the objective is to maximize power, let us use arithmetic mean temperature differences and a 100 percent heat transfer effectiveness in both the evaporator and condenser. These simplifying assumptions lead to $T_{ce} = T_1$ and:

$$\text{COP} = T_1/(T_{hc} - T_1) \quad (9)$$

$$W_r = (P_1/\alpha_r\eta_r)((T_{hc} - T_1)(T_0/T_1^2 - T_1^{-1}) \quad (10)$$

for, respectively, the coefficient of performance and the refrigeration power. The optimality rule, which specifies the optimum heat rejection temperature T_{hc} in terms of the refrigeration temperature T_1, is in this case given by the solution of the canonical second-degree polynomial:

$$T_{hc} = [b + (b^2 - 4c)^{1/2}]/2 \quad (11)$$

where:

$$b = (3T_0^2 + T_1^2)/(T_0 + T_1) \quad (12)$$

$$c = T_0\cdot T_1(3T_0 - T_1)/(T_0 + T_1) \quad (13)$$

III Numerical Example

The numerical data used in this example are the following:

$$C_{pa} = 1.005, \quad C_{pc} = 1.033,$$

$$C_{pt} = 1.108, \quad R = 0.2871, \quad \text{in kJ/kg}\cdot\text{K}$$

$$\eta_c = 0.85, \quad \eta_t = 0.90, \quad \eta_{pc} = 0.96, \quad \eta_{pt} = 0.98,$$

$$\alpha_c = 0.2779, \quad \alpha_t = 0.2591, \quad (1+f) = 1.03$$

$$T_0 = 300\text{ K}, \quad T_3 = 1200\text{ K}.$$

Case 1: $\eta_r = 0.60$; Case 2: $\eta_r = 0.85$.

The overall heat transfer coefficient considered, from boiling and condensing refrigerant to air, is 0.050 kW/m$^2\cdot$K, and the heat transfer area density is 350 m^2/m^3, which is a little conservative for state-of-the-art compact heat exchangers.

Note: The values of the specific heat integrated averages to be used in actual cycle evaluations will depend on the compressor and turbine exit temperatures, still unknown initially. A few iterations will therefore be needed in order to make these data consistent with the numerical solution to be obtained.

The results of the calculations are plotted in Figs. 3–7.

IV Results

(*a*) Maximum Net Power Per Unit Volumetric Air Flow Rate. Figure 3 shows the overall net power per unit volumetric air flow rate versus T_1, for the two isentropic refrigeration coefficients considered; the 60 percent efficiency is probably a little conservative, while the 85 percent efficiency is probably a little optimistic for the optimum refrigeration temperature expected.

Case 1 achieves a maximum of 357.2 kW/(m^3/s) at T_1 = 235 K; this is 87.7 kW/(m^3/s) or 33 percent higher than the base case without air refrigeration for which the net power supplied is 269.5 kW/(m^3/s) at $T_1 = T_0$ = 300 K. The corresponding mean heat rejection temperature T_{hc} is 372.9 K. At this maximum power, the refrigeration power is 94.7 kW/(m^3/s), the refrigeration load is 96.8 kW/(m^3/s), and the heat rejection load 191.5 kW/(m^3/s). The arithmetic mean temperature differences in the condenser and evaporator are respectively 36.5 and 32.5 K. The estimated heat transfer areas are 105.1 and 59.6 m^2, respectively, for the condenser and the evaporator. The corresponding heat exchanger volumes are 0.30 and 0.17 m^3. The ratio of net power gain obtained to refrigeration power supplied is 0.93.

Case 2 achieves a maximum of 397.8 kW/(m^3/s) at T_1 = 214.5 K, which is 128.3 kW/(m^3/s) or 48 percent higher than the base case without air refrigeration. The corresponding mean heat rejection temperature T_{hc} is 399.7 K. At this maximum power, the refrigeration power is 141.8 kW/(m^3/s), the refrigeration load is 139.5 kW/(m^3/s) and the heat rejection load 281.3 kW/(m^3/s). The arithmetic mean temperature differences in the condenser and evaporator are respectively 49.9 and 42.8 K. The estimated heat transfer areas are 112.9 and 65.3 m^2, respectively, for the condenser and the evaporator. The corresponding heat exchanger volumes are 0.32 and 0.19 m^3.

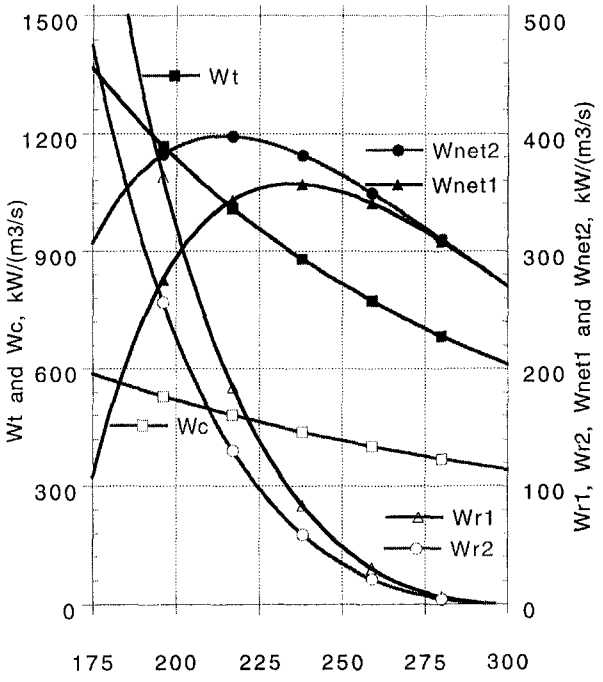

Fig. 3 Power versus refrigeration temperature

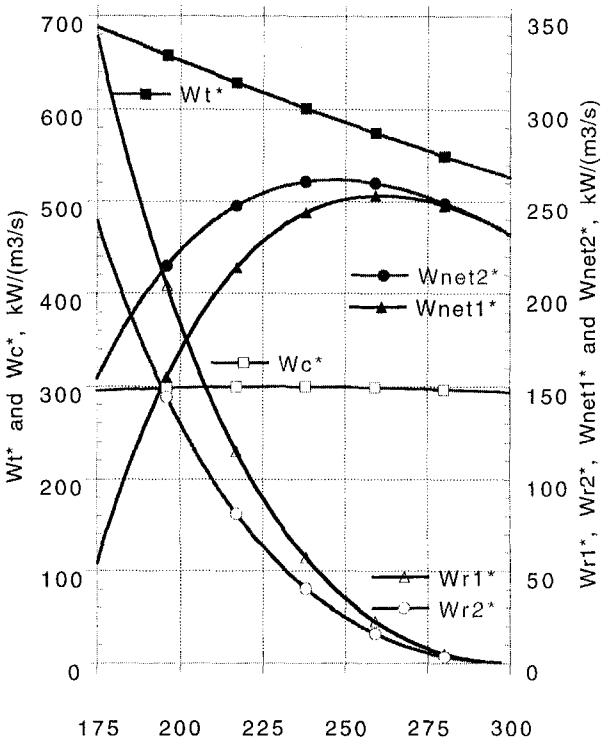

Fig. 4 Specific power versus refrigeration temperature

The ratio of net power gain obtained to refrigeration power supplied is 0.90.

Admittedly, the refrigeration power requirements for temperatures below 225 K appear to be prohibitively high; similarly, the mean heat rejection temperatures corresponding to these power maxima are unusually high; but, considering that cost optimization solutions will result from a compromise between maximum power and maximum efficiency, lower refrigeration power requirements and lower heat rejection temperatures are expected to be optimum.

(*b*) Maximum Specific Net Power per Unit Mass Air Flow Rate. Figure 4 shows the specific net power per unit mass air flow rate versus T_1, for the two isentropic refrigeration coefficients considered. Here, the compressor specific power is

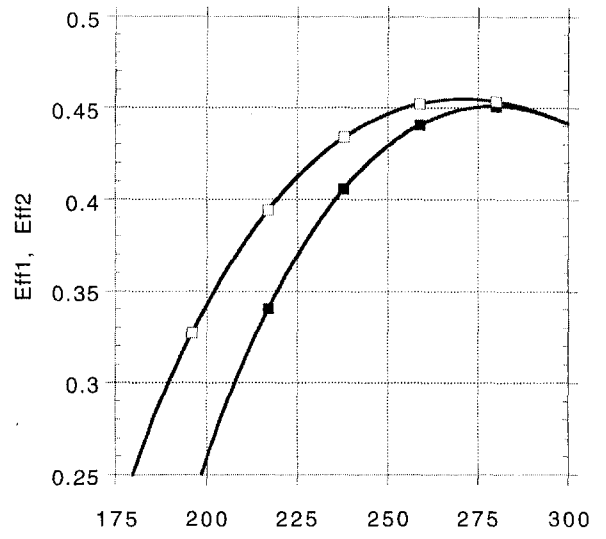

Fig. 5 Thermal efficiency versus refrigeration temperature

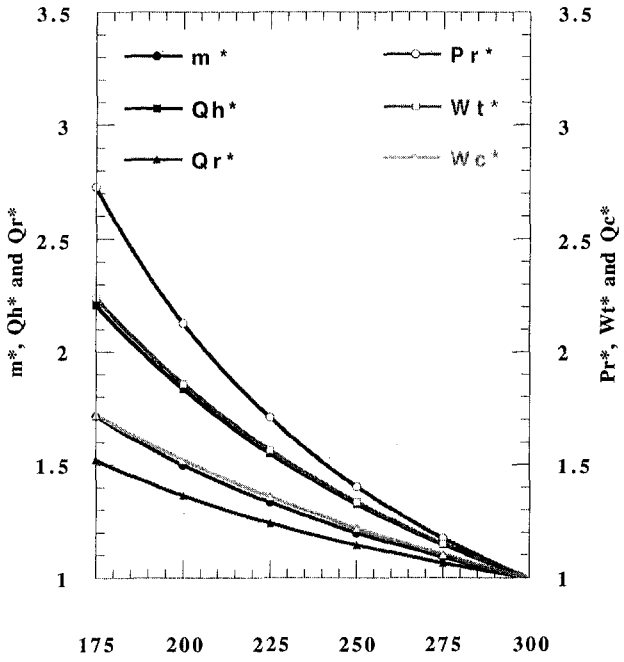

Fig. 6 Relative size parameters versus refrigeration temperature

seen to be nearly constant, but it actually reaches a very flat maximum of 299.8 kW/(kg/s) at T_1 = 230 K; as the refrigeration temperature decreases, the compressor power tends to increase with the increasing compression ratio, and decrease at the same time with respect to the refrigeration temperature. This maximum is 2.0 percent higher than the specific value achieved at 300 K.

Case 1 achieves a maximum of 253.3 kW/(kg/s) at T_1 = 260.5 K; this is 21.2 kW/(kg/s) or 9 percent higher than the base case without air refrigeration for which the net power supplied is 232.1 kW/(kg/s) at $T_1 = T_0$ = 300 K. The corresponding mean heat rejection temperature T_{hc} is 342.3 K. At this maximum power, the refrigeration power is only 20.8 kW/(kg/s), the refrigeration load is 39.7 kW/(kg/s), and the heat rejection load 60.5 kW/(kg/s). The arithmetic mean temperature differences in the condenser and evaporator are respectively 21.2 and 19.8 K. The estimated heat transfer areas are respectively 57.0 and 40.2 m^2, for the condenser and the evaporator. The corresponding heat exchanger volumes are 0.16 and 0.11 m^3. The ratio of net power gain obtained to refrigeration power supplied is 1.02.

Case 2 achieves a maximum of 261.7 kW/(m^3/s) at T_1 = 247 K, which is 29.6 kW/(kg/s) or 13 percent higher than the base case without air refrigeration. The corresponding mean heat rejection temperature T_{hc} is 358.1 K. At this maximum power, the refrigeration power is 28.2 kW/(kg/s), the refrigeration load is 53.3 kW/(kg/s), and the heat rejection load 81.5 kW/(kg/s). The arithmetic mean temperature differences in the condenser and evaporator are respectively 29.1 and 26.5 K. The estimated heat transfer areas are respectively 56.1 and 40.2 m^2, for the condenser and the evaporator. The corresponding heat exchanger volumes are 0.16 and 0.11 m^3. The ratio of net power gain obtained to refrigeration power supplied is 1.05.

(*c*) **Thermal Efficiency.** Figure 5 shows the behavior of thermal efficiency versus refrigeration temperature; the maxima achieved are, respectively: 45.1 percent at T_1 = 279 K for case 1 and 45.5 percent at T_1 = 279 K for case 2; thermal efficiency 44.1 percent at T_1 = 300 K = T_0. This indicates that refrigeration, and refrigeration efficiency, has a minor effect on the maxima achieved; but thermal efficiency drops off drastically as refrigeration temperature decreases below 250 K. This is a further indication that an optimum cost compromise between specific power and thermal efficiency could call for inlet air refrigeration in the neighborhood of 240 K with an isentropic efficiency of about 70 percent.

(*d*) **Variation of System Size Parameters With Refrigeration Temperature.** This comparison attempts to give a preliminary idea about the physical size of the gas turbine system main components as would be induced by inlet air refrigeration. These parameters are defined as ratios of: air mass flow rate, combustor thermal power, regenerator thermal power, compression ratio, turbine power and compressor power at T_1, to their corresponding values at T_0 = 300 K, per unit volumetric air flow rate; they are shown in Fig. 6.

The compression ratio is seen to increase the fastest with decreasing refrigeration temperature; next to it, combustor thermal power and turbine mechanical power increase at the same rate; then compressor power and air mass flow rate increase also at the same rate. Combustor size is seen to increase the least. At T_1 = 240 K, for instance, turbine power would have increased by about 45 percent and compressor power by about 30 percent.

V Comparison and Discussion of the Results

The results presented in this preliminary work are obtained from a conceptual cycle point of view and, consequently, only broad and brief comparisons with other gas turbine systems would be appropriate in this presentation.

A first comparison can be made in terms of specific work and thermal efficiency achieved by the conservative case considered for this cycle, that is with a refrigeration efficiency of 60 percent. The specific work values are respectively 357 kJ/m^3 and 253 kJ/kg, and thermal efficiency 45 percent. For a compression Cooled Regenerative Cycle with a Variable Geometry (CCR-VG), McCoy (1981) reported a maximum thermal efficiency of 36 percent for a 4 × 5000 hp COGAG system installed in a 2000-ton escort ship. No specific power figure was mentioned in the paper.

For a design of a Compact Helium Closed Cycle Gas Turbine for marine propulsion, with the same turbine inlet temperature (1200 K) and same compressor and turbine isentropic efficiencies (respectively 85 and 90 percent), Spurrier (1979) reported

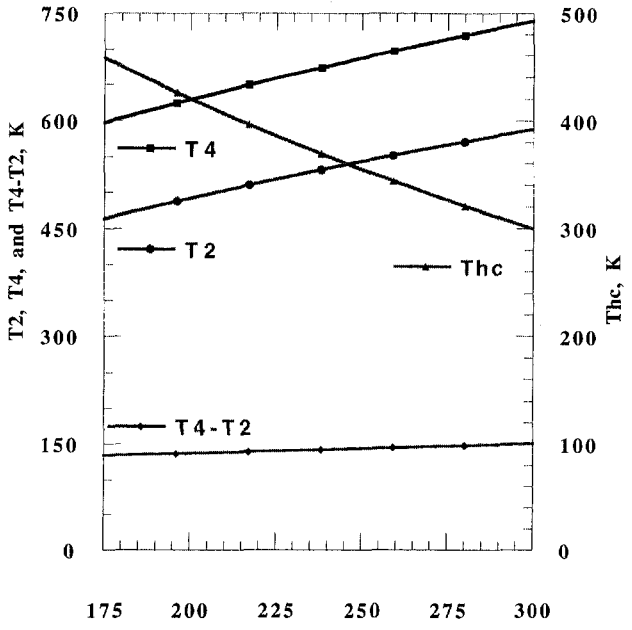

Fig. 7 Temperatures versus refrigeration temperature

a 39 percent thermal efficiency. The specific power calculated from the reported data is 945.2 kW per $kg \cdot s^{-1}$ of helium.

With the high compressor ratios considered in this conceptual cycle, $P_r = 13.3$ at $T_1 = 240$ K for instance, the cycle performances could further be increased by compressor intercooling as indicated by the high compressor exit temperature shown in Fig. 7.

VI Conclusion

The conceptual gas turbine cycle with inlet air refrigeration, optimized on net power criteria in this paper, presents realistic potentialities to develop gas turbine systems for baseload power plants and large propulsion systems with high thermal efficiency and specific power per unit volumetric air flow rate. Furthermore, these performances will be obtained year round, virtually unaffected by ambient air conditions, provided the refrigeration system is conservatively dimensioned. This system performance will be improved by compressor intercooling, which will further increase the optimum compression ratio.

Although these results are only preliminary, they could prove this conceptual cycle to be a potential alternative to baseload power generation in hot climates and arid lands, where sufficient water heat sinks are scarce. If the ice formation problem at the compressor inlet is more potential than effective, particularly in dry climates, this cycle could be also worth considering for propulsion systems of large land vehicles and naval units.

Acknowledgments

The author gratefully acknowledges the support of Ecole Centrale-Paris and Laboratoire EM.2.C during the first half of 1994. The basic idea for this research comes from a study done for Saint-Gobain Emballages in January–February 1994.

References

Ait-Ali, M. A., 1979, "Optimum Liquefaction Cycles of Natural Gas," PhD Dissertation, Dept. of Mech. Engrg., Stanford University, Palo Alto, CA.

Ait-Ali, M. A., 1995, "Finite-Time Optimum Refrigeration Cycles," *J. Appl. Phys.*, Vol. 77(9).

Curzon, F. L., and Ahlborn, B., 1975, "Efficiency of a Carnot Engine at Maximum Power Output," *Am. J. Phys.*, Vol. 43, pp. 22–24.

De Lucia, M., Bronconi, R., and Carnevale, E., 1994, "Performance and Economic Enhancement of Cogeneration Gas Turbine Through Compressor Inlet Air Cooling," ASME JOURNAL OF ENGINEERING FOR GAS TURBINES AND POWER, Vol. 116, pp. 360–365.

Ibrahim, O. M., Klein, S. A., and Mitchell, J. W., 1991, "Optimum Heat Power Cycles for Specified Boundary Conditions," ASME JOURNAL OF ENGINEERING FOR GAS TURBINES AND POWER, Vol. 113, pp. 514–521.

McCoy, A. W., 1981, "Regenerative Gas Turbines for Naval Escort Ships," ASME Paper No. 81-GT-115.

Ondryas, I. S., Wilson, D. A., Kayamoto, M., and Haub, G. L., 1993, "Options in Gas Turbine Power Augmentation Using Inlet Air Chilling," ASME JOURNAL OF ENGINEERING FOR GAS TURBINES AND POWER, Vol. 113, pp. 203–211.

Rice, I. G., 1982, "The Reheat Gas Turbine With Steam-Blade Cooling—A Means of Increasing Reheat Pressure, Output, and Combined Cycle Efficiency," ASME JOURNAL OF ENGINEERING FOR POWER, Vol. 104, pp. 9–22.

Spurrier, F. R., 1979, "A Compact Closed Gas Turbine for Marine Propulsion," ASME Paper No. 79-GT-62.

Wu, C., and Kiang, R. L., 1991, "Power Performance of a Nonisentropic Brayton Cycle," ASME JOURNAL OF ENGINEERING FOR GAS TURBINES AND POWER, Vol. 113, pp. 501–504.

APPENDIX 1

Refrigeration Cycle Power Requirements

The power requirements of the inlet air refrigeration cycle need to be evaluated as a function of the refrigeration temperature T_1 in order to be subtracted from the power delivered by the turbine and thus obtain the overall net power of the cycle as a function of T_1. The link between the two systems is the evaporator of the refrigeration cycle, for which the energy balance is given by the following equation based on a Logarithmic Mean Temperature Difference (LMTD):

$$C_{pa}(P_1V_1/RT_1)(T_0 - T_1) = UA[(T_0 - T_1) - (T_1 - T_{ce})] \times 1/\ln[(T_0 - T_{ce})/(T_1 - T_{ce})] \quad (14)$$

Air admitted into the refrigeration cycle, then into the compressor, is assumed to behave as an ideal gas with no pressure drop allowance in the evaporator, for which the heat conductance is UA. Solving this equation for T_{ce} gives the refrigerant lower isotherm in the evaporator as:

$$T_{ce} = [T_1 \exp(XT_1) - T_0]/[\exp(XT_1) - 1] \quad (15)$$

In a Carnot refrigeration cycle, the coefficient of performance (COP) is equal to the ratio of the refrigerant lower isotherm T_{ce} and the temperature difference $(T_{hc} - T_{ce})$ between the two isotherms, that is:

$$\text{COP} = T_{ce}/(T_{hc} - T_{ce}) \quad (16)$$

Replacing for T_{ce} from Eq. (15) gives:

$$\text{COP} = [(T_{hc}(\exp(XT_1) - 1)/(T_1 \exp(XT_1) - T_0) - 1] \quad (17)$$

The actual refrigeration power of a vapor compression refrigeration cycle is then obtained by assuming a cycle isentropic efficiency η_r defined by the ratio of the Carnot cycle refrigeration power to the power actually required:

$$W_r/V_1 = (P_1/R)C_{pa}\eta_r^{-1}(T_0/T_1 - 1) \times [(T_{hc}(\exp(XT_1) - 1)/(T_1 \exp(XT_1) - T_0) - 1)] \quad (18)$$

where the parameter X is defined by Eq. (3).

APPENDIX 2

Thermal Efficiency for a Regenerative Gas Turbine Cycle

With reference to the T–s diagram of Fig. 2, the compressor and turbine exit temperatures are obtained by replacing for the optimum value of the compression ratio as given by Eq. (4), in the well-known adiabatic relations:

$$T_2 = T_1(\eta_c + (\eta_{pc} \cdot P_r)^{\alpha c} - 1)/\eta_c \quad (19)$$

$$T_4 = T_3(1 + \eta_t(\eta_{pt} \cdot P_r)^{-\alpha t} - \eta_t) \quad (20)$$

Hence,

$$T_2 = T_1(1 - 1/\eta_c) + [(\eta_{pc}/\eta_{pt})^{\alpha c \cdot \alpha t}(T_1/\eta_c)^{\alpha t}(\eta_t T_3(1 + f))^{\alpha c}]^{1/(\alpha c + \alpha t)} \quad (21)$$

$$T_4 = T_3(1 - \eta_t) + [(\eta_{pc}/\eta_{pt})^{\alpha c \cdot \alpha t}(T_1/\eta_c)^{\alpha t}(\eta_t T_3)^{\alpha c}(1 + f)^{-\alpha t}]^{1/(\alpha c + \alpha t)} \quad (22)$$

The potential temperature difference for regeneration is then expressed as:

$$T_4 - T_2 = \{T_3(1 - \eta_t) - T_1(1 - 1/\eta_c) + [(\eta_{pc}/\eta_{pt})^{\alpha c \cdot \alpha t}(T_1/\eta_c)^{\alpha t}(\eta_t T_3)^{\alpha c}]^{1/(\alpha c + \alpha t)} \times ((1 + f)^{-\alpha t/(\alpha c + \alpha t)} - (1 + f)^{\alpha c/(\alpha c + \alpha t)})\} \quad (23)$$

We note that for isentropic turbine and compressor, and with negligible pressure losses and fuel-to-air mass ratio, the potential temperature difference for regeneration is zero, as

should be expected, for a maximum net power ideal gas turbine cycle.

The heat rate supplied by the regenerator is given by the product of the potential temperature difference as expressed by Eq. (23) and the products of combustion thermal capacitance, times the regenerator effectiveness:

$$Q_r/V_1 = C_{pt}(P_1/RT_1)(1 + f)(T_4 - T_2)\epsilon_r \qquad (24)$$

Thermal power supplied to the working fluid of this regenerative gas turbine cycle is given by:

$$Q_h/V_1 = C_{pt}(P_1/RT_1)(1 + f)[(T_3 - T_2) - (T_4 - T_2)\epsilon_r] \qquad (25)$$

After replacing for T_2 from Eq. (21) and for the potential temperature difference from Eq. (23), the expression of the thermal power supplied to the combustor becomes:

$$\begin{aligned} Q_h/V_1 &= C_{pt}(1 + f)(P_1/R)T_3(1 - \epsilon_r(1 - \eta_t))/T_1 \\ &\quad - \epsilon_r[(\eta_{pc}/\eta_{pt})^{\alpha c \cdot \alpha t}((1 + f)\eta_c)^{\alpha c}(\eta_t T_3/T_1)^{\alpha c}]^{1/(\alpha c + \alpha t)} \\ &\quad - (1 - \epsilon_r)\{(1 - 1/\eta_c) \\ &\quad + [(\eta_{pc}/\eta_{pt})^{\alpha c \cdot \alpha t}((1 + f)\eta_t T_3/T_1)^{\alpha c}\eta_c^{-\alpha t}]^{1/(\alpha c + \alpha t)}\} \end{aligned} \qquad (26)$$

The cycle thermal efficiency is obtained by dividing the overall net power delivered by the cycle by the thermal power supplied, that is, by dividing Eq. (5) by Eq. (26). The results are represented in Fig. 3 for the data of the numerical example considered.

The potential temperature difference for regeneration is shown in Fig. 7 with the compressor and turbine exit temperatures T_2 and T_4. It is seen to increase only slightly, from 139 K at T_1 = 175 K to 150 K at T_1 = 300 K. At constant turbine inlet temperature, compressor intercooling would lead to higher optimum compression ratios and lower turbine exit temperatures; this could actually reduce the regeneration potential and make it cost ineffective.

K. Ito
Professor.
Mem. ASME

R. Yokoyama
Associate Professor.
Mem. ASME

Department of Energy Systems Engineering,
Osaka Prefecture University,
1-1, Gakuen-cho, Sakai, Osaka, 593 Japan

Y. Matsumoto
Manager,
Technical Research Center,
The Kansai Electric Power Co., Inc.,
3-11-20, Nakoji, Amagasaki,
Hyogo, 661 Japan

Effect of Steam-Injected Gas Turbines on the Unit Sizing of a Cogeneration Plant

The effect of installing steam-injected gas turbines in a cogeneration plant is analyzed with respect to unit sizing and operational planning. An optimization method is used to determine the capacities of gas turbines and other auxiliary machinery in consideration of their operational strategies for variations of electricity and thermal energy demands. Through a numerical study on a plant for district heating and cooling, it is clarified how the installation of steam-injected gas turbines in place of simple-cycle ones can improve the economic and energy-saving properties. The influence of the capital cost of steam-injected gas turbines on the unit sizing and the above-mentioned properties is also clarified.

Introduction

For the purpose of energy-efficient utilization, gas turbine cogeneration plants have been installed widely in industrial and commercial sectors. The economic and energy-saving properties of cogeneration plants are affected significantly by their operational flexibility for seasonal and hourly variations of energy demands. So far simple-cycle gas turbine cogeneration units, which are equipped with gas turbines alone as prime movers and with waste heat recovery boilers, have been installed conventionally. These units have a disadvantage in that they cannot change the heat-to-power ratio flexibly to respond to variations of electricity and thermal energy demands. As a result, in cases where thermal energy demand is relatively lower than electricity demand, for example, they must be operated at a part-load status with low power-generating efficiency, or at the rated load status with a large amount of heat disposal. This affects the economic and energy-saving properties.

Steam-injected gas turbines (STIG) are expected to give a solution to this problem. They aim to increase electrical output and generating efficiency by injecting superheated steam into combustors of gas turbines, and it enables us to change the heat-to-power ratio flexibly by adjusting steam injection. Additional flexibility can be obtained by adjusting supplemental firing with duct burners of waste heat recovery boilers. Thus the high operational flexibility of STIG units gives a potential for improving the economic and energy-saving properties of cogeneration plants.

To improve the performance of STIG units, thermodynamic characteristics have been analyzed by many researchers (Fraize and Kinney, 1979; Brown and Cohn, 1981; Larson and Williams, 1987; Noymer and Wilson, 1993; Rice, 1993a–c). In addition to the thermodynamic analysis, operational problems have been discussed for the purpose of cogeneration application, and optimization approaches have been adopted to improve the economic and energy-saving properties for STIG units (Maher et al., 1987; Baken and Haspel, 1988) and total cogeneration plants with STIG units (Ito et al., 1995). In order to utilize the high operational flexibility of STIG units, both unit sizing and operational planning are very important. However, no investigation has been made into optimal equipment capacities of cogeneration plants with STIG units. The sizes of STIG units currently available are limited. However, in developing a new STIG unit, considerating surrounding conditions such as energy demands and utility rates, it is necessary to find an appropriate size. Moreover, if we had more sizes available in the future, it would be possible to determine optimal capacities of STIG units in cogeneration plants.

The objective of this paper is to present an optimal unit sizing method for cogeneration plants with STIG units, and to investigate the effect of installing STIG units in a cogeneration plant from the viewpoint of both unit sizing and operational planning. A numerical study is carried out on a plant for district heating and cooling, and the influence of capital cost of STIG units on the unit sizing, and on the economic and energy-saving properties of the cogeneration plant, is examined.

Plant Configuration

STIG Unit. Figure 1 illustrates the configuration of a STIG unit. Similarly to a simple cycle gas turbine unit, this unit is equipped with a gas turbine generator and a waste heat recovery boiler. Electrical output can be increased by superheating steam generated with the waste heat recovery boiler and injecting it into a combustor of the gas turbine. Steam output can also be increased by supplemental firing with duct burners of a secondary combustor. The unit can operate within a wide range of electrical and steam outputs by adjusting the natural gas consumption for main and supplemental firing, and the amount of injected steam. Surplus exhaust heat is disposed of through exhaust gas dumpers. Feedwater is needed to supply water consumed for steam injection.

Total Cogeneration Plant. Figure 2 illustrates the configuration of the total cogeneration plant investigated in this paper. Although only one unit is illustrated for each kind of equipment, multiple units may be installed. Electricity is supplied to users by operating gas turbine generators in cogeneration units and purchasing electricity from an outside electric power company. Electricity is also used to drive electric compression refrigerators, pumps, cooling towers, and other auxiliary machinery in the plant. Steam generated by waste heat recovery boilers in cogeneration units is used for several purposes. When steam is in short supply, it is supplemented by gas-fired auxiliary boilers. Electric compression and steam absorption refrigerators are installed to supply cold water for space cooling. Steam is used for space heating and other miscellaneous purposes.

Contributed by the International Gas Turbine Institute for publication in the JOURNAL OF ENGINEERING FOR GAS TURBINES AND POWER. Manuscript received by the International Gas Turbine Institute April 1995. Associate Technical Editor: L. A. Riekert.

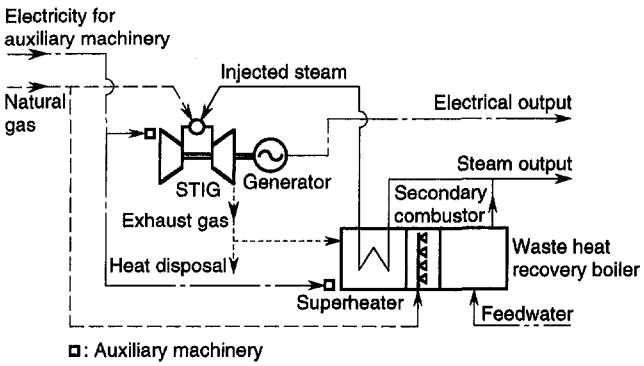

Fig. 1 Configuration of STIG unit

Optimal Unit Sizing Method

The basic idea of the optimal unit sizing method presented here is based on the method for simple-cycle gas turbine cogeneration plants (Yokoyama et al., 1994). Only an outline of the method is presented here.

Unit Sizing Problem. Equipment capacities and utility maximum demands are determined so as to optimize a selected objective function, in consideration of equipment operational strategies corresponding to seasonal and hourly variations of energy demands. Equipment includes gas turbine cogeneration units, as well as apparatus for purchasing electricity, gas-fired auxiliary boilers, electric compression refrigerators, and steam absorption refrigerators. Utilities include purchased electricity, natural gas, and water.

The annual operational hours in a year are discretized by setting D representative days and by dividing each day into H time periods, and the annual operational hour for the hth time period on the dth representative day is designated by T_{dh}. Energy demands are estimated for each time period on each representative day, and the operational strategy is assessed correspondingly. In addition to average energy demands, peak energy demands in summer and winter should be taken into account so that energy will be supplied during the peak periods.

The annual total cost is adopted as the objective function to be minimized from the economic viewpoint. The annual total cost is evaluated as the sum of the annual capital cost and annual operational cost on the basis of the annualized costs method. The annual capital cost of each piece of equipment is considered as a function of its capacity. The annual operational cost of each utility is the sum of the customer/demand charges and energy charge. The demand charge is considered as a function of the utility maximum demand, and the energy charge is calculated from the plant's operational strategy. Thus the objective function is expressed by

$$J = F(\mathbf{x}) + \sum_{d=1}^{D} \sum_{h=1}^{H} V_{dh}(\mathbf{x}, \mathbf{y}_{dh}, \mathbf{z}_{dh}) T_{dh}, \qquad (1)$$

where F is the sum of the annual capital cost and the annual customer/demand charges, and it is a function of the vector composed of equipment capacities and utility maximum demands $\mathbf{x}$. The function V_{dh} is the hourly energy charge, and it is expressed explicitly only by utility consumption. However, the constraints described below make it a function of $\mathbf{x}$, and the continuous variable vector $\mathbf{y}_{dh}$ and binary variable vector $\mathbf{z}_{dh}$, which express respectively energy flow rates and on/off status of operation of equipment for the corresponding time period.

As constraints, it is necessary to consider the performance characteristics of each piece of equipment and energy balance relationships of each energy flow for each time period on each representative day. First, performance characteristics of equipment are expressed as relationships between flow rates of input and output energy, using the continuous variable vector $\mathbf{y}_{dh}$. Here, the binary variable vector $\mathbf{z}_{dh}$ is also used to incorporate the on/off status of operation into these relationships. Since performance characteristics of equipment change with capacities, parameters expressing performance characteristic values are considered as functions of capacities $\mathbf{x}$. Next, energy balance relationships are expressed as linear equations with energy flow rates $\mathbf{y}_{dh}$.

For example, performance characteristics of a STIG unit can be formulated as follows: For a certain capacity, electrical and steam output is related to the natural gas consumption for main and supplemental firing, and the amount of injected steam. Here, binary variables are also used to express the on/off status of gas turbine operation, steam injection, and supplemental firing. Electricity consumption for auxiliary machinery and feedwater consumption is also related to the continuous and binary variables given above. These equations are generalized to express performance characteristics of a STIG unit of any capacity by defining performance characteristic values as functions of capacity. For example, the electrical output at the rated load status without steam injection is selected as capacity.

This formulation results in the following set of constraints:

$$\mathbf{C}_{dh}(\mathbf{x}, \mathbf{y}_{dh}, \mathbf{z}_{dh}) = \mathbf{0}, \quad (d = 1, \ldots, D; h = 1, \ldots, H), \qquad (2)$$

where $\mathbf{C}_{dh}$ is the vector composed of constraint functions.

Unknown variables are composed of the vector expressing equipment capacities and utility maximum demands $\mathbf{x}$, and the vectors expressing the operational strategy, $\mathbf{y}_{dh}$ and $\mathbf{z}_{dh}$. Although the capacity of each piece of equipment is selected from

Nomenclature

$\mathbf{C}_{dh}$ = vector composed of constraint functions
D = number of representative days per year
E = electric power, MWh/h
$\bar{E}_{GT}$ = electrical output at rated load status without steam injection of gas turbine cogeneration unit, MWh/h
F = sum of annual capital cost and customer/demand charges, \$/y
H = number of time periods per day
J = objective function (annual total cost), \$/y
Q = heat flow rate, MWh/h
T_{dh} = annual operational hour, h/y
V_{dh} = hourly energy charge, \$/h
$\mathbf{x}$ = vector composed of continuous variables for equipment capacities and utility maximum demands
$\mathbf{y}_{dh}$ = vector composed of continuous variables for energy flow rates
$\mathbf{z}_{dh}$ = vector composed of binary variables for on/off status of operation
α = ratio of capital unit costs of cogeneration units

Subscripts

d = index for representative day
h = index for time period

Equipment Symbols (Subscripts)

BA = gas-fired auxiliary boiler
CU = gas turbine cogeneration unit
EP = equipment for purchasing electricity
PC = pump for space cooling
RE = electric compression refrigerator
RS = steam absorption refrigerator

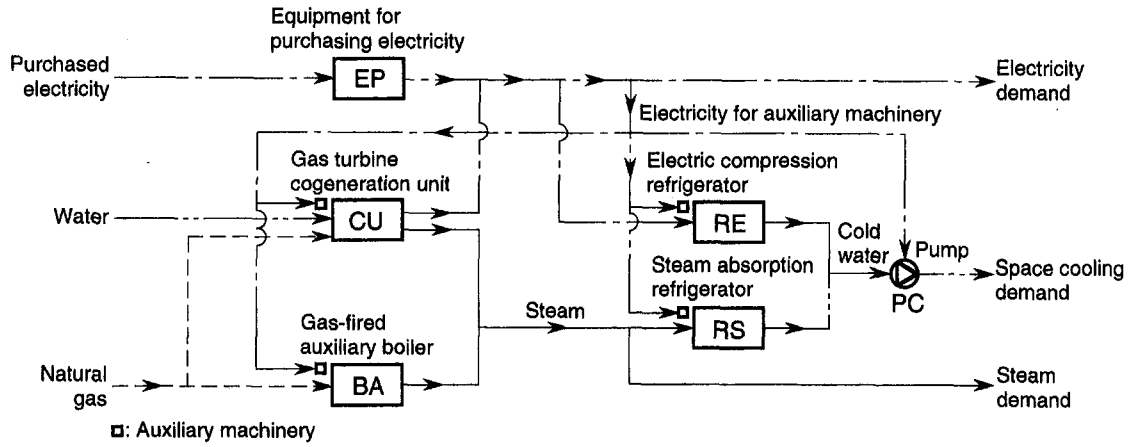

Fig. 2 Configuration of total cogeneration plant with STIG units

a set of discrete values in the practical design, it is regarded as a continuous variable here.

Hierarchical Optimization Method. In order to solve the problem efficiently, a hierarchical optimization method is employed here: Equipment capacities and utility maximum demands are determined in the unit sizing problem at the upper level; the operational strategy is assessed in the operational planning problem at the lower level; both levels are interconnected with each other by a penalty method.

At the upper level, the optimal unit sizing problem is formulated as a nonlinear programming one, in which optimal values of equipment capacities and utility maximum demands are searched so as to minimize the annual total cost. The sequential linear programming method is adopted as a solving method of the nonlinear programming problem (Cheney and Goldstein, 1959).

At the lower level, for a plant with the equipment capacities and utility maximum demands given at each searching step, the operational strategy is assessed using an optimal operational planning method proposed by the authors (Ito et al., 1990), and the annual energy charge is evaluated. The optimal operational planning problem is formulated as a mixed-integer linear programming problem, and it is solved by the branch and bound method (Garfinkel and Nemhauser, 1972). The specific algorithm adopted here is based on the Land–Doig (1960) method.

Numerical Study

A numerical study is carried out to investigate the effect of installing STIG units in a cogeneration plant by using the method presented above. A cogeneration plant used for district heating and cooling is selected as an example.

Input Data

Energy Demands. In the district considered here, four office buildings and two hotels are to be constructed. The total floor area is about 384,000 m^2. For simplicity, it is assumed that the plant begins to supply energy to all buildings at the same time. Table 1 gives the annual total and hourly maximum values of electricity, space cooling, and steam demands estimated for the district. Figure 3 shows the load duration curves indicating the annual variations of hourly energy demands. Here, a weekday, a Saturday, and a holiday are considered as representative days for each month; i.e., the operational strategy is investigated on 36 representative days throughout a year. Hourly energy demands are given as input data for each representative day. In addition to these average energy demands, peak energy demands in summer and winter are also given by multiplying the average energy demands on a weekday in August and January by 1.2, respectively.

Table 1 Annual total and hourly maximum values of energy demands

Energy	Annual total value GWh/y	Hourly maximum value MWh/h
Electricity	73.29	20.56
Space cooling	27.28	31.54
Steam *	31.24	28.84

* Energy flow rate of 1 MWh/h is equivalent to mass flow rate of 1.53×10^3 kg/h.

Alternative Plants. It is assumed that two gas turbine cogeneration units are installed, and that one unit is installed for other kinds of equipment, for simplicity. In order to investigate the effect of STIG units, the following three alternative plants are selected here:

1 Plant A: both cogeneration units are STIG units;
2 Plant B: one is a STIG unit, and the other is a simple-cycle gas turbine unit; and
3 Plant C: both are simple-cycle gas turbine units.

Here, it is assumed that the capacities of two cogeneration units are the same for each plant, and that a simple-cycle gas turbine unit is composed of a simple-cycle gas turbine generator and a conventional waste heat recovery boiler.

Performance and Cost. Performance characteristics and capital costs of equipment are given as functions of their capacities. They are summarized in Table 2. Nonlinear curve fitting is adopted for performance characteristics of STIG and simple-cycle gas turbine units on the basis of real data (Ito et al., 1995). For example, the following features are considered: the power-generating efficiency at the rated load status without steam injection tends to increase with capacity, and conversely

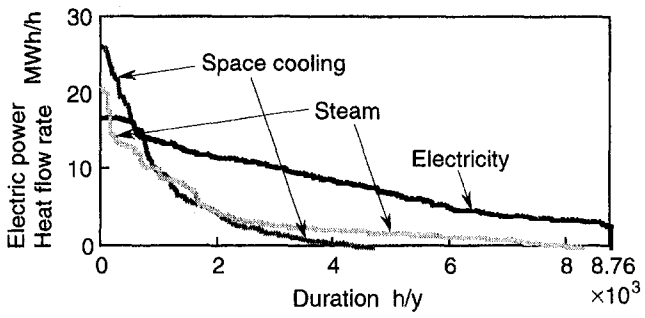

Fig. 3 Load duration curves of energy demands

Table 2 Performance characteristic values and capital unit costs of equipment

Equipment	Performance characteristic value	Capital unit cost
STIG cogeneration unit	Power-generating efficiency $0.197\bar{E}_{GT}^{0.21}$ * Waste heat recovery efficiency $0.568\bar{E}_{GT}^{-0.04}$ * (Rated load status without steam injection) Power-generating efficiency $\dfrac{0.197\bar{E}_{GT}^{0.21}+0.029\bar{E}_{GT}^{-0.04}}{1+0.071\bar{E}_{GT}^{-0.04}}$ * (Rated load status with steam injection)	$1760\times10^3\alpha$ \$/MW
Simple-cycle gas turbine cogeneration unit	Power-generating efficiency $0.197\bar{E}_{GT}^{0.21}$ * Waste heat recovery efficiency $0.568\bar{E}_{GT}^{-0.04}$ * (Rated load status)	1760×10^3 \$/MW
Gas-fired auxiliary boiler	Thermal efficiency 0.90	53×10^3 \$/MW
Electric compression refrigerator	Coefficient of performance 3.60	172×10^3 \$/MW
Steam absorption refrigerator	Coefficient of performance 1.20	413×10^3 \$/MW
Equipment for purchasing electricity	—	450×10^3 \$/MW
Pump	Electricity consumption rate 0.025 MW/MW	—

* $\bar{E}_{GT}$: capacity (electrical output at the rated load status without steam injection) of gas turbine cogeneration unit.

the waste heat recovery efficiency on the same condition tends to decrease; steam injection increases electrical output while it needs additional natural gas consumption. Linear curve fitting is adopted for performance characteristics of other kinds of equipment. Linear functions are used to express the relationship between capital cost and capacity for all kinds of equipment. Here, a parametric study is carried out with respect to the ratio of capital unit costs of cogeneration units α defined by

$$\alpha = \frac{\text{Capital unit cost of STIG units}}{\text{Capital unit cost of simple-cycle gas turbine units}}. \quad (3)$$

The rates of utilities are standard ones used in Japan, and they are given in Table 3. In evaluating the annual total cost, it is assumed that the life of equipment is 15 y, the salvage value of equipment is zero, and the interest rate is 0.1.

Results and Discussion. Figure 4 shows the optimal values of equipment capacities and utility maximum demands in relation to the ratio of capital unit costs of cogeneration units α. Comparisons are made between plants A and C, and plants B and C in Figs. 4(a) and 4(b), respectively. Since plant C has no STIG units, the optimal values are not affected by α. Since plants A and B have STIG units, the optimal values vary with α. The optimal capacity per unit (without steam injection) is shown for gas turbine cogeneration units. The figures do not include the optimal capacities for electric compression and steam absorption refrigerators. The optimal capacities for these refrigerators are almost equal to zero and the maximum value of space cooling demand, respectively, for all plants and all values of α.

The capacity of STIG units for plant A is lower than that of simple-cycle gas turbine units for plant C, and it decreases with an increase in α. On the other hand, the capacity of a STIG unit and a simple-cycle gas turbine unit for plant B is a little higher than that for plant C, and it is almost constant regardless an increase in α. The reason for this result will be described below.

Figure 5 shows the relationships between the annual total costs for plants A and B, and the ratio of capital unit costs of cogeneration units α. The annual total costs for plants A and B are normalized by that for plant C. The annual total cost for plant A exceeds that for plant C in the range of α more than 1.4, while the annual total cost for plant B is lower than that for plant C in the range of α adopted here. This is because the first STIG unit contributes significantly to enhancing the operational flexibility regarding the heat-to-power ratio and consequently reducing the operational cost, but further enhancement in operational flexibility is not necessary and the second one only increases the annual capital cost. This is also related to the above-stated results on optimal capacities of gas turbine cogeneration units.

Figure 6 shows the relationships between the annual primary energy consumption for plants A and B, and the ratio of capital unit costs of cogeneration units α. The annual primary energy consumption is selected as an evaluation criterion for energy-saving property, and it is normalized by that for plant C. Here, it is assumed that the thermal efficiency of purchased electricity is 0.388. Unlike the above-stated economic property, the energy-saving property is not significantly affected by α, and the annual primary energy consumption for plants A and B remains lower than that for plant C. This is because the annual primary energy consumption depends essentially on the operational strategy, and a large amount of exhaust heat, which must be disposed of in plant C, can be utilized in plants A and B due to high operational flexibility by steam injection. An increase in the annual primary energy consumption with α in plant A is due to a decrease in the capacity of STIG units, as shown in Fig. 4(a).

To confirm this theory, the operational strategies for some cases are examined in detail. Figures 7(a–c) show the load duration curves of electricity supply and exhaust heat utilization for optimal operational strategies of plants A to C, respectively. The cases where the ratio of capital unit costs of cogeneration units α is 1.2 are shown for plants A and B. In these figures, E_{main1} and E_{main2} are the electric power generated without steam injection, E_{inj1} and E_{inj2} are the electric power generated addition-

Table 3 Rates of utilities

Utility	Unit cost		
	Customer charge	Demand charge	Energy charge
Purchased electricity	—	13.92×10^3 \$/(MW·month)	86.16 (Jul.~Sep.) \$/MWh 78.32 (Other months)
Natural gas	288 \$/month	9.6 (Apr.~Oct.) \$/(m³/h·month) 25.6 (Other months)	0.247 \$/m³
Water	—	—	2.8 \$/m³

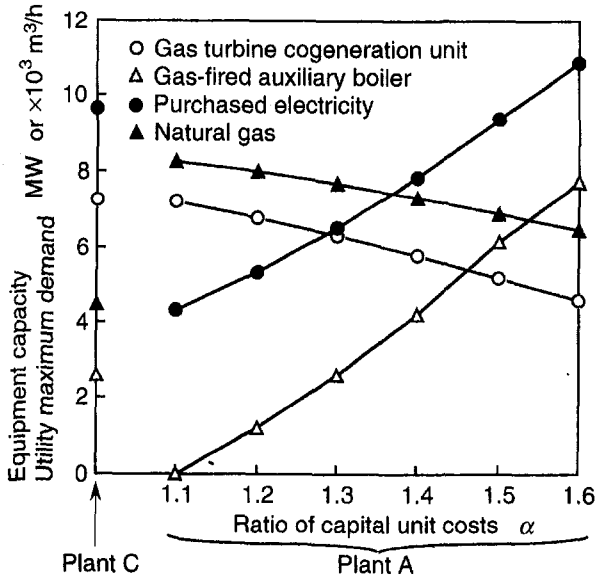

Fig. 4(*a*) Plants A and C

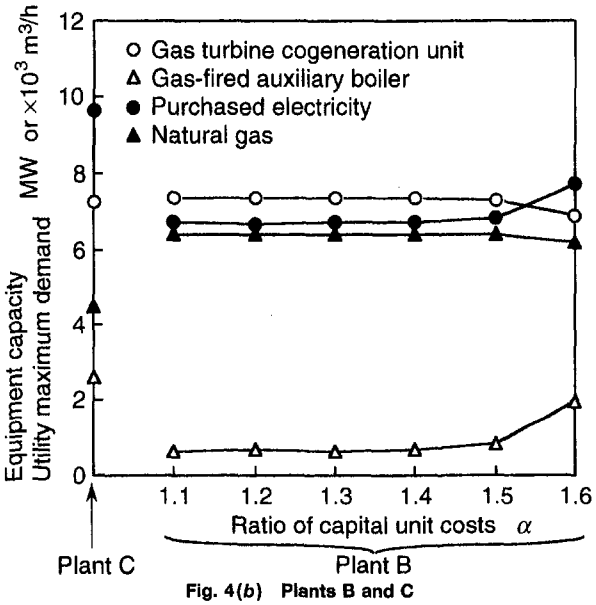

Fig. 4(*b*) Plants B and C

Fig. 4 Optimal values of equipment capacities and utility maximum demands versus ratio of capital unit costs of cogeneration units α

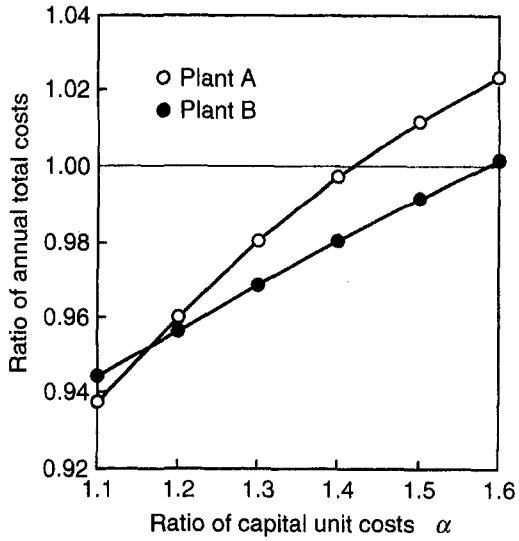

Fig. 5 Ratio of annual total costs versus ratio of capital unit costs of cogeneration units α

ally with steam injection, and E_{buy} is the electric power purchased from an outside electric power company. In addition, Q_{sup1} and Q_{sup2} are the heat flow rates of steam supplied for thermal energy demand, Q_{inj1} and Q_{inj2} are the heat flow rates of steam used for steam injection, and Q_{disp} is the heat flow rate of steam disposed of, which is converted from the heat flow rate of exhaust gas.

In plant C, cogeneration units are operated at the rated load status in case of high electricity demand. However, this operation produces a large amount of heat disposal because the heat-to-power ratio cannot be changed. On the other hand, cogeneration units tend to be shut down in case of low electricity demand. This is because the power-generating efficiency of gas turbine generators at part-load status is lower than that at the rated load status.

In plants A and B, cogeneration units produce no heat disposal, and tend to be operated at part-load status even during periods of low electricity demand. The operational hours of both cogeneration units for plants A and B are longer than those for plant C. This is because surplus steam can be utilized for steam injection to increase the electric power. However, the operational hour of the second STIG unit in plant A is much shorter than that of the first one. Consequently, the effect of installing the second one is relatively small, and plant A is inferior to plant B in both economic and energy-saving properties.

Conclusions

By using an optimal unit sizing method, the effect of installing steam-injected gas turbine units in a cogeneration plant has been investigated from the viewpoints of both unit sizing and operational planning. A numerical study has been carried out on a plant for district heating and cooling, and the influence of capital cost of STIG units has been examined on the unit sizing, and economic and energy-saving properties of the cogeneration plant. The following main results have been obtained here:

1 The installation of STIG units can enhance the operational flexibility regarding the heat-to-power ratio, and consequently

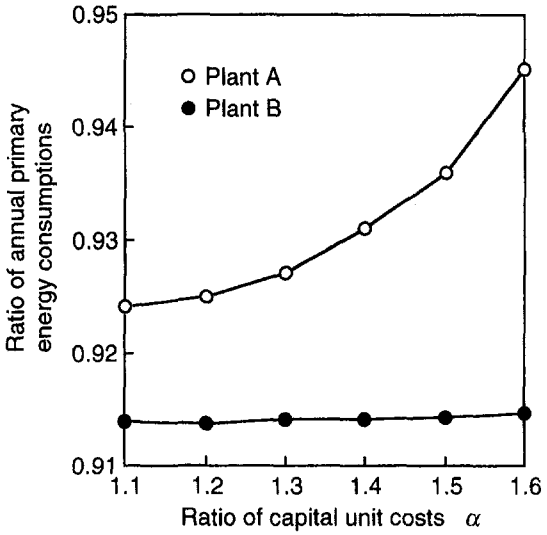

Fig. 6 Ratio of annual primary energy consumptions versus ratio of capital unit costs of cogeneration units α

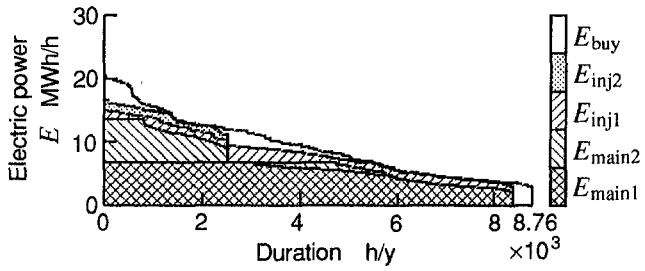

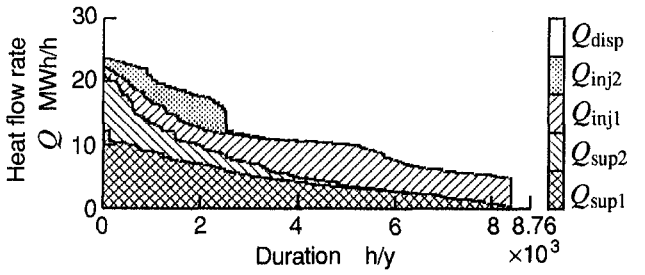

Fig. 7(*a*) Plant A (α = 1.2)

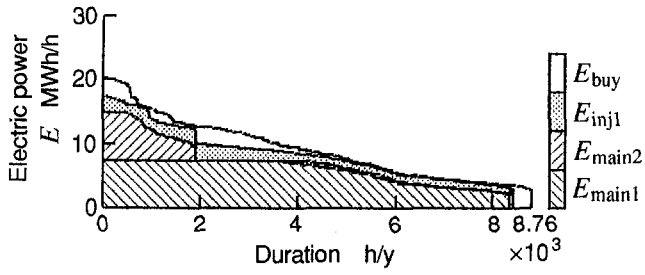

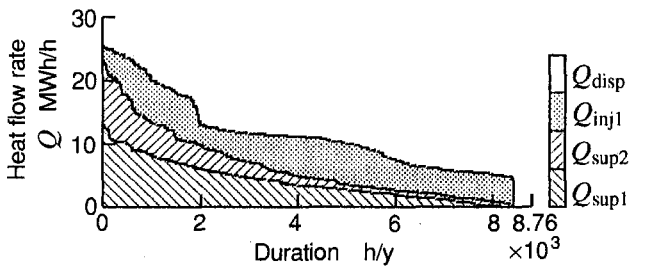

Fig. 7(*b*) Plant B (α = 1.2)

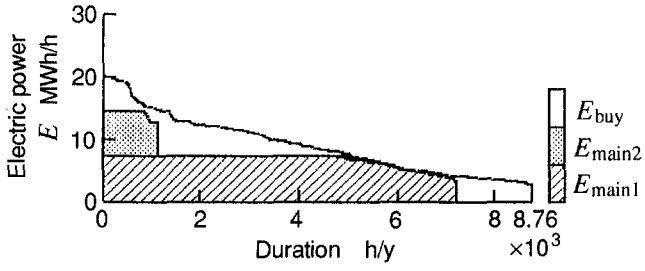

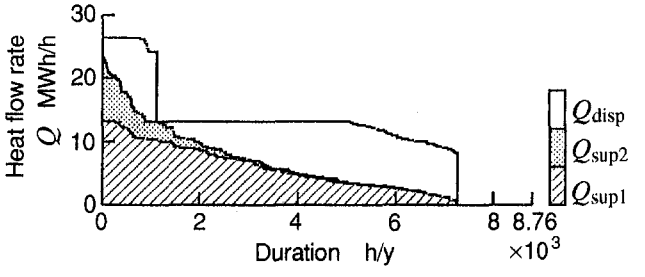

Fig. 7(*c*) Plant C

Fig. 7 Load duration curves of electricity supply and exhaust heat utilization for optimal operational strategies

reduce the operational cost. However, it may be disadvantageous in annual total cost, which depends on an increase in the capital cost of STIG units.

2 The installation of multiple STIG units may be excessive, because the installation of the first unit may enhance the operational flexibility enough to correspond to seasonal and hourly variations of energy demands, and further enhancement in operational flexibility may not be necessary.

3 The energy-saving property for a STIG cogeneration plant remains better than that for a simple-cycle gas turbine cogeneration plant, and it is not significantly affected by the capital cost of STIG units.

References

Baken, J. A. M., and Haspel, B. van den, 1988, "Optimized Operation of Steam-Injected Gas Turbine Cogeneration Units," *Proc. 2nd International Symposium and Exposition on Turbomachinery, Combined-Cycle Technologies and Cogeneration,* pp. 259–265.

Brown, D. H., and Cohn, A., 1981, "An Evaluation of Steam Injected Combustion Turbine Systems," ASME JOURNAL OF ENGINEERING FOR POWER, Vol. 103, pp. 13–19.

Cheney, E. W., and Goldstein, A. A., 1959, "Newton's Method for Convex Programming on Tchebycheff Approximation," *Numerical Mathematics,* Vol. 1, pp. 253–268.

Fraize, W. E., and Kinney, C., 1979, "Effects of Steam Injection on the Performance of Gas Turbine Power Cycles," ASME JOURNAL OF ENGINEERING FOR POWER, Vol. 101, pp. 217–227.

Garfinkel, R. S., and Nemhauser, G. L., 1972, *Integer Programming,* Wiley, New York, pp. 5–7.

Ito, K., Yokoyama, R., Akagi, S., and Matsumoto, Y., 1990, "Influence of Fuel Cost on the Operation of a Gas Turbine-Waste Heat Boiler Cogeneration Plant," ASME JOURNAL OF ENGINEERING FOR GAS TURBINES AND POWER, Vol. 112, pp. 122–128.

Ito, K., Yokoyama, R., and Matsumoto, Y., 1995, "Optimal Operation of Cogeneration Plants With Steam-Injected Gas Turbines," ASME JOURNAL OF ENGINEERING FOR GAS TURBINES AND POWER, Vol. 117, pp. 60–66.

Land, A. H., and Doig, A. G., 1960, "An Automatic Method of Solving Discrete Programming Problems," *Econometrica,* Vol. 28, pp. 497–520.

Larson, E. D., and Williams, R. H., 1987, "Steam-Injected Gas Turbines," ASME JOURNAL OF ENGINEERING FOR GAS TURBINES AND POWER, Vol. 109, pp. 55–63.

Maher, K. J., Ehmke, H. J., and Gibson, D. C., 1987, "Optimum Operation of a Steam Injected Gas Turbine," presented at the USSR/Australia Workshop on Advanced Energy Technologies.

Noymer, P. D., and Wilson, D. G., 1993, "Thermodynamic Design Considerations for Steam-Injected Gas Turbines," ASME Paper No. 93-GT-432.

Rice, I. G., 1993a, "Steam-Injected Gas Turbine Analysis: Part I—Steam Rates," ASME Paper No. 93-GT-132; published as "Steam-Injected Gas Turbine Analysis—Steam Rates," ASME JOURNAL OF ENGINEERING FOR GAS TURBINES AND POWER, Vol. 117, 1995, pp. 347–353.

Rice, I. G., 1993b, "Steam-Injected Gas Turbine Analysis: Part II—Steam-Cycle Efficiency," ASME Paper No. 93-GT-420.

Rice, I. G., 1993c, "Steam-Injected Gas Turbine Analysis: Part III—Steam-Regenerated Heat," ASME Paper No. 93-GT-421.

Yokoyama, R., Ito, K., and Matsumoto, Y., 1994, "Optimal Sizing of a Gas Turbine Cogeneration Plant in Consideration of Its Operational Strategy," ASME JOURNAL OF ENGINEERING FOR GAS TURBINES AND POWER, Vol. 116, pp. 32–38.

Measured Force/Current Relations in Solid Magnetic Thrust Bearings

P. E. Allaire

R. L. Fittro

E. H. Maslen

Mechanical, Aerospace, and Nuclear Engineering Department, University of Virginia, Charlottesville, VA 22903

W. C. Wakefield

Proctor & Gamble, Hunt Valley, MD 21030

When magnetic bearings are employed in a pump, compressor, turbine, or other rotating machine, measurement of the current in the bearing coils provides knowledge of the forces imposed on the bearings. This can be a significant indicator of machine problems. Additionally, magnetic bearings can be utilized as a load cell for measuring impeller forces in test rigs. The forces supported by magnetic bearings are directly related to the currents, air gaps, and other parameters in the bearings. This paper discusses the current/force relation for magnetic thrust bearings. Force versus current measurements were made on a particular magnetic bearing in a test rig as the bearing coil currents were cycled at various time rates of change. The quasi-static force versus current relations were measured for a variety of air gaps and currents. The thrust bearing exhibits a hysteresis effect, which creates a significant difference between the measured force when the current is increasing as compared to that when the current is decreasing. For design current loops, 0.95 A to 2.55 A, at the time rate of change of 0.1 A/s, the difference between increasing and decreasing current curves due to hysteresis ranged from 4 to 8 percent. If the bearing is operated in small trajectories about a fixed (nonzero) operation point on the F/I (force/current) curve, the scatter in the measurement error could be expected to be on the order of 4 percent. A quasi-static nonlinear current/force equation was developed to model the data and curve-fit parameters established for the measured data. The effects of coercive force and iron reluctance, obtained from conventional magnetic materials tests, were included to improve the model, but theoretically calculated values from simple magnetic circuit theory do not produce accurate results. Magnetic fringing, leakage, and other effects must be included. A sinusoidal perturbation current was also imposed on the thrust bearing. Force/current magnitude and phase angle values versus frequency were obtained for the bearing. The magnitude was relatively constant up to 2 Hz but then decreased with frequency. The phase lag was determined to increase with frequency with value of 16 deg at 40 Hz. This effect is due to eddy currents, which are induced in the solid thrust-bearing components.

Introduction

Magnetic bearings have been used in supporting shaft forces in compressors, pumps, turbines, and other rotating machines. Normally a magnetic thrust bearing is employed to provide an axial load capacity in a rotating machine (Allaire, 1989; Allaire et al., 1989). Figure 1 shows the geometry of a magnetic thrust bearing. Proper design of the bearing requires detailed knowledge of the force that results when a current is applied. Simple magnetic circuit analysis is often employed for preliminary thrust bearing design (Allaire et al., 1994a). This paper discusses measurements of the current/force relation in a magnetic thrust bearing and an extension of simple circuit analysis to account for other effects.

In recent years, magnetic bearings have begun to be used for the measurement of forces as well, including load cells in impeller test rigs, excitation for system identification and monitoring. The use of a magnetic bearing as an excitation force has been described by Ulbrich (1988). Wagner and Pietruszka (1988) developed a magnetic bearing to be used for the measurement of fluid forces in turbocompressor applications. Imlach et al. (1991) described the use of magnetic bearings to measure force, stiffness, and damping in a canned motor pump. Hawkins et al. (1991) have also employed magnetic bearings as a known force input device for the identification of rotor dynamic coefficients in a test stand. Humphris (1992) described the use of magnetic bearings as a diagnostic tool for rotating shafts. Feng et al. (1982) and Verhoeven et al. (1993) employed magnetic bearings in two test rigs for the identification of long seals and impeller/casing interactions. Hawkins and Imlach (1993) described an experimental method for the measurement of the frequency dependent force displacement transfer function of a magnetic bearing/controller system.

Test rigs have been developed for measuring thrust and radial forces by several investigators. A review of journal articles related to pump impeller forces up to 1984 is given by Flack and Allaire (1984). Several works have appeared in the literature since that time. An example is Jery et al. (1985) reporting on a strain gage-based test rig. Rigs of this type require very careful construction to minimize structural interactions that contribute to uncertainties in the measurements. Testing has also been limited to impellers with relatively large clearances compared to industrial practice.

The current/force relation is an important topic for magnetic bearings. However, there have been few studies reported on accurately determining the characteristics of this relation for specific magnetic bearing configurations and comparing this to a theoretical model. Some preliminary results on this topic were reported by Allaire et al. (1994b). Many effects such as nonlinearities, eddy currents, hysteresis, fringing, leakage, and frequency effects are not included in these simple models.

Contributed by the International Gas Turbine Institute and presented at the 40th International Gas Turbine and Aeroengine Congress and Exhibition, Houston, Texas, June 5–8, 1995. Manuscript received by the International Gas Turbine Institute February 13, 1995. Paper No. 95-GT-400. Associate Technical Editor: C. J. Russo.

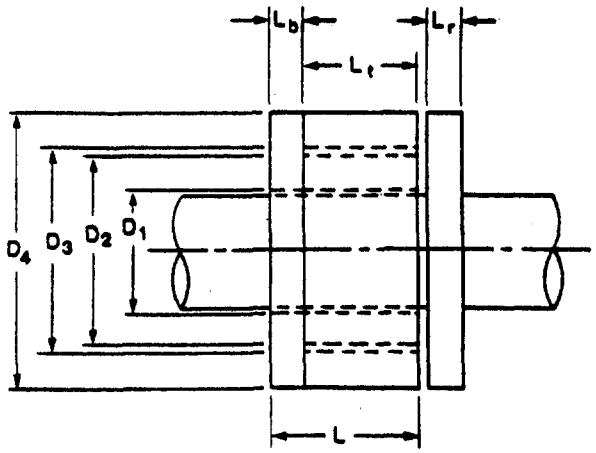

Fig. 1 Side view of thrust bearings

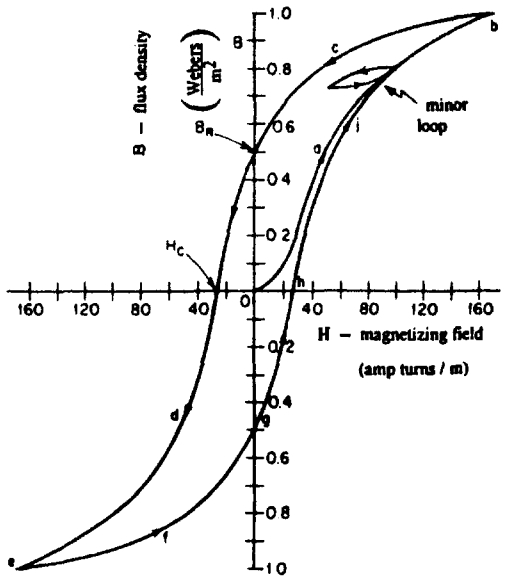

Fig. 2 *B-H* curve for typical magnetic material

Hysteresis and eddy current effects are important in magnetic bearing characterization. The *B-H* curve of any magnetic material exhibits hysteresis, which affects the current/force relation. A hysteresis curve for a typical magnetic material is shown in Fig. 2. The increasing H values follow a different curve than the decreasing H values. The area between the curves represents the energy loss during the cycle.

Eddy current effects also degrade magnetic bearing performance (Zmood et al., 1987). Williams and Trumper (1993) have investigated material/air gap hysteresis effects in a laminated stack similar to a radial bearing. Keith (1993) conducted an extensive study of eddy current and hysteresis effects on current/force relations in a two-pole magnetic configuration similar to a magnetic thrust bearing. He found that eddy current effects in solid pole pieces, with a 0.51 mm (10 mils) gap, dominated the current/force relation as the frequency increased above approximately 2 Hz. Keith noted that this produces a significant phase lag in the actuator. Knowledge of the phase lag found in the thrust bearing affects the feedback control loop design.

If a magnetic thrust bearing is perfectly axisymmetric and the coil currents are held constant, there will be no eddy current effects present. However, thrust bearings in industrial use are subject to time-varying forces. The coil currents are changed to adjust the bearing load capacity in response to the applied load (Allaire et al., 1997). These time-varying currents generate hysteresis and eddy current effects in thrust bearings. In turn, these induced eddy currents produce induced magnetic fields opposing the applied magnetic field. These effects were studied in the magnetic thrust bearing described here. Both of these phenomena are crucial to accurate modeling of the current/force relation in force test rigs and operating industrial bearings.

Thrust Test Rig

The magnetic thrust bearing geometry is shown in Fig. 1. The stator is composed of an inner toroid, a base plate, outer toroid, and a coil of wire. The rotor is simply a flat disk fixed to the shaft (also called a thrust disk or thrust runner). The magnetic thrust bearing had an outer diameter of D_4 = 89.5 mm (3.50 in.), D_3 = 78.5 mm (3.09 in.), D_2 = 60.9 mm (2.40 in.), inner diameter of D_1 = 44.4 mm (1.75 in.), axial lengths of L = 26.4 mm (1.04 in.) and L_b = 7.1 mm (0.28 in.). The thrust collar (runner) had axial length L_r = 14.2 mm (0.56 in.). It was designed for a thrust load of F = 187 N (42 lbf). The coils consisted of 300 turns of #22 wire secured in the bearing by a thin stainless steel retainer (slotted to avoid eddy currents in the retainer). The operating current (design bias current) was I_0 = 1.75 A within the operating range of 0.95 A to 2.55 A. The nominal operating air gap of the bearing was g_0 = 0.762 mm (0.030 in.). The coercive force and relative permeability of the magnetic material have been measured independently via a Rowland ring test as 5.15 Oe (410 A/m) and 1376, respectively. All magnetic components were constructed of conventional solid soft iron material rather than laminated. The stator may be solid or divided into sectors to reduce eddy currents. This work considers only solid thrust bearing components.

A load cell was attached to the movable crosshead (on an Instron Universal Testing Machine) and the thrust bearing fixed to the base of the machine. Figure 3 shows a drawing of the test setup. Calibration of the testing apparatus was accomplished by hanging known weights from the collar holder and measuring the force. Great care, using shims around the circumference of the bearing, was taken to ensure that the thrust collar and bearing were parallel.

Current Cycle: Quasi-Static Results

Measurements of current/force relations were made for a wide range of air gaps and currents (Wakefield, 1994). At low

Nomenclature

A_g = pole cross-sectional area (one pole)
b_1 = hysteresis offset
b_2 = equivalent iron gap offset
B = magnetic flux density
D_1 = bearing inner diameter
D_2 = coil inner diameter
D_3 = coil outer diameter
D_4 = bearing outer diameter
F = force
F_0 = nominal force
g = air gap (one)
g_0 = nominal air gap
H_c = coercive force (field intensity)
I = current
I_c = effective current
I_0 = nominal current
L = total axial stator length = $L_b + L_t$
L_r = thrust collar length
L_i = length of magnetic path in iron
N = number of turns
R_g = air gap reluctance = $g/(\mu_0 A_g)$
R_i = iron reluctance = $L_i/(\mu_0 \mu_r A_g)$
γ = force proportionality constant
μ_0 = permeability of free space
μ_r = relative permeability

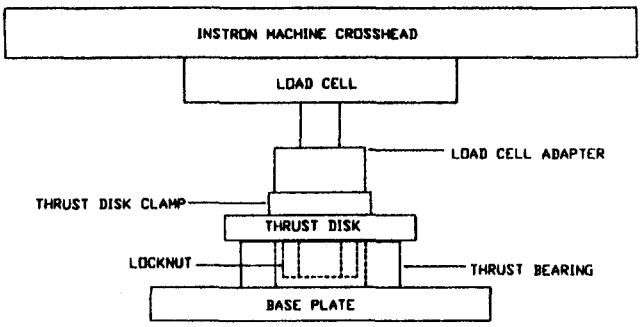

Fig. 3 Drawing of thrust bearing test setup

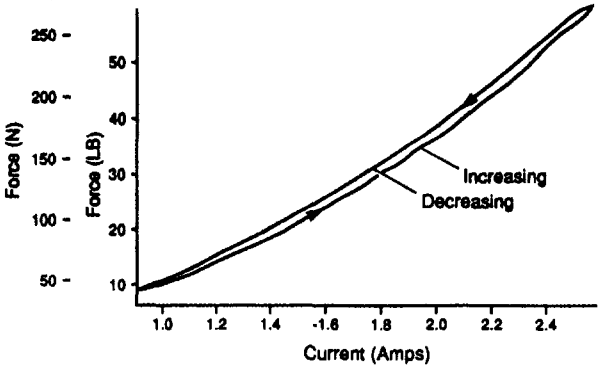

Fig. 5 Measured force versus current with air gap 0.762 mm (0.030 in.), current 0.95 A to 2.15 A

frequencies, the predominant effect is due to hysteresis. Current cycles were run at a quasi-static rate of 0.1 A/s and at lower current rates. All of the results within a certain range gave essentially the same results indicating that only hysteresis effects were being measured. The results presented in this paper are for two current loop tests. Figure 4 shows force/current values for an air gap of 0.762 mm (30 mils) and a major current loop from −2.55 A to 2.55 A. For the same air gap, results for a minor loop of 0.95 A to 2.55 A (the design range for this bearing) are given in Fig. 5. Before testing, a de-gaussing procedure was followed to bring the *B-H* curve to remove any residual magnetism effects in the material.

The shape of each force/current plot was the same for increasing and decreasing currents. For comparison purposes, the force was evaluated at the design bias current value of 1.75 A as the perturbation current was increasing and decreasing. The difference between the two curves was as high as 12.6 percent for major current loops such as the one shown in Fig. 4 but reduced to 4.7 percent for minor loops more likely to be encountered in actual use as illustrated in Fig. 5. The repeatability of the curves was very high, indicating that the loop effect at this low cycle rate was due to hysteresis rather than eddy currents.

Quasi-Static Current/Force Model

Magnetic bearings, when operated single-sided as in this case, are nonlinear. The force is related to the square of the coil currents (Allaire et al., 1994a). When the bearing is double acting, the net effect is to linearize the actuator so that the force-current relation is approximately linear. A typical equation for the flux density B in the magnetic circuit is given by

$$B = \frac{NI}{2A_g R_g} \tag{1}$$

where it is assumed that all of the flux is contained in the two air gaps and there is no hysteresis. Then the force F which attracts the rotor in a single-sided stator is given by

$$F = \frac{B^2 A_g}{\mu_0} = \frac{\mu_0 N^2 I^2 A_g}{4g^2} \tag{2}$$

This simple formula is inadequate to model the effects seen in the experimental data just presented.

Two primary effects must be included in the quasi-static equation above: iron reluctance and iron hysteresis effects. The iron reluctance effect R_i can be included in the denominator of the flux equation, summed with the air gap reluctance, and the iron hysteresis effect can be modeled as an effective current I_c.

$$B = \frac{N(I + I_c)}{A_g(2R_g + R_i)} \tag{3}$$

For this bearing, the air gap length is 0.762 mm (0.030 in.), the air gap area is 1,368 mm^2 (2.12 in.^{2}) and the air gap reluctance is $R_g = 4.43 \times 10^5$ A-turns/weber for one air gap. In the iron, the iron path length is 83.8 mm (3.3 in.), the same area, and the reluctance of $R_i = 3.5 \times 10^4$ A-turns/weber. As the magnetic field H decreases in the magnetic material, there will be a coercive force H_c remaining when zero magnetic flux density is reached. This may be represented as an effective current I_c where

$$I_c = \frac{H_c}{N} L_e = \frac{H_c}{N}\left(2g + \frac{L_i}{\mu_r}\right) \tag{4}$$

where L_e is the effective magnetic gap length. For this bearing, $L_e = 1.585$ mm (0.0624 in.) and $I_c = 0.0022$ A. This corresponds to the current required to return the magnetic flux density B to zero. If the material has the magnetic field intensity H decreased gradually in an oscillating fashion, the *B-H* curve will return to the origin of the *B-H* plot. However, magnetic bearings are typically operated so that the material has a coercive force present as shown by the measurements. In this case, the flux equation must be modified to include the corresponding effective current.

The force equation, Eq. (2), was modified to include the additional terms with the result

$$F(I, g) = \frac{\mu_0 N^2 (I + I_c)^2 A_g}{4\left(g + \frac{L_i}{2\mu_r}\right)^2} \tag{5}$$

This is the general form employed in this paper.

Normally there is an operating point for a thrust bearing about a nominal value for current I_0, and gap g_0. Let the nominal force be that due to the air gap reluctance only with the result:

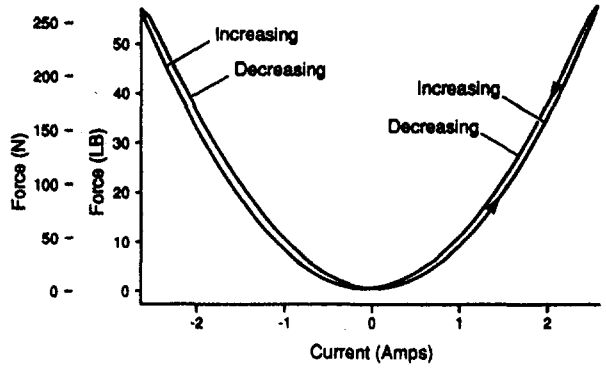

Fig. 4 Measured force versus current with air gap 0.762 mm (0.030 in.), current −2.55 A to 2.55 A

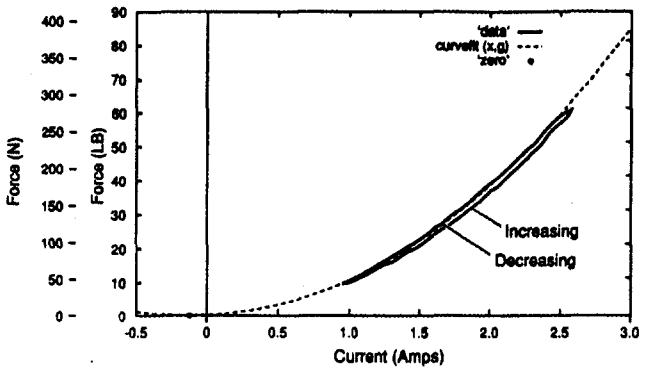

Fig. 6 Least-squares curve fit and typical measured current cycle

$$F_0 = \frac{\mu_0 N^2 I_0^2 A_g}{4 g_0^2} \tag{6}$$

For the bearing tested in this work, $I_0 = 1.75$ A, $g_0 = 0.762$ mm (30 mils) and $F_0 = 203.8$ N (45.8 lb).

It is appropriate to employ a dimensionless form of the force equation. Define the dimensionless force as:

$$\bar{F}(\bar{I}, \bar{g}) = \frac{\left(\bar{I} + \frac{I_c}{I_0}\right)^2}{\left(\bar{g} + \frac{L_i}{2\mu_r g_0}\right)^2} \tag{7}$$

where

$$\bar{I} = \frac{I}{I_0}, \quad \bar{g} = \frac{g}{g_0}$$

This suggests the generic form of the quasi-static current/force relation employed in this paper to fit the measured data for the tested single-sided magnetic thrust bearing:

$$\bar{F}(\bar{I}, \bar{g}) = \gamma\left(\frac{\bar{I} + b_1}{\bar{g} + b_2}\right)^2 \tag{8}$$

where $b_1 = I_c/I_0$ and $b_2 = L_i/(2\mu_r g_0)$. The primary variables are the current and air gap length. Here γ is a dimensionless constant of proportionality, b_1 represents an offset in the B-H curve for the magnetic material due to hysteresis effects, and b_2 represents the ratio of equivalent magnetic length to the nominal air gap.

A least squares curve fit of the data from the thrust bearing measurements produced the following values for the current/force equation:

$$\gamma = 0.996$$
$$b_1 = 0.0718$$
$$b_2 = 0.3247 \tag{9}$$

Figure 6 shows a comparison of the curve fit with one of the measured current loops. The zero point indicates the equivalent coercive current I_c. The theoretical value for b_1 using the value of 0.0022 A found earlier gives $b_1 = 0.0012$ rather than the value given above. This is an error of 98 percent. Similarly for the theoretically calculated term $b_2 = 0.040$ and the error here is 88 percent. The errors are due to magnetic fringing, leakage and other factors not completely obvious to the authors at this point in time.

Many data runs were employed to develop the curve fit. In each case, only measurements with the design current range, 0.95 A to 2.55 A, were used, with the current changing at 0.1 A/s. Equal numbers of increasing and decreasing current data were averaged to produce the numerical values in Eq. (9). A statistical error analysis was also conducted. The distribution of error was noticeably bimodal with a mean of 0.3 percent and a standard deviation of 3.8 percent. The bimodal distribution suggests the superposition of two normal distributions with differing mean values. The experimental data were taken for force/current trajectories essentially on the same hysteresis loop from 0.95 A to 2.55 A. The separation between the two halves of the hysteresis loops, one with increasing current and the other with decreasing current, is believed to have induced the bimodal distribution.

Uncertainty Analysis

An uncertainty analysis was conducted to determine the extent to which uncertainty in the calibration data produces uncertainty in the calibration parameters (γ, b_1, b_2) and the extent to which this model uncertainty, coupled with the measurement uncertainty during the execution of the actual experiment, will lead to uncertainty in the measured forces. This analysis resulted in an expected mean error of zero and a standard deviation of 3.96 percent. This result is consistent with the observed distribution, implying that the only major (nonrandom) source of error in the measurements is due to hysteresis.

Frequency Effects

Eddy currents develop due to time-varying currents in the bearing coil. The induced flux in the stator opposes the applied flux to reduce the generated magnetic bearing load capacity. The resulting frequency response effects can cause a magnetic bearing performance to deviate significantly from expected values. Eddy current effects were explored by cycling the coil current through the design range of 0.95 A to 2.55 A at various frequencies. Figure 7 shows the force/current plots for 0.1, 1.0 and 10.0 Hz with an air gap of 0.762 mm (30 mils). The difference in the loop segments becomes larger as the frequency increases. This is due to higher eddy current effects as the time rate of change of the electric field increases.

The ratio of force to current was evaluated for a range of frequencies. The current value versus frequency was generated by comparison of the measured current signal to a sinusoidal reference. A similar method was used for the force value. A ratio of these values was then taken. The magnitude is plotted in Fig. 8 and the phase angle is plotted in Fig. 9. The magnitude is relatively constant over the frequency range up to 2 Hz but drops off approximately 28 percent at 40 Hz. Binns et al. (1985) report a similar 10 dB/decade roll-off for eddy currents in other configurations.

The phase angle approximately follows a one-half power function with frequency. It drops off to approximately 16 deg

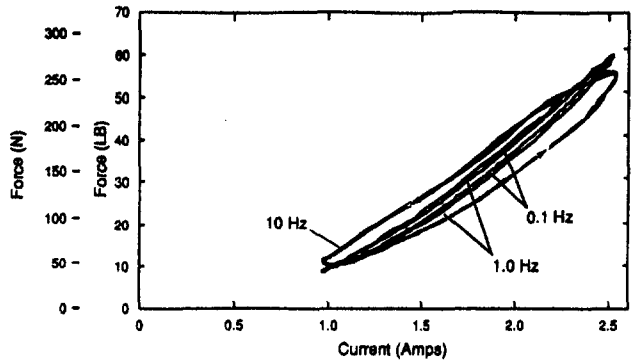

Fig. 7 Measured force versus sinusoidal current at 0.1, 1.0, 10 Hz with air gap 0.762 mm (0.030 in.) current 0.95 A to 2.55 A

at 40 Hz. A least-squares curve fit to the phase angle data gives the results

$$\phi = -1.039\omega^{1/2} - 2.0135 \quad (10)$$

as shown in Fig. 9. This phase lag versus frequency trend is consistent with eddy current effects in other applications (Binns et al., 1985). A linear model was also curve fit to the data as illustrated in Fig. 9 but the fit is not very good. This decreased force/current magnitude and phase lag versus frequency is due primarily to tangential eddy currents developed in the solid thrust bearing stator. The induced flux in the stator opposes the applied flux to reduce the generated magnetic bearing load capacity.

The pump test rig in which these bearings will be employed runs at approximately 10 Hz with a blade pass frequency of approximately 40 Hz. Overall, the large drop-off of phase angle at the running frequency and blade pass frequency makes this particular bearing not a particularly good choice for the purpose of measuring forces. An alternative bearing employing a less lossy material is currently under testing.

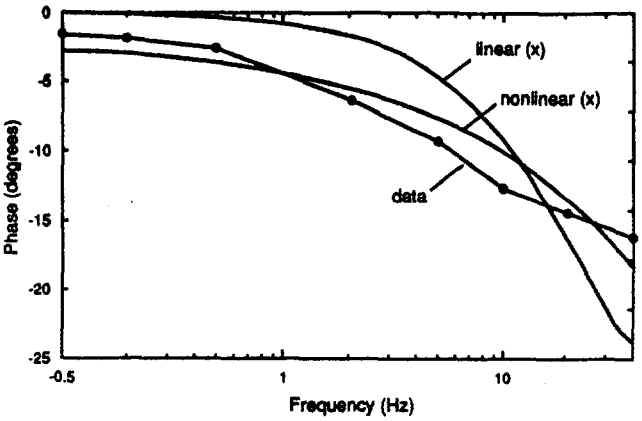

Fig. 9 Phase angle of force/current ratio versus frequency with linear and half frequency curve fits

Conclusions

Numerous papers, noted in the introduction, either propose or have reported the use of magnetic bearings to determine external forces in a rotating machine or component. However, not much has been reported in the literature on verifying the theoretical equations apparently employed to extract the data. The deviations from the simple force/current relations normally quoted for magnetic thrust bearing load capacity must be taken into account when using magnetic bearings as load cells. However, testing can be carried out to quantify hysteresis and eddy current effects. Knowledge of these effects allows for the redesign of magnetic bearings to reduce uncertainties.

A specific solid magnetic thrust bearing was constructed and tested. The quasi-static current versus force relations were measured for a variety of currents and air gaps. A relatively accurate overall quasi-static force/current relation was developed that modeled the bimodal error distribution with a standard deviation of approximately 4 percent. It is important to discuss the significance of the bimodal nature of the error in regard to measurement of forces in rotating machines through measurement of the magnetic bearing currents. If the bearing is operated in small trajectories about a fixed, nonzero operation point on the current/force curve, the scatter in the error could be expected to be on the order of 4 percent but the error may not have zero mean. Further, the actual mean error will depend upon the specific current/force trajectory used to reach the operating point.

A nonlinear model of the current/force relation was developed for quasi-static changes. Conventional magnetic property tests were conducted to measure the coercive force and relative permeability. Simple magnetic circuit theory was employed to determine the parameters in the nonlinear current/force relation but the results differed from the experimentally measured parameters by large percentages. It is apparent that magnetic fringing, leakage, and other effects must be included for an accurate theoretical model.

A sinusoidally varying current was also imposed upon the thrust bearing. As the frequency increases, eddy currents are introduced into the solid thrust bearing components producing significant phase lag. This bearing demonstrated poor frequency response results in the operating frequency range of its design. No model of the eddy currents has been developed yet. For more accurate measurement of thrust bearing forces, eddy current effects must be reduced as much as possible. Alternatives include selection of less lossy materials and segmentation of stator components of the thrust bearing.

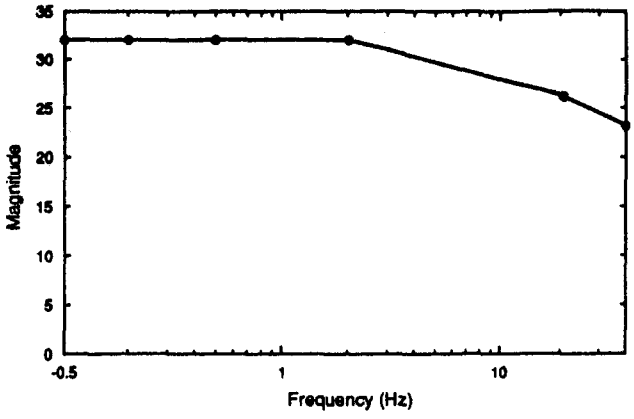

Fig. 8 Magnitude of force/current ratio versus frequency

Acknowledgments

This work was partially supported by a grant from NASA Lewis Research Center with Dr. Gerald Brown as project supervisor.

References

Allaire, P. E., 1989, "Design and Test of a Magnetic Thrust Bearing," *Journal of the Franklin Institute,* Vol. 326, No. 6, Dec.

Allaire, P., Imlach, J., McDonald, J., Humphris, R., Lewis, D., Blair, B., Claydon, J., and Flack R., 1989, "Design, Construction, and Test of a Magnetic Bearing in an Industrial Canned Motor Pump," *Proc. Texas A&M Pump Symposium,* Houston, TX, May.

Allaire, P. E., Maslen, E. H., Humphris, R. R., Knospe, C. R., and Lewis, D. W., 1994a, "Magnetic Bearings," *Handbook of Lubrication and Tribology,* Vol. III, CRC Press, pp. 577–600.

Allaire, P. E., Fittro, R. L., Maslen, E. H., and Wakefield, W. C., 1994b, "Current/Force Relations in Solid Magnetic Bearings," *Proc. REVOLVE '94,* Calgary, Alberta, June 7–9.

Allaire, P. E., Maslen, E. H., Lewis, D. W., and Flack, R. D., 1997, "Magnetic Thrust Bearing Operation and Industrial Pump Application," ASME JOURNAL OF ENGINEERING FOR GAS TURBINES AND POWER, Vol. 119 this issue, pp. 168–173.

Binns, K. J., Lawrenson, P. J., and Trowbridge, C. W., 1985, *The Analytical and Numerical Solution of Electric and Magnetic Fields,* Wiley, New York.

Feng, T. Neumer, T., Nordman, R., Verhoeven, J., and De Vis, D., 1992, "Identification of Fluid/Structure Interactions in Centrifugal Pumps," presented at the Fifth International Conference on Vibrations in Rotating Machinery, Bath, England, Sept. 7–10.

Flack, R. D., and Allaire, P. E., 1984, "Lateral Forces on Pump Impellers: A Literature Review," *Shock and Vibration Digest,* Vol. 16, No. 1, pp. 5–14.

Hawkins, L. A., Murphy, B. T., and Lang, K. W., 1991, "The Rocketdyne Multifunction Tester: Operation of a Radial Magnetic Bearing as an Excitation Source," *Proc. ROMAG '91, Magnetic Bearings and Dry Gas Seals International Conference,* University of Virginia, Mar. 13–15, pp. 1–13.

Hawkins, L. A., and Imlach, J., 1993, "Development of Experimental Method for Measurement of Magnetic Bearing Transfer Function Characteristics," *Proc.*

MAG '93, Magnetic Bearings, Magnetic Drives, and Dry Gas Seals Conference & Exhibition, July, Technomics Publishing Co., pp. 188–197.

Humphris, R. R., 1992, "A Device for Generating Diagnostic Information for Rotating Machinery," *Proc. MAG '92, Magnetic Bearings, Magnetic Drives, and Dry Gas Seals Conference & Exhibition,* July, Technomics Publishing Co., pp. 123–135.

Imlach, J., Blair, B. J., and Allaire, P. E., 1991, "Measured and Predicted Force and Stiffness Characteristics of Industrial Magnetic Bearings," ASME *Journal of Tribology,* Vol. 113, pp. 784–788.

Jery, B., Brennan, C. E., Caughey, T. E., and Acosta, A. J., 1985, "Forces in Centrifugal Pump Impellers," *Proc. Second International Pump Symposium,* Texas A&M University, pp. 21–29.

Keith, F. J., 1993, "Implicit Flux Feedback Control for Magnetic Bearings," Ph.D. Thesis, University of Virginia, June.

Lashley, C. M., Ries, D. M., Zmood, R. B., Kirk, J. A., and Anand, D. K., 1989, "Dynamics Considerations for a Magnetically Suspended Flywheel," *Proc. 24th IECEC.*

Ulbrich, H., 1988, "New Test Techniques Using Magnetic Bearings," *Proc. First International Conference on Magnetic Bearings,* June, Springer-Verlag, pp. 281–289.

Verhoeven, J. J., De Vis, D., and Nordman, R., 1993, "Development and Operating Experience of a 5000 kW Test Boilerfeed Pump on Active Magnetic Bearings," *Proc. Mechanical Engineers,* C439/004.

Wagner, N. G., and Pietruszka, W. D., 1988, "Identification of Rotor Dynamic Parameters on a Test Stand With Active Magnetic Bearings," *Proc. First International Conference on Magnetic Bearings,* June, Springer-Verlag, pp. 289–302.

Wakefield, W. C., 1994, "Magnetic Bearings/Load Cells for a Centrifugal Pump: Design Construction and Testing," M. S. Thesis, University of Virginia.

Williams, M. E., and Trumper, D. L., 1993, "Materials for Efficient High-Flux Magnetic Bearing Actuators," NASA Conference on Magnetic Suspension, Seattle, WA, Aug.

Zmood, R. B., Anand, D. K., and Kirk, J. A., 1987, "The Influence of Eddy Currents on Magnetic Actuator Performance," *Proc. IEEE,* Vol. 75, No. 2, Feb.

Damage Tolerance Based Life Prediction in Gas Turbine Engine Blades Under Vibratory High Cycle Fatigue

D. P. Walls

R. E. deLaneuville

S. E. Cunningham

Advanced Life Systems and Methods,
United Technologies Pratt & Whitney,
West Palm Beach, FL 33410

A novel fracture mechanics approach has been used to predict crack propagation lives in gas turbine engine blades subjected to vibratory high cycle fatigue (HCF). The vibratory loading included both a resonant mode and a nonresonant mode, with one blade subjected to only the nonresonant mode and another blade to both modes. A life prediction algorithm was utilized to predict HCF propagation lives for each case. The life prediction system incorporates a boundary integral element (BIE) derived hybrid stress intensity solution, which accounts for the transition from a surface crack to corner crack to edge crack. It also includes a derivation of threshold crack length from threshold stress intensity factors to give crack size limits for no propagation. The stress intensity solution was calibrated for crack aspect ratios measured directly from the fracture surfaces. The model demonstrates the ability to correlate predicted missions to failure with values deduced from fractographic analysis. This analysis helps to validate the use of fracture mechanics approaches for assessing damage tolerance in gas turbine engine components subjected to combined steady and vibratory stresses.

Introduction

Vibration in gas turbine engines is known to be a potential cause of component failure. Turbine blades are particularly susceptible to damage by vibratory high cycle fatigue due to the large range in frequency responses excited by rotation. Further, these vibratory stresses are superimposed on cyclic and steady stresses induced by thermal and mechanical loads at each throttle setting.

Conventional methods for predicting turbine blade failure due to high cycle fatigue have been limited to modified Goodman plot approaches, which bound the allowed vibratory stress as a function of the steady stress to give a minimum of 10^7 cycles of life. However, the use of the Goodman diagram for assessing design margin in engine components subjected to HCF has recently been challenged as the best approach. As an alternative, fracture-mechanics-based criteria have been proposed to enable the determination of crack or flaw size limits in critical locations exposed to combined steady and vibratory environments. *The use of these fracture mechanics criteria, however, needs to be validated with data from actual engine components exposed to real engine operating conditions.*

Predicting the damage tolerance of turbine airfoils is further complicated by the advances in turbine blade materials, which have addressed the need for higher strength at higher temperatures. Directionally solidified and single crystal nickel superalloys have been developed and are now in use because of their improved creep capability and fatigue strength at elevated temperatures over conventionally cast alloys. In addition to the anisotropy of material properties, these alloys also exhibit fracture properties, which vary with operating temperature, stress state, and frequency. In particular, several different fracture modes have been characterized and described in detail (Telesman and Ghosn, 1989; Cunningham et al., 1993, 1994). Applications related to these fracture modes in life prediction approaches are described by Cunningham and DeLuca (1995). Fracture mode dependence on environment has also been characterized (DeLuca and Cowles, 1989). In general, accurate life predictions for directionally solidified and single-crystal nickel alloys require the ability to predict what mode of fracture operates at a particular condition. This is due to the fact that cracks propagate at different rates and along different paths, depending on the fracture mode.

The role these fracture modes play in analyzing in-service failures can also be very important. Often in failure analysis, temperatures, steady stresses, and vibratory conditions are not well known and are only assumed or estimated. In these alloys, the characteristics of the fracture features are distinctly different in well-defined ranges of operating conditions. By careful interrogation of a post-failure fracture surface, one can distinguish the range of operating conditions by correlating the fracture features to known calibrated ranges of conditions that give those features.

Advances in crack growth testing technology have provided a means to address HCF crack growth life. Automated methods for tracking crack growth and closed-loop feedback load control have enabled the characterization of crack growth in the nonlinear near-threshold region.[1] In this region, crack growth rates are sufficiently slow to enable measurable crack growth even as a consequence of a high-frequency vibration.

In the following, a novel fracture mechanics approach has been used to estimate the vibratory fatigue capability of advanced turbine blade materials. This approach extends the fracture mechanics concept of crack growth rate dependence on the stress intensity to enable high cycle fatigue life prediction when a turbine blade is exposed to multiple vibratory stress conditions. It incorporates understanding of fracture mode behavior in nickel superalloys to relate the resultant fracture behavior in

Contributed by the International Gas Turbine Institute and presented at the 40th International Gas Turbine and Aeroengine Congress and Exhibition, Houston, Texas, June 5–8, 1995. Manuscript received by the International Gas Turbine Institute March 27, 1995. Paper No. 95-GT-244. Associate Technical Editor: C. J. Russo.

[1] The stress intensity threshold is the stress intensity below which cracks do not advance faster than 10^{-10} in. cycle.

blade tests to the model developed. The results show the approach has the ability to estimate the damage tolerance of turbine blades subjected to various modes of vibratory high cycle fatigue and represents a viable alternative for assessing damage tolerance in turbine airfoils.

Life Prediction Methodology

The fracture mechanics life prediction model developed in this study was comprised of three components, including an analytic stress intensity solution for a blade attachment geometry, an empirical material crack growth model, and an algorithm to sum damage on a cycle by cycle basis. The stress intensity solution incorporated the elevated local stress and concomitant die-out in the vicinity of the blade attachment contact through a finite element analysis. The finite element stress field was subsequently imported into a two-dimensional boundary integral element (BIE) code to evaluate the stress intensity as a function of crack length. The two-dimensional nature of the BIE code restricted the determination of the stress intensity solution to that of a through crack. To increase the robustness of the fracture model to include the surface flaw geometry generally observed during early stages of crack growth, a scaling approach was employed to map the through-crack solution to a surface crack solution through the assumed relation:

$$K_{\text{Surface}} = K_{\text{BIE}} \cdot \frac{F_{\text{Surface}}}{F_{\text{Edge}}} \tag{1}$$

Here, K is the stress intensity factor and F is the crack size and geometry-dependent shape factor defined herein as

$$F = \frac{K}{\sigma\sqrt{\pi a}} \tag{2}$$

where σ and a represent the applied stress and crack length, respectively.

In an effort to simulate the steep stress gradient associated with contact stresses, the shape factors for surface and edge cracks in remote *bending* fields were employed. Finally, the surface crack shape factor incorporated crack aspect ratios measured directly from striations of typical blade fracture surfaces.

To account for later stages of crack growth, it was recognized that the surface crack ultimately grows to encompass a perpendicular edge of the fracture plane, thereby becoming a corner crack and, providing the material toughness is not exceeded, progresses through the blade root thickness, thereby becoming an edge crack. Thus it is anticipated that the BIE solution should transition to corner and edge crack solutions under far field stress levels. Accordingly, analytic stress intensity solutions for corner and edge cracks were joined with the BIE solution to form the hybrid stress intensity model presented in Fig. 1. Note

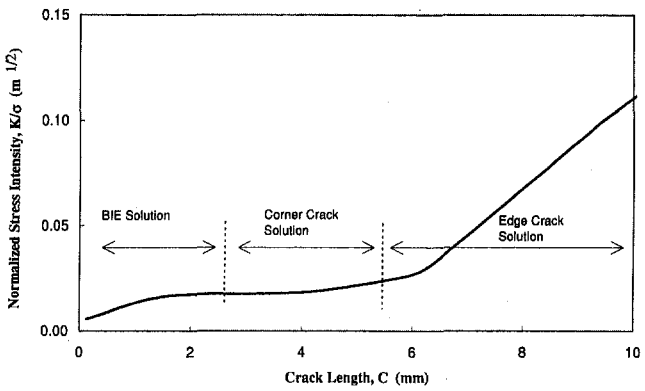

Fig. 1 Plot of normalized stress intensity versus crack length showing the transition from the boundary integral element solution to the analytic corner and edge crack solutions

Table 1 Summary of loading conditions

Loading Mode	Blade #1	Blade #2
Non-Resonant	350 MPa p-p	175 MPa p-p
Resonant	NONE	295 MPa p-p
LCF	0-875 MPa	0-875 MPa

that empirically measured crack aspect ratios were incorporated into the corner crack solution. In addition, whereas the BIE solution was normalized to the local surface contact stress of the blade attachment, it was deemed appropriate to normalize the corner and edge crack solutions to the far-field stress, owing to the larger size relative to the fracture plane dimensions.

To allow for crack growth life prediction, the stress intensity at each crack size was uniquely related to a crack growth rate, da/dN, through a material crack growth model for the blade alloy. The material model utilized a least-squares fit between laboratory specimen data and a hyperbolic sine function of the form

$$\log\,(da/dN) = C_1 \sinh\,(C_2(\log\,(\Delta K) + C_3)) + C_4 \tag{3}$$

where C_1, C_2, C_3, and C_4 are selected to provide optimal fit over the threshold, stage II and stage III growth regimes. In addition, C_1–C_4 incorporate a functional dependence on temperature, R-ratio, and frequency to allow interpolation to specific engine operating conditions.

Finally, the stress intensity solution and material crack growth model were incorporated into a damage accumulation algorithm to compute the crack extension associated with a given number of HCF loading cycles, N_L

$$N_L = \int_{a_o}^{a_f} \frac{da}{\phi\{\Delta K(\sigma_{\text{HCF}})\}} \tag{4}$$

where σ_{HCF} is the vibratory stress amplitude, a_o and a_f are the crack lengths at the beginning and end of the loading, and the function $\phi(\Delta K)$ is evaluated through Eq. (3).

The damage accumulation scheme also allows for prediction of blade life under multiple fatigue loading modes, typically associated with fighter engine missions, through a linear summation technique of the form

$$\sum_{\text{Missions}} \sum_{i} \int_{a_o}^{a_f} \frac{da}{\phi\{\Delta K(\sigma_i)\}} \tag{5}$$

Comparison With Data

Experimental. To evaluate the predictive capability of the fracture model, blades were subjected to two different types of vibratory loading mode typically found in engine operating environments. In the first case, the loading consisted of a high amplitude nonresonant vibration (NRV). The NRV stress level was increased well above that typically measured under nominal engine conditions such that propagation would occur from a 0.75 mm preflaw. In the second case, both the nonresonant and a resonant vibratory mode were alternately applied, each for a specific dwell period. In this instance, the nonresonant stress amplitude was lowered to a level representative of engine operating conditions while the resonant mode amplitude was large enough to propagate from the preflaw. Finally, in both cases, several large-amplitude cycles were applied following the vibratory dwell, indicative of the low cycle fatigue (LCF) cycles associated with large throttle excursions in engine missions. The loading is summarized in Table 1. Each blade was subsequently subjected to repeated vibratory/LCF missions until failure. Following fracture at the blade attachment, extensive fractography was performed in an attempt to relate fracture surface features to the applied loading.

Fracture surfaces of each blade are shown in Fig. 2. Notably, the blade subjected to the high nonresonant levels exhibited a total of 3–5 distinguishable propagation arrest marks. The propagation arrest marks are deemed due to the largest LCF cycle associated with the completion of each mission sequence. Accordingly, the region between each arrest is due to HCF propagation during the NRV dwell period. At higher resolution, the surface is seen to exhibit an ancillary transprecipitate noncrystallographic (TPNC)[2] type fracture mode, representative of high ΔK crack growth in this material. The blade subjected to the combined vibratory mission showed a markedly different fracture surface morphology. Notably, two distinctive propagation bands were observed, occurring in an alternating pattern. The narrow band exhibited a monoplanar TPNC fracture mode while the wider band exhibited the ancillary TPNC mode, indicative of a higher ΔK propagation. In addition, the narrow banding was not observed until the crack had grown to 5.1 mm. Thus it was deduced that the wide and narrow banding represent the resonant and NRV vibratory modes, respectively. In total, 95 propagation arrest features were noted on the stage II fracture surface prior to fast fracture, suggesting 95 completed mission sequences to blade failure.

Correlation With Fracture Model. The vibratory dwell times per mission, stress amplitudes, and LCF amplitudes were utilized in the fracture model to allow a prediction of the number of loading missions to failure from the pre-existing flaw size. The predictions were then compared with the number of missions to failure in each blade deduced from the fractography. For the blade exposed only to NRV stresses, the model predicts four *completed* mission sequences to failure. This result is in reasonable agreement with the 3–5 propagation arrest marks observed on the fracture surface. While NRV propagation occurs from the initial flaw in the NRV loaded blade, the fractography suggests NRV driven crack propagation does not occur until larger crack sizes are reached in the combined loading blade. To validate this, the model was to used to *predict* the crack length at which NRV driven propagation would commence. This was accomplished by noting that the stress intensity at the onset of crack propagation is equal to the material threshold stress intensity:

[2] TPNC fracture occurs in the intermediate temperature region (600°F–1600°F) and is characterized by the crack tip progressing across the precipitate and matrix phases without regard to crystallographic features. In monoplanar TPNC, observed at lower values of ΔK, the cracking is limited to a single plane and the fracture surface appears smooth and shiny. At higher values of ΔK, ancillary TPNC is observed. In this case, the crack tip proceeds across many surfaces and the fracture surface appears much rougher.

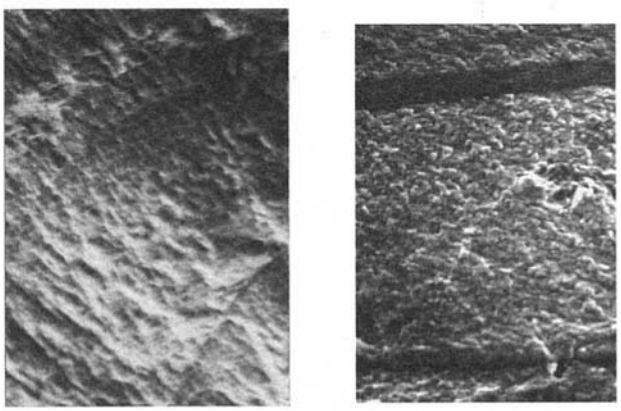

Fig. 2 Micrographs showing the fracture surfaces of (*A*) the blade subjected to only the NRV loading and (*B*) the blade subjected to the combined vibratory loading. The narrow banding observed in (*B*) is deduced to be the NRV propagation region.

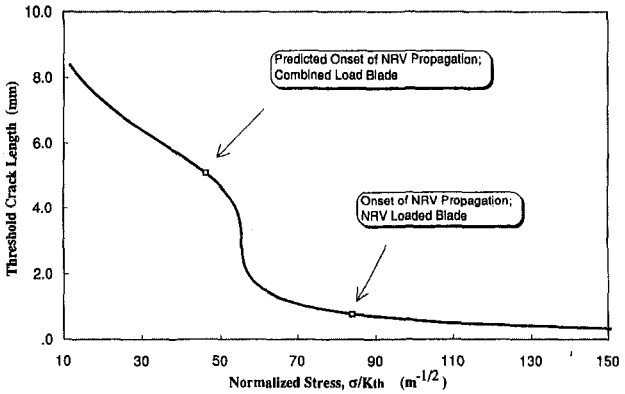

Fig. 3 The normalized stress intensity solution of Fig. 1 with stress intensity, *K*, replaced by the threshold value. The plot represents the crack length at which crack propagation will commence for a given applied stress amplitude.

$$K_{th} = \sigma_{nrv}\sqrt{a_{nrv}}F \tag{6}$$

where a_{nrv} represents the crack length at the onset of NRV propagation. Thus, the threshold crack length in each blade is related by the ratio of shape factors through

$$\frac{(a_{nrv})_2}{(a_{nrv})_1} = \left[\frac{F_1(\sigma_{nrv})_1}{F_2(\sigma_{nrv})_2}\right]^2 \tag{7}$$

This approach allows a direct prediction of the threshold crack length in the combined load blade, eliminating uncertainties in the material threshold stress intensity. To facilitate evaluation of Eq. (7), the normalized stress intensity curve was replotted as threshold crack length versus normalized stress (Fig. 3). The crack length at the onset of propagation in the NRV loaded blade (i.e., the preflaw size) combined with the NRV stress amplitudes in both blades predicts HCF propagation due to the NRV stresses in the combined load blade to commence at a crack length of 5.5 mm. This is in reasonable agreement with the value of 5.1 mm measured from the fractography, indicative of the predictive capability of the fracture model.

Finally, the stress amplitudes and individual dwell times of both the NRV and resonant loads, along with the LCF amplitudes, were inserted into the fracture model to predict the number of missions to failure in the combined load blade. The model predicts blade failure in 103 complete missions, compared to 95 missions evaluated from the fractography. The favorable agreement between the fracture model and the missions of crack propagation life deduced from the fracture surface features illustrates the potential capability of developing a damage tolerant design/life system approach to vibration driven HCF propagation.

Conclusions

A fracture mechanics approach has been developed to enable damage tolerance life prediction of gas turbine engine blades subjected to vibratory high cycle fatigue. The approach incorporates numerically derived stress intensity solutions calibrated with measured crack shapes, permits combinations of different cyclic amplitudes and frequencies, and incorporates the threshold stress intensity concept for estimating crack sizes which are not expected to propagate. Results using this technique have been compared with data from actual engine hardware subjected to HCF and LCF cycles.

Several key conclusions are noted. The first is related to the method's ability to estimate high cycle fatigue life of parts using fracture mechanics. When combined with mission information and fractography of the damaged parts, the algorithm gave results that correlated well with the actual lives of individual

blades subjected to combinations of different vibratory modes. While the data are currently limited to two mission definitions, the results lend support for the use of fracture mechanics for estimating cyclic life of cracks propagating due to combined LCF and HCF.

A second conclusion stems from the use of the threshold stress intensity factor for estimating the crack size a part can sustain without crack growth. The good agreement of the estimated threshold crack size for NRV stresses in the combined load blade with the crack length determined from the fracture surface indicates that the threshold stress intensity method is a potentially powerful tool for assessing design margin and inspection requirements for HCF.

Finally, although the use of nickel superalloys tends to complicate the analytical portion of component design, their unique fracture properties have actually aided in the life prediction analysis and validation performed here. The detailed characterization of different fracture modes induced by particular operating conditions has enabled the differentiation by cycle type of the onset of crack growth. This result underscores the importance of understanding the basic mechanisms of fracture and fatigue when setting design margins and evaluating component cyclic life.

References

Cunningham, S. E., DeLuca, D. P., and Haake, F. K., 1993, *Crack Growth and Life Prediction in Single Crystal Nickel Superalloys, Vol. I,* P&W Internal Report FR-22593-1, Mar.

Cunningham, S. E., DeLuca, D. P., Hindle, E. H., III, Sheldon, J. W., and Haake, F. K., 1994, *Crack Growth and Life Prediction in Single Crystal Nickel Superalloys, Vol. II,* P&W Internal Report, Mar.

Cunningham, S. E., and DeLuca, D. P., 1995, "Assessing Crack Growth Behavior Under Continuous Temperature Gradients," *Second Symposium on Thermo Mechanical Fatigue Behavior of Materials,* M. J. Verrilli and M. G. Castelli, eds., American Society for Testing and Materials, Philadelphia, submitted for publication.

DeLuca, D. P., and Cowles, B. A., 1989, in: *Hydrogen Effects on Material Behavior,* N. R. Moody and A. W. Thompson, eds., Warrendale, PA, pp. 603–613.

Telesman, J., and Ghosn, L. J., 1989, "The Unusual Near-Threshold FCG Behavior of a Single Crystal Superalloy and the Resolved Shear Stress as the Crack Driving Force," *Engineering Fracture Mechanics,* Vol. 34, pp. 1183–1196.

G. N. Balaji

J. H. Griffin

Department of Mechanical Engineering,
Carnegie Mellon University,
Pittsburgh, PA 15213

Resonant Response of a Tapered Beam and Its Implications to Blade Vibration

The resonant response characteristics of a tapered beam are studied using Euler–Bernoulli beam theory. The sensitivity of the beam's maximum stress to variations in its geometry is studied for three types of harmonic pressure loading. The implications to the response of airfoil chordwise bending modes are discussed.

1 Introduction

In 1990 six American gas turbine manufacturers participated in a workshop at Carnegie Mellon University in which they ranked the relative importance of various types of blade vibration problems. They concluded that the fatigue failure of airfoils due to high-frequency *tip modes* was their single most important structural problem. Tip modes, which include chordwise bending modes, are modes in which the displacement at either the leading or trailing edge blade tip is accentuated. Modern blading is more likely to fail from high vibratory response in these types of modes because of the design trend toward wider chords and fewer blades. The use of wider chord vanes and blades tends to make the excitation more severe and make the blade's tip modes more likely to respond. Larger vanes increase the strength of the vane wake and, since there are fewer vanes, it also tends to generate lower frequency excitations on neighboring rotor stages. Because compressor blades, in particular, have highly tapered, long chords with thin leading and trailing edges, they tend to have a number of tip modes with natural frequencies that can be excited by the vane wakes in the operating range of the engine. The workshop participants reported that a characteristic of the resonant response of these high-frequency modes is that there tends to be a high degree of variability from blade to blade in the magnitude of the resonant stress. Their experience indicates that only a part of that variation can be attributed to system dynamics and traditional stage mistuning. Following the workshop, a study was initiated to develop a better fundamental understanding of tip mode vibration. This paper documents the results of the first phase of that study.

The objective of the work reported here is to determine the effect of taper and tip thickness on the maximum resonant stress of a tapered beam subjected to externally applied harmonic pressure distributions and to investigate its possible implications to blade vibration. Tapered beams are of interest since their geometry is similar to that of the leading or trailing edge of an airfoil. As a result, airfoil chordwise bending modes should exhibit similar sensitivity to changes in chordwise taper and leading or tailing edge thickness. As a result, the tapered beam provides a simplified, first-order model of an airfoil's behavior that should provide insight into the sensitivity of the airfoil's response to geometric perturbations.

The sensitivity of the response to geometric changes also depends on the type of excitation that is applied. The spatial distributions of the excitation pressures used in this study are: a constant pressure to serve as a baseline, a leading edge type pressure distribution, and a trailing edge type pressure distribution. Consequently, the relative importance of each type of excitation in terms of how it affects tip mode response will be assessed.

While the free vibration of a tapered beam was originally addressed by Nicholson as early as 1917, and extensive studies were later conducted by Cranch and Adler (1956), Conway and Dubil (1965), and Sanger (1968), the forced response of tapered beams was only recently analyzed by Roy and Ganesan (1992). Roy and Ganesan discuss the amplitude of response of the tapered beam with different thickness profiles that are subjected to a simple sinusoidal harmonic loading. However, they do not investigate the vibratory stresses in the beam, the sensitivity of the beam to geometric perturbations, or the effect of aerodynamic type pressure fields, which are the focal points of the work reported here.

In the next section, the tapered beam problem will be formulated and a formal solution developed for its resonant response. In section 3, the solution will be specialized for sharply pointed beams, the location and magnitude of the maximum stress will be determined, and the relative importance of the three different types of pressure distributions assessed. In section 4 the effect of blunting the sharp tip will be investigated. The results of the study will be summarized and its possible implications to airfoil resonant response will be discussed in the final section.

2 Formulation

The geometry of a beam with a linear height variation is depicted in Fig. 1. From Euler–Bernoulli beam theory, the equation of motion is

$$\frac{\partial^2}{\partial x^2}\left(EI(x)\frac{\partial^2 u}{\partial x^2}\right) = -\rho A(x)\frac{\partial^2 u}{\partial t^2} + p(x, t)b \qquad (1)$$

for $t > 0$ and $a < x < L$. $u(x, t)$ is the transverse displacement, E is Young's modulus, b is the width, ρ is the density, and $p(x, t)$ is the pressure. If the height of the beam $h(x)$ is equal to sx, then the section modulus I equals $b(sx)^3/12$ and the area A equals bsx.

Because of the way the linear height variation has been described, the beam would be sharply pointed if the parameter, a, were zero. Physically, $a \geq 0$ and $\alpha = a/L$ is the *truncation ratio*. The truncation ratio determines the amount of the material removed from the tip, and can also be used to describe the thickness of the tip.

Using the normalized coordinate $\xi = x/L$, the equation of motion is rewritten as

$$\frac{\partial^2}{\partial \xi^2}\left(\xi^3\frac{\partial^2 u}{\partial \xi^2}\right) = -\gamma^2\xi\frac{\partial^2 u}{\partial t^2} + \tilde{p}(\xi, t) \qquad (2)$$

Contributed by the International Gas Turbine Institute and presented at the 40th International Gas Turbine and Aeroengine Congress and Exhibition, Houston, Texas, June 5–8, 1995. Manuscript received by the International Gas Turbine Institute March 31, 1995. Paper No. 95-GT-453. Associate Technical Editor: C. J. Russo.

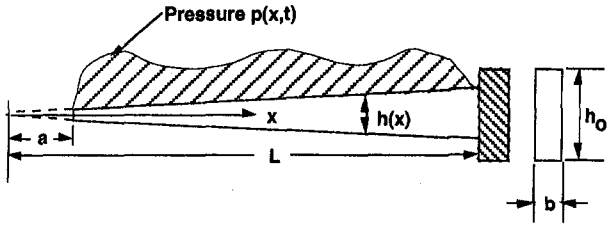

Fig. 1 Geometry of a tapered beam

for $t > 0$ and $\alpha < \xi < 1$, where

$$\gamma^2 = \frac{12\rho L^2}{Es^2}$$

and

$$\tilde{p}(\xi, t) = \frac{12Lp(\xi, t)}{Es^3}$$

The response of the beam may be represented as a linear combination of its normal modes, i.e.,

$$u(\xi, t) = \sum_{i=1}^{\infty} u_n(t)\phi_n(\xi) \tag{3}$$

where, in general, the normal modes are eigenfunctions of the form (Sanger, 1968)

$$\phi_n(\xi) = \frac{1}{\lambda_n\sqrt{\xi}}[J_1(\lambda_n\sqrt{\xi}) + B_nY_1(\lambda_n\sqrt{\xi}) + C_nI_1(\lambda_n\sqrt{\xi}) + D_nK_1(\lambda_n\sqrt{\xi})] \tag{4}$$

J, Y, I, and K are Bessel functions of the first and second kind. The specific values of the constants B_n, C_n, and D_n, and the eigenvalues λ_n depend on α and the boundary conditions. For now, it is assumed that suitable boundary conditions are specified so that the modes are orthogonal.

Substituting Eq. (3) into Eq. (1) and utilizing orthogonality, a set of uncoupled equations for the modal displacements u_n are obtained of the form

$$\ddot{u}_n(t) + \omega_n^2 u_n(t) = f_n(t) \tag{5}$$

where

$$\omega_n^2 = \frac{\lambda_n^4}{16\gamma^2}$$

and

$$f_n(t) = \frac{\int_\alpha^1 \tilde{p}(\xi, t)\phi_n(\xi)d\xi}{I_n}$$

$$I_n = \int_\alpha^1 \xi(\phi_n(\xi))^2 d\xi$$

Incorporating modal damping, the equation of motion is rewritten as

$$\ddot{u}_n(t) + 2\zeta_n\omega_n\dot{u}_n(t) + \omega_n^2 u_n(t) = f_n(t) \tag{6}$$

If the forcing pressure distribution is harmonic, $\tilde{p}(\xi, t) = \tilde{P}(\xi)e^{i\omega t}$, then the generalized force is given by

$$f_n = \frac{\tilde{P}_n}{\gamma^2 I_n} e^{i\omega t},$$

where

$$\tilde{P}_n = \int_\alpha^1 \tilde{P}(\xi)\phi_n(\xi)d\xi$$

and the steady-state response of the beam is

$$u_n(t) = U_n e^{i\omega t} \tag{7}$$

Equations (6) and (7) imply

$$(\omega_n^2 - \omega^2 + 2i\omega\omega_n\zeta_n)U_n = \frac{\tilde{P}_n}{\gamma^2 I_n} \tag{8}$$

For small values of damping, the resonant response frequency is approximately ω_n and the resonant amplitude of the modal displacement is

$$U_n^* = \left(\frac{1}{2\zeta_n}\right)\frac{1}{\omega_n^2}\frac{\tilde{P}_n}{\gamma^2 I_n} \tag{9}$$

3 Resonant Response of Pointed Beams

In this section, the resonant response of pointed beams will be determined in order to serve as a baseline case. The importance of the different types of pressure fields will be established.

3.1 Normal Modes of Vibration. The normal modes of vibration of the tapered pointed cantilever beam can be specialized from Eq. (4) and may be written as (Cranch and Adler, 1956)

$$\phi_n(\xi) = \frac{2}{\lambda_n\sqrt{\xi}}[J_1(\lambda_n\sqrt{\xi}) + C_nI_1(\lambda_n\sqrt{\xi})] \tag{10}$$

where the mode shapes have been normalized to have unit tip displacement. The natural frequencies are related to the eigenvalues by

$$\omega_n = \frac{\lambda_n^2 h_o}{4L^2}\sqrt{\frac{E}{12\rho}} \tag{11}$$

The modal stresses in the beam can be related to the displacements by

$$\sigma_x = \frac{M_n(\xi)h(\xi)}{I(\xi)} \tag{12}$$

where

$$M_n(\xi) = \frac{EI(\xi)}{L^2}\frac{d^2\phi_n(\xi)}{d\xi^2}$$

Thus, the modal stresses can be written as

$$\sigma_x(\xi) = \frac{Es\lambda_n^2}{8L}\sigma_n(\xi) \tag{13}$$

where

$$\sigma_n(\xi) = \frac{2}{\lambda_n\sqrt{\xi}}[J_3(\lambda_n\sqrt{\xi}) + C_nI_3(\lambda_n\sqrt{\xi})]$$

σ_n will be referred to as the *modal stress function.*

The displacements and stress functions of the modes exhibit a strong degree of similarity for the case of the sharply pointed beam. This similarity will be explored in the next section in order to establish a general relationship between the maximum modal stress and the tip displacement of the beam.

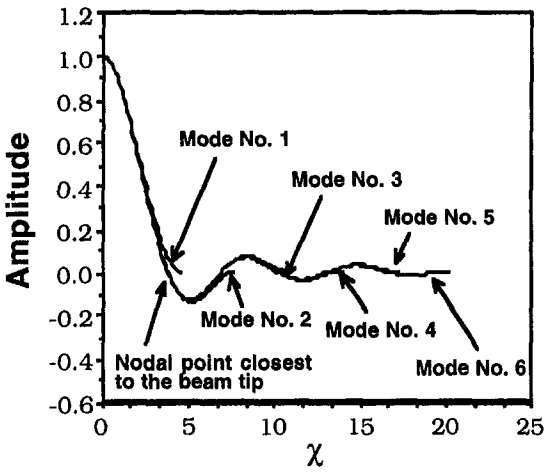

Fig. 2 Mode shapes for the cantilever beam

3.2 The Maximum Modal Stress and Its Location. From Eqs. (10) and (13) it is clear that the modal displacements and stresses are functions of the variable

$$\chi = \lambda_n \sqrt{\xi} \tag{14}$$

Using χ, the mode shapes and the modal stress function can be rewritten as

$$\phi_n(\chi) = \frac{2}{\chi}\left[J_1(\chi) + C_n I_1(\chi)\right] \tag{15}$$

$$\bar{\phi}_n(\chi) = \frac{2}{\chi}\left[J_3(\chi) + C_n I_3(\chi)\right] \tag{16}$$

The first seven modal displacements and modal stress functions are plotted as a function of χ in Figs. 2 and 3. In these figures the functions are only displayed over physically meaningful values of χ. When plotted in this manner it is apparent that in the near field, χ small, all modes behave in a similar fashion. This occurs because only the coefficient C_n varies with the mode number n in expressions (15) and (16), and it plays a limited role in the functions' near-field behavior. From Fig. 3 it is clear that the maximum value of the modal stress function, σ^0, is approximately equal to 0.22 for all modes, but, especially for the higher ($n > 1$) modes. Let $(\sigma_n)_{\max}$ be the maximum value of the modal stress when the beam resonates in the nth mode. From Eq. (13) it can be related to the resonant displacement of the beam as

$$(\sigma_n)_{\max} = \frac{Es\lambda_n^2}{8L}\sigma^0 U_n^* \tag{17}$$

or alternatively using Eqs. (2) and (5) as

$$(\sigma_n)_{\max} = 0.38 U_n^* \omega_n \sqrt{\rho E} \tag{18}$$

This is similar to Ungar's result (1962) for simply supported, uniform beams, i.e., he found that $(\sigma_n)_{\max} = U_n^* \omega_n \sqrt{3\rho E}$. However, for the case of tapered beams the ratio of stress to maximum displacement is smaller since the tip is considerably more flexible.

From Figs. 2 and 3, it can be observed that the distance to the first nodal point and the distance to the maximum stress location is nearly the same for all modes, but especially for $n > 1$. In fact, it can be shown numerically that the maximum stress occurs at a value of χ equal to approximately 0.95 of the distance to the first nodal point. Since χ is proportional to $\sqrt{\xi}$, this means physically that the maximum modal stress occurs at a distance from the tip of the beam, which is approximately 89 percent of the distance to the first nodal point.

The magnitude and location of the maximum stress were calculated when other boundary conditions were applied at $\xi = 1$. Each case exhibited results for the higher modes that were essentially the same as those discussed in this section. Consequently, it can be concluded that the maximum stresses in all but the lowest modes are approximately given by Eq. (17) or (18), and, in fact, is to a great extent independent of the constraints applied away from the tip.

3.3 Maximum Resonant Stress. From Eqs. (9) and (17), the maximum resonant stress in the tapered beam is given by

$$(\sigma_m)_{\text{peak}} = \frac{24}{s^2}\left(\frac{1}{2\zeta_m}\right)\delta_m \tag{19}$$

where the expression has been simplified to

$$\delta_m = \frac{\sigma^0 P_m}{\lambda_m^2 I_m} \quad \text{and} \quad P_m = \int_0^1 P(\xi)\phi_m(\xi)d\xi \tag{20}$$

and where $P(\xi)$ is the original, physical pressure distribution. From Eq. (19) it can be observed that the resonant stresses depend on three factors. First, they are directly proportional to the dynamic amplification factor, $1/(2\zeta_m)$. This dependence will not be investigated in this study. Second, they are inversely proportional to the square of the slope ($s = h_0/L$) and for small values of s, the stresses are very sensitive to variations in h_0, the thickness at the root of the beam. Last, they are proportional to δ_m, the *stress participation factor.* The stress participation factor directly evaluates the influence of the type of pressure distribution on the resonant stress. This dependence will be explored in the next section.

3.4 Calculation of Stress Participation Factors. The stress participation factors are determined for the three types of pressure distributions defined as (Dowell et al., 1989)

Baseline case of constant pressure: $p(\xi, t) = P_0 e^{i\omega t}$

Leading edge type pressure: $p(\xi, t) = \frac{P_1}{\sqrt{\xi}} e^{i\omega t}$

Trailing edge type pressure: $p(\xi, t) = P_2\sqrt{\xi} e^{i\omega t}$ (21)

In each case, the constants P_i are chosen so that the average pressure distribution acting on the beam is equal to one.

The participation factors were computed for each type of pressure distribution and the results plotted as a function of

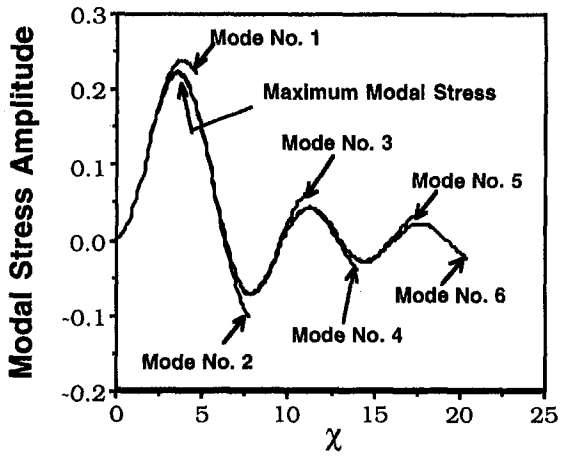

Fig. 3 Modal stresses for the cantilever beam

mode number in Fig. 4. (The points are connected artificially by lines to identify better the type of pressure distribution applied.)

For the case of constant pressure, the odd modes show a higher participation than the even modes. Consequently, for this type of pressure distribution, the odd modes would tend to be more critical than the even-numbered ones.

For a trailing edge type pressure distribution, the participation factors for odd modes were again more critical than those for the even-numbered modes. However, the blades tended to respond considerably less than if a constant pressure were applied with the same average value. This occurs because the applied pressures are smaller near the tip where the displacement is highest and, consequently, the generalized force is smaller. Since for the higher frequency modes the displacements tend to be progressively more localized near the tip, the generalized force decreases as the mode number increases and the participation factors decrease accordingly. From a vibratory response point of view, trailing edge type pressure fields provide the least critical source of excitation.

For a leading edge type of pressure distribution, the participation factors of the higher modes were of the same magnitude as that of the first mode. This could be expected since this type of distribution produces a singularity at the free tip of the beam, which is similar in effect to the application of a delta function at the beam tip. Delta functions tend to excite all modes equally, which is nearly true in this case. This is a matter of serious concern as it implies that the peak vibratory stresses due to higher modes could be quite large.

From a resonant response point of view, the critical case is a thin leading edge with pressure distributions that are highly localized at the tip. According to the previous analyses all modes, including the higher frequency ones, may be excited to nearly the same degree. In theory for a perfectly pointed beam, the location of the maximum stress occurs closer to the tip as the mode number increases. In fact, however, airfoils are not perfectly pointed as their tips are cut off and slightly rounded. By truncating the sharp tips in this manner, the higher frequency modes may be preferentially affected. This effect is investigated in the next section.

4 Resonant Response of Truncated Beams

In this section, the effect of removing a portion of the sharp tip is investigated. Truncating the beam in this manner will be shown to be equivalent to increasing the tip's thickness.

4.1 Normal Modes of Vibration. The normal modes of vibration of a tapered truncated cantilever beam are

$$\phi(\xi) = \frac{1}{\phi_n^0}\frac{1}{\lambda_n\sqrt{\xi}}\left[J_1(\lambda_n\sqrt{\xi}) + B_nY_1(\lambda_n\sqrt{\xi}) + C_nI_1(\lambda_n\sqrt{\xi}) + D_nK_1(\lambda_n\sqrt{\xi})\right] \quad (22)$$

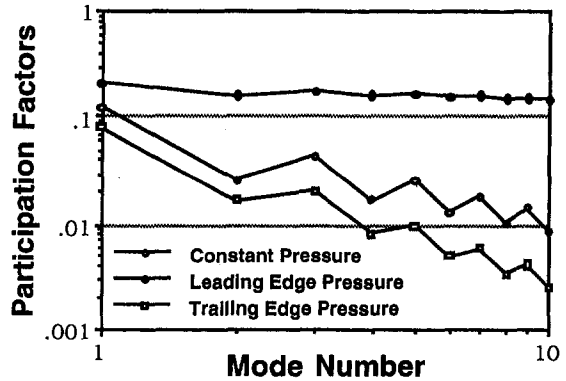

Fig. 4 Stress participation factors

where $\alpha < \xi < 1$ and

$$\phi_n^0 = \frac{1}{\lambda_n\sqrt{\alpha}}\left[J_1(\lambda_n\sqrt{\alpha}) + B_nY_1(\lambda_n\sqrt{\alpha}) + C_nI_1(\lambda_n\sqrt{\alpha}) + D_nK_1(\lambda_n\sqrt{\alpha})\right]$$

where the purpose of ϕ_n^0 is to normalize the modes so that they have unit tip displacement. Analogous to Eq. (13), the modal stresses are again of the form

$$\sigma_x(\xi) = \frac{Es\lambda_n^2}{8L}\sigma_n(\xi) \quad (23)$$

except that the modal stress function is given by

$$\sigma_n(\xi) = \frac{1}{\phi_n^0}\frac{1}{\lambda_n\sqrt{\xi}}\left[J_3(\lambda_n\sqrt{\xi}) + B_nY_3(\lambda_n\sqrt{\xi}) + C_nI_3(\lambda_n\sqrt{\xi}) + D_nK_3(\lambda_n\sqrt{\xi})\right]$$

4.2 Scaling of Mode Shapes and the Modal Stress Function. The location and the magnitude of the maximum modal stress are now more difficult to determine since an additional parameter α has been introduced. In section 3.2, it was observed that the location of the maximum stress for a mode depended on the location of the first nodal point. Let ξ_ϕ be the distance to the first nodal point of a mode, ξ_σ be the distance to the point where the modal stress is a maximum, and $\mu = \xi_\sigma/\xi_\phi$. Define the maximum value of $\sigma_n(\xi)$ for $\alpha < \xi < 1$ as σ^α. After some investigation, it was found that the μ and σ^α could best be described in terms of the *truncation factor*, κ, which combines two parameters. The truncation factor is defined as

$$\kappa(\alpha) = \frac{\alpha}{\xi_\phi(\alpha) - \alpha} \quad (24)$$

μ and σ^α were calculated for a series of cantilevered beams and plotted as functions of κ for the first seven modes in Fig. 5. With the exception of the first mode, μ and σ^α are essentially the same for all modes. The different behavior of the first mode is probably due to the fact that the constraints at its first nodal point are different from those of the interior nodal points associated with the higher modes.

Thus, if the tip displacement in the nth mode U_n^* is known, then analogous to Eq. (17) the maximum stress in the beam is given by

$$(\sigma_n(\alpha))_{\max} = \frac{Es\lambda_n^2}{8L}\sigma^\alpha U_n^* \quad (25)$$

4.3 Maximum Resonant Stress. Analogous to section 3.3, the maximum resonant stress for truncated beams is given by

$$(\sigma_n)_{\text{peak}} = \frac{24}{s^2}\left(\frac{1}{2\zeta_n}\right)\delta_n(\alpha) \quad (26)$$

where

$$\delta_n(\alpha) = \frac{\sigma^\alpha P_n}{\lambda_n^2 I_n} \quad (27)$$

The stress participation factor $\delta_n(\alpha)$ depends on the type of pressure loading and the truncation ratio, α. It was found in section 3.4 that a leading edge pressure distribution most strongly excited the critical high frequency modes. $\delta_n(\alpha)$ was calculated for this critical case for the first seven modes. In these calculations the pressure remained singular at the beam tip, i.e., $P(\xi) = P_1/\sqrt{\xi - \alpha}$, and P_1 was set equal to $0.5/\sqrt{1-\alpha}$ so that the net force remained constant. The results are depicted in Fig. 6 in which $\delta_n(\alpha)$ is plotted as a

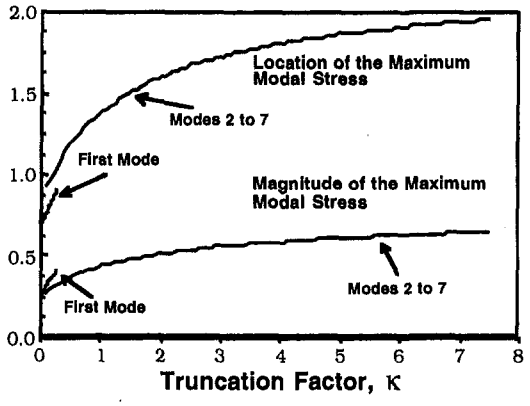

Fig. 5 Location and magnitude of the maximum modal stress

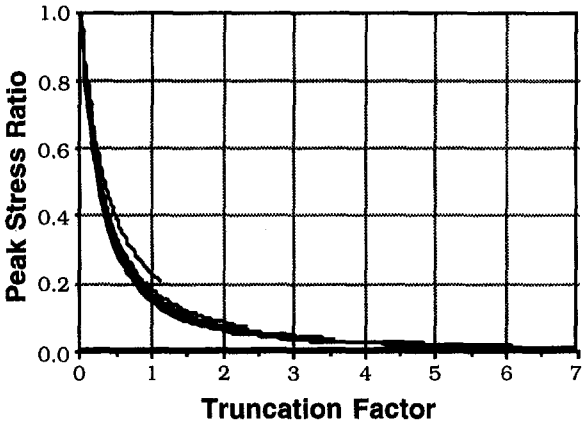

Fig. 7 Reduction in stress participation factor

function of the mode number for α varying from 0 to 10 percent. It shows that in the range of values simulated, increasing α uniformly caused $\delta_n(\alpha)$ to decrease. Furthermore, the decrease is more rapid when the mode number is higher.

The information in Fig. 6 is consolidated when $\delta_n(\alpha)/\delta_n(0)$ are plotted as functions of the truncation factor κ as shown in Fig. 7. Figure 7 provides a fairly general result. For example, it indicates that, except for the first mode, removing material from the tip so that κ equals 10 percent will reduce the resonant vibratory stress by 80 percent.

An alternative physical interpretation of these results is to consider the effect of keeping the length of the beam and its base thickness fixed and thickening its tip. If h_t and h_0 are the thicknesses of the beam at its tip and base, respectively, then $\alpha = h_t/h_0$. Thus, Figs. 6 and 7 also effectively describe the effect of changing the beam's tip thickness on the stress participation factor. Note that, in this case, the slope s decreases as α increases since $s = h_0(1 - \alpha)/L$ and that from Eq. (26) this will have some effect on the magnitude of the resonant stress.

While the results indicated in Fig. 7 are quite general, they are not in the best form for use by engineers. An alternative way of viewing this data would be to pose the question, "What thickness ratio is required to reduce the resonant stress by a certain percent?" For example, the thickness ratio, h_t/h_0, that is required to reduce the resonant stress by 50 percent is plotted as a function of the mode number in Fig. 8. The least-squares fit of the data, indicated in Fig. 8 as a solid straight line, yields the result that to reduce the resonant stress in the nth mode by at least 50 percent the thickness ratio should satisfy

$$\frac{h_t}{h_0} \geq \left(\frac{5}{n}\right)^{1.85} \tag{28}$$

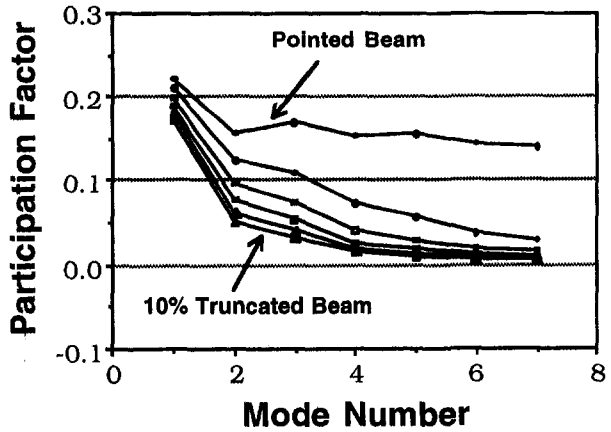

Fig. 6 Effect of truncation on stress participation factors

It is clear from Eq. (28) that the response of the higher frequency modes is very sensitive to small changes in the thickness of the tip.

5 Conclusions

A study of the resonant stress that occurs in linearly tapered beams was conducted in which the beams were subjected to three different types of loading. The load distributions were chosen to represent the type of pressure fields that occur on the leading and trailing edges of airfoils as well as a baseline constant pressure case. These cases were investigated because the beam's response should provide a first order model of the behavior of high frequency, chordwise bending modes in airfoils.

Expressions were derived using a normal mode expansion for the beam's resonant displacement. In order to relate the displacement to stress, the modal stress function was examined to determine the magnitude and location of the maximum stress in the beam. For the case of a sharply pointed beam, the magnitude of the maximum stress was found to be approximately $0.38\omega_n\sqrt{\rho E}$ times the tip displacement and it occurs at a location that is approximately 89 percent of the distance to the first nodal point. In the case of a truncated beam, the magnitude and location of the maximum stress were found to be functions of a single parameter, the truncation factor, κ.

Using these results, expressions were derived for the maximum resonant stress under the assumption that the modal damping factors either remain constant or can be independently calculated. The resonant stress of the nth mode was found to be inversely proportional to the square of the taper parameter, s, and proportional to a stress participation factor, δ_n. The stress participation factor was calculated for sharply pointed beams for three types of pressure distributions. It was found to decrease

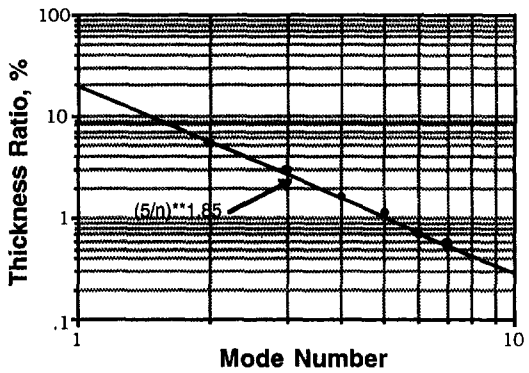

Fig. 8 Tip thickness required to reduce stress by a factor of two

fairly rapidly for the higher modes, except for the critical case of a leading edge type pressure distribution. For this case, δ_n was nearly constant as n increased. This suggests that an important source of excitation for chordwise bending modes in airfoils may be the pressure fields near their leading edge.

A practical method for reducing tip mode response that is used by airfoil designers is to blunt the sharp edge by either thickening or removing part of its tip. It was found that both treatments are essentially equivalent and that they are predicted to reduce the resonant response of the tapered beam significantly in the case of a leading edge-type pressure distribution. It was shown that the responses of all of the higher frequency modes were similarly reduced if the participation factors were plotted as a function of the truncation factor, κ. Results that were not shown indicated that similar blunting of the beam when it is subjected to a trailing edge type pressure distribution could lead to an increase in vibratory response. Thus, the type of pressure loading should be taken into account when trying to remedy a resonant response problem by changing an airfoil's geometry.

A goal of this work was to obtain a more basic understanding of chordwise bending modes in airfoils, and, in particular, to establish possible sources of the large variability that has been observed in their resonant response. A key result in this regard may be the consolidated plot of the normalized stress participation factor as a function of the truncation factor, κ, as displayed in Fig. 7. Because the participation factor varies rapidly when κ is small, it is clear that the response of a specific high frequency mode would be highly sensitive to variations in the tip's thickness if its nominal thickness corresponded to a κ value in this range, e.g., $\kappa_{\text{nom}} = 0.2$. Typically, for any given design, there will be one or possibly a group of neighboring modes that satisfy this requirement and exhibit corresponding increased sensitivity to thickness variations.

Because of the simplified nature of the model, it is clear that this study is preliminary in nature. Two issues that bear on its accuracy are how well Euler–Bernoulli beam theory represents tapered beams, and to what extent the behavior of tapered beam modes represent actual blades. A significant number of independent calculations were performed on tapered beam geometries using a commercial finite element program in order to check the accuracy of the results. The tapered beam geometry was represented using a relatively fine mesh of two-dimensional, quadrilateral elements. It was observed that for the modes discussed in this paper, the participation factors that were calculated using finite elements agreed reasonably well with those predicted by Euler–Bernoulli beam theory and that, as a result, all of the trends were the same as those presented in this paper. Thus, it was concluded that Euler–Bernoulli theory provides a reasonably accurate representation of the modes and beam geometries of interest and, of course, has the advantage of providing much more general results than can be obtained from numerical simulations.

A more serious concern is to what extent the behavior of tapered beams represents that of blades. This issue is complex and remains to be studied. However, it is important to understand that the purpose of a simple model, such as that presented here, is to provide insights into some of the physical mechanisms that should also be factors affecting the behavior of the more complex, real system. In this sense the simple model provides a context for the subsequent study of the actual system.

Acknowledgments

This work was supported by the GUIde Consortium on the Forced Response of Bladed Disks. Support for the Consortium is provided by its industrial members: AlliedSignal Engines, Allison Engine Company, General Electric Aircraft Engines, Pratt & Whitney, Textron Lycoming, Westinghouse Electric Corporation, NASA, and the U.S. Air Force. Special acknowledgment is given to the members of the Steering Committee for their suggestions and practical knowledge of the problem discussed.

References

Conway, H. D., and Dubil, J. F., 1965, "Vibration Frequencies of Truncated-Cone and Wedge Beams," ASME *Journal of Applied Mechanics,* Vol. 87, pp. 932–934.

Cranch, E. T., and Adler, A. A., 1956, "Bending Vibrations of Variable Section Beams," ASME *Journal of Applied Mechanics,* Vol. 78, pp. 103–108.

Dowell, E. H., Curtiss, H. C., Scanlan, R. H., and Sisto, F., 1989, *A Modern Course in Aeroelasticity,* Kluwer Academic Publishers, Boston, 2nd ed.

Nicholson, J. W., 1917, "The Lateral Vibrations of Bars of Variable Section," *Proc. Royal Society of London, England,* Vol. 93, Series A, pp. 506–519.

Roy, P. K., and Ganesan, N., 1992, "Some Studies on the Response of a Tapered Beam," *Computers and Structures,* Vol. 45, No. 1, pp. 185–195.

Sanger, D. J., 1968, "Transverse Vibration of a Class of Nonuniform Beams," *Journal Mechanical Engineering Science,* Vol. 10, No. 2, pp. 111–120.

Ungar, E. E., 1962, "Maximum Stresses in Beams and Plates Vibrating at Resonance," ASME *Journal of Engineering for Industry,* Vol. 84, pp. 149–155.

C.-C. Lin
Ford Motor Company,
Dearborn, MI
Assoc. Mem. ASME

M. P. Mignolet

Associate Professor,
Dept. of Mechanical and
Aerospace Engineering,
Arizona State University,
Tempe, AZ 85287-6106
Mem. ASME

An Adaptive Perturbation Scheme for the Analysis of Mistuned Bladed Disks

In this paper, a novel perturbation technique is introduced for the determination of the forced vibration response of mistuned bladed disks. The proposed technique is adaptive in the sense that the level of approximation can be varied at will to accommodate any specificities of the tuned system and/or of the existing mistuning. This versatility of the proposed approach not only guarantees the reliability of the computed response but also leads to an excellent compromise between accuracy and computational effort. Numerical results are presented that demonstrate both the reliability of the computed response and the computational saving obtained by relying on the suggested perturbation technique as opposed to a straightforward steady-state analysis.

Introduction

In the context of turbomachinery, the term mistuning refers to small blade-to-blade variations in their mechanical properties such as mass, damping, and/or natural frequencies. These small imperfections, which are usually a consequence of the manufacturing process and/or in-service wear, have a surprisingly large effect on both the free (mode shapes) and forced (steady-state amplitude of response) vibration of bladed disks (see, for example, Whitehead, 1966; Ewins and Han, 1984; Kielb and Kaza, 1984; Basu and Griffin, 1986; Wei and Pierre, 1988a, b; Afolabi, 1988; Sinha and Chen, 1989; Mignolet and Lin, 1993; Lin and Mignolet, 1996). In particular, it has been found (Basu and Griffin, 1986) that the steady-state amplitude of vibration of certain blades can be as large as 2.43 times the value computed on the basis of identical blades (tuned system). Paradoxically, it has been shown that mistuning often has a beneficial effect on flutter; it pushes the appearance of this phenomenon to a higher flow velocity.

These findings indicate that a careful structural dynamics analysis of a *given* bladed disk must rely on accurate estimates of the structural parameters of the systems (mass, damping coefficient, and stiffness). The identification technique recently devised by Mignolet and Lin (1997) can, for example, be used to produce these parameters.

If the objective of the structural dynamic analysis is to validate a proposed design for an *ensemble* of conceptually identical bladed disks, it is required in view of the observations given above to

1 include mistuning in the modeling of the disk and
2 proceed with a random analysis since the imperfections arising in the manufacturing process and/or in service are unlikely to be predictable.

From a computational point of view, both of these analysis requirements have a disastrous effect. Indeed, in the absence of mistuning, the perfect periodicity of the bladed disk allows the determination of its dynamic response by investigating only one typical blade. The inclusion in the model of blade-to-blade variations in structural properties destroys the symmetry of the system and thus leads to an increase in the number of degrees-of-freedom to be considered by a factor of N, the number of blades. Associated with this magnification of the problem size is an increase in computational effort proportional, in general, to N^2.

The determination of the distribution of the amplitudes of blade response corresponding to random structural properties of the disk is a prerequisite for the failure and fatigue analysis of an ensemble of mistuned bladed disks. Unfortunately, such a probabilistic study is very difficult to achieve in an analytical way, as demonstrated by the recent efforts of Huang (1982), Sinha and Chen (1989), Mignolet and Lin (1993) and Lin and Mignolet (1996). On this basis, the Monte Carlo simulation technique has often been used to produce the necessary distribution of blade amplitudes of response. That is, many sets of the random structural parameters of the disk are first synthesized. Then, the amplitudes of response of the blades corresponding to each individual set of blade properties are computed, and, finally, a statistical analysis of the produced population of amplitudes is performed. Clearly, the Monte Carlo technique is both versatile and simple, but it is also costly computationally. In fact, it is not unusual that 100, 1000, or more sets of blade parameters be required to obtain an accurate estimate of the distribution of the amplitudes of blade response.

On the basis of these observations, the aim of the present investigation is to propose a novel perturbation-based simulation scheme that provides a dramatic reduction in the computational effort necessary to produce an accurate estimate of the distribution of the amplitudes of blade response.

Mistuned Bladed Disk Modeling

Neglecting the effects of possible nonlinearities associated with the structure, the fluid, and their interaction and relying on an appropriate discretization, e.g., finite elements, it is found that a bladed disk can be modeled as a multi-degree-of-freedom system whose equations of motion can be written as

$$M\ddot{\underline{X}} + C\dot{\underline{X}} + K\underline{X} = \underline{F}. \tag{1}$$

In this relation, the symbol $\underline{X}(t)$ denotes the time-dependent response vector corresponding to the external loading $\underline{F}(t)$. Further, the symbols M, C, and K, designate the mass, damping, and stiffness matrices.

An alternative representation of the equations of motion, Eq. (1), can be obtained by analyzing the behavior of a given blade. Specifically, assume first that p degrees-of-freedom have been used to model each of the N blades. Then, partitioning the Np

Contributed by the International Gas Turbine Institute and presented at the 40th International Gas Turbine and Aeroengine Congress and Exhibition, Houston, Texas, June 5–8, 1995. Manuscript received by the International Gas Turbine Institute March 1, 1995. Paper No. 95-GT-455. Associate Technical Editor: C. J. Russo.

$\times 1$ vectors $\underline{X}(t)$, $\underline{F}(t)$, and the $Np \times Np$ matrices M, C, and K into $p \times 1$ and $p \times p$ blocks, it is found that

$$M_{jj}\ddot{\underline{X}}_j + C_{jj}\dot{\underline{X}}_j + K_{jj}\underline{X}_j + \sum_{\substack{l=1 \\ l\neq j}}^{N} [M_{jl}\ddot{\underline{X}}_l + C_{jl}\dot{\underline{X}}_l + K_{jl}\underline{X}_l] = \underline{F}_j \quad (2)$$

for $j = 1, \ldots, N$, where

$$\underline{X}(t) = \begin{bmatrix} \underline{X}_1(t) \\ \underline{X}_2(t) \\ \cdot \\ \cdot \\ \cdot \\ \underline{X}_N(t) \end{bmatrix} \quad \underline{F}(t) = \begin{bmatrix} \underline{F}_1(t) \\ \underline{F}_2(t) \\ \cdot \\ \cdot \\ \cdot \\ \underline{F}_N(t) \end{bmatrix} \quad (3)$$

and D_{jl} denotes the jl block element of dimension $p \times p$ of an arbitrary matrix D. According to the above equations, the bladed disk can be viewed as a set of N p-degree-of-freedom systems coupled to one another through the off-diagonal block elements M_{jl}, C_{jl}, and K_{jl}, $j \neq l$.

In the absence of mistuning, the N blades have perfectly identical geometric and material properties and the disk dynamic model, Eq. (1) or (2), must be invariant with respect to a rotation by an angle $s(2\pi/N)$ with $s = 0, 1, 2, \ldots, N$. This physical requirement implies mathematically that

$$M_{(j+s)(l+s)} = M_{jl} \quad C_{(j+s)(l+s)} = C_{jl} \quad \text{and} \quad K_{(j+s)(l+s)} = K_{jl} \quad (4)$$

for all j and l and $s = 1, 2, \ldots, N$, or equivalently that the block elements M_{jl}, C_{jl}, and K_{jl} do not depend independently on the indices j and l but rather on the difference $j - l$, i.e.,

$$M_{jl} = \bar{M}_{j-l} \quad C_{jl} = \bar{C}_{j-l} \quad K_{jl} = \bar{K}_{j-l}. \quad (5)$$

Further, the periodicity of the system implies that the $p \times p$ matrices $\bar{M}_j$, $\bar{C}_j$, and $\bar{K}_j$ must also satisfy the conditions

$$\bar{M}_{j+N} = \bar{M}_j \quad \bar{C}_{j+N} = \bar{C}_j \quad \bar{K}_{j+N} = \bar{K}_j \quad j = 1, 2, \ldots, N. \quad (6)$$

The introduction of mistuning in the system, for example, in the form of small blade-to-blade variations in the mass distribution, the damping modeling, and/or the natural frequencies, destroys the rotational symmetry of the disk and invalidate the use of the relations (5). In their place, the mistuned block elements M_{jl}, C_{jl}, and K_{jl} can be expressed in terms of their tuned counterparts as

$$M_{jl} = \bar{M}_{j-l} + \delta M_{jl}, \quad C_{jl} = \bar{C}_{j-l} + \delta C_{jl}, \quad \text{and} \quad K_{jl} = \bar{K}_{j-l} + \delta K_{jl} \quad (7)$$

where the deviations δM_{jl}, δC_{jl}, and δK_{jl} are associated with the mistuning. The elements of these $p \times p$ matrices will be modeled in the present investigation as zero mean random variables with a given joint probability density function.

Modal Analysis of the Tuned and Decoupled Systems

The strong connection between the forced response of a lightly damped multi-degree-of-freedom system and its modal characteristics, i.e., mode shapes and natural frequencies, motivates the review of the free vibration of two limiting models of the bladed disk, i.e., the tuned and the decoupled systems.

Tuned System. Combining Eqs. (2) and (5), it is found that the free vibration of the undamped tuned disk is governed by the set of differential equations

$$\bar{M}_0\ddot{\underline{X}}_j + \bar{K}_0\underline{X}_j + \sum_{\substack{l=1 \\ l\neq j}}^{N} [\bar{M}_{j-l}\ddot{\underline{X}}_l + \bar{K}_{j-l}\underline{X}_l] = \underline{0} \quad j = 1, 2, \ldots, N. \quad (8)$$

The convolution character of this equation suggests introducing the discrete Fourier transforms

$$\bar{M}^{(r)} = \sum_{j=1}^{N} \bar{M}_j e^{i(2\pi/N)jr} \quad (9)$$

$$\bar{K}^{(r)} = \sum_{j=1}^{N} \bar{K}_j e^{i(2\pi/N)jr} \quad (10)$$

and

$$\underline{X}^{(r)}(t) = \sum_{j=1}^{N} \underline{X}_j(t) e^{i(2\pi/N)jr} \quad (11)$$

where r is an integer index, $r = 0, 1, 2, \ldots, N-1$, referred to as the engine order, and $i = \sqrt{-1}$.

To formulate the equations of motion, Eq. (8), in terms of $\bar{M}^{(r)}$, $\bar{K}^{(r)}$, and $\underline{X}^{(r)}(t)$, multiply first Eq. (8) by $e^{i(2\pi/N)jr}$ and sum the resulting relations for $j \in [1, N]$. Finally, using the periodicity of the $p \times p$ matrices $\bar{M}_j$ and $\bar{K}_j$, Eq. (6), it is found that

$$\bar{M}^{(r)}\ddot{\underline{X}}^{(r)} + \bar{K}^{(r)}\underline{X}^{(r)} = \underline{0} \quad r = 0, 1, 2, \ldots, N-1. \quad (12)$$

Thus, the introduction of the Fourier transforms, Eqs. (9)–(11), has led to the reduction of the Np coupled differential equations, Eq. (8), into N uncoupled sets of p coupled differential equations.

For each value of $r \in [0, N-1]$, there exist p natural frequencies $\omega_{l,r}$, $l = 1, 2, \ldots, p$, of the rth reduced system, Eq. (12). These values and the corresponding mode shapes, $\underline{\phi}_{l,r}$, are such that

$$\det [\bar{K}^{(r)} - \omega_{l,r}^2 \bar{M}^{(r)}] = 0 \quad l = 1, 2, \ldots, p \quad (13)$$

and

$$[\bar{K}^{(r)} - \omega_{l,r}^2 \bar{M}^{(r)}]\underline{\phi}_{l,r} = \underline{0} \quad l = 1, 2, \ldots, p. \quad (14)$$

Considering the multiplicity of a given natural frequency, it is first observed that the periodicity of the matrices $\bar{M}_j$ and $\bar{K}_j$, Eq. (6), implies that

$$\bar{M}^{(N-r)} = [\bar{M}^{(r)}]^* \quad \text{and} \quad \bar{K}^{(N-r)} = [\bar{K}^{(r)}]^* \quad (15)$$

where the superscript * denotes the operation of complex conjugation. Then, noting that the natural frequencies are all real, it is found that

$$\begin{aligned} 0 &= \det [\bar{K}^{(r)} - \omega_{l,r}^2 \bar{M}^{(r)}] \\ &= \det [[\bar{K}^{(N-r)}]^* - \omega_{l,r}^2 [\bar{M}^{(N-r)}]^*] \\ &= \{\det [\bar{K}^{(N-r)} - \omega_{l,r}^2 \bar{M}^{(N-r)}]\}^*. \end{aligned} \quad (16)$$

Thus, $\omega_{l,r}$ is also a natural frequency of the $N-r$th reduced system independently of l, or equivalently,

$$\omega_{l,N-r} = \omega_{l,r} \quad \text{for } \textit{all} \quad l = 1, 2, \ldots, p \quad \text{and} \quad r = 1, 2, \ldots, N-1. \quad (17)$$

This result indicates that the natural frequencies corresponding to any index $r \neq 0$ and $r \neq N/2$ are automatically repeated.

A simple relationship between the mode shapes $\underline{\phi}_{l,r}$ and $\underline{\phi}_{l,N-r}$ can also be derived. Specifically, it is found in general that

$$\underline{\phi}_{l,N-r} = \underline{\phi}_{l,r}^* = \underline{\phi}_{l,r}^{(R)} - i\underline{\phi}_{l,r}^{(I)} \quad (18)$$

where $\underline{\phi}_{l,r}^{(R)}$ and $\underline{\phi}_{l,r}^{(I)}$ denote the real and imaginary parts of $\underline{\phi}_{l,r}$. When the global mass and stiffness matrices are symmetric, the block elements $\bar{M}_j$ and $\bar{K}_j$ also satisfy the conditions

$$\bar{M}_j = \bar{M}_{-j} = \bar{M}_{N-j} \quad \text{and} \quad \bar{K}_j = \bar{K}_{-j} = \bar{K}_{N-j} \quad j = 1, 2, \ldots, N \quad (19)$$

from which it is concluded that the $p \times p$ matrices $\bar{M}^{(r)}$ and $\bar{K}^{(r)}$ are real. This additional property implies in turn that the mode shapes $\underline{\phi}_{l,r}$ are also real so that

$$\underline{\phi}_{l,r}^{(I)} = 0 \quad \text{for } all \quad l = 1, 2, \ldots, p \quad \text{and}$$

$$r = 1, 2, \ldots, N-1 \quad (20a)$$

and

$$\underline{\phi}_{l,N-r} = \underline{\phi}_{l,r} \quad \text{for } all \quad l = 1, 2, \ldots, p \quad \text{and}$$

$$r = 1, 2, \ldots, N-1. \quad (20b)$$

The determination of the *system* mode shapes $\Phi_{l,r}$ can be achieved directly from their counterparts, $\underline{\phi}_{l,r}$, for the reduced systems described by Eq. (12). Consider first the case $r = 0$ and assumed that the natural frequency $\omega_{l,0}$ is not repeated. Then, the corresponding free response of the entire disk originates only from the vector $\underline{X}^{(0)}(t)$ since Eq. (12) yields only the trivial solution $\underline{X}^{(r)}(t) = 0$ for all values $r \neq 0$. Thus, inverting Eq. (11), it is found that

$$\underline{X}_j(t) = \frac{1}{N}\sum_{r=0}^{N-1} \underline{X}^{(r)}(t) e^{-i(2\pi/N)jr} = \left[\frac{\alpha_0}{N}\underline{\phi}_{l,0}\right] e^{i\omega_{l,0}t} \quad (21)$$

where α_0 is an arbitrary scalar constant, so that

$$\underline{\Phi}_{l,0} = \frac{1}{N}\begin{bmatrix} \underline{\phi}_{l,0} \\ \underline{\phi}_{l,0} \\ \cdot \\ \cdot \\ \cdot \\ \underline{\phi}_{l,0} \end{bmatrix} \quad l = 1, 2, \ldots, p. \quad (22)$$

Proceeding similarly in the case $r = N/2$ when N is even, it is found that

$$\begin{aligned} \underline{X}_j(t) &= \frac{1}{N}\sum_{r=0}^{N-1} \underline{X}^{(r)}(t) e^{-i(2\pi/N)jr} \\ &= \left[\frac{1}{N}\underline{\phi}_{l,(N/2)} e^{-i(2\pi/N)j(N/2)}\alpha_{N/2}\right] e^{i\omega_{l,(N/2)}t} \\ &= \left[\frac{(-1)^{j+1}}{N}\underline{\phi}_{l,(N/2)}\alpha_{N/2}\right] e^{i\omega_{l,(N/2)}t} \end{aligned} \quad (23)$$

where $\alpha_{N/2}$ is an arbitrary scalar. Thus,

$$\underline{\Phi}_{l,(N/2)} = \frac{1}{N}\begin{bmatrix} \underline{\phi}_{l,(N/2)} \\ -\underline{\phi}_{l,(N/2)} \\ \cdot \\ \cdot \\ \cdot \\ -\underline{\phi}_{l,(N/2)} \end{bmatrix} \quad l = 1, 2, \ldots, p. \quad (24)$$

For an arbitrary value of r, $r \neq 0$ and $r \neq N/2$, there are two contributions to the response vector $\underline{X}_j(t)$, namely those associated with $\underline{X}^{(r)}(t)$ and $\underline{X}^{(N-r)}(t)$. Thus,

$$\begin{aligned} \underline{X}_j(t) &= \frac{1}{N}[\underline{X}^{(r)}(t) e^{-i(2\pi/N)jr} + \underline{X}^{(N-r)}(t) e^{-i(2\pi/N)j(N-r)}] \\ &= \frac{1}{N}[\alpha_r \underline{\phi}_{l,r} e^{-i(2\pi/N)jr} + \alpha_{N-r}\underline{\phi}_{l,(N-r)} e^{-i(2\pi/N)j(N-r)}] e^{i\omega_{l,r}t} \end{aligned} \quad (25)$$

where α_r and α_{N-r} are two arbitrary scalars. Since the natural frequency $\omega_{l,r}$ is of multiplicity two, it is associated with two separate mode shapes, which can be determined from this equation by selecting for example $\alpha_r = \alpha_{N-r}$ and $\alpha_r = -\alpha_{N-r}$. These choices lead, in conjunction with Eq. (18), to the following solutions:

$$\underline{X}_j(t) = \begin{cases} 2\alpha_r \dfrac{1}{N}\left[\underline{\phi}_{l,r}^{(R)} \cos\dfrac{2\pi}{N}jr + \underline{\phi}_{l,r}^{(I)} \sin\dfrac{2\pi}{N}jr\right] e^{i\omega_{l,r}t} \\ \qquad \text{for} \quad \alpha_r = \alpha_{N-r} \\ -2i\alpha_r \dfrac{1}{N}\left[\underline{\phi}_{l,r}^{(R)} \sin\dfrac{2\pi}{N}jr - \underline{\phi}_{l,r}^{(I)} \cos\dfrac{2\pi}{N}jr\right] e^{i\omega_{l,r}t} \\ \qquad \text{for} \quad \alpha_r = -\alpha_{N-r} \end{cases} \quad (26)$$

and the corresponding mode shapes

$$\underline{\Phi}_{l,r} = \begin{bmatrix} \underline{\phi}_{l,r}^{(R)} \cos\dfrac{2\pi}{N}r + \underline{\phi}_{l,r}^{(I)} \sin\dfrac{2\pi}{N}r \\ \underline{\phi}_{l,r}^{(R)} \cos\dfrac{4\pi}{N}r + \underline{\phi}_{l,r}^{(I)} \sin\dfrac{4\pi}{N}r \\ \cdot \\ \cdot \\ \cdot \\ \underline{\phi}_{l,r}^{(R)} \end{bmatrix} \quad (27a)$$

and

$$\underline{\Phi}_{l,N-r} = \begin{bmatrix} \underline{\phi}_{l,r}^{(R)} \sin\dfrac{2\pi}{N}r - \underline{\phi}_{l,r}^{(I)} \cos\dfrac{2\pi}{N}r \\ \underline{\phi}_{l,r}^{(R)} \sin\dfrac{4\pi}{N}r - \underline{\phi}_{l,r}^{(I)} \cos\dfrac{4\pi}{N}r \\ \cdot \\ \cdot \\ \cdot \\ -\underline{\phi}_{l,r}^{(I)} \end{bmatrix}. \quad (27b)$$

It is finally reminded that when the global mass and stiffness matrices M and K are symmetric, the vector $\underline{\phi}_{l,r}^{(I)}$ vanishes identically and a simplification of the system mode shapes is obtained.

Decoupled System. When the coupling terms in both the global mass (M) and stiffness (K) matrices are small, i.e., when

$$|\max \lambda(M_{jl})| \ll [\min \lambda(M_{jj}) \min \lambda(M_{ll})]^{1/2}$$

$$\text{for } all \quad j \neq l \quad (28)$$

and

$$|\max \lambda(K_{jl})| \ll [\min \lambda(K_{jj}) \min \lambda(K_{ll})]^{1/2}$$

$$\text{for } all \quad j \neq l \quad (29)$$

where $\lambda(D)$ denotes the eigenvalues of an arbitrary matrix D, the equations of motion, Eq. (2), can be approximated by the following N uncoupled sets of differential equations:

$$M_{jj}\ddot{\underline{X}}_j + K_{jj}\underline{X}_j = 0 \quad j = 1, 2, \ldots, N. \quad (30)$$

Each of these uncoupled p-degree-of-freedom systems is characterized by natural frequencies $\omega_{l,j}$ and mode shapes $\underline{\phi}_{l,j}$, $l = 1, 2, \ldots, p$, that satisfy the equations

$$\det [K_{jj} - \omega_{l,j}^2 M_{jj}] = 0 \quad (31)$$

and

$$[K_{jj} - \omega_{l,j}^2 M_{jj}]\underline{\phi}_{l,j} = \underline{0}. \tag{32}$$

If the natural frequency $\omega_{l,j}$ is not repeated, the response of the entire disk at that frequency originates only from the vector $\underline{X}_j(t)$ since Eq. (30) yields only the trivial solution $\underline{X}_k(t) = 0$ for $k \neq j$. Then,

$$\underline{X}_j(t) = \alpha_j' \underline{\phi}_{l,j} e^{i\omega_{l,j}t} \tag{33}$$

where α_j' is an arbitrary scalar, and

$$\underline{X}(t) = \begin{bmatrix} \underline{0} \\ \cdot \\ \underline{0} \\ \underline{X}_j(t) \\ \underline{0} \\ \cdot \\ \underline{0} \end{bmatrix} = \alpha_j' \begin{bmatrix} \underline{0} \\ \cdot \\ \underline{0} \\ \underline{\phi}_{l,j} \\ \underline{0} \\ \cdot \\ \underline{0} \end{bmatrix} e^{i\omega_{l,j}t}. \tag{34}$$

It is finally concluded that the system mode shape $\underline{\Phi}_{l,j}$ associated with the natural frequency $\omega_{l,j}$ is

$$\underline{\Phi}_{l,j} = \begin{bmatrix} \underline{0} \\ \cdot \\ \underline{0} \\ \underline{\phi}_{l,j} \\ \underline{0} \\ \cdot \\ \underline{0} \end{bmatrix} l = 1, 2, \ldots, p \quad j = 1, 2, \ldots, N. \tag{35}$$

The Adaptive Perturbation Scheme

The large increase in the computational effort that is associated with mistuning has motivated various investigators (Huang, 1982; Wei and Pierre, 1988a, b, 1990; Sinha and Chen, 1989; Mignolet and Lin, 1993; Lin and Mignolet, 1996) to propose perturbation-based techniques for the determination of the forced response of mistuned bladed disks. In view of the large effect that even a small level of mistuning has on both the free and forced vibration responses of the system, it is doubtful that a straightforward, regular perturbation approach would be successful. Indeed, Wei and Pierre (1988b) have demonstrated that truncated Taylor series approximations of the response of the blades in terms of the small perturbations of their structural properties are accurate only when the blade-to-blade coupling is very large with respect to the standard deviation (root mean square value) of the mistuned parameters. In the opposite limit of a very small coupling, these authors demonstrated that both the free and forced vibration of the disk can be qualitatively well understood by considering the decoupled mistuned system as the "base system" and treating the known blade-to-blade coupling terms as the perturbation parameters. These results clearly indicate that there is no perturbation scheme that can be employed in all situations or, equivalently, that is uniformly valid in the parameter space. A similar conclusion could be reached from the investigations conducted by Happawana et al. (1991), Mignolet and Lin (1993), and Natsiavas (1993) in which two distinct perturbation schemes were used simultaneously to produce an overall reliable estimate of the structural dynamic response of the system.

To understand the need for the combined use of two different perturbation schemes, note first that the steady-state response of the disk to a harmonic excitation of frequency ω can be written as the sum of modal contributions, each of which is computed from the transfer function of the equivalent modal single-degree-of-freedom system. Further, this function possesses a very sharp peak near the corresponding natural frequency when the associated damping ratio is small, as is usually the case in turbomachinery applications. Thus, the modal contributions associated with natural frequencies $\omega_{l,j} \approx \omega$ are very sensitive to small changes in the values of $\omega_{l,j}$ while those corresponding to $\omega_{l,j} \not\approx \omega$ display a much weaker dependence on variations of the frequencies $\omega_{l,j}$. Then, the effect of mistuning on a modal contribution is large if $\omega_{l,j} \approx \omega$ but small otherwise. On the basis of this observation, it is concluded that an accurate perturbation strategy for the steady-state structural dynamic analysis of mistuned bladed disks must rely on a separate treatment of the modal contributions associated with natural frequencies $\omega_{l,j}$ that are close and far from the excitation frequency, ω.

The focus of the present method on the natural frequencies of the bladed disk motivates the analysis of the system not in the physical coordinates, $\underline{X}(t)$, as in Eq. (1), but rather in terms of a set of variables $\underline{q}(t)$ that accurately represent the contributions of the various mode shapes in the response. These new coordinates can be related to the physical ones by the relation

$$\underline{X}(t) = T\underline{q}(t) \tag{36}$$

where T denotes a $Np \times Np$ transformation matrix as yet unspecified.

Selecting the columns of T to be the mode shapes of the *mistuned* bladed disk leads of course to a set of variables $\underline{q}(t)$ that correspond exactly to the system's modal coordinates. The use of this transformation in connection with a Monte Carlo study would however lead to a tremendous computational effort as the mode shapes of every bladed disk considered would have to be determined. Thus, for such simulation analyses, the columns of T should:

1 not change from one bladed disk to another
2 represent reliable approximations of the mode shapes of the mistuned disks considered.

In view of the comprehensive qualitative analysis performed by Wei and Pierre (1988a, b), it is suggested to choose the columns of the transformation matrix T to be

(*i*) the mode shapes of the *tuned* system when the coupling terms M_{jl}, C_{jl}, and K_{jl}, $j \neq l$, are *larger* (have larger eigenvalues) than their mistuning counterparts δM_{jj}, δC_{jj}, and δK_{jj}

(*ii*) the mode shapes of the *decoupled* system when the coupling terms M_{jl}, C_{jl}, and K_{jl}, $j \neq l$, are *smaller* (have smaller eigenvalues) than their mistuning counterparts δM_{jj}, δC_{jj}, and δK_{jj}.

Introducing this change of variables, Eq. (36), into Eq. (1) and premultiplying the resulting relations by T^T leads to the transformed equations of motion

$$M'\ddot{\underline{q}} + C'\dot{\underline{q}} + K'\underline{q} = \underline{F}' \tag{37}$$

where

$$M' = T^T M T \quad C' = T^T C T \quad K' = T^T K T$$
$$\text{and} \quad \underline{F}' = T^T \underline{F}. \tag{38}$$

An alternative representation of Eq. (37) can be obtained by partitioning the vectors $\underline{q}$, $\underline{F}'$ and the matrices M', C', and K' into $p \times 1$ and $p \times p$ block elements as in Eqs. (2) and (3). It is then found that

$$M_{jj}'\ddot{\underline{q}}_j + C_{jj}'\dot{\underline{q}}_j + K_{jj}'\underline{q}_j + \sum_{\substack{l=1 \\ l \neq j}}^{N} [M_{jl}'\ddot{\underline{q}}_l + C_{jl}'\dot{\underline{q}}_l + K_{jl}'\underline{q}_l] = \underline{F}_j'. \tag{39}$$

When the excitation vector, $\underline{F}(t)$, is a single frequency harmonic function of the form

$$\underline{F}(t) = \underline{F}_C \cos \omega t + \underline{F}_S \sin \omega t \tag{40}$$

the steady-state response of the bladed disk can be written in the form

$$\underline{q}_j(t) = \underline{U}_j \cos \omega t + \underline{V}_j \sin \omega t. \tag{41}$$

Introducing Eqs. (40) and (41) in Eq. (39) leads to the $2Np \times 2Np$ linear system of equations

$$H\underline{Z} = \underline{\tilde{F}} \tag{42}$$

where the $2Np$ vectors $\underline{Z}$ and $\underline{\tilde{F}}$ are defined as

$$\underline{Z} = \begin{bmatrix} \underline{U}_1 \\ \underline{V}_1 \\ \underline{U}_2 \\ \underline{V}_2 \\ \cdot \\ \cdot \\ \cdot \\ \underline{U}_N \\ \underline{V}_N \end{bmatrix} \quad \text{and} \quad \underline{\tilde{F}} = \begin{bmatrix} \underline{F}'_{1C} \\ \underline{F}'_{1S} \\ \underline{F}'_{2C} \\ \underline{F}'_{2S} \\ \cdot \\ \cdot \\ \cdot \\ \underline{F}'_{NC} \\ \underline{F}'_{NS} \end{bmatrix} \tag{43}$$

and the $2p \times 2p$ block element H_{jl} of the matrix H is

$$H_{jl} = \begin{bmatrix} K'_{jl} - \omega^2 M'_{jl} & \omega C'_{jl} \\ -\omega C'_{jl} & K'_{jl} - \omega^2 M'_{jl} \end{bmatrix}. \tag{44}$$

Considering the magnitude of the terms H_{jl}, it is first noted for the base configuration, which is the tuned system when the coupling is stronger than the mistuning and the decoupled system in the reverse case, that the matrix $H = \bar{H}$ is block diagonal, i.e.,

$$\bar{H}_{jl} = 0 \quad \text{for} \quad j \neq l. \tag{45}$$

Further, the lowest eigenvalue of the matrix $\bar{H}_{jj}$ will be "small" when the excitation frequency is close to one of the natural frequency $\omega_{l,j}$ of the corresponding reduced system, Eq. (12) or (30), but will otherwise be "large." This disparity in the magnitudes of the diagonal elements of the base impedance matrix $\bar{H}_{jj}$ renders the formulation of a reliable perturbation scheme difficult.

To remedy this situation, it is suggested to partition the response vector $\underline{q}(t)$ not in terms of the variables $\underline{q}_j$, $j = 1, 2, \ldots, N$ as in Eq. (39), but rather in terms of the components $\underline{q}_S$ and $\underline{q}_L$, which are associated with small and large diagonal elements of $\bar{H}$, respectively. That is,

$$\underline{q}(t) = \begin{bmatrix} \underline{q}_S(t) \\ \underline{q}_L(t) \end{bmatrix} \tag{46}$$

where $\underline{q}_S(t)$ and $\underline{q}_L(t)$ are vectors of dimensions $d \times 1$ and $(Np - d) \times 1$, respectively. This partition can be achieved directly from the physical variables $\underline{X}(t)$ by selecting the transformation matrix T to be

$$T = [\Phi_S \quad \Phi_L] \tag{47}$$

where Φ_S and Φ_L denote the $Np \times d$ and $Np \times (Np - d)$ matrices whose columns are the system mode shapes associated with the natural frequencies $\omega_{l,j}$ that are close to (for Φ_S) and far from (for Φ_L) the excitation frequency ω.

Proceeding with this partitioning, it is found that the linear system of equations (42) becomes

$$\begin{bmatrix} H_{SS} & H_{SL} \\ H_{LS} & H_{LL} \end{bmatrix} \begin{bmatrix} \underline{Z}_S \\ \underline{Z}_L \end{bmatrix} = \begin{bmatrix} \underline{\tilde{F}}_S \\ \underline{\tilde{F}}_L \end{bmatrix} \tag{48}$$

where the matrices H_{SS}, H_{SL}, H_{LS}, and H_{LL} are of respective dimensions $2d \times 2d$, $2d \times 2(Np - d)$, $2(Np - d) \times 2d$, and $2(Np - d) \times 2(Np - d)$, while the vectors $\underline{Z}_S$, $\underline{Z}_L$, $\underline{\tilde{F}}_S$, and $\underline{\tilde{F}}_L$ have $2d$, $2(Np - d)$, $2d$, and $2(Np - d)$ components.

The computation of the steady-state components $\underline{Z}_S$ and $\underline{Z}_L$ can now be performed by perturbation technique. To this end, note first that the inverse of the matrix H can, by relying on the Frobenius–Schur formula, be expressed as

$$H^{-1} = \begin{bmatrix} H_{SS} & H_{SL} \\ H_{LS} & H_{LL} \end{bmatrix}^{-1} = \begin{bmatrix} G_{SS} & G_{SL} \\ G_{LS} & G_{LL} \end{bmatrix} \tag{49}$$

where

$$G_{SS} = [H_{SS} - H_{SL}H_{LL}^{-1}H_{LS}]^{-1} \tag{50a}$$

$$G_{SL} = -G_{SS}H_{SL}H_{LL}^{-1} \tag{50b}$$

$$G_{LS} = -H_{LL}^{-1}H_{LS}G_{SS} \tag{50c}$$

and

$$G_{LL} = H_{LL}^{-1} + H_{LL}^{-1}H_{LS}G_{SS}H_{SL}H_{LL}^{-1}. \tag{50d}$$

It is then found from Eqs. (48)–(50) that the response of the system can be evaluated as

$$\underline{Z}_S = G_{SS}\underline{\tilde{F}}_S + G_{SL}\underline{\tilde{F}}_L = G_{SS}[\underline{\tilde{F}}_S - H_{SL}H_{LL}^{-1}\underline{\tilde{F}}_L] \tag{51}$$

and

$$\underline{Z}_L = G_{LS}\underline{\tilde{F}}_S + G_{LL}\underline{\tilde{F}}_L = H_{LL}^{-1}[\underline{\tilde{F}}_L - H_{LS}\underline{Z}_S]. \tag{52}$$

Next, note by construction that the matrix $H_{LL} = \bar{H}_{LL}$ corresponding to the base system is diagonal and contains only large terms. Then, considering its perturbed counterpart

$$H_{LL} = \bar{H}_{LL} + \delta H_{LL} \tag{53}$$

where δH_{LL} contains the mistuning terms when the coupling is larger than the mistuning and the coupling terms in the reverse situation, it is found that H_{LL} is strongly diagonal dominant so that

$$H_{LL}^{-1} = [\bar{H}_{LL} + \delta H_{LL}]^{-1} = \bar{H}_{LL}^{-1}[I_{2(Np-d)} + \delta H_{LL}\bar{H}_{LL}^{-1}]^{-1}$$
$$\approx \bar{H}_{LL}^{-1} - \bar{H}_{LL}^{-1}\delta H_{LL}\bar{H}_{LL}^{-1} + \ldots + (-1)^k\bar{H}_{LL}^{-1}[\delta H_{LL}\bar{H}_{LL}^{-1}]^k \tag{54}$$

where $I_{2(Np-d)}$ denotes the identity matrix of dimensions $2(Np - d) \times 2(Np - d)$. Keeping $k + 1$ terms in the Taylor series yields kth order approximations of the matrices G_{SS}, G_{LS}, G_{SL}, and G_{LL} through Eq. (50) and of the response vector $\underline{Z}$ from Eqs. (51) and (52).

Note finally that the proposed perturbation technique reduces, in the case $d = 0$, to either the "classical perturbation method" (when the coupling terms are larger than the mistuning) or the "modified perturbation method" (when the mistuning is larger than the coupling terms), as defined by Wei and Pierre (1988a).

Perturbation Technique: Synopsis

Given the model of a set of mistuned bladed disks, their steady-state responses can be obtained by this adaptive perturbation technique, which can be summarized as follows:

1 Determine the base configuration. It represents the tuned system if the blade-to-blade coupling terms are larger than

the mistuning components, and the decoupled system in the reverse situation.

2 Determine the natural frequencies and mode shapes of the base system by relying either on Eqs. (9)–(11), (13), (14), (22), (24), and (27) (tuned system) or Eqs. (31), (32), and (35) (decoupled system).
3 Determine the number d of natural frequencies $\omega_{l,j}$ that are close to the excitation frequency ω.
4 Create the transformation matrix T according to Eq. (47).
5 Determine the transformed global matrices M', C', K', and vector F' according to Eq. (38).
6 Determine the impedance matrix H and the excitation vector $\bar{F}$ from Eqs. (43) and (44). Identify their partitions H_{SS}, H_{SL}, H_{LS}, H_{LL}, $\bar{F}_S$, and $\bar{F}_L$ using Eq. (48).
7 Identify the diagonal matrix $\bar{H}_{LL}$ corresponding to the base configuration, see Eq. (53), and compute its inverse $\bar{H}_{LL}^{-1}$.
8 Select an order k and determine the corresponding approximation of the matrix H_{LL}^{-1} from the Taylor series, Eq. (54).
9 Compute the response of the system in the modal coordinates, $q(t)$, from Eq. (50a), (51), and (52).
10 Finally, determine the response of the system in the physical coordinates, $\underline{X}(t)$, by using Eq. (36).

Numerical Results

To investigate the reliability and computational efficiency of the proposed adaptive perturbation technique, the one-degree-of-freedom per blade model shown in Fig. 1 has been considered. Although simple, this system has been found in numerous studies (Wei and Pierre, 1988a, b; Sinha and Chen, 1989; Mignolet and Lin, 1993; Lin and Mignolet, 1996; among others) to qualitatively display the peculiarities of mistuned bladed disks.

Following Sinha and Chen (1989) and Mignolet and Lin (1993), the disk was assumed to support 24 blades, i.e., $N = 24$, of identical masses, $m = 0.0114$ kg, and damping coefficients, $c_j = c = 1.443$ N s/m and $c_C = 0$, but dissimilar natural frequencies. Specifically, the stiffnesses k_j were modeled as independent random variables uniformly distributed in the interval $k_j \in [430{,}000 - 8{,}000\sqrt{3},\ 430{,}000 + 8{,}000\sqrt{3}]$ N/m which correspond to a mean stiffness of $k_t = 430{,}000$ N/m and a standard deviation of 8,000 N/m. The system was subjected to an rth engine order excitation of the form

$$F_j(t) = F_0 \cos(\omega_r t - \psi_{j,r}) \tag{55}$$

where ω_r is the rth natural frequency of the tuned system, which is such that

$$\omega_r^2 = \frac{k_t}{m} + 4\frac{k_C}{m}\sin^2\frac{\pi r}{N} \tag{56}$$

and

$$\psi_{j,r} = \frac{2\pi}{N} r(j-1). \tag{57}$$

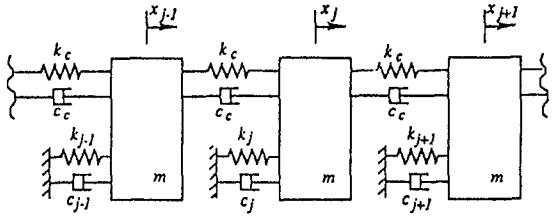

Fig. 1 Model of bladed disk

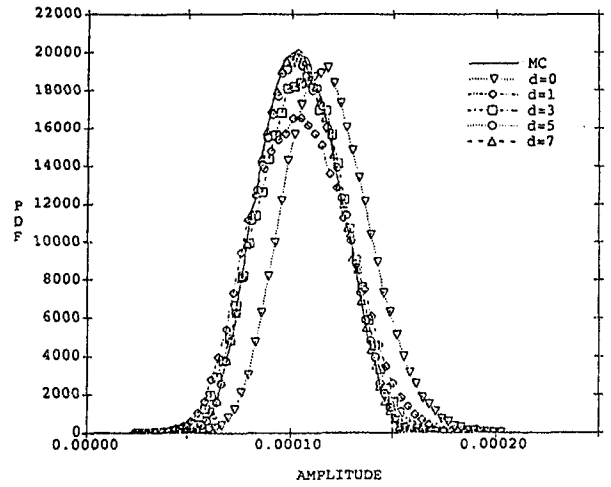

Fig. 2 Probability density function of blade amplitude, k_c = 45,430 N/m, c = 1.443 Ns/m, zeroth engine order excitation

The value of the coupling stiffness k_C was first set to

$$k_C = 45{,}430 \text{ N/m} \tag{58}$$

which corresponds to the physical bladed disk considered by Sinha and Chen (1989) and Mignolet and Lin (1993). Since the standard deviation of the mistuning is only 8000 N/m, the base configuration for the system should be selected as the tuned disk. Shown in Figs. 2 and 3 are the distributions of the amplitudes of blade response obtained by a complete Monte Carlo simulation (curve labeled "MC") and by the present adaptive perturbation technique with different numbers of close natural frequencies, d.

It is seen from Figs. 2 and 3 that an extremely reliable approximation of the distribution of blade amplitudes is obtained by selecting as few as two close frequencies, i.e., $d = 2$, although only one term was selected to compute H_{LL}^{-1}, i.e., $k = 0$ in Eq. (54). Note also that the matrix G_{SS} was approximated in the form

$$G_{SS} = H_{SS}^{-1} + H_{SS}^{-1}H_{SL}H_{LL}^{-1}H_{LS}H_{SS}^{-1} \tag{59}$$

to provide an approximation of the response vector $\underline{Z}$ that is consistently of zeroth order. For comparison, also included on these figures are the curves labeled $d = 0$, which correspond to

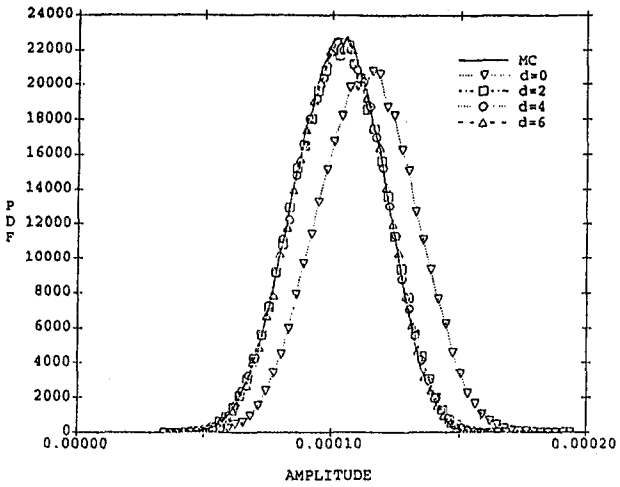

Fig. 3 Probability density function of blade amplitude, k_c = 45,430 N/m, c = 1.443 Ns/m, third engine order excitation

Table 1 Computational efficiency of the adaptive perturbation technique for various engine order excitations (r) and various numbers of close natural frequencies (d), k_c = 45,430 N/m, c = 1.443 Ns/m, zeroth order approximation

r	d	$\frac{(CPU\ time)_{Perturbation}}{(CPU\ time)_{Monte\ Carlo}}$
0 (Fig. 2)	0	0.018
	1	0.025
	3	0.063
	5	0.112
	7	0.169
3 (Fig. 3)	0	0.033
	2	0.054
	4	0.102
	6	0.156

the classical perturbation method as defined by Wei and Pierre (1988a).

Considering the CPU times, it is seen from Table 1 that the present perturbation technique yields a dramatic computational saving; the accurate distributions corresponding to $d = 5$ and $d = 4$ for the zeroth and third engine order excitations, respectively, require only 11.2 and 10.2 percent of the Monte Carlo CPU time! These results were obtained by running, on a VAX 6000-430 with operating system VAX/VMS version 5.5-2, FORTRAN programs that were written carefully, but no attempt was made to optimize them.

It would appear from Figs. 2 and 3 that the chosen number of close frequencies d should depend on the engine order. In fact, these results and others not presented here clearly demonstrate that a larger value of d is required for $r = 0$. This observation is readily justified by noting from Eq. (56) that the natural frequencies ω_r are closest to each other around $r = 0$, $r = N/2$, and $r = N - 1$ and furthest around $r = N/4$ and $r = 3N/4$. Then, the number d of natural frequencies that are considered close to the excitation frequency should be slightly larger around $r = 0$, $r = N/2$, or $r = N - 1$ and could be smaller around $r = N/4$ and $r = 3N/4$.

To investigate the reliability of the proposed perturbation technique when the coupling terms are smaller than the mistuning, the value of the stiffness k_C was arbitrarily set to k_C = 2000 N/m and the damping coefficients were again selected to be equal and $c_j = c = 0.7215$ Ns/m. Shown in Figs. 4 and 5 are the distributions of blade amplitudes obtained by a Monte Carlo simulation and by the adaptive perturbation technique for zeroth and third engine orders, respectively. Note again the excellent matching between these two sets of curves. A comparison of the CPU times, shown in Table 2, indicates again that a dramatic computational saving can be obtained by relying on the proposed method. Comparing Figs. 2 and 4 or 3 and 5, it is seen that a decrease in the values of k_C and c has led to an increase of the domain of observed values of the amplitude of blade response and, consequently, to a decrease of the corresponding values of the probability density function.

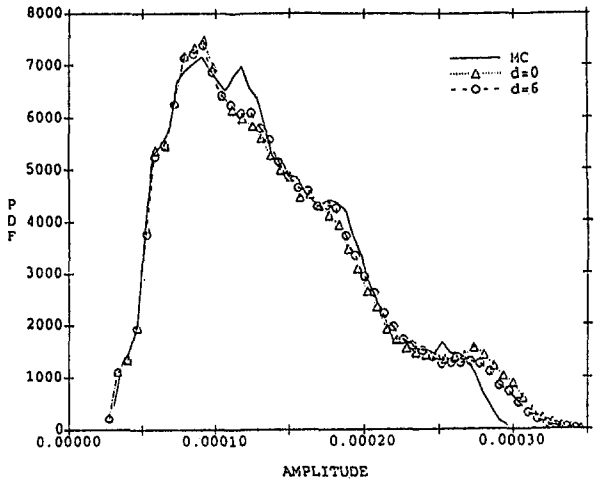

Fig. 4 Probability density function of blade amplitude, k_c = 2,000 N/m, c = 0.7215 Ns/m, zeroth engine order excitation

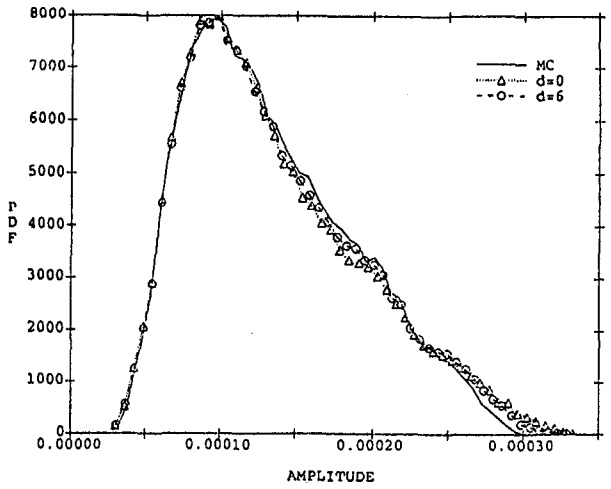

Fig. 5 Probability density function of blade amplitude, k_c = 2,000 N/m, c = 0.7215 Ns/m, third engine order excitation

Summary

A novel perturbation-based technique has been described for the determination of the distribution of the amplitudes of blade response in an ensemble of mistuned bladed disks. Central to the present approach is the observation that small variations of a natural frequency of the system created by the random mistuning lead to a large change in its corresponding modal contribution to the disk's response *only* if the natural frequency is close to the excitation frequency.

On this basis, it was first suggested to analyze the dynamics of the bladed disk in terms of the modal coordinates corresponding to a base configuration, which is the tuned disk when the blade-to-blade coupling is large with respect to the level of mistuning and the decoupled system in the reverse situation. The formulation of the method then proceeds with a partition of the modal impedance matrix into blocks associated with

Table 2 Computational efficiency of the adaptive perturbation technique for various engine order excitations (r) and various numbers of close natural frequencies (d), k_c = 2,000 N/m, c = 0.7215 Ns/m, second order approximation

r	d	$\frac{(CPU\ time)_{Perturbation}}{(CPU\ time)_{Monte\ Carlo}}$
0 (Fig. 4)	0	0.130
	6	0.405
3 (Fig. 5)	0	0.133
	6	0.370

natural frequencies that are either close or far from the excitation frequency. Finally, the effect of the latter group of modes is computed by a perturbation expansion to yield a reliable approximation of the disk's steady-state response.

The technique described is adaptive in the sense that the number of natural frequencies that are considered close to the excitation frequency can be varied at will to ensure the reliability of the computed response.

Numerical results have demonstrated that the proposed method can yield reductions in the computing time by an order of magnitude without compromising the accuracy of the estimated distribution of the amplitudes of blade response.

References

Afolabi, D., 1988, "A Note on the Rogue Failure of Turbine Blades," *Journal of Sound and Vibration,* Vol. 122, No. 3, pp. 535–545.

Basu, P., and Griffin, J. H., 1986, "The Effect of Limiting Aerodynamic and Structural Coupling in Models of Mistuned Bladed Disk Vibration," ASME *Journal of Vibration, Acoustics, Stress, and Reliability in Design,* Vol. 108, pp. 132–139.

Ewins, D. J., and Han, Z. S., 1984, "Resonant Vibration Levels of a Mistuned Bladed Disk," *Journal of Sound and Vibration,* Vol. 106, pp. 211–215.

Happawana, G. S., Bajaj, A. K., and Nwokah, O. D. I., 1991, "A Singular Perturbation Perspective on Mode Localization," *Journal of Sound and Vibration,* Vol. 147, pp. 361–365.

Huang, W.-H., 1982, "Vibration of Some Structures With Periodic Random Parameters," *AIAA Journal,* Vol. 20, No. 7, pp. 1001–1008.

Kielb, R. E., and Kaza, K. R. V., 1984, "Effects of Structural Coupling on Mistuned Cascade Flutter and Response," ASME JOURNAL OF ENGINEERING FOR GAS TURBINES AND POWER, Vol. 106, pp. 17–24.

Mignolet, M. P., and Lin, C.-C., 1993, "The Combined Closed Form—Perturbation Approach to the Analysis of Mistuned Bladed Disks," ASME *Journal of Turbomachinery,* Vol. 115, pp. 771–780.

Mignolet, M. P., and Lin, C.-C., 1997, "Identification of Structural Parameters in Mistuned Bladed Disks," ASME *Journal of Vibration and Acoustics,* in press.

Lin, C.-C., and Mignolet, M. P., 1996, "Effects of Damping and Damping Mistuning on the Forced Vibration Response of Bladed Disks," *Journal of Sound and Vibration,* Vol. 193, No. 2, pp. 525–543.

Natsiavas, S., 1993, "Mode Localization and Frequency Veering in a Nonconservative Mechanical System With Dissimilar Components," *Journal of Sound and Vibration,* Vol. 165, No. 1, pp. 137–147.

Sinha, A., and Chen, S., 1989, "A Higher Order Technique to Compute the Statistics of Forced Response of a Mistuned Bladed Disk Assembly," *Journal of Sound and Vibration,* Vol. 130, No. 2, pp. 207–221.

Wei, S.-T., and Pierre, C., 1988a, "Localization Phenomena in Mistuned Assemblies With Cyclic Symmetry. Part I: Free Vibrations," ASME *Journal of Vibration, Acoustics, Stress, and Reliability in Design,* Vol. 110, pp. 429–438.

Wei, S.-T., and Pierre, C., 1988b, "Localization Phenomena in Mistuned Assemblies With Cyclic Symmetry. Part II: Forced Vibrations," ASME *Journal of Vibration, Acoustics, Stress, and Reliability in Design,* Vol. 110, pp. 439–449.

Wei, S.-T., and Pierre, C., 1990, "Statistical Analysis of the Forced Response of Mistuned Cyclic Assemblies," *AIAA Journal,* Vol. 28, No. 5, pp. 861–868.

Whitehead, D. S., 1966, "Effect of Mistuning on the Vibration of Turbomachines Blades Induced by Wakes," *Journal of Mechanical Engineering Science,* Vol. 8, No. 1, pp. 15–21.

A Reduced Order Approach for the Vibration of Mistuned Bladed Disk Assemblies

M.-T. Yang

J. H. Griffin

Department of Mechanical Engineering,
Carnegie Mellon University,
Pittsburgh, PA

A reduced order approach is introduced in this paper that can be used to predict the steady-state response of mistuned bladed disks. This approach takes results directly from a finite element analysis of a tuned system and, based on the assumption of rigid blade base motion, constructs a computationally efficient mistuned model with a reduced number of degrees of freedom. Based on a comparison of results predicted by different approaches, it is concluded that: The reduced order model displays structural fidelity comparable to that of a finite element model of the entire bladed disk system with significantly improved computational efficiency; and under certain circumstances both the finite element model and the reduced order model predict quite different response from simple spring-mass models.

1 Introduction

The resonant amplitudes of turbine blades tend to be sensitive to minor variations in the blade properties. It is realized that, because of the rotational periodicity of its geometry, a bladed disk usually has natural frequencies that are clustered in narrow ranges. When the natural frequencies of a system are close together, slight variations in the system's structural properties can cause large changes in its modes, and, consequently, its dynamic response. The sensitivity of a bladed disk's dynamic response to small variations in the frequencies of the blades is referred to in the literature as the *blade mistuning* problem and has been studied extensively; for example, refer to Dye and Henry (1969), Ewins (1988), Fabunmi (1980), Griffin and Hoosac (1984), or Ottarsson and Pierre (1993). It is important to understand mistuning since it can result in large blade-to-blade variations in the vibratory response and the high response blades can fail from high cycle fatigue.

Much of the work that has been done in mistuning utilizes spring-mass models to represent bladed disks in order to reduce the number of degrees of freedom and to make the problem computationally tractable; for examples, refer to the previously cited papers. The model's parameters, such as the mass and the spring constants, are chosen in an ad hoc manner and one must question the ability of such simple models to represent such complex systems accurately. While some attempt has been made to corroborate the accuracy of spring-mass models by comparing predictions with specific test data, for example Griffin (1988), such work is relatively scarce.

Efforts have been made to develop more structurally accurate models for bladed disks by using plate elements to represent the disk and beam elements to represent the blades; for examples refer to Kaza and Kielb (1984), and Rzadkowski's two papers (1994a, b). While there can be blade configurations for which the beam representation may be adequate, plate, thick shell, and even solid elements are often needed to represent modern low-aspect-ratio blades. The finite element method could be a possible choice to model a whole bladed disk accurately, but it is recognized that the time cost and the storage space required to run these programs would be prohibitively high. For example, one could imagine using the Monte-Carlo approach of Griffin and Hoosac (1984) with detailed finite element models of the entire mistuned bladed disk. Such an approach would involve the analysis of hundreds of mistuned disks in order to determine the statistical variations in the blades' vibratory response. Clearly, such computations are currently beyond the capabilities of even supercomputers and would be hardly suitable for use as a design tool. Furthermore, because of the extremely large number of degrees of freedom involved and the closeness of the natural frequencies, one must question whether such results would even be numerically accurate.[1]

The limitations associated with spring-mass and beam models and the direct finite element approach motivate us to consider the possibility of developing a new model for analyzing mistuned bladed disks. Our goal is to develop a methodology that will take the results directly from a finite element analysis of a tuned system and construct a computationally efficient mistuned model with a reduced number of degrees of freedom. The intent is that the approach will display structural fidelity comparable to a finite element model and computational efficiency more comparable to that of a spring-mass model.

2 Approach for Reducing the Number of Degrees of Freedom

In the study of the steady-state response of complex structures, one widely used analytical approach is the *receptance method* (Bishop and Johnson, 1960). The receptance method is based on the observation that the dynamic response of every substructure is determined by how it interacts with its environment at its boundaries. If the substructure interacts with its environment only at limited areas, it is convenient to express the degrees of freedom of the entire substructure in terms of the degrees of freedom of its interfaces. The benefit of this method is that when several substructures interact with each other, it is only necessary to solve for the degrees of freedom associated with the interfaces. Once the degrees of freedom of the interfaces are determined, the response of all substructures and, consequently, the whole structure may be calculated. To apply the receptance method to the mistuned bladed disk, it is

Contributed by the International Gas Turbine Institute and presented at the 40th International Gas Turbine and Aeroengine Congress and Exhibition, Houston, Texas, June 5–8, 1995. Manuscript received by the International Gas Turbine Institute March 31, 1995. Paper No. 95-GT-454. Associate Technical Editor: C. J. Russo.

[1] In contrast, the reduced order model uses finite element generated modes for a single cantilevered blade and for a tuned disk. The modes of the tuned disk can be calculated using a single disk segment with cyclic symmetric boundary conditions. Disk modes calculated in this manner do not exhibit numerical instabilities since for a specified cyclic constraint their natural frequencies are well separated.

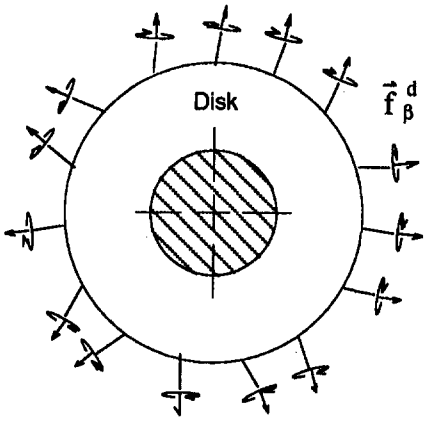

Fig. 1 Disk substructure

divided into two substructures—the disk[2] (Fig. 1) and the blades (Fig. 2). Modal analysis is then used to determine the substructures' behavior in terms of the degrees of freedom of the interfaces. A receptance approach was formulated for mistuned, shrouded bladed disks by Menq et al. (1986). They then specialized the formulation to the case of a tuned system and used it to solve for the vibratory response of a tuned shrouded stage in which the blade was represented using beam elements. In general, however, the direct receptance approach has two shortcomings:

1 The substructures' modes have to be free at the disk–blade interfaces in order to be admissible. This works reasonably well for the disk since the blades provide relatively little constraint at its rim and, consequently, only a few families of disk modes are required to represent its response. However, it is undesirable to use the free–free blade model. Because blades generally vibrate close to the clamped–free condition, a large number of the free–free modes are needed to achieve a good representation of its vibratory response.
2 A direct application of the receptance method results in a formulation with a reduced number of degrees of freedom. However, depending on the number of nodes at the blade interface, the number can still be quite large, especially if solid elements are used to model the blade's neck. Since it is undesirable to restrict the approach to blade models with only a few nodes at the disk–blade interface, the receptance method needs to be modified in order to make it even more efficient. This is done using the following simplifying assumption.

It is assumed that the disk–blade interfaces undergo rigid body type translations and rotations. The blade vibration is then determined as a combination of blade base motion and clamped–free blade modes. As will be shown, this approach results in a formulation that has a relatively small number of degrees of freedom (six times the number of blades) and is, consequently, computationally efficient. In addition, since the blade is represented in terms of its clamped–free modes, its response can be quickly characterized with only a few modes.

3 Mathematical Formulation

3.1 Disk Equation. If the disk substructure is subjected to a harmonic excitation, its response is given by the receptance matrix $\mathbf{R}$, i.e.,

$$\begin{Bmatrix} \vec{u}_\alpha^{\,d} \\ \vec{u}_\beta^{\,d} \end{Bmatrix} = \begin{bmatrix} \mathbf{R}_{\alpha,\alpha}^d \mathbf{R}_{\alpha,\beta}^d \\ \mathbf{R}_{\beta,\alpha}^d \mathbf{R}_{\beta,\beta}^d \end{bmatrix} \begin{Bmatrix} \vec{f}_\alpha^{\,d} \\ \vec{f}_\beta^{\,d} \end{Bmatrix} \tag{1}$$

[2] Note the cross-hatching in Fig. 1 indicates that in this model the disk is fully constrained at its bore.

where $\vec{u}^d$, $\vec{f}^{\,d}$, and $\mathbf{R}^d$ are the displacement, the external force, and the receptance associated with the disk. The subscript α denotes the group of nodes that do not interact with other substructures and the subscript β denotes the group of nodes that reside at the disk–blade interfaces. Since the only external forces on the disk are the interactive forces at the disk–blade interfaces

$$\vec{f}_\alpha^{\,d} = \vec{0} \tag{2}$$

Equations (1) and (2) imply that

$$\vec{u}_\beta^{\,d} = \mathbf{R}_{\beta,\beta}^d \vec{f}_\beta^{\,d} \tag{3}$$

To formulate the disk equation in a more reduced order form, i.e., a formulation with six degrees of freedom per interface, the following two relations are introduced:

$$\vec{u}_\beta^{\,d} \approx \mathbf{Q}_{\beta,o}^d \vec{u}_o^{\,d} \tag{4}$$

$$\vec{f}_o^{\,d} = \Sigma_{o,\beta}^d \vec{f}_\beta^{\,d} \tag{5}$$

where $\vec{u}_o^{\,d}$ is a vector whose components are the six equivalent rigid body-type motions of the disk at the interfaces and $\vec{f}_o^{\,d}$ is the resultant forces on the disk at the interfaces. $\Sigma_{o,\beta}^d$ is a matrix that effectively sums the various nodal forces to get the resultant forces and moments that act on the disk. $\mathbf{Q}_{\beta,o}^d$ is the transpose of $\Sigma_{o,\beta}^d$. The detailed derivations of these matrices are provided by Yang (1994). The inverse relations of equations (4) and (5) are

$$\vec{u}_o^{\,d} = \mathbf{Q}_{\beta,o}^{d+} \vec{u}_\beta^{\,d} \tag{6}$$

$$\vec{f}_\beta^{\,d} = \Sigma_{o,\beta}^{d+} \vec{f}_o^{\,d} \tag{7}$$

where $\mathbf{Q}_{\beta,o}^{d+}$ and $\Sigma_{o,\beta}^{d+}$ are the generalized inverses of the matrices $\mathbf{Q}_{\beta,o}^d$ and $\Sigma_{o,\beta}^d$. Their expressions are

$$\mathbf{Q}_{\beta,o}^{d+} = (\mathbf{Q}_{\beta,o}^{dT} \mathbf{Q}_{\beta,o}^d)^{-1} \mathbf{Q}_{\beta,o}^{dT} \tag{8}$$

$$\Sigma_{o,\beta}^{d+} = \Sigma_{o,\beta}^{dT} (\Sigma_{o,\beta}^d \Sigma_{o,\beta}^{dT})^{-1} \tag{9}$$

In essence, Eqs. (6) and (7) state that $\vec{u}_o^{\,d}$ is the least-squares fit of $\vec{u}_\beta^{\,d}$ and $\vec{f}_\beta^{\,d}$ is the non-self-equilibrated forces estimated from $\vec{f}_o^{\,d}$. There are many possible choices of the distributed force $\vec{f}_\beta^{\,d}$. The reason that only the non-self-equilibrated forces were used is that, because of *Saint Venant's Principle,* the self-equilibrated forces die off quickly away from the interfaces and their global effect on the system should be relatively small. Substituting Eqs. (6) and (7) into Eq. (3) results in the reduced order receptance formulation for the disk

$$\vec{u}_o^{\,d} = \mathbf{R}_{o,o}^d \vec{f}_o^{\,d} \tag{10}$$

where

$$\mathbf{R}_{o,o}^d = \mathbf{Q}_{\beta,o}^{d+} \mathbf{R}_{\beta,\beta}^d \Sigma_{o,\beta}^{d+} \tag{11}$$

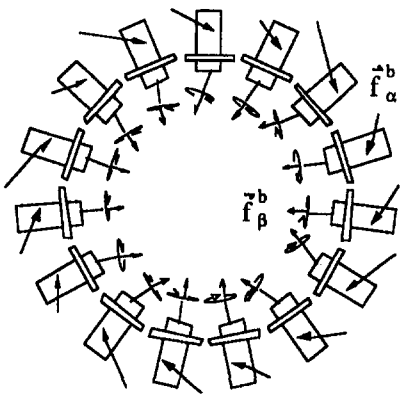

Fig. 2 Blade substructure

By applying standard modal analysis, the disk receptance $\mathbf{R}^d_{\beta,\beta}$ can be written as

$$\mathbf{R}^d_{\beta,\beta} = \sum_j \frac{\vec{\phi}^{\,d}_{j,\beta}\vec{\phi}^{\,dT}_{j,\beta}}{m^d_j(\omega^{d2}_j - \Omega^2 + 2i\Omega\omega^d_j\zeta^d_j)} \tag{12}$$

where Ω is the excitation frequency, $\vec{\phi}^{\,d}_j$ is the jth disk mode, and m^d_j, ζ^d_j, and ω^d_j are the modal mass, modal damping ratio, and natural frequency of the jth disk mode. Combining Eqs. (11) and (12), the reduced order disk receptance can be written as

$$\mathbf{R}^d_{o,o} = \sum_j \frac{\vec{\phi}^{\,d}_{j,o}\vec{\phi}^{\,dT}_{j,o}}{m^d_j(\omega^{d2}_j - \Omega^2 + 2i\Omega\omega^d_j\zeta^d_j)} \tag{13}$$

where $\vec{\phi}^{\,d}_{j,o}$, the jth reduced order disk modes, is written as

$$\vec{\phi}^{\,d}_{j,o} = \mathbf{Q}^{d+}_{\beta,o}\vec{\phi}^{\,d}_{j,\beta} \tag{14}$$

3.2 Blade Equation. Consider a single blade whose base is constrained to move in a plane undergoing small, harmonic translations and rotations. Let $\vec{u}^b_o$ be the six-degree-of-freedom displacement vector of the blade base and, again, denote the group of nodes that do not interact with the disk by the subscript α and the group of nodes that reside at the interface by β. The receptance equation for the blade can be written as

$$\vec{u}^b_\alpha - \mathbf{Q}^b_{\alpha,o}\vec{u}^b_o = \mathbf{R}^b_{\alpha,\alpha}(\vec{f}^{\,b}_\alpha + \Omega^2\mathbf{M}^b_{\alpha,\alpha}\mathbf{Q}^b_{\alpha,o}\vec{u}^b_o) \tag{15}$$

$$\vec{u}^b_\beta = \mathbf{Q}^b_{\beta,o}\vec{u}^b_o \tag{16}$$

where $\vec{u}^b$, $\vec{f}^{\,b}$, and $\mathbf{R}^b$ are the displacement, the external force, and the receptance associated with the blade. $\mathbf{M}^b_{\alpha,\alpha}$ is the blade mass matrix associated with the group-α nodes. $\mathbf{Q}^b_{\alpha,o}$ and $\mathbf{Q}^b_{\beta,o}$ are geometric functions such that $\mathbf{Q}^b_{\alpha,o}\vec{u}^b_o$ and $\mathbf{Q}^b_{\beta,o}\vec{u}^b_o$ describe the motion of the entire blade provided that the blade follows the motion of its base and does not deform. The term $\Omega^2\mathbf{M}^b_{\alpha,\alpha}\mathbf{Q}^b_{\alpha,o}\vec{u}^b_o$ in the right-hand side of Eq. (15) describes the inertial force introduced by the blade base motion. Rearranging Eq. (15), the motion of the group-α nodes $\vec{u}^b_\alpha$ can be expressed in terms of the external excitation force $\vec{f}^{\,b}_\alpha$ and the blade base motion $\vec{u}^b_o$, i.e.,

$$\vec{u}^b_\alpha = \mathbf{R}^b_{\alpha,\alpha}\vec{f}^{\,b}_\alpha + (\Omega^2\mathbf{R}^b_{\alpha,\alpha}\mathbf{M}^b_{\alpha,\alpha} + \mathbf{I})\mathbf{Q}^b_{\alpha,o}\vec{u}^b_o \tag{17}$$

From modal analysis, the receptance $\mathbf{R}^b_{\alpha,\alpha}$ can be written as

$$\mathbf{R}^b_{\alpha,\alpha} = \sum_j \frac{\vec{\phi}^{\,b}_{j,\alpha}\vec{\phi}^{\,bT}_{j,\alpha}}{m^b_j(\omega^{b2}_j - \Omega^2 + 2i\Omega\omega^b_j\zeta^b_j)} \tag{18}$$

where $\vec{\phi}^{\,b}_j$ is the jth mode for a blade clamped at its base, and m^b_j, ζ^b_j, and ω^b_j are the modal mass, modal damping ratio, and natural frequency of the jth blade mode.

The resultant force on the blade base, $\vec{f}^{\,b}_o$, is needed in order to assemble the entire system. To determine $\vec{f}^{\,b}_o$ consider the blade as an object that can move and deform in space. The forces acting on the blade are the excitation force $\vec{f}^{\,b}_\alpha$ on the airfoil and the interactive force $\vec{f}^{\,b}_o$ at the interface. Since linear and angular momentum have to be conserved, one can deduce that

$$\Sigma^b_o(-\Omega^2\mathbf{M}^b\vec{u}^b) = \Sigma^b_o\vec{f}^{\,b} = \Sigma^b_{o,\alpha}\vec{f}^{\,b}_\alpha + \vec{f}^{\,b}_o \tag{19}$$

where Σ^b_o is a geometric function that calculates the resultant force and moment about the blade base O. Substituting Eqs. (16) and (17) into Eq. (19), $\vec{f}^{\,b}_o$ can be expressed in terms of the blade base motion $\vec{u}^b_o$ and the external excitation $\vec{f}^{\,b}_\alpha$, i.e.,

$$\vec{f}^{\,b}_o = \mathbf{Z}^{\,b}_{o,o}\vec{u}^b_o + \mathbf{H}^b_{o,\alpha}\vec{f}^{\,b}_\alpha \tag{20}$$

where

$$\mathbf{Z}^{\,b}_{o,o} = -\Omega^2\Sigma^b_o\mathbf{M}^b\mathbf{Q}^b_o - \Omega^4\Sigma^b_{o,\alpha}\mathbf{M}^b_{\alpha,\alpha}\mathbf{R}^b_{\alpha,\alpha}\mathbf{M}^b_{\alpha,\alpha}\mathbf{Q}^b_{\alpha,o} \tag{21}$$

$$\mathbf{H}^b_{o,\alpha} = -\Omega^2\Sigma^b_{o,\alpha}\mathbf{M}^b_{\alpha,\alpha}\mathbf{R}^b_{\alpha,\alpha} - \Sigma^b_{o,\alpha} \tag{22}$$

Equation (20) describes the relation between the interactive force $\vec{f}^{\,b}_o$, the blade base motion $\vec{u}^b_o$, and the external excitation $\vec{f}^{\,b}_\alpha$ for a single blade. Clearly, similar equations apply for all blades. In fact, Eqs. (20), (21), and (22) describe the motions of all of the blades provided the vectors represent the collections of the corresponding vectors of individual blades and the matrices become block diagonal matrices with the corresponding matrices of individual blades at the diagonal.

3.3 Assembling the Substructures. Equations (10) and (20) describe the relations between the interactive forces and the motion of the interfaces for the disk and the blades, respectively. Since there are four unknown vectors, $\vec{u}^d_o$, $\vec{f}^{\,d}_o$, $\vec{u}^b_o$, and $\vec{f}^{\,b}_o$ to be determined, there need to be two additional constraints. The first is Newton's law of interactive forces, i.e.,

$$\vec{f}^{\,d}_o = -\vec{f}^{\,b}_o \tag{23}$$

The second one is Hooke's law, which provides a constitutive relation at the interfaces, i.e.,

$$\vec{f}^{\,d}_o = \mathbf{K}_{o,o}(\vec{u}^d_o - \vec{u}^b_o) \tag{24}$$

where $\mathbf{K}_{o,o}$ is the stiffness matrix associated with the attachment at the disk-blade interfaces.[3] By solving Eqs. (10), (20), (23), and (24) simultaneously, the four unknowns can be expressed in terms of the external excitation force $\vec{f}^{\,b}_\alpha$, i.e.,

$$\vec{u}^b_o = -(\mathbf{R}^d_{o,o} + \mathbf{K}^{-1}_{o,o})[\mathbf{I} + \mathbf{Z}^{\,b}_{o,o}(\mathbf{R}^d_{o,o} + \mathbf{K}^{-1}_{o,o})]^{-1}\mathbf{H}^b_{o,\alpha}\vec{f}^{\,b}_\alpha \tag{25}$$

$$\vec{f}^{\,b}_o = [\mathbf{I} + \mathbf{Z}^{\,b}_{o,o}(\mathbf{R}^d_{o,o} + \mathbf{K}^{-1}_{o,o})]^{-1}\mathbf{H}^b_{o,\alpha}\vec{f}^{\,b}_\alpha \tag{26}$$

$$\vec{u}^d_o = -\mathbf{R}^d_{o,o}[\mathbf{I} + \mathbf{Z}^{\,b}_{o,o}(\mathbf{R}^d_{o,o} + \mathbf{K}^{-1}_{o,o})]^{-1}\mathbf{H}^b_{o,\alpha}\vec{f}^{\,b}_\alpha \tag{27}$$

$$\vec{f}^{\,d}_o = -[\mathbf{I} + \mathbf{Z}^{\,b}_{o,o}(\mathbf{R}^d_{o,o} + \mathbf{K}^{-1}_{o,o})]^{-1}\mathbf{H}^b_{o,\alpha}\vec{f}^{\,b}_\alpha \tag{28}$$

The vibration of the blades can then be easily derived by substituting Eq. (25) into Eq. (17).

3.4 Remarks on the Mathematical Approach. There are several advantages of using the reduced order formulation (Eqs. (17) and (25)) to solve the blade mistuning problem:

1 The coefficient matrices $\mathbf{R}^d_{o,o}$, $\mathbf{Z}^{\,b}_{o,o}$, and $\mathbf{H}^b_{o,\alpha}$ are calculated from the substructures' modes. Since the frequency range is usually limited to a narrow range near a particular engine order crossing, only a few dominant modes need to be included in the calculation and, consequently, the computational cost is low.
2 For blade mistuning problems, the disk is treated as a cyclic symmetric structure. As a result, its modes can be calculated efficiently by applying cyclic symmetric boundary conditions on a disk segment corresponding to a single blade.
3 The most computationally intensive part of this approach lies in computing the inverse of the matrix $[\mathbf{I} + \mathbf{Z}^{\,b}_{o,o}(\mathbf{R}^d_{o,o} + \mathbf{K}^{-1}_{o,o})]$ in Eq. (25). This is a square matrix with a dimension equal to six times the number of the blades. In many problems the rigidity of the disk is such that only three degrees of freedom are needed to describe the blade's motion at its base, two rotations and a translation normal to the disk. In either case the number of degrees of freedom is orders of magnitude smaller than for a finite element model for an entire mistuned bladed disk.
4 The reduced order method is especially computationally efficient when running Monte Carlo simulations of blade mistuning since the disk's modes and the nominal blade's modes only need to be calculated once. The coefficient matrices associated with the blades ($\mathbf{Z}^{\,b}_{o,o}$ and $\mathbf{H}^b_{o,\alpha}$) are

[3] If the attachment is infinitely stiff, then Eq. (24) implies that the displacements in the blade and disk are equal, and, consequently, Eq. (24) becomes a continuity requirement.

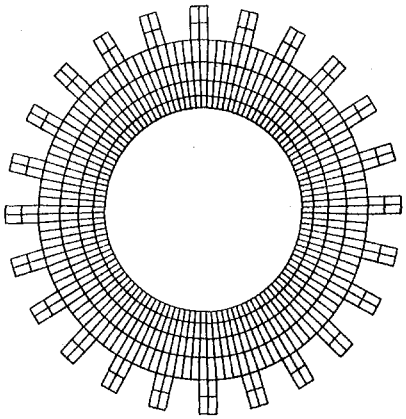

Fig. 3 Finite element model of test problem

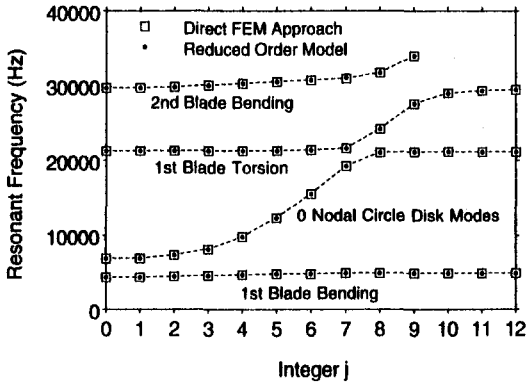

Fig. 5 Tuned system frequencies

calculated by changing the cantilever blade frequencies in the receptance calculation for each blade. On the other hand, a direct simulation using finite element models would require completely new calculations for each mistuned stage.

4 Comparison of Results

A computer code named LMCC (Linear Mistuning Computer Code) has been developed based on the reduced order approach. A test problem was developed that was sufficiently simple that a finite element solution of the complete bladed disk could be determined, Fig. 3. The test problem is analyzed using: (1) modal summation based on a direct finite element analysis, (2) LMCC, and (3) the computer code BLDVIB, which calculates the response of a mass-spring model of the bladed disk, Fig. 4. The development of BLDVIB is documented by Griffin and Hoosac (1984). The vibratory response of more than one hundred different resonant crossings have been examined of which the examples presented in this section are representative.

The geometry of the test problem was chosen so that the following requirements were satisfied:

1 The disk and the nominal blade have natural frequencies that are representative of a turbopump. Both the blades and disk are assumed to have material properties associated with a super nickel alloy.
2 The test problem represents a realistic three-dimensional structure with low aspect ratio, platelike blades. A test problem consisting of beam-type blades would not be appropriate since a goal is to check the validity of the simplifying constraint that the bases of the blades move as rigid bodies. The "blades" are 2.54 cm high by 1.27 cm wide and are 0.381 cm thick. The "disk" has inner and outer radii of 7.62 cm and 12.7 cm, and is 2.03 cm thick. The disk is constrained at its inner radius.
3 The entire system does not have too many degrees of freedom. As a result the entire bladed disk can be directly analyzed by finite elements without expending too much computational time or having numerical stability problems.

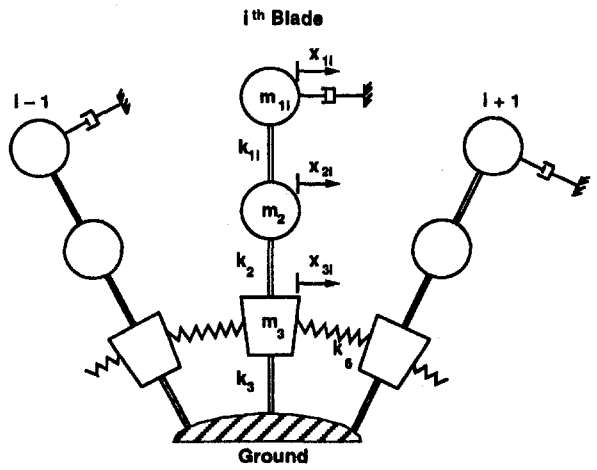

Fig. 4 Spring-mass model used by Hoosac and Griffin

There are still several parameters of the reduced order model that need to be determined before the algorithm can be implemented. The attachment stiffness matrix $\mathbf{K}_{o,o}$ is set to infinity to represent the simplified geometry of the test problem, i.e., the blade and disk nodes at the interface are identical. The other parameters that need to be determined are the damping ratios of the substructures' modes. It is assumed that both the blades and the disk have the same damping ratio. Its value is chosen so that the resonant response predicted by LMCC for the tuned system is the same as that predicted by the finite element method.

4.1 Tuned Response. First a comparison will be made between LMCC and the finite element method based on the natural frequencies of a tuned bladed disk. LMCC does not readily compute natural frequencies. However, if the system is lightly damped they can be inferred by the system's resonant frequencies since they can be calculated using LMCC's forced response algorithm. Figure 5 shows a comparison of natural frequencies. The integer "j" refers to the engine order of the excitation which excites the jth nodal diameter mode. The mode shapes can be described in terms of how the strain energy is primarily distributed in the system. For example, for j equal to one, the lowest frequency mode is essentially a first cantilevered bending mode, the second mode is a disk mode, and the third mode is essentially a blade torsional mode. The mode shapes are described in more detail by Yang (1994).

In comparing the frequencies that were calculated, it is clear that, overall, the two methods agree reasonably well. However, the reduced order approach tends to predict slightly higher frequencies, probably because of the assumption of rigid blade base motion, which tends to overconstrain the system. Note that the reduced order model represents the structure's response over a wide range of frequencies and nodal diameters. Results from the spring-mass model are not shown since the natural frequencies of the tuned system are part of the input parameters to the method and not calculated results.

The nominal properties of the spring-mass model were calculated using the approach given by Griffin (1988). Initially, the spring-mass model predicted a spurious second mode, which had to be eliminated by varying some of the parameters. Figure

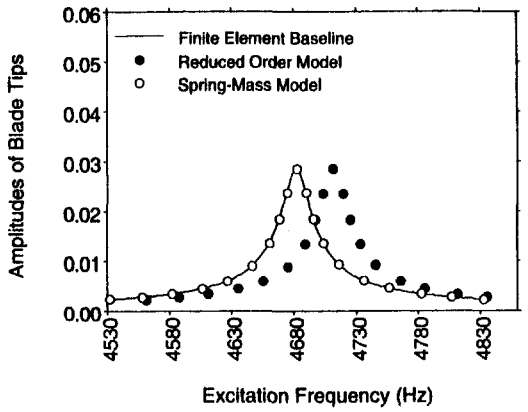

Fig. 6 Tuned response curves

6 shows representative response curves of the tuned system as predicted by the three different methods. For this particular case, the bladed disk is subjected to a fourth engine order excitation and the blades vibrate predominantly in their first bending mode. It appears that the three methods agree well with each other, although the response predicted by the reduced order model is at a slightly higher frequency.

4.2 Mistuned Response. The finite element model is mistuned by varying the elastic modulus of the material in each blade. This same effect is simulated in LMCC by changing the natural frequencies of each blade when calculating its receptance. In the case of BLDVIB the stiffness, k_{1i}, of each blade was altered to produce the same frequency distribution. Figure 7 shows representative response curves of the blades as predicted by the three methods. In this case the bladed disk is subjected to a fourth engine order excitation and the blades predominantly vibrate in their first bending mode. Clearly, the agreement of all three methods is quite good. In general, it was observed that the reduced order model and the spring-mass model give comparable results when the blades respond predominantly in their first bending modes.

Figure 8 depicts representative response curves when the blades are excited in their first torsional mode. It is clear from the plots that the reduced order model works much better than the spring-mass model in representing the response of the system. This case differs from the bending mode case in that the disk is effectively much stiffer. This stiffness effect is discernible from the fact that the percentage change in the frequencies of the four and five diameter modes of the tuned system (Fig. 5) is an order of magnitude smaller for the torsional modes, 0.075 percent, than for the first bending modes, 1.5 percent. For a stiff disk, the spring-mass model predicts that the blades essentially respond as isolated mistuned blades on a rigid foundation. However, both the finite element and LMCC results indicate that there is still significant interaction between the blades that results in complex system dynamics that is not captured by the simple spring-mass models.[4]

4.3 Limitations of the Reduced Order Model. Additional simulations were made with both thicker and thinner disks. In general, finite element and LMCC results agreed quite well except for one case when the thickness of the disk is halved. In the case in question, the tuned system exhibits frequency veering for the third and fourth modes when j is in the range of 2 to 6, Fig. 9. As a result, the bladed disk has two families of modes that are close together and that respond to the excitation. Because of the closeness of the frequencies, the resulting vibration contains significant amounts of both blade torsion and disk modes. Figure 10 shows the response curves predicted by the three different models. It appears that neither the reduced order model nor the spring-mass model successfully predicts the correct results. One problem with the LMCC model is that it does not predict the separation in the frequencies of the two families of modes very accurately when $\mathbf{K}_\infty$ is infinitely stiff, Fig. 9. This problem was addressed by introducing a finite value of the blade attachment stiffness matrix so that the frequency difference for the tuned system's response more closely approximates that of the finite element model, Fig. 9. Figure 10(d) shows the response curves predicted by the reduced order model when the attachment stiffness has been adjusted. The results from the reduced order model agree somewhat better with the finite element results, but not as well as in the other cases examined.

4.4 Execution Time Comparison. There are two principal advantages of the reduced order model approach that lead to increased computational efficiency. The first is that the num-

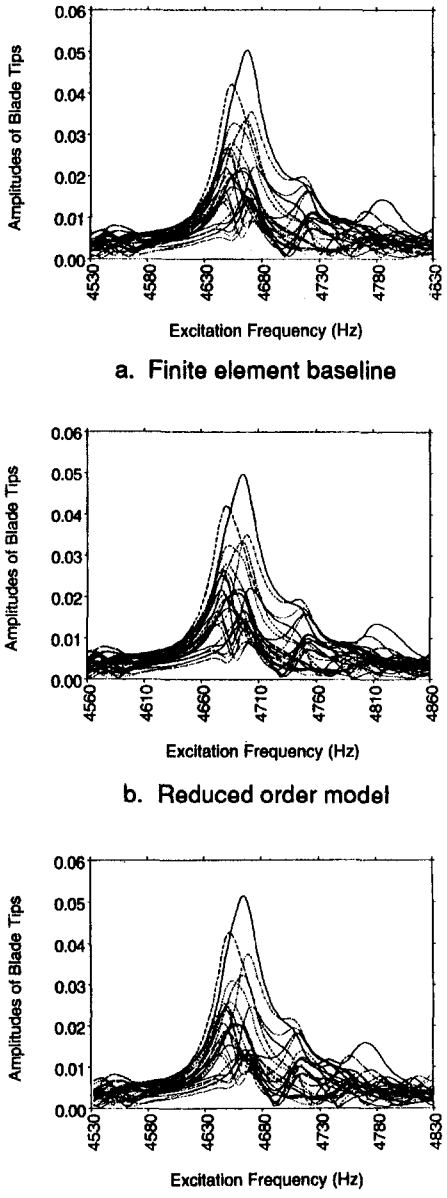

Fig. 7 Mistuned response curves for blades in first bending

[4] Simulations were also made of the response of the mistuned system in first bending with a stiffer disk. In this case all three methods predicted that the blades would respond as isolated blades. Again, the spring-mass model worked quite well for first bending.

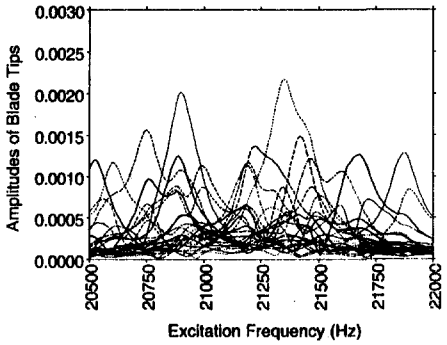

a. Finite element baseline

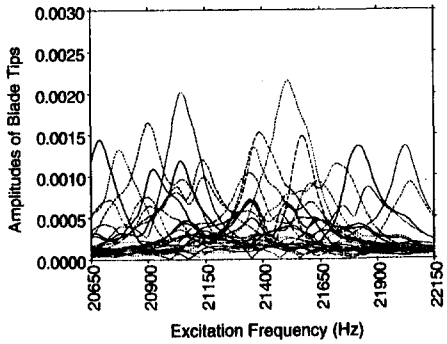

b. Reduced order model

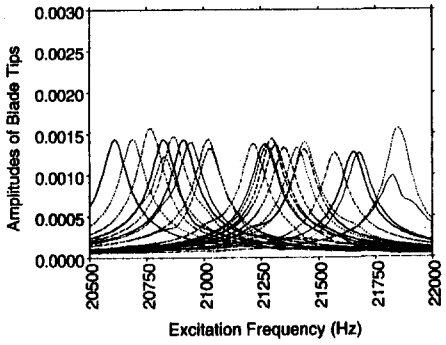

c. Spring-mass model

Fig. 8 Mistuned response curves for blades in first torsion

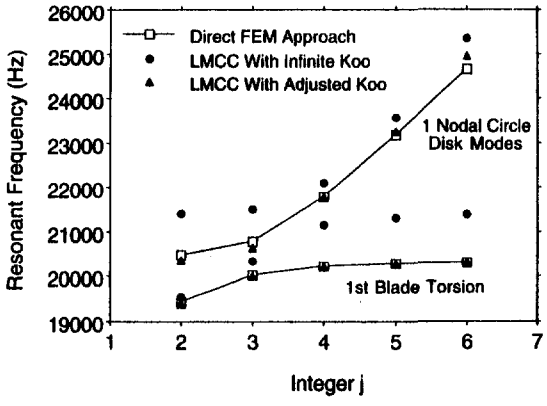

Fig. 9 Tuned system frequencies when the disk thickness is reduced by a factor of two

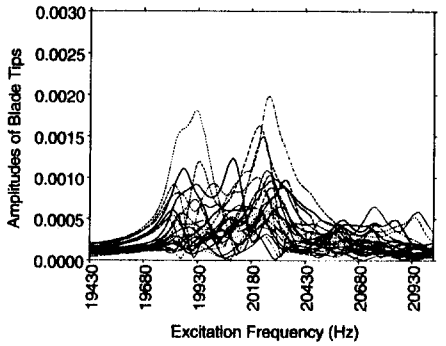

a. Finite element baseline

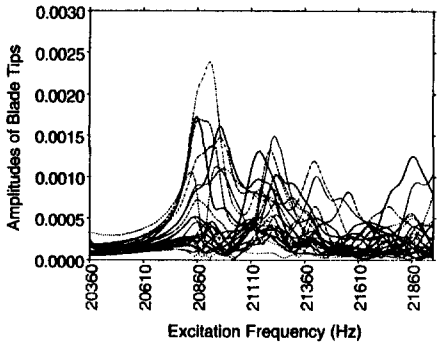

b. Reduced order moel

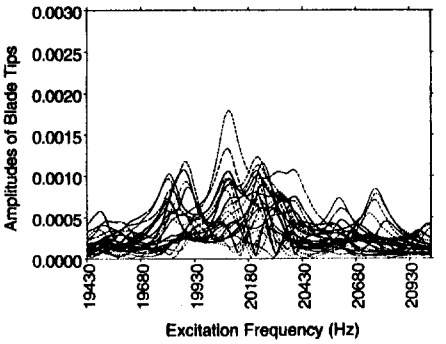

c. Spring-mass model

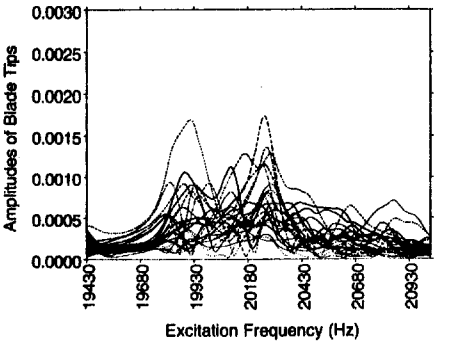

d. Reduced order model using adjusted K_{oo}

Fig. 10 Mistuned response curves for coupled disk and torsion modes

ber of degrees of freedom that must be determined (three or six per blade) in the forced response analysis is independent of the refinement of the finite element model of the blade and disk models that are used to calculate its input. Thus, LMCC is especially efficient when compared to a direct finite element solution of a bladed disk that has a large number of elements. Second, the most computationally expensive part of the calcula-

tion with LMCC is in calculating the modes of the clamped blade and tuned disk using finite elements. Since this needs to be done only once, LMCC becomes progressively more efficient when more mistuned bladed disks are simulated in a specific Monte Carlo analysis. An estimate of the relative run times of LMCC and a finite element analysis using modal superposition for a representative case indicates that LMCC would be two to three orders of magnitude faster for a one hundred bladed disk simulation.

Conclusions

A new reduced order approach has been developed for analyzing the forced response of mistuned bladed disks. The reduced order model is based on the idea of decomposing the bladed disk into substructures and representing the response in terms of the degrees of freedom associated with their interfaces. It further assumes that the blade bases undergo rigid body-type motions. The blade vibration may then be expressed as a combination of blade base motion and cantilever blade modes. This approach results in only six equivalent degrees of freedom, three rotations and three translations, at each disk–blade interface. Because of the reduction in the number of unknowns, the reduced order model provides a formulation which can be solved efficiently by computers. An advantage of this formulation is that the reduced order model is directly calculated from finite element analyses of a single clamped blade and a tuned disk without any additional ad hoc assumptions.

Comparisons of results from direct finite element simulations and the reduced order model indicate that, in general, the reduced order model agrees quite well with the finite element baseline. An exception to this agreement occurred when modes from two different families (one predominantly blade modes and one predominantly disk modes) were close in frequency and excited simultaneously. Comparisons were also made with results from spring-mass models. The spring-mass models predicted good results when the blades were responding predominantly in first bending, but did not predict the response when the disk was stiff and the blades were responding predominantly in first torsion.

Acknowledgments

This work was supported by NASA Contract NAS8-38348 under the direction of L. Kiefling and K. Mims of NASA Marshall Space Flight Center.

One of the authors, J. H. Griffin, wishes to acknowledge his discussions of reduced order models with Professor C. Pierre from the University of Michigan. Professor Pierre has ongoing research in the area of reduced order modeling of mistuned systems. His approach is similar in some respects to that reported here. At the time of the discussions in January 1993 both approaches had been extensively and independently formalized. As a result of their discussion, they agreed that they would acknowledge each other's work when publishing their results. The authors are not aware of any publication of Professor Pierre's work on reduced order modeling that has appeared in the open literature.

References

Bishop, R. E. D., and Johnson, D. C., 1960, *Mechanics of Vibration,* Cambridge University Press.

Dye, R. C. F., and Henry, T. A., 1969, "Vibration Amplitudes of Compressor Blades Resulting From Scatter in Blade Natural Frequencies," *Transactions of the ASME,* Vol. 91, pp. 182–188.

Ewins, D. J., 1988, "Structural Dynamic Characteristics of Bladed Assemblies," *ALGOR Manual on Aeroelasticity in Axial-Flow Turbomachines,* Vol. 2, Specialized Printing Service Ltd., Loughton, pp. 15-1 to 15-37.

Fabunmi, J. A., 1980, "Forced Vibrations of a Single Stage Axial Compressor Rotor," ASME JOURNAL OF ENGINEERING FOR POWER, Vol. 102, pp. 322–328.

Griffin, J. H., and Hoosac, T. M., 1984, "Model Development and Statistical Investigation of Turbine Blade Mistuning," ASME *Journal of Vibration, Acoustics, Stress, and Reliability in Design,* Vol. 106, pp. 204–210.

Griffin, J. H., 1988, "On Predicting the Resonant Response of Bladed Disk Assemblies," ASME JOURNAL OF ENGINEERING FOR GAS TURBINES AND POWER, Vol. 110, pp. 45–50.

Kaza, K. R. V., and Kielb, R. E., 1984, "Flutter of Turbofan Rotors With Mistuned Blades," *AIAA Journal,* Vol. 22, No. 11.

Menq, C. H., Griffin, J. H., and Bielak, J., 1986, "The Forced Response of Shrouded Fan Stages," ASME *Journal of Vibration, Acoustics, Stress, and Reliability in Design,* Vol. 108, No. 1, pp. 50–55.

Ottarsson, G., and Pierre, C., 1993, "A Transfer Matrix Approach to Vibration Localization in Mistuned Blade Assemblies," ASME Paper No. 93-GT-115.

Rzadkowski, R., 1994a, "The General Model of Free Vibrations of Mistuned Bladed Discs, Part I: Theory," *Journal of Sound and Vibration,* Vol. 173, No. 3, pp. 377–393.

Rzadkowski, R., 1994b, "The General Model of Free Vibrations of Mistuned Bladed Discs, Part II: Numerical Results," *Journal of Sound and Vibration,* Vol. 173, No. 3, pp. 395–413.

Wagner, L. F., 1993, "Vibration Analysis of Grouped Turbine Blades," Ph.D. Thesis, Carnegie Mellon University, Pittsburgh, PA.

Yang, M.-T., 1994, "A Reduced Order Approach for the Forced Vibration Analysis of Mistuned Bladed Disk Assemblies," Ph.D. Thesis, Carnegie Mellon University, Pittsburgh, PA.

P. E. Allaire

E. H. Maslen

D. W. Lewis

R. D. Flack

Department of Mechanical, Aerospace, and Nuclear Engineering, ROMAC Laboratories, University of Virginia, Charlottesville, VA 22903

Magnetic Thrust Bearing Operation and Industrial Pump Application

Magnetic bearings represent a new bearing technology, which has some advantages over conventional fluid film and rolling element bearings for some applications. The paper describes the basic concepts of magnetic thrust bearing operation involving the magnetic actuator, electronic controls, power amplifier, and sensor. The magnetic actuator is a magnetic circuit, which generates attractive forces. These support the rotating shaft. While it is often thought that magnetic bearings are highly nonlinear devices, this paper demonstrates that they are linear in both the perturbation flux and current when used in a double acting configuration. Electronic feedback controls are used to stabilize the bearing. Example design parameters are presented for an application to an industrial canned motor pump.

Introduction

The first magnetic bearing in the United States to support a high-speed centrifuge rotor axially was constructed at the University of Virginia in 1935–9 [1]. Other magnetic bearings were constructed in Germany at about the same time. As reliable electronic components became available at a reasonable cost, magnetic bearing applications were reported by academic researchers and industrial firms. Applications have extended to compressors, pumps, turboexpanders, gas turbines, turbomolecular vacuum pumps, x-ray tubes, and many others. A recent study of aircraft gas turbine engines indicates that the elimination of the oil supply and associated components with magnetic bearings could reduce the engine weight by approximately one fourth.

Canned pumps, used in chemical and petrochemical industrial plants, have a rotating component (motor rotor plus pump impeller) that is surrounded by the working fluid, such as water, oil, sulfuric acid, and hydrochloric acid. Figure 1 shows a diagram of an industrial canned motor pump supported in magnetic bearings [2]. The stator of the pump is canned, typically with stainless steel or similar metal, pierced only by the inlet and exit pipes. This exterior canning prevents the working fluid from leaking into the atmosphere and avoids the need for a mechanical seal placed at the point where the shaft exits from the pump to its drive motor. For many years, industrial firms have desired to find an alternative pump with no leakage and long life. One such alternative is the magnetic bearing supported canned pump.

While common canned pumps have offered a potential solution to the emission problem, their sleeve bearings are lubricated with the process fluids, which normally are poor lubricants. As a result, the bearings often wear or overheat and fail. A major chemical company found that the average life of existing canned pumps for a specific application was 11 months in their chemical plants.

In addition to avoiding leakage and increased life, magnetic bearings offer further benefits of diagnostic capability and vibration control. Pump vibration amplitude is automatically monitored by the bearing sensors. Also, the bearing coil currents can be used to continuously monitor pump forces and to determine when problems have occurred.

To evaluate industrial performance, two pumps were retrofitted with magnetic bearings. The first pump was a laboratory prototype [2–4] and the second is currently in field testing in an industrial chemical plant [3].

Recently, magnetic bearings have begun to be employed in pumps for power plant applications. A 600 hp multistage boiler feedpump supported in magnetic bearings has been installed in the Greenridge plant of the New York State Electric & Gas Company [5–6].

A magnetic bearing system consists of four basic components: (1) magnetic actuator, (2) electronic control, (3) power amplifier, and (4) shaft position sensor. In many ways, magnetic bearing components resemble electric motors. The basic magnetic actuator is constructed of magnetic material electromagnetically activated by a coil of wire. As shown in Fig. 2, the stator component is normally composed of horseshoe-shaped magnets and the rotor component is a piece of magnetic material to complete the magnetic path. An air gap separates the nonmoving and moving parts of the bearing.

To keep the rotor from contacting the stator, a position sensor signal is used as input for an electronic control circuit to adjust the coil currents. If the rotor is too close to the stator, the coil current is reduced. Alternatively, if the rotor is too far away from the stator, the coil current is increased.

It is commonly thought that magnetic bearings are inherently nonlinear devices, where the force is proportional to the square of the magnetic flux density or coil current and inversely proportional to the air gap. However, when used in the typical double acting configuration common in industrial applications, they become linear in the perturbation (control) flux density and linear in the perturbation current rather than nonlinear.

Basic Actuator Theory

Initial design of magnetic bearings is performed using a simple magnetic circuit analysis (model) [7, 8]. The theoretical model of the thrust bearing used in this article employs this model of the thrust or radial bearing to illustrate the principles involved in magnetic bearing design. It is essentially a one-dimensional flux model taken along the centerline of the magnetic material and in the air gaps. This is then verified with a magnetic finite element analysis if necessary. Finally, test measurements are made on the actual bearing to verify the load capacity, etc.

Contributed by the International Gas Turbine Institute and presented at the 39th International Gas Turbine and Aeroengine Congress and Exposition, The Hague, The Netherlands, June 13–16, 1994. Manuscript received by the International Gas Turbine Institute February 4, 1994. Paper No. 94-GT-38. Associate Technical Editor: E. M. Greitzer.

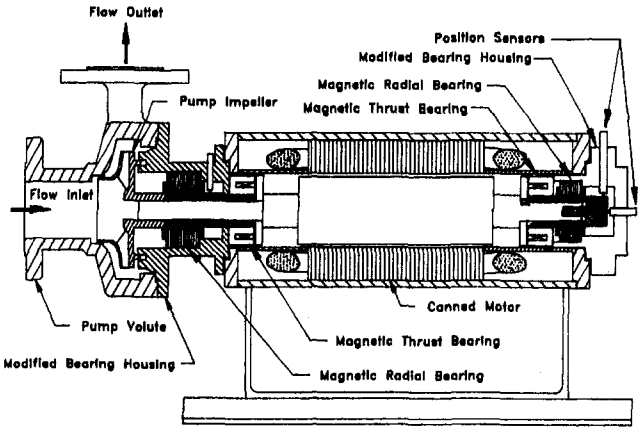

Fig. 1 Canned pump retrofitted with magnetic bearings

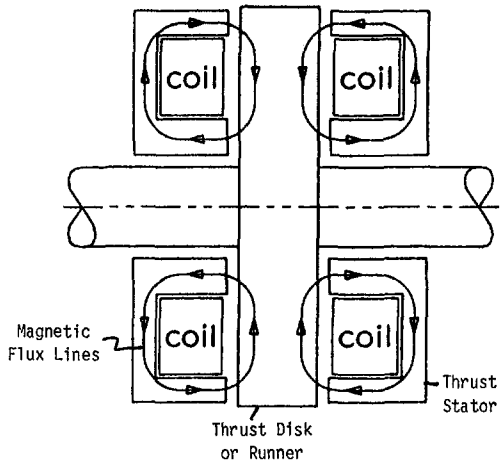

Fig. 2 Basic double-acting magnetic actuator geometry

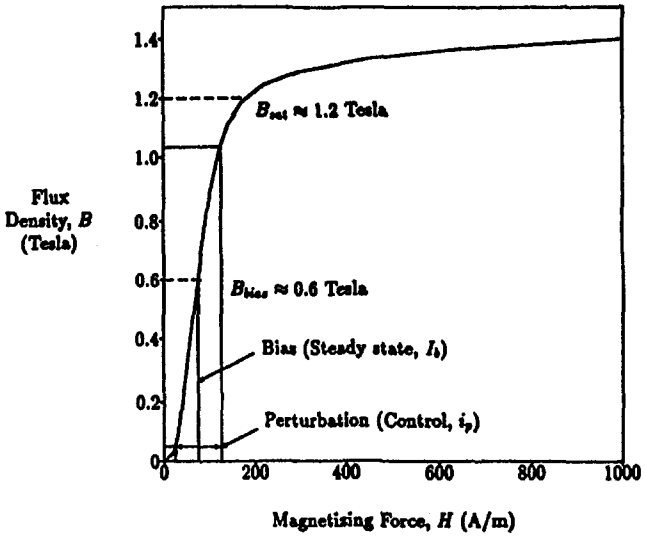

Fig. 3 Magnetic flux density B versus magnetic field intensity H for silicon iron

Several assumptions are made in the following: (1) Flux levels are always below saturation level; (2) shaft motions are small compared to the steady-state air gap dimension; (3) the flux distribution is relatively uniform in stator cross sections; and (4) leakage is small. In actual magnetic bearing analysis, some or all of the above assumptions may be violated by a particular bearing design. This does not mean that the bearing will not operate, but it does mean that a more complex finite element analysis must be carried out.

The magnetic part of the circuit, illustrated in Fig. 2, is constructed of ordinary magnetic material such as silicon steel or higher saturation level magnetic materials such as Vanadium Permendur. The air gap has thickness g and area A_g.

Magnetic flux is produced in each horseshoe-shaped section of the actuator by a coil of N turns of wire with a current i flowing through it. A power amplifier produces the desired current in the coil. The flux path of length L goes through the horseshoe, through the air gaps at the end of each pole face of the horseshoe magnet, and through the rotor. The magnetic field intensity H induced by N wires carrying current i wrapped around a closed magnetic path of length L is given by $H = Ni/L$. The quantity Ni is called the magnetomotive force MMF.

The magnetic flux ϕ in the circuit equals the flux density B times the pole face area A_g, which is also the area of one air gap in the magnetic circuit. In magnetic circuits, most of the magnetic resistance (called the reluctance) resides in the air gaps. Air and other nonferrous materials have nearly the same magnetic properties as free space. The flux density in such materials is related to the magnetic field intensity by the linear relation (valid for many nonmagnetic materials) $B = \mu_0 H$ where μ_0 is the permeability of free space (air).

Magnetic bearings are normally constructed of a ferrous magnetic material and the air gaps made as small as practical to minimize the required magnetomotive force. Nearly always, the magnetic flux in magnetic bearings is determined by the air gap and the reluctance of the magnet iron can be neglected compared to that in the air gap.

The typical ferrous magnetic material employed in a magnetic actuator has a magnetization curve, plotted as B versus H, as illustrated in Fig. 3. The B–H curve is roughly linear for much of the range of B. The slope of this curve in the linear range is called the permeability of the material, μ. Often, this is expressed as the product of the permeability of free space, μ_0, times a relative permeability for the material, μ_r. The B–H relation is $B = \mu_0 \mu_r H$. Silicon steel (often called soft magnet iron) has a relative permeability of 1000 to 5000.

At higher values of B, the B–H curve is no longer linear. The level of flux, which can be produced in the magnetic material as the magnetic field intensity H increases, approaches a point where the B–H curve deviates significantly from the linear

Nomenclature

A = air gap area, m^2
B = flux density, Tesla = Wb/m^2
D = diameter, m
F = force, N
g = length of air gap, m
G = transfer function
H = magnetic field intensity, amp-turns/m
i = current, amps
K_i = current gain, N/amp
K_x = position stiffness, N/m
L = length of magnetic circuit, m
M = mass, kg
MMF = magnetomotive force, amp-turns
N = number of turns, turns
V = voltage, volts
ϵ = position, m
e = fringing and leakage derating factor
μ = permeability, H/m
ϕ = magnetic flux, Wb = N-m/amp
ω = frequency, rad/s
τ = time constant

value. The knee of the curve is called the saturation point. For silicon steel, this typically occurs in the range of 1.5 to 1.7 Tesla (1 Tesla = 10,000 Gauss). With the advanced magnetic materials such as Vanadium Permendur, this value may be as high as 2.2 to 2.4 Tesla. When the bearing operation drives the material to that point, it acts as if it has an air core. The required magnetomotive force is then quite high and not economical.

The flux density B in each air gap is given by $B = \mu_0 Ni/(2g)$ as induced by N total turns of wire encircling the magnetic circuit. The force F which attracts the rotor to the stator and permits the actuator to act as a bearing, is given by

$$F = \frac{B^2 A_g}{\mu_0} = \epsilon \frac{\mu_0 N^2 i^2 A_g}{4g^2} \tag{1}$$

The force is proportional to the square of Ni and inversely proportional to the square of gap g. It would appear from this result that magnetic bearings are very nonlinear devices. However, a closer examination of a double-acting bearing later in this section reveals a different result.

Magnetic circuits have effects such as fringing and leakage that are modeled with a derating factor ϵ. The derating factor is usually taken as 0.9 for thrust bearings. A detailed finite element magnetic field solution will give more accurate results, but the derating factor is sufficient for the basic magnetic circuit analysis presented here.

Actual operation of the magnetic bearing involves superposition of two fluxes: a bias flux and a perturbation (control) flux $B = B_b + B_p$. The bias flux density B_b is a steady-state flux level induced in the air gap by a bias i_b (steady-state) current in the coil. The perturbation flux density B_p is a time-varying control flux density developed by the perturbation (control) current i_p in the coil. The total current in the coils is $i = i_b + i_p$. The two respective fluxes are

$$B_b = \frac{\mu_0 N i_b}{2g}; \quad B_p = \frac{\mu_0 N i_p}{2g} \tag{2}$$

Usually, the bias flux level B_b is set at about one half of the magnetic saturation level shown in Fig. 3, allowing for relatively large perturbation flux levels up and down from the bias level. The associated force expression of Eq. (1) becomes

$$F = \frac{A_g (B_b + B_p)^2}{\mu_0} \tag{3}$$

Electromagnetic forces are only attractive so actuators must be placed on both sides of the moving components in a double-acting arrangement, as illustrated in Fig. 2. The net force F_N is given by

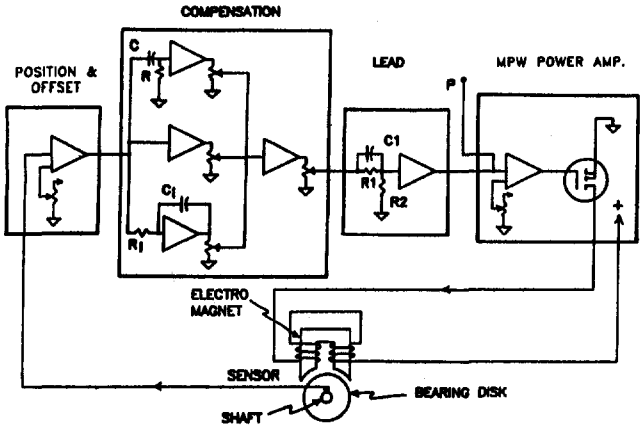

Fig. 4 Electronic feedback control circuit diagram for canned pump application

$$F_N = F_2 - F_1 = \left[\frac{A_g B^2}{\mu_0}\right]_2 - \left[\frac{A_g B^2}{\mu_0}\right]_1 \tag{4}$$

Assuming that the gap areas are the same in both actuators and substituting in Eq. (4) gives

$$F_N = \frac{A_g}{\mu_0}[(B_b + B_p)^2 - (B_b - B_p)^2] \tag{5}$$

The two sides operate off of a common control so that a positive perturbation flux (or associated perturbation current) on one side is exactly the negative of the other side. This expression can be expanded and then simplified to give

$$F_N = \frac{4A_g B_b B_p}{\mu_0} = \epsilon \frac{\mu_0 A_g N^2 i_b i_p}{g^2} \tag{6}$$

In this derivation, it is assumed that the gap is large compared to the amplitude of thrust collar motion; usually the gap is an order of magnitude larger.

This is the net force expression in terms of either flux or magnetomotive force. The bias flux density B_b is constant, so the net force F_N is directly proportional to the perturbation (control) flux B_p or the perturbation (control) current i_p.

The maximum force capability of magnetic bearings occurs when the magnetic material is saturated and will not develop any more flux. Then the maximum force of the double-acting magnetic bearing will be obtained with zero flux on one side and maximum flux on the other side. The maximum force expression becomes

$$F_{\max} = \frac{B_{\text{sat}}^2 A_g}{\mu_0} \tag{7}$$

This is the force limit on magnetic bearings. Magnetic bearings will not produce force beyond this level without a very large magnetomotive force to drive the flux level higher.

Magnetic bearings have a backup bearing system, which acts when the maximum force limit is exceeded. Typically, the backup bearing clearance is chosen as one half of the magnetic bearing geometric clearance. More restrictive maximum force limits may arise from inadequate power amplifier response rate, as discussed later in this article.

Magnetic actuator forces change with both current and air gap thickness [7]. The current gain K_i (change in magnetic force due to a change in coil current) is the more important factor for magnetic bearings. Alternatively, K_x is called the position stiffness (the change in force due to a change in air gap thickness) and is less important.

The current gain within the linear flux range, for all four air gaps in a double-acting bearing, is

$$K_i = \frac{\partial F_N}{\partial i_p} = \epsilon \frac{\mu_0 A_g N^2 i_b}{g_0^2} \tag{8}$$

The current gain is positive for a magnetic bearing. The second term on the right side of Eq. (8), the linearized expression for the current gain, is independent of the perturbation current but linearly related to the bias current. Thus the magnetic actuator should not be designed with a very low bias current to avoid poor response when a change in force is required. If i_b is one half of the saturation value, the dynamic range of the actuator is a maximum. When the total current on the unloaded side of the bearing is zero ($i_b - i_p = 0$), that side of the bearing is turned off; at the same time the loaded side of the bearing is approaching saturation.

The next parameter is the position stiffness. The gap thicknesses on either side of the bearing may be written as $g_1 = g_0 + x$ and $g_2 = g_0 - x$. The steady-state gap thickness is g_0 and the rotor position is x, measured from the centered position.

The position stiffness, for all four air gaps in a double acting bearing, is

$$K_x = -\frac{\partial F_N}{\partial x} = -\epsilon \frac{\mu_0 A_g N^2 i_b^2}{g_0^3} \tag{9}$$

The position stiffness is negative. As the moving component moves closer to one side, the force increases tending to pull it further in that same direction, unlike a mechanical spring, which tends to return it to the center.

Since the shaft position change x is typically small compared to the gap dimension g, the linearized expression given on right of Eq. (9) is valid over the range of operation of most magnetic bearings. With these two parameters, the net force is given by

$$F_N = K_i i_p - K_x x \tag{10}$$

The next section discusses the control circuit, which adjusts the current term in this equation.

The rate at which the bearing must change force, called the force slew rate, depends upon the rate of change of applied forces on the rotor as must be determined in the rotor/bearing dynamic design process. The force slew rate is equal to the net steady state force times the frequency of the applied force. The required time rate of change of current, known as the current slew rate, to produce this rate of change of force is

$$\tau_i = \frac{\tau_f}{K_i} = \frac{F_s \omega}{K_i} \tag{11}$$

Since this required current slew rate is inversely proportional to the current gain, a magnetic bearing with low K_i must have a high voltage power supply to drive it at a high current slew rate.

Sensors, Controllers, and Power Amplifiers

The electronic circuit that controls the current in the stator coils has three components: sensor, controller, and power amplifier [8]. It determines coil current in the actuator based upon the rotor (either thrust disk or radial shaft disk) position. The general equation (employing Laplace transforms where s is the complex frequency) for the control circuit is $i_p(s) = G(s)x(s)$ where the overall controller transfer function is $G(s)$. If there is no feedback controller employed, the negative position stiffness K_x of the actuator from Eq. (9), shows that the actuator is unstable. The primary purpose of the feedback control is to stabilize the rotor and keep it centered.

Position sensors are used to monitor rotor position continuously. Most commonly, eddy current sensors of construction similar to the bearings themselves are employed. The sensor has a small output voltage proportional to the shaft position. The equation is $V_s(s) = K_s x(s)$ where K_s is the sensor gain. There is a high frequency rolloff in the sensor amplifier so the transfer function representing the sensor system is

$$\frac{V_s(s)}{x(s)} = \frac{K_s}{1 + \tau_s s} \tag{12}$$

where the denominator terms indicate the rolloff time constant times the frequency.

The transfer function from the controller output voltage to the sensor output voltage is

$$\frac{V_c(s)}{V_s(s)} = G_c(s) \tag{13}$$

Figure 3 shows an example control circuit diagram. The basic control algorithm for magnetic bearings is a PID (proportional-integral-derivative) control written as

$$G_c(s) = \frac{K_p + K_{ic}/s + K_d s}{1 + b_{c1} s + b_{c2} s^2} \tag{14}$$

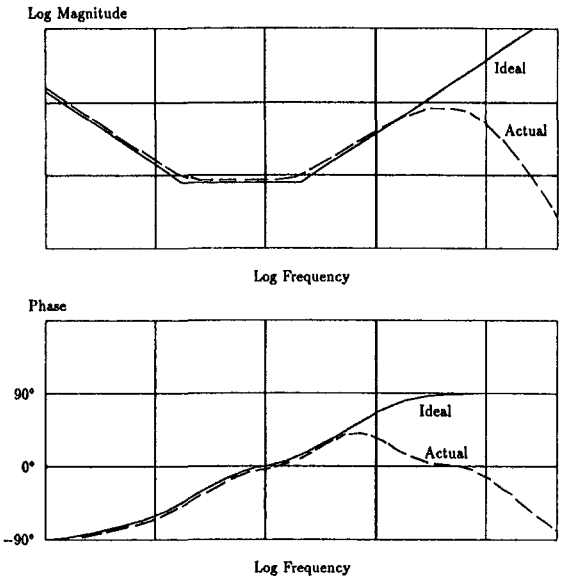

Fig. 5 Magnitude and phase diagram of ideal and actual PID controller

where K_p is the proportional gain constant (similar to a stiffness term), K_{ic} is the integral gain constant (associated with low frequency centering of the shaft), and K_d is the derivative gain constant (similar to a damping term). More details of this type of controller are given in [7, 8] and by other authors in [9, 10].

If the shaft is off center due to some static force acting on it, such a gravity sag, the control loop keeps on increasing the magnetic force to return it to the desired position. At low frequency, the PID phase lag is 90 deg. At high frequency, the PID phase lead is 90 deg as needed to stabilize the magnetic bearing-control loop. Figure 5 shows a plot of the ideal PID controller amplitude and phase angle versus frequency. The frequency indicated is the vibration frequency of some excitation rather than the shaft rotating frequency.

It is impossible to construct an electronic circuit (PID) with infinite gain at infinite frequency. There is always some rolloff at high frequency as illustrated in Fig. 4. Typically, this may be modeled as some second-order denominator term in the Eq. (14), where b_{c1} and b_{c2} are constants determined from the controller circuit design. Generally, this high frequency rolloff is placed so that the magnetic bearing frequencies that need to be controlled, such as machine operating speed, are below the rolloff frequency but higher frequencies, such as high shaft natural frequencies, are not controlled. In the intermediate frequency range, problems can arise that must be dealt with by more advanced controls techniques.

The output from the control circuit is typically a small voltage proportional to the desired current required for the bearing coils. The current is usually rather large, on the order of amps, so a power amplifier (and possibly a preamplifier) is required for each bearing coil. The transfer function of the amplifier is

$$\frac{i_p(s)}{V_c(s)} = \frac{K_a}{1 + \tau_a s} \tag{15}$$

where K_a is the amplifier gain and τ_a is the time constant of the amplifier high frequency roll off characteristic. Usually, there will be one amplifier per coil (or per quadrant in a radial bearing) in the magnetic actuator.

The overall transfer function for the sensor, controller, and power amplifier is

$$\frac{i_p(s)}{x(s)} = \frac{i_p(s)}{V_c(s)} \frac{V_c(s)}{V_s(s)} \frac{V_s(s)}{x(s)} \tag{16}$$

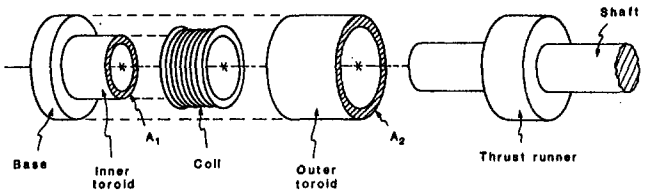

Fig. 6 Exploded view of single-acting magnetic thrust bearing

and the resulting transfer function is

$$G(s) = \frac{K_s}{1 + \tau_s s} \frac{K_p + K_i/s + K_d s}{1 + b_{c1}s + b_{c2}s^2} \frac{K_a}{1 + \tau_a s} \tag{17}$$

While this is a typical magnetic bearing control circuit design, there are many possible variations. More advanced control systems are also employed using state space methods. The following net force expression, from Eq. (10), governs the bearing static and dynamic operation

$$F_N = K_i G(s) X(s) + K_x X(s) \tag{18}$$

Industrial Canned Motor Pump Application

As indicated in the introduction, two pumps were constructed. The first pump was a conventional centrifugal overhung single-stage 20 Hp pump with a design flow rate of 300 gal/min in water at 120 ft of head. Figure 1 shows a diagram of the magnetic bearing supported pump. The overall length of the pump was 21 in. and the motor diameter was 8 in. Both the stator and rotor of the three-phase synchronous motor were canned with stainless steel cans. A return flow line cooled the motor.

New bearing support sections were constructed to accommodate the magnetic bearings and sensors [2]. Two single-acting thrust bearings, one on each end of the motor rotor, and two radial magnetic bearings were placed in approximately the same locations as the original sleeve bearings. Five standard industrial eddy current position sensors were used, one for each coordinate axis, to provide the feedback signal for the magnetic bearings.

Thrust Bearings

The basic thrust bearing geometry for the canned pump in Fig. 6 consists of an electromagnetic stator and a thrust collar placed on the rotor. The stator and rotor are separated by a nonmagnetic gap to allow for rotation without physical contact. The stator is composed of an inner and outer toroid connected by a common base. The inner and outer toroids and base may be constructed of one piece or separate pieces assembled together. The thrust collar is attached to the shaft. In many applications, the thrust bearing is double-acting with the thrust collar between two stators.

A coil of wire between the inner and outer toroids produces the magnetomotive force to drive the bearing. As an example, consider the magnetic thrust bearing employed in the prototype industrial canned pump as shown in Fig. 6: $N = 576$ turns and $i = 1.5$ amps where #28 wire was employed. This produces an magnetomotive force of MMF $= Ni = 864$ amp-turns.

The magnetic flux path goes through the outer stator toroid, through the outer air gap, through the thrust collar, back through the inner air gap, and returns to the stator inner toroid. The thrust face outer and inner gap areas are given by:

$$A_{go} = \frac{\pi}{4}(D_4^2 - D_3^2) \quad A_{gi} = \frac{\pi}{4}(D_2^2 - D_1^2) \tag{19}$$

where the diameters for the canned pump application are, shown in Fig. 7, as

$D_1 = 41.1$ mm (1.62 in.) $D_2 = 67.3$ mm (2.65 in.)

$D_3 = 67.3$ mm (2.96 in.) $D_4 = 92.1$ mm (3.62 in.)

In this design, the cross-sectional area of the flux path is made the same, as closely as possible, over the length of the magnetic circuit. The outer and inner toroid areas are equal, with value

$$A_{go} = A_{gi} = A_g = 2.230 \text{ mm}^2 \ (3.45 \text{ in.}^2)$$

The other thrust bearing dimensions are

$L = 40.4$ mm (1.59 in.) = Axial length

$L_t = 29.8$ mm (1.17 in.) = Coil axial length

$L_c = 10.7$ mm (0.42 in.) = Thrust collar length

The flux path cross-sectional area in the end and thrust disk is close to that in the toroids.

The air gap g was chosen to be 0.508 mm (0.020 in.) for the canned motor pump thrust bearing. The flux density is $B = 1.068$ Tesla (10,680 Gauss) at the nominal operating point. At this point, the flux level should be compared to the saturation flux of the material. In the case of the canned motor pump example, the magnetic bearings were constructed from silicon steel. For this material, the saturation level is 1.2 to 1.6 Tesla or well above the operating flux level.

The nominal operating ideal force that can be taken by the thrust bearing is calculated from Eq. (1) as 2020 N (456 lb). This assumes that only one side of the double-acting thrust bearing is on while the other side is off. Using a typical thrust bearing derating factor of 0.9, the operating actual force is $F_N = 1818$ N (410 lb). If the current capability of the coil and associated electronic supply system are sufficient to push the flux density up to 1.6 Tesla, the peak force that can be taken by this single-sided thrust bearing is $F_{max} = 2720$ N (612 lb).

The current gain formula is given by Eq. (8). For the canned motor pump the numerical value is $K_i = 2{,}430$ N/amp (544 lb/amp). The position stiffness is obtained from Eq. (9). Again taking the canned motor pump example, $K_x = -7.15 \times 10^6$ N/m (−41,200 lb/in.). These parameters are then employed in designing the control system. Length limitations do not permit a full discussion of the controller design for the pump application.

Conclusions

The principles of operation of magnetic thrust bearings have been presented. Some new insights have been gained as to the linearity of double acting thrust bearings. The successful

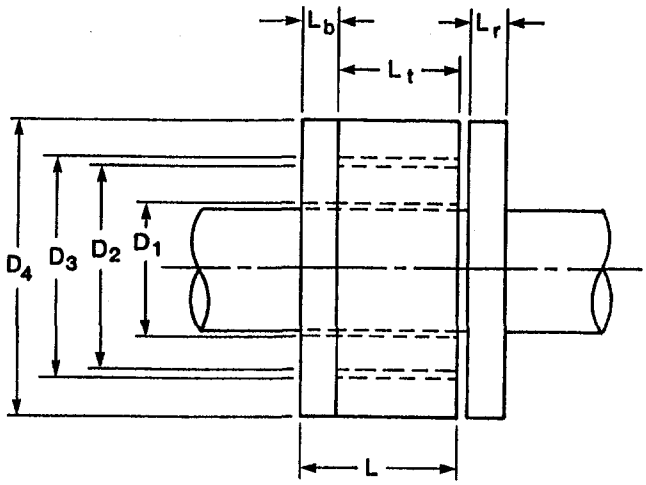

Fig. 7 Diameters and lengths of thrust bearing

application of magnetic thrust bearings in an industrial canned motor pump has been presented.

Acknowledgments

The authors would like to thank the Virginia Center for Innovative Technology, Kingsbury Inc., Exxon Chemical Co., Goulds Pump Co., NASA Lewis Research Center, and the U.S. Army Research Center for partial funding of the work reported in this article.

References

1 Allaire, P. E., Humphris, R. R., and Lewis, D. W., "Professor Jesse W. Beams and The First Practical Magnetic Suspension," *Proc. International Symposium on Magnetic Suspension Technology,* NASA Conference Publication 3152, Langley Research Center, Aug. 19–23, 1991.

2 Allaire, P., Imlach, J., McDonald, J., Humphris, R., Lewis, D., Banerjee, B., Blair, B., Claydon, J., and Flack, R., "Design, Construction and Test of a Magnetic Bearing in an Industrial Canned Motor Pump," *Proc. Texas A&M Pump Symposium,* Houston, TX, May 1989.

3 Imlach, J., Humphris, R., Blair, B., Allaire, P., and Lewis, D., "Testing of a Magnetic Bearing Equipped Canned Motor Pump for Installation in the Field," *Proc. Second International Symposium on Magnetic Bearings,* Tokyo, Japan, July 1990, pp. 39–46.

4 Imlach, J., Blair, B. J., and Allaire, P. E., "Measured and Predicted Force and Stiffness Characteristics of Industrial Magnetic Bearings," ASME *Journal of Tribology,* Vol. 113, Oct. 1991, pp. 784–788.

5 Cooper, P., et al., "A Boiler Feed Pump Employing Active Magnetic Bearings," in: *Advances in Steam Turbine Technology for Power Generation,* ASME, Oct. 1990, pp. 203–209.

6 Cooper, P., and Jones, G., "Operating Experience, Including Transient Response, of a Magnetic-Bearing-Equipped Boiler Feed Pump," *Proceedings of MAG '93—Magnetic Bearings, Magnetic Drives and Dry Gas Seals,* P. Allaire, ed., July 29–31, 1993, Alexandria Virginia, published by Technomic Publishing Co., pp. 19–28.

7 Allaire, P. E., Mikula, A., Banerjee, A., and Lewis, D. W., "Design and Test of a Magnetic Thrust Bearing," *Journal of the Franklin Institute,* Vol. 326, No. 6, Dec. 1989.

8 Humphris, R. R., Kelm, R. D., Lewis, D. W., and Allaire, P. E., "Effect of Control Algorithms on Magnetic Bearing Properties," ASME JOURNAL OF ENGINEERING FOR GAS TURBINES AND POWER, Vol. 108, Oct. 1986, pp. 624–632.

9 Ulbrich, H., "Elements of Active Vibration Control for Rotating Machinery," NASA Technical Memorandum 10 23 68, 1990.

10 Ulbrich, H., "Active Bearing Support for Rotating Machine Elements," *Journal of Machine Vibration,* Springer Verlag, 1992, pp. 2–12.

Design and Analysis of a Sensorless Magnetic Damper

H. M. Chen
Mechanical Technology Inc.,
Latham, NY 12110

An analytical method for designing magnetic bearing controllers with no displacement sensors has been developed and laboratory tested. The method was applied to the design of a sensorless magnetic damper for replacing a rolling element bearing of a vertical rotor with a large unbalance. The synchronous vibration force transmitted to ground was predicted to be reduced by a factor of ten.

Introduction

An industrial vertical rotor supported by rolling element bearings was originally designed to operate below its first critical speed. Since the rotor accumulated unbalance during operation, which was a potential problem, it was proposed that a soft magnetic bearing replace the lower rolling element bearing. The magnetic bearing (hereafter referred to as a damper) tends to make the rotor spin at its mass center and reduces the unbalance force to ground by an order of magnitude.

The damper is an actively controlled electromagnetic device, and its desired stiffness and damping properties can be readily achieved by using a conventional PID controller with displacement sensors. However, because these sensors are expensive and unreliable in the hot, hostile environment around the rotor, there is high incentive to design a "sensorless" controller.

Whereas a conventional PID controller processes rotor displacement signals with proportional, integral, and derivative filters, a sensorless controller applies a totally different algorithm. Henrikson et al. (1974) and Robinson (1976) worked with thrust magnetic bearing controllers and measured velocity instead of displacement. Velocity can be measured by using a permanent magnet moving inside a coil, which is a simple, rugged measurement device. Also, because it needs no significant signal conditioning, it is inexpensive. Vischer and Bleuler (1990), Bleuler and Vischer (1991), and Mizuno et al. (1992) used a state observer method in their sensorless magnetic bearing work. As described by Mizuno et al., there are five or six observer parameters to be determined for each control axis; thus, tuning the controller when using a state observer is difficult.

Herein, the author adopts a velocity feedback method similar to the Henrikson and Robinson approaches. Instead of measuring directly, however, velocity is recreated by an estimator (Okada et al., 1992) using back electromotive force (EMF) and current signals in the magnetizing coils. To facilitate tuning, an analytical process was developed to minimize the number of free parameters in each control axis.

Sensorless Control Method

The following discussion assumes a basic understanding of the laminated rotor and stator cores, magnetizing coils, power electronics, and power supply associated with magnetic bearings. We will therefore assume certain parameters without discussing them, such as current stiffness, K_i, and magnetic stiffness, K_m. The three major elements of sensorless control that we will concentrate on are the velocity feedback controller, the velocity estimator, and the self-starter.

Contributed by the International Gas Turbine Institute and presented at the 40th International Gas Turbine and Aeroengine Congress and Exhibition, Houston, Texas, June 5–8, 1995. Manuscript received by the International Gas Turbine Institute February 13, 1995. Paper No. 95-GT-180. Associate Technical Editor: C. J. Russo.

Figure 1 shows a sensorless control system diagram where the rotor is represented by a rigid mass, M, without considering its bending modes. Assuming that a good velocity signal is available, magnetic levitation can be achieved by feeding back the velocity signal through the two-part velocity feedback controller and to the power amplifiers. The purpose of the first controller element, which is a first-order low-pass filter with a time constant, $1/C$, and a gain, G_v, is to cut down the high-frequency feedback of the velocity and to avoid high-frequency noise or bending mode resonances that may saturate the power amplifier and cause system instability. One or more notch filters may still be needed for controlling some structure-related, high-frequency resonances. The second controller element is the zero-force-seeking loop (Henrikson, 1974), which has a positive feedback with loop gain, G_cG_e, greater than 1.0. The positive feedback is also low passed with a time constant, $1/A$, which is much longer than $1/C$. The zero-force-seeking loop, by itself, is unstable; its output latches to $\pm$ maximum values. Similarly, the rotor alone in the magnetic field set up by the bias currents is also unstable. When the feedback loop is closed with properly chosen parameters, the system can be made stable. The characteristic equation of the dynamic system is represented by:

$$1 + KS(S + A)/(S^2 - 1)(S - A_r)(S + C) = 0 \quad (1)$$

where

$A_r = (G_cG_e - 1)A$,
$K = G_sG_aG_cG_vCK_i/MB^2$, and
$B = \sqrt{K_m/M}$

In Eq. (1), the Laplace variable, S, as well as A, A_r, and C are all normalized by the artificial parameter, B, called the bias frequency, which is a measure of the strength of the bias flux in the magnetic device. It has been assumed that in the low-frequency range of interest, the power amplifiers have practically a constant sensitivity, G_a. Without losing generality, G_a can be assumed as 1 ampere per volt. Similarly, the velocity estimator sensitivity is assumed at 1 volt per inch per second (0.4 volts per centimeter per second), and the feed forward gain G_c at 1 volt per volt. There are now four parameters remaining in Eq. (1) that have to be determined for stable control. These parameters are A, A_r, C, and K, all nondimensional. The root-locus plot of Fig. 2 is typical with variable gain, K, and fixed values for A, A_r, and C. There is a range of K values for which the system will have one or two pairs of well-damped roots. For example, for $K = 15$, as shown in Fig. 2, the two pairs of complex conjugate roots are both well damped. For different combinations of A, A_r, and C values, the shapes of the root loci are different. One can choose the desired shapes from a precalculated, nondimensional data bank and determine the four parameters.

Figure 3 shows the velocity estimator, which is another important element of sensorless control. A magnetizing coil wound

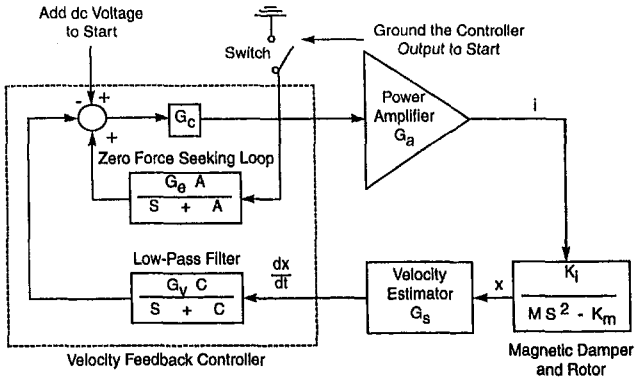

Fig. 1 Sensorless control system diagram

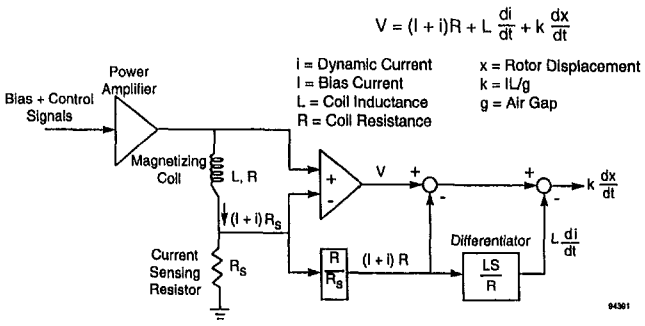

Fig. 3 Velocity estimator

on a stator core with a nominal air gap, g, to a rotor core has an inductance, L, and a wire resistance, R. The voltage signal across the coil, V, comprises three components: the voltage drop due to current flow, the back EMF due to dynamic current driven through by the power amplifier, and the back EMF due to flux variation in cores due to rotor motion. The last component is proportional to rotor velocity and is extracted by the velocity estimator. In order to eliminate the first two components, the current through the coil is measured using a resistor, R_s. The elimination process is self-explanatory, as shown in Fig. 3. Okada et al. (1992) used such a velocity estimator in an analog circuit for a vibration suppression actuator. A major drawback of this estimator is the sensitivity of the coil resistance to temperature, which is detailed later in describing a sensorless experiment.

Since the sensorless control is activated by velocity, the rotor at rest needs a "kick" to get the magnetic levitation started. Before kicking the rotor, one has to know which side of the magnets the rotor is resting or leaning on. The kick should be in the direction to free the rotor. This information is available if the bias currents to different quadrants of the bearing are turned on sequentially. In other words, the rotor will rest on the electromagnet turned on first. In addition to these logic functions, the self-starter is required to add a d-c voltage, V_{dc}, at the zero-force-seeking loop input and ground the zero-force-seeking loop output momentarily, as shown in Fig. 1. The polarity of the d-c voltage is decided by the side on which the rotor rests. The magnitude is determined by the allowable static rotor position shift, X_{dc}, as represented by:

$$X_{dc} = \{G_a V_{dc}/(G_c G_e - 1)\}(K_i/K_m) \qquad (2)$$

It should be emphasized that the velocity-controlled magnetic bearing has an implicit "zero position reference" where the static forces on the rotor balance each other. X_{dc} is a deviation from this zero position reference. The self-starter kicks the rotor with V_{dc}. When levitation is achieved, the rotor position is off by X_{dc}. Therefore, in the final step, the self-starter turns off the V_{dc} at the zero-force-seeking-loop input.

Experiment

Tests on a single control axis were successfully performed using the setup shown in Fig. 4, verifying the sensorless control theory above. The right side of the photo shows a fabricated column suspended vertically between two electromagnets. The column is made of two 8-in. (20 cm)-long aluminum rods and two steel end-plates and weighs about 2.5 oz (70 g). The bias and control coils are separate. The total air gap is 0.120 in. (3.05 mm), 0.045 in. (1.14 mm) on the top, and 0.075 in. (1.91 mm) at the bottom. The left side of the photo shows the analog circuitry of the velocity feedback controller, the velocity estimator, and the power amplifier.

Figure 5 shows how, in theory, variations in the low-pass filter gain, G_v affect response. During testing, the sinusoidal sweep indicated a damped peak response at 65 Hz (410 rad/s) when $G_v = 0.6$. As the gain was reduced, the peak response dropped and suddenly shifted in frequency. Finally, with $G_v = 0.3$, the system went into a sustained resonance at 22 Hz (140 rad/s). These observations showed good correlation with the calculated result in Fig. 5. When the gain was on the high side, the second mode was less damped and showed up in forced response. When the gain was between 0.4 and 0.5, both modes were well damped and showed no response. When the gain was

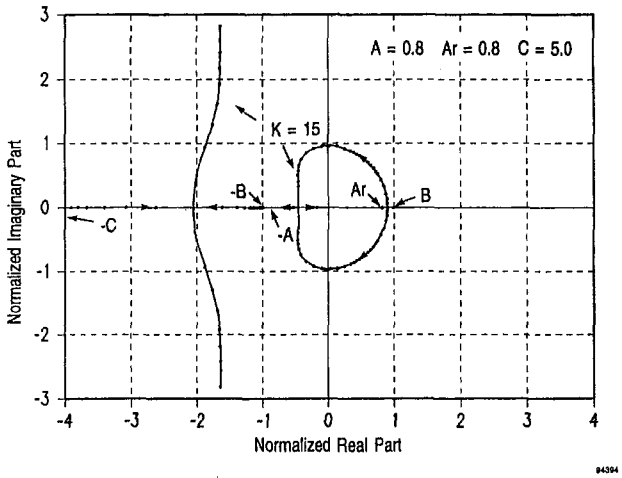

Fig. 2 Typical normalized root-locus plot

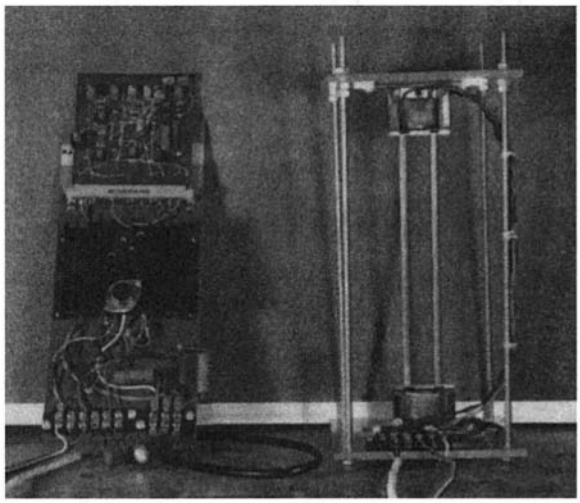

Fig. 4 Experimental setup

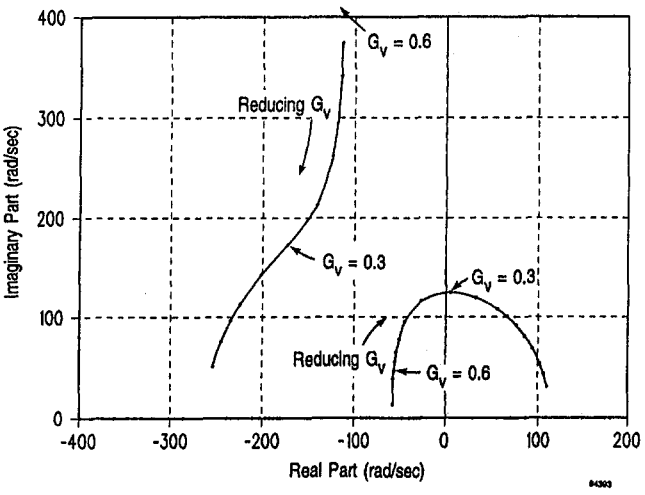

Fig. 5 Root-locus plot for sensorless demonstration

low, the first mode became less damped and dominated the response.

Another interesting observation was that the suspended column moved up, closing the top air gap when weights were added to the column. This is a distinctive feature of sensorless or velocity-controlled magnetic bearings. If the bias fluxes are large, the d-c stiffness of the sensorless bearing is also large, as if there were "integral" control (Mizuno et al., 1992). The tests also revealed a serious problem associated with the velocity estimator. The usual material for the coils is copper, and since the resistance of copper changes significantly with temperature, the velocity estimator had to be tuned differently for cold and warm coils. An apparent remedy is to avoid or eliminate the voltage drop signal, $(I + i)R$. In the following damper design, search coils are added to the damper to avoid the voltage drop due to the currents while retaining the collocation of the velocity signal. Note that a search coil picks up flux variation signals at the air gap. It has a high-impedance output and, thus, the current flow inside is insignificant.

Magnetic Damper Design

The mathematical model of the vertical rotor retrofitted with a magnetic damper is presented in Fig. 6. The upper ball bearing taking both radial and thrust loads is much stiffer radially than the lower magnetic damper. Therefore, the first rotor critical vibration has a mode shape of a swinging wheel and shaft pivoted at the upper bearing. The modal mass seen by the damper is approximately:

$$M = (M_w l^2 + I_w)/l_1^2 \tag{3}$$

where M_w and I_w are the mass and transverse mass moment of inertia, respectively, of the large wheel.

Also shown in Fig. 6 are the four E-shaped stator cores of the damper. Each stator core has a large magnetizing coil and a small sensing coil. The three relevant damper parameters, M, K_i, and K_m are 300 lb (136 kg), 54 lb/A (240 N/A), and 4500 lb/in. (7.89×10^5 N/m), respectively.

The rotor runs normally at 3000 rpm (50 Hz); the bias frequency, B, is about 12 Hz. In this case, one would choose a well-damped first mode with a modal frequency less than B, and an overdamped second mode to ensure that a second mode does not show up at all. The most important goal is to achieve the softest possible damper at the running frequency (50 Hz). Damper dynamic stiffness can be represented by:

$$K_{\text{dyn}} = KS(S + A)/(S - A_r)(S + C) - 1 \tag{4}$$

where K_{dyn} is normalized with respect to the magnetic stiffness, K_m.

This equation provides a quick check of the dynamic stiffness at any frequency, once the values of A, A_r, C, and K are chosen and satisfy the stability from a root-locus plot. The normalized velocity feedback controller parameters ($A = 0.8$; $A_r = 0.2$; $C = 4.0$; and $K = 8.0$) are selected to achieve low dynamic stiffness at 3000 rpm.

The damper dynamic properties as functions of speed are plotted in Fig. 7 where the real and imaginary parts of the dynamic stiffness, $K_m K_{\text{dyn}}$, are plotted separately as functions of rotor speed. Note that the total dynamic stiffness at 3000 rpm is about 22,500 lb/in. (3.95×10^6 N/m) or about $\frac{1}{20}$ of the ball bearing stiffness.

Using an unbalance response program, rotor responses were calculated for the separate cases of the lower bearing as a ball bearing and when a magnetic bearing was substituted. Figure 8 compares the forces and rotor displacement at the lower bearings, assuming an unbalance of 1.0 oz-in. (72 g-cm) at the wheel. Each ball bearing has a radial stiffness of 500,000 lb/in. (8.77×10^7 N/m) and a negligible amount of damping. The rotor with two ball bearings experiences the first critical at about 3400 rpm and is sensitive to unbalance at the running speed. At the same speed, the rotor with the damper transmits much lower force through the lower support while it whirls more freely at the support.

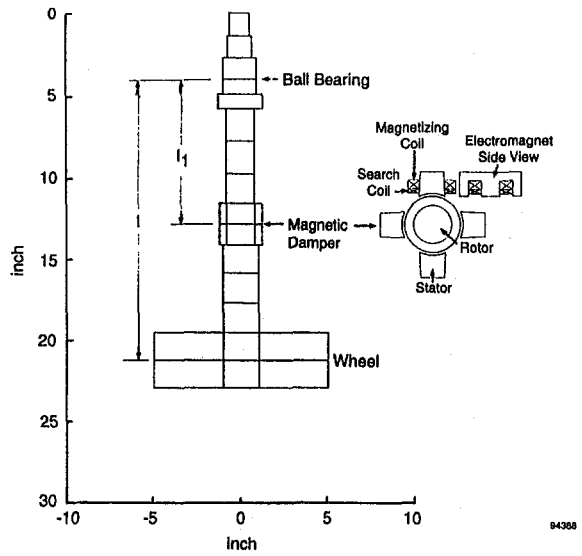

Fig. 6 Mathematical rotor and damper models

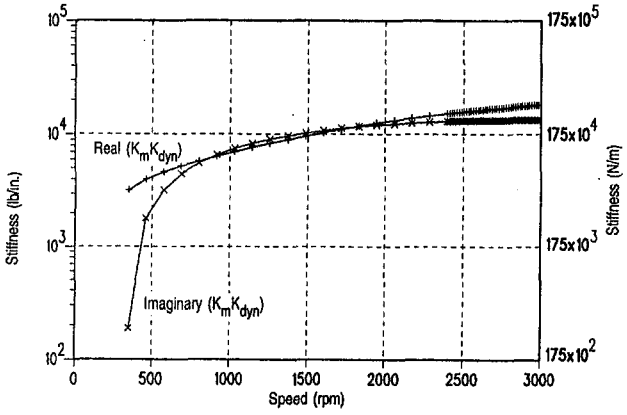

Fig. 7 Dynamic properties of a magnetic damper

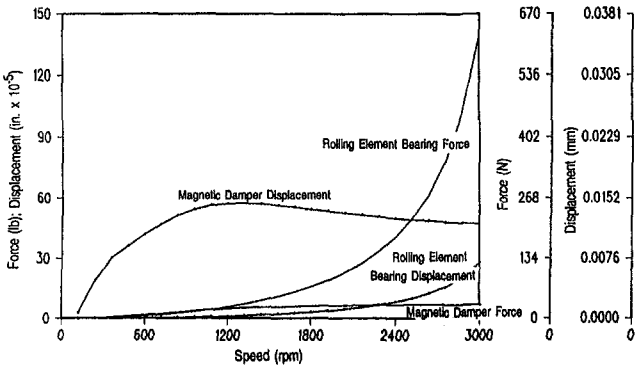

Fig. 8 Lower support force and displacement

Conclusions

The unique design methodology for sensorless magnetic bearings presented herein separates control into three elements. Dividing control among a velocity feedback controller, a velocity estimator, and a self-starter minimizes the number of free parameters that have to be chosen at one time in the design process and makes the control tuning process straightforward.

A common problem of sensorless control—the sensitivity of wire resistance to coil temperature—was revealed during experimentation. This sensitivity makes tuning the velocity estimator unreliable. There are two ways to address the problem: by adding temperature compensation for the parameter, R, by tapping a temperature related signal in the coils, or by avoiding the voltage drop signal due to current flowing through by the use of search coils, as was done in the damper design described above.

References

Bleuler, H., and Vischer, D., 1991, "Magnetic Bearings With Minimum Hardware Requirement," presented at ROMAG'91 Magnetic Bearing & Dry Gas Seals Conference, Washington DC, Mar. 13–15.

Henrikson, C. H., et al., 1974, "Magnetically Suspended Momentum Wheels for Spacecraft Stabilization," presented at AIAA 12th Aerospace Science Meeting, Washington, DC, Paper No. 74–128.

Mizuno, T., et al., 1992, "Towards Practical Applications of Self-Sensing Magnetic Bearings," presented at 3rd International Conference on Active Magnetic Bearings, Alexandria, VA, July 29–31.

Okada, Y., et al., 1992, "Electromagnets as Velocity Sensors and Vibration Control Actuators," *Electromagnetic Forces and Applications,* Elsevier Science Publications, pp. 171–174.

Robinson, A. A., 1976, "Magnetically Suspended Momentum Wheel for Satellite Stabilization," *Proc. 2nd Conference on Advanced Magnetic Materials and Applications,* Sept., IEE Conference Publication 142, pp. 131–134.

Vischer, D., and Bleuler, H., 1990, "A New Approach to Sensorless and Voltage Controlled AMBs Based on Network Theory Concepts," *Proc. 2nd International Symposium on Magnetic Bearings,* July, University of Tokyo.

Vibration and Control of a Flexible Rotor in Magnetic Bearings Using Hybrid Method and H^∞ Control Theory

T. N. Shiau
Department of Mechanical Engineering,
National Chung Cheng University,
Chia Yi, Taiwan

G. J. Sheu

C. D. Yang

Institute of Aeronautics and Astronautics,
National Cheng Kung University,
Tainan, Taiwan

The vibration and active control of a flexible rotor system with magnetic bearings are investigated using Hybrid Method (HM) and H^∞ control theory with consideration of gyroscopic effect. The hybrid method, which combines the merits of the finite element method (FEM) and generalized polynomial expansion method (GPEM) is employed to model the flexible rotor system with small order of plant. The mixed sensitivity problem of H^∞ control theory is applied to design the control of system vibration with spillover phenomena for the reduced order plant. The H^2 control design is also employed for comparison with the H^∞ design. The experimental simulation is used to illustrate the effects of control design. It is shown that the H^∞ controller design can be very effective to suppress spillover phenomena. In addition, the H^∞ control design has robustness to the variation of the model parameters. The application of the hybrid method (HM) together with H^∞ control design is highly recommended for vibration control of flexible rotor systems with magnetic bearings.

Introduction

Recently magnetic bearings have been developed in high-speed turbomachines such as gas turbines, jet engines, pumps, and machine tools. The advantages of using magnetic bearings are that they need no lubrication, consume less power, and possess long life compared to conventional bearings such as rolling element bearings and fluid film bearings. Furthermore, magnetic bearings have manipulatable stiffness and damping to cope with the rotordynamic problems of instability and unbalance. The most popular and practical type of magnetic bearing is the active magnetic bearing (AMB), which will be considered in this study.

The design of active magnetic bearing has been investigated by many authors (Allaire et al., 1981, 1983; Salm and Schweitzer, 1984; Nonami et al., 1990). The AMB geometry is shown in Fig. 1 and several electromagnets are arranged radially around the shaft. The current and thus the force can be continuously adjusted by a design controller (Stanway and Burrows, 1981; Humphris et al., 1986; Okada et al., 1992). The stiffness and damping of magnetic bearings can be changed over a wide range of parameters to attenuate the rotor vibrations. The magnetic force acting on the shaft is produced by signals proportional to a combination of shaft displacement and velocity (PD controllers). Since PD controllers can only take a few specifications into account, the closed-loop stability cannot be guaranteed. Zames (1981) introduced a systematic approach to the regulator problem involving model uncertainties and general external signals using Hardy space H^∞. The controller is designed to minimize the disturbance, which causes the maximal damage to the plant. This "minimax" optimization problem is characteristic of H^∞ control (Doyle et al., 1989, 1992). The vibration control based on the reduced order model using H^∞ control theory has been studied by Nonami et al. (1991a) and Cui and Nonami (1992). The spillover control of magnetic levitation systems was also studied by Nonami et al. (1991b) using H^∞ control theory.

Various methods for the dynamic analysis of rotor-bearing systems have been developed and used widely during the past few decades. The present paper will be concerned with using the finite element method (FEM) (Nelson and McVaugh, 1976; Nelson, 1980) and the generalized polynomial expansion method (GPEM) (Shiau and Hwang, 1993). Moreover, a concept that combines the merits of FEM and GPEM will be used to model the rotor system to reduce the system order. The H^∞ mixed sensitivity method is used to control system design for the reduced order model. The method is expected to suppress the spillover effect and to be a powerful robustness to the parameter variation of a rotor system with magnetic bearings.

Equation Formulation

The rotor bearing system can be modeled as an assemblage of rigid disks, flexible shaft elements with distributed mass and stiffness, and discrete bearings. The Timoshenko beam element is employed to simulate the rotor system. The gyroscopic moments, rotatory inertia, and shear deformation of the shaft are taken into consideration in this study. For simplicity, the following assumptions are made:

1 Field fringing and leakage effects are neglected.
2 Magnetic flux density and field density are uniform through the core and gap.
3 The attractive forces are proportional to the square of the coil current (Maxwell's theorem).
4 The induced voltages of electromagnets are ignored.
5 Both AMB have the same characteristics.
6 Only small vibrations near equilibrium are considered.
7 The shaft with rigid disks attached is flexible.
8 Torsional vibration and axial vibration are neglected.

The set of linearized second-order differential equations characterizing the behavior of a rotor system under control can be written as:

$$[M]\{\ddot{p}\} + ([C] - \Omega[G])\{\dot{p}\} + [K]\{p\} = [B]\{u\} + \{Q\} \quad (1)$$

Contributed by the International Gas Turbine Institute and presented at the 39th International Gas Turbine and Aeroengine Congress and Exposition, The Hague, The Netherlands, June 13–16, 1994. Manuscript received by the International Gas Turbine Institute February 4, 1994. Paper No. 94-GT-57. Associate Technical Editor: E. M. Greitzer.

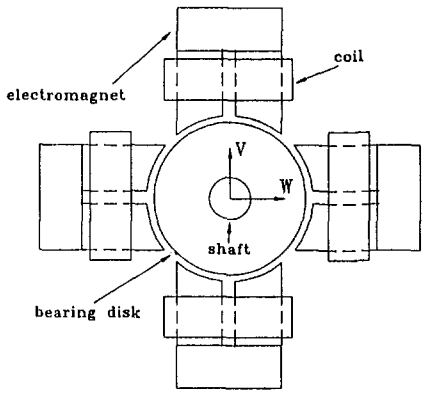

Fig. 1 Magnetic bearing geometry

where Ω is the shaft rotational speed; $[M]$, $[C]$, $[G]$, and $[K]$ are the symmetric positive definite mass, symmetric positive semidefinite damping, skew symmetric gyroscopic, and symmetric positive semidefinite stiffness matrices, respectively, with all dimensions $4(N_e + 1) \times 4(N_e + 1)$ (Nelson, 1980). The $4(N_e + 1) \times 1$ generalized translational and rotational displacement vector is denoted by $\{p\}$. The control force distribution matrix and the control force vector are denoted by $[B]$ and $\{u\}$, respectively. $\{Q\}$ denotes the external force vector such as unbalance force, disturbance etc.

Model of Magnetic Bearing System. The basic active magnetic bearing equations are developed based on Maxwell's law. A small purturbed motion about equilibrium position is assumed, and the linearization technique will be applied. It is also assumed that the flux levels are well below saturation in the core material. Then, the total magnetic flux in an air gap is given by

$$\phi = \frac{\mu_o ANI}{H} \tag{2}$$

where μ_0, A, N, I, and H are the permeability, the face area, number of winding turns, the coil current, and the gap thickness, respectively. The attractive force of an electromagnet is

$$F = \frac{\phi^2}{2\mu_o A} \tag{3}$$

Substitution of ϕ into Eq. (3) for two air gaps gives

$$F = \frac{\mu_o AN^2 I^2}{H^2} \tag{4}$$

If vibration near equilibrium is small, F, H, and I can be given as follows:

$$F = F_s + f, \quad I = I_s + i, \quad H = H_s - h \tag{5}$$

where F_s, I_s, and H_s are the steady-state attractive force, current, and gap thickness, respectively. f, i, and h are the control attractive force, control current, and control gap thickness, respectively.

For small motion, $I_s \gg i$, and $H_s \gg h$, the Taylor series expansion is applied for small values of i and h. This yields the following attractive control forces in linear form:

$$F = \frac{\mu_o AN^2 (I_s + i)^2}{(H_s - h)^2} \approx \frac{\mu_o AN^2 I_s^2}{H_s^2}\left(1 + 2\frac{h}{H_s} + 2\frac{i}{I_s}\right)$$

$$= F_s + f \tag{6}$$

There are two independent parameters in Eq. (6), i.e., position h and current i. We define the position stiffness K_h and current stiffness K_i as follows:

$$K_h = -\frac{\partial F}{\partial h}, \quad K_i = -\frac{\partial F}{\partial i}$$

Substitution of Eq. (6) yields

$$K_i = -\frac{2\mu_o AN^2 I_s}{H_s^2}$$

$$K_h = -\frac{2\mu_o AN^2 I_s^2}{H_s^3}$$

The control attractive force f can be rewritten as:

$$f = -K_i i - K_h h \tag{7}$$

System Equations of Motion. The model of flexible rotor with magnetic bearings system using the finite element method (FEM) can be shown as Eq. (1). It is noted that the external force of the disturbance is neglected in the study. A typical property of many practical AMB systems is the displacement at the AMB coils, which can be measured. It is assumed that

Nomenclature

$a_n(t)$, $b_m(t)$ = coefficients of polynomial
$[B]$ = control force distribution matrix
$[C]$, $[K]$ = system damping and stiffness matrices, respectively
d = diameter of the shaft
E = modulus of elasticity
F_s, I_s, H_s = steady-state attractive force, steady-state current, and steady-state gap thickness, respectively
f, i, h = control attractive force, control current, and control gap thickness, respectively
$G(s)$ = nominal plant
$[GC]$, $[GK]$ = generalized system damping and stiffness matrices, respectively
$[GM]$, $[GG]$ = generalized system mass and gyroscopic matrices, respectively
$\{g\}$ = generalized coordinate vector
H = gap thickness
I_p = disk polar inertia
$K(s)$ = controller
K' = transverse shear form factor
K_h, K_i = position and current stiffness, respectively
$[M]$, $[G]$ = system mass and gyroscopic matrices, respectively
N = number of winding turns
N_e = number of element
N_p = number of polynomial terms
$P(s)$ = augmented plant
$\{p\}$ = displacement vector
$\{Q\}$ = external force vector
$S(s)$ = sensitivity function
$T(s)$ = complementary sensitivity function
$[T]$ = transformed matrix
$\{u\}$ = control force vector
(V, W) = translations in (Y, Z) directions
$W_1(s)$ = sensitivity weighting function
$W_3(s)$ = complementary sensitivity weighting function
y = measured output vector
(B, Γ) = small angle rotations about (Y, Z) axes
$\Delta_m(s)$ = multiplicative uncertainty
μ_o = permeability
Ω = rotational speed

the outputs are measured from the magnetic bearings. With the control input $\{u\}$ designed for the magnetic bearings and combining the magnetic bearing force, Eq. (1) can be rewritten as:

$$[M]\{\ddot{p}\} + ([C] - \Omega[G])\{\dot{p}\} + [K]\{p\} = [B]\{u\} \quad (8)$$

where

$$\{p\} = \{V_1, W_1, B_1, \Gamma_1, \ldots, V_{(N_e+1)}, W_{(N_e+1)}, B_{(N_e+1)}, \Gamma_{(N_e+1)}\}$$

$$[B] = \begin{bmatrix} 1 & 1 & 0 & 0\cdots 0 & 0 & 0 & 0 \\ 0 & 0 & 0 & 0\cdots 1 & 1 & 0 & 0 \end{bmatrix}^T_{4(N_e+1)\times 2}$$

$$\{u\} = \{f_l, f_r\}^T$$

$f_l = -K_i i_l - K_h h_l$: control forces at the left side of AMB

$f_r = -K_i i_r - K_h h_r$: control forces at the right side of AMB

Rearranging Eq. (8) yields:

$$[M]\{\ddot{p}\} + ([C] - \Omega[G])\{\dot{p}\} + ([K] + [K1])\{p\} = -K_i[B]\{i\} \quad (9)$$

where

$$[K1] = \text{diag}\,(K_h, K_h, 0, 0, \ldots, K_h, K_h, 0, 0)_{4(N_e+1)\times 4(N_e+1)}$$

$$\{i\} = \{i_l, i_r\}^T$$

i_l: control current at the left side of AMB

i_r: control current at the right side of AMB

Let the measured output vector y be expressed as:

$$y = \{V_l, V_r\}^T = [C1]\{p\} \quad (10)$$

where

$$[C1] = \begin{bmatrix} 1 & 0 & 0 & 0\cdots 0 & 0 & 0 & 0 \\ 0 & 0 & 0 & 0\cdots 1 & 0 & 0 & 0 \end{bmatrix}^T_{4(N_e+1)\times 2}$$

One crucial drawback of the controller design approach is that the high order model control scheme will require a considerable computation time for estimating the nonmeasured state variables and calculating the corresponding controller output signals. Hence, low order discrete-time dynamic output control schemes must be sought in order to simplify the control task. A hybrid method (HM), which combines the merits of FEM and the Generalized Polynomial Expansion Method (GPEM) of Shiau and Hwang (1989, 1993), is employed to reduce the system order.

Model Reduction Technique: Hybrid Method (HM). Based on the GPEM, the translational deflections along the rotating shaft can be expressed as a series of polynomials associated with time coefficient functions $a_n(t)$, $b_m(t)$:

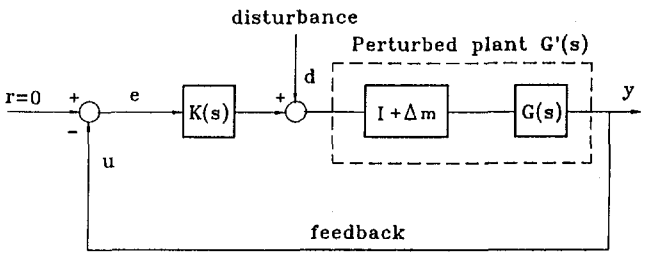

Fig. 2 Block diagram of MIMO feedback control system, where G is the nominal plant and Δ_m(s) is the multiplicative uncertainty

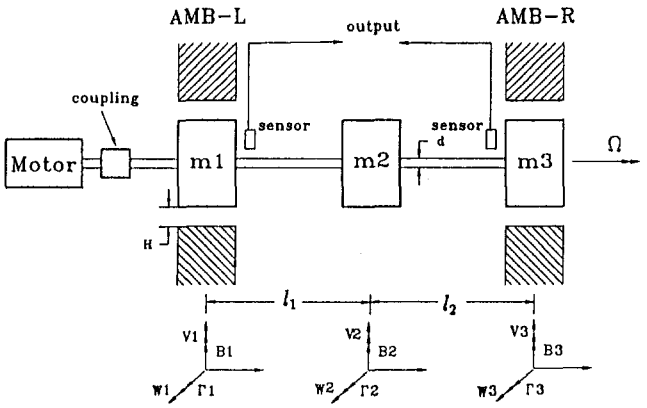

Fig. 3 Model of flexible rotor with magnetic bearing system

$$V(x, t) = \sum_{n=1}^{N_p} a_n(t)x^{n-1} \quad (11)$$

$$W(x, t) = \sum_{m=1}^{N_p} b_m(t)x^{m-1} \quad (12)$$

The expressions of rotational deflections are geometrically related to translational deflections by the following equations:

$$\Gamma(x, t) = \frac{\partial V(x, t)}{\partial x} = \sum_{n=1}^{N_p} (n-1)a_n(t)x^{n-2} \quad (13)$$

$$B(x, t) = -\frac{\partial W(x, t)}{\partial x} = -\sum_{m=1}^{N_p} (m-1)b_m(t)x^{m-2} \quad (14)$$

The equation of motion, based on FEM for a flexible rotor with the magnetic bearing system under control, is of the form:

$$[M]\{\ddot{p}\} + ([C] - \Omega[G])\{\dot{p}\} + ([K] + [K1])\{p\} = -K_i[B]\{i\} \quad (15)$$

where

$$\{p\} = \{V_1, W_1, B_1, \Lambda_1, \ldots, V_{(N_e+1)}, W_{(N_e+1)}, B_{(N_e+1)}, \Gamma_{(N_e+1)}\}$$

The Hybrid Method combines the merits of FEM and GPEM. It simply describes the system equation of motion using FEM first and applies the GPEM to reduce the system degrees of freedom. Applying the GPEM, the physical coordinate vector $\{p\}$ can be expressed in terms of generalized coordinate at nodal point i in the following forms:

Table 1 Specifications of simulation model

Parameters		Value	Unit
Mass	$m_1 = m_3$	1.5	Kg
Mass	m_2	0.75	Kg
Length	$l_1 = l_2$	0.5	m
Diameter	d	0.02	m
Gap Length	H_s	0.0015	m
Bias Current	I_s	1.0	A
Position Stiffness	K_h	10^5	N/m
Current Stiffness	K_i	100	N/A
Modulus of Elasticity	E	$2.1 * 10^{11}$	$N * m^{-2}$
Moment of Inertia	$I_{p1} = I_{p3}$	0.01	$Kg * m^{-4}$
Moment of Inertia	I_{p2}	0.005	$Kg * m^{-4}$
Shaft Density	ρ	7806	$Kg * m^{-3}$
Rotational Speed	Ω	1000	rad/sec
Damping ratio	ζ	0.1%	

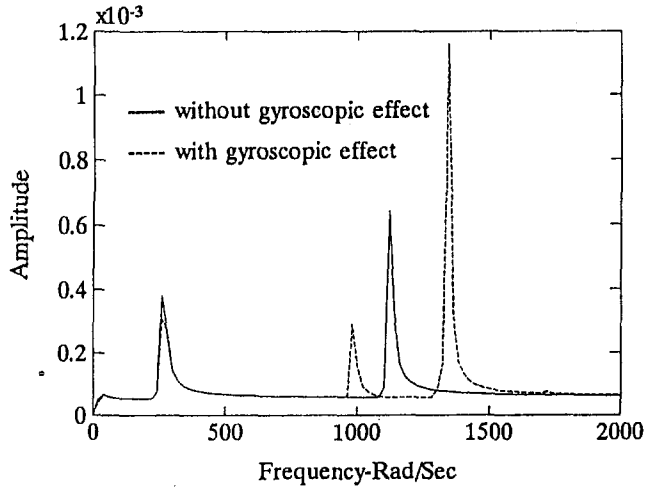

Fig. 4 System unbalance responses

$$V_i(x_i, t) = \sum_{n=1}^{N_p} a_n(t) x_i^{n-1}$$

$$W_i(x_i, t) = \sum_{m=1}^{N_p} b_m(t) x_i^{m-1}$$

$$\Gamma_i(x_i, t) = \sum_{n=1}^{N_p} (n-1) a_n(t) x_i^{n-2}$$

$$B_i(x_i, t) = -\sum_{m=1}^{N_p} (m-1) b_m(t) x_i^{m-2}$$

These equations can be expressed in matrix form:

$$\{p\}_{4(N_e+1)\times 1} = [T]_{4(N_e+1)\times 2N_p}\{g\}_{2N_p\times 1} \tag{16}$$

where $\{p\}$ and $\{g\}$ are physical and generalized coordinate vectors, respectively. The generalized coordinate vector $\{g\}$ and each element of matrix $[T]$, t_{ij} are given below:

$$\{a\}^T = \{a_1, a_2, \ldots, a_{N_p}\}$$

$$\{b\}^T = \{b_1, b_2, \ldots, b_{N_p}\}$$

$$\{g\}^T = \{a^T, b^T\}$$

$$t_{4i-3,j} = t_{4i-2,j+N_p} = (x_i)^{j-1}, \quad j = 1, 2, \ldots, N_p$$

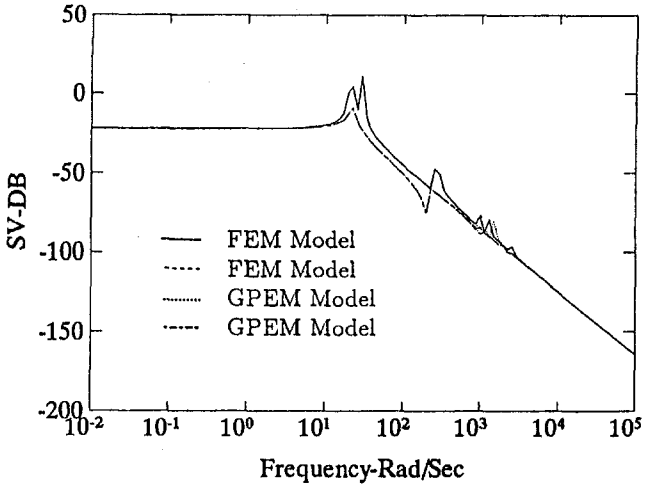

Fig. 5 Frequency responses of full order modal (FEM) and reduced-order model (GPEM)

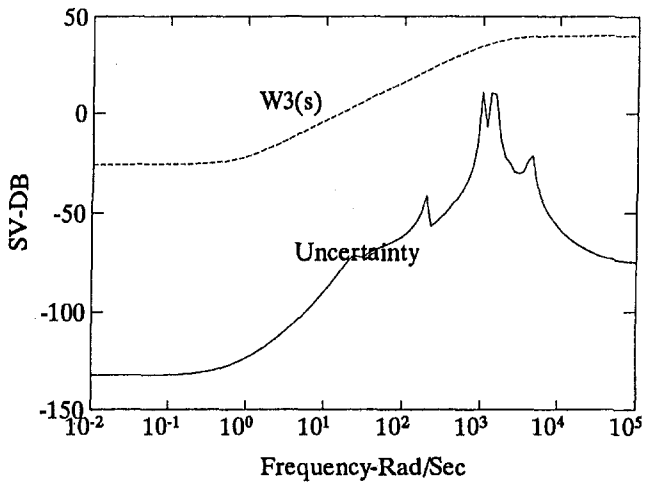

Fig. 6 Frequency responses of $\Delta_m(s)$ between FEM and GPEM and $W_3(s)$

$$t_{4i-1,j+N_p} = -(j-1)(x_i)^{j-2}, \quad j = 1, 2, \ldots, N_p$$

$$t_{4i,j} = (j-1)(x_i)^{j-2}, \quad j = 1, 2, \ldots, N_p$$

other elements = 0

Substituting Eq. (16) into Eq. (9) and premultiplying $[T]^T$ yields

$$[GM]\{\ddot{g}\} + ([GC] - \Omega[GG])\{\dot{g}\} + [GK]\{g\} = -K_i[T]^T[B]\{i\} \tag{17}$$

where

$$[GM] = [T]^T[M][T]$$

$$[GG] = [T]^T[G][T]$$

$$[GC] = [T]^T[C][T]$$

$$[GK] = [T]^T([K] + [K1])[T]$$

The coefficient matrices shown in Eq. (15) are of dimension $4(N_e + 1) \times 4(N_e + 1)$. However, the coefficient matrices shown in Eq. (17) are of dimension $2N_p \times 2N_p$. One of the advantages of using GPEM is that the order of the rotor system can be greatly reduced if $2N_p \ll 4(N_e + 1)$. This provides a good opportunity to reduce the order of the rotor system without loss of accuracy (Shiau and Hwang, 1993).

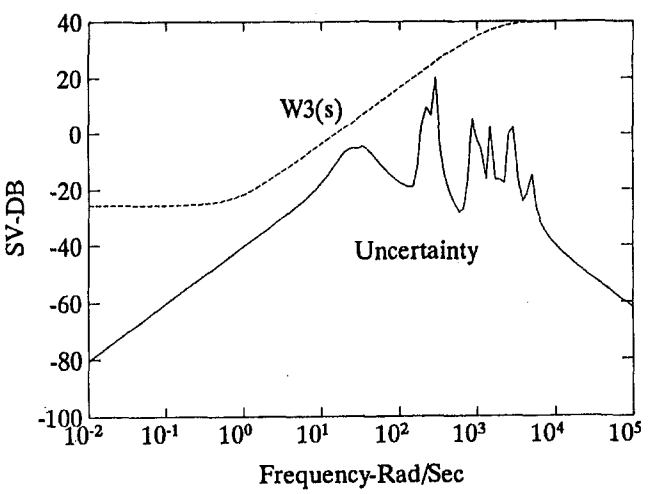

Fig. 7 Frequency responses of $\Delta_m(s)$ due to gyroscopic effect change (Ω: 1000 rad/s → 2000 rad/s) and $W_3(s)$

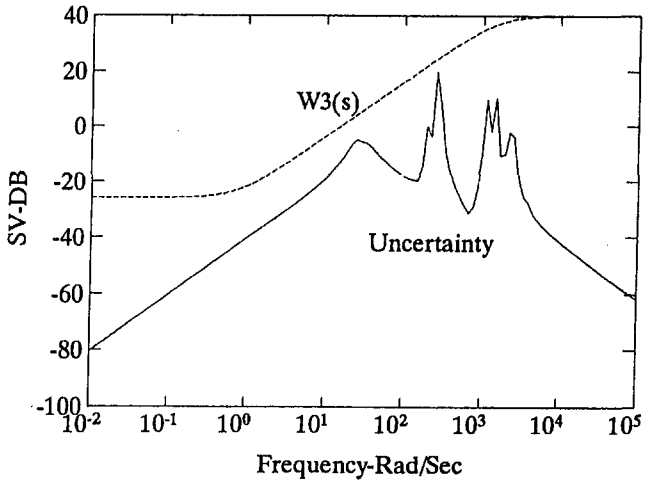

Fig. 8 Frequency responses of $\Delta_m(s)$ due to gyroscopic effect change (Ω: 1000 rad/s → 0 rad/s) and $W_3(s)$

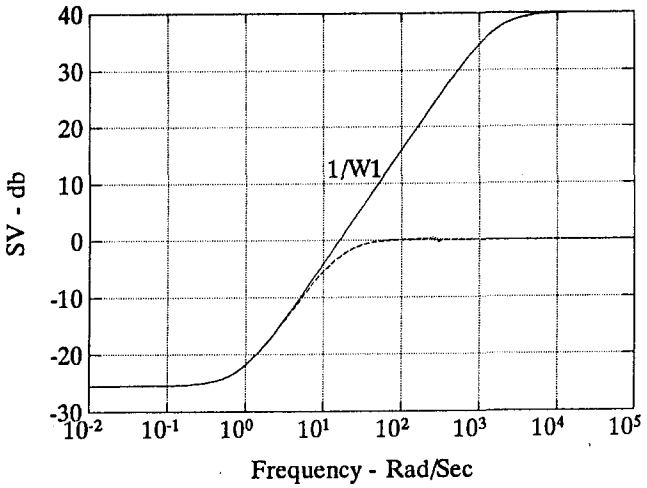

Fig. 9 Sensitivity function and $W_1^{-1}(s)$ of H^∞ control design

State Space Formulation. Choosing $x_p = \{\dot{p}, p\}^T$ as a state vector for the plant and $u = \{i\}$, one obtains the following state space realization based on the FEM model:

$$\dot{x}_p = A_p x_p + B_p u$$
$$y_p = C_p x_p \tag{18}$$

where

$$A_p = \begin{bmatrix} [M]^{-1}(\Omega[G] - [C]) & -[M]^{-1}([K] + [K1]) \\ 0 & I \end{bmatrix}_{8(N_e+1)\times 8(N_e+1)}$$

$$B_p = \begin{bmatrix} -K_i[M]^{-1}[B] \\ 0 \end{bmatrix}_{8(N_e+1)\times 2}$$

$$C_p = [0 \quad [C1]]_{2\times 8(N_e+1)}$$

The order of the flexible rotor shown in Eq. (18) is $8(N_e + 1)$. Choosing $x_{p'} = \{g, g\}^T$ as a state vector and $u = \{i\}$, the rotor system in state realization for the HM model becomes:

$$\dot{x}_{p'} = A_{p'} x_{p'} + B_{p'} u$$
$$y_{p'} = C_{p'} x_{p'} \tag{19}$$

where

$$A_{p'} = \begin{bmatrix} [GM]^{-1}(\Omega[GG] - [GC]) & -[M]^{-1}[GK] \\ 0 & I \end{bmatrix}_{4N_p\times 4N_p}$$

$$B_{p'} = \begin{bmatrix} -K_i[GM]^{-1}[T]^T[B] \\ 0 \end{bmatrix}_{4N_p\times 2}$$

$$C_{p'} = [0 \quad [C1][T]]_{2\times 4N_p}$$

It is shown from Eq. (19) that the order of the GPEM model is $4N_p$. Usually, the practical rotor system is of $4N_p \ll 8(N_e + 1)$.

Design of H^∞ Controller

The H^∞ technique not only offers the trade-off between performance and the control effort, but also compromises with the capability of stabilizing the plant disturbance. Such a control problem is called a performance robust problem. The content system is constructed by solving a mixture H^∞ norm minimization problem of sensitivity and complementary sensitivity functions. H^∞ control theory is applied to actively control the vibration of a multi-input and multi-output flexible rotor model to suppress spillover phenomena.

Robust Stabilization Problem. Generally, it is very difficult to identify the system parameters properly for a flexible rotor system with actuator dynamics. On the other hand, the control system is designed based on the reduced model that omits higher modes. For these reasons, it is necessary to know how the modeling errors might adversely affect the performance of control system. It is also necessary for the active rotor control system to have a strong robustness. The robust stability is studied using small gain theory. The well-known feedback system is shown in Fig. 2. Since $G(s)K(s)(I + G(s)K(s))^{-1}$ and Δ_m are assumed stable, based on the small gain theory, then the feedback perturbation system will remain internally stable under the multiplicative perturbation Δ_m if

$$\|\Delta_m[G(s)K(s)(I + G(s)K(s))^{-1}]\|_\infty < 1 \tag{20}$$

If the upper bound of $\Delta_m(s)$ is known, one can choose

$$\text{Sup } \bar{\sigma}\{\Delta_m(jw)\} \le W_3(jw) \tag{21}$$

Then the the sufficient condition for feedback perturbation system to be robustly stable can be expressed as follows:

$$\|W_3(s)T(s)\|_\infty < 1 \tag{22}$$

In Eq. (22), $T(s) = G(s)K(s)(I + G(s)K(s))^{-1}$ is the com-

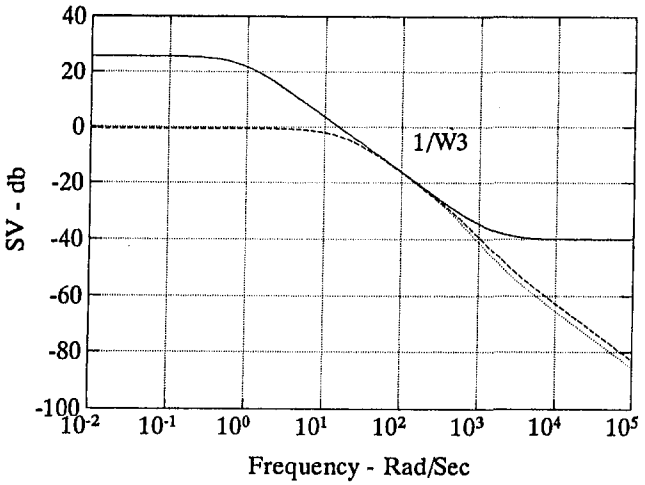

Fig. 10 Complementary sensitivity function and $W_3^{-1}(s)$ of H^∞ control design

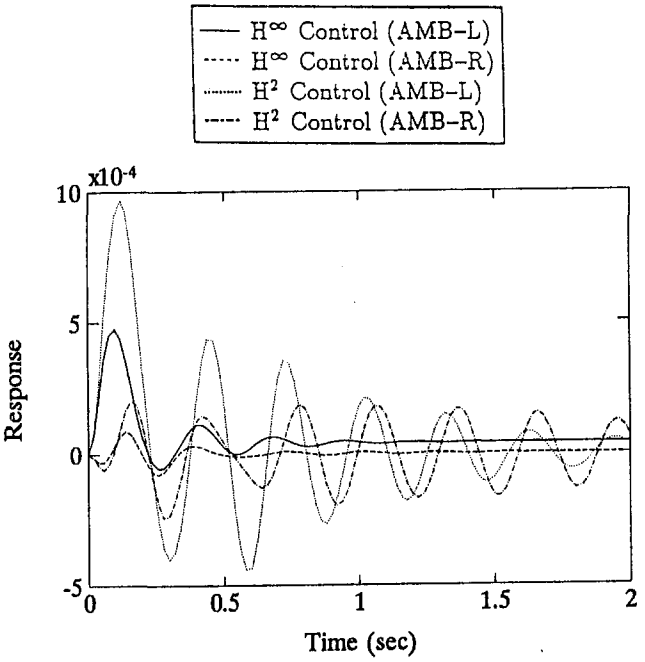

Fig. 11(a)

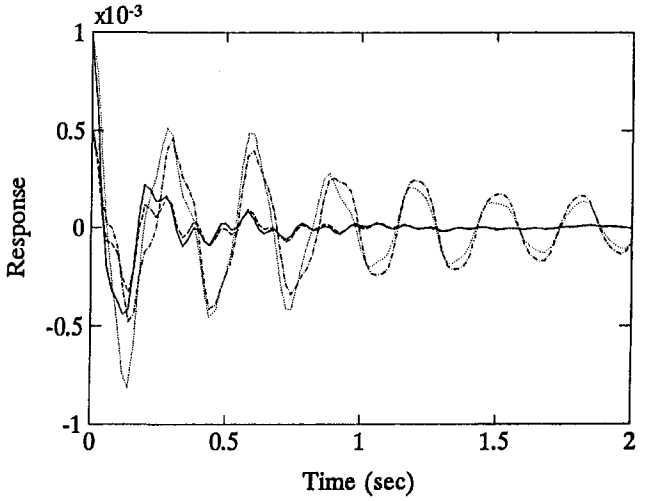

Fig. 11(b)

Fig. 11 Dynamic responses of the shaft at magnetic bearing positions using H^2 and H^∞ control design with two conditions: (*a*) step disturbance, (*b*) lift-off

plementary sensitivity function, and $W_3(s)$ the complementary sensitivity weighting function, defining the robustness specification. The smaller $T(s)$ is, the larger the allowable variation $\Delta_m(s)$ will be. This implies that better robust stability will be obtained.

Tracking Performance Problem. The problem of improving the response performance is to design a controller $K(s)$ to minimize $\|S(s)\|_\infty$ subject to the condition of stability of the closed-loop system for given plant $G(s)$. The sensitivity function $S(s)$ defines the gain of tracking error $e(s)$. For good tracking performance, the value of $\|S(s)\|_\infty$ must be very small within the bandwidth. Therefore, Sup $\bar{\sigma}\{S(jw)\}$ must be limited, and if the upper bound is chosen as $W_1^{-1}(s)$, i.e.,

$$\text{Sup } \bar{\sigma}\{S(jw)\} < W_1^{-1}(jw) \tag{23}$$

then

$$\|S(s)W_1(s)\|_\infty < 1 \tag{24}$$

where $W_1(s)$ is the sensitivity weighting function for tracking performance specification. From this discussion, if the functions of $W_1(s)S(s)$ and $W_3(s)T(s)$ are minimized simultaneously, the closed-loop system will be robustly stable and of good response performance. This is the mixed sensitivity problem with sufficient conditions to design a controller to satisfy

$$\left\| \begin{matrix} W_1(s)S(s) \\ W_3(s)T(s) \end{matrix} \right\|_\infty < 1 \tag{25}$$

Numerical Simulation

The primary purpose of this study is to design a controller based on the reduced order model of HM using H^∞ control theory. It is expected to prevent the flexible rotor instability with spillover phenomena.

A simple flexible rotor suspended by two active magnetic bearings, as shown in Fig. 3, is considered. The parameters of

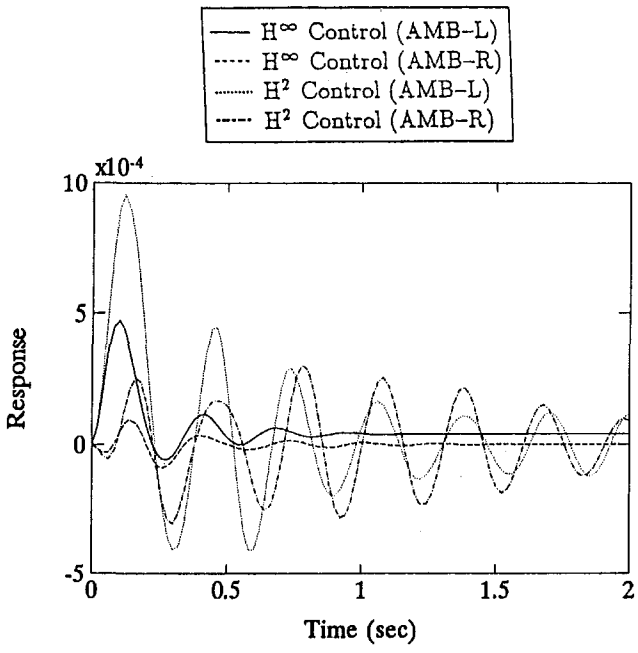

Fig. 12(a)

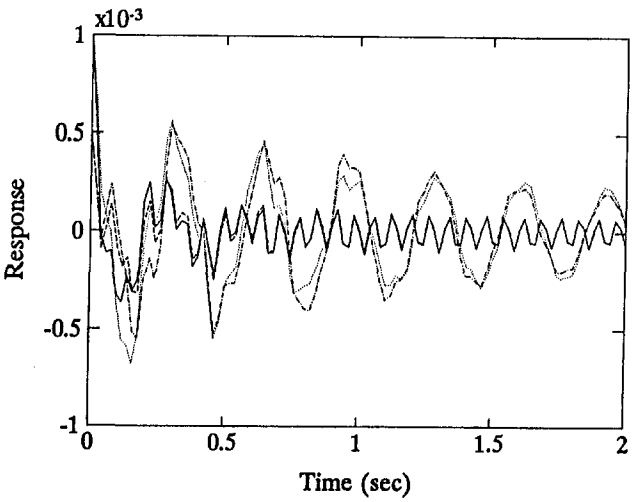

Fig. 12(b)

Fig. 12 Dynamic responses of the shaft at magnetic bearing positions with mass variation ($m_2 \rightarrow 2m_2$) using H^2 and H^∞ control design with two conditions: (*a*) step disturbance, (*b*) lift-off

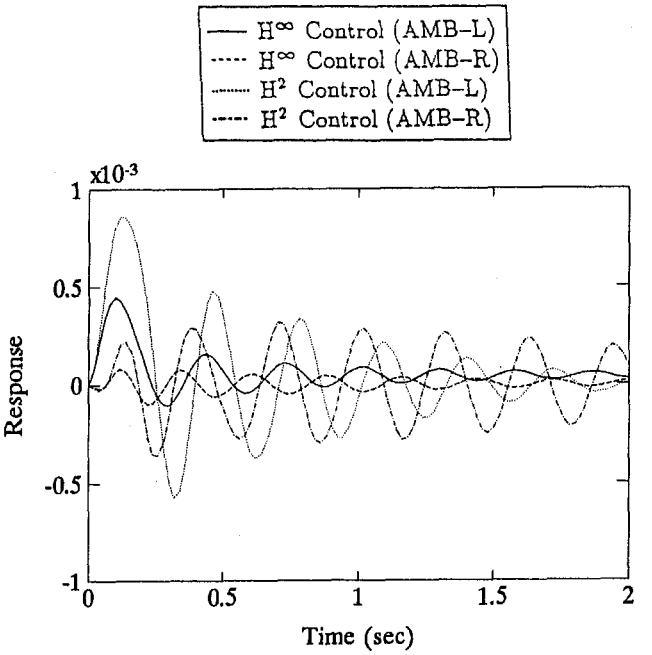

Fig. 13(a)

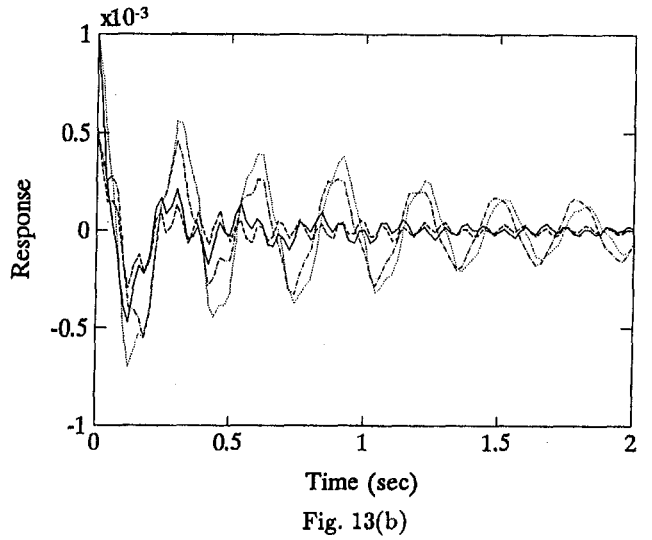

Fig. 13(b)

Fig. 13 Dynamic responses of the shaft at magnetic bearing positions with gyroscopic variation (Ω: 1000 rad/s → 2000 rad/s) using H^2 and H^∞ control design with two conditions: (*a*) step disturbance, (*b*) lift-off

the rotor system are listed in Table 1. The system is modeled with two elements and each nodal point is of four degrees of freedom. Figure 4 shows the unbalance response of the flexible rotor with unbalance 10^{-4} kg · m at the center disk for the consideration of gyroscopic effect and without gyroscopic effect. Because of the gyroscopic effect, it tends to stiffen the rotor in forward whirl and soften it in backward whirl, thus raising and lowering the critical speeds of the forward and backward modes, respectively. It is shown that the gyroscopic effects are more pronounced at high rotational speed. This study will concern H^∞ control design of flexible rotors with gyroscopic effects.

In order to include primary flexible modes, $N_p = 5$ for the GPEM model is chosen. The frequency responses for FEM and GPEM systems are shown in Fig. 5. It is shown that the lower modes obtained from the GPEM model are well compared to the FEM model. The frequency response of multiplicative uncertainty $\Delta_m(s)$ for the difference between FEM and GPEM is shown in Fig. 6. Suppose that the operation range for Ω is 0 rad/s to 2000 rad/s, and the design rotational speed for Ω is 1000 rad/s. The multiplicative uncertainty induced from gyroscopic effects by variation of rotational speed is plotted in Figs. 7 and 8. From Eq. (21), the weighting function $W_3(s)$ must be chosen as the envelope of $\Delta_m(s)$, which leads to

$$W_3(s) = \frac{100s + 80}{s + 1550} I_2, \quad W_1(s) = \frac{s + 1601}{100s + 85} I_2 \quad (26)$$

The design specifications for H^∞ control design based on a reduced model are to stabilize the unstable modes and to suppress spillover phenomena. From Figs. 9 and 10, it is found that the cost function of the mixed sensitivity problem shown in Eq. (25) is satisfied.

Two control design methods using H^∞ and H^2 theory are applied to simulate the response with disturbance or initial condition. Figures 11(*a*, *b*) show the response performance of a

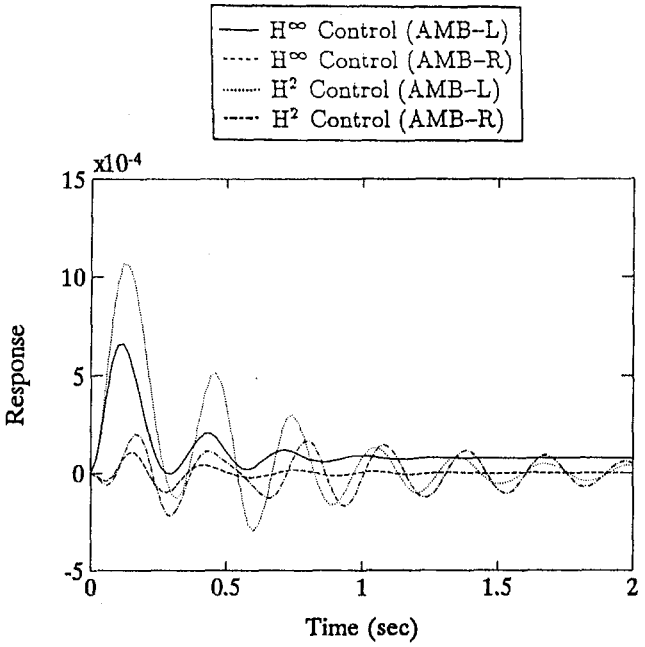

Fig. 14(a)

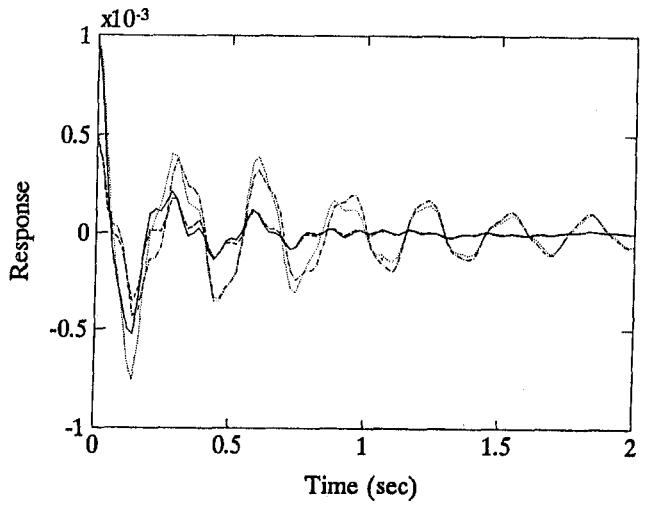

Fig. 14(b)

Fig. 14 Dynamic responses of the shaft at magnetic bearing positions with current stiffness variation ($K_i \rightarrow 0.5\ K_i$) using H^2 and H^∞ control design with two conditions: (*a*) step disturbance, (*b*) lift-off

closed-loop system due to step disturbance at the left magnetic bearing and the response of the initial displacement at lift-off, respectively. The initial values of the displacements are $V_l = 10^{-3}$ m and $V_r = 5 \times 10^{-4}$ m. It is found that the unstable modes are stabilized in both control design methods and the spillover phenomenon caused by the truncation of flexible modes does not occur. It implies that H^∞ design is more effective and powerful for the existence of $\Delta_m(s)$.

For the actual machines, it is of concern whether the effect of controller performance robustness gets to be worse with system parameter variations. Figures $12(a, b)$ show the responses due to step disturbance and lift-off, respectively, when the mass of the central disk becomes twofold. If the rotational speed Ω equals 2000 rad/s, the responses due to step disturbance and lift-off are shown in Figs. $13(a, b)$, respectively. The responses due to step disturbance and lift-off with current stiffness variation ($K_i \rightarrow 0.5\ K_i$) are shown in Figs. $14(a, b)$, respectively. The results show that H^∞ control has powerful robustness to system parameter variation, because the responses of the closed-loop system with different variations are almost the same.

As the results demonstrated by the example, GPEM is recommended to simplify the control task. From the viewpoint of robustness for suppressing the spillover phenomena and system parameter variation, the H^∞ control method is a useful and powerful control algorithm for the flexible rotor system with magnetic bearings.

Conclusions

The active vibration control of flexible rotor system with magnetic bearings has been investigated with the consideration of gyroscopic moment effect in this study. Using FEM together with GPEM, the flexible rotor can be modeled for small-order plants. The H^∞ control theory is applied to suppress the vibration of rotor system actively with spillover phenomena. The results can be summarized as follows:

1 The GPEM technique, which can greatly reduce the order of the rotor system, is employed to simplify the control design for flexible rotor system with magnetic bearings.
2 Because the controller design specification can be included in H^∞ control design to account for the effects of dynamic uncertainty, the suppression of spillover phenomena is very effective. The results show that the rotor system remains robustly stable with good performance under H^∞ control design based on the reduced-order model.
3 Since the system order can be greatly reduced using GPEM and many dynamic uncertainties can be taken into account in H^∞ control design, it is highly recommended to apply the GPEM together with H^∞ control theory to increase the performance of flexible rotor system with magnetic bearings.

References

Allaire, P. E., Lewis, D. W., and Jain, V. K., 1981, "Feedback Control of Single Mass Rotor on Rigid Supports," *Journal of Franklin Institute,* Vol. 312, pp. 1–11.

Allaire, P. E., Lewis, D. W., and Knight, J. D., 1983, "Active Vibration Control of a Single Mass Rotor on Flexible Supports," *Journal of Franklin Institute,* Vol. 315, pp. 211–222.

Cui, W. M., and Nonami, K., 1992, "H^∞ Control of Flexible Rotor–Magnetic Bearing Systems," presented at the The Third Symposium on Motion and Vibration Control, Japan.

Doyle, J. C., Glover, K., Khargonekar, P. P., and Francis, B. A., 1989, "State-Space Solutions to Standard H^2 and H^∞ Control Problems," IEEE *Transactions on Automatic Control,* Vol. 34, No. 8, pp. 832–847.

Doyle, J. C., Francis, B. A., and Tannenbaum, A. R., 1992, *Feedback Control Theory,* Macmillan Publishing Company.

Humphris, R. R., Kelm, R. D., Lewis, D. W., and Allaire, P. E., 1986, "Effect of Control Algorithms on Magnetic Journal Bearing Properties," ASME JOURNAL OF ENGINEERING FOR GAS TURBINES AND POWER, Vol. 108, pp. 625–632.

Nelson, H. D., and McVaugh, J. M., 1976, "The Dynamics of Rotor Bearing Systems Using Finite Elements," ASME *Journal of Engineering for Industry,* Vol. 98, pp. 593–600.

Nelson, H. D., 1980, "A Finite Rotating Shaft Element Using Timoshenko Beam Theory," ASME *Journal of Mechanical Design,* Vol. 102, pp. 793–803.

Nonami, K., Yamanaka, T., and Tominaga, M., 1990, "Vibration and Control of a Flexible Rotor Supported by Magnetic Bearings," JSME *International Journal,* Series III, Vol. 33, No. 4, pp. 475–482.

Nonami, K., Wang, J. W., Sampei, M., and Mita, T., 1991a, "Active Vibration Control of Flexible Rotor Using H^∞ Control Theory," *Rotating Machinery and Vehicle Dynamics,* ASME DE-Vol. 35, pp. 85–91.

Nonami, K., Wang, J. W., and Yamazaki, S., 1991b, "Spillover Control of Magnetic Levitation Systems Using H^∞ Control Theory," *Transactions of the Japan Society of Mechanical Engineers,* Series C, Vol. 57, No. 534, pp. 568–575.

Okada, Y., Nagai, B., and Shimane, T., 1992, "Cross-Feedback Stabilization of the Digitally Controlled Magnetic Bearing," ASME *Journal of Vibration and Acoustics,* Vol. 114.

Salm, J., and Schweitzer, G., 1984, "Modelling and Control of a Flexible Rotor With Magnetic Bearings," Third International Conference on Vibrations in Rotating Machinery, Institution of Mechanical Engineers, York, Paper No. c277/80.

Shiau, T. N., and Hwang, J. L., 1989, "A New Approach to the Dynamic Characteristic of Undamped Rotor Bearing System," ASME *Journal of Vibration, Acoustics, Stress, and Reliability in Design,* Vol. 111, pp. 379–385.

Shiau, T. N., and Hwang, J. L., 1993, "Generalized Polynomial Expansion Method for the Dynamic Analysis of Rotor Bearing System," ASME JOURNAL OF ENGINEERING FOR GAS TURBINES AND POWER, Vol. 115, pp. 209–217.

Stanway, R., and Burrows, C. R., 1981, "Active Vibration Control of a Flexible Rotor on Flexibly-Mounted Journal Bearings," ASME *Journal of Dynamic Systems, Measurement, and Control,* Vol. 103, pp. 383–388.

Zames, G., 1981, "Feedback and Optimal Sensitivity: Model Reference Transformations, Multiplicative Seminorms, and Appropriate Inverses," IEEE *Transaction on Automatic Control,* Vol. AC-23, pp. 301–320.

Multi-objective Optimization of a Flexible Rotor in Magnetic Bearings With Critical Speeds and Control Current Constraints

Ting Nung Shiau

Chun Pao Kuo

Department of Mechanical Engineering,
National Chung Cheng University,
Chia Yi, Taiwan

Jiunn Rong Hwang

Institute of Aeronautics and Astronautics,
National Cheng Kung University,
Tainan, Taiwan

This paper presents the single objective optimization and the multi-objective optimization for a flexible rotor system with magnetic bearings. The weight of rotor shaft and the transmitted forces at the magnetic bearings are minimized either individually or simultaneously under the constraints on the critical speeds and the control currents of magnetic bearings. The design variables are the cross-sectional area of the shaft, the bias currents of magnetic bearings, and the positions of the disk and the magnetic bearings. The dynamic characteristics are analyzed using the generalized polynomial expansion method and the sensitivity analysis is also studied. For single objective optimization, the method of feasible directions (MFD) is applied. For multi-objective optimization, the weighting method (WM), the goal programming method (GPM), and the fuzzy method (FM) are employed. It is found that the system design can be significantly affected by the choices of the bias currents of magnetic bearings, the position of the disk with unbalance, and the magnetic bearings. The results also show that a better compromised design can always be obtained for multi-objective optimization.

Introduction

The dynamic behavior of flexible rotor system with magnetic bearings has been investigated for over three decades. The feasibility of using magnetic bearings has been widely demonstrated. Many advantages over conventional bearings, such as oil-film and rolling-element types, are becoming apparent. Because of no contact, they require no lubricant and consume less power. Furthermore, they have manipulable stiffness and damping to cope with rotordynamic instability and imbalance sensitivity, which are common to rotating machinery. These characteristics lead the magnetic bearings to the status of practical engineering. The purpose of this study is to develop an efficient algorithm for the optimum design of flexible rotor system with magnetic bearings under critical speed constraints and control current constraints.

The optimization design of a structural system usually requires three steps. The first step is to analyze the system dynamic behavior. In the past, a variety of methods for the determination of the critical speeds, modes, and unbalance response of rotor-bearing systems have been successfully developed. These methods can be divided into two categories. The first is the discretization method, which models the rotor systems into many finite degrees of freedom, and two techniques are usually used: one is the state vector-matrix method (Myklestad, 1944; Prohl, 1945; Ruhl and Booker, 1972; Lund, 1974a, b), the other is the direct stiffness method (Nelson and McVaugh, 1976; Childs, 1978; Nelson, 1980; Adams, 1980; Childs and Gravis, 1982). The second is the analytical method (Gladwell and Bishop, 1959; Dimentberg, 1961; Eshleman and Eubanks, 1969), which models the rotor systems as distributed parameter systems. The former is described with a set of ordinary differential equations, and the latter a set of partial differential equations. The generalized polynomial expansion method (Shiau and Hwang, 1989, 1993), which has been shown of better merit compared with other methods, is employed to analyze the dynamic characteristics of the system.

The second step is to choose the design variables and the constraints. Some authors (Childs and Gravis, 1982; Shiau and Hwang, 1988, 1990; Shiau and Chang, 1993) have shown that the system parameters including the geometry of system, coefficients of bearings, inertia properties of rigid disk, and the distribution of the mass and stiffness of rotating assemblies have significant influence on the dynamic characteristics of a rotor-bearing system. It is important to choose the most effective parameters as the design variables and carry out the system sensitivity analysis. The sensitivity analysis has been investigated by Lund (1979), Fritzen and Nordman (1982), Rajan et al. (1986, 1987), Shiau and Hwang (1988, 1990), and Shiau and Chang (1993). The design variables considered in this paper include the cross-sectional area of shaft, the bearing stiffnesses, the positions of bearings and disks, and the bias currents of the magnetic bearings. The constraints on the system critical speeds as well as the control currents of magnetic bearings are employed.

The third step is to develop the redesign algorithm to achieve the optimum design stage. Both the single objective optimization and multi-objective optimization are considered in this study. In single objective optimization, the method of feasible direction (MFD) (Zoutendijk, 1960) is employed to perform the design. In multi-objective optimization, it is required to find a set of nondominated solutions (Duckstein, 1984). The weighting method (WM) (Chankong and Haimes, 1983), the goal programming method (GPM) (Krishnamurty and Turcic, 1987; Kaplan and Rao, 1987), and the fuzzy method (FM) (Wang and Wang, 1985; Rao, 1987) are employed to perform the design. Two examples are employed to demonstrate the merits of the present design algorithm.

Dynamic Analysis

A typical rotor-bearing system is shown in Fig. 1, which consists of disks, shaft elements with distributed mass and stiff-

Contributed by the International Gas Turbine Institute and presented at the 39th International Gas Turbine and Aeroengine Congress and Exposition, The Hague, The Netherlands, June 13–16, 1994. Manuscript received by the International Gas Turbine Institute February 26, 1994. Paper No. 94-GT-297. Associate Technical Editor: E. M. Greitzer.

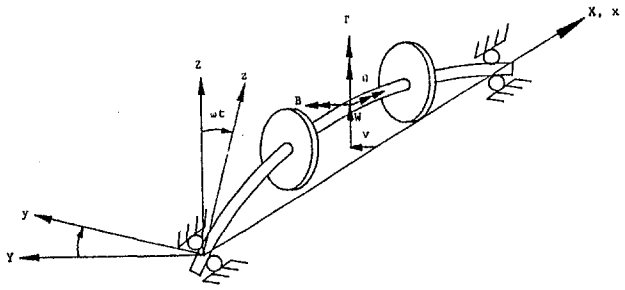

Fig. 1 Typical rotor configuration and coordinates

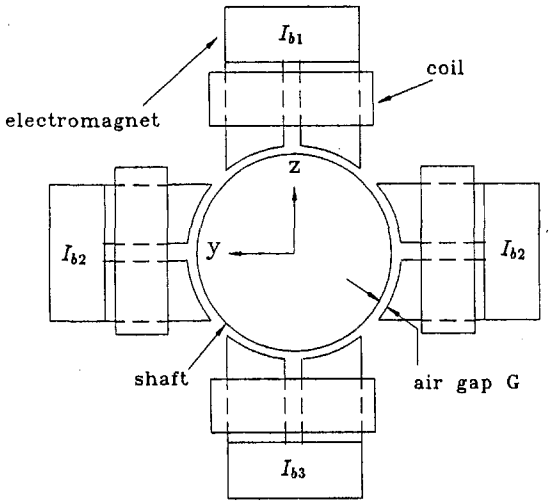

Fig. 2 Geometric configuration of magnetic bearing

ness, and discrete bearings. Two reference frames are adopted: one is the Newtonian reference frame $X-Y-Z$ and the other is rotating reference frame $x-y-z$. Both the X and x axes are collinear and coincident with the undeformed bearing centerline. The rotating frame rotates about the X axis with a whirl speed of ω.

The magnetic bearing considered in this study is shown in Fig. 2, and consists of four electromagnets. It is assumed that the force generated in the magnetic bearing is a nonlinear function of the current in the coils and the rotor displacements. The force of the jth magnetic bearing in the Z direction is of the following form (Maslen et al., 1989):

$$F_{zj} = f[(I_{b1} + i_z)/(G - Z)]^2 - f[(I_{b3} - i_z)/(G + Z)]^2 - W_g \quad (1)$$

where $f = \mu_o A_g N^2/2$ is a constant, $W_g = f(I_{b1}^2 - I_{b3}^2)/G^2$ is the static load, I_{b1}, I_{b3} are the bias currents of magnetic bearing, i_z is control current in the Z direction, G is air gap, μ_o is magnetic permeability of air, A_g is area of each air gap perpendicular to the magnetic flux, and N is number of coil turns per pole pair. For a magnetic bearing system with $Z \ll G$ and $i_z \ll I_{b1}$ and I_{b3}, Eq. (1) can be linearized as follow:

$$F_{zj} = K_{iz} i_z + K_{mz} Z \quad (2a)$$

where

$$K_{iz} = \frac{2f(I_{b1} + I_{b3})}{G^2} \quad (2b)$$

$$K_{mz} = \frac{2f(I_{b1}^2 + I_{b3}^2)}{G^3} \quad (2c)$$

Note that the net upward magnetic pull due to I_{b1} and I_{b3} balances the static load, W_g, in Eq. (1). In this study, the control current i_z is considered to be proportional to displacement Z and velocity $\dot{Z}$ as

$$i_z = -C_d Z - C_v \dot{Z} \quad (3)$$

where C_d and C_v are proportional constants. Substituting Eq. (3) into Eq. (2a), the force becomes:

$$F_{zj} = -C_v K_{iz} \dot{Z} - (C_d K_{iz} - K_{mz}) Z \quad (4)$$

Nomenclature

$a_n(t)$, $b_m(t)$ = generalized coordinates
A = cross-sectional area of the shaft
A_g = area of air gap perpendicular to the magnetic flux
$[C]$ = damping matrix of bearing
C_{yyj}^b, C_{zzj}^b = damping of the jth magnetic bearing
$e(x)$ = eccentricity of the shaft at position x
e_i^d = eccentricity of the ith disk
E = elastic modulus of the shaft
$F(\underline{X})$ = objective function
$\overline{F}_j^b$ = transmitted force at jth magnetic bearing
F_{yy}, F_{zz} = magnetic bearing force in the y, z directions
g_j = the jth constraint
$[G]$ = gyroscopic matrix
G = nominal air gap ($x = 0$)
i_y, i_z = control current in y, z directions, respectively
I_{b1}, I_{b2}, I_{b3} = coil bias currents
I_D, I_P = diametral and polar moment of inertia of the shaft per unit length
I_{Di}^d, I_{Pi}^d = diametral and polar moment of the ith disk
$[K_s]$ = stiffness matrix of shaft
K_{iy}, K_{iz} = current stiffness
K_{my}, K_{mz} = magnetic stiffness
K_{yyj}^b, K_{zzj}^b = stiffness of the jth magnetic bearing
l = total length of the shaft
l_i = length of the ith shaft element
$[M]$ = mass matrix
N = number of coil turns per pole pair
N_b, N_d, N_e = total number of disk, magnetic bearings, and shaft elements
N_o = number of objectives
N_P = number of polynomial terms
$\underline{Q}_f$, $\underline{Q}_b$ = magnitude of steady state forward and backward response
r_o, r_I = outer radius and inner radius of shaft element
T = total kinetic energy
U = total potential energy
V, W = translational displacement in Y and Z directions, respectively
$W(\underline{X})$ = total shaft weight
$\overline{W}_c$ = weight reduced coefficient
$X-Y-Z$ = fixed reference frame
$x-y-z$ = rotating reference frame
x_i^b, x_i^d = positions of the ith magnetic bearing and disk
B, Γ = angle rotations about Y, Z axes
μ_o = magnetic permeability of air
ρ = mass density per unit volume of the shaft
ω, Ω = whirl speed and spin speed
ω_n^c = the nth critical speed

Similarly, the magnetic force in the Y direction can be expressed as

$$F_{yj} = -C_v K_{iy}\dot{Y} - (C_d K_{iy} - K_{my})Y \tag{5a}$$

where

$$K_{iy} = \frac{4fI_{b2}}{G^2} \tag{5b}$$

$$K_{my} = \frac{4fI_{b2}^2}{G^3} \tag{5c}$$

Equations (4) and (5a) imply that the magnetic bearing is of damping constants $C^b_{yyj} = C_v K_{iy}$, $C^b_{zzj} = C_v K_{iz}$ and stiffness $K^b_{yyj} = C_d K_{iy} - K_{my}$, $K^b_{zzj} = C_d K_{iz} - K_{mz}$. These coefficients depend on the changes of constants C_d and C_v.

The dynamic behavior of flexible rotor systems with magnetic bearings are analyzed based on the following assumptions: (1) The shear effect of the flexible shaft is neglected; (2) the shaft with rigid disks attached is flexible and supported by the orthotropic bearings as well as magnetic bearings; (3) lateral displacements are so small that the deflections and forces are assumed in the $Y-Z$ plane; (4) torsional vibration and axial vibration are neglected. We consider the translational and rotational displacements of any cross section of the shaft, (V, W) and (B, Γ) which are expressed as functions of position along the rotating axis x and time t, i.e.

$$V = V(x, t), \quad W = W(x, t)$$
$$\mathrm{B} = \mathrm{B}(x, t), \quad \Gamma = \Gamma(x, t) \tag{6}$$

The rotations (B, Γ) are geometrically related to the translations (V, W) by the following equations:

$$\mathrm{B}(x, t) = -\frac{\partial W(x, t)}{\partial x}$$
$$\Gamma(x, t) = \frac{\partial V(x, t)}{\partial x} \tag{7}$$

To derive the equations of motion, the Lagrangian approach is employed. This requires the calculation of the kinetic and potential energies of the system. These energy functions can be expressed in terms of the displacements and their derivatives. The total kinetic energy (T) consists of the kinetic energy of shaft (T_s), the disk (T_d), and the eccentricity (T_e). Similarly, the total potential energy (U) have the components of the strain energy of the shaft (U_s) and the bearings (U_b). They are expressed as

$$T = T_s + T_d + T_e \tag{8a}$$

$$U = U_s + U_b, \tag{8b}$$

and the corresponding energy components are shown by Shiau and Hwang (1993). The dissipation function (F) due to bearing damping is given by

$$F = \sum_{j=1}^{N_b} \{\tfrac{1}{2} c^b_{yyj}\dot{V}_j^2 + \tfrac{1}{2} c^b_{zzj}\dot{W}_j^2 + c^b_{yzj}\dot{V}_j\dot{W}_j\} \tag{9}$$

The generalized polynomial expansion method (GPEM) (Shiau and Hwang, 1993), which describes the translations and the rotations as follows:

$$V(x, t) = \sum_{n=1}^{N_p} a_n(t)x^{n-1}$$
$$W(x, t) = \sum_{m=1}^{N_p} b_m(t)x^{m-1} \tag{10a}$$

$$\mathrm{B}(x, t) = -\frac{\partial W(x, t)}{\partial x} = -\sum_{m=2}^{N_p} (m-1)x^{m-2}b_m(t)$$
$$\Gamma(x, t) = \frac{\partial V(x, t)}{\partial x} = \sum_{n=2}^{N_p} (n-1)x^{n-2}a_n(t), \tag{10b}$$

is employed. The coefficients $a_n(t)$ and $b_m(t)$ are the generalized coordinates and the integer N_p is the number of polynomials.

Substituting Eqs. (10a) and (10b) and their derivatives into the total kinetic energy, potential energy, and dissipation energy and using the Lagrangian approach,

$$\frac{d}{dt}\frac{\partial}{\partial \dot{q}_i}(T-U) - \frac{\partial}{\partial q_i}(T-U) + \frac{\partial F}{\partial \dot{q}_i} = 0, \tag{11}$$

where the generalized coordinates q_i can be any of a_n or b_m with $n, m = 1, N_p$, the equations of motion may be expressed as follow for constant rotating speed:

$$\begin{pmatrix} M & 0 \\ 0 & M \end{pmatrix}\begin{pmatrix} \underline{\ddot{a}} \\ \underline{\ddot{b}} \end{pmatrix} + \Omega\begin{pmatrix} 0 & G \\ -G & 0 \end{pmatrix}\begin{pmatrix} \underline{\dot{a}} \\ \underline{\dot{b}} \end{pmatrix} + \begin{pmatrix} C_{yy} & C_{yz} \\ C_{zy} & C_{zz} \end{pmatrix}\begin{pmatrix} \underline{\dot{a}} \\ \underline{\dot{b}} \end{pmatrix}$$
$$+ \begin{pmatrix} K_s + K_{yy} & K_{yz} \\ K_{zy} & K_s + K_{zz} \end{pmatrix}\begin{pmatrix} \underline{a} \\ \underline{b} \end{pmatrix} = \begin{pmatrix} \underline{R}_a \\ \underline{R}_b \end{pmatrix} \tag{12}$$

where the $N_p \times 1$ vectors $\underline{a}$, $\underline{b}$, $\underline{R}_a$, and $\underline{R}_b$ are of the form

$$\underline{a} = \{a_1, a_2, \ldots, a_{N_p}\}^T$$
$$\underline{b} = \{b_1, b_2, \ldots, b_{N_p}\}^T \tag{13a}$$

$$\underline{R}_a = \{R_{a1}, R_{a2}, \ldots, R_{aN_p}\}^T$$
$$\underline{R}_b = \{R_{b1}, R_{b2}, \ldots, R_{bN_p}\}^T \tag{13b}$$

and the expressions of the $N_p \times N_p$ matrices M, G, C_{yy}, C_{yz}, C_{zz}, K_s, K_{yy}, K_{yz}, and K_{zz}, and the components of $\underline{R}_a$ and $\underline{R}_b$ are shown by Shiau and Hwang (1993).

For the simplicity and convenience, the $N_p \times 1$ complex vector $\underline{P}$ and its conjugate $\underline{\tilde{P}}$ are introduced, which are defined as

$$\underline{P} = \underline{a} + i\underline{b}$$
$$\underline{\tilde{P}} = \underline{a} - i\underline{b} \tag{14}$$

and the shaft is considered without eccentricity. Equation (12) can be rewritten as

$$[M]\underline{\ddot{P}} + ([C_1] - i\Omega[G])\underline{\dot{P}} + ([C_2] + i[C_{yz}])\underline{\dot{\tilde{P}}}$$
$$+ ([K_s] + [K_1])\underline{P} + ([K_2] + i[K_{yz}])\underline{\tilde{P}} = \underline{R}e^{i\Omega t} \tag{15}$$

where the $N_p \times N_p$ matrices $[K_1]$, $[K_2]$, $[C_1]$, and $[C_2]$ are all real and symmetric matrices and of the form

$$[K_1] = \tfrac{1}{2}([K_{yy}] + [K_{zz}]), \quad [K_2] = \tfrac{1}{2}([K_{yy}] - [K_{zz}])$$
$$[C_1] = \tfrac{1}{2}([C_{yy}] + [C_{zz}]), \quad [C_2] = \tfrac{1}{2}([C_{yy}] - [C_{zz}]) \tag{16a}$$

and the $N_p \times 1$ vector $\underline{R}$ is defined as

$$\underline{R} = \{R_1, R_2, \ldots, R_{N_p}\}^T \tag{16b}$$

where

$$R_j = \sum_{i=1}^{N_d} e_i^d m_i^d \Omega^2 e^{i\phi_i} x_i^{j-1}$$

The critical speeds of the damped system governed by Eq. (12) is calculated by neglecting the forcing terms. Defining $\underline{q} = \{\underline{d} \quad \dot{\underline{b}} \quad \underline{a} \quad \underline{b}\}^T$, Eq. (12) can be rewritten in the first-order form

$$[\bar{M}]\dot{\underline{q}} + [\bar{K}]\underline{q} = \{0\} \tag{17}$$

where

$$[\bar{M}] = \begin{pmatrix} [M] & 0 & 0 & 0 \\ 0 & [M] & 0 & 0 \\ 0 & 0 & [I] & 0 \\ 0 & 0 & 0 & [I] \end{pmatrix}$$

$$[\bar{K}] = \begin{pmatrix} [C_{yy}] & [C_{yz}] + \Omega[G] & [K_s] + [K_{yy}] & [K_{yz}] \\ [C_{zy}] - \Omega[G] & [C_{zz}] & [K_{zy}] & [K_s] + [K_{zz}] \\ -[I] & 0 & 0 & 0 \\ 0 & -[I] & 0 & 0 \end{pmatrix} \tag{18}$$

Let

$$\underline{q} = \underline{q}_0 e^{\sigma t} \tag{19}$$

where

$$\sigma = \alpha + i\omega \tag{20}$$

Substituting Eq. (19) into Eq. (17), we find

$$(\sigma[\bar{M}] + [\bar{K}])\underline{q}_0 = \{0\} \tag{21}$$

The critical speeds and corresponding mode shapes can be obtained by solving the eigenvalue problem for specified rotational speeds.

The steady-state unbalance response of the system governed by Eq. (15) can be assumed of the form

$$\underline{P} = \underline{Q}_f e^{i\Omega t} + \underline{Q}_b e^{-i\Omega t} \tag{22}$$

where $\underline{Q}_f$ and $\underline{Q}_b$ are complex vectors that describe the amplitude and phase of forward and backward circular motion, respectively. Substituting Eq. (22) into Eq. (15) yields:

$$\begin{aligned} [A_1]\underline{Q}_f + [B_1]\bar{\underline{Q}}_b &= \underline{R} \\ [A_2]\underline{Q}_b + [B_2]\bar{\underline{Q}}_f &= \underline{0} \end{aligned} \tag{23}$$

where the $N_p \times N_p$ matrices $[A_1]$, $[A_2]$, $[B_1]$, and $[B_2]$ are of the form

$$\begin{aligned} [A_1] &= -\Omega^2[M] + \Omega^2[G] + [K_s] + [K_1] + i\Omega[C_1] \\ [A_2] &= -\Omega^2[M] - \Omega^2[G] + [K_s] + [K_1] - i\Omega[C_1] \\ [B_1] &= [K_2] - \Omega[C_{yz}] + i([K_{yz}] + \Omega[C_2]) \\ [B_2] &= [K_2] + \Omega[C_{yz}] + i([K_{yz}] - \Omega[C_2]) \end{aligned} \tag{24}$$

Solving for $\underline{Q}_f$ and $\underline{Q}_b$ in Eq. (23) and combining Eqs. (22), (14), and (10a), one can obtain the translations (V, W) of the system.

With knowing the translational displacements, one can simply find the transmitted force at the jth magnetic bearing, which is of the form

$$\begin{aligned} F^b_{yyj} &= K^b_{yyj}V(x^b_j, t) + C^b_{yyj}\dot{V}(x^b_j, t) \\ F^b_{zzj} &= K^b_{zzj}W(x^b_j, t) + C^b_{zzj}\dot{W}(x^b_j, t) \end{aligned} \tag{25}$$

where F^b_{yyj} and F^b_{zzj} are the components of the transmitted force of the jth bearings in Y and Z direction, respectively.

Optimization Approach

The objective functions in this study, $\underline{F}(\underline{X})$, include the total weight of the shaft $W(\underline{X})$ and/or the transmitted forces through the jth magnetic bearings $\|F^b_j(\underline{X})\|$. Since the objective functions number more than one, the multiobjective optimization techniques are employed. The design variables, x_i, are chosen to be the most sensitive parameters. Since the cross-sectional area of the shaft is proportional to the weight of the shaft, and the bias currents of magnetic bearing play an important role in the change of the critical speeds and the transmitted forces through the magnetic bearings, they are taken as the system design variables. The positions of the disks and the bearings are also considered as the design variables to enlarge the design capability. The major design constraints of this problem include the constraints on critical speeds and control currents of magnetic bearings, and the side constraints. The reason for chosing the constraints on control currents is to ensure the satisfaction of $i \ll I_{bj}$.

The constraints on critical speeds can be expressed as

$$\begin{aligned} g_1(\underline{X}) &= \omega^c_{1F} - \frac{\Omega_{\text{low}}}{a_1} \le 0 \\ g_2(\underline{X}) &= a_2 \cdot \Omega_{\text{high}} - \omega^c_{2B} \le 0 \end{aligned} \tag{26}$$

where Ω_{low} and Ω_{high} are the lower and upper bounds of the operating speed range of the existent rotor system. The first forward and the second backward critical speeds are denoted by ω^c_{1F} and ω^c_{2B}, respectively. It should be noted that one can also choose ω^c_{2F} as the upper bound instead of ω^c_{2B}. The jth constraints, which describe the limitations on control currents of magnetic bearings, can be expressed as follows:

$$\begin{aligned} g_j(\underline{X}) &= i_{yl} - i_c \le 0 \quad j \in J \\ g_j(\underline{X}) &= i_{zl} - i_c \le 0 \quad j \in J \end{aligned} \tag{27}$$

where i_{yl} and i_{zl} are the control currents of the lth magnetic bearing along the Y axis and Z axis, respectively. The upper bound of the control current of magnetic bearing is denoted by i_c. The optimum design problem becomes

$$\text{Minimize: } W(\underline{X}) = \sum_{i=1}^{N_e} \rho_i l_i A_i$$

and/or

$$\|F^b_j(\underline{X})\|$$

Subject to:

$$\begin{aligned} g_1(\underline{X}) &= \omega^c_{1F} - \frac{\Omega_{\text{low}}}{a_1} \le 0 \\ g_2(\underline{X}) &= a_2 \cdot \Omega_{\text{high}} - \omega^c_{2B} \le 0 \\ g_j(\underline{X}) &= i_{yl} - i_c \le 0, \quad l = 1, N_b \\ g_j(\underline{X}) &= i_{zl} - i_c \le 0, \quad l = 1, N_b \end{aligned}$$

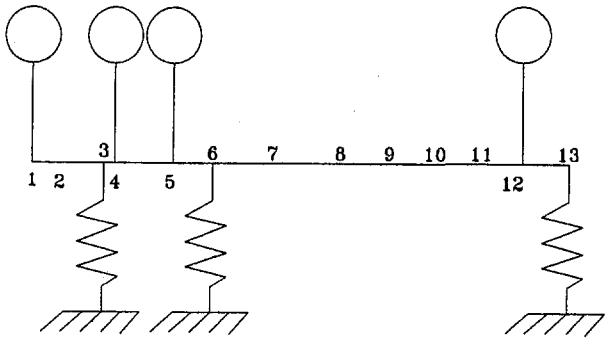

Fig. 3 Rotor model for Example 1

$$\underline{X} = \underline{X}_l = \{A_i, I_{bjk};\ i = 1, N_e, j = 1, 2, k = 1, N_b\}$$

$$\text{or} \quad \underline{X} = \underline{X}_l \cup \{x_l^b, x_m^d;\ l = 1, N_b, m = 1, N_d\}$$

$$x_i^l \le x_i \le x_i^u, \quad i = 1, n$$

where N_e, N_b, and N_d are the total number of shaft elements, the magnetic bearings, and the disks respectively. The total number of design variables is denoted by n. The rest of parameters are introduced in the nomenclature.

For the single objective optimization, the method of feasible direction (MFD) (Zoutendijk, 1960) is applied. For multi-objective optimization, the basic concept is to transform the vector optimization to a scalar optimization. Three methods including the Weighting Method (WM), the Goal Programming Method (GPM), and the Fuzzy Method (FM) are employed to perform the multi-objective optimization (Shiau and Chang, 1993).

Numerical Results and Discussion

Two examples are employed to demonstrate the merits of the design algorithm. The first example considers a single spool system with magnetic bearings located at stations 3, 6, and 13; see Fig. 3. The second example, as shown in Fig. 4, is a stepped rotor with magnetic bearings located at stations 11 and 15.

Example 1: In this example, the magnetic bearings are referred to as No. 1, No. 2, and No. 3, respectively. The shaft is divided into 12 elements, and the cross-sectional area of each element is uniform with outer radius fixed by 2.95 cm. Moreover, four disks with fixed masses are located at stations 1, 4, 5, and 12. The fourth disk is of unbalance 5×10^{-5} m. The rotating speed is 1500 rad/s. The details of rotor configuration are listed in Table 1. The constants a_1 and a_2, shown in Eq. (26), are chosen to be $a_1 = 1.2$, $a_2 = 1.3$, i.e., the first forward critical speed ω_{1F}^c is at least lower than Ω_{low} by a factor 1.2 while the second backward critical speed is at least 30 percent higher than Ω_{high}. The rotational speed range is given by $\Omega_{\text{low}} = 830.0$ rad/s and $\Omega_{\text{high}} = 1770.0$ rad/s. The constraint function of Eq. (26) can be rewritten as

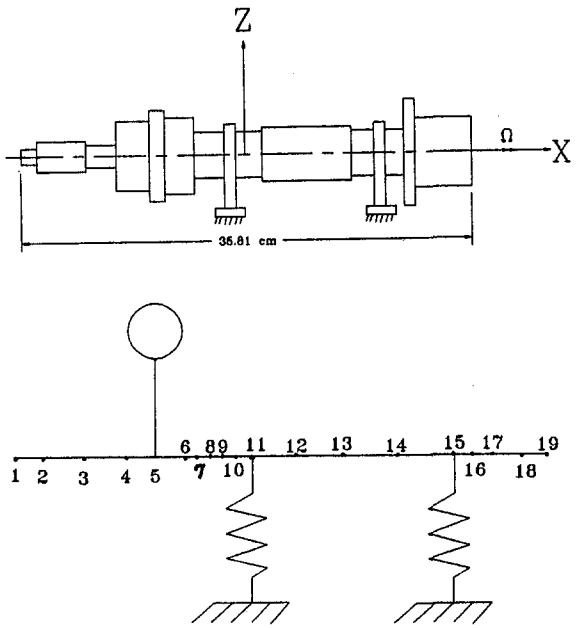

Fig. 4 System configuration and model for Example 2

Table 1 Initial configuration data of rotor system for Example 1

Element node no.	Node location (cm)	Bearing & disk	Outer radius (cm)	Inner radius (cm)
1	0.0	Disk No.1	2.95	1.882
2	4.29		2.95	1.940
3	8.89	Bearing No.1	2.95	1.466
4	10.49	Disk No.2	2.95	1.660
5	20.17	Disk No.3	2.95	2.151
6	27.69	Bearing No.2	2.95	2.690
7	44.20		2.95	2.690
8	59.44		2.95	2.690
9	74.68		2.95	2.690
10	89.92		2.95	2.690
11	105.16		2.95	1.420
12	120.14	Disk No.4	2.95	1.880
13	127.94	Bearing No.3		

Density = 8193.0 Kg/m^3 ; Elastic modulus = 2.069×10^{11} N/m^2

Disk :

	Location (cm)	Mass (Kg)	Polar inertia (Kg·cm^2)	Diametral inertia (Kg·cm^2)
No.1	0.0	11.38	0.1953	0.0982
No.2	10.49	7.88	0.1670	0.0835
No.3	20.17	7.70	0.1761	0.0880
No.4	120.14	21.70	0.4448	0.2224

Bearing :

	Location (cm)	I_{b1} (A)	I_{b2} (A)
No.1	8.89	21.0	21.0
No.2	27.69	16.0	16.0
No.3	127.94	20.0	20.0

$$g_1(\underline{X}) = \omega_{1F}^c - 691.67 \text{ rad/s} \le 0$$

$$g_2(\underline{X}) = 2301.00 \text{ rad/s} - \omega_{2B}^c \le 0 \qquad (28)$$

The constant, i_c shown in Eq. (27), is chosen as 0.6. Thus Eq. (27) can be rewritten as

$$g_3(\underline{X}) = i_{y1} - 0.6A \le 0; \quad g_6(\underline{X}) = i_{z2} - 0.6A \le 0$$

$$g_4(\underline{X}) = i_{z1} - 0.6A \le 0; \quad g_7(\underline{X}) = i_{y3} - 0.6A \le 0$$

$$g_5(\underline{X}) = i_{y2} - 0.6A \le 0; \quad g_8(\underline{X}) = i_{z3} - 0.6A \le 0$$

The side constraints are given by

$$1.42 \text{ cm} \le r_{Ii} \le 2.69 \text{ cm}, \quad i = 1, 12 \qquad (29a)$$

$$10.0A \le I_{bij} \le 21.0A, \quad i = 1, 3, j = 1, 2 \qquad (29b)$$

For magnetic bearing, the constants f, G, C_d, and C_v shown in Eqs. (1) and (3) are chosen to be $f = 0.0002$, $G = 0.001$, $C_d = 41000$, and $C_v = 0.3$. The computing system used in this study is a VAX-8600.

Table 2 Initial and final design of example 1 for different single objective designs

	Initial		Final					
Shaft			W		F_1^b		F_2^b	
Element	Inner Radius (cm)							
1	1.882		2.690		1.442		2.189	
2	1.940		2.589		1.420		1.420	
3	1.466		2.205		2.537		2.026	
4	1.660		2.021		2.690		2.690	
5	2.151		2.690		2.690		2.690	
6	2.690		2.690		2.690		2.690	
7	2.690		2.690		2.690		2.690	
8	2.690		2.690		2.667		2.690	
9	2.690		2.690		2.690		2.690	
10	2.690		2.690		2.690		2.690	
11	1.420		2.690		1.420		1.420	
12	1.880		2.690		1.420		1.420	
Magnetic	Bias Current (A)							
Bearing	I_{b1}	I_{b2}	I_{b1}	I_{b2}	I_{b1}	I_{b2}	I_{b1}	I_{b2}
1	21.0	21.0	21.0	21.0	21.0	19.8	21.0	20.8
2	16.0	16.0	15.6	15.6	17.0	17.1	16.5	18.2
3	20.0	20.0	20.4	20.4	20.4	20.4	20.0	20.0
	Critical Speed (rad/sec)							
ω_{1F}^c	992		611		654		656	
ω_{2B}^c	2397		2399		2398		2401	
Magnetic	Control Current (A)							
Bearing	i_y	i_z	i_y	i_z	i_y	i_z	i_y	i_z
1	0.08	0.08	0.04	0.04	0.03	0.03	0.03	0.03
2	0.13	0.13	0.11	0.11	0.09	0.09	0.09	0.09
3	0.0	0.0	0.0	0.0	0.03	0.03	0.03	0.03
	Shaft Weight (kg)							
W	10.235		5.081		9.159		8.791	
W_c			50.35%		10.51%		14.11%	
	Transmitted Force (N)							
F_1^b	681.4		358.8		232.5		234.9	
F_2^b	1023.8		858.1		716.4		714.0	
F_3^b	8.1		1.1		248.0		229.4	
$VAX-8600\ CPU(sec)$			1284		1149		1126	

Table 3 Initial and final design of Example 1 for multi-objective optimization design

Multiobjective: W and F_2^b								
	Initial		Final					
Shaft			WM		GPM		FM	
Element	Inner Radius (cm)							
1	1.882		2.690		2.690		2.690	
2	1.940		2.413		2.195		1.436	
3	1.466		2.023		2.348		1.680	
4	1.660		2.690		2.690		2.690	
5	2.151		2.690		2.690		2.690	
6	2.690		2.690		2.690		2.690	
7	2.690		2.690		2.690		2.690	
8	2.690		2.690		2.690		2.690	
9	2.690		2.690		2.690		2.690	
10	2.690		2.690		2.690		2.690	
11	1.420		2.690		2.690		2.690	
12	1.880		2.690		2.690		1.420	
Magnetic	Bias Current (A)							
Bearing	I_{b1}	I_{b2}	I_{b1}	I_{b2}	I_{b1}	I_{b2}	I_{b1}	I_{b2}
1	21.0	21.0	21.0	21.0	21.0	21.0	10.0	10.0
2	16.0	16.0	21.0	21.0	17.3	17.3	10.0	10.0
3	20.0	20.0	20.4	20.4	20.4	20.4	21.0	20.0
	Critical Speed (rad/sec)							
ω_{1F}^c	992		609		610		623	
ω_{2B}^c	2397		2400		2400		2350	
Magnetic	Control Current (A)							
Bearing	i_y	i_z	i_y	i_z	i_y	i_z	i_y	i_z
1	0.08	0.08	0.03	0.03	0.03	0.03	0.07	0.07
2	0.13	0.13	0.10	0.10	0.10	0.10	0.14	0.14
3	0.0	0.0	0.0	0.0	0.0	0.0	0.0	0.0
	Shaft Weight (kg)							
W	10.235		5.120		5.180		6.672	
W_c			49.92%		49.33%		34.81%	
	Transmitted Force (N)							
F_1^b	681.4		283.5		281.3		305.7	
F_2^b	1023.8		816.9		816.2		847.5	
F_3^b	8.1		17.4		18.7		12.7	
$VAX-8600\ CPU(sec)$			1101		1834		2468	

For the single objective optimization, the total weight of the shaft, the transmitted force of No. 1 magnetic bearing, and the transmitted force of No. 2 magnetic bearing are individually minimized. The method of feasible direction (MFD) is employed. The initial data and optimum results using the MFD for the three different objectives are shown in Table 2.

It shows that the individual objective can be significantly reduced and the optimum weight is less than that shown by Shiau and Chang (1993) for the conventional bearing case. This is because the bias currents of magnetic bearings have been added as the design variables. For the multi-objective optimization, the total weight of the shaft, the transmitted force of No. 1 magnetic bearing, and the transmitted force of No. 2 magnetic bearing are investigated. The design variables are chosen to be the cross-sectional area of each shaft element and the bias currents of No. 1 magnetic bearing and No. 2 magnetic bearing. Applying the weighting method (WM), the goal programming method (GPM), and the fuzzy method (FM), the optimum results shown in Tables 3 and 4. The results show that the total weight of the shaft, the transmitted force of No. 1 magnetic bearing, and the transmitted force of No. 2 magnetic bearing can be reduced simultaneously.

Example 2: The stepped rotor bearing system shown in Fig. 4 is considered. The magnetic bearings located at stations 11 and 15 are referred to as No. 1 and No. 2, respectively. The shaft is divided into 18 elements, and the cross-sectional areas are different. Moreover, one disk with fixed mass is located at station 5. The disk is of unbalance 1×10^{-4} m located on it. The rotating speed is 3000 rad/s. The details of the rotor configuration are listed in Table 5. The constants a_1 and a_2 are chosen to be $a_1 = 1.2$, $a_2 = 1.2$. The rotational speed range is given by $\Omega_{\text{low}} = 2400.0$ rad/s and $\Omega_{\text{high}} = 3500.0$ rad/s. Thus Eq. (26) can be rewritten as

$$g_1(\underline{X}) = \omega_{1F}^c - 2000.0 \text{ rad/s} \le 0$$

$$g_2(\underline{X}) = 4200.0 \text{ rad/s} - \omega_{2B}^c \le 0 \qquad (30a)$$

Table 4 Initial and final design of Example 1 for multi-objective optimization design

Multiobjective: W, F_1^b, and F_2^b								
	Initial		Final					
Shaft			WM		GPM		FM	
Element	Inner Radius (cm)							
1	1.882		2.690		2.670		2.688	
2	1.940		1.420		1.420		2.561	
3	1.466		1.420		2.690		2.558	
4	1.660		2.690		2.690		2.662	
5	2.151		2.690		2.690		2.690	
6	2.690		2.690		2.690		2.690	
7	2.690		2.690		2.690		2.690	
8	2.690		2.690		2.690		2.690	
9	2.690		2.690		2.690		2.690	
10	2.690		2.690		2.690		2.690	
11	1.420		1.420		2.690		1.476	
12	1.880		2.690		2.690		1.711	
Magnetic	Bias Current (A)							
Bearing	I_{b1}	I_{b2}	I_{b1}	I_{b2}	I_{b1}	I_{b2}	I_{b1}	I_{b2}
1	21.0	21.0	21.0	20.7	21.0	20.6	21.0	21.0
2	16.0	16.0	21.0	21.0	20.3	21.0	16.0	16.0
3	20.0	20.0	20.4	20.4	20.4	20.4	20.0	20.0
	Critical Speed (rad/sec)							
ω_{1F}^c	992		644		610		658	
ω_{2B}^c	2397		2493		2396		2326	
Magnetic	Control Current (A)							
Bearing	i_y	i_z	i_y	i_z	i_y	i_z	i_y	i_z
1	0.08	0.08	0.03	0.03	0.03	0.03	0.03	0.03
2	0.13	0.13	0.09	0.09	0.10	0.10	0.09	0.09
3	0.0	0.0	0.03	0.03	0.0	0.0	0.03	0.03
	Shaft Weight (kg)							
W	10.235		7.674		5.459		7.792	
W_c			25.02%		46.66%		23.87%	
	Transmitted Force (N)							
F_1^b	681.4		282.0		269.6		246.4	
F_2^b	1023.8		744.3		810.7		729.2	
F_3^b	8.1		240.5		18.6		217.8	
VAX-8600 CPU (sec)			601		3020		1846	

Table 5 Multi-stepped rotor configuration data for Example 2

Element node no.	Node location (cm)	Bearing & disk	Outer radius (cm)	Inner radius (cm)
1	-17.90		0.51	
2	-16.63		1.02	
3	-12.82		0.76	
4	-10.28		2.03	
5	-9.01	Disk No.1	2.03	1.52
6	-7.74		3.30	
7	-7.23		3.30	1.52
8	-6.47		2.54	1.78
9	-5.20		2.54	
10	-4.44		1.27	
11	-1.39	Bearing No.1	1.27	
12	1.15		1.52	0.52
13	4.96		1.52	0.52
14	8.77		1.27	
15	10.80	Bearing No.2	1.27	
16	12.58		3.81	
17	13.60		2.03	1.52
18	16.64		2.03	1.52
19	17.91			

Density = 7806.0 Kg/m^3 ; Elastic modulus = 2.078×10^{11} N/m^2

Disk :

	Location (cm)	Mass (Kg)	Polar inertia (Kg·m^2)	Diametral inertia (Kg·m^2)
No.1	-9.01	1.401	0.0020	0.00136

Bearing :

	Location (cm)	I_{b1} (A)	I_{b2} (A)
No.1	-1.39	6.0	6.0
No.2	10.80	6.0	6.0

The constant i_c shown in Eq. (27) is chosen as 0.6. Thus in this case, Eq. (27) can be rewritten as

$$g_3(\underline{X}) = i_{y1} - 0.6A \le 0; \quad g_5(\underline{X}) = i_{y2} - 0.6A \le 0$$

$$g_4(\underline{X}) = i_{z1} - 0.6A \le 0; \quad g_6(\underline{X}) = i_{z2} - 0.6A \le 0 \quad (30b)$$

The side constraints of design variables are given by

$$0.0 \text{ cm} \le r_{li} \le 0.31 \text{ cm}, \quad i = 1, 4$$

$$0.0 \text{ cm} \le r_{li} \le 1.83 \text{ cm}, \quad i = 5, 6$$

$$0.0 \text{ cm} \le r_{li} \le 2.34 \text{ cm}, \quad i = 7, 8$$

$$0.0 \text{ cm} \le r_{li} \le 1.07 \text{ cm}, \quad i = 9, 16$$

$$0.0 \text{ cm} \le r_{li} \le 1.83 \text{ cm}, \quad i = 17, 18 \quad (31a)$$

$$1.00 \text{ A} \le I_{bij} \le 15 \text{ A}, \quad i = 1, 2; \quad j = 1, 2$$

$$-4.44 \text{ cm} \le x_1^b \le 1.15 \text{ cm} \quad (31b)$$

$$8.77 \text{ cm} \le x_2^b \le 13.60 \text{ cm} \quad (31c)$$

$$-12.82 \text{ cm} \le x_1^d \le -6.47 \text{ cm} \quad (31d)$$

The behavior constraints stated by Eqs. (30a) and (30b) and the side constraints of Eqs. (31a) and (31b) are considered as the system constraints for case 1. For case 2, Eqs. (31c) and (31d) are added as the side constraints. For magnetic bearing, the constants f, G, C_d, and C_v shown in Eqs. (1) and (3) are chosen to be $f = 0.0001$, $G = 0.001$, $C_d = 20000$, and $C_v = 0.7$. The computing system used in this study is a VAX-8600.

For convenience, the coefficient W_ϵ is introduced, which is the percentage of weight saving, and is defined as

$$W_\epsilon = \frac{W_{in} - W_{opt}}{W_{in}} \times 100 \text{ percent} \quad (32)$$

where W_{in} is initial weight, and W_{opt} is optimum weight.

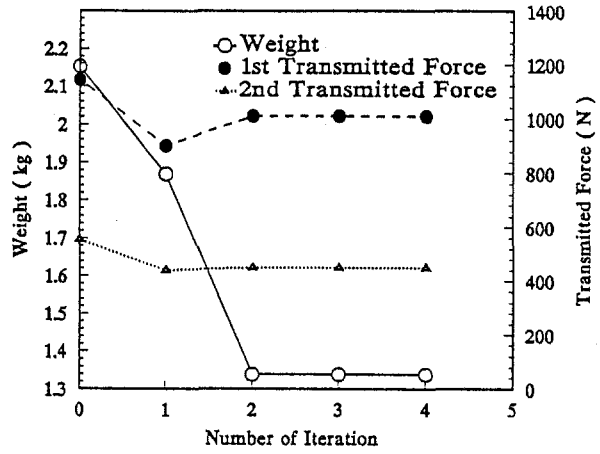

(5a)

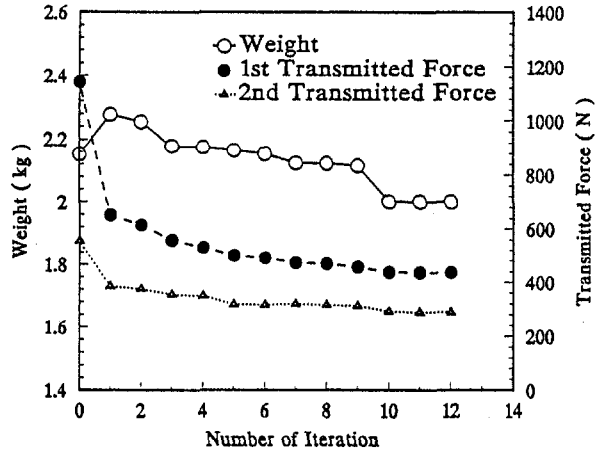

(5b)

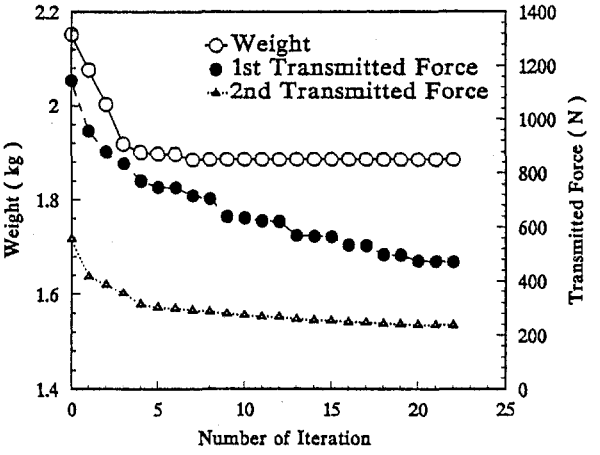

(5c)

Fig. 5 Design history of Example 2 for single objective: (*a*) total weight of the shaft; (*b*) transmitted force of No. 1 magnetic bearing; (*c*) transmitted force of No. 2 magnetic bearing

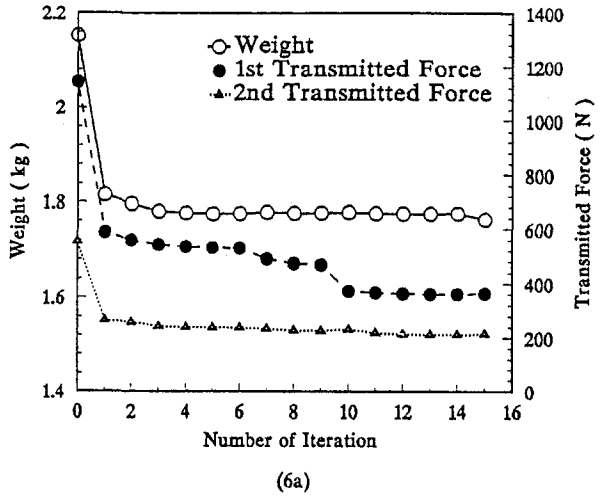

(6a)

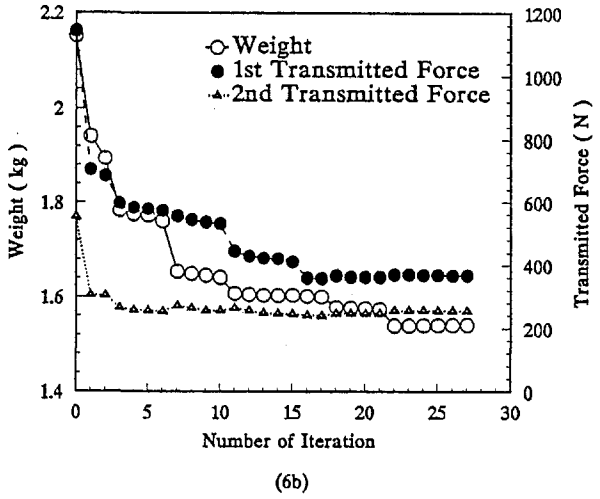

(6b)

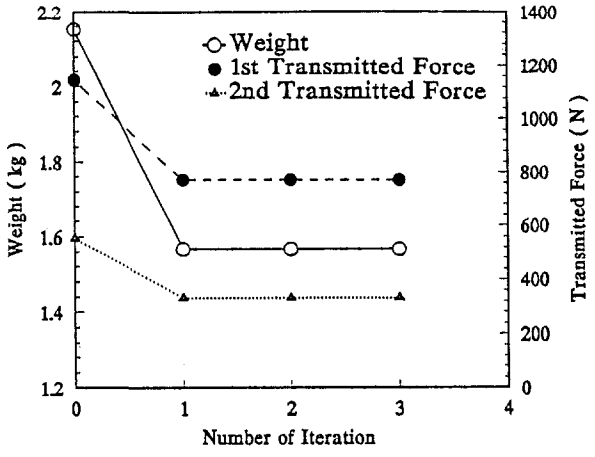

(6c)

Fig. 6 Design history of Example 2 for multi-objective optimization: (*a*) Weighting Method (WM); (*b*) Goal Programming Method (GPM); (*c*) Fuzzy Method (FM)

(*i*) *Case 1.* In this example, the total weight of the shaft, the transmitted force of No. 1 magnetic bearing, and the transmitted force of No. 2 magnetic bearing is individually considered as the objective function. The design history for the weight minimization case is given in Fig. 5(*a*). It is noted that the transmitted forces of No. 1 and No. 2 magnetic bearings can be also reduced when the total weight of the shaft is minimized.

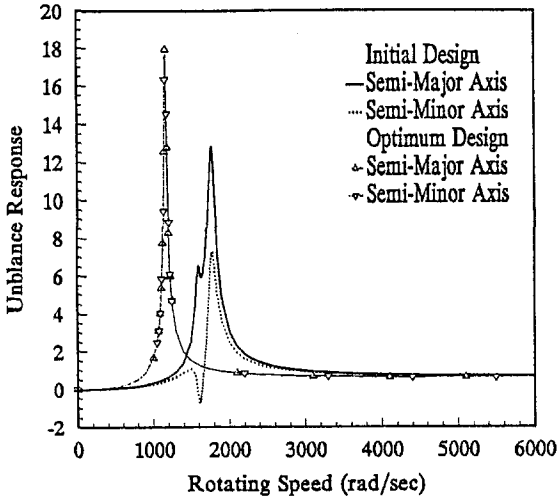

Fig. 7 Unbalance response of initial design and optimum design with mass eccentricity 1×10^{-4} m for Example 2

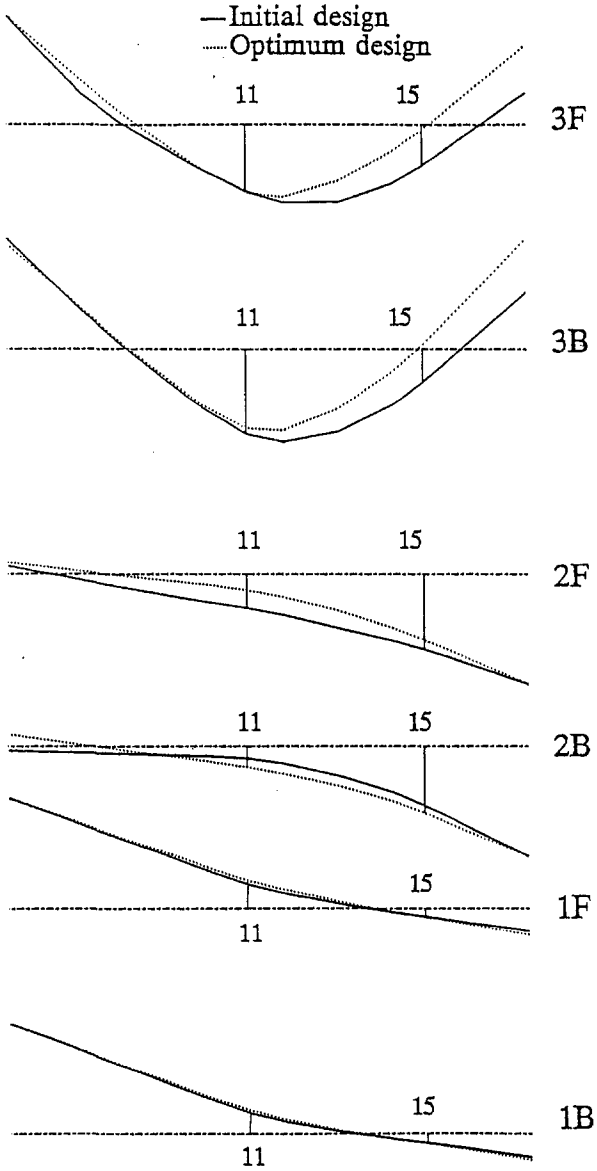

Fig. 8 Mode shapes of initial design and optimum design for Example 2

Figures 5(b) and 5(c) show the design histories of single objective with the minimization of transmitted force at No. 1 and No. 2 magnetic bearings, respectively. For multi-objective optimization, the total weight of the shaft, the transmitted forces at No. 1 and No. 2 magnetic bearings are simultaneously considered as objectives. The design variables are chosen to be the cross-sectional area of each shaft element, the bias currents of No. 1 and No. 2 magnetic bearings. By applying the weighting method (WM), the goal programming method (GPM), and the fuzzy method (FM), the objectives can be reduced and the design histories of using these methods are shown in Figs. 6(a–c). The results indicate that the optimum inner radius of shaft elements for multi-objective optimization are larger than those of weight minimization case but smaller than those of minimization of transmitted force. However, the final bias currents of magnetic bearing for multi-objective optimization are smaller than that of weight minimization case. It also indicates that the total weight of the shaft, and the transmitted forces at No. 1 and No. 2 magnetic bearings can be simultaneously reduced. For the weighting method, the transmitted forces of two magnetic bearings are smaller than the other two methods. For the goal programming method, the total weight of the shaft is smaller than the other two methods. For the fuzzy method, the CPU time is much smaller than the other two methods. These imply that the choice of multi-objective optimization technique is case dependent.

The unbalance responses of initial and optimum design using the Weighting Method are shown in Fig. 7. The results indicate that the response obtained from the optimum design is larger than the initial design. The mode shapes of initial and optimum design using the Weighting Method are shown in Fig. 8.

(ii) *Case 2.* The positions of the magnetic bearings and of the disk are added to be design variables. For the single objective optimization, a comparison between case 1 and case 2 is given by Table 6. For weight minimization case, the optimum weight equals 1.339 kg. For the other two objectives, the final objective values in case 2 are much smaller than the final objective values in case 1. This implies that the adding of the positions of the disks and of the magnetic bearings as design variables give more flexibilities of the design.

For the multi-objective optimization, a comparison of the results for case 1 and case 2 is given by Table 7. The optimum results shown in case 2 are much smaller than those of case 1, especially for the Weighting Method. This implies that the positions of the disks and of the magnetic bearings can significantly affect the system design.

Conclusions

In this study, the Generalized Polynomial Expansion Method is employed to perform the dynamic analysis of flexible rotor systems with magnetic bearings. Both the single objective optimization and multi-objective optimization are studied. The objective functions include the total weight of the shaft, and/or the transmitted forces of No. 1 and No. 2 magnetic bearings. The behavior constraints are the limitations on the critical speeds and control currents of No. 1 and No. 2 magnetic bearings. The design variables are the cross-sectional areas of shaft elements, the bias currents and positions of magnetic bearings, as well as disk positions. The method of feasible direction (MFD) is applied to achieve the optimal design for single objective optimization. For multi-objective optimization, the techniques of the Weighting Method, the Goal Programming Method, and the Fuzzy Method are employed.

Three examples are employed to demonstrate the efficiency and accuracy of present algorithm. The results are summarized as follows:

1 The bias currents of magnetic bearings can significantly affect the system dynamic behaviors. The choice of bias currents as design variables is suggested.
2 For single objective optimization, the total weight of the shaft can be considerably reduced with a little decrease of transmitted forces. However, the transmitted force can be reduced a lot with slight decrease of the total weight of the shaft.
3 To reduce the total weight of the shaft and the transmitted forces of two magnetic bearings simultaneously, the multi-objective optimization is applied. The results show that a better compromised design can be always obtained. It is also found that the system design can be significantly affected by the choices of the positions of disk with unbalance, and of the magnetic bearings with the minimization of transmitted forces considered, as well as the bias currents of magnetic bearings.

Table 6 Comparison of single objective optimization with different design values for Example 2

	Initial	Final		
		W	F_1^b	F_2^b
	Shaft Weight (kg)			
W^*	2.152	1.339	2.001	1.886
W^{**}	2.152	1.339	1.806	2.017
W_ϵ^*		37.8%	7.0%	12.4%
W_ϵ^{**}		37.8%	16.1%	6.3%
	Transmitted Force (N)			
F_1^{b*}	1143.1	1009.0	435.3	470.9
F_1^{b**}	1143.1	956.5	122.5	379.9
F_2^{b*}	554.0	450.3	288.5	236.7
F_2^{b**}	554.0	437.2	296.1	56.3
$VAX-8600\ CPU^*\ (sec)$		609	2149	4126
$VAX-8600\ CPU^{**}\ (sec)$		710	9054	4670

* Design Variable: r_{il} and l_{bij}
** Design Variable: r_{il}, l_{bij}, x_j^b, and x^d

Table 7 Comparison of multiobjective optimization with different design values for Example 2

	Initial	Final		
		WM	GPM	FM
	Shaft Weight (kg)			
W^*	2.152	1.763	1.541	1.567
W^{**}	2.152	1.351	1.465	1.561
W_ϵ^*		18.0%	28.4%	27.2%
W_ϵ^{**}		37.2%	31.9%	27.5%
	Transmitted Force (N)			
F_1^{b*}	1143.1	364.2	368.0	771.4
F_1^{b**}	1143.1	227.3	263.3	679.6
F_2^{b*}	554.0	214.8	254.6	332.5
F_2^{b**}	554.0	96.5	119.8	274.0
$VAX-8600\ CPU^*\ (sec)$		2964	5146	450
$VAX-8600\ CPU^{**}\ (sec)$		4298	2644	611

* Design Variable: r_{il} and l_{bij}
** Design Variable: r_{il}, l_{bij}, x_j^b, and x^d

References

Adams, M. L., 1980, "Nonlinear Dynamics of Flexible Multi-Bearing Rotors," *Journal of Sound and Vibration,* Vol. 71(1), pp. 129–144.

Chankong, V., and Haimes, Y. Y., 1983, *Multiobjective Decision Making: Theory and Methodology,* North-Holland.

Childs, D. W., 1978, "The Space Shuttle Main Engine High-Pressure Fuel Turbopump Rotor Dynamic Instability Problem," ASME JOURNAL OF ENGINEERING FOR POWER, Vol. 100, pp. 48–57.

Childs, D. W., and Gravis, K., 1982, "A Note on Critical-Speed Solutions for Finite-Element-Based Rotor Models," *Journal of Mechanical Design,* Vol. 104, No. 1, pp. 412–415.

Dimentberg, F. M., 1961, *Flexural Vibrations of Rotating Shafts,* Butterworth, London.

Duckstein, L., 1984, *Multiobjective Optimization in Structural Design: The Model Choice Problem,* Wiley, New York.

Eshleman, R. L., and Eubanks, R. A., 1969, "On the Critical Speeds of a Continuous Rotor," ASME *Journal of Engineering for Industry,* Vol. 91, pp. 1180–1188.

Fritzen, C. P., and Nordman, R., 1982, "Influence of Parameter Changes to Stability Behavior of Rotor," NASA Conference Publication 2250, *Rotor-Dynamic Instability Problems in High-Performance Turbomachinery,* Texas A & M Univ., College Station, pp. 284–297.

Gladwell, G. M. L., and Bishop, R. E. D., 1959, "The Vibration of Rotating Shafts Supported in Flexible Bearings," *Journal of Mechanical Engineering Science,* Vol. 1, pp. 195–206.

Kaplan, R. L., and Rao, S. S., 1987, "Nonlinear Goal Programming Techniques in the Synthesis of Mechanism," *Proc. ASME Design Automation Conference,* pp. 173–180.

Krishnamurty, S., and Turcic, D. A., 1987, "Nonlinear Goal Programming Techniques in the Synthesis of Mechanism," *Proc. ASME Design Automation Conference,* pp. 173–180.

Lund, J. W., 1974a, "Stability and Damped Critical Speeds of a Flexible Rotor in Fluid-Film Bearings," ASME *Journal of Engineering for Industry,* Vol. 96, pp. 509–517.

Lund, J. W., 1974b, "Modal Response of a Flexible Rotor in Fluid-Film Bearings," ASME *Journal of Engineering for Industry,* Vol. 96, pp. 525–533.

Lund, J. W., 1979, "Sensitivity of the Critical Speeds of a Rotor to Changes in Design," ASME *Journal of Mechanical Design,* Vol. 102, pp. 115–121.

Maslen, E., Hermann, P., Scott, M., and Humphris, R. R., 1989, "Practical Limits to the Performance of Magnetic Bearings: Peak Force, Slew Rate, and Displacement Sensitivity," ASME *Journal of Tribology,* Vol. 111, pp. 331–336.

Myklestad, N. O., 1944, "A New Method of Calculating Natural Modes of Uncoupled Bending Vibration of Airplane Wings and Other Types of Beams," *Journal of Aeronautical Science,* pp. 153–162.

Nelson, H. D., and McVaugh, J. M., 1976, "The Dynamics of Rotor-Bearing Systems Using Finite Elements," ASME *Journal of Engineering for Industry,* Vol. 98, pp. 593–600.

Nelson, H. D., 1980, "A Finite Rotating Shaft Element Using Timoshenko Beam Theory," ASME *Journal of Mechanical Design,* Vol. 102, pp. 793–803.

Prohl, M. A., 1945, "A General Method for Calculating Critical Speeds of Flexible Rotors," ASME *Journal of Applied Mechanics,* Vol. 12, pp. A-142-A-148.

Rajan, M., Nelson, H. D., and Chen, W. J., 1986, "Parameter Sensitivity in Dynamics of Rotor-Bearing Systems," ASME *Journal of Vibration, Acoustics, Stress, and Reliability in Design,* Vol. 108, pp. 197–206.

Rajan, M., Rajan, A. D., Nelson, H. D., and Chen, W. J., 1987, "Optimal Placement of Critical Speed in Rotor Bearing System," ASME *Journal of Vibration, Acoustics, Stress, and Reliability in Design,* Vol. 109, pp. 152–157.

Rao, S. S., 1987, "Multiobjective Optimization of Fuzzy Structure Systems," *Int. J. for Num. Methods in Engineering,* Vol. 24, pp. 1157–1171.

Ruhl, R. L., and Booker, J. F., 1972, "A Finite Element Model for Distributed Parameters Turborotor Systems," ASME *Journal of Engineering for Industry,* Vol. 94, pp. 128–132.

Shiau, T. N., and Hwang, J. L., 1988, "Minimum Weight Design of a Rotor Bearing System With Multiple Frequency Constraints," ASME JOURNAL OF ENGINEERING FOR GAS TURBINES AND POWER, Vol. 110, No. 4, pp. 592–599.

Shiau, T. N., and Hwang, J. L., 1989, "A New Approach to the Dynamic Characteristic of Undamped Rotor Bearing Systems," ASME *Journal of Vibration, Acoustics, Stress, and Reliability in Design,* Vol. 111, pp. 379–385.

Shiau, T. N., and Hwang, J. L., 1990, "Optimum Weight Design of a Rotor Bearing System With Dynamic Behavior Constraints," ASME JOURNAL OF ENGINEERING FOR GAS TURBINES AND POWER, Vol. 112, pp. 454–462.

Shiau, T. N., and Chang, J. R., 1993, "Multiobjective Optimization of Rotor Bearing System with Critical Speeds Constraints," ASME JOURNAL OF ENGINEERING FOR GAS TURBINES AND POWER, Vol. 115, pp. 246–255.

Shiau, T. N., and Hwang, J. L., 1993, "Generalized Polynomial Expansion Method for the Dynamic Analysis of Rotor Bearing System," ASME JOURNAL OF ENGINEERING FOR GAS TURBINES AND POWER, Vol. 115, pp. 209–217.

Wang, G. Y., and Wang, W. Q., 1985, "Fuzzy Optimum Design of Structures," *Eng. Opt.,* Vol. 8, pp. 291–300.

Zoutendijk, G., 1960, *Methods of Feasible Directions,* Elsevier, Amsterdam.

An Evaluation of Indentation and Finishing Properties of Bearing Grade Silicon Nitrides

J. F. Dill
Mechanical Technology Inc.,
Latham, NY 12110

M. N. Gardos
Hughes Aircraft Co.,
El Segundo, CA 90245

R. G. Hardisty
Spheric Engineering Ltd.,
Crawley, West Sussex, United Kingdom

This paper describes the results of studies of the machining performance and the indentation hardness and fracture toughness of different silicon nitride materials as part of an effort to better define the optimum machining conditions for bearing components. This work builds on prior efforts by two of the authors, Gardos and Hardisty (1993) who formulated a simple relationship between diamond grinding performance of silicon nitride bearing balls and a wear equation first detailed by Evans and Wilshaw (1976). The goal of this present work was to determine the general applicability of such a relationship, i.e., could simple indentation studies be used to define finishing conditions for different silicon nitride materials? The availability of such a simple test would reduce the time required for developing an acceptable process when a supplier changes his formulation, or when a new material becomes available. Quicker development of optimum finishing conditions would eventually result in a lower-cost product for users. The initial study by Gardos and Hardisty (1993) was based on limited data taken at a fixed set of conditions. This study expanded the range of conditions evaluated and the number of ceramic materials studied in an effort to define the universality of the relationship between grinding wear, hardness, and toughness. This study has shown that no simple relationship like that first envisioned by the authors exists. The results showed that the grinding wear of the individual silicon nitride materials increased at different rates as a function of load. Because of the differences found in the load dependence of grinding rates, no simple relationship between hardness, fracture toughness, and grinding rate could be found that fit the data over the range of conditions studied. This work is part of an ARPA funded effort to provide a tribological performance database on ceramic-bearing materials, including their grinding and finishing properties, and their interaction with standard bearing steels.

Introduction

One issue in the manufacturing of high-quality bearing balls from silicon nitride that faces a ball finisher is that each ceramic supplier produces its own composition of material. Consequently, the properties of those materials that can perform acceptably in a bearing vary sufficiently that the finishing process can differ widely for acceptable bearing grade silicon nitride materials from different suppliers, much like different types of bearing steels (M-50, 52100, 440C) differ in their finishing processes. Under an ARPA Bearing Technology Program, MTI, Hughes Aircraft, and Spheric Engineering have been investigating whether indentation measurements of fracture toughness and hardness could be used to provide guidance on the finishing properties and therefore the machine setup parameters for materials with differing properties.

While each silicon nitride studied has the potential to perform well in a bearing application, the optimum ball manufacturing process will differ significantly depending on the specific properties of the ceramic. As shown by Gardos and Hardisty (1993), the polishing rate of the ceramic ball blank material at a fixed set of conditions can vary by at least a factor of three among known acceptable silicon nitride materials. If those fixed conditions are the optimum one for both materials, obviously a formulation that can be finished in one third the time would be favored. On the other hand, if by changing conditions the relative processing rate of the two materials changes substantially, the selection of the best material formulation is less clear cut.

The purpose of the study reported here was to provide a more controlled, in-depth investigation and analysis of the machining properties of bearing grade ceramics in a ball finishing type of operation than the previous work. The present studies have involved two baseline bearing production materials, Toshiba TSN-03H and Norton Advanced Ceramics NBD-200, along with a third experimental material from CERCOM designated PSG-H. When this entire ARPA program is completed, the results will be published in a Hybrid Bearing User's Guide along with specifications for the testing of ceramic bearing materials. This paper will present the results of the ball finishing studies to date and discuss the implications of those studies in overall ball manufacturing.

Work conducted at Hughes Aircraft involved detailed studies of the fracture toughness and hardness of the silicon nitride materials using carefully controlled indentation techniques. Spheric Engineering, a commercial ceramic ball finisher, evaluated wear rates in the finishing process as a function of load using a specially instrumented ball finishing machine. The Hughes and Spheric data were then reviewed and analyzed by MTI, and comparisons were made with the previous work. MTI was also responsible for the procurement and control of the samples. All materials were supplied blind to Hughes and Spheric and access to each other's interim results was restricted until all data were complete.

Indentation Studies of Fracture Toughness and Hardness

In the original ball finishing work of Gardos and Hardisty (1993), indentation measurements were made by R. Cundill of

Contributed by the International Gas Turbine Institute and presented at the 40th International Gas Turbine and Aeroengine Congress and Exhibition, Houston, Texas, June 5–8, 1995. Manuscript received by the International Gas Turbine Institute March 18, 1995. Paper No. 95-GT-389. Associate Technical Editor: C. J. Russo.

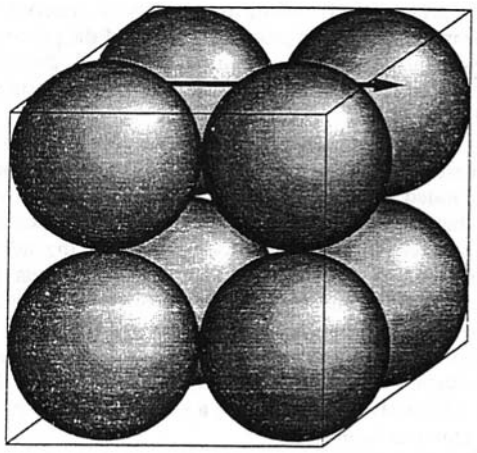

Fig. 1 Ball mounting configuration

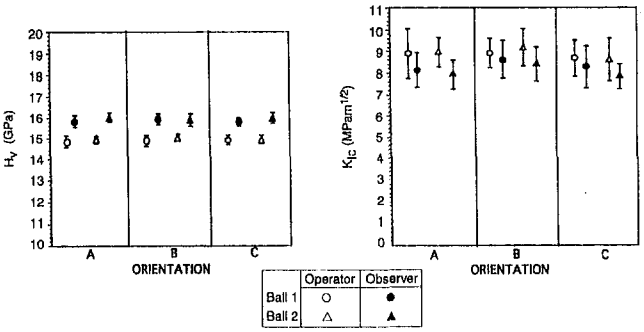

Fig. 2 Operator effects on indentation results

SKF Engineering Research Center. In the current study a series of measurements was made on each test material by operators from CERCOM (who were trained by SKF in their procedure) and from Hughes Aircraft (who had expertise in indentation studies of ceramic materials). The indentation procedure used was identical to the process first developed by SKF specifically for bearing grade silicon nitride. Two operators were used for the indentation measurements to evaluate the reproducibility in the values obtained between the two operators using the same apparatus. Further studies are under way to evaluate the comparison between hardness and fracture toughness values from a second indentation machine at Hughes Aircraft with those measured at CERCOM to assess site-to-site variability of results using a standard procedure.

To insure hard mounting of the samples and provide an ability to evaluate whether microstructural variations existed either in individual balls or from one ball to another, a group of eight ball blanks from each material were mounted against each other in a cube configuration as shown in Fig. 1. These balls were then encased in plastic, which was color coded to maintain traceability. The cubes of balls were ground flat such that the bulk material on each ball blank was exposed on three sides of the cubes with sufficient plastic remaining to hold the balls in place. Once the ball blanks were ground to basic size, the surfaces were carefully polished to remove any possible damage from the grinding process and to provide the proper surface finish for the indentation studies.

Indentation values of K_{Ic} and H_v are sensitive to a number of factors including the operator, the equipment, the load, the atmospheric environment (humidity in particular), and the use or non-use of a dye penetrant to highlight the cracks produced. In addition to these experimental factors, the absolute values calculated will depend on which equation is used in the analysis. At least four different methods are commonly used for analyzing indentation data on silicon nitride. While the equation used will change the absolute values, it will not generally change the relative values. A note of caution: Silicon nitride materials suppliers in fact use different techniques for measuring and calculating their values of K_{Ic} and H_v, making direct comparison of manufacturer supplied values of these quantities difficult. One justification for this study of indentation properties was that data from suppliers could not be used reliably to compare and analyze the machining results.

The general form of the equation for calculating fracture toughness, which is the primary variable of interest in these studies, takes the form of:

$$K_{Ic} = X(P/c^{1.5})$$

where P is the indentation load, c is the crack extension, and X is a calibration factor, which varies depending on the equation selected for the analysis. For this study a calibration factor developed by SKF (R. Cundill, private communication) specifically for bearing-grade silicon nitrides was used. The value of this calibration factor is:

$$X = 0.305\ (E/H_v)^{0.4}$$

where E is the elastic modulus of the material and H_v is the Vickers hardness calculated from the indentation.

Previous indentation studies on bearing grade silicon nitride materials have shown that K_{Ic} reaches a steady-state value at a 5 kg indentation load while for some materials H_v may continue to change up to a 10 kg load. In the present work a 5 kg indentation load was used. Further work is planned to investigate the load effects on indentation measurements in silicon nitride. For statistical purposes, a total of five indentations were made by each operator. A comparison of the measured values reflects a consistent, although small difference in the hardness and fracture toughness values determined by the two operators. The results of the measurements of hardness and fracture toughness for the two operators are presented graphically in Fig. 2 and tabularly in Table 1.

Ball Finishing Studies

The ball finishing process used by Spheric and other ball finishers involves the lapping of rough balls (or ball blanks) between grooved plates using loose abrasive. Depending on the size of the ball, and quantity, lapping plates with single or multiple grooves are used. Plate diameters range from a few inches for single groove finishing of small balls to approximately four feet for multigroove finishing of large balls. The number of balls in a machine load can also vary from ten to several million in steel ball finishing.

Table 1 Indentation measurement results

Supplier/ Matl I.D.	Vickers Hardness (GPa) by Source			Fracture Toughness [MPa(m)$^{0.5}$] by Source		
	Supplier	CERCOM	Hughes	Supplier Value/Rank	CERCOM Value/Rank	Hughes Value/Rank
Toshiba / TSN-03H	14.78*	15.41	15.59	6.75* / 1	8.50 / 1	7.13 / 2
CERCOM / PSG-H	14.51**	14.83	15.41	5.28** / 2	6.37 / 3	6.09 / 3
CERBEC / NBD-200	15.48***	16.09	16.30	4.70*** / 3	7.64 / 2	7.15 / 1

* Niihara Method, 20Kg load, 30 sec. dwell time
** 1 Kg load per ASTM C849 for microhardness,
5 Kg load using A.G. Evans equation per ASTM STP 678.
*** Hardness Per ASTM E92, Fracture Toughness Per Indentation Anstis Calculation (10kg Load, 10 Sec. dwell)

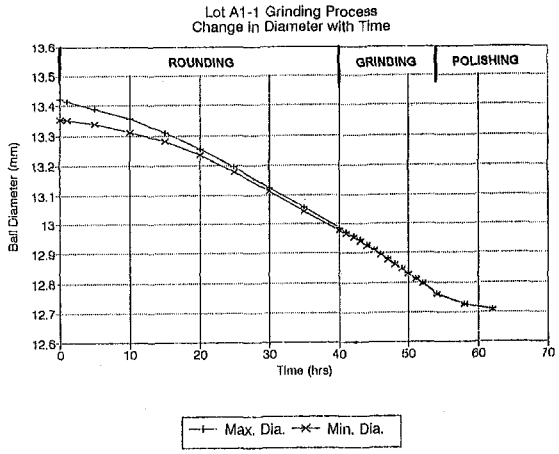

Fig. 3 Grinding rate data for TSN-03H

A single groove finishing machine was selected for these finishing studies because it requires a manageable number of balls, and because every ball undergoes the same process since they all cycle in the same groove. This type of machine is an ideal research vehicle and was used essentially unchanged for the prior studies by Gardos and Hardisty (1993). To permit evaluation of the bearing performance of the balls produced in this ball processing research, a decision was made to use 0.5-in.-dia balls as test samples since this is the standard ball size used in the NTN Bower RCF test for evaluating the rolling contact fatigue and wear properties of steel and ceramic bearing materials. While this size ball is presently on the large size end of the primary industrial market for ceramic balls, the use of a standard test was considered a significant benefit. Furthermore, the fundamental results on ball finishing should not be affected by the ball size. The selection of a 0.5-in.-dia ball also permitted a direct comparison of the results obtained during this more controlled study with those of the initial Hughes study, which also used 0.5-in.-dia balls.

In the ball finishing process, the bottom plate in the standard machine is rotated by a drive motor while the top plate remains static. A load is applied to the top plate via a spring, allowing the top plate to "float" while remaining under load. Abrasive is normally applied manually at predetermined intervals and lubricant is applied by drip feed. Neither the lubricant nor the abrasive are recycled in an effort to prevent contamination.

The production process to make a finished ball from a rough blank can be divided into three different stages as shown in Fig. 3. These include:

- Rounding: During this portion of the process the sizes of the blanks are equalized and the majority of the sphericity error is removed.
- Grinding: During this portion of the process the ball size is reduced from the blank size to very close to the final desired ball size. While this step is generally described as grinding, it is a lapping process as are all elements of the ball finishing process. The term grinding is used to describe the fact that the majority of material removal occurs at this stage. During this portion of the process the sphericity, ball size, and ball size variation are all improved to a point where only minor changes are needed in the final polishing process to achieve the final desired ball grade.
- Polishing: During this portion of the process, the primary emphasis is on achieving the desired final surface finish on the balls. Small improvements may also be made in the sphericity and size to achieve the desired final ball grade, but in general the amount of material removal is very small during the final polishing steps.

For the present study, all measurements of material removal rate were made during the grinding portion of the process where the ball size and sphericity variations are small; thus the measurements could be related to an overall rate of uniform material removal from the ball surface.

A single groove finishing machine was modified to provide better process controls for the finishing studies; the modifications included improved speed control, reduced vibration through better mounting and isolation of the machines, improved load control and monitoring through the addition of pneumatic load cylinders for load application and load cells for load measurement, and computer control of both the abrasive and lubricant addition amount and timing. To insure that the machine modifications didn't affect the basic process, the instrumented machines were checked by running several loads of Toshiba TSN-03H balls for which a known standard production process exists at Spheric.

Cast iron machine plates and a light hydrocarbon oil were used for all tests. A diamond abrasive of 45 μm grit size was used for the rounding and grinding processes. A 1 μm grit size was used for the finishing process. The first set of tests evaluated the grinding rate for each material under the same set of fixed load conditions used in the previous study. A total of three machine loads of each material were evaluated at the standard conditions. The second set of tests evaluated the effect of load on the grinding process while keeping the variables of speed, lubricant, and abrasive addition fixed. Load was the primary variable since it is known to have the most significant influence on the processing time. To provide the best comparison between the different materials, the process was also standardized by recutting the v-grooves in the plates to the same condition at the start of each test.

A typical result of the finishing rate studies for TSN-03H at the standard conditions of 1 kg/ball load on the single groove machine is shown in Fig. 3. To measure finishing rates, the machine was stopped at regular intervals during the process. All of the balls were removed from the machine, cleaned, and inspected dimensionally. Once the balls were measured, they were returned to the machine with new abrasive and lubricant additions. The measurement of grinding rate was made by a linear fit to the data points during the grinding process.

The dependence of material removal rates on load for Toshiba TSN-03H, CERBEC NBD-200 and CERCOM PSG-H is depicted in Fig. 4. The new wear rate values are within 10 percent of the previous measurements at 1 kg/ball load for TSN-03H and CERBEC NBD-200. A detailed discussion of these load-dependent results is given in the next section.

Comparison of Results

As shown in Fig. 5, when the wear rate data from the finishing studies at 1 kg/ball load are combined with the new Hughes

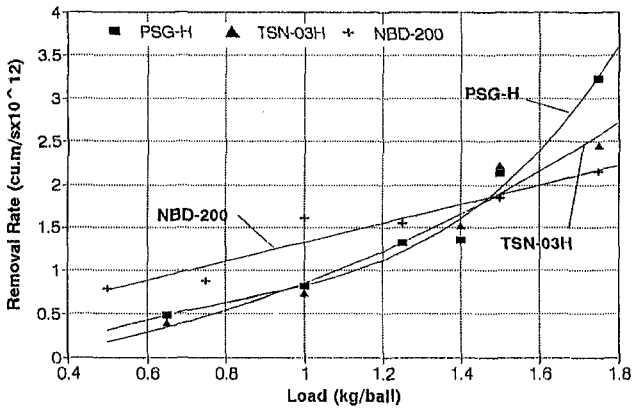

Fig. 4 Load dependence of material removal rates

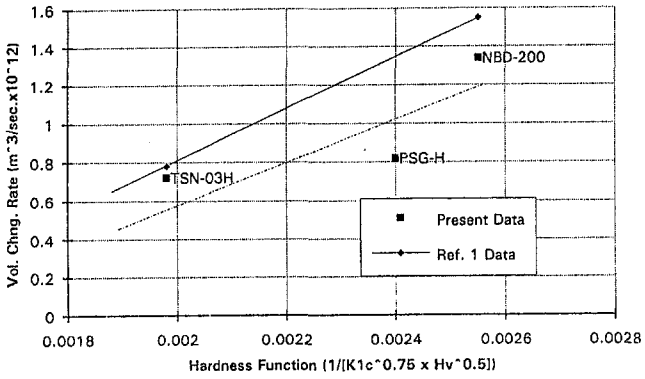

Fig. 5 Fit of grinding rate data at 1 kg/ball load to Evans–Wilshaw function

data for K_{Ic} and H_v, a plot very similar to that reported in the 1993 study is achieved. Both the original data and the results of this study are included in the figure for comparison.

Despite the close agreement between the new data and the old data at 1 kg/ball load, a similar set of curves cannot be generated for other loads. As can be seen in Fig. 4, the different materials exhibit significantly different grinding rate behavior as a function of load. The NBD-200 material from Norton Advanced Ceramics showed a nearly linear dependence of grinding rate with load. In contrast, the other silicon nitrides from Toshiba and CERCOM, exhibited a nonlinear dependence of grinding rate on load. The grinding rate for Norton's material was two times that of the Toshiba material at 1 kg/ball. At 1.5 kg/ball the rates were approximately equal and at 1.75 kg/ball load the Toshiba grinding rate was approximately 10 percent higher than that of the Norton material. Further study of a wider range of material microstructures and material removal rates are needed if correlations between composition and finishing behavior are to be established.

The results of this study clearly indicate that a simple Evans–Wilshaw type model for the grinding rate is not adequate since the nature of the relationship changes depending on load. At low loads, the Evans–Wilshaw hardness–toughness grinding rate relationship like that reported by Gardos and Hardisty was obtained. At midrange loads, the grinding rate was the same for materials with significantly different physical properties and finally at the highest loads, the materials with higher fracture toughness (as measured by indentation methods) exhibited the highest rather than the lowest grinding rates. Clearly a more complex model needs to be developed for the grinding process.

In the present study, the measurements of K_{Ic} and H_v were made at a single set of fixed conditions. However, it is known that for some silicon nitride materials the values obtained will depend on the indentation load. Further investigation of the load dependence of the indentation properties will be evaluated to determine whether they can be used to understand the grinding rate results phenomenologically. It seems unlikely that a direct correlation can be made between the load dependence of such macroscopic measurements of hardness and fracture toughness and the details of the microscopic materials processes that are involved in the ball grinding process. Such data, however, may be very useful for determining the best load regime to use for ball grinding and polishing steps.

Conclusions

A number of conclusions can be drawn from the ball finishing load dependence results and about the utility of measurements of indentation studies of fracture toughness and hardness for defining the basic finishing characteristics for a given silicon nitride bearing material:

- The simple correlation of grinding rate to the Evans–Wilshaw factor does not apply. The original results seem to be a fortuitous result of the load per ball selected for the study.
- It is unlikely that any simple correlation can be found between physical properties and grinding rate of silicon nitride materials that differ in composition and structure.
- Further study into whether there is a correlation between the load dependence of the grinding rate and the composition of the silicon nitride could be a fruitful avenue for evaluation. The two silicon nitrides with similar chemistry and glassy phase content (Toshiba TSN-03H, and CERCOM PSG-H with roughly 10 percent of Al_2O_3/Y_2O_3 based glassy phase) behaved relatively similarly, while the only ceramic studied with a MgO binder and a lower level of glassy phase (roughly 5 percent) exhibited very different behavior. Evaluation of a wider range of silicon nitride formulations would be needed to determine if a grouping of behavior can be made by composition.
- The increase in grinding rate of the Al_2O_3/Y_2O_3 binder materials is reminiscent of the load sensitivity of the wear rates of these materials observed previously in rolling contact fatigue testing by Dill (1996). More detailed materials evaluation studies of the material removal processes in these two cases are needed to determine if there is any relationship to the rolling contact fatigue versus load behavior.
- The use of a single groove finishing machine for establishing grinding and polishing conditions for ball processing on new materials may be of benefit prior to finishing large multigroove loads of these expensive materials. The single groove finishing rates proved to be very reproducible from load to load when the process was well controlled.

Acknowledgments

The efforts described in this paper are based on data funded by ARPA as part of their Ceramic Bearing Technology Initiative. The MTI/ARPA Ceramic Bearing Technology Program is technically monitored by Mr. Karl Mecklenburg of the Air Force Materials Laboratory at Wright Patterson Air Force Base and managed by Dr. William Coblenz of ARPA/MSD.

References

Dill, J. F., 1996, "Hybrid Bearing Technology for Advanced Turbomachinery: Rolling Contact Fatigue Testing," ASME JOURNAL OF ENGINEERING FOR GAS TURBINES AND POWER, Vol. 118, pp. 173–178.

Evans, A. G., and Wilshaw, T. R., 1976, "Quasi-Static Particle Damage of Brittle Solids—I. Observations, Analysis and Implications," *Acta Metallurgica,* Vol. 24, pp. 939–956.

Gardos, M. N., and Hardisty, R. G., 1993, "Fracture Toughness- and Hardness-Dependent Polishing Wear of Silicon Nitride Ceramics," *STLE Tribology Transactions,* Vol. 36, No. 4, pp. 652–660.

K. C. Liu

C. R. Brinkman

Metals and Ceramics Division,
Oak Ridge National Laboratory,
Oak Ridge, TN 37831

J.-L. Ding

S.-B. Lin

Department of Mechanical
and Materials Engineering,
Washington State University,
Pullman, WA 99164

Predictions of Tensile Behavior and Strengths of a Si_3N_4 Ceramic at High Temperatures Based on a Viscoplastic Model

Tensile deformation and rupture behavior were simulated using a viscoplastic model developed recently. The model was formulated based on the state variable approach, which provides flexibility and versatility for characterizing the time-dependent behavior of ceramic materials under general thermomechanical loading conditions. Simulations portrayed by the model were compared with experimental tensile data obtained under two different tensile stressing rates. Results showed that the model was capable of simulating deformation behavior for all practical engineering purposes, but estimated high-temperature fracture strengths somewhat conservatively.

Introduction

Existing engineering design methods can treat time-dependent material behavior such as creep in the design and analysis of ceramic structural components. However, life prediction and reliability estimation are implemented with poststructural analysis data, using a Weibull-based statistical model (Cuccio et al., 1994). Loading history dependency and viscoplastic effects on structural performance of ceramic components at high temperature are often simplified or ignored as minor details due to the lack of appropriate provisions in the existing design analysis techniques.

Deformation and rupture behavior of ceramic materials such as silicon nitride (Si_3N_4) at high temperatures are generally sensitive to loading or stressing rate. The sensitivity is attributed to the viscous behavior of an amorphous intergranular second-phase material used as a densification aid in the fabrication process. In tensile testing at low temperatures, most ceramic materials behave as elastic solids. At high temperatures, the materials may still behave elastically if stressing rate is sufficiently high. However, the range of elastic response decreases and inelastic deformation becomes discernible before rupture occurs as stressing rate decreases. A viscoplastic model (Ding et al., 1994a) was developed recently for use in characterizing creep and creep rupture behavior of a grade of Si_3N_4 ceramic material, commercially known as GN-10 Si_3N_4,[1] subjected to general thermomechanical loading conditions.

This paper demonstrates that the model, by the nature of the formulation methodology known as the state variable approach (Rice, 1971), is capable of predicting the time-dependent viscoplastic behavior in uniaxial monotonic tension (also known as dynamic fatigue behavior in the ceramic industries), ultimate tensile rupture strength, and rupture time. Comparisons are made between predictions and experimental data obtained at elevated temperatures using different stressing rates, and results are discussed.

Viscoplastic Model

A refined model (Ding et al., 1994b) capable of predicting both creep deformation and creep rupture life was developed based on creep data obtained for GN-10 Si_3N_4, using the state variable approach. Besides the inelastic strain variable (ϵ), the model employs two state variables, namely, a hardening variable (δ) and a damage variable (ω) to characterize the current mechanical state of the material. The model consists of three equations in a rate form as shown in the following. Equation (1) is a flow rule that describes the inelastic strain rate ($\dot{\epsilon}$) as a function of the hardening variable, applied stress (σ), and temperature (T); Eqs. (2) and (3) are two evolution rules for the two state variables:

$$\dot{\epsilon} = \frac{d\epsilon}{dt} = \frac{\dot{\epsilon}_0 (54)^n \left(\frac{\sigma - \sigma_{th}}{54} - c \right)^n e^{-Q_\epsilon / RT}}{\delta}, \tag{1}$$

$$\dot{\delta} = \frac{d\delta}{dt} = \frac{\dot{\delta}_0 e^{-Q_\delta / RT}}{\delta^m} = \frac{\beta}{\delta^m}, \tag{2}$$

$$\dot{\omega} = \frac{d\omega}{dt} = \frac{\dot{\omega}_0 \left(\frac{\sigma}{54} \right)^\nu e^{-Q_\omega / RT}}{\delta (1 - \omega)}, \tag{3}$$

where

$$\begin{aligned}
\dot{\epsilon}_0 &= e^{78.08} \text{ for } T \le 1200°C, \\
&= e^{21.93} \text{ for } T > 1200°C; \\
\sigma_{th} &= 1765.8 - 1.12T \text{ MPa for } T \le 1250°C, \\
&= 516.9 - 0.3T \text{ MPa for } T > 1250°C; \\
c &= 0 \text{ and } n = 1 \text{ for } \sigma \le \sigma_{\text{trans}}, \\
&= 1 \text{ and } n = 1.32 \text{ for } T \le 1250°C \text{ and } \sigma > \sigma_{\text{trans}}, \\
&= 1 \text{ and } n = 1.7 \text{ for } T > 1250°C \text{ and } \sigma > \sigma_{\text{trans}}; \\
\sigma_{\text{trans}} &= 1848.3 - 1.12T \text{ MPa for } T \le 1250°C, \\
&= 1108.1 - 0.634T \text{ MPa for } T > 1250°C; \\
Q_\epsilon &= 957.4 \text{ kJ/mole for } T \le 1200°C, \\
&= 270 \text{ kJ/mole for } T > 1200°C; \\
m &= \tfrac{1}{3}; \\
\dot{\delta}_0 &= e^{93.5} \text{ for } T \le 1200°C, \\
&= e^{-1.26} \text{ for } T > 1200°C; \\
Q_\delta &= 1174 \text{ kJ/mole for } T \le 1200°C, \\
&= 13.26 \text{ kJ/mole for } T > 1200°C; \\
\dot{\omega}_0 &= e^{103.46}; \\
\nu &= 10.47; \\
Q_\omega &= 1497 \text{ kJ/mole.}
\end{aligned}$$

[1] GN-Si_3N_4 was engineered and is marketed by AlliedSignal Ceramic Components, Torrance, California.

Contributed by the International Gas Turbine Institute and presented at the 40th International Gas Turbine and Aeroengine Congress and Exhibition, Houston, Texas, June 5–8, 1995. Manuscript received by the International Gas Turbine Institute February 22, 1995. Paper No. 95-GT-388. Associate Technical Editor: C. J. Russo.

t is in h, ϵ in microstrain, T the absolute temperature in K, R the gas constant, σ_{th} the threshold stress below which creep is assumed to be negligible, and σ_{trans} the transition stress above which the creep rate is a linear function of stress and a nonlinear function otherwise.

The hardening variable that characterizes the internal state of creep resistance is assumed to be $\delta = 1$ at the initial state of the material but δ increases monotonically under stress and thermal exposure as time elapses. The damage variable that characterizes the state of internal damage is assumed to vary from $\omega = 0$ at the initial state of the material to $\omega = 1$ that, according to Eq. (3), yields $\dot{\omega} = \infty$ signifying a rupture failure.

It should be noted that Eqs. (1) and (3) are individually coupled with Eq. (2) through δ but mutually independent from each other. This implies that creep deformation and fracture are assumed to be two independent processes. The justification for such formulation was based on postmortem examinations of previous experimental results (Ding et al., 1994c), which indicate that the fracture failure of the material in tension is caused primarily by localized damage such as the growth of a dominant pre-existing internal defect rather than distributed damage induced by void nucleation, growth and coalescence, although the latter damage process may be occurring concurrently but contributing neither overwhelmingly nor synergistically to the ultimate failure. Decoupling of Eqs. (1) and (3) is plausible for the case of tensile loading in view of the short rupture lifetime that is usually required. The hardening of grain boundary phase was found to be the major factor that enhanced the resistances of both creep and creep fracture of GN-10 ceramic. The creep rate and damage rate are, therefore, assumed to be inversely proportional to δ, as expressed in Eqs. (1) and (3), respectively. Detailed discussions concerning the formulation of the model are given elsewhere (Ding et al., 1994b).

The viscoplastic model presented in earlier sections was tailored to best represent the creep behavior that exhibits monotonically decreasing creep. For some ceramic materials that exhibit a relatively brief period of primary creep followed by an extensive period of steady-steady creep, the model can be modified to approximate the creep behavior without the loss of generality in the present application because tensile fracture is accomplished in a short period of time and the steady-state creep rate does not significantly influence the final outcome.

Experimental Details

Material and Specimen. The material used in this study was a high grade of hot isostatically pressed (HIP) Si_3N_4, marketed as GN-10, which contains small amounts of Y_2O_3 and SrO as densification aids. Nominal density was 3.23 g/cm^3. A fracture surface (Fig. 1) shows prismatic grains on the order of 1 to 1.5 μm in diameter and an average aspect ratio of about 4, nearly isotopically distributed with well-dispersed pores typically smaller than 1 μm in diameter.

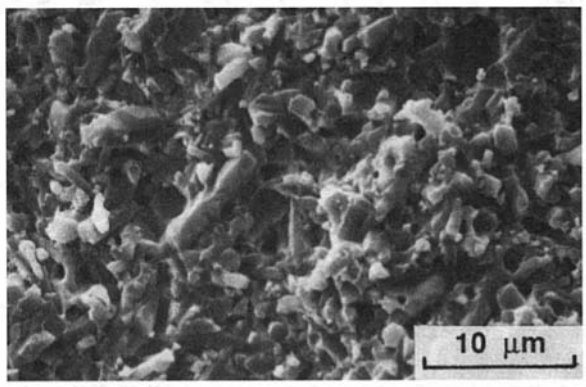

Fig. 1 A high magnification SEM micrograph of a typical fracture surface

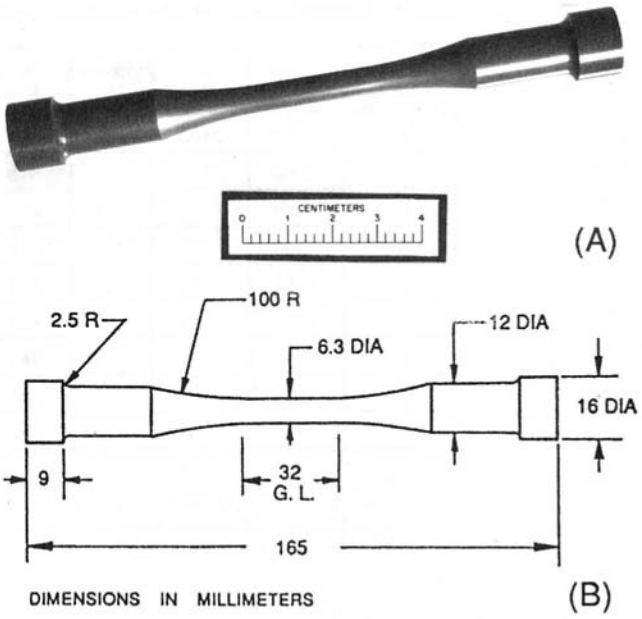

Fig. 2 (*A*) A buttonhead tensile specimen and (*B*) specimen geometry

Buttonhead specimens (Fig. 2(*a*)) were machined from tiles having a nominal size of 190 mm × 100 mm × 20 mm thickness, without any postsintering heat treatment. The specimen

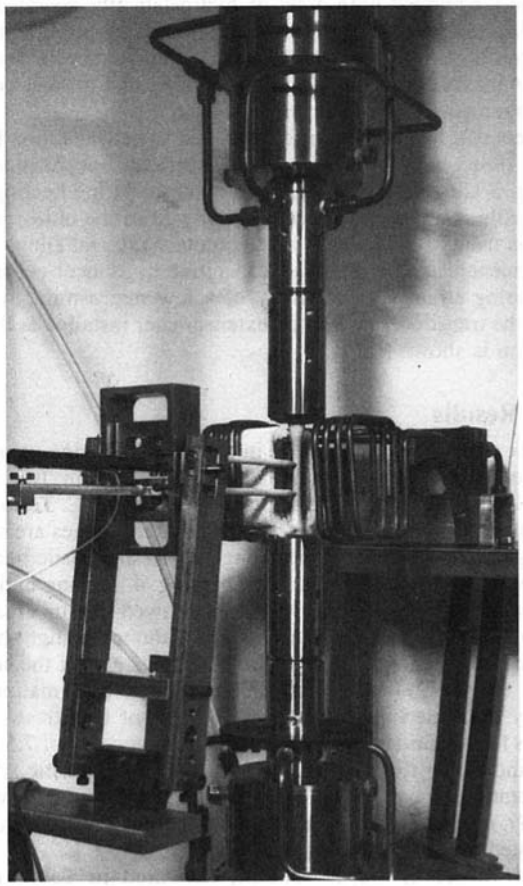

Fig. 3 Load-train assembly for ceramic tensile testing at elevated temperatures using induction heating, and a mechanical extensometer installed at the test position

Table 1 Summary of experimental results on GN-10 Si_3N_4 tested in tension at elevated temperatures

Specimen No.	Temp. °C	K MPa/min	E GPa	σ_f MPa	Σ_f MPa	$1-\Sigma_f/\sigma_f$	ϵ_f 10^{-6}	ϵ_{pl} 10^{-6}	t_r s
A	1150	2100	284	585	930	+0.59	1973	0	16.7
C	1200	"	236	516	634	+0.23	2226	0	14.7
E	1250	"	217	473	445	-0.06	2277	0	13.5
G	1300	"	208	518	325	-0.37	2302	0	16.5
B	1150	7.5	237*	521	490	-0.06	2403	0	4167
D	1200	"		527	393	-0.25	2733	316	4216
F	1250	"		361	279	-0.23	2855	1136	2888
H	1300	"		256	199	-0.22	2826	1540	2048
J	"	"		270	199	-0.26	2857	1500	2160

Notes: K = Stressing rate
E = Elastic modulus; * indicates apparent elastic modulus.
σ_f = Experimental fracture strength
Σ_f = Predicted fracture strength
ϵ_f = Strain at fracture
ϵ_{pl} = Plastic strain
t_r = Time to failure

(Fig. 2(*b*)) has a 6.3 mm gage diameter and a 32 mm uniform gage section. All circumferential grinding marks in the reduced gage section were removed by final longitudinal grinding with the grinding wheel placed in alignment with the specimen axis until the specimen surface had a finish of 0.4 μm (rms). Neither postmachining heat treatment nor surface polishing was given to the specimen gage section.

Testing Equipment and Method. All testing was performed using a closed-loop controlled electrohydraulic testing machine equipped with a set of hydrostatically operated self-aligning specimen grippers in the load-train assembly (Fig. 3). The self-aligning specimen gripper is a unique device designed to eliminate bending in the test specimen due to load column misalignment (Liu and Brinkman, 1986).

Specimen heating was accomplished by an induction heater (Liu, 1988) with a SiC susceptor. A ceramic specimen visible in Fig. 3 is flanked by two induction coils during heating.

Tensile strain was measured directly from the uniform gage section using a mechanical extensometer (Liu and Ding, 1993) instrumented with a sensitive capacitive transducer capable of measuring strain with accuracy of a few microstrain. A view from the transducer end of the extensometer installed at the test position is shown in Fig. 3.

Test Results

Nine specimens were tested in monotonic tension using two different stressing rates of 7.5 and 2100 MPa/min, two specimens each at 1150, 1200, 1250, and three at 1300°C. Test results are summarized in Table 1, and stress–strain curves are shown in Fig. 4. The influence of stressing rate on the tensile behavior of this material is clearly indicated in Fig. 4. Testing under the high stressing rate of 2100 MPa/min showed that this material behaved virtually like an elastic solid, although a slight hint of plastic deformation was perceptible near the end of the stress–strain curve (*G*) obtained at 1300°C. Plastic deformation was clearly illustrated in the high stress range of the stress–strain curves for specimens tested at the low stressing rate of 7.5 MPa/min, indicating the material behaved as a viscoplastic solid at temperatures above 1150°C. The fracture strength (σ_f), rupture time (t_r), fracture strain (ϵ_f), and plastic strain (ϵ_{pl}) are also tabulated in Table 1.

The values of elastic moduli, tabulated in Table 1 and plotted in Fig. 5, were determined directly from the stress–strain curves (*A*, *C*, *E*, and *G*) of the specimens tested under the high stressing rate. These values were correspondingly in good agreement with those determined from the low stress portion of the stress–strain curves (*D*, *F*, *H*, and *J*) below σ_{th}, where creep was virtually negligible. However, the apparent elastic modulus for curve *B* was much lower than the elastic modulus for curve *A*. The dynamic effect was partially responsible for the discrepancy but only in small part. A large part of the difference was most likely attributed to material variation because the high stressing rate used in this experiment was still far below the so-called dynamic range where the stress wave travels at much higher speed. The cause of the discrepancy is not known due to the limited number of tests. For the present study, the difference in the modulus values is of secondary importance.

Model Prediction and Discussion

Because the viscoplastic model presented in an earlier section was formulated to simulate the material behavior under general thermomechanical loading conditions, applications to constant stressing-rate tension in isothermal condition can be implemented rather straightforwardly by integrating the three basic equations. To this end, however, σ and δ must be expressed as functions of time. Under constant stressing-rate

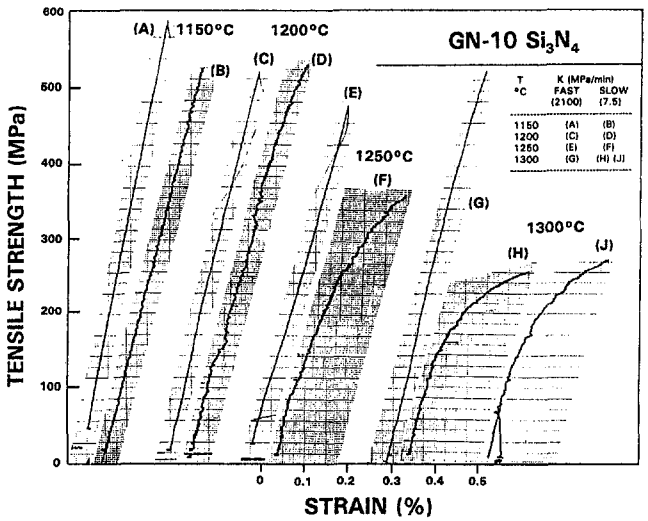

Fig. 4 Uniaxial tensile stress–strain curves of GN-10 Si_3N_4 tested at elevated temperatures using two different stressing rates

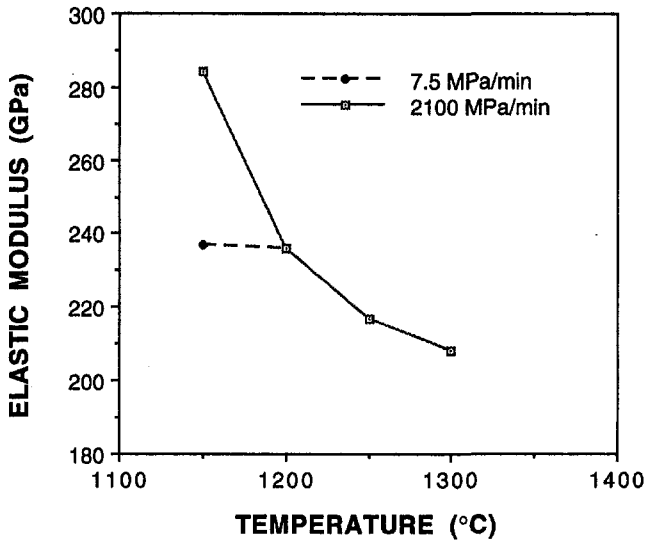

Fig. 5 Elastic modulus of GN-10 was found to be a function of temperature

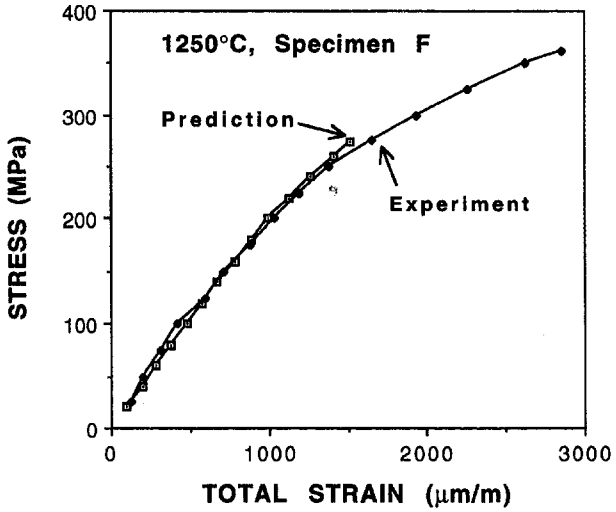

Fig. 7 Comparison of experimental tensile stress–strain curve of GN-10 Si_3N_4 at 1250°C and simulation

loading, tensile stress can be calculated from a simple relation such as

$$\sigma = \int_0^t \dot{\sigma}\ (=\text{const})d\tau = Kt, \tag{4}$$

where constant K is the stressing rate. Analogously, if tensile loading is applied under an isothermal condition as the cases being considered here, an explicit expression for δ in terms of t can be derived by an integration of Eq. (2) as

$$\delta = [1 + (1 + m)\beta t]^{1/(1+m)}, \tag{5}$$

where β represents the numerator of Eq. (2). With the aid of Eqs. (4) and (5), Eqs. (1) and (3) can be integrated independently to obtain two equations for ϵ and ω, respectively, as functions of time t. The time to tensile rupture (t_r) is determined from the ω equation by setting $\omega = 1$. The total tensile strain is the sum of the viscoplastic strain ϵ calculated from the ϵ equation and the elastic strain σ/E, where E is the elastic modulus of the material. Tensile fracture strength and fracture strain are calculated, respectively, from Eq. (4) and the ϵ equation at time $t = t_r$.

Simulations were performed for the tensile stress–strain curves illustrated in Fig. 4, using the analytical model. The experimental stress–strain curves obtained for specimens tested at the high stressing rate (2100 MPa/min) were well reproduced by simulated curves, which also showed a stress–strain relation that was virtually linear as those exhibited in Fig. 4. However, tensile fracture strengths were overestimated for lower temperatures (>1200°) and underestimated for higher temperatures by about +60 to −37 percent as indicated in Table 1.

Although not shown, curve B was also well simulated by a stress–strain curve, which was essentially linear, but the stress–strain slope for the simulation was slightly steeper compared to that of curve B because the elastic modulus of curve A was used in the simulation.

Viscoplasticity is clearly discernible from experimental stress–strain curves obtained for specimens tested at the low stressing rate of 7.5 MPa/min. To facilitate comparison, experimental curves obtained at 1200, 1250, and 1300°C and corresponding simulations are plotted for each temperature in Figs. 6–8. Although simulations somewhat underpredict actual

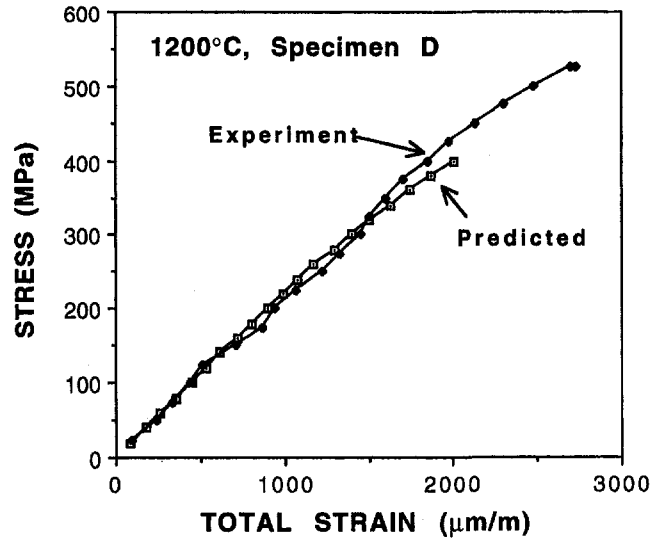

Fig. 6 Comparison of experimental tensile stress–strain curve of GN-10 Si_3N_4 at 1200°C and simulation

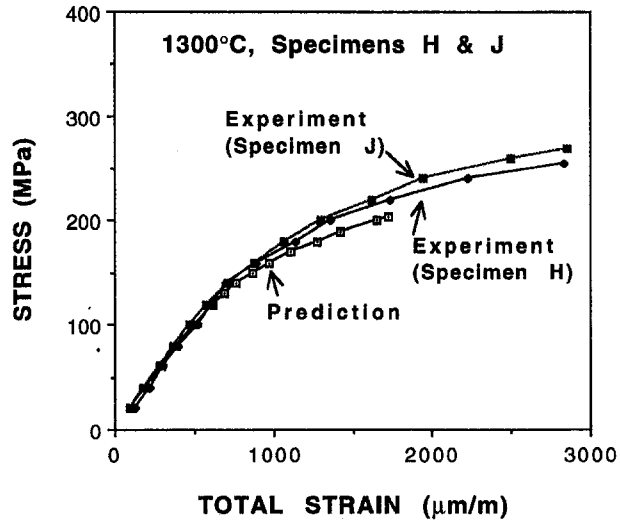

Fig. 8 Comparison of experimental tensile stress–strain curve of GN-10 Si_3N_4 at 1300°C and simulation

stress–strain behavior in all three cases, essential features of the actual viscoplastic behavior of the material are well reproduced. The fracture strengths are again underpredicted by about 25 percent. It should be noted that all the constants used in the model were determined based on creep curves and creep rupture data, which represent long-term material properties. In contrast, tensile rupture data must be characterized as short-term material properties, which may not be well represented by the model that was primarily formulated to delineate the long-term material behavior. For this reason, life predictions by the model for extremely short-term tests were less accurate, but reasonable in all cases investigated. Another reason is that the parameters in Eq. (3) were determined from a small database, which contained noticeable scatter.

Conclusions

Tensile behavior was investigated on GN-10 Si_3N_4 ceramic at elevated temperatures in the range of 1150 to 1300°C. Two different stressing rates were used. Tensile behavior was shown to be sensitive to stressing rate in the temperature range above 1150°C. The material virtually behaved as an elastic solid at all the temperatures tested when specimens were loaded at a rate of 2100 MPa/min. However, the range of elastic response decreased and the material behaved as a plastic solid when specimens were loaded at 7.5 MPa/min. The elastic modulus of GN-10 at high temperatures was found to be a function of temperature.

A viscoplastic model developed recently for characterization of creep deformation and creep rupture behavior of the same material was used to simulate the experimental tensile stress–strain behavior and to predict the fracture strength. Results showed the model was quite capable of simulating deformation behavior for all practical engineering applications, but estimated the high-temperature fracture strength somewhat conservatively.

Acknowledgments

Research sponsored by the U.S. Department of Energy, Assistant Secretary for Energy Efficiency and Renewable Energy, Office of Transportation Technologies, as part of the Advanced Automotive Materials Program, under contract No. DE-AC05-96OR22464 with Lockheed Martin Energy Research Corporation. We wish to thank Drs. A. A. Wereszczak, C. H. Hsueh, and B. G. Gieseke for reviewing the manuscript.

References

Cuccio, J., Peralta, A., Song, J., Brehm, P., Johnson, C., Tucker, W., and Fang, H., 1994, "Probabilistic Methods for Ceramic Component Design and Implications for Standards," *LifePrediction Methodologies and Data for Ceramic Materials,* C. R. Brinkman and S. F. Duffy, eds., American Society for Testing and Materials, Philadelphia, PA, ASTM STP 1201, pp. 291–308.

Ding, J. L., Liu, K. C., and Brinkman, C. R., 1994a, "A Comparative Study of Existing and Newly Proposed Models for Creep Deformation and Life Prediction of Si_3N_4," *ibid.,* pp. 62–83.

Ding, J. L., Liu, K. C., and Brinkman, C. R., 1994b, "A Phenomenological High-Temperature Deformation and Life Prediction Model for Advanced Silicon Nitride Ceramics," *Proc. Symposium on Durability and Damage Tolerance,* ASME Winter Annual Meeting, Nov. 6–11, Chicago, IL.

Ding, J. L., Liu, K. C., and Brinkman, C. R., 1994c, "Creep and Creep Rupture of an Advanced Silicon Nitride Ceramic," *J. American Ceramic Society,* Vol. 77, No. 4, pp. 867–874.

Liu, K. C., and Brinkman, C. R., 1986, "Tensile Cyclic Fatigue of Structural Ceramics," *Proc. 23rd Automotive Technology Development Contractors' Coordination Meeting,* Society of Automotive Engineers, Warrendale, PA, P-165, pp. 279–284.

Liu, K. C., 1988, "Ceramic Specimen Heating by Induction Power," *International Journal of High Technology Ceramics,* Vol. 4, pp. 203–210.

Liu, K. C., and Ding, J. L., 1993, "A Mechanical Extensometer for High-Temperature Tensile Testing of Ceramics," *Journal of Testing and Evaluation,* JTEVA, Vol. 21, No. 5, Sept., pp. 406–413.

Rice, J. R., 1971, "Inelastic Constitutive Relations for Solids: An Internal Variable Theory and Its Applications to Metal Plasticity," *Journal of Mechanics and Physics of Solids,* Vol. 19, pp. 433–455.

K. Reifsnider

K. Liao

M. McCormick

A. Tiwari

Materials Response Group,
Virginia Polytechnic Institute
and State University,
Blacksburg, VA 24061

Fiber Fracture in Continuous Fiber Ceramic Composites: Concepts and Observations

The knowledge of fiber behavior in CMCs is rather modest, and models tend to be based on concepts that are less than complete. The present paper addresses several aspects of this problem. Fundamental assumptions for tensile strength models are discussed, and some basic modeling approaches are described. The effects of fiber fracture on the quasi-static stress–strain behavior are described (from physical measurements), and some models of that behavior discussed. Finally, a summary of the "state of affairs" for this subject will be attempted, and the needs for further investigation, especially to support improved modeling, will be presented.

Physical Aspects

Many ceramic composite material systems are designed to be fiber dominated, i.e., the reinforcing fibers sustain loads after the matrix cracks, and the strength of the composite is dominated by the fiber strength. Hence, information about the fracture of fibers, especially under the long-term application of mechanical loading, and especially in high-temperature environments that are common for such materials, is critical for the understanding and modeling of the performance of such material systems. The physical nature of the present subject is indicated in Fig. 1. Figure 1(a) shows the fracture plane of a Nicalon/glass ceramic composite. It is seen that matrix cracks form in planes transverse to the fibers that are aligned with the direction of loading in this case. These matrix cracks typically form at of the order of one third to one half of the failure load, and reach a saturation spacing controlled by the nature of the transfer of stress between the fibers and matrix (Aveston et al., 1971). For loading above that level, the fibers support the load, and the matrix acts to transfer stress back into the fibers in regions surrounding fiber breaks (that do not occur in the matrix-crack plane). When a sufficient number of fibers break, the accumulation of fractures creates an unstable condition, which leads to fracture, with broken fiber fragments pulling out of the matrix regions as shown in Fig. 1(a).

If the interface (or interphase region) between the fibers and matrix is "weak" (or very compliant), the matrix is less "efficient" at transferring stress back into the fiber around a fiber fracture point, and the distance between fiber fractures along the length of the fibers is large. However, if the fibers are well bonded to the matrix (or tightly gripped by residual stresses), then the fibers may fracture many times. A typical fiber fracture pattern near the point of specimen fracture is shown in Fig. 1(b). In general, the fibers may break into fragments of the order of 10–100 times the fiber diameter.

Stress Redistribution

In CMCs, the matrix stiffness is typically similar to the fiber stiffness. Hence, the stress in the fibers is greatly affected by the formation of matrix cracks; for a fiber volume fraction of 50 percent, the matrix may be supporting on the order of half the load. It is, therefore, essential to estimate the load redistribution closely as a function of increasing load level if the fiber-controlled strength is to be correctly calculated. One approach to that objective is to reduce the "effective stiffness" of the matrix as cracks form. But then, the question becomes how to estimate the "rate" of matrix crack formation as a function of loading.

An alternative approach is to assume that when the stress in the matrix reaches the average strength of the matrix material, it remains at that value throughout any remaining increases of load level. The physical logic of this concept is based on the argument that the average stress in the cracked ply or element cannot exceed the average strength, and the matrix continues to support stress, on the average, by shear transfer from the fibers (and adjacent plies, if present). Then a computational scheme can be constructed that adjusts the matrix stiffness as applied loading increases to keep the average matrix stress (calculated from plate theory or laminate analysis) constant. The success of this approach can be determined by comparing the resulting specimen (global) stiffness to measured values as a function of loading.

However, the data shown in Fig. 1(b) clearly indicate that the fibers break into small pieces, indicating that stiffness change due to fiber fracture must also be considered. Hence, the global stiffness must also be reduced using a "short fiber" model in which the relative stiffness is determined by the aspect ratio of the fiber fragments, and decreases as the fiber fragment length decreases. If the probability of fiber fracture, $P(\sigma)$, is known, then the ratio of current to initial fiber aspect ratio AR can be given by

$$\frac{\mathrm{AR}_\sigma}{\mathrm{AR}_o} = 1 - \frac{(\mathrm{AR}_o - \mathrm{AR}_f)P(\sigma)}{\mathrm{AR}_o}$$

where AR_f is the final value of the aspect ratio just prior to fracture. The stiffness of a unidirectional composite as a function of fiber aspect ratio (alone) can be determined from elasticity solutions of the transient stress problem (Carman and Reifsnider, 1992). For present purposes, we can approximate that dependence with a shear-lag model (Cox, 1952) with the relationship

$$\frac{E_f'}{E_f} = 1 - \frac{\tanh\left(Sr_0 \dfrac{\mathrm{AR}_\sigma}{2}\right)}{Sr_0 \dfrac{\mathrm{AR}_\sigma}{2}}$$

$$S = \sqrt{\frac{2\pi G_m}{\left(\dfrac{r_1}{r_o} - 1\right) E_f A}}$$

Contributed by the International Gas Turbine Institute and presented at the 40th International Gas Turbine and Aeroengine Congress and Exhibition, Houston, Texas, June 5–8, 1995. Manuscript received by the International Gas Turbine Institute February 8, 1995. Paper No. 95-GT-228. Associate Technical Editor: C. J. Russo.

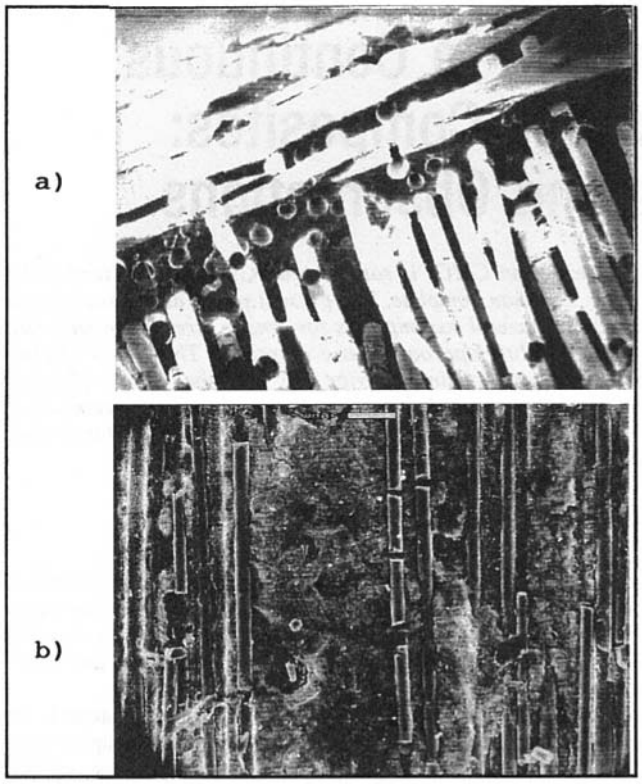

Fig. 1 Fracture plane (*a*) and fiber fracture pattern (*b*) in a Nicalon/CASS laminate

where E_f is the modulus of the unbroken fiber, G_m is the matrix shear modulus, r_0 is the fiber radius, r_1 is the mean spacing between fibers, and A is the cross-sectional area of the fiber.

Using the combined stiffness change from matrix cracking (calculated by keeping the matrix stress constant) and the stiffness reduction due to the reduction of fiber aspect ratios determined from the equations given above, a prediction of the global stiffness change with increasing load can be calculated. A comparison of such a calculation for a cross-ply Nicalon/CAS system (shown in Fig. 1(*b*)) is shown in Fig. 2. Stiffness change due to matrix cracking was modeled by keeping the 90-deg ply-stress constant after crack initiaton. Experimental data have been taken from Tiwari et al. (1995). The agreement is seen to be remarkably good, suggesting that the average stress distributions from such a model (especially in the fibers) is also reasonably close to reality.

The onset of matrix cracks and their progression have been successfully monitored by an acousto-ultrasonic (AU) NDE technique as shown by the authors in previous work (Tiwari et al., 1995; Henneke et al., 1993). The nonlinear behavior observed in a stress–strain curve for a unidirectional ceramic composite has been predominantly attributed to the effect of matrix cracks. This effect of matrix cracks on the stress–strain curve has been previously modeled (by the acousto-ultrasonic stress–strain response or "AUSSR" model) with the help of real-time AU data. The AUSSR model predicts the strain response to increasing stress levels by incorporating damage modes and their effect upon the global strain response of a laminate with the help of real-time AU data into classical laminated plate theory. The ply properties are varied according to real-time AU data by varying E_m and G_m of the matrix to take into account the occurrence of matrix cracks. The change in the elastic moduli due to matrix cracks causes the nonlinear zone of the stress–strain curve generated by the model, and closely fits the experimental data for unidirectional materials. We will briefly describe a modified AUSSR model that incorporates the fiber breaks during matrix cracking by altering the effective fiber volume fraction using AU data. Unlike polymeric composites, around 23 percent of the fibers break during matrix cracking. Researchers have speculated about fiber breaks in ceramic composites and their effect on the stress–strain curve. Real-time AU parameters along with the AUSSR models and SEM microphotographs provide further proof of the large amount of fiber breaks (23 percent) during matrix cracking, and help in understanding the failure process in ceramic composites. The prediction of composite stiffness by Cox's (1952) model for aligned short fiber composite compares well with experimental data. The modified AUSSR model attempts to describe the damage mechanisms occurring by assessing the combined effect of matrix cracks and fiber breakage on the global strain response of the laminate to increasing loads. This work represents an integration of measured experimental damage with analytical modeling to produce a better physical understanding of the damage development process in ceramic composites.

The AUSSR model was formulated to study the failure mechanisms of unidirectional Nicalon/CAS-II ceramic composites. The model uses real-time AU data along with classical laminated plate theory (CLPT) to predict the strains measured at the outer plies in the gage section for a given load. A Weibull distribution was used to approximate the variation of the real-time AU parameter with increasing stress levels. Researchers have shown that the matrix crack density plotted versus stress follows a Weibull distribution; hence, a two-parameter Weibull distribution was chosen here. The AU parameter SWF ($M0$) is the zeroth moment of the frequency spectrum of the received AU signal; it represents the energy content of the received AU signal (Tiwari et al., 1995). Figure 3 shows the degradation of SWF values for a typical unidirectional Nicalon/CAS-II ceramic composite laminate and the corresponding Weibull distribution curve with Weibull shape parameter $\alpha = 15$ and location parameter $\beta = 235$ MPa selected to approximate this degradation curve. The elastic moduli of the matrix material, E_m and G_m, used in classical laminated plate theory fortran code were varied over the same stress range from 100 to 0 percent using the same Weibull parameters $\alpha = 15$ (shape parameter) and $\beta = 235$ MPa (location parameter). Here it is assumed that the matrix degrades in a similar fashion to the real-time AU parameter SWF ($M0$). This assumption takes into account the effect of matrix cracking and its contribution to the observed global strains. Strains are then predicted for each increment of stress using laminated plate theory and the variation of matrix proper-

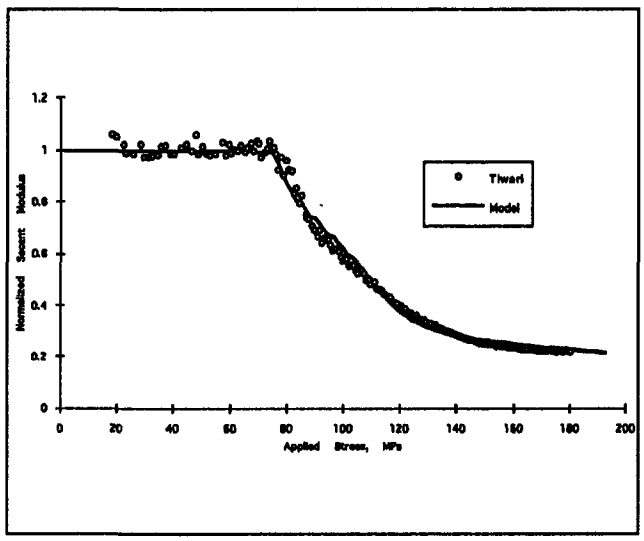

Fig. 2 Predicted and observed global stiffness change as a function of applied load level for a Ni/CAS composite laminate under quasi-static loading

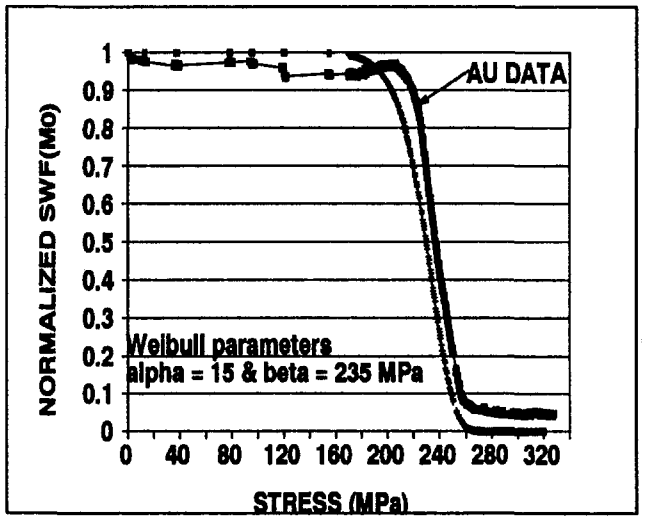

Fig. 3 Degradation of stress wave factor as a function of applied loading

ties using Weibull parameters obtained from real-time AU data. The results of this calculation are shown in Fig. 4, together with the actual observed stress–strain curve.

The initial predicted linear portion of the curve (E_c = 136 GPa) closely approximates the real data (E_c = 131 GPa). A few fiber breaks caused by residual stresses in a virgin specimens may be responsible for a slight decrease in the initial stiffness. The changes in the slopes in the nonlinear zone follow the same trends to 0.35 percent strain. The slope of the second linear zone of the AUSSR-predicted curve is $\nu_f E_f$ (fiber volume fraction * elastic moduli of fiber = 77 GPa) and is stiffer than the corresponding slope (52 GPa) of the measured data.

Results from AU have shown the occurrence of local fiber breaks together with matrix cracking in this range. The difference between the compliance of the specimen compared to the AUSSR model is due to the loss of load-bearing fibers because of the fiber breaks occurring during loading, and is unaccounted for in this model. The AUSSR model was modified to account for the average number of fiber breaks occurring during matrix cracking using data obtained from real-time AU tests as shown in Fig. 4. The effective fiber volume fraction was recalculated and the AUSSR model predictions were modified accordingly as described in a previous work by the authors (Tiwari et al., 1995; Henneke et al., 1993). The effective fiber volume fraction ($\zeta\nu_f$ = 0.31) was calculated by assuming the broken fibers (23 percent) are not load bearing and hence behave as a material filling up the volume without sharing any load.

The Weibull parameters α and β account for the effect of matrix cracking and the effective fiber volume fraction accounts for the fiber breaks. The predictions of the modified AUSSR and the previous AUSSR model are shown in Fig. 4. The modified AUSSR model predictions better approximate the experimental stress strain curve for a unidirectional SiC/CAS-II ceramic composite. The underlying assumption is that all fiber breaks that occur during matrix cracking occur at one stress level after the saturation of matrix cracks, and hence a jump in strain value is seen at that stress level in the modified AUSSR model predictions. The effective fiber volume fractions could instead be altered when the sharp peaks corresponding to fiber breaks are observed during static tests to obtain an improved further-modified AUSSR model prediction. The slope of the second linear zone ($\zeta\nu_f E_f$ = 61 GPa) is nearer to the experimental data (52 GPa) than the other unmodified AUSSR model.

The AU results need to be corroborated by verifying the amount of fiber breaks at saturation of matrix cracks. An unidirectional Nicalon/CAS-II specimen was loaded to saturation of matrix cracks and then etched to expose the broken fibers. SEM photomicrograph of the etched sample (Fig. 1(*b*)) shows the occurrence of periodic fiber breaks with an average length of 100 μm. The composite at this stage can be analyzed as short fibers perfectly aligned in the loading direction. Using Cox's model (discussed earlier) for short fiber composite, an elastic modulus of 53 GPa (E_c = 53 GPa) for the composite laminate with aligned broken fibers (l = 100 μm) was obtained. The final stiffness value obtained from Cox's model closely approximates the experimental slope of 52 GPa.

Tensile Strength After Matrix Cracking

Figure 5 shows a schematic diagram of the situation to be considered. If the CMC is correctly designed, as discussed above, to avoid immediate failure when the matrix cracks form, then the question of tensile strength becomes more complex. It involves the possibility of fibers breaking in the matrix regions between the matrix cracks, and the debonding and slipping of the fibers in the matrix material.

For our present purposes, we will consider the model of Liao et al. (Liao, 1994), which is conceptually similar to an earlier model published by Curtin (1991). The present approach is based on the following premises:

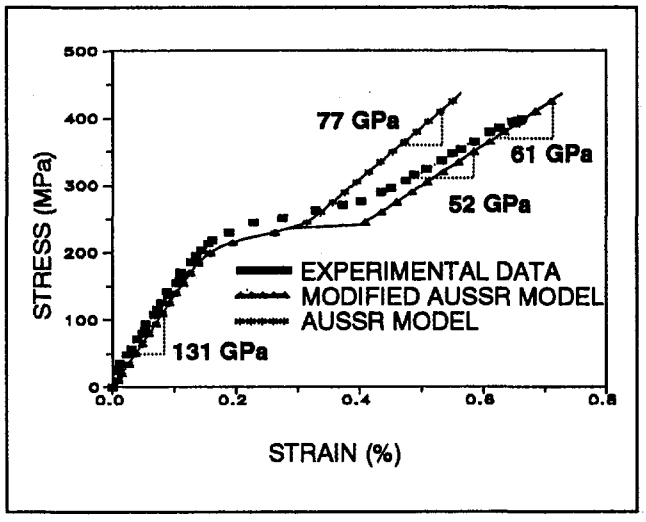

Fig. 4 Predicted and observed stress–strain curve for a SIC/CAS-II ceramic composite

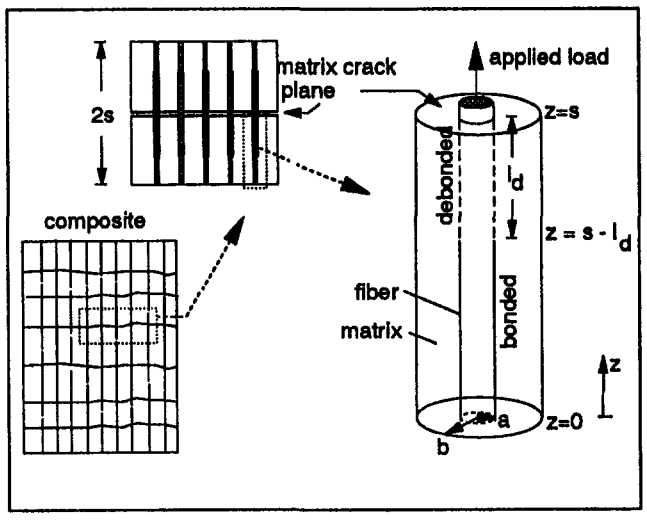

Fig. 5 Schematic diagram of global, local, and fiber-matrix conditions that control the strength of CMCs after matrix crack saturation

1 Calculations begin with a stage where multiple matrix cracking has already occurred and is saturated (Fig. 5); the influence of fiber fracture prior to the matrix cracking load is ignored.

2 The fiber/matrix interface is assumed to be partially debonded when multiple matrix cracking occurs. Further loading results in an increase in debonding length, which is determined by an interfacial shear strength approach: The debonding length increases when the fiber/matrix shear stress at the debonding front exceeds the interfacial shear strength.

3 The stress distributions for both the debonded and the bonded region of an intact fiber are described by an approximate elasticity solution wherein the Poisson's effect is considered.

4 For each small load increment, the probability of fiber fracture and the mean fracture location is calculated for each of the three regions of an intact fiber, i.e., the fiber within the matrix crack plane, the debonded region, and the bonded region. Each broken fiber that bridges a matrix crack supports a normal load of $(2\pi r\delta\tau)$ at the matrix crack plane, where r is the radius of the fibers, delta is the length of the broken fiber from the break to the matrix crack plane, and τ is the interfacial shear stress. The rest of the applied load on the composite is shared equally between all the remaining intact fibers (in contrast to the local stress concentration model discussed below). It can be shown that the probability of fiber fracture within the matrix crack plane is negligible (Liao, 1994). Also, total debonding of the fiber/matrix interface occurs at relatively low load beyond the start of matrix cracking.

5 The effect of fiber fracture on tensile strength for fibers adjacent to, but outside the representative volume (the length of which is the average matrix crack spacing, with a transverse matrix crack in the middle) is considered. Those broken within an "ineffective length" (designated at the matrix crack plane of the representative volume, encompassing several matrix blocks depending on the interfacial shear stress and current load) are considered broken within the representative volume because they are not supporting the stress that an intact fiber would support (although they are "intact" within the representative volume). Such an effect is ignored in most other tensile strength models for CMC (Sutcu, 1989; Schwietert and Steif, 1990; Weitsman and Zhu, 1992).

6 The fraction of intact fibers and the total load that is carried by the unbroken fibers are evaluated at each load increment. Failure of the composite is defined when the total load reaches a maximum.

The details of the analysis associated with this approach appear in a dissertation recently published by Liao (1994). Some typical results are shown here using properties of a Ni/LASS II system. In Fig. 6 the fiber failure ratio for several different values of the Weibull modulus of fiber, m, are plotted with increasing applied load. It is seen that, at a relatively low load, there are fewer fiber failures in fibers with higher m values, since their strength distribution is more uniform than those with lower m values (for a constant value of characteristic fiber strength). As the applied load is increased, there is a transition point where it takes more load to break fibers with lower m value, owing to the fact that the wider spread of the Weibull distribution for that case implies that there are more strong fibers toward the tail of the density function. As a result, the composite acquired higher predicted strength when the fiber strength distribution has a lower m value, and vice versa.

The effect of the fiber/matrix interfacial shear stress on the composite tensile strength is only influenced by the effect of fiber debonding and fiber/matrix sliding. Hence, the model predicts that a higher composite strength is attained for a system with a higher interfacial shear stress. However, a higher interfacial shear stress may not be a favorable condition for the toughness of the composite, characterized by the total pull-out work, as shown in Fig. 7, where normalized pull-out work is plotted

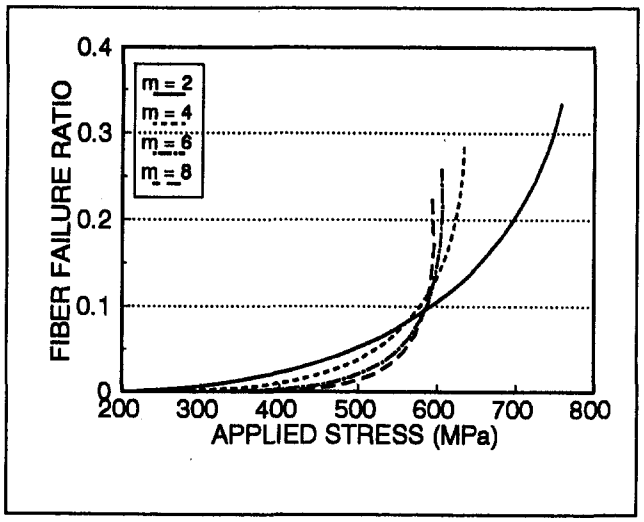

Fig. 6 Predicted dependence of the ratio of broken to unbroken fibers on load global load level

against applied stress for several interfacial shear stress values. It is seen from Fig. 7 that a lower interfacial shear stress increases the toughness. However, the model does not explicitly balance those influences.

This model can also be applied to the case of cyclic (fatigue) loading. For that purpose, the following assumptions are made:

1 The fatigue model is developed from the tensile strength model based on the fact that damage events (transverse matrix cracking, fiber/matrix debonding, and fiber fracture) are similar in tensile loading and tensile fatigue.

2 Two additional features are considered in the fatigue model: the degradation of the fiber/matrix interfacial shear stress and the degradation of the characteristic fiber strength with applied cycles. The former is the result of continued sliding between the debonded fibers and the surrounding matrix; the latter is attributed to flaw development in the fibers during repeated loading or other fiber degradation mechanisms such as oxidation. Although it is quite possible that these two factors are coupled, for simplicity, they are considered separately in the model. Decreasing fiber/matrix interfacial shear stress has the effect of reducing the load supported by an individual broken fiber at the matrix crack plane, implying that intact fibers are under higher stress with applied cycles (i.e., more susceptible to fracture). The effect of decreasing characteristic fiber strength is obvious.

3 As no experimental data currently exist to determine how the fiber/matrix interfacial shear stress and the characteristic fiber strength vary with applied cycles, a linear logarithmic function is assumed for both.

The Weibull modulus m of the reinforcing fibers has a significant influence on the predicted life of unidirectional CMCs, as shown in Fig. 8, where the ratios of intact fibers for several m values are plotted against applied cycles. The underlying logic is similar to the case of tensile strength: There are more stronger fibers in the tail of the density function to sustain local loads, assuming that the average fiber strength remains unchanged for different m values.

Effect of Local Stress Concentrations

As indicated above, if the fibers are bonded or gripped tightly by the matrix in a CMC, the matrix cracks simply propagate through the fibers and fail the composite in a very brittle manner (Warren, 1992). We can discuss the important parameters of this problem with the following simplified model (for a more

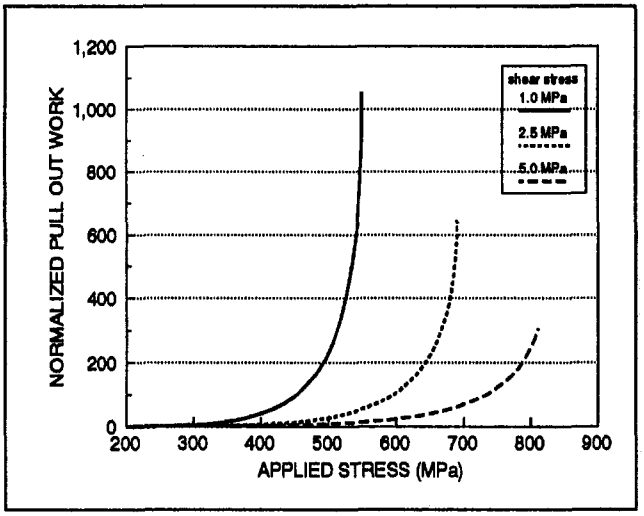

Fig. 7 Relative toughness as a function of the level of interfacial shear stress, as represented by the fiber-pull-out work versus applied load level

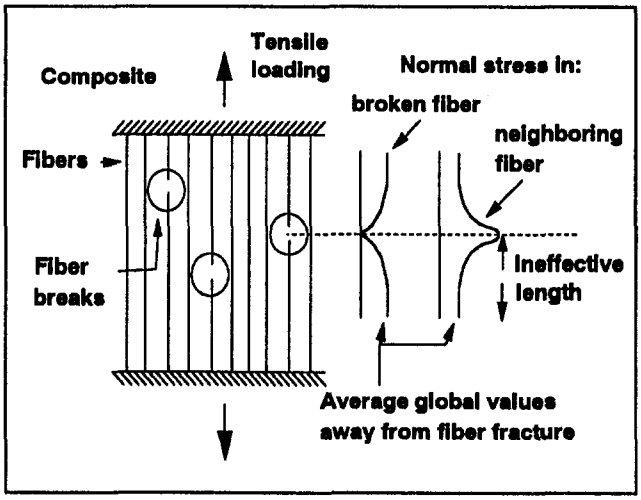

Fig. 9 Tensile strength problem in the fiber direction

complete version, see Gao and Reifsnider, 1993). For the purpose of our discussion, we will assume that the "ineffective length" over which stress is transferred back into a broken fiber can be calculated from an elasticity solution (or from a suitably accurate approximate solution of that sort). We seek, then, to formulate a model that correctly represents the influence of constituent properties, geometry, and arrangement (including the interphase region) on the balance between making the ineffective length small to avoid having the entire length of the fiber lost when a single fracture point develops, and making the ineffective length large so that the local stress concentration does not cause brittle fracture when a single fracture point develops. The ineffective length can be changed by altering the fiber, matrix, and interphase properties. In CMCs, for example, a fiber coating such as carbon is typically used to reduce the strength of the fiber-matrix interphase so that brittle fracture is avoided. But how long should the ineffective length be, i.e., what is the correct way to make the composite for optimum strength (not just to avoid a specific type of failure)?

Figure 9 depicts the problem at hand. The stress in the broken fiber builds back up to the undisturbed level by shear transfer from the surrounding matrix, composite, and interphase region. That rate of buildup is directly proportional to the stress concentration in the next nearest fibers; if the buildup occurs over a short distance, the stress concentration in the neighboring fibers is great and they tend to break causing very brittle composite behavior.

However, if the buildup occurs over a large distance (i.e., very low fiber-matrix coupling by the interphase region), the strength of each fiber is lost completely when the first local fiber break occurs. Most fiber strength models consider only limited aspects of this problem. For example, any "complete" model would indicate that the fiber-matrix interaction should be compliant or weak enough to avoid transmitting a stress concentration to the next unbroken fiber, but stiff and strong enough to provide some shear transfer to the matrix so that the fibers can break more than once, i.e., so that the composite is stronger than a simple rope of fibers without any matrix. Surprisingly, very few models predict such an "optimum" condition in terms of the material properties and local geometries of the problem (Gao and Reifsnider, 1993). Batdorf has considered the effect of local stress concentration and the statistical distribution of strength of the fibers, but his model does not treat the effect of changing ineffective length at the local level as a function of load level associated with fiber-matrix sliding (Batdorf, 1982). Curtin considers the latter aspect, but the question of stress concentration is not addressed (Curtin, 1991). A model of tensile strength that builds on those three models is presented below.

We begin by writing the probability of failure of the fibers in a composite in terms of the applied stress, in the following form:

$$P(\sigma) = 1 - \exp[-\delta k \sigma^m]$$

where δ is the local ineffective length normalized by the reference length, L, $k = 1/\sigma_o^m$ (where σ_o is the Weibull characteristic strength of the fibers), and m is the Weibull shape parameter of the fiber strength distribution. As suggested by Curtin and Batdorf, we approximate this expression (for small values of the arguments) by

$$P(\sigma) \doteq k\delta\sigma^m$$

and claim that the number of single fiber breaks at that applied stress is equal to that probability times the total number of fibers, N. To consider the effect of one fiber break on another, we postulate that in the overstress region the fiber stress in the next nearest fiber has a linear distribution (as suggested by

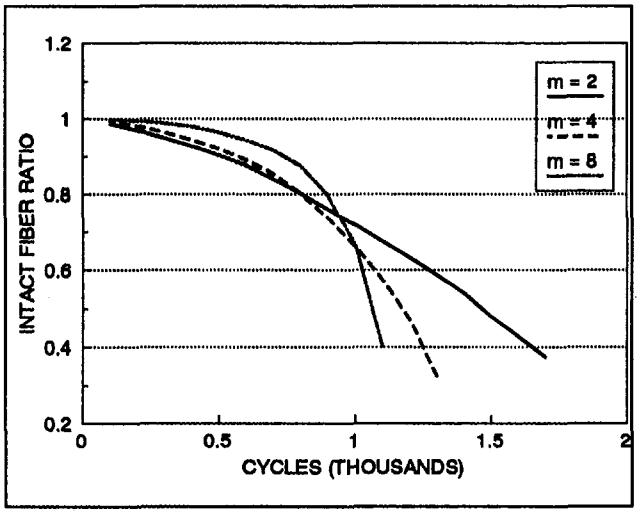

Fig. 8 Unbroken fiber ratio (proportional to remaining strength) versus cycles of fatigue loading for several values of Weibull modulus

Batdorf—a "correct" distribution could be used if known) so that that function has the form

$$f(x) = C_1 + \frac{x}{(\delta_1/2)}(1 - C_1)$$

where (again using the notation of Batdorf) C_1 is the stress concentration in the next nearest fiber to a single fiber fracture, and δ_1 is the associated ineffective length. For such a distribution, it can be shown that

$$P(\sigma) = k\lambda_1(C_1\sigma)^m; \quad \lambda_1 = \frac{\delta_1(C_1^{m+1} - 1)}{(m + 1)(C_1 - 1)C_1^m}$$

Then the probability that each single fiber fracture will form a double fiber fracture (or "doublet" as Batdorf calls it) can be written as

$$P_{1-2}(\sigma) = k\lambda_1(C_1\sigma)^m$$

where n_1 is the number of next nearest fibers around each single fiber fracture, and the number of "doublets" can be written as $Q_2 = Q_1P_{1-2}(\sigma)$. Then in general, one can write

$$Q_{i+1} = Q_i n_i k\lambda_i(C_i\sigma)^m$$

where Q_i is the number of i-fiber-neighboring-breaks (or "iplets"). Now we depart from the Batdorf approach and claim, first, that the condition of unstable fiber fracture (composite system fracture) can be assessed by requiring that *all* next nearest fibers break around any group of n broken fibers, i.e.,

$$Q_{n+1} = Q_n n_n \Rightarrow Q_n n_n k\lambda_n(C_n\sigma_c)^m = Q_n n_n$$

where Q_{i+1} is the number of neighboring fiber breaks when the applied stress has reached the critical level, σ_C. Then we can solve for that critical "composite strength" to obtain

$$\sigma_c = \frac{1}{(k\lambda_n)^{1/m}C_n} = \frac{\sigma_o}{\lambda_n^{1/m}C_n}$$

Now if we substitute the earlier form for λ_n, and simplify the expression, we obtain

$$\sigma_c = \frac{\sigma_o}{[(\delta_n/(m + 1))(C_n^m + C_n^{m-1} + \ldots + 1)]^{1/m}}$$

We note in passing that if there are no local stress concentrations, the sum in the denominator of that expression becomes $m + 1$, and the strength expression becomes nearly identical to the classical bundle strength estimate for that limiting condition. We also note that this simple expression predicts a maximum (optimum) in the strength of the composite as the ineffective length and the local stress concentration are varied, as shown by Fig. 10 (for $m = 2$). Hence, such an expression correctly follows the physics that we know controls the situation, and guides us in the choice of material parameters to avoid excessive local stress concentrations on the one hand and excessively long ineffective lengths on the other.

However, at this point we encounter the limits of current mechanics models in that no closed-form solutions for the stress concentrations or the ineffective lengths are available for the case when several fibers are broken locally. For our case, we can approach the question of the ineffective length by using Curtin's model to write the following relationship

$$\lambda_n \rightarrow \frac{2}{L}\left(\frac{\hat{D}E_f\epsilon}{4\tau_o}\right)$$

(with the definition that $\hat{D}$ is an "effective" fiber diameter that has been adjusted to account for the fact that multiple fibers are broken in the critical region that initiates unstable fracture). Then if we claim that $E_f\epsilon \rightarrow \sigma_o$ when the applied stress reached the critical level, σ_C, we obtain the estimated strength expression

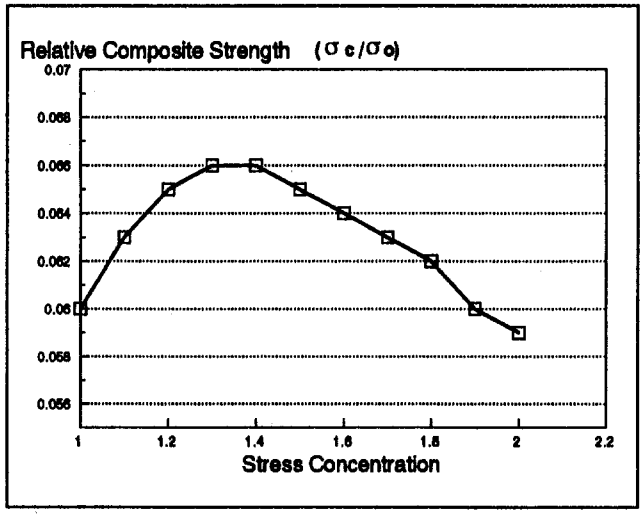

Fig. 10 Global composite strength as a function of local stress concentration caused by n broken fibers

$$\sigma_c = \sigma_o^{(m-1)/m}\left(\frac{L2\tau_o}{\hat{D}}\right)^{1/m}\frac{(1 + m)^{1/m}}{[C_n^m + C_n^{m-1} + \ldots + 1]^{1/m}}$$

that compares nearly term by term with the expression given by Curtin, except for the dependence on the stress concentration, and the effect of fiber slipping which he incorporates. If we adopt those two "correction factors" from Curtin's work, the final expression becomes

$$\sigma_c = \sigma_o^{m/(m+1)}\left(\frac{2\tau_o L}{\hat{D}}\right)^{1/(m+1)}\left(\frac{2}{m + 2}\right)^{1/(m+1)} \times \left(\frac{m + 1}{m + 2}\right)\frac{(1 + m)^{1/m}}{[C_n^m + C_n^{m-1} + \ldots + 1]^{1/m}}$$

This expression has numerous advantages for the estimation of static strength, and for use in the estimation of remaining strength under long-term mechanical and thermal loading. Most important, it is explicit in the dependence on the microproperties that control that strength or remaining strength, such as the interfacial shear stress/strength τ_o and the local stress concentration, C_n. In principle, the local stress concentration can be calculated, so that the only unknown for a given material system that is difficult to obtain is the critical number of broken fibers in a local region when unstable fracture ensues. As it happens, that number has been measured for some systems, and varies over a small range for those cases (Razvan, 1992; Tamuzh, 1981). Most important, our closed-form strength expression above shows an optimum ("correct") choice for the material properties involved, including the interfacial strength that should be used to balance the local stress concentration against long ineffective lengths that reduce the bundle strength of the system.

Summary of Concepts

The discussions and data presented above provide the following perspectives on the function and importance of fibers in continuous fiber-reinforced ceramic matrix composites:

1 Fibers control the density and influence of matrix cracks that develop at applied load levels above the matrix crack initiation point.

2 Matrix cracking greatly changes the stress in the fibers.

3 The interaction of the fibers and matrix (controlled by the relative stiffness of the fibers and matrix and the fiber-matrix interphase region) controls the stress in the fibers, especially the local stress (and stress redistribution) in the neighborhood of fiber fractures.

4 The statistical variation of fiber strength plays an important role in CMC composite strength and life.

5 CMC composites should be "designed" to balance the tendency for brittle fracture against the tendency for the fibers to operate as a "bundle" (or rope) without the benefit of interaction with the matrix. This design is often controlled by the nature of the fiber-matrix interphase region, typically created by fiber coatings such as carbon.

6 Models exist, and others are being developed, that can specify the correct choices for constituent and interphase properties, geometry, and arrangements to obtain optimum strength and life (remaining strength) for CMCs. The existing models (and the understandings that support them) are incomplete, but a solid foundation for this effort exists. The models presented in the present paper add quantification of changes in axial stiffness due to fiber breaks, the effect of local stress concentrations caused by fiber fracture on composite strength, and the fraction of fibers broken as a function of quasi-static applied load level to other available representations.

Acknowledgments

The authors gratefully acknowledge the support of the Oak Ridge National Laboratory Fossil Energy Program under contract No. 19X-SL758C, the National Science Foundation Science and Technology Center for High Performance Polymeric Adhesives and Composites under grant No. DMR9120004, the Babcock and Wilcox Corporation under contract No. 90189/CDR1286, and the Virginia Center for Innovative Technology under grant No. MAT-94-015.

References

Aveston, J., Cooper, G. A., and Kelly, A., 1971, "Single and Multiple Fracture," *Proc. Conf. on the Properties of Fiber Composites,* IPC Science and Technology Press, Guildford.

Batdorf, S. B., 1982, "Tensile Strength of Unidirectionally Reinforced Composites," *J. Reinforced Plastics and Composites,* Vol. 1.

Carman, G., and Reifsnider, K., 1992, "Micromechanics of Short-Fiber Composites," Vol. 43, pp. 137–146.

Cox, H. L., 1952, "The Elasticity and Strength of Paper and Other Fibrous Materials," *British Journal of Applied Physics,* Vol. 3, pp. 72–79.

Curtin, W. A., 1991, "Theory of Mechanical Properties of Ceramic-Matrix Composites," *J. Am. Ceram. Soc.,* Vol. 74, No. 11, pp. 2837–2845.

Gao, Z., and Reifsnider, K., 1993, "Micromechanics of Tensile Strength in Composite Systems," ASTM STP 1156, W. W. Stinchcomb and N. E. Ashbaugh, eds., Am. Soc. for Testing and Materials, Philadelphia, Vol. 4, pp. 453–470.

Henneke, E. G., Vary, A., and Tiwari, A., 1993, "Modelling of Stress-Strain Response of Ceramic Composites by Acousto-Ultrasonic Parameters," *Sixth Annual HITEMP Conference Proceedings,* Cleveland, OH.

Liao, K., 1994, "Tensile and Uniaxial/Multiaxial Fatigue Behavior of Ceramic Matrix Composites at Ambient and Elevated Temperatures," PhD Dissertation, Virginia Tech, Blacksburg, VA.

Razvan, A., 1992, "Fiber Fracture in Continuous-Fiber Reinforced Composite Materials During Cyclic Loading," Dissertation, Engineering Science and Mechanics, College of Engineering, Virginia Polytechnic Institute and State University.

Schwietert, H. R., and Steif, P. S., 1990, "A Theory for the Ultimate Strength of a Brittle-Matrix Composite," *Journal of the Mechanics and Physics of Solids,* Vol. 38, No. 3, pp. 325–343.

Sutcu, M., 1989, "Weibull Statistics Applied to Fiber Failure in Ceramic Composites and Work of Fracture," *Acta Metallurgica,* Vol. 37, No. 2, pp. 651–661.

Tamuzh, V., 1981, *Proc. 2nd U.S.A.-U.S.S.R. Symp. on Fracture of Composite Materials,* Lehigh University.

Tiwari, A., Reifsnider, K. L., and Henneke, E. G. II, 1995, "Modeling Mechanical Response of SiC/CAS-II Ceramic Composites Under Quasi-Static Loads Using A Real-Time Acousto-Ultrasonic NDE Technique," accepted for publication in *Journal of Composite Materials,* June.

Warren, R., 1992, "Fundamental Aspects of the Properties of Ceramic Matrix Composites," in: *Ceramic Matrix Composites,* R. Warren, ed., Blackie Press, London, pp. 64–114.

Weitsman, Y. L., and Zhu, H., 1992, "Multifracture of Ceramic Composites," Oak Ridge National Laboratory Contract Report, ORNL-6703.

On the Relative Roles of Fuel Spray Kinetic Energy and Engine Speed in Determining Mixing Rates in D.I. Diesel Engines

W. J. Smith

D. J. Timoney

Department of Mechanical Engineering, University College Dublin, Belfield, Dublin 4, Ireland

This paper describes an attempt to separate out and to quantify the relative importance of fuel injection characteristics and in-cylinder air motion as factors influencing the rate of fuel–air mixing and of combustion in high-speed D.I. diesel engines, where bulk swirling air motion is absent. Tests on a 121 mm bore × 139 mm stroke, 1.6 liter, single-cylinder engine at constant engine speed reveal substantially shorter fuel–air mixing times as the mean fuel injection kinetic energy (M.I.K.E.) is increased. Also, tests at constant injection kinetic energy but with varying engine speed (involving different fuel injection system builds at each speed) show that fuel–air mixing times are reduced at higher engine speeds. From these trends it is concluded that, while injection kinetic energy is the dominant factor in determining fuel–air mixing rates in D.I. diesels, small-scale turbulent air motions, the intensity and structure of which are related to engine speed, also exert an important influence on the mixing rate.

Introduction

A major portion of the combustion process in Direct Injection (D.I.) diesel engines takes place in diffusion flames (Kamimoto and Kobayashi, 1991; Ikegami et al., 1988; Plee and Ahmad, 1983). Rates of chemical reaction and of heat release are therefore controlled by rates of fuel–air mixing. The physical effects that "drive" the fuel–air mixing in a given engine geometry are not understood in detail, but appear to be related to:

(*i*) the fuel injection process
(*ii*) air motion effects (swirl, squish, and turbulence), and
(*iii*) combustion chamber geometry.

Despite intensive research effort over many years, the relative influences of these individual effects on rates of combustion are still poorly understood. This paper describes the results of an engine-based experimental study designed specifically to isolate and quantify the independent influences of fuel injection characteristics and of piston-generated air turbulence on the rate of mixing and combustion.

Present State of Knowledge

The effects of fuel injection system parameters on rates of mixing and combustion and on exhaust emissions have been thoroughly investigated and are now reasonably well documented (e.g., Beck et al., 1988; Doyle et al., 1989; Herzog, 1989; Nakakita et al., 1991; Needham et al., 1990; Russell et al., 1989; Ball, 1981; Krieger, 1989; Zelenka et al., 1990). Experimental studies have clearly established the desirability of achieving very high fuel injection system pressures, which, in turn, yield high velocities of fuel injection into the combustion chamber.

The contribution of air motion effects to mixing is generally less clear-cut but appears to vary significantly with engine size. For example, a combination of experiment and analysis (Ball, 1981; Timoney, 1985a) implied that bulk air motion effects had a relatively small influence in a larger (216 mm bore), slower speed engine but a very much more substantial influence in a smaller, higher speed "swirling" DI engine (121 mm bore).

Distinguishing between the influences of fuel injection and air motion is not a straightforward matter and certainly does not seem to have been clearly explained in the existing literature. This paper describes an attempt to examine the effects of engine speed changes (and hence changes in piston-generated turbulence) on combustion rate, independently of the combustion chamber shape, fuel injection rate and bulk air motion, at least for the case of a relatively small (121 mm bore), high-speed D.I. diesel engine.

Experimental Program

Description of Experimental Apparatus. The experimental data were obtained using a Ricardo E16, single-cylinder, two-valve, D.I. diesel research engine of 121 mm bore × 139 mm stroke, 1.6 liter swept volume. The compression ratio was 15.9 and a cylindrical "deep bowl" piston cavity 63.4 mm diameter × 26.9 mm deep was used.

For all test cases discussed here, the engine was fitted with a *zero-swirl inlet port,* and external boost air was supplied at 0.5 bar above atmospheric for all tests. Air intake manifold temperatures were in the range 22–25°C. Fueling was constant at 70 mm^3 per injection for all tests, giving trapped air–fuel ratios close to 48:1. This relatively lean air–fuel ratio was necessary to protect the cylinder pressure transducer from excessively high in-cylinder soot levels. Zero swirl levels were confirmed on a Ricardo steady flow test rig, using an impulse type swirl meter (Tippelman, 1977).

A C.A.V. "Majormec" fuel injection pump was used in conjunction with a variety of plunger diameters (and hence nominal pumping rates). Fuel injection pump plunger diameters of 10, 11, and 12 mm were used together with a 4 hole × 0.28 mm dia × 140 deg cone angle injector nozzle, yielding maximum fuel-line pressures of 300–700 bar. Nozzle opening pressure (NOP) was set to either 210 or 340 bar by omitting or inserting a shim between the injector needle and its return spring.

Contributed by the Internal Combustion Engine Division and presented at the Internal Combustion Engine Division 1995 Spring Technical Conference, Marietta, Ohio, April 23–26, 1995. Manuscript received by the Internal Combustion Engine Division February 1995. Associate Technical Editor: W. K. Cheng. Paper No. 95-ICE-8.

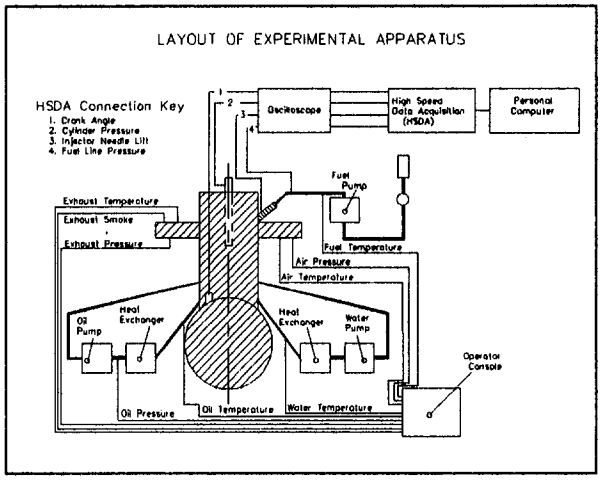

Fig. 1 Layout of experimental apparatus

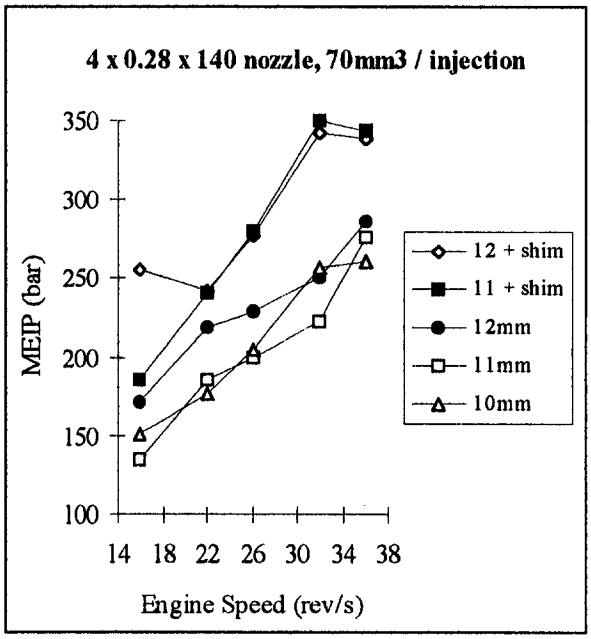

Fig. 2 Variation of M.E.I.P. with engine speed and fuel injection pump plunger diameter

Cylinder pressure was detected with a Kistler piezoelectric transducer (model 6121) and fuel line pressure was sampled at a point about 160 mm from the injector with an Intersonde Type 21 transducer. A Ricardo needle lift transducer was fitted to the injector. Fuel line pressure, needle lift, and cylinder pressure data were recorded at intervals of one half-degree crank angle, using a high-speed data acquisition system (HSDA), and stored on floppy disks before being transferred to a desktop PC for subsequent analysis. A schematic diagram of the experimental apparatus is shown in Fig. 1.

Design of the Experimental Program. The test program covered a range of engine speeds from 16 to 36 rev/s (960 to 2160 rpm). Fuel injection timing was adjusted at each test condition to give start of cylinder pressure rise at TDC (±0.5 deg).

The primary objective of the test program was to obtain data from tests where:

1 the engine speed was held constant and the fuel spray kinetic energy was varied; and

2 the fuel spray kinetic energy was held constant and the engine speed was varied.

The first objective was achieved by using different fuel injection pump plungers and/or different injector nozzle opening pressures to alter the spray kinetic energy, at a given engine speed.

With a given fuel system build, the fuel spray kinetic energy tends to increase with increasing engine speed. The second objective was achieved therefore by using a high-rate fuel pump build at low engine speeds and lower-rate builds as the engine speed was increased. The magnitude of the fuel spray kinetic energy was initially estimated using the mean effective injection pressure (M.E.I.P.) computation outlined by Ball (1981). M.E.I.P. is the mean pressure difference that would be required to force the known fuel quantity through the nozzle orifice area during the measured injection period. The variation in M.E.I.P. with engine speed for a range of fuel pump builds and at a fueling rate of 70 mm^3/injection is shown in Fig. 2.

Nomenclature

M.E.I.P. = Mean Effective Injection Pressure (mean pressure drop required to force the measured fuel volume per injection through the injector nozzle hole area in the measured injection period)

M.I.K.E. = Mean Injection Kinetic Energy, kJ/kg (computed from instantaneous injection rate data)

Results and Data Analysis

At each test condition, cylinder pressure, needle lift, and fuel line pressure were measured over 100 consecutive engine cycles. An ensemble average for each channel was then obtained and this average was employed for all subsequent analysis. The raw cylinder pressure data were smoothed using a cubic spline technique, and the resultant pressure trace was used to compute the instantaneous heat release rate at each test condition using the one-dimensional heat release analysis program HREL (Timoney, 1987b). Based on the results of the heat release calculation, a *mixing time* was calculated as being the time interval between the start of needle lift (the start of fuel–air mixing) and the point where the heat release computed by HREL was equal to 80 percent of the calorific value of the injected fuel quantity. The 80 percent point was chosen (rather than 90 or 100 percent) in order to avoid well-known difficulties associated with the computation of heat release rates during the final stages of combustion (Timoney, 1987b). The results of this analysis are presented in Fig. 3, which shows the variation in computed mixing time as a function of M.E.I.P. for a range of engine speeds. Note that no bulk air swirl was present and that any in-cylinder gas motions present before start of injection must be presumed to be due to squish or to piston motion (where the latter includes turbulence generated by intake valve flows that has not fully decayed).

It is clear from Fig. 3 that the time required to mix the fuel and air depends strongly on both the M.E.I.P. and the engine speed. It is also evident that the magnitude of the engine speed effect is at least as great as that of M.E.I.P.

For example, increasing the M.E.I.P. by 50 percent from 200 bar to 300 bar has a significantly smaller effect on the mixing time than increasing the engine speed by approximately the same percentage from 22 rev/s to 32 rev/s (45 percent increase).

On studying these results, the authors were not satisfied that the M.E.I.P. calculation gave an accurate estimate of the kinetic energy associated with an unsteady, transient fuel injection process. In order to quantify this parameter more accurately, they

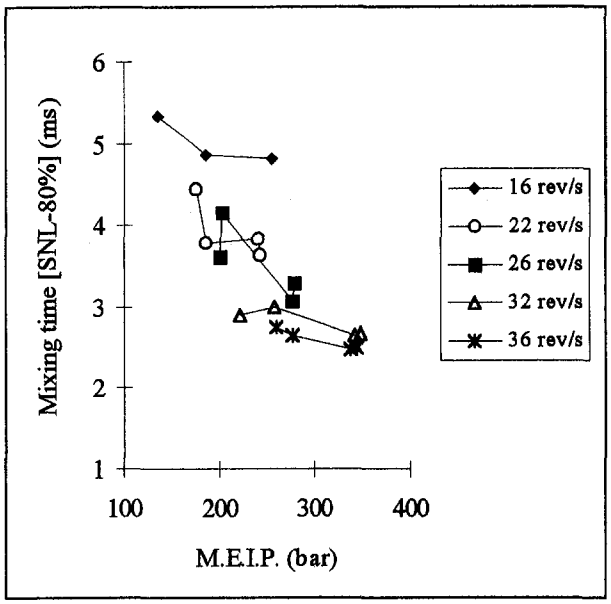

Fig. 3 Variation of fuel–air mixing time with engine speed and mean effective injection pressure

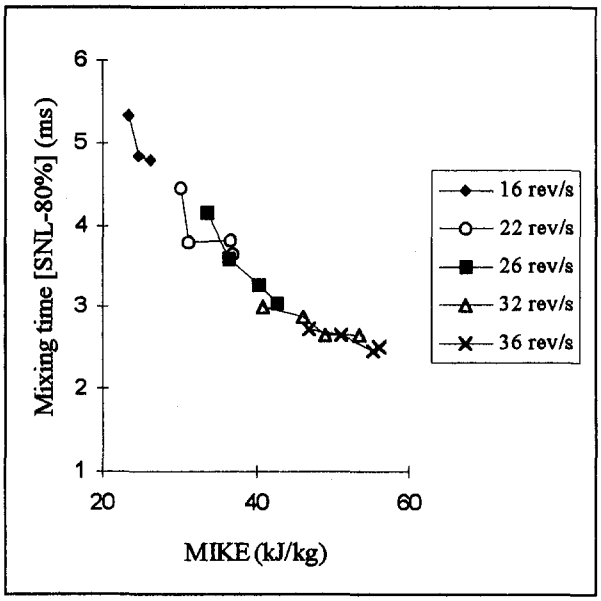

Fig. 4 Variation of mixing time with M.I.K.E. at constant engine speed

constructed a computer model (INJECT), which used the measured fuel line pressure, measured needle lift, and measured cylinder pressure data to predict the instantaneous injection rate throughout the injection period. The program uses a method of characteristics technique to compute the instantaneous fuel pressure at the nozzle orifices from the measured fuel line pressure data, and combines this with the measured cylinder pressure and needle lift to compute instantaneous injection rate and kinetic energy (Smith and Timoney 1991, 1992; Timoney and Smith, 1993).

Using INJECT, the mass-weighted mean kinetic energy of the fuel spray could be computed, and this parameter was denoted M.I.K.E. (mean injection kinetic energy). This parameter has the units of kJ/kg, and represents the kinetic energy of the injected fuel per unit mass. An equivalent mean injection pressure can be computed by multiplying the M.I.K.E. by the fuel density. So for diesel fuel with a density of 845 kg/m^3, a M.I.K.E. of 10 kJ/kg is equivalent to a mean pressure drop of 84.5 bar across the nozzle orifices.

When the fuel spray kinetic energy is computed in this manner, the trends apparent from Fig. 3 change very significantly. Figure 4 shows the variation in computed mixing time as a function of M.I.K.E. for a range of engine speeds.

A casual glance at Fig. 4 would suggest that increases in mixing rate are associated solely with increases in the kinetic energy of the fuel spray and that engine speed-related air motion effects were of little or no significance. However, it should be remembered that, due to the manner in which the tests were performed, M.I.K.E. and engine speed are highly correlated, i.e., high M.I.K.E. values are obtained at high engine speeds, and vice versa.

Figure 5 presents data from tests that have the same M.I.K.E. at different engine speeds. These tests represent a subset of those plotted in Fig. 4, and clearly indicate that the engine speed, as well as the M.I.K.E., exerts a significant influence on the fuel–air mixing rate.

Because the inadequacies of the M.E.I.P. calculation as a measure of fuel spray kinetic energy were not known until the experimental program had been completed, the engine speed variations achieved at a given M.I.K.E. are relatively small. Nonetheless, the trend for all the available data clearly shows that the mixing time reduces (i.e., mixing rate increases) as the engine speed is increased.

Careful examination of Fig. 5 reveals that a M.I.K.E. of 55 kJ/kg was computed for *two* test points at an engine speed of 36 rev/s. Despite the fact that different fuel injection system builds were employed (11 mm plunger for test 1011 and 12 mm plunger for test 1021), yielding quite different injection rate diagrams (as shown in Fig. 7 of Timoney and Smith, 1993), the mixing times were almost identical. The authors feel that this result strongly supports their hypothesis that M.I.K.E. exerts a first-order influence on the fuel–air mixing rate in nonswirling D.I. diesel engines.

The two data points shown on Fig. 5 at 22 rev/s with M.I.K.E. values of 37 kJ/kg are the cause of some concern in that they upset an otherwise consistent trend. For these two tests the mixing times are significantly different, despite the fact that the M.I.K.E. and the engine speed are the same, as should be the bulk air motion, the start of combustion timing, and the fueling quantity. It is difficult, therefore, to explain the disparity in the

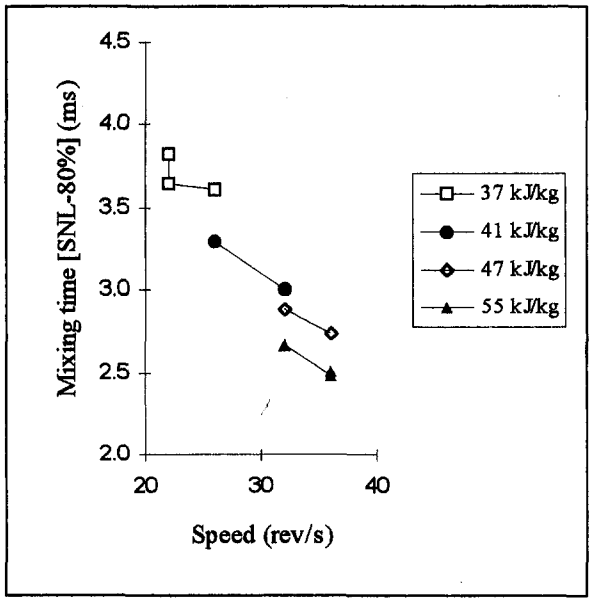

Fig. 5 Variation of mixing time with engine speed at constant M.I.K.E.

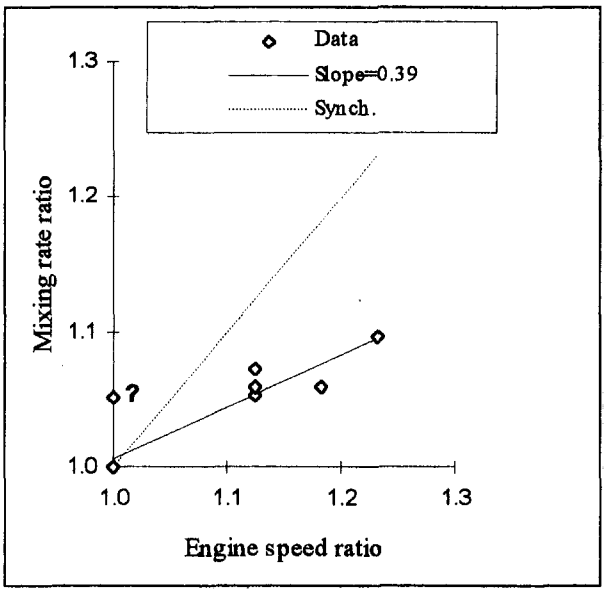

Fig. 6 Dimensionless presentation of data from Fig. 5

fuel–air mixing rates for these tests. No satisfactory explanation is available at the time of writing.

In order to quantify the magnitude of the apparent engine-speed related effect, the data from Fig. 5 can be shown on a dimensionless plot (Fig. 6). Using the data for the lowest engine speed at a particular M.I.K.E. level as the baseline, the engine-speed ratio of other tests at the same M.I.K.E. is plotted along the abscissa, and the corresponding mixing-time ratio is plotted along the ordinate. Repeating this exercise for each line of constant M.I.K.E. produces the data points of Fig. 6. Note that the line drawn through the points is not a regression line, as it ignores the presence of the data point marked "?". This arises from the above-mentioned pair of data points at 22 rev/s. Also plotted in Fig. 6 is a line denoted "synch." This is the slope of a line when the mixing rate scales linearly with engine speed.

It is apparent from Fig. 6 that there does seem to be a general trend of increasing mixing rate with increased engine speed. The slope of the trend line suggests that doubling the engine speed—while maintaining M.I.K.E. at a fixed level—would increase the fuel–air mixing rate by 39 percent.

Discussion

Taken together, the trends shown in Figs. 4, 5, and 6 suggest the following:

1 **At a constant engine speed, increasing the mean fuel injection kinetic energy (M.I.K.E.) increases the fuel–air mixing rate and therefore yields a shorter 0–80 percent mixing time.**

This conclusion is consistent with the widely accepted principle that increased injection pressures give rise to shorter combustion periods in D.I. diesel combustion systems, but emphasizes the importance of kinetic energy rather than the mean effective injection pressure parameter. Given that spray kinetic energy per unit mass and nozzle pressure drop are both related directly to the square of the injection velocity, the difference in slopes between corresponding constant speed lines of Figs. 3 and 4 are of particular interest. For example, at 16 rev/s, a change of injection system build from 11 mm plunger at 210 bar NOP (Test 985) to 11 mm plunger at 340 bar NOP (Test 1025) to 12 mm plunger at 340 bar NOP (Test 1015) yielded changes in M.E.I.P. from 135 (100 percent) to 186 (137 percent) to 255 bar (189 percent) but changes in M.I.K.E. of 23.3 kJ/kg (100 percent) to 24.8 (106 percent) to 26.3 (113 percent).

The data plotted in Fig. 4 strongly suggest that M.I.K.E. is the dominant factor governing fuel–air mixing rates in non-swirling D.I. diesel combustion systems. The mechanisms that might give rise to this phenomenon are thought to be:

(*i*) Higher fuel spray velocities associated with an increase in M.I.K.E. lead to more rapid and effective bulk distribution of the fuel in the surrounding air;

(*ii*) Higher-velocity sprays are more turbulent, leading to increased air entrainment, and to the generation of higher turbulence levels in the surrounding air (e.g., Kamimoto, 1991);

(*iii*) As discussed by Timoney (1987c) there is a theoretical minimum energy required to distribute the fuel throughout the air in a finite time. The actual energy supplied is very many times larger than this and a "mixing efficiency" can be defined which is the ratio of these two figures. Assuming that the mixing efficiency of a given injection system/combustion chamber configuration is determined primarily by its combined geometry, increasing the kinetic energy of the fuel spray will tend to promote more rapid mixing.

2 **At a constant M.I.K.E., increasing the engine speed increases the rate of fuel–air mixing.**

This conclusion is less likely to be expected by those familiar with Direct Injection combustion systems, since the causative mechanisms are not so readily apparent. It is of course possible that the increased mixing rate observed in Fig. 5 as engine speed is increased, is in fact linked to some other aspect of combustion system, and that the connection with engine speed is purely coincidental. A plausible mechanism is therefore required to explain how an increase in piston speed might assist the fuel–air mixing process. The authors suggest that small-scale turbulent air motions, induced by the motion of the piston, represent such a mechanism.

It has been established for a variety of combustion chamber shapes in open chamber engines that the intensity of in-cylinder turbulence scales more or less linearly with piston speed (Arcoumanis and Whitelaw, 1987; Catania and Mittica, 1987; Heywood, 1986; Lancaster, 1976; Witze, 1977). It is also accepted that the combustion process in D.I. diesel engines is characterized by random turbulent mixing between turbulent eddies having different concentrations (Ikegami et al., 1988; Magnussen and Hjertager, 1976), and that the fuel–air mixing rate is the primary factor governing the fuel burning rate (Heywood, 1986). More recently, Konno observed that turbulence exerts a major influence both on the rate and on the completeness of combustion during the diffusion combustion phase (Konno et al., 1992).

It has been explicitly or implicitly accepted in most of these studies, however, that the turbulence required for successful combustion is generated almost exclusively by the fuel sprays and perhaps by the combustion process itself, perhaps with a secondary contribution from the collapse of bulk air flow structures such as swirl (e.g., Bazari, 1992; Beck et al., 1988; Plee and Ahmad, 1983). Combustion models constructed on this basis would not, however, be able to predict the engine-speed related trend observed in Figs. 5 and 6. For example, Chikahisa et al. (1992) computed fuel vapor distribution at nonflame conditions, for two different engine speeds but with the same injection velocity (and M.I.K.E.). Although heat release computations were not included in this paper, the fuel vapor distributions do not suggest an improvement in the mixing rate; rather the reverse, since an air turbulence term is not included in the model.

Some support for the hypothesis put forward by the present authors that small-scale piston-induced turbulence contributes significantly to fuel–air mixing is available from the fact that re-entrant and square-lobed piston bowls, which enhance air turbulence during the injection and combustion phases, are becoming widespread (e.g., Ikegami et al., 1990; Sakata et al., 1990). Further support may be found in the results of some unusual experiments by Konno et al. (1992) and Nagano et al. (1994).

There is some support, therefore, for the hypothesis that the increased fuel–air mixing rate associated with increased engine speed at constant M.I.K.E. is related to piston-generated turbulence. Doubts arise, however, when the magnitude of the kinetic energy associated with this turbulence is compared to that of the fuel sprays. The latter is typically three orders of magnitude greater than the turbulent kinetic energy of the charge air at TDC compression (e.g., Timoney, 1987c). It may therefore appear difficult to justify the inclusion of air turbulence effects in a combustion model. As shown by Timoney (1987c), the energy available in even the most feeble fuel spray massively exceeds the theoretical minimum required for efficient mixing. The structure and distribution of the turbulent flow field, therefore, would seem to be highly significant.

However, it has been observed (Catania and Mittica, 1987, 1990) that the micro-time scale of the instantaneous velocity fluctuation in reciprocating engines exhibits an approximately inverse scaling law with engine speed. A less than inverse scaling law was also deduced for the dependence of the micro-time scale of *cycle-resolved* turbulence on engine speed in the same paper. This concentration of turbulent energy in smaller structures as engine speed increases is exactly what is required to enhance fuel–air mixing at the molecular level. Turbulent air motions are also distributed throughout the mixing/combustion chamber, rather than concentrated in dense sprays and clouds of vapor. The turbulent kinetic energy is therefore optimally positioned to assist in the mixing process.

A very large body of literature has been published on experimental and theoretical aspects of diesel engine combustion, and much of this has been summarized by Ramos (1989). It is evident that much of the modeling effort has been directed toward the study of atomization and sprays, often with emphasis on droplet–turbulence interactions and spray interaction with swirl. However, high-speed combustion photographs show that recognizable spray jets disappear relatively early on in the combustion process, especially after spray impingement on the chamber walls. This is true particularly for small high-speed engines under conditions of high load, where oxygen availability is low. Therefore, a large portion of fuel–air mixing/heat release occurs outside of the sprays. There can be no doubt that spray-related effects set the initial conditions for the fuel–air mixing process and these are clearly vital to the efficacy of the overall process, but there seems to be plenty of scope for other factors to become dominant later on.

Conclusions

The authors have performed a unique series of experiments on a 1.6 liter, single-cylinder D.I. diesel research engine, covering engine speeds from 16 to 36 rev/s (960 to 2160 rpm) with a variety of fuel pumping rates but for a *nonswirling* engine build. Subsequent analysis of the instantaneous fuel injection characteristics using an injection rate analysis program has furnished evidence in support of the following:

- At a constant engine speed, increasing the *mean fuel injection kinetic energy* (M.I.K.E.) increases the fuel–air mixing rate and therefore yields a shorter mixing (or heat release) time.
- At a constant fuel injection kinetic energy, increasing the engine speed increases the fuel–air mixing rate. This effect is believed to be a result of the influence of piston-generated turbulence. This turbulence is not normally "designed in" to achieve maximum benefit. More detailed study of the mechanisms in operation here may lead to the development of better combustion systems for high-speed direct injection diesel engines.

Acknowledgments

W. J. Smith would like to express his gratitude to the Irish Electricity Supply Board for their support through the University College Dublin Newman Scholar scheme, without which much of the work presented in this paper could not have been completed. The authors would also like gratefully to acknowledge the assistance and support provided by Ricardo Consulting Engineers, Sussex, U.K., in whose laboratories all of the experimental work was carried out.

References

Arcoumanis, C., and Whitelaw, J. H., 1987, "Fluid Mechanics of Internal Combustion-Engines—a Review," *Proc. Inst. Mech. Engrs.,* Vol. 201, No. C1.

Ball, W. F., 1981, "Einflusse des Einspritzdruckes auf die Verbrennung bei Dieselmotoren mit Direkteinspritzung ohne Luftdroll," *MTZ,* Vol. 42, No. 4, pp. 141–149.

Ball, W. F., and Timoney, D. J., 1981, "The Performance of a Quiescent Direct Injection Diesel Combustion System and Its Comparison With Prediction," presented at CIMAC, Helsinki, 8–12 June.

Bazari, Z., 1992, "A DI Diesel Combustion and Emissions Predictive Capability for Use in Cycle Simulation," SAE Paper No. 920462.

Beck et al., 1988, "Effects of Fuel Injection on Diesel Combustion," SAE Paper No. 880299.

Catania, A. E., et al., 1992, "Time-Frequency Spectral Structure of Turbulence in an Automotive Engine," SAE Paper No. 920153.

Catania, A. E., and Mittica, A., 1987, "Induction System Effects on Small-Scale Turbulence in a High-Speed Diesel Engine," ASME JOURNAL OF ENGINEERING FOR GAS TURBINES AND POWER, Vol. 109, pp. 491–502.

Catania, A. E., and Mittica, A., 1990, "Autocorrelation and Autospectra Estimation of Reciprocating Engine Turbulence," ASME JOURNAL OF ENGINEERING FOR GAS TURBINES AND POWER, Vol. 112, pp. 357–368.

Chikahisa et al., 1992, "Combustion Similarity for Different Size Diesel Engines: Theoretical Prediction and Experimental Results," SAE Paper No. 920465.

Doyle et al., 1989, "Application of an Advanced In-Line Injection System to a Heavy Duty Diesel Engine," SAE Paper No. 891847.

Herzog, P., 1989, "The Ideal Rate of Injection for Swirl Supported Diesel Engines," presented at IMechE Seminar on Diesel Fuel Injection Systems, London, 10–11 Oct.

Heywood, J. B., 1986, "Fluid Motion Within The Cylinder of Internal Combustion Engines—The 1986 Freeman Scholar Lecture," ASME *Journal of Fluids Engineering,* Vol. 109, pp. 3–35.

Ikegami et al., 1988, "Diesel Combustion and the Pollutant Formation as Viewed From Turbulent Mixing Concept," SAE Paper No. 880425.

Ikegami et al., 1990, "Combustion Chamber Shape and Pressurised Injection in High-Speed Direct Injection Diesel Engines," SAE Paper No. 900440.

Kamimoto, T., and Kobayashi, H., 1991, "Combustion Processes in Diesel Engines," *Prog. Energy Combust. Sci.,* Vol. 17, pp. 163–189.

Konno et al., 1992, "Reduction of Smoke and NO_x by Strong Turbulence Generated During the Combustion Process in D.I. Diesel Engines," SAE Paper No. 920467.

Krieger, K., 1989, "Diesel Fuel Injection Systems for Heavy Duty Engines," presented at IMechE Seminar on Diesel Fuel Injection Systems, London, 10–11 Oct.

Lancaster, D. R., et al., 1976, "Effects of Turbulence on Spark-Ignition Engine Combustion," SAE Paper No. 760160.

Lancaster, D. R., 1976, "Effects on Engine Variables on Turbulence in a Spark-Ignition Engine," SAE Paper No. 760159.

Magnussen, B. F., and Hjertager, B. H., 1976, "On Mathematical Modelling of Turbulent Combustion With Special Emphasis on Soot Formation and Combustion," *16th Symposium (International) on Combustion,* The Combustion Institute.

Nagano et al., 1994, "Reduction of Exhaust Emissions by Air-Jet Turbulence in a DI Diesel Engine: Application to an In-Line 6-Cylinder Engine," *JSAE Review 15,* pp. 9–14.

Nakakita et al., 1991, "Effects of High Pressure Fuel Injection on the Combustion and Exhaust Emissions of a High-Speed Diesel Engine," *JSAE Review,* Vol. 12, No. 1, pp. 18–25, Jan.

Needham, J. R., et al., 1990, "Injection Timing and Rate Control—A Solution for Low Emissions," SAE Paper No. 900854.

Needham, J. R., and Whelan, S., 1994, "Meeting the Challenge of Low Emissions and Fuel Economy With the Ricardo Four-Valve High-Speed Direct Injection Engine," *Proc. Instn. Mech. Engnrs Part D,* Vol. 208, pp. 181–190.

Plee, S. L., and Ahmad, T., 1983, "Relative Roles of Premixed and Diffusion Burning in Diesel Combustion," SAE Paper No. 831733.

Ramos, J. I., 1989, *Internal Combustion Engine Modelling,* Hemisphere Publishing Corporation.

Russell et al., 1989, "Rate Modulation for Direct Injection Diesel Engines," presented at IMechE Seminar on Diesel Fuel Injection Systems, London, 10–11 Oct.

Sakata et al., 1990, "Development of Toyota Reflex Burn (TRB) System in DI Diesel," SAE Paper No. 900658.

Smith, W. J., and Timoney, D. J., 1991, "Fuel Injection Rate Analysis Using Measured Data," IMechE Paper C430/057, *IMechE Proceedings Computers in Engine Technology.*

Smith, W. J., and Timoney, D. J., 1992, "Fuel Injection Rate Analysis—A New Diagnostic Tool for Combustion Research," SAE Paper No. 922224.

Timoney, D. J., 1985a, "Engine Speed-Related Effects in D.I. Diesel Combustion," presented at the International Symposium on Advanced Engine Research (ISER), University of Wisconsin, Madison, U.S.A., Sept.

Timoney, D. J., 1985b, "Smoke and Fuel Consumption Measurements in a Direct Injection Diesel Engine With Variable Swirl," SAE Paper No. 851542.

Timoney, D. J., 1987a, "Effects of Important Variables on Measured Heat Release Rates in a D.I. Diesel," SAE Paper No. 870271.

Timoney, D. J., 1987b, "Problems With Heat Release Analysis in D.I. Diesels," SAE Paper No. 870270.

Timoney, D. J., 1987c, "Energetics of Fuel-Air Mixing in D.I. Diesel Engines," *Proc. International Centre for Heat and Mass Transfer, 26,* D. Brian Spalding and N. H. Afgan, ed., Hemisphere Publishing Corporation, pp. 189–199.

Timoney, D. J., and Smith, W. J., 1987, "Influence of Turbulence in a D.I. Diesel," *Proc. NATO Advanced Study Institute on Combusting Flow Diagnostics,* Montechoro, Portugal, Apr.

Timoney, D. J., and Smith, W. J., 1993, "Relationships Between Instantaneous Fuel Injection Rate and Exhaust Emissions From a D.I. Diesel Combustion System," 20e Conseil International des Machines a Combustion (CIMAC-20), London, May, Paper D80.

Tippelman, G., 1977, "A New Method of Investigation of Swirl Ports," SAE Paper No. 770404.

Witze, P. O., 1977, "Measurement of the Spatial Distribution and Engine Speed Dependence of Turbulent Air Motion in an I.C. Engine," SAE Paper No. 770220.

Zelenka et al., 1990, "Ways Towards the Clean Heavy Duty Diesel," SAE Paper No. 900602.

Comparison of Emissions and Efficiency of a Turbocharged Lean-Burn Natural Gas and Hythane-Fueled Engine

J. F. Larsen

J. S. Wallace

Department of Mechanical Engineering,
University of Toronto,
Toronto, Ontario, Canada

An experiment was conducted to evaluate the potential for reduced exhaust emissions and improved efficiency, by way of lean-burn engine fuelling with hydrogen supplemented natural gas (Hythane). The emissions and efficiency of the Hythane fuel (15 percent hydrogen, 85 percent natural gas by volume), were compared to the emissions and efficiency of pure natural gas using a turbocharged, spark ignition, 3.1 L, V-6 engine. The feasibility of heavy duty engine fueling with Hythane was assessed through testing conducted at engine speed and load combinations typical of heavy-duty engine operation. Comparison of the efficiency and emissions at MBT spark timing revealed that Hythane fueling of the test engine resulted in consistently lower brake specific energy consumption and emissions of total hydrocarbons (THC), carbon monoxide (CO), and carbon dioxide (CO_2), at a given equivalence ratio. There was no clear trend with respect to MBT oxides of nitrogen (NO_x) emissions. It was also discovered that an improved NO_x-THC tradeoff resulted when Hythane was used to fuel the test engine. Consequently, Hythane engine operating parameters can be adjusted to achieve a concurrent reduction in NO_x and THC emissions relative to natural gas fueling.

Introduction

Ever since the invention of the "horseless carriage," gasoline and diesel fuel have enjoyed a virtual monopoly on fueling of automobile power plants. Within the past decade, however, growing environmental awareness has resulted in the enaction of more stringent regulations governing the tailpipe emissions of automobiles. In turn, this legislation has inspired efforts to search for viable, less polluting alternative fuels.

In an effort to harness the low emissions potential of hydrogen, without dealing with the complications associated with a dedicated hydrogen-fueled vehicle, some research has been focused on assessing the benefits of hydrogen-supplemented hydrocarbon fuels. Most promising of these fuels is Hythane, a mixture of hydrogen and natural gas. Since natural gas exists in a gaseous state (except under extremely low temperatures), it can be easily mixed with hydrogen, a convenience not shared by the liquid hydrocarbon fuels. The primary benefit of Hythane stems from the notion that the hydrogen portion of the mixture will burn without producing any hydrocarbon (HC) or carbon monoxide (CO) emissions. Due to the faster flame speed and broader flammability limits of hydrogen, addition of hydrogen to natural gas should result in an overall increase in the laminar burning velocity and lean operating limit; these factors will serve to decrease oxides of nitrogen (NO_x) emissions, while maintaining lower levels of total hydrocarbons (THC) in the engine exhaust. The increase in hydrogen-to-carbon ratio that results from hydrogen supplementation will also yield lower carbon dioxide (CO_2) emissions. Furthermore, at low enough hydrogen concentrations, Hythane fuel can be metered (e.g., by mixer or port injectors), without need for the elaborate fueling strategies required of pure hydrogen fueling.

Several studies have been conducted in an effort to assess the potential of Hythane as an alternative to natural gas fueling of engines. The studies can essentially be divided into two groups: stoichiometric fueling and lean-burn operation. All of the stoichiometric studies (Eccleston and Fleming, 1972; Foute et al., 1992; Strothers, 1993; Swain et al., 1993; Cattelan and Wallace, 1994) indicate that stoichiometric Hythane fueling slightly reduces the engine-out levels of hydrocarbons and carbon monoxide during open-loop engine operation. The studies are divided, however, on the effect that Hythane fueling has on engine-out NO_x emissions. Eccleston and Fleming (1972) and Swain et al. (1993) report that NO_x emissions are about the same for natural gas and Hythane fueling, while Foute et al. (1992), Strothers (1993), and Cattelan and Wallace (1994) found increased NO_x emissions during Hythane fueling. Cattelan and Wallace (1994) also report that under closed-loop engine operation, catalytic conversion of NO_x, THC, and CO occurs with almost 100 percent efficiency for both Hythane and natural gas fueling, resulting in no discernible difference in exhaust emissions between the two fuels. Most would agree that there is little apparent benefit to using Hythane in stoichiometrically fueled engines; for open-loop operation, the small reductions in CO and total hydrocarbon emissions are offset, in some instances, by an increase in NO_x emissions. Additionally, under closed-loop operation there does not seem to be any difference in exhaust emissions between Hythane and natural gas fueling.

Many have postulated that the real advantage of Hythane is its ability to allow for ultralean fueling of an engine. To this end, three of the aforementioned studies (Eccleston and Fleming, 1972; Strothers, 1993; Swain et al., 1993) have also researched lean Hythane operation. All of these studies illustrate similar trends in the emissions results; for a given fuel–air equivalence ratio, THC emissions are substantially lower for Hythane fueling, NO_x emissions are higher for Hythane fueling, and CO emissions are about the same for natural gas and Hythane fueling. The real benefit of Hythane, though, is thought to arise from its extended lean operating limit, which Strothers (1993) indicates is 6.3–12.5 percent leaner than the lean op-

Contributed by the Internal Combustion Engine Division and presented at the Internal Combustion Engine Division 1995 Spring Technical Conference, Marietta, Ohio, April 23–26, 1995. Manuscript received by the Internal Combustion Engine Division November 1994. Associate Technical Editor: W. K. Cheng.

Table 1 Engine specifications

Engine make	General Motors
Engine type	Water cooled, four stroke, 60° V-6, spark ignition
Displacement	3146 cm^3
Bore	89 mm
Stroke	84 mm
Compression ratio	8.8:1
Valve actuation	Hydraulic lifters

erating limit of natural gas. At leaner operating conditions, NO_x can be reduced below the levels of NO_x at the lean operating limit of natural gas. At leaner operating conditions, NO_x can be reduced below the levels of NO_x at the lean operating limit of natural gas fueling, while maintaining a THC advantage and low CO emissions. Strothers (1993) and Swain et al. (1993) further reported that engine efficiency was improved through use of Hythane.

The objective of this study is to compare the exhaust emissions and efficiency of a turbocharged Hythane and natural gas fueled engine operated at lean equivalence ratios. An assessment concerning the viability of Hythane as an alternative to natural gas will also be made. The primary focus of this investigation is on the emissions and efficiency at mid and high engine loads, and serves to supplement the research conducted by Strothers (1993) and Swain et al. (1993). Although tests were conducted at light load, small fluctuations in engine torque led to excessive scatter in the brake specific emissions data. When analyzed on a concentration (ppm) basis, however, the light load exhaust emissions exhibit trends similar to those found at the full and half load test conditions.

Experimental Apparatus

The engine used for testing was a General Motors 3.1 liter, turbocharged, six-cylinder, four-stroke, spark ignition engine. Engine specifications are listed in Table 1. For the most part, the engine was left in its stock configuration, but a few changes were deemed necessary in order to optimize the engine for lean-burn operation. To achieve reasonable power output at lean equivalence ratios, a turbocharger was installed between the fuel mixer and throttle. To allow access to engine control parameters, a specialized ECM (engine control module) controlled by a Heads-Up Display (HUD) was used in place of the stock ECM. Due to the software imposed spark advance limit of 50 deg BTDC for the HUD, an aftermarket spark timing (ST) advance module was used in conjunction with the HUD when a spark advance in excess of 50 deg BTDC was required.

The engine speed was controlled by a water brake dynamometer. Engine load was regulated by a PID (Proportional-Integral-Derivative) controlled turbocharger wastegate (at wide open throttle) or by manually varying the throttle position (at part throttle operation). Engine speed and torque were measured using a dynamometer mounted Hall effect sensor and strain gage, respectively.

Engine exhaust gas was extracted from the exhaust pipe about 1.25 m downstream of the exhaust manifold. The sample was dried in a refrigeration type drier, and analyzed to determine the dry emissions of nitric oxide, oxides of nitrogen, total hydrocarbons (in ppm C), carbon monoxide, carbon dioxide, hydrogen, and oxygen. Emissions measurements were made using a chemiluminescence analyzer for NO and NO_x, a flame ionization detector (FID) for THC, a nondispersive infrared (NDIR) analyzer for CO and CO_2, a thermal conductivity detector (TCD) for hydrogen, and a paramagnetic analyzer for O_2. Before collecting any emissions data, the engine was operated until the oil and coolant temperatures had stabilized at their respective set points.

Table 2 Composition and other properties of the test fuels

	HYTHANE	NG
Hydrogen content (%)	15.4	0.0
Methane content (%)	79.67	94.17
Ethane content (%)	2.17	2.57
Propane content (%)	0.223	0.263
Butane content (%)	0.0530	0.0627
Pentane content (%)	0.0119	0.0141
Hexane content (%)	0.0030	0.0036
Heptane content (%)	0.0006	0.0007
Oxygen content (%)	0.108	0.128
Nitrogen content (%)	1.92	2.27
Carbon dioxide content (%)	0.436	0.515
Molecular mass (g/mol)	14.65	16.95
Hydrogen-to-carbon ratio	4.27	3.91
Lower heating value (MJ/kg)	48.75	47.21

The fuel–air equivalence ratio (ϕ) was measured using a commercially available wide-range oxygen sensor (NTK MO-1000), and was also calculated from the exhaust gas composition. Airflow was measured with a hot-wire flow meter, and the fuel consumption was calculated from the ϕ and airflow measurements.

The gaseous fueling system used to meter the Hythane and natural gas fuels consisted of a coolant heated high-pressure regulator (IMPCO HPR-3000), a two-stage low pressure regulator (IMPCO PEV-E) and an air valve type fuel mixer (IMPCO CA-125). The test fuels were purchased prebottled in standard gas cylinders, stored at a maximum pressure of about 16.5 MPa. In order to insure fuel consistency from test to test, all of the natural gas, including that contained in the Hythane fuel, was drawn from the same stock. The Hythane fuel had a certified hydrogen content of 15.4 ± 0.3 percent. The composition and some other properties of the test fuels are listed in Table 2.

Experimental Design

An experiment was designed to allow comparison of engine exhaust emissions and efficiency between natural gas and Hythane fueling of the test engine. The experiment comprised two distinct phases: The first phase was aimed at examining the MBT (minimum spark advance for best torque) emissions and efficiency trends within a broad range of fuel–air equivalence ratios near the lean operating limit, and the second phase involved a statistical comparison of engine emissions and efficiency between natural gas and Hythane fueling.

Central to the experimental design was selection of an appropriate test matrix. For this study, a test matrix was devised to examine the effect of varying the engine operating parameters (ϕ and ST) for each fuel (Hythane and natural gas), at three engine operating conditions (8 percent load, 1200 rpm; 50 percent load, 2000 rpm; 100 percent load, 1500 rpm). The test matrix, which is divided into six blocks, is shown in Table 3. Each block represents a unique combination of engine operating condition and fuel type. The selection of the three engine operating conditions was guided by the SAE Recommended Practice for Diesel Engine Emissions Measurement (SAE J1003

Table 3 Experimental test matrix

	NATURAL GAS	HYTHANE
1200 rpm, 10 N·m	Condition 1	Condition 2
2000 rpm, 65 N·m	Condition 3	Condition 4
1500 rpm, 130 N·m	Condition 5	Condition 6

FEB84), and are meant to be representative of engine operation under the following distinctly different circumstances commonly encountered by heavy-duty engines:

(*i*) Light load at fast idle engine speed (Conditions 1 and 2, Table 3); representative of driving a transmission power-take-off (e.g., to operate a hydraulic pump).
(*ii*) Medium load at high engine speed (Conditions 3 and 4, Table 3); representative of highway cruising.
(*iii*) High load at medium engine speed (Conditions 5 and 6, Table 3); representative of climbing a steep hill while hauling a heavy load.

The maximum load (100 percent load) was determined through preliminary engine testing to be 130 N · m, and corresponds to the maximum value of engine torque that could be achieved at all test points within the Condition 5 and Condition 6 test matrix blocks. Consequently, the torque corresponding to half load (50 percent load) and low load (8 percent load) engine operation are 65 N · m and 10 N · m, respectively. The corresponding bmep values are 5.14 atm (75.6 psi), 2.57 atm (37.8 psi), and 0.395 atm (5.81 psi) for the full-load, half-load, and low-load operating conditions, respectively.

Within each matrix block, tests were conducted for 25 different combinations (test points) of ϕ and ST, with the exception of test Condition 2, which comprised of 30 test points. The range of ϕ and ST values used was determined through preliminary testing of the engine. The same five spark timing values were used for each test block: 30, 35, 40, 45, and 50 deg before top dead center (BTDC). For the full and half-load operating conditions, tests were conducted at equivalence ratios ranging from 0.709 to 0.637 for natural gas, and from 0.667 to 0.599 for Hythane. At low load, equivalence ratios ranging from 0.769 to 0.667 for natural gas, and from 0.714 to 0.606 for Hythane were tested.

In an effort to minimize the differences in emissions and efficiency of Hythane and natural gas due to variations in atmospheric conditions, Hythane and natural gas tests for each speed and load combination were conducted on the same day, with the exception of the low-load, fast idle speed combination. Additionally, all ϕ and ST combinations within each test matrix block were run in random sequence, so that the influence of any uncontrollable variables (e.g., atmospheric conditions) was randomized.

Results

The results of this research are divided into two sections: Experimental Test Matrix Results, which examines the emissions and efficiency trends and trade-offs (at MBT) between Hythane and natural gas fueling of the test engine, and Results of Statistical Testing, which analyzes the statistical differences between the Hythane and natural gas emissions and efficiency.

Experimental Test Matrix Results

MBT Spark Timing. For spark ignition engines, there is some value of spark timing at each operating point that maximizes bmep, and the minimum amount of spark advance required to achieve maximum bmep is referred to as MBT (minimum advance for best torque). In most cases, the torque curve is relatively flat in the region of the maximum value, so a few degrees of spark advance, or retard, from MBT can be tolerated without significantly affecting engine torque. In practice, MBT spark timing is usually taken to be a few (no exact quantitative definition has been established) degrees retarded from the value that maximizes bmep, in order to take advantage of the lower NO_x emissions inherent of less advanced timings. Despite the potential for reduced emissions, it is best to keep an engine timed as closely as possibly to MBT, since maximum engine efficiency, and consequently minimum BSEC, coincide with the occurrence of peak torque. With this in mind, MBT serves as a logical, and convenient reference point at which the emissions and efficiency of different fuels, such as natural gas and Hythane, can be compared.

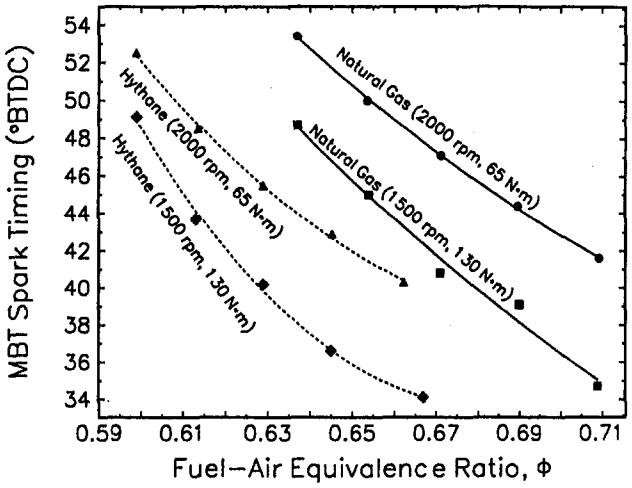

Fig. 1 MBT spark timing versus ϕ for full and half-load test conditions

Figure 1 is a plot showing the variation in MBT with changes in ϕ, for the full-load and half-load test conditions. Each curve, independent of engine load and fuel type, exhibits an increase in MBT spark timing as the equivalence ratio is leaned. The increased heat capacity of the excess air results in lower combustion temperatures; as a result, energy release occurs more slowly, and the duration required for completion of the combustion process increases. Klimstra (1985) has demonstrated that maximum engine efficiency occurs when the combustion heat release is centered about 7–8 deg after top dead center (ATDC), a point referred to as the optimum combustion phasing angle. Consequently, as ϕ is leaned and combustion duration increases, MBT spark advance must increase in order to keep the heat release centered about the optimum combustion phasing angle. Figure 1 also indicates that at a given equivalence ratio, MBT for natural gas is about 9 deg more advanced than MBT for Hythane. The curves also reveal that MBT for the midload operating conditions require 4–5 deg more advance than MBT for the full-load conditions. This trend is common to all homogeneous charge SI engines because the lower cylinder temperature and pressure present at lighter loads results in increased combustion duration.

Oxides of Nitrogen (NO_x) Emissions. The brake specific oxides of nitrogen ($BSNO_x$) emissions at MBT are plotted against equivalence ratio for the full-load and half-load operating conditions in Fig. 2. For a given fuel–air equivalence ratio, it might be expected that natural gas, which has an inherently longer combustion duration (and hence lower cylinder temperatures) than Hythane, should yield lower NO_x emissions. However, the reactions governing NO_x formation are time, as well as temperature dependent, so the longer combustion duration may offset the temperature decrease to some extent. Figure 2 shows that NO_x emissions are in fact higher for Hythane fueling at the full-load condition within the range of overlapping equivalence ratios. For the half-load test condition, however, Hythane emissions of NO_x are actually lower than the natural gas emissions. The advantage of Hythane fueling comes by way of its extended lean limit, where the heat capacity of the excess air leads to a decrease in flame temperature; NO_x emissions at the leanest Hythane test points are lower than the NO_x emissions at the leanest natural gas test points. The absolute differences in MBT $BSNO_x$ emissions between each fuel are actually quite small, as are the $BSNO_x$ emissions themselves. For this reason, judgment about which fuel has the potential for lowest NO_x

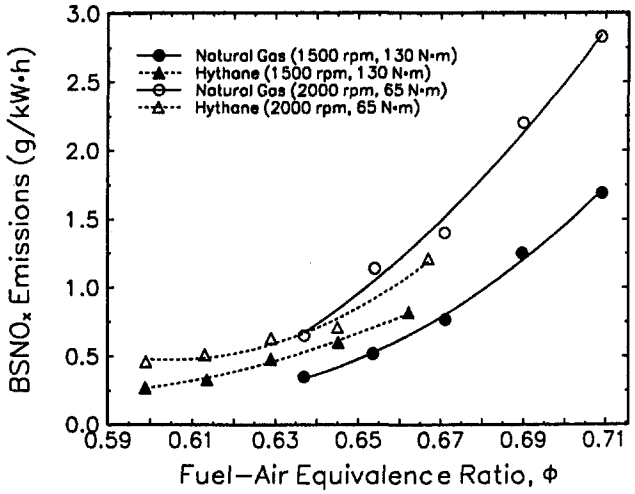

Fig. 2 MBT $BSNO_x$ emissions versus ϕ for full and half-load test conditions

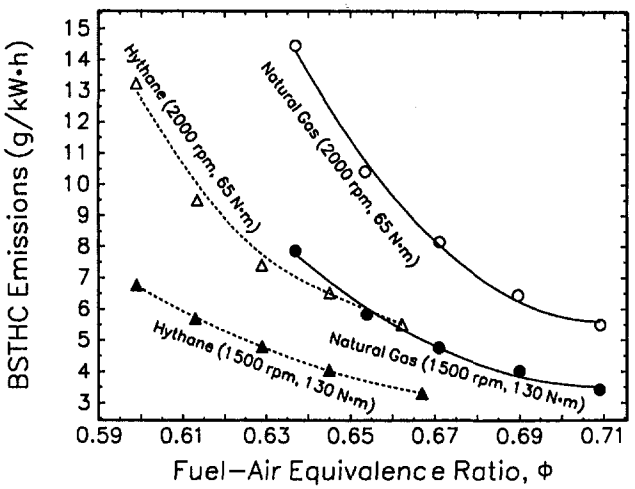

Fig. 4 MBT BSTHC emissions versus ϕ for full and half-load test conditions

emissions is reserved for the section detailing the results of statistical testing.

Figure 3 is a plot of the NO_2 fraction of NO_x as a function of NO_x concentration, and includes all of the test matrix data points. The curve illustrates that for low NO_x concentrations, NO_2 comprises the vast majority of NO_x, and for higher NO_x concentrations, the NO_2 content levels out at about 20 percent. Another point of interest is that NO_2 formation is strictly a function of the NO_x concentration, and is independent of speed, load and fuel type.

Total Hydrocarbon (THC) Emissions. There are four potential sources of hydrocarbon emissions that relate to the engine under test: flame quenching (partial burn and misfire), crevice hydrocarbon storage, scavenging losses, and exhaust valve leakage. Prior to commencement of testing, an engine leak-down test confirmed that the intake and exhaust valves were sealing adequately, thereby eliminating exhaust valve leakage as a significant source of hydrocarbon emissions. Scavenging losses are also thought to be negligible for two reasons: a reduced overlap camshaft was installed in the engine, and the maximum MAP used during testing was a relatively low 134 kPa (19.4 psia). Consequently, flame quenching and crevice storage remain as the only sources likely to have a significant effect on the engine-out THC emissions.

The THC emissions at MBT are plotted against equivalence ratio in Fig. 4, for the half-load and full-load operating conditions. Both conditions exhibit the same trend; Hythane fueling of the test engine results in substantially lower brake specific total hydrocarbon (BSTHC) emissions than natural gas fueling. In an effort to assess the relative contribution of each THC emissions source (flame quenching and crevice storage), Fig. 5 was constructed. Figure 5 is a plot of MBT exhaust port temperature as a function of equivalence ratio, for the half-load and full-load test conditions. The curves indicate that the exhaust port temperature is independent of fuel type; for a given speed, load and equivalence ratio, exhaust port temperatures are roughly the same for both Hythane and natural gas fueling. This fact has important implications, because the exhaust port temperature is an indicator of the extent to which post-combustion oxidation of the crevice gases is likely to occur. For the half-load and full-load operating conditions, this means that the crevice hydrocarbons, if indeed a significant proportion of the overall THC levels, should be oxidized to a similar degree for both Hythane and natural gas fueling of the test engine. The fact that the hydrocarbon content of Hythane is only 85 percent (as opposed to natural gas, which has a hydrocarbon content close to 100 percent), might suggest that the Hythane crevice gases should have a lower hydrocarbon content than those of natural gas. The reduced hydrocarbon content of Hythane is

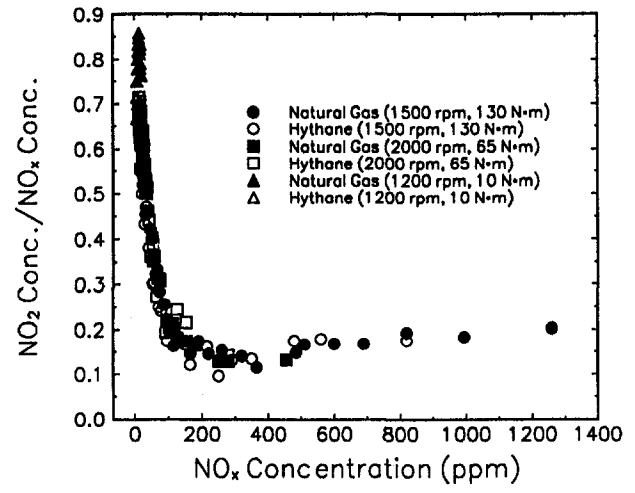

Fig. 3 NO_2 fraction of NO_x versus NO_x concentration for all test conditions

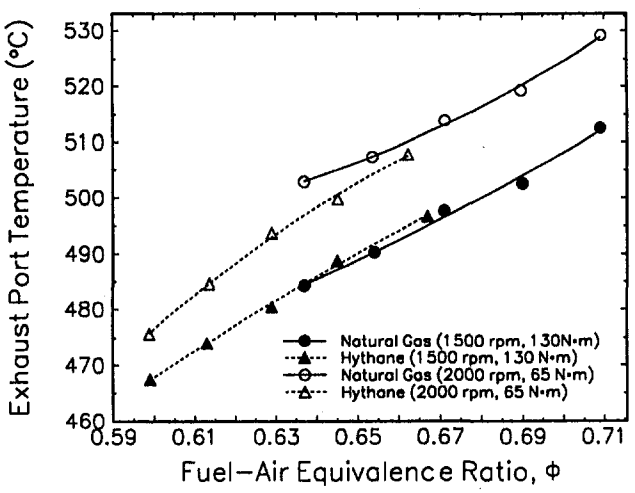

Fig. 5 Exhaust port temperature versus ϕ for full and half-load test conditions

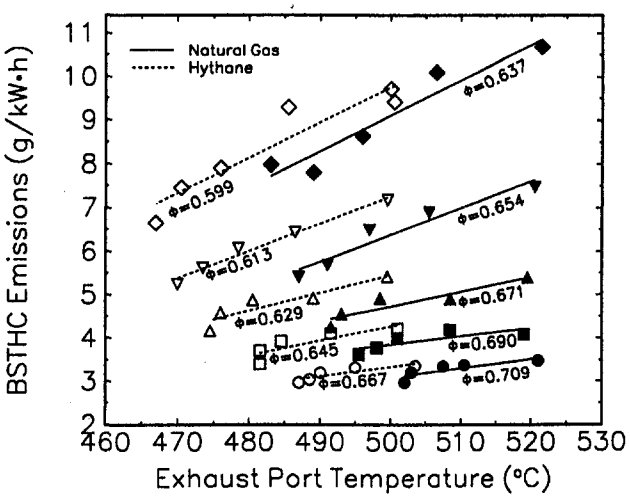

Fig. 6 BSTHC emissions versus exhaust port temperature at full-load engine operation

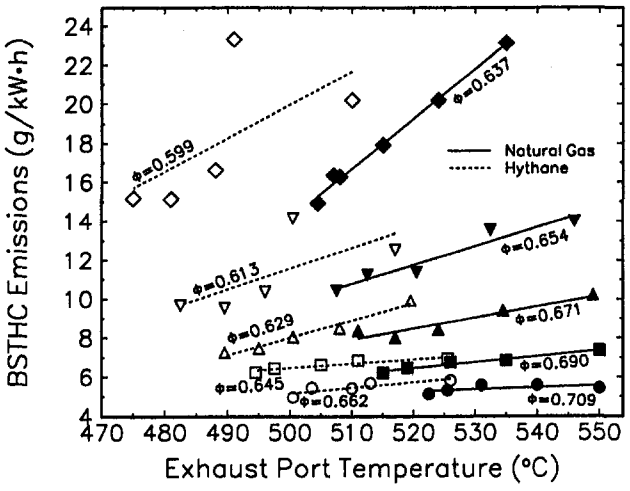

Fig. 7 BSTHC emissions versus exhaust port temperature at half-load engine operation

offset, however, by denser crevice packing; peak cylinder pressures are higher for Hythane fueling, at a given equivalence ratio, due to its shorter combustion duration.

In a natural gas fueled spark ignition engine having good combustion quality (i.e., no partial burn), the vast majority of unburned hydrocarbon emissions are attributable to the storage and subsequent release of unburned fuel–air mixture from the combustion chamber crevices (Thompson and Wallace, 1994). Furthermore, the absolute concentration of exhaust unburned hydrocarbons is dictated by the extent to which the returning crevice gases are oxidized. The degree of postcombustion crevice gas oxidation is dependent, in turn, upon the in-cylinder temperature history starting from the time of crevice gas release; higher temperatures lead to increased crevice hydrocarbon oxidation rates. Providing that good combustion quality can be maintained, a natural gas fueled SI engine will, therefore, exhibit a decrease in THC emissions as expansion temperatures increase, an effect that has been demonstrated by Jääskeläinen and Wallace (1994) using a stoichiometrically fueled engine operated with varying amounts of EGR. The extent of the THC decrease will depend on the equivalence ratio; as ϕ is leaned, the decrease in expansion temperatures will cause the rate of postcombustion oxidation to slow considerably.

To examine the dependence of the test engine BSTHC emissions on expansion temperature at different equivalence ratios, Figs. 6 and 7 were constructed using the test matrix data. In this case, exhaust port temperature was used as an indicator of expansion temperature since no in-cylinder temperature measurements were made. The plots illustrate that for both full-load (Fig. 6) and half-load (Fig. 7) operation, BSTHC emissions increase as the exhaust port temperature rises. This implies that some source other than crevice storage, namely flame quenching (i.e., partial burn), must be contributing significantly to the overall THC emissions. The slope of each curve in Figs. 6 and 7, hereafter referred to as the *partial burn index,* can be thought of as a qualitative measure of the ratio of the hydrocarbons resulting from partial burn to the crevice storage hydrocarbons; at the richest equivalence ratios tested, the BSTHC versus port temperature curves are relatively flat, suggesting that partial burn does not make a large contribution to the overall THC levels. However, as the equivalence ratio is leaned and combustion duration increases, the partial burn index of each curve in Figs. 6 and 7 rises to reflect the increased significance of partial burn. Another important observation concerning Figs. 6 and 7 is that for both fuels at full and half-load operation, the Hythane and natural gas partial burn indices are the same (i.e., the BSTHC versus exhaust port temperature curves are parallel) at similar BSTHC levels. Coupled with the previous inference that crevice hydrocarbon emissions will be approximately the same for both fuels, this means that for a given level of total hydrocarbon emissions, the extent of partial burn must also be similar. Figure 8, which is a plot of MBT BSTHC emissions as a function of MBT spark timing for both fuels at the full and half-load operating conditions, validates this hypothesis. The graph shows that for each load the natural gas and Hythane curves lie on top of one another. In other words, at a given combustion duration (which is reflected by the degree of MBT spark advance), the hydrocarbon emissions at each load are roughly the same for both fuels. As a consequence, the lower THC emissions that result from Hythane fueling (see Fig. 4) can be primarily attributed to differences in combustion duration. The presence of the hydrogen in the Hythane fuel serves to decrease combustion duration, which results in reduced partial burn, and hence lower THC emissions.

Carbon Monoxide (CO) Emissions. The brake specific carbon monoxide (BSCO) emissions at MBT are plotted versus equivalence ratio for both fuels, at the full-load and half-load operating conditions, in Fig. 9. The trends among both operating conditions are similar; relative to natural gas, Hythane fueling results in substantially reduced MBT carbon monoxide emissions for a given equivalence ratio.

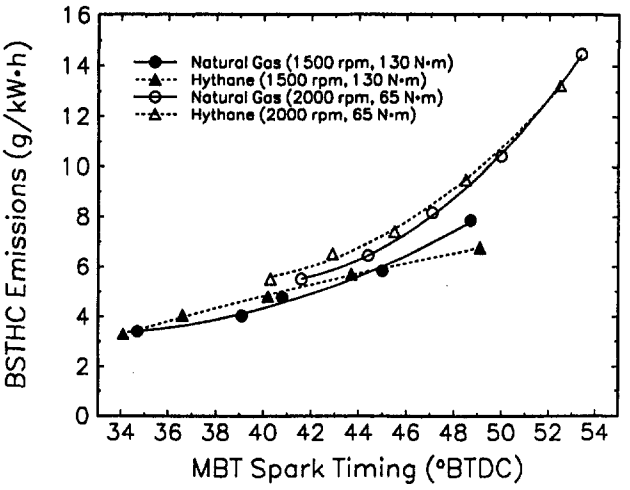

Fig. 8 MBT BSTHC emissions versus MBT spark timing for full and half-load test conditions

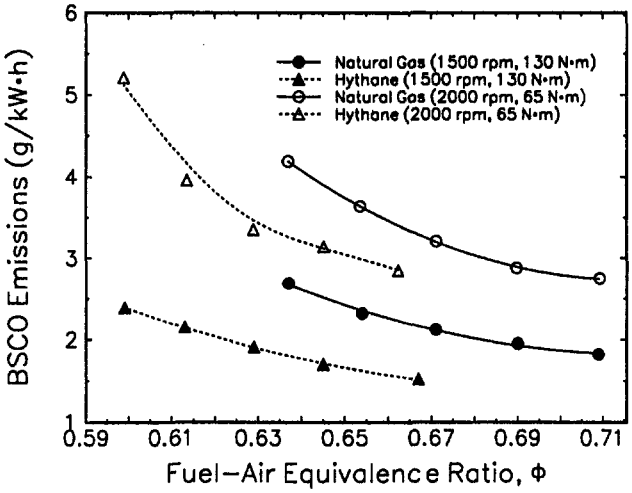

Fig. 9 MBT BSCO emissions versus ϕ for full and half-load test conditions

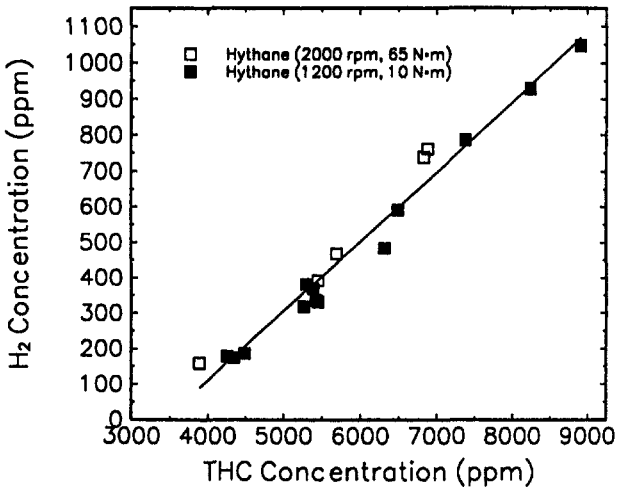

Fig. 11 H_2 concentration versus THC concentration at half and low-load test conditions

The dominant oxidation path for CO can be represented by the following reaction:

$$CO + OH \leftrightarrow CO_2 + H \quad (1)$$

Much like the reactions governing NO_x formation, reaction (1) competes unsuccessfully, at first, with the hydrocarbon oxidation reactions, for its share of available radicals (in this case OH radicals). Oxidation of CO begins only relatively late in the reaction process, after all of the original fuel and intermediate HC compounds have been consumed. As a result, the presence of unoxidized hydrocarbons in the reaction zone inhibits CO oxidation. Figure 10 is a plot of the $CO-CO_2$ ratio as a function of THC concentration, which includes all test matrix data points, and clearly illustrates that the $CO-CO_2$ ratio for both fuels rises as hydrocarbon emissions increase. Figure 10 also reveals, however, that the $CO-CO_2$ ratios for each fuel increase at different rates, indicating that some mechanism, apart from hydrocarbon inhibition, contributes to the regulation of CO oxidation.

An important point to note about the primary CO oxidation reaction (1), is that it proceeds quickly enough to maintain equilibrium throughout the expansion stroke (Newhall, 1969).

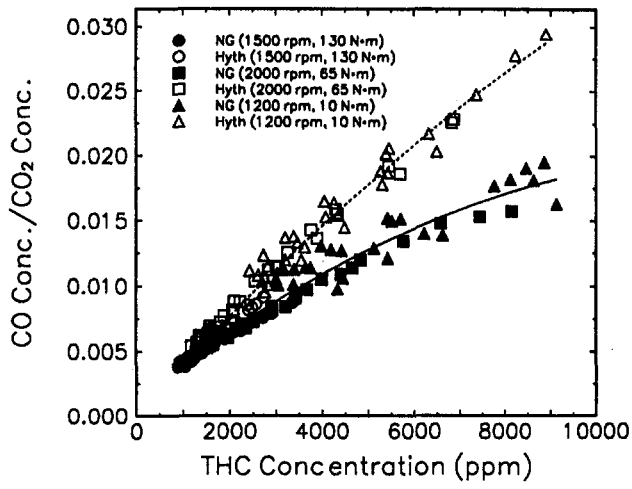

Fig. 10 CO fraction of CO_2 versus THC concentration for all test conditions

Consequently, the $CO-CO_2$ ratio is dictated solely by the relative concentration of OH and H radicals, as follows:

$$\frac{[CO]}{[CO_2]} = \frac{1}{K}\frac{[H]}{[OH]} \quad (2)$$

where K is the equilibrium constant for reaction 1, and [CO], $[CO_2]$, [H], and [OH] are the respective concentrations of carbon monoxide, carbon dioxide, monatomic hydrogen, and hydroxyl radical. In turn, the concentration of each radical species (OH and H) is controlled by the partial equilibrium established by the following bimolecular reactions (Newhall, 1969):

$$OH + H \leftrightarrow H_2 + O \quad (3)$$

$$OH + O \leftrightarrow O_2 + H \quad (4)$$

$$OH + H_2 \leftrightarrow H_2O + H \quad (5)$$

$$OH + OH \leftrightarrow H_2O + O \quad (6)$$

Like reaction (1), the forward and reverse reaction rates for reactions (3) through (6) are extremely fast, which means that reactions (3), (4), (5), and (6) are kinetically limited by the availability of each reacting species. It is perhaps this limitation that accounts for the differing Hythane and natural gas $CO-CO_2$ ratios. The test matrix data reveal that molecular hydrogen is present in measurable quantities only during Hythane fueling of the test engine at half-load and low-load operation; the H_2 gas chromatograph detected no hydrogen in the engine exhaust during any of the natural gas fueled tests or full-load Hythane tests. The measured H_2 concentration is plotted as a function of THC concentration in Fig. 11. The figure illustrates that the H_2 concentration rises linearly with increasing hydrocarbon concentration. The fact that measurable quantities of hydrogen appear only during half and low-load Hythane operation, and that H_2 emissions correlate so well with THC concentration, suggest that partial burn (as opposed to a hydrogen producing chemical reaction) is the dominant mechanism regulating exhaust H_2 levels. As substantial quantities of unburned hydrogen become available in the postcombustion environment, it is possible that reaction (5) accelerates (since it is no longer kinetically limited due to H_2 unavailability) and causes the partial equilibrium among reactions (3) to (6) to shift toward increased H concentration, and subsequently reduced OH concentration. Referring to Eq. (2), it is evident that as the equilibrium H concentration rises (and hence OH concentration falls), the $CO-CO_2$ ratio will increase. Furthermore, as unburned H_2 concentrations continue to rise in conjunction with increasing THC concentration, the equilibrium H concentration should rise cor-

respondingly, causing a divergence of the Hythane and natural gas $CO-CO_2$ curves as is depicted in Fig. 10.

Engine Efficiency (BSEC). In terms of measurable quantities, brake specific energy consumption is defined as follows:

$$\text{BSEC [kJ/kW·h]} = \frac{(\dot{m}_{\text{fuel}})(\text{LHV}_{\text{fuel}})}{\text{BP}} \quad (7)$$

where

$\dot{m}_{\text{fuel}}$ = mass fuel flow rate into engine [g/s]
LHV = lower heating value of fuel [MJ/g]
BP = brake power produced by the engine [kW]

Of key importance is the fact that BSEC is defined in terms of the total quantity of fuel inducted into the engine. As a consequence, any fuel that remains unoxidized (i.e., shows up as unburned hydrocarbons and/or unburned hydrogen in the engine exhaust) or is not fully oxidized, as is indicated by the presence of CO in the exhaust, results in an efficiency loss and hence increased BSEC. Plotted in Fig. 12, is the MBT brake specific energy consumption as a function of equivalence ratio, for the full and half-load operating conditions. The figure illustrates that there is little difference in BSEC, between Hythane and natural gas fueling, at the full-load condition. However, at the half-load condition, there is a noticeable BSEC decrease that results from Hythane fueling of the test engine.

To ascertain whether or not the level of unoxidized hydrocarbons, hydrogen, and carbon monoxide is the only factor responsible for the BSEC difference, it is useful to discuss energy consumption in terms of the fuel energy that actually participates in the combustion process. To this end, brake specific combustion energy utilization (BSCEU) was defined as follows:

BSCEU = (energy content of fuel inducted into engine)

$$- \text{(energy content of unburned HC, } H_2 \text{ and CO)}$$

$$\text{BSCEU [MJ/kW·h]} = \text{BSEC} - (\text{LHV}_{\text{NG}})(\text{BSHC}) - (\text{LHV}_{\text{CO}})(\text{BSCO}) - (\text{LHV}_{\text{H}_2})(\text{BSH}_2) \quad (8)$$

where:

LHV_{NG} = lower heating value of natural gas [kJ/g] (see Table 2)
BSHC = brake specific hydrocarbon emissions [g/kW·h]
LHV_{CO} = lower heating value of carbon monoxide (10.1 kJ/g)

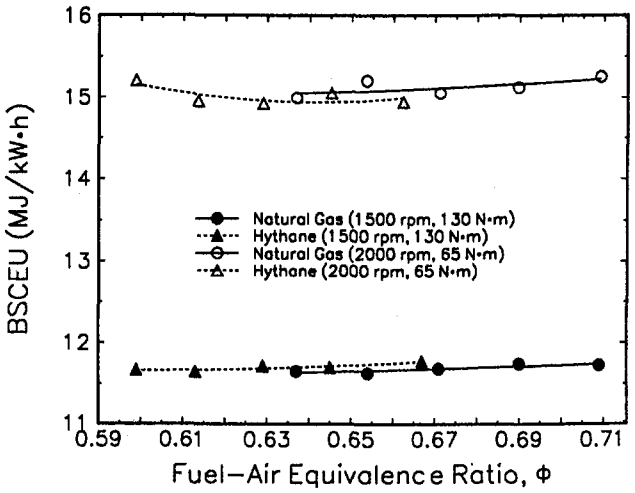

Fig. 13 MBT BSCEU versus ϕ for full and half-load test conditions

BSCO = brake specific carbon monoxide emissions [g/kW·h]
LHV_{H_2} = lower heating value of hydrogen (120.0 kJ/g)
BSH_2 = brake specific hydrogen emissions [g/kW·h]

It should be noted that the definition of BSCEU does not account for any fuel that undergoes postcombustion oxidation. Clearly, any fuel that is oxidized after the completion of combustion, in the exhaust ports for example, does not contribute to the engine work output. Consequently, BSCEU, as derived above, will tend to overestimate the amount of fuel energy that performs useful work on the pistons. However, postcombustion hydrocarbon oxidation in lean fueled engines, which is hampered by the inherently low postcombustion temperatures, is likely negligible relative to the quantity of fuel that remains unoxidized. Figure 13 is a plot of BSCEU versus equivalence ratio, for both fuels, at the full and half-load operating conditions. The figure illustrates that there is very little difference in BSCEU between the fuels, at both loads. It follows, therefore, that the BSEC difference between Hythane and natural gas fueling that was observed at half-load engine operation is due predominantly to the differences in wasted energy that exits the engine in the form of unburned hydrocarbons, hydrogen and carbon monoxide. It is also clear why BSEC is greater for natural gas than Hythane at a given equivalence ratio; the longer combustion duration inherent of natural gas fueling results in higher unburned fuel and carbon monoxide emissions, and hence greater energy wastage.

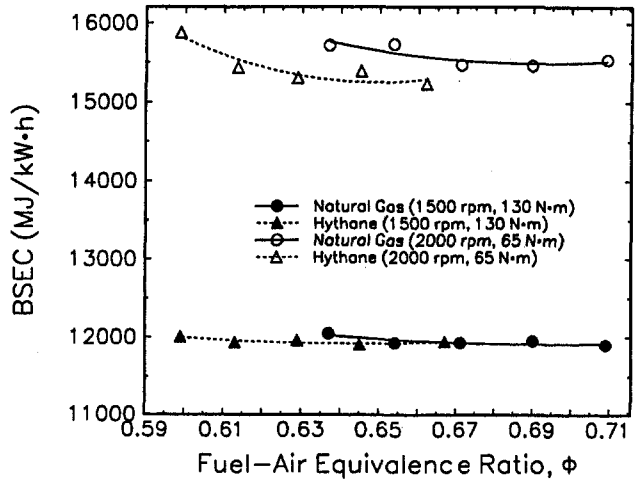

Fig. 12 MBT BSEC versus ϕ for full and half-load test conditions

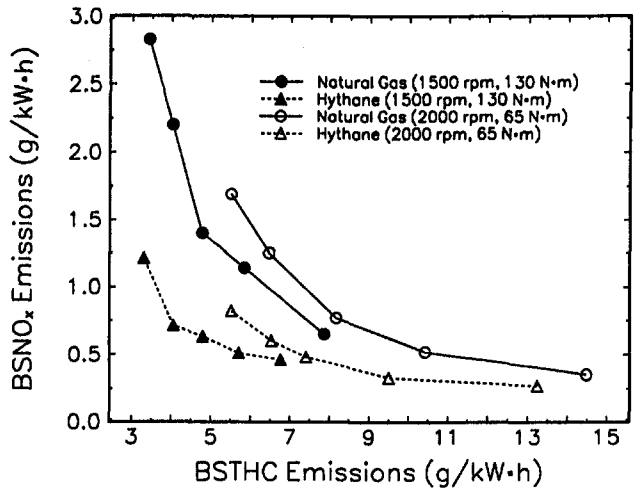

Fig. 14 $BSNO_x$-BSTHC tradeoff for full and half-load test conditions

Table 4 Statistically significant differences (at 95 percent C.L.) between Hythane and natural gas exhaust emissions and efficiency for half-load operating condition (2000 rpm, 65 N · m)

	Mean Value for Natural Gas Fuelling	Mean Value for Hythane Fuelling	S.S. Difference (NG - Hythane)	Percentage of NG Emissions
$BSNO_X$ (g/kW·h)	0.558	0.369	0.177	31.73%
BSTHC (g/kW·h)	10.27	9.589	0.559	5.44%
BSCO (g/kW·h)	3.798	3.987	-0.162	-4.27%
BSEC (kJ/kW·h)	15428	15228	161.1	1.04%

NO_x-THC Tradeoff. Figure 14 illustrates the tradeoff between brake specific THC and NO_x emissions at MBT. The reason for the drastic trade-off among the two emissions should be clear; the combination of engine operating parameters that favors low NO_x emissions (retarded ST and lean ϕ) is exactly that which results in high THC levels. Of utmost importance is the fact that the Hythane curves for full-load and half-load operation lie to the left of, and below the natural gas curves. This means that during Hythane fueling, it is possible to achieve simultaneously lower NO_x and THC emissions than during natural gas fueling.

Results of Statistical Testing. The NO_x–THC emissions tradeoff outlined in the preceding paragraph was used to guide selection of engine operating points to be tested statistically. In order to minimize BSEC, MBT spark timing was used for each test point, so the key was to choose an equivalence ratio that provided satisfactorily low emissions. Carbon monoxide emissions are of little concern (since they are readily oxidized by a catalytic converter) and the brake specific energy consumption at MBT is about the same at all equivalence ratios, so the only remaining factors influencing the selection of test point equivalence ratios were THC and NO_x emissions. An important fact that further simplified equivalence ratio selection, is that the majority of THC emissions are in the form of methane (CH_4), which is generally considered to be nonreactive in the atmosphere (though there is mounting concern over its possible effectiveness as a greenhouse gas). As a result, it makes sense to operate the engine as lean as possible, stability permitting, so as to minimize NO_x emissions, which are a stringently regulated exhaust pollutant. During previous testing, it was discovered that an MBT spark timing of about 50 deg BTDC corresponds with the limit of stable engine operation at the full and half-load operating conditions, for both Hythane and natural gas. For this reason, it was decided to use an MBT spark timing of 50 deg BTDC for each of the statistical test points, and the equivalence ratio corresponding to MBT at each operating condition was determined from the MBT versus ϕ curves in Fig. 1. The values of equivalence ratio used for statistical testing at the half-load test condition (2000 rpm, 65 N · m) were 0.654 and 0.608 for natural gas and Hythane, respectively. At the full-load test condition (1500 rpm, 130 N · m), respective equivalence ratios of 0.631 and 0.598 were used for natural gas and Hythane fueling.

For each fuel, repetitive tests were conducted at the full and half-load operating conditions using the previously outlined operating parameters. Nine tests were performed at Condition 5 (1500 rpm, 130 N · m, natural gas fueling), eight tests were performed at Condition 6 (1500 rpm, 130 N · m, Hythane fueling) and ten tests were run at each of Conditions 3 (2000 rpm, 65 N · m, natural gas fueling) and 4 (2000 rpm, 65 N · m, Hythane fueling). A computer program was used to determine whether or not the differences between Hythane and natural gas emissions, at each load, were statistically significant (S.S.) at the 95 percent confidence level. For any emissions differences found to be statistically significant, the extent of the S.S. differences was calculated. The results of the statistical testing are summarized in Table 4 for the half-load operating condition, and in Table 5 for the full-load operating condition. The first two columns of each table contain the mean value of each emission for natural gas and Hythane fueling. The S.S. differences (at the 95 percent confidence level) between fuels, for each emission, are shown in the third column of Tables 4 and 5. The S.S. differences are tabulated as natural gas emissions minus Hythane emissions; consequently, all positive values in the third column are representative of lower emissions under Hythane fueling, and negative values are indicative of lower emissions under natural gas fueling. The final column of each table contains the emissions differences expressed as a percentage of the natural gas emissions. A positive value indicates the percentage by which Hythane emissions were lower than natural gas emissions, and a negative value represents the percentage by which Hythane emissions were higher than natural gas emissions.

The results of the statistical testing reveal that all exhaust emissions, with the exception of CO, were lower when the test engine was fueled with Hythane. At the half-load operating condition (2000 rpm, 65 N · m) during Hythane fueling, the following statistically significant (at the 95 percent confidence level) emissions reductions were observed: a 31.73 percent decrease in $BSNO_x$ and a 5.44 percent decrease in BSTHC. Hythane fueling at the full-load test condition (1500 rpm, 130 N · m) resulted in the following statistically significant (at the 95 percent confidence level) emissions reductions: a 13.27 percent decrease in $BSNO_x$ and a 12.97 percent decrease in BSTHC. There was no S.S. difference in CO emissions or BSEC at full-load operation, but at half-load operation, Hythane BSCO emissions were 4.27 percent higher than natural gas BSCO emissions. Hythane fueling at the half-load test condition resulted in a 1.04 percent decrease in BSEC relative to natural gas fueling.

Conclusions

The results of the matrix and statistical testing clearly demonstrate the potential of Hythane to reduce the exhaust concentrations of regulated pollutants and increase the efficiency of a spark ignition engine. The emissions of primary concern in a lean-fueled engine are hydrocarbons and NO_x; consequently, the discovery that simultaneously lower levels of NO_x and hy-

Table 5 Statistically significant differences (at 95 percent C.L.) between Hythane and natural gas exhaust emissions and efficiency for full-load operating condition (1500 rpm, 130 N · m)

	Mean Value for Natural Gas Fuelling	Mean Value for Hythane Fuelling	S.S. Difference (NG - Hythane)	Percentage of NG Emissions
$BSNO_X$ (g/kW·h)	0.539	0.455	0.072	13.27%
BSTHC (g/kW·h)	8.624	7.327	1.118	12.97%
BSCO (g/kW·h)	3.124	3.144	no S.S. diff.	---
BSEC (kJ/kW·h)	12126	12119	no S.S. diff.	---

drocarbon emissions can be achieved during Hythane fueling has important implications. In fact, Hythane fueling exhibited statistically significant reductions of 13–32 percent in NO_x emissions and 5–13 percent in THC emissions. Although the percentage differences in NO_x emissions are quite substantial, the absolute concentration of oxides of nitrogen found in the engine exhaust, during statistical testing, was only on the order of 50 ppm; if reduced NO_x emissions were the only objective in the search for an alternative to natural gas fuel, one could argue that the differences in NO_x emissions are not large enough to offset the added cost of Hythane. On the other hand, the differences in THC emissions were far more substantial than the NO_x emissions differences. But since the primary component of the THC emissions is methane, which is considered to be nonreactive in the atmosphere, the THC emissions are of little concern in terms of their likelihood to participate in the formation of photochemical smog. One benefit of lower THC emissions, however, is a marginal improvement in fuel economy. It is unlikely though, that this advantage by itself would justify the added expense of Hythane fuel.

Acknowledgments

The authors gratefully acknowledge financial support for the project from the Alternative Energy Division of CANMET, part of Natural Resources Canada. The advice and technical support for the engine control system provided by General Motors of Canada is also appreciated, and in particular we would like to thank John Christie, Rick Gibson, and Kirk Burcar for their assistance. Additional thanks are extended to Hannu Jääskeläinen and Alex Cattelan at the University of Toronto for many helpful suggestions and discussions.

References

Cattelan, A. I., and Wallace, J. S., 1994, "Hythane and CNG Fuelled Engine Exhaust Emission and Engine Efficiency Comparison," presented at the Tenth World Hydrogen Energy Conference, Cocoa Beach, FL.

Eccleston, D. B., and Fleming, R. D., 1972, "Clean Automotive Fuel," U.S. Bureau of Mines Automotive Exhaust Emissions Program, Technical Progress Report 48.

Foute, S., Knowlton, T., Lynch, F., Ragazzi, R., and Raman, V., 1992, "The Denver Hythane Project—Recent Progress," presented at the Tenth Anniversary Conference, Industry and Hydrogen, Kananaskis, Alberta, Canada.

Glassman, I., 1987, *Combustion,* Academic Press, Inc., Orlando, FL.

Heywood, J. B., 1988, *Internal Combustion Engine Fundamentals,* McGraw-Hill, Inc., New York.

Jääskeläinen, H. E., and Wallace, J. S., 1994, "Examination of Charge Dilution With EGR to Reduce NO_x Emissions From a Natural Gas Fueled 16 Valve DOHC Four-Cylinder Engine," SAE Paper No. 942006.

Klimstra, J., 1985, "The Optimum Combustion Phasing Angle—A Convenient Engine Tuning Criterion," SAE Paper No. 852090.

Milton, B. E., and Keck, J. C., 1984, "Laminar Burning Velocities in Stoichiometric Hydrogen and Hydrogen–Hydrocarbon Gas Mixtures," *Combustion and Flame,* Vol. 58, pp. 13–22.

Newhall, H. K., 1969, "Kinetics of Engine-Generated Nitrogen Oxides and Carbon Monoxide," *Proc. 12th Symposium on Combustion,* pp. 603–613.

Strothers, R., 1993, "Hythane—Its Potential as a Fuel for Internal Combustion Engines," Final Report for ORTECH Corporation Project Number 600197.

Swain, M. R., Yusuf, M. J., Dülger, Z., and Swain, M. N., 1993, "The Effects of Hydrogen Addition on Natural Gas Engine Operation," SAE Paper No. 932775.

Thompson, N. D., and Wallace, J. S., 1994, "Effect of Engine Operating Variables and Piston and Ring Parameters on Crevice Hydrocarbon Emissions," SAE Paper No. 940480.

Problems of Forecasting the Future of Advanced Engines and Engine Characteristics of the Hydrogen Injection With LH_2 Tank and Pump

S. Furuhama
Musashi Institute of Technology,
Setagaya-ku,
Tokyo, Japan

Introduction

When the history of the vehicle engine during the last half century is reviewed, a number of research and development efforts have resulted in various useful improvements. From the author's personal point of view, the electronic-controlled fuel injection device is the most distinguished accomplishment for the vehicle engine.

On the other hand, wrong evaluations for some of the technologies have brought large investment losses to many engine manufacturers in the world. Figure 1 is the famous future forecast of the automobile engine published by Eaton Corp. in 1973. It is obvious that none of the engines that had been expected promising at that time were as popular in market as the forecast. Another more recent example is a ceramic engine, which once attracted much attention but now is being removed from the list of future advanced engines. In the case of the ceramic engine, the technology evaluation in the early stage was not done properly. In the first part of this article, scientific explanation will be made to explain why some of the initially promising engines were not able to replace conventional reciprocating engine.

Various discussions and forecasts have been published with respect to future vehicle engines with alternative fuels, such as an electric-powered engine and a hydrogen engine. It seems extremely important that each of the technologies be appropriately evaluated from the scientific viewpoint. It should be emphasized that the primary conditions required for the automobile engine are light weight and high power output. It will be discussed in the second part of the article that the only alternative fuel engine that satisfies these conditions with the present technology level is a hydrogen injection engine with a LH_2 tank and a LH_2 pump. The summary of the author's research work on this type of hydrogen engine will be also presented.

Examples of Misevaluated Advanced Engines

Wankel Rotary Engine. The Wankel rotary engine has raised much expectation as an innovative engine to replace the reciprocating engine. However, its practical use is so limited that the market share is far smaller than that predicted in Fig. 1. The main cause of such a disappointing result is that fundamental knowledge of the engine tribology theory was not sufficient. In other words, the blow-by amount through gas seals is much larger and the hydrodynamic lubrication for the rotary engine is much inferior to that for the piston ring. The piston ring tribology research the author has been working on can well explain the difference between the two types of engine.

Blow-by

(1) Blow-by Characteristics of a Piston Ring. The passage of blow-by gas through a piston ring is from passages ① to ⑤ as shown in Fig. 2. Among the five passages, the gap ⑤ is much smaller than the other four; in the case of the ring for 80 mm cylinder bore, the area of ⑤ is merely 0.09 mm^2. This theory was verified both analytically and experimentally by Furuhama (1956a, 1961). Figure 3 (Furuhama, 1974) is a typical measured result. Based on these results, it can be concluded that the blow-by amount under the normal engine operation is less than 1 percent of the intake air, and that the power loss caused by the blow-by is negligibly small.

(2) Blow-by in a Rotary Engine. Since the combustion chamber of the Wankel rotary engine is rectangular, the seals at its corners should have a complicated structure, as shown in Fig. 4. As a result of the structure, there are many passages for the blow-by and the total blow-by area is also large.

The gap g_1 of the apex seal ③ may be slightly smaller than the gap g of the piston ring (Fig. 2). However, the apex seal ③ makes an oscillation motion against the sliding surface ① with the maximum angle $\phi\ m \fallingdotseq 25$ deg, and the gas pressure P_1 reaches its maximum near the angle $\phi\ m$. As a result, c_1 becomes as large as 2 to 2.5 mm, and the blow-by area $c_1 g_1$ is much larger than that of the piston ring. There are two such large blow-by paths in a combustion chamber.

There are two gaps, whose area is $c_2 g_2$, between the side seal and the corner seal. The leakage through the gap e of the corner bolt ④ occurs at four locations. The total amount of blow-by through these gaps, although it could not be directly measured as in the case of the reciprocating engine, was estimated by various assumptions, static measurements, and the measurement under partially operating conditions. The result is shown in Fig. 5 (Furuhama, 1973).

According to the estimation in Fig. 5, the blow-by amount in the rotary engine is 10 times or more as large as that in the reciprocating engine. Eberle and Klomp (1973) at GM then reported that their estimated blow-by amount reached about 20 times as large. The large blow-by amount in the rotary engine causes such problems as decrease in engine power and deterioration in durability because the blow-by gas contains the component to increase wear.

Lubrication

(1) Piston Ring Lubrication. The piston ring sliding surface (width B) forms an ideal profile shown in Fig. 6 after completion of running-in process, according to Furuhama

Contributed by the Internal Combustion Engines Division and presented as the Calvin Rice Lecture at the 1995 Spring Technical Conference, Marietta, Ohio, April 23–26, 1995. Manuscript received by the Internal Combustion Engines Division January 1995; revision received September 1996. Associate Technical Editor: W. K. Cheng.

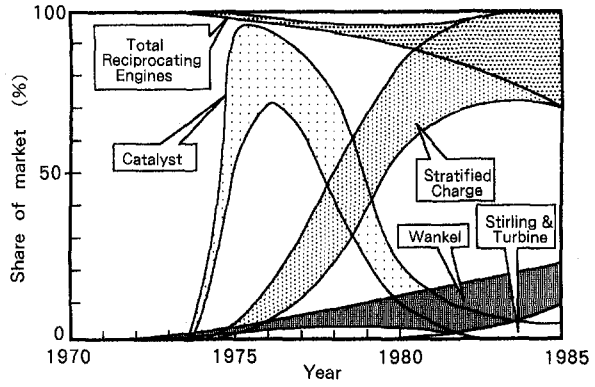

Fig. 1 Range of expected market penetration (by Eaton Corp., Feb. 1973)

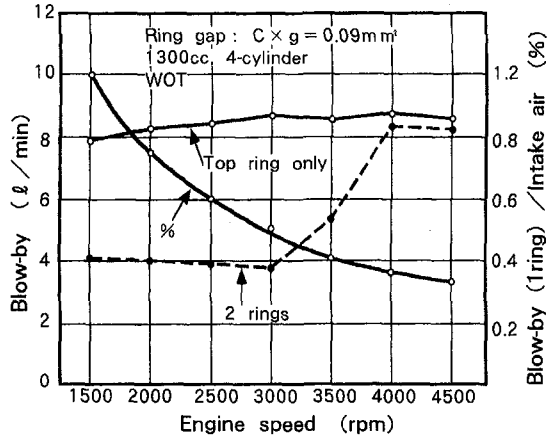

Fig. 3 Measured blow-by characteristics of a gasoline engine

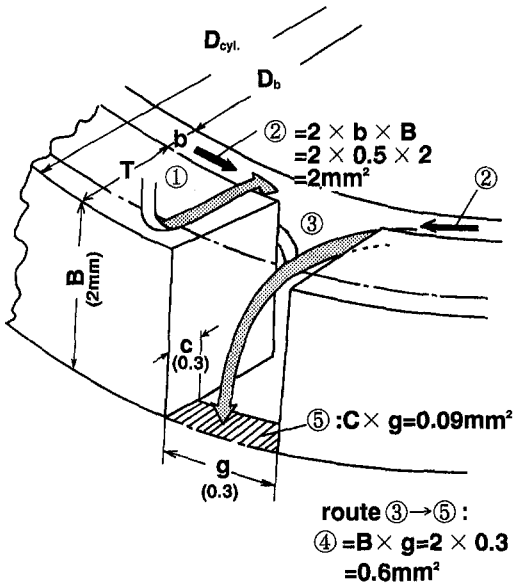

Fig. 2 Passage of blow-by gas through a piston ring

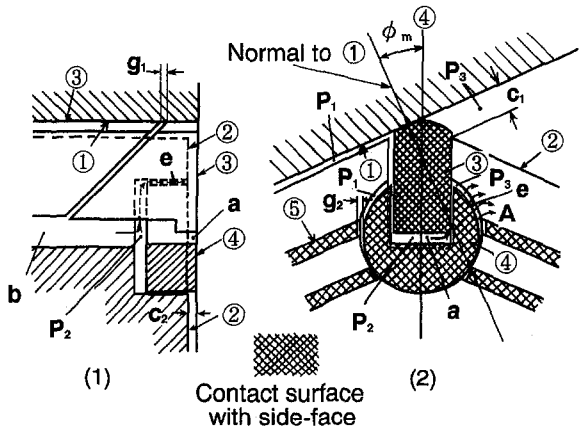

Fig. 4 Blow-by passages through a corner of rotor in NSU·KKM 613

(1956a, 1978). This profile can be empirically expressed by $e = B/1000$. The hydrodynamic lubrication theory indicates that the oil film thickness h_2 becomes optimum when $h_2 = e$, under steady-state condition and for the given $\mu U/W$ and B, where μ, U, and W are viscosity, velocity, and load, respectively. On the other hand, the oil film thickness under the actual engine operation can be calculated as shown in Fig. 7, which illustrates that this profile is almost ideal and that the tangential angle ϕ in Fig. 6 is nearly equal to the maximum tilted angle of the piston against the cylinder bore.

There is another function in the piston ring. When the piston reaches TDC and BDC, the ring stops in a moment and the oil film thickness h_2 approaches to zero. However, the contraction of h_2 results in squeeze action, which forms oil film. The thickness of such oil film h_2 is approximately proportional to $B^{1.5}$.

(2) Lubrication of Apex Seal (Furuhama, 1980). As previously mentioned, the apex seal in the rotary engine makes an oscillating motion against the sliding surface. Because of the oscillatory motion, the formed profile cannot be an ideal one with a small e, which is the case of the piston ring, but the profile becomes a circular shape with its radius of curvature equal to 4 mm. As a result of such profile, the apex seal and the sliding surface makes nearly a line contact, and the calculated oil film thickness turns out to be the one shown in Fig. 8, in spite of its continual motion. According to the calculation, the minimum value of h_2 is as small as 0.05 μ m, which is virtually a metal contact.

In addition, the amount of oil consumption for the rotary engine is considerably larger than that for the reciprocating engine. This is because of structure and function of the oil seals and because the apex seal slides over the hot combustion chamber wall to which a spark plug is installed.

Ceramic Engine. A ceramic engine was introduced as an adiabatic high thermal efficiency engine. However, the merit of the ceramic engine had not been realized, although ceramic material itself has still promising future for different purposes.

Effect of Wall Thermal Conductivity on Engine Heat Loss. In general, the heat loss through combustion chamber walls amounts to 15 to 30 percent of the total combustion heat, hence its reduction should be effective to thermal efficiency improve-

Nomenclature

BF = backfire
CH_2 = compressed hydrogen
EM = external mixing
HPI = high-pressure injection
LH_2 = liquid hydrogen
LPI = low-pressure injection
MH = metal hydride
PI = preignition

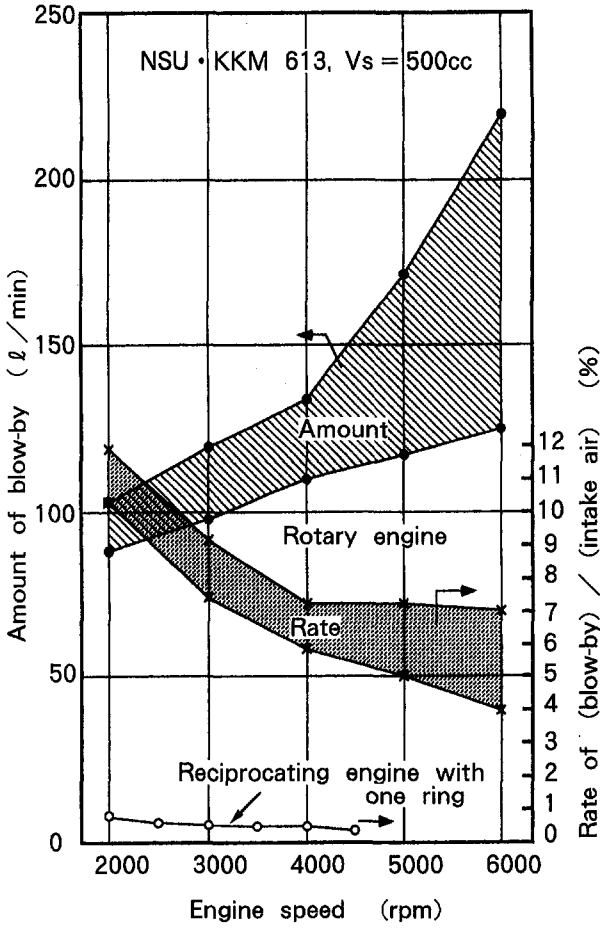

Fig. 5 Estimated range of total blow-by in rotary engine

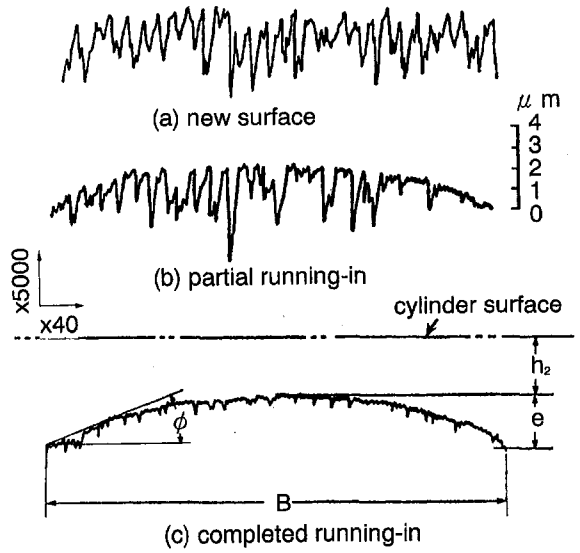

Fig. 6 Running-in process of piston ring sliding surface

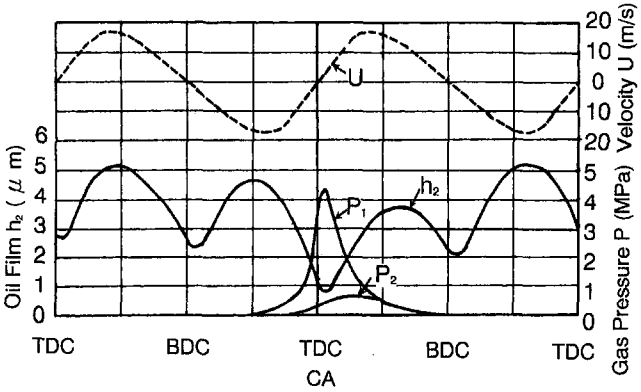

Engine: D × S = 80 × 80 mm, 4000 rpm
Ring: B = 1.5 mm, Tension = 9.8 N
Oil Viscosity = 7.06 × 10^{-3} Pa•s

Fig. 7 Minimum oil film thickness (h_2) formed on the piston ring

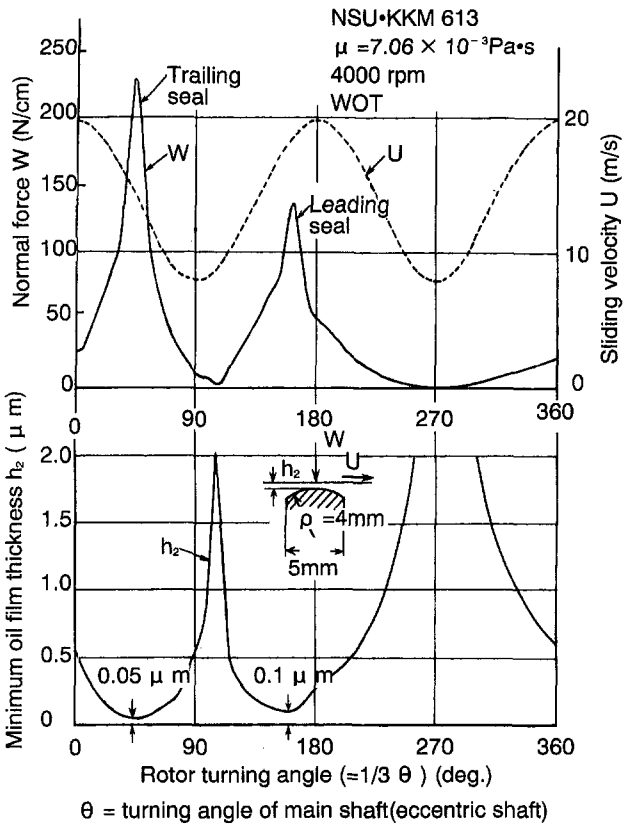

Fig. 8 Minimum oil film thickness (h_2) formed on the apex seal

ment. Since ceramics have low thermal conductivity and are highly heat proof, use of the ceramics as combustion chamber walls seemed a beneficial idea.

However, heat transfer analysis can reveal the following problem. Figure 9 shows a simple steady-state model, where the combustion chamber is the right side of the wall (thickness δ = 10 mm), and the coolant is flowing in the left side. The amount of heat flux through the wall Q is expressed by Eqs. (1) and (2), as a function of gas-side heat transfer coefficient α_H, thermal conductivity of the wall λ_w, and coolant side heat transfer coefficient α_c.

$$Q = \alpha_H(T_1 - T_2) = K(T_1 - T_4) \quad (1)$$

$$K = 1/(1/\alpha_H + \delta/\lambda_w + 1/\alpha_c) \quad (2)$$

In Eq. (1), T_1 and T_2 are space-and-time-averaged temperatures of hot working gas and hot gas side wall, respectively. It is important to note that α_H is determined only by hot gas properties and flow conditions and is independent of λ_w. The calculated temperature in various conditions are plotted in Fig. 9. The result shows that even if the wall λ_w were one-tenth of

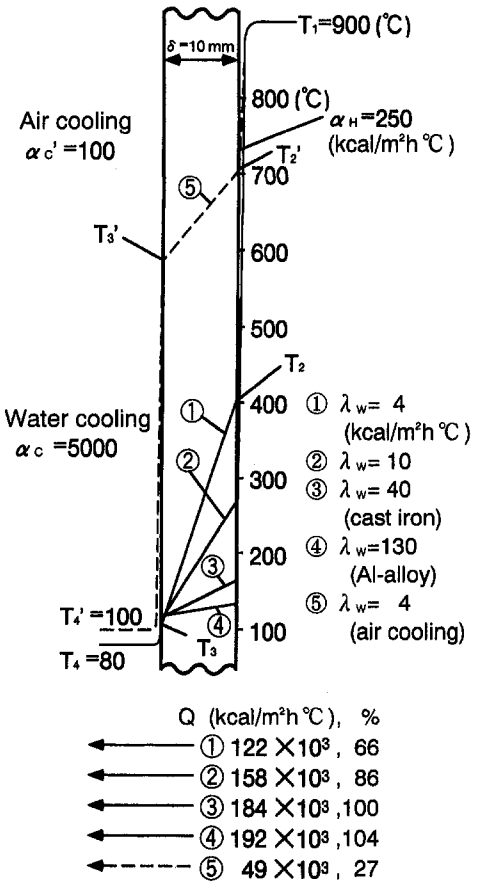

Fig. 9 Effect of wall λ_w on the overall heat transfer

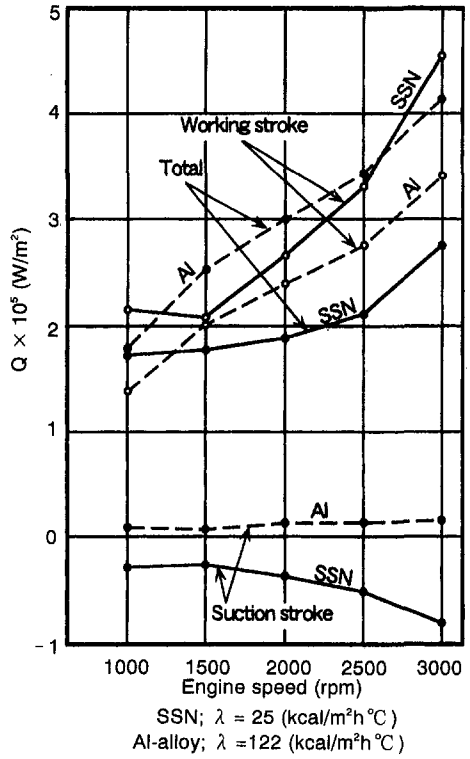

Fig. 10 Comparison of heat transfer Q between AL alloy and SSN piston during each stroke in operating diesel engine

that for cast iron, the heat flux Q would be decreased only to 66 percent, but that the wall temperature T_2 would rise from 163°C to 410°C.

In the case without cooling water, i.e., with air cooling, even though the heat flux would be reduced to 27 percent, the wall temperature T_2 would increase as high as 706°C, as shown by a dotted line in Fig. 9. Such high wall temperature deteriorates engine durability so significantly that the engine fails to function.

Heat Loss Measurement in the Operating Ceramic Engine. The heat transfer in the actual engine is highly unsteady; the hot gas temperature and the heat loss amount considerably varies with time. Thus, Furuhama and Enomoto (1987) made a heat flux measurement using a DI diesel engine with $D \times S$ = 104 × 118 mm. 4.5-mm-thick SSN ceramic (λ = 29.3 W/mK) was united to the piston crown with an air layer between them. Thin-film thermocouples were embedded to measure the instantaneous surface temperature, from which the instantaneous heat flux was calculated. The measurement results were compared with those from Al alloy in Fig. 10.

The comparison in Fig. 10 revealed that, although the heat transfer over the total cycle was decreased by using SSN, the heat transfer during the working stroke was the true energy loss, for SSN, it was larger than its counterpart for Al alloy. It seems because the high-temperature gas near the SSN wall makes the combustion flame approach the wall and enhances the heat transfer rate. This experimental result markedly discouraged the ceramic engine development. There have been no experimental reports showing the increased thermal efficiency by ceramic engines.

Requirements for Future Automobile Engine

The improper evaluation explained in the previous chapter should not be repeated when the future alternative fuel engine is selected. In addition, considering the increase of population and automobiles in the world, there is not much time before the earth environment is totally deteriorated. In order to avoid such catastrophe, the proper candidate should be selected based on scientific evaluations, and R&D for its practical use should be started as early as possible.

In the following sections, alternative fuel engines considered as promising future engine candidates will be evaluated from the technological viewpoints. In the discussion, however, the cost and safety will be excluded because they cannot be quantitatively evaluated.

Pollutive Emission. Since lean combustion can be realized by natural gas, its emission rates of CO, HC, and NO_x can be considerably reduced under low load operation. However, the emission rates under high load are almost the same as that for gasoline. In addition, reduction of CO_2 production is not noticeable, as shown in Table 1, where the CO_2 production rate for natural gas is 0.79 of that for oil under the same amount of heat generation. Since natural gas is also fossil fuel, it cannot be the primary candidate of alternative automobile fuel from an energy conservation point of view.

Table 1 CO_2 produced by various fuel combustion: Q = calorific value of 1 l gasoline = 7800 kcal

Fuel	Typical molecule	CO_2 kg/Q	Ratio of gasoline
Coal	C	3.53	1.56
Gas oil	$C_{16}H_{34}$	2.33	1.03
Gasoline	C_8H_{18}	2.27	1.00
Methanol	CH_3OH	2.25	0.99
Natural gas	CH_4	1.80	0.79
Hydrogen	H_2	0	0

Table 2 Weight ΔW of fuel and storage equivalent to 30 l gasoline

Fuel tank	Fuel		Tank wt. (kg)	Total wt. ΔW(kg)
	Vol.(ℓ)	Wt.(kg)		
Gasoline	30	22	5	27
Methanol	62	49	8	57
Hydrogen				
MH		8.2	764	772
CH_2(15MPa)	670	8.2	755	763
LH_2	115	8.2	65	73
Battery(※)				1360

(※) Assumption: The energy density is 40Wh/kg and the power conversion efficiency is 5 times as large as that of gasoline
MH: Metal hydride, CH_2: Compressed gas, LH_2 : Liquid

In the case of hydrogen, the emission rates of CO, HC, CO_2, and particulates are almost zero, and NO_x emission rate can be also significantly reduced, as discussed later.

An electric vehicle produces none of these pollutive emissions.

Weight and Power Output. It has not been properly understood that the total weight ΔW of fuel and tank is an important factor to determine the suitability of automobile fuel. Table 2 compares ΔW for various alternative fuels with that for 30 l gasoline. In the case of a battery and motor, battery weight ΔW is 50 times as large as that of 30 l gasoline and its tank. If the maximum allowable ΔW for an automobile of 1500 kg (W) is set 300 kg, the battery must be as small as that comparable to 6 l gasoline.

In the case of hydrogen, if metal hydride (MH) or 15 MPa compressed hydrogen (CH_2) is chosen as a storage method, ΔW in both cases is about 29 times as large as that for the 30 l gasoline system. From this comparison, it can be concluded that both of the above hydrogen systems such as MH and CH_2, are not suitable for practical automobiles.

Running Performance. The running performance of automobiles is significantly affected by the vehicle weight. In this section, an analytical approach will be made how ΔW affects the running performance. When the vehicle weight W is 1500 kg, the running resistance R of the vehicle can be expressed by the following three resistances while neglecting air resistance. They are:

Rolling resistance

$$R_r = \mu_r(W + \Delta W)g$$

Ascending resistance

$$R_s = \sin\theta(W + \Delta W)g$$

Accelerating resistance

$$R\alpha = \alpha(W + \Delta W)$$

where μ, g, θ, and α are rolling resistance coefficient, gravitational acceleration, slope angle, and starting acceleration, respectively. All of the three resistances are proportional to ($W + \Delta W$).

Starting Acceleration (α). When a vehicle is started on the road with $\theta = 0$, the resistance for the maximum acceleration is expressed by $Rm = (\mu_r g + \alpha)(W + \Delta W)$. In the case, where $\Delta W = 0$, $\mu_r = 0.02$, and $\alpha = 2.5$ m/s^2, Rm becomes 4044 N. Thus, the starting acceleration α can be expressed as a function of ΔW:

$$\alpha = 4044/(1500 + \Delta W) - 0.196 \quad [\mathrm{m/s^2}] \qquad (3)$$

This equation indicates that α is determined by ΔW, regardless of fuel type. The calculated results in Fig. 11 show that α is lowered by 17 percent for $\Delta W = 300$ kg and by 31 percent for $\Delta W = 600$ kg.

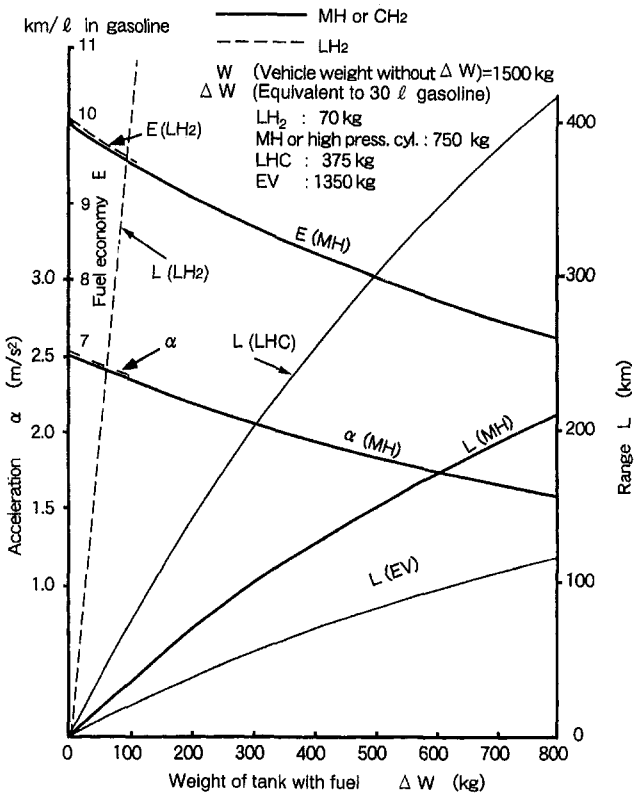

Fig. 11 Effect of fuel tank weight on L, α, E, in the case of each storage

Fuel Economy (E). The fuel economy of a vehicle E, which is defined as the traveling distance by the fuel equivalent to 1 l gasoline, can be expressed by the following equation if the vehicle travels in the same running condition:

$$E = V/(\beta P) = C_1/R = C_2/(W + \Delta W) \qquad (4)$$

In this equation, V, β, and P are vehicle speed, engine fuel consumption [l/kWh], and engine power (= RV), respectively, and C_1 and C_2 are constants. Assuming $E_0 = 10$ km/l when $\Delta W = 0$,

$$E = 15000(1500 + \Delta W) \quad [\mathrm{km}/l] \qquad (5)$$

Figure 12 illustrates fuel economy data for American gasoline vehicles in 1976. The dotted line in Fig. 12 is Eq. (5), which agrees with the mean value of the data. Equation (5) is also a

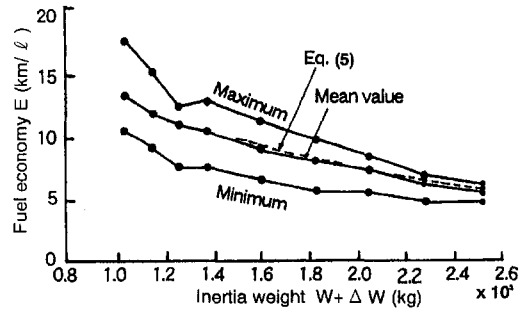

Fig. 12 Relation between the weight and the fuel economy of American gasoline vehicles in 1976

Table 3 History of R & D hydrogen vehicle at Musashi Institute of Technology

1970	Start of H_2-engine R & D. Research on BF and H_2-O_2 engine.
1974	Musashi-1 small truck with ten CH_2-(7N m^3)cyl. ΔW = 550kg.
1975	Musashi-2 Nissan car with 230 ℓ LH_2 -tank 140K-H_2 EM engine. Running the whole distance of 2800km along the West Coast of U.S.A.
1976	R & D of 2-stroke engine with LPI and LH_2-pump.
1978	Musashi-3 Suzuki minicar with 65 ℓ LH_2-tank and LH_2 pump and LPI 2-stroke engine.
1980	Research on engine power, PI and NOx in LPI 2-stroke engine.
1982	Musashi-5 HPI Pi = 6MPa, platinum hot wire ignition in 2-stroke engine, 82 ℓ LH_2-tank, operated at 4th WHEC
1983	R & D of hot wire endurance, injection and NOx HPI engine.
1984	Musashi-6 Nissan car with 4-stroke, HPI Pi = 8MPa, platinum hot wire, operated at 5th WHEC Research on LH_2-pump, injection, combustion and thermodynamics.
1986	Musashi-7 Hino truck, HPI with ceramic glow ignition, operated at Vancouver fair. R & D of ignition devices, cylinder reciprocating LH_2-pump, gas compression, NOx, hybrid of HPI and EM and mixture formation.
1990	Musashi-8 Nissan sport car Pi = 10MPa, spark ignition, 100 ℓ LH_2, operated at 8th WHEC. R & D of injection and spark timing control, new injection and NOx controls.
1993	Musashi-9 refrigerator truck with 360 ℓ LH_2, PHI and cooling system. Running the whole distance of 14km with 1/10 slope and demonstrating the cooling ability by LH_2. Research on BF, LH_2-pump friction and hybrid of HPI and EM.

function of only ΔW, and its calculated result is shown in Fig. 11.

Range (L). Range L of a vehicle is defined as the traveling distance with one charged fuel, and is expressed by:

$$L = E\Delta W/d = E_0 W \frac{\Delta W}{d\cdot(W + \Delta W)} \quad [\text{km}] \qquad (6)$$

where d is the weight ΔW per equivalent energy to 1 l gasoline.

The values of d[kg/l] for various fuels are shown below:

Gasoline: 0.9, LH_2: 2.33, MH or CH_2: 25,

LHC: 12.5 and EV: 45.

LHC is an imaginary tank containing twice as much high-pressure hydrogen as 30 MPa and with the same weight as standard hydrogen tank. EV is an electric vehicle.

The calculated range L by Eq. (6) for each fuel system is also compared in Fig. 11. Since fuel economy E is decreased as ΔW increases, range L does not increase as a linear function of ΔW. Figure 11 shows that EV with ΔW = 300 kg can travel only 55 km, and that for EV to have 100 km range. ΔW should be 620 kg. This result indicates that EV is unsuitable for passenger cars or trucks. In the case of MH and CH_2, according to Fig. 11, ΔW needs 300 kg for L = 100 km, and to double the L (= 200 km), the required ΔW sharply increases to 750 kg, which is half of W. In addition, when ΔW = 750 kg, E and α are decreased by 33 and 36 percent, respectively. This result points out that practical use of MH or CH_2 is difficult to realize.

On the other hand, LH_2 can achieve more than 400 km range when ΔW = 100 kg. In the range of ΔW = 100 kg, the decrease of E and α is small. From this comparison, it can be concluded that it is only LH_2 that satisfies the necessary condition of ΔW for practical use.

Research and Development of Hydrogen Engines at Musashi Institute of Technology

History. Just a quarter century ago, research on hydrogen engines started at the Internal Combustion Engine Laboratory at Musashi Institute of Technology. The history of the research work is tabulated in Table 3. The research and development work has been conducted by two different but interlinked approaches. One is the fundamental research carried out in the laboratory. The other approach is to fabricate a full-scale test vehicle to participate in demonstration events such as WHEC (World Hydrogen Energy Conference). The on-road operation of the test vehicle revealed new problems, then their causes and countermeasures were investigated in the laboratory.

The first hydrogen engine used CH_2 and an external mixture (EM) method, but CH_2 was soon changed to LH_2 for increasing the range L. The combination of LH_2 and EM caused severe backfire (BF). Although a method of supplying cooled hydrogen to an intake port was developed as a countermeasure against BF, its effect was not sufficient. Then, after experiencing low-pressure injection (LPI) with LH_2 pump, a combination of HPI with a LH_2 pump and spark ignition was finally developed. This system was capable of high power output without any abnormal combustions. Research and development on its fundamental phenomena and on the improvements of engine performance have been continued at Musashi Institute of Technology.

Fundamental Characteristics of Hydrogen Engine

Chemical Equation. When fuel CxHy is completely burned with an excess air ratio λ ($\lambda \geqq 1$), this chemical reaction is expressed by the following equation:

$$\mathrm{CxHy} + \lambda(x + 0.25y)(\mathrm{O_2} + 3.76N_A) \rightarrow x\mathrm{CO_2} + 0.5y\mathrm{H_2O} + (x + 0.25y)3.76\lambda \times \{N_A + (\lambda - 1)\mathrm{O_2})\} + Q_0 \qquad (7)$$

In this equation, x = 8 and y = 18 for gasoline, x = 16 and y = 34 for gas oil, and for hydrogen x = 0 and y = 2. If λ = 1 with hydrogen, Eq. (7) turns out to be:

$$\mathrm{H_2} + 0.5(\mathrm{O_2} + 3.76N_A) \rightarrow \mathrm{H_2O} + 1.88N_A + Q_0 \qquad (8)$$

where N_A denotes average molecular weight of all molecules in

Table 4 Fuel properties for engine

Fuel Typical molecule	Hydrogen H_2	Gasoline C_8H_{18}	Gas oil $C_{16}H_{34}$
Stoichiometric A/F m_v vol.	2.38	59.5	116.6
Stoichiometric A/F m_m wt.	34.2	15.1	14.9
Inflammability limit λ —	10	1.3	
Lower calorific value H_u MJ/kg	120.1	44.5	44.3
Molecular weight f kg/kmol	2.016	114.2	226.4
Molecular calorific value =fH_u MJ/kmol	242.1	5,080	10,030
V_m=Mixture vol./H_2kmol =3.38 × 22.4N m^3/kmol	75.76	1,356	2,636
Q_m=Mixture Calorific value =fH_u/V_m kJ/N m^3	3,200	3,750	3,810
V_a=Air vol./H_2 kmol =2.38 × 22.4 N m^3/kmol	53.35	1,334	2,614
Q_a=Calorific value/airkmol =fH_u/V_a kJ/N m^3	4,540	3,810	3,840
Increase in number of mol after combustion γ_0 %	- 14.8	5.79	6.38

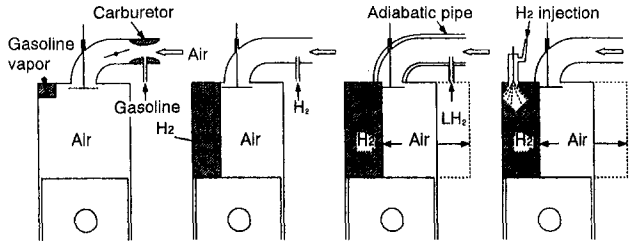

Fig. 13 Output power with various fuel supply methods in $1 / V_s$

Table 5 Viscosity of various substances in phase of liquid and (gas) at standard pressure

Substance	Temp. K	Density ρ kg/ m³	Viscosity μ 10^{-6} kg/ms	Kinetic viscosity $\nu = \mu / \rho$ 10^{-6} m²/s
Hydrogen H_2	20	71	13.2	0.19
(gas)	300	0.082	9.0	109.5
Gas oil $C_{16}H_{34}$	300	810	2,400	3.0
Methane CH_4	100	440	144	0.33
(gas)	300	0.644	11.2	17.3
Nitrogen N_2	70	841	217	0.26
(gas)	300	1.123	17.9	15.9
Oxygen O_2	70	1,237	364	0.294
(gas)				
Water H_2O	293	1,000	1,000	1.0
Air				
(gas)	300	1.161	18.62	16.04
Engine oil	373	850	7,500	8.8

air except O_2, and the value of N_A is 28.17. The amount of Q_0, which is heat generation per 1 kmol hydrogen, is 242.2 × MJ.

The air–fuel ratio under $\lambda = 1.0$, which is denoted by m_v (volume ratio) and m_m (mass ratio), is generally expressed by the following relations.

$$m_v = 4.76(x + 0.25y) \tag{9a}$$

$$m_m = 137.9(x + 0.25y)/(12.01x + 1.008y) \tag{9b}$$

Values of m_v and m_m for various fuels are listed in Table 4.

Power. The m_v values shown in Table 4 illustrate that the volume ratio of gasoline vapor in the fuel/air mixture is only 1.65 percent, while that of hydrogen amounts to 30 percent. Because of this difference, the intake air volume for hydrogen is 70 percent of that for gasoline, and as a result, the hydrogen engine output power becomes 85 percent of that for the gasoline engine on the same stroke volume (V_s) basis. Figures 13(a) and 13(b) schematically explain this phenomenon.

On the other hand, if LH_2 is directly introduced to the engine to increase the mixture density, as shown in Fig. 13(c), the engine output power becomes larger by 22 percent than that for the gasoline engine, and larger by 43 percent than the case where gaseous hydrogen at room temperature is mixed with air. Figure 13(d) illustrates the system in which hydrogen is injected into the cylinder during the compression stroke. In this case, approximately the same power output as 13(c) can be obtained, according the calculation.

The adverse effects of backfire (BF) and pre-ignition (PI) should be taken into consideration. Occurrence of BF makes the external mixture (EM) system require λ to be larger than 1.5, and reduces the power output to about a half of that for the gasoline engine. The pre-ignition restricts the maximum output power, even if the LPI system is adopted.

Decrease in Mols After Combustion (Pichainarong, 1990). The difference in number of mols Δn between the right-hand side and the left-hand side in Eq. (7) is expressed by $\Delta n = 0.25\,y - 1$, regardless of λ. In the case of hydrogen combustion, Δn turns out to be −0.5 and the mols after combustion decrease by 15 percent, while the combustion of gasoline or gas oil increases the mols by about 6 percent at $\lambda = 1$. The effects of such reduction on the power output is also examined.

When the mixture with n_1 mols, Cv_1 (Molal Constant Volume Specific Heat) and temperature T_1 is burned to become the products with n_2, Cv_2, and T_2 under constant volume (V) reaction, the generated heat Q can be expressed by $Q = n_2Cv_2T_2 - n_1Cv_1T_1$. Assuming $n_1Cv_1T_1 = Q_0$ regardless of fuel type and using the perfect gas equation $PV = nRT$, the pressure after combustion P_2 turns out to be

$$P_2 = (R/V)(Q + Q_0)/Cv_2 \tag{10}$$

Since the difference of Cv_2 ($=Cp_2 - 8.32$ kJ/kmolK) among different fuels is very small as shown in Fig. 14, the decrease in mols after combustion does not directly affect P_2 or the power output.

Viscosity. Viscosity μ and kinematic viscosity $\nu = \mu/\rho$ of various substances under both liquid and gaseous states are listed in Table 5. When the surface, which has a profile shown by II, is sliding with a constant speed U along the flat surface I as shown in Fig. 15, the minimum lubricant film thickness h_m can be approximately expressed by;

$$h_m = C_1\sqrt{\mu U/W} \tag{11}$$

where C_1 is a constant. If h_m is less than a certain limit, the sliding surface becomes burnt. Using Eq. (11), the friction force R is expressed by;

$$R = B\mu U/h_m = C_2\sqrt{\mu UW} \tag{12}$$

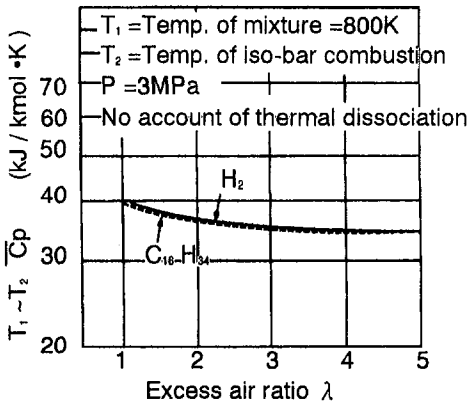

Fig. 14 Comparison in $\bar{C}p$ between H_2 and $C_{16}H_{34}$

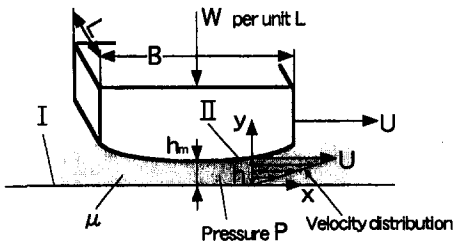

Fig. 15 Lubricating surface model

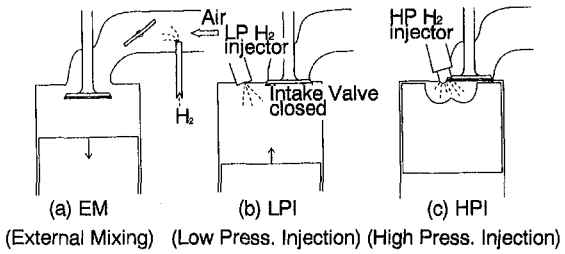

Fig. 16 Basic systems of hydrogen supply into engine

When fluid is flowing through the clearance h with velocity $U = 0$ and the pressure gradient dP/dx, the flow rate per unit length L q becomes

$$q = \frac{dP}{dx}\frac{h^3}{12\,\mu} \tag{13}$$

These relationships have the following influences on a hydrogen engine and its components.

(1) Leakage Through Narrow Clearance. The leakage flow rate of LH_2 is much larger than those of other liquid, according to Table 5 and Eq. (13). In comparison with liquid natural gas (LNG), liquid nitrogen (LN_2), water and gas oil, it is 11, 16, 76, and 182 times as much, respectively. Because of such large leakage, a high-pressure LH_2 pump requires a very narrow clearance, i.e., if the LH_2 clearances h is so small as 0.45 of LNG, 0.4 of LN_2, or 0.18 of gas oil, the leakage volumetric flow rate of hydrogen becomes equal to those of the above liquid.

On the other hand, in the case of gaseous hydrogen, its leakage volumetric flow rate is only 1.25 times and 2.1 times as much as those of natural gas (NG) and air, respectively. On a mass flow basis, it becomes 0.16 and 0.15 in comparison with NG and air.

(2) Clearance Between Piston and Cylinder of LH_2 Pump. The LH_2 pump developed at Musashi Institute of Technology has a piston with 15 to 20 mm diameter. For this pump, it was found that the optimum diametrical clearance is 4 ~ 5 μm. If the clearance is further decreased, the leakage would be reduced, but at the same time, the friction force should be increased, as pointed out by Eq. (12). This large friction heat vaporizes a part of sucked LH_2 and deprives the pumping function. Such inability of LH_2 pump is called "Gas Compression," and selection of the clearance dimension is one of the keys for LH_2 pump design.

The predicted h_m by Eq. (11) for LH_2 pump is only 1/13.5 of that for a diesel engine injection pump. The piston and the cylinder of LH_2 pump virtually cause solid-to-solid friction, thus they would get burned if they were made of metals. From this reason, superior self-lubricating material must be chosen for LH_2 pump.

Combustion in Hydrogen Engine

Backfire (BF) Mechanism (Furuhama, 1977b). Typical fuel supply systems for hydrogen are illustrated in Fig. 16. System (*a*) is external mixture (EM), in which the supply system is very simple because hydrogen is capable of ultralean combustion, and as a result, its mixture ratio does not need precise control. However, because of BF, the output power becomes about half as large as that for a gasoline engine. When Musashi-2, the first LH_2 full-scale test car, participated in SEED rally in 1975 and was driven along the west coast in the U.S.A., fierce BF often occurred and caused various troubles. It was a lesson that BF must be completely avoided for a hydrogen vehicle.

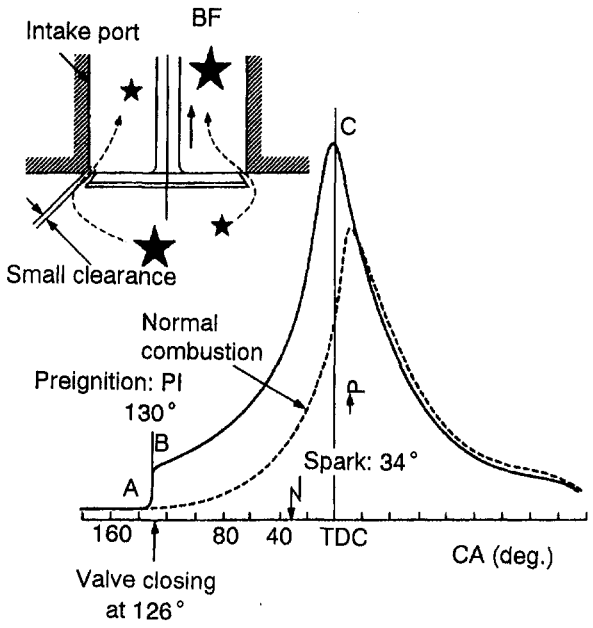

Fig. 17 BF phenomenon

In EM systems, when hydrogen/air mixture formed in an intake manifold is taken into a cylinder, pre-ignition (PI) occurs far prior to spark timing 34° BTDC, as shown by the indicator diagram in Fig. 17. If the PI occurs at 130° BTDC before the intake valve is closed at 126° BTDC, the ignited flame propagates through the valve clearance to the mixture inside the

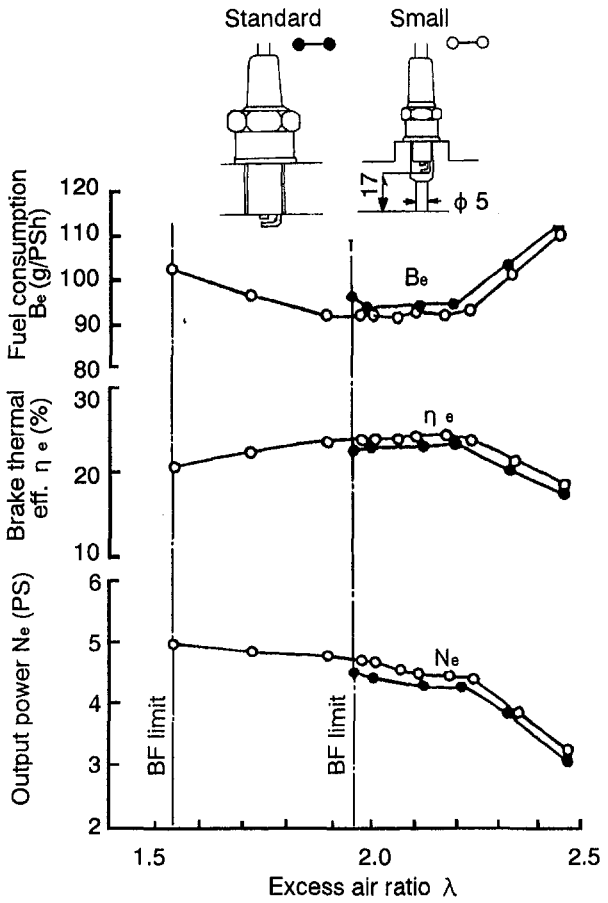

Fig. 18 Effect of small plug on BF control

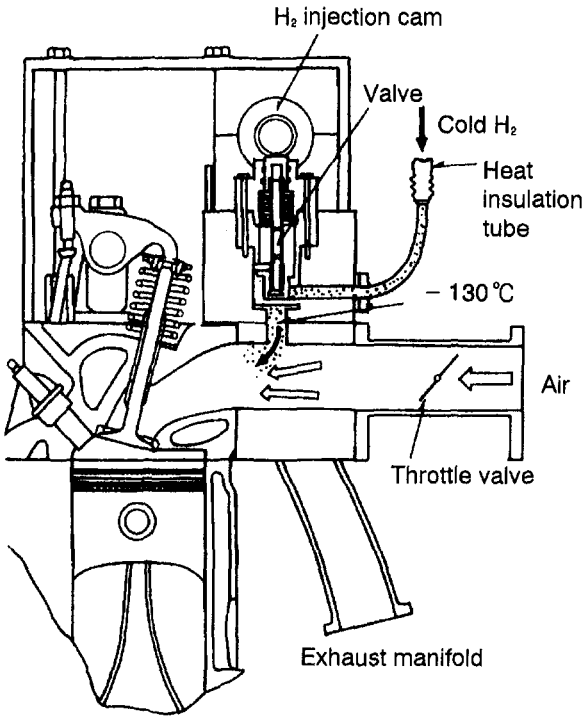

Fig. 19 Low temperature H_2 supply into EM system (Musashi-2)

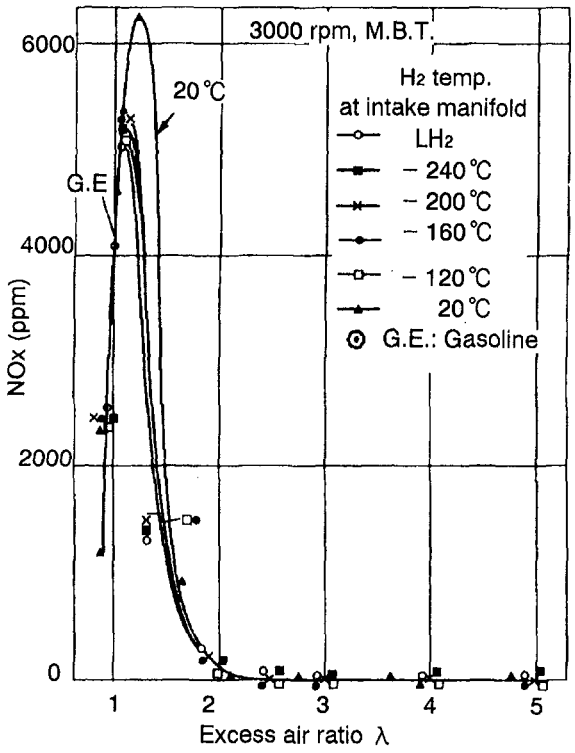

Fig. 20 Effect of λ and H_2 temperature on NO_x content in case of EM

manifold. This is a BF phenomenon, which can be regarded as a pre-ignition at a very early stage. For a hydrogen engine, why and where such pre-ignition occurs has been an important but unsolved problem.

Furuhama et al. made a hypothesis that the spark plug electrode was an ignition source of BF and, based on the hypothesis, they installed a smaller plug in the innermost position of the ϕ 5 mm hole, as shown in Fig. 18. As a result of this modification, the BF limit was shifted to the richer side, i.e., from $\lambda = 2$ to 1.55, but BF was not able to be completely prevented. Another hypothesis was recently made by Koyanagi et al. (1994) at Musashi I.T. According to them, measurements of OH radical indicated that the moderately burning flame at the piston top land seems to be an ignition source. The investigation is currently in progress.

Since the cause of BF has not been clarified yet, its determinative countermeasures have not been found out. Mercedes-Benz (Withalm and Gelse, 1986) reported that water injection into an intake manifold was effective for BF prevention. Amount of injected water was relatively large, 5 to 10 percent of the air mass flow rate when $\lambda = 1$. This made water injection control difficult, corresponding to various power outputs. Injected water also made lubrication oil cloudy and caused rust. Although efforts were made to establish this technology, the development seems terminated at present. Musashi-2 (Furuhama, 1975) adopted a system in which cooled hydrogen at about −130°C was supplied to an intake port only when intake valves were open. This system is illustrated in Fig. 19. However, no effects were attained against BF.

NO_x Emission Characteristics in EM System (Furuhama, 1977a). For EM, the mixture ratio under combustion is uniformly distributed throughout the cylinder. Because of this, NO_x emission is not effectively reduced by lowering the hydrogen inlet temperature, as shown in Fig. 20. On the other hand, in the range of lean combustion with $\lambda \geqq 2$, NO_x emission becomes significantly small. This result indicates that as long as EM hydrogen engines are used under low power output, there would be no problems of NO_x emission and BF.

Low Pressure Hydrogen Injection (LPI) Two Stroke Engine (Furuhama, 1978; Furuhama et al., 1981; Furuhama and Kobayashi, 1982). A system shown in Fig. 16(*b*), in which air alone is taken in, then hydrogen is injected into the cylinder after the intake valve is closed, can completely avoid the BF. In addition, high power output can be possible, as indicated in Fig. 13(*d*), and PI can be restrained to some extent. This system was applied to Musashi-3's two stroke engine. The engine and fuel supply system of Musashi-3, shown in Fig. 21, has the following characteristics.

In the case of gasoline engines, unless injection takes place during the scavenging period, the ignition becomes unstable,

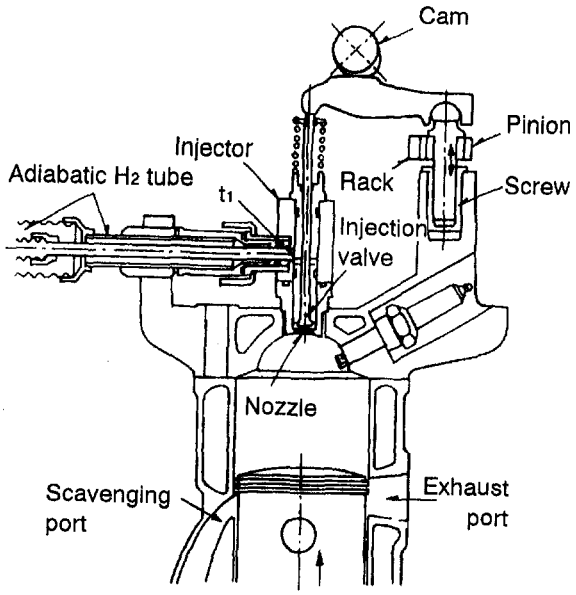

Fig. 21 Cooled H_2 LPI 2-stroke engine (Musashi-3)

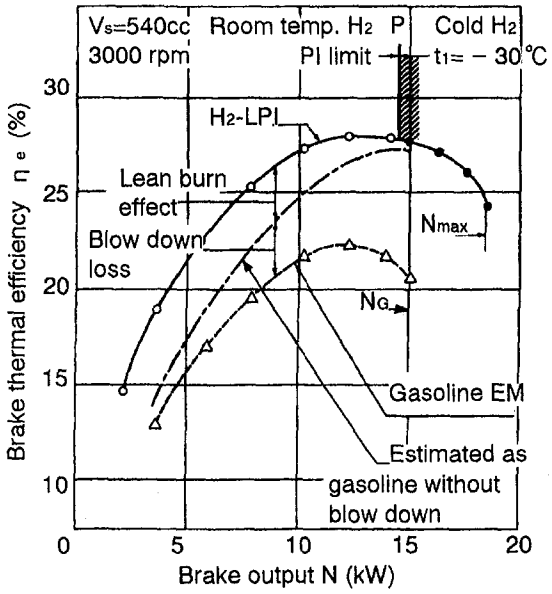

Fig. 22 High performance of two-stroke cooled-H_2 LPI engine

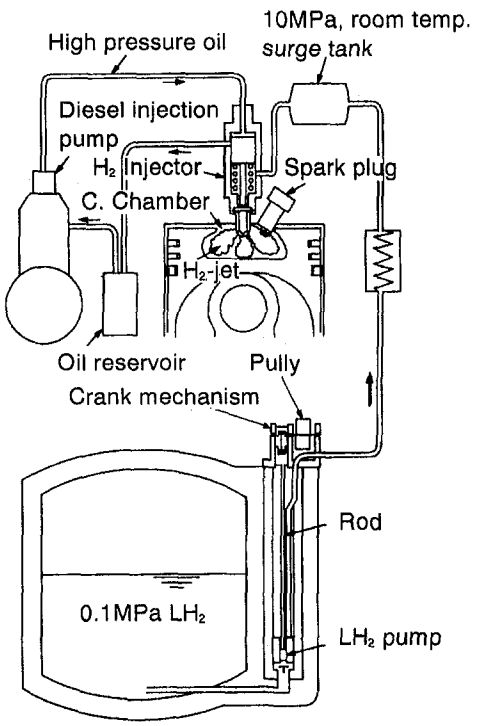

Fig. 24 HPI engine fuel system

and as a result, the fresh air and fuel blow down without combustion. Hydrogen engines, on the other hand, make stable ignition possible even when injection takes place after the exhaust ports are closed. Because of this ignition characteristic, the loss of air and fuel can be prevented, and ultralean combustion can be realized. In addition, internal EGR with this engine is effective to reduce NO_x and to suppress PI.

Figure 22 shows measurement results of this engine. According to the figure, PI occurs at the output power close to the maximum power of the gasoline engine N_G, but by lowering hydrogen temperature to −30°C at the injection valve inlet, operation under the theoretically maximum power becomes possible without PI. Comparing this result with Fig. 19, it is revealed that cold hydrogen injection is far more effective than cooling of intake mixture by the cold hydrogen. Similarly, this system is more effective to NO_x reduction. It is shown in Fig. 23 that two-stroke engines exhaust less NO_x than four-stroke engines both for hydrogen and gasoline mainly because of the internal EGR.

Apparatus for High Pressure Injection (HPI). The discussion above indicates that high-performance hydrogen engines without abnormal combustion can be realized by HPI shown in Fig. 16(*c*). Thus, the final goal at Musashi Institute of Technology was set at HPI engines, and a HPI engine was first applied

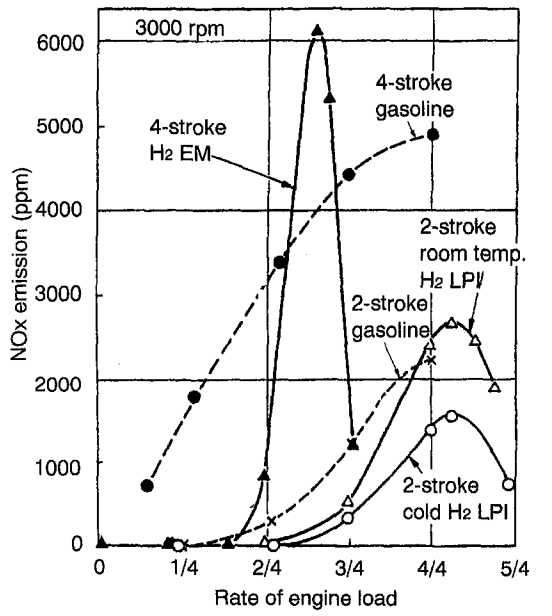

Fig. 23 Comparison of NO_x among various engines

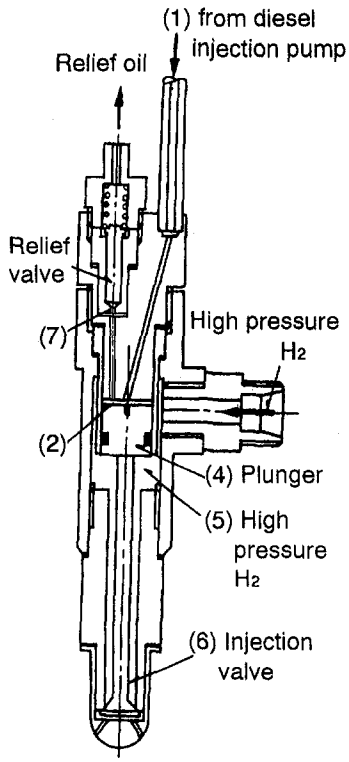

Fig. 25 High-pressure H_2 injector without coil spring

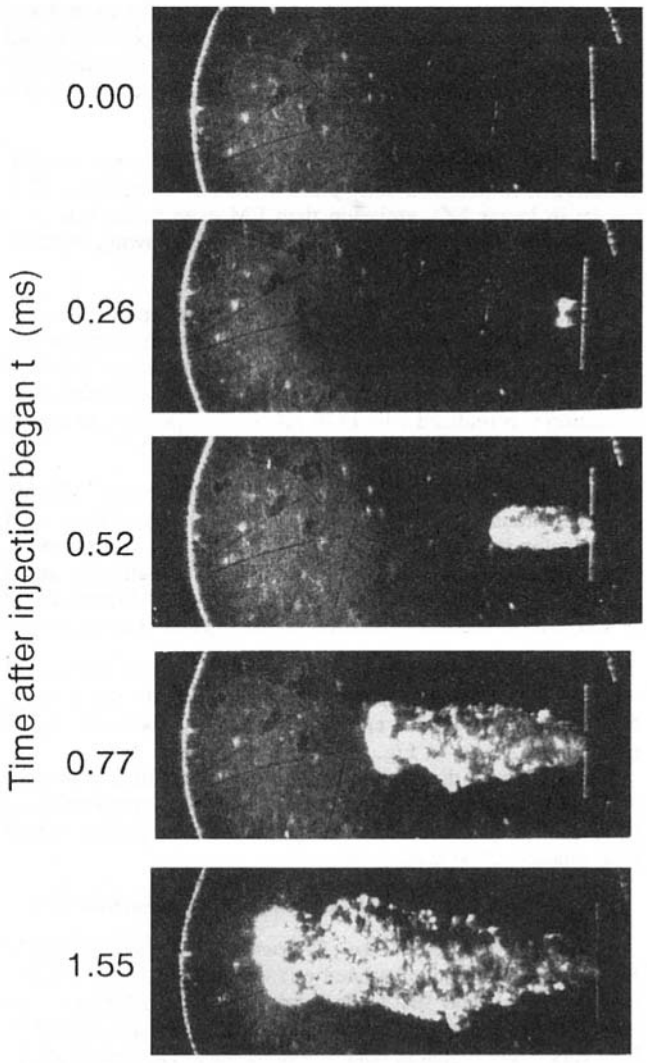

Fig. 26 Schlieren photo of H_2 growth progress

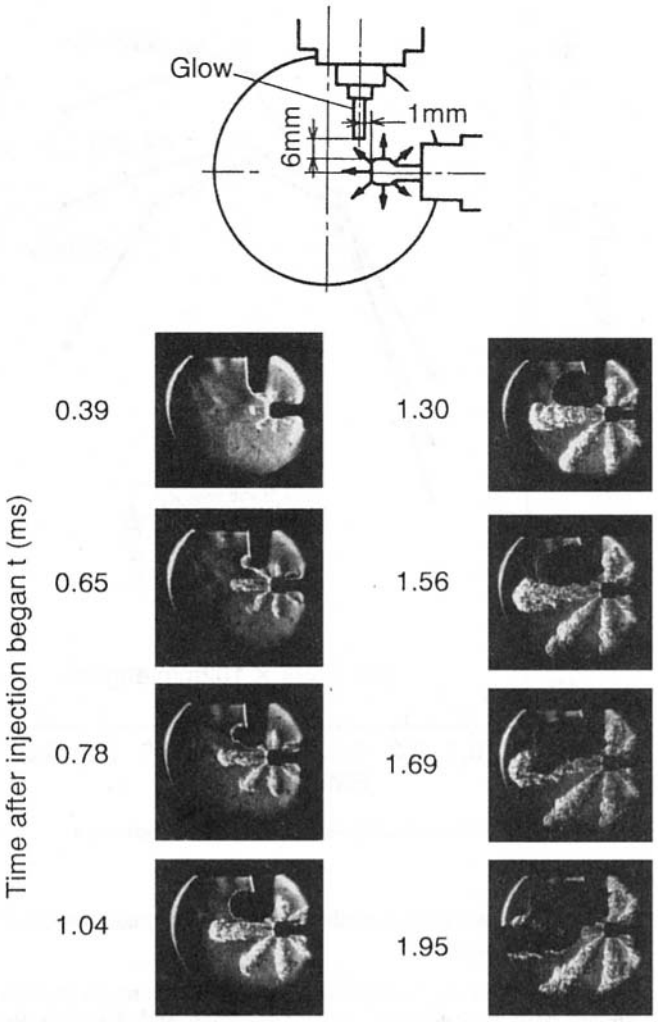

Fig. 27 Flame propagation of H_2 jet in constant-volume stationary cavity

to Musashi-5 in 1982 (Furuhama and Kobayashi, 1982, 1984). The engine system applied to Musashi-8 and 9 is shown in Fig. 24 (Furuhama et al., 1991). An LH_2 pump is inserted into 100 l LH_2 tank. LH_2 pressure is raised to 10 MPa by the LH_2 pump and the high-pressure LH_2 is introduced to a surge tank. A hydrogen injection valve equipped inside an injector is opened by gas oil pressure wave from a diesel engine injection pump and the injected hydrogen is ignited by spark.

The injector, which is the most crucial component, was recently modified, as shown in Fig. 25. In this system, a pressure wave traveling through a high-pressure tube (1), enters a small room (2), pushes down a plunger (4), and opens an injection valve (6). When the oil supply in the tube (1) is stopped, an oil relief through a small hole (7) decreases pressure in (2), and the hydrogen pressure in (5) closes the injection valve.

Mixture Formation and Flame Propagation of Hydrogen Jet. The density of gas oil droplet in diesel engines is 40 times as large as that of air, whereas hydrogen jet density is only 0.07 of air density. As a result, hydrogen jet penetration is not as strong. In addition, as discussed in the previous paragraph regarding the viscosity of hydrogen, the low Reynolds number (Re) makes transition to turbulent flow difficult, which seems a reason for slow combustion of hydrogen jets. Figure 26 is schlieren photographs taken by Fukuma and Furuhama (1987) when a hydrogen jet was injected into a constant volume chamber. It was found out from this visualization that the maximum velocity at the jet tip was as low as 44 m/s and that the turbulence near the jet boundary was also small. Another experimental result by Fukuma et al. (1986) is shown in Fig. 27. According to this result, one of the jets was ignited at 0.65 ms after the injection, but the flame did not propagate to the next jet though the flame was close to the next jet.

However, the experiment using an operating engine by Pichainarong et al. (1990) revealed that hydrogen jet combustion could be promoted as a result of increase in the injection pressure P_i as shown in Fig. 28. They succeeded in improving the performance under high load by reducing the diameter D_1 of the piston cavity inlet as shown in Fig. 29. These results indicate

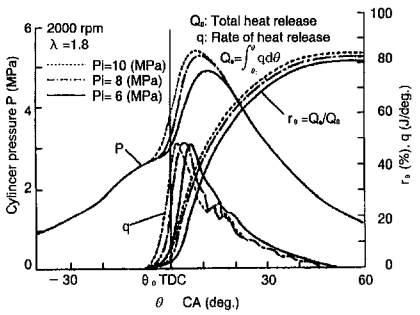

Fig. 28 Effect of P_i on the combustion heat release

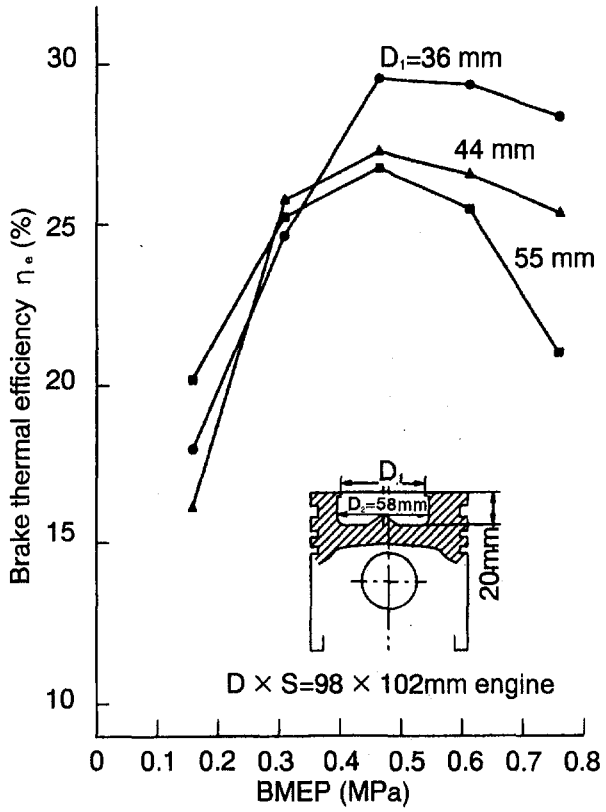

Fig. 29 Effect of cavity entrance D_1 on the engine η e

that there exists a unique method of mixture formation suitable for hydrogen engines.

Ignition Methods for Hydrogen Jet. HPI hydrogen engines should have two devices: one for injection and the other for ignition. In this section, the development of ignition methods will be summarized. The ignition method used for Musashi 5 and 6 was a relatively simple hot surface method, which was an electric heater made by winding a platinum wire around a ceramic rod. The life was, however, extremely short. In the next test vehicle, Nino truck Musashi-7, a ceramic glow enclosing a tungsten wire, which is often used for a diesel starter, was adopted. This alternation made the life longer, but it was not sufficiently long.

In general, a stable ignition can be obtained if the surface temperature is higher than 900°C, whereas sufficient life time can be guaranteed only if it is lower than 800°C. From this disagreement, spark ignition was applied to Musashi-8 and 9, in which small energy consumption and long life were realized. In order to make the spark ignition method work properly, the following two conditions were required. First, the spark gap should be located as close as possible to one jet hole, in order to minimize the ignition delay. Second, since the spark ignition timing must be determined according to the injection timing, their optimum combination should be selected. Figure 30 shows experimental results by Kobayashi et al. (1989). In Fig. 30(a), where the jet reached a spark gap at t = 0.3 ms after it leaves a jet hole, and the spark was discharged at the same moment, immediate and stable ignition was obtained. In Fig. 30(b), where the spark was discharged at halfway of the jet stream at t = 0.95 ms, the ignition was delayed and unstable. If the spark timing was further delayed, as shown in Fig. 30(c), where t = 1.3 ms, ignition did not take place because the mixture was too rich.

The experimental results using Musashi-8 by Furuhama et al. (1991) are shown in Fig. 31, where L is an injection valve lift and V is an ignition voltage. According to this experiment conducted by an operating engine, if the injection timing θ_i and spark timing θ_s were the same, stable ignition was obtained, but if θ_s is later than θ_i by 3° (0.5 ms), the ignition became delayed and was sometimes missed.

NO_x Characteristics in HPI Engine. In the case of HPI, unlike EM, combustion takes place at the rich mixture jet. This results in larger NO_x emission than EM even under low load with large λ, as shown in Fig. 32. Thus the following countermeasures were tested.

(1) EGR. Since the hydrogen does not contain sulfur, serious wear is not caused. In addition, since the exhaust gas has large amounts of H_2O in it, its vaporization latent heat can be made use of. Because of these advantages, significant NO_x reduction was realized with EGR rate α = 15 percent, as shown in Fig. 33(a). The decrease in η_c was also small.

(2) Injection of Low Temperature Hydrogen. Figure 33(b) demonstrates that lowering hydrogen temperature t_1 at the injector inlet is effective to NO_x reduction. Furthermore, since jet temperature at the injection hole is higher by about 90°C than at the injector inlet, more effective reduction could be obtained if thermal insulation of the injector was improved.

(3) Hybrid of HPI With EM. When a part of fuel is EM with air, the initial combustion becomes moderate. As a result, NO_x emission during the entire combustion can be significantly reduced, as shown in Fig. 34.

Three methods discussed in this section were all effective for NO_x reduction of HPI engines. Therefore, the combination of two or three of these methods will be able to further reduce total amount of NO_x emission.

Decrease in Temperature of Mixture and Burned Gas

(1) High Output by Low Temperature Hydrogen Supply. Figure 35 shows the calculated mixture temperature T when 1 kg air at 300 K and 101.3 kPa is mixed with 29.24 g hydrogen at T_H. In this figure, ΔT is the temperature decrease caused by LH_2 vaporization (latent heat = 445 kJ/kg). The lowest possible temperature of the mixture is 210 K, 90 K lower than room temperature 300 K. Since the density of the mixture is in inverse proportion to the temperature T, the output power will increase as T decreases. ϕ_c at T = 210 K, the power becomes 1.44 times as large as that at 300 K and 1.22 times as large as that for gasoline engines, according to the calculation.

(2) Reduction of Burned Gas Temperature. As burned gas temperature increases, BF and PI become more likely, and the amount of NO_x emission also increases. Calculation was carried out for the combustion process where 1 kg air at 300 K and 101.3 kPa was adiabatically compressed with the compression ratio 12:1 to become 770 K (T_2), then the constant pressure combustion with heat generation Q = 3510/λ took place and increased the temperature to the maximum level T_4. This process is shown in Fig. 36.

In the case of EM, the relationship between T_2 and T_4 can be expressed by $T_4 = T_2 + 3510/(\lambda + 0.02924)C_p$, assuming C_p is a constant equal to the average value over the process ② to ③ The line AB in Fig. 37 illustrates T_4 as function of Q or λ. The point B corresponds to T_4 with λ = 2, at which NO_x emission becomes very small. The point (8) with λ = 1.5 roughly indicates the BF limit, and the corresponding T_4 value is 2400 K, which is 420 K lower than A. The T_4 value marked by (2) is obtained when the intake mixture (λ = 1) is cooled by LH_2, and is 155 K lower than A. On the other hand, 5 percent water injection decreases T_4 to the point (3), which is 255 K lower than A. In this case, 110 K of 255 K reduction is because of water vaporization, and the rest is because water addition increases working substances.

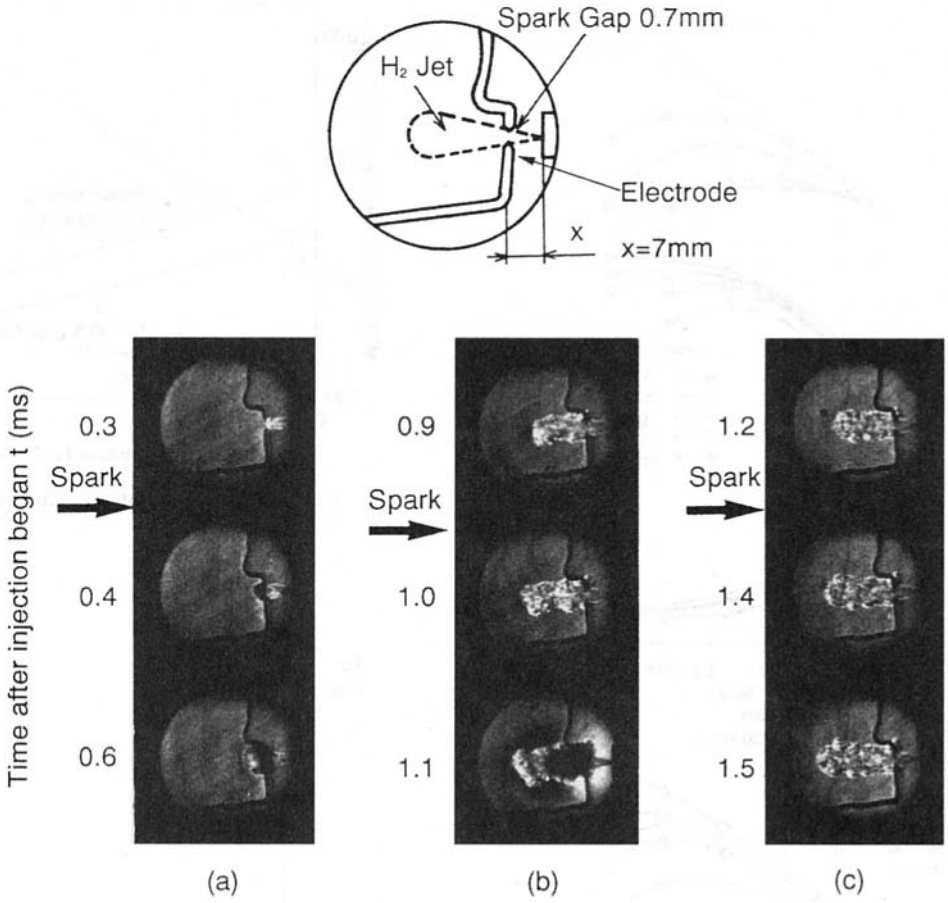

Fig. 30 Effect of spark timing on the ignitability of H_2 jet

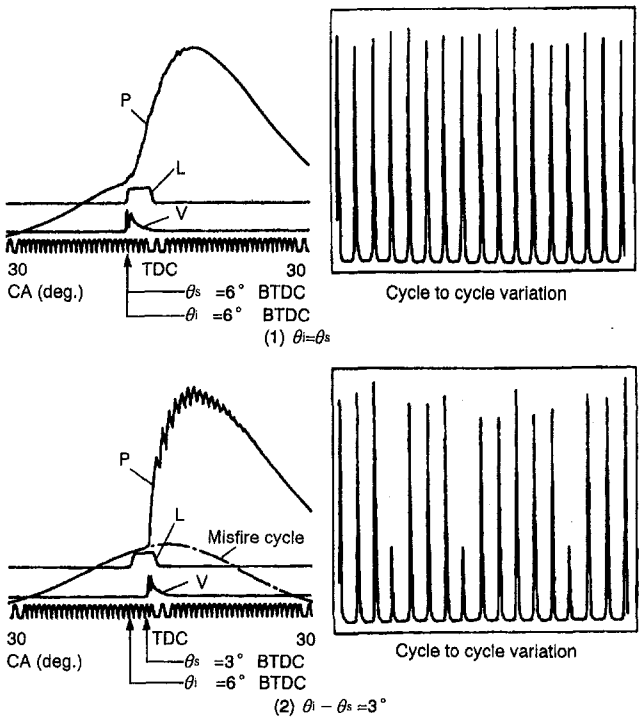

Fig. 31 Effect of spark timing on the combustion of HPI engine

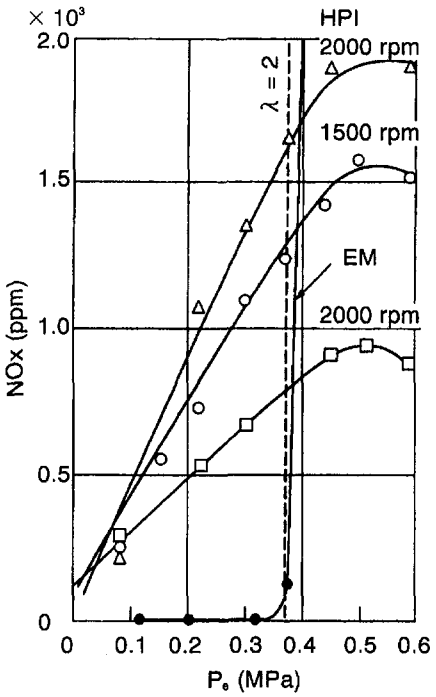

Fig. 32 NO_x characteristics of HPI engine

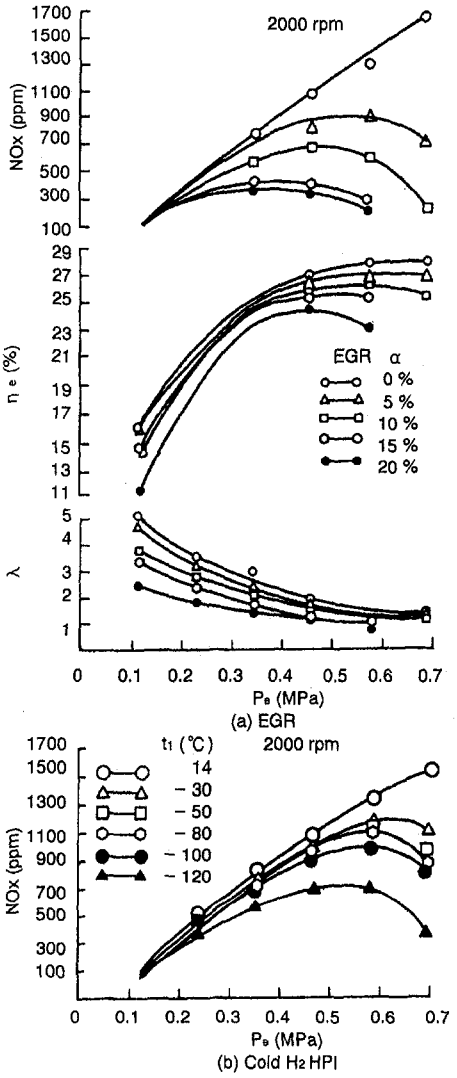

Fig. 33 Effect of EGR and cold H_2 on the NO_x control in HPI

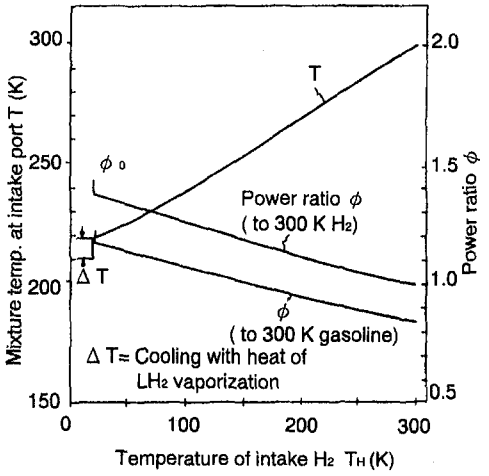

Fig. 35 Power up by introduction of cold H_2

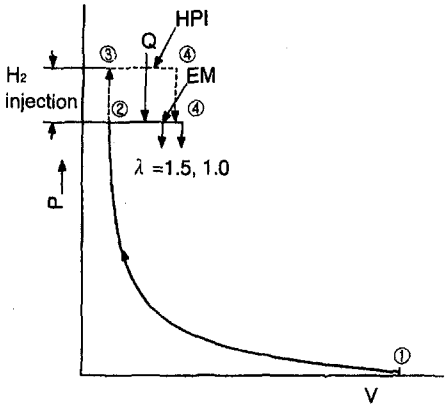

Fig. 36 P–V diagram for calculation of T_4

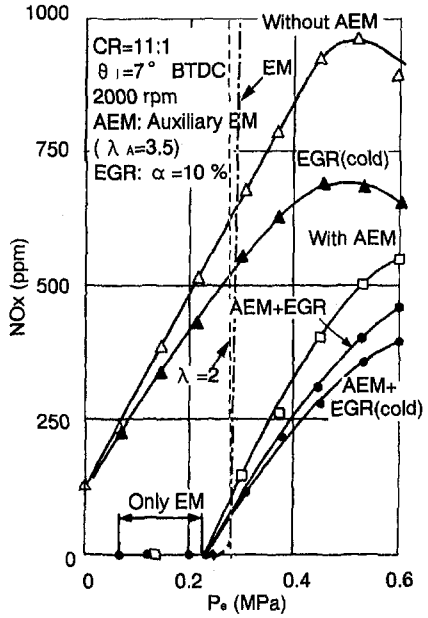

Fig. 34 Effect of auxiliary EM (AEM) and EGR on the NO_x control

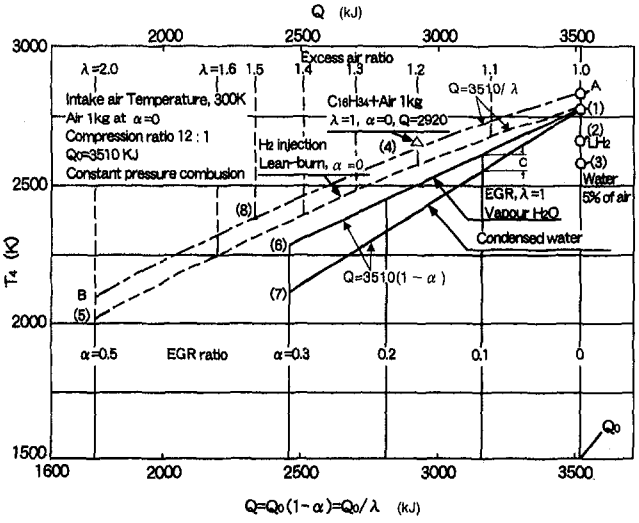

Fig. 37 Comparison of the effect of several methods on the calculated combustion gas temperature T_4

The combustion process for HPI is illustrated by a dotted line in Fig. 37, where it is assumed that hydrogen at 350 K is injected during the process ② to ③ in Fig. 36. The increase in

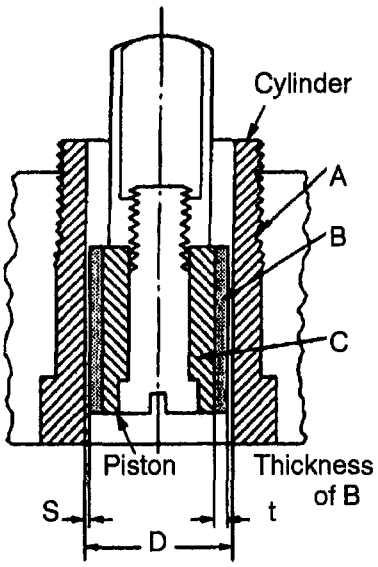

A: Stainless steel, B: Synthetic resin
C: Invar

$$t=\frac{D}{2}\left(\frac{\alpha_A-\alpha_C}{\alpha_B-\alpha_C}\right) \quad -(14)$$

Fig. 38 LH_2 pump consisting of three kinds of material

moles raises the mixture pressure, but since the injected hydrogen temperature (350 K) is lower than the air temperature at ②, the mixture temperature T_3 becomes lower than T_2, and T_4 after combustion also decreases to the point (1) in Fig. 37. The resultant T_4 temperatures marked by (1)–(5) are lower by about 60 K at the same Q than those for EM.

The process for HPI with EGR was then examined. When the amount of new intake air is decreased under EGR ratio α and $\lambda = 1$, the heat generation Q can be expressed by $Q = 3510\ (1 - \alpha)$. In the case of EGR, as α increases, moles of H_2O in the working substances increase, which results in larger C_p and lower T_4. This effect can be obtained only by α, not by λ. In addition, if the exhaust gas used for EGR is cooled and its water vapor is condensed, the effect to reduce T_4 becomes larger. In Fig. 37, the calculation results with and without water condensation are plotted. Results (1)–(6) are the calculated T_4 without condensation as a function of α and Q, and the results (1)–(7) are the corresponding T_4 with condensation. According to the results, α is more effective to T_4 reduction than λ for the same amount of Q (power output).

LH_2 Pump (Furuhama et al., 1984). As discussed before, hydrogen injection into a cylinder is the most desirable system to realize high power output without abnormal combustion. In addition, weight comparison indicates that an LH_2 tank is a storage method with the smallest weight. In order to apply these two systems to vehicle engines, an LH_2 pump is the required device. Invention and development of the LH_2 pump and injection system are the most noticeable achievement at Musashi Institute of Technology. The following are some of the development results.

1 Since low hydrogen viscosity often caused the sliding surface to be burned, as discussed in the previous paragraph regarding the viscosity of hydrogen, a synthetic material was used for piston outer surface in order to prevent the burned surface.

2 Since the synthetic material has a large thermal expansion coefficient α, it is rather difficult to maintain a proper clearance between the piston outer surface and the metal cylinder inner surface. Material C with extremely small α was inserted into the inside of the piston, as illustrated in Fig. 38. This design succeeded in keeping the clearance satisfying Eq. (14) over the all temperature range.

3 The LH_2 pump at the early development stage had a long connecting rod, which connected a reciprocating piston in the pump and a crank shaft located in the upper part of the tank. However, it was found out that the rod was bent by the increased compression force, which increased the friction with the cylinder wall. Generated heat as a result of the large friction caused "gas compression" and the LH_2 pump lost its function. As a countermeasure against it, the cylinder A was reciprocated by the rod (5), while the piston (B) was made stationary as shown in Fig. 39.

Summary

This paper briefly presents some of the major results of hydrogen engine research and development, which the author has been conducting during a long period of time by the countless helps of many assistants and students. The followings are their summary.

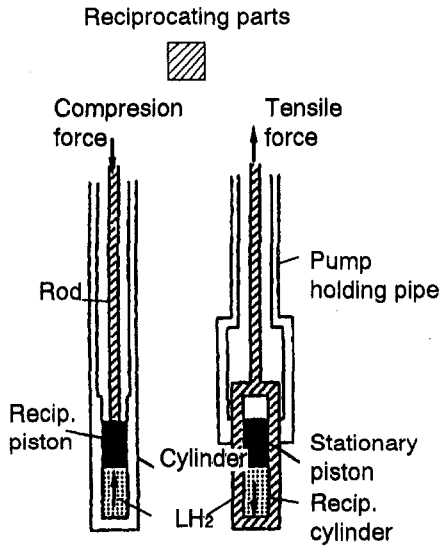

(a) Piston recip. (b) Cylinder recip.

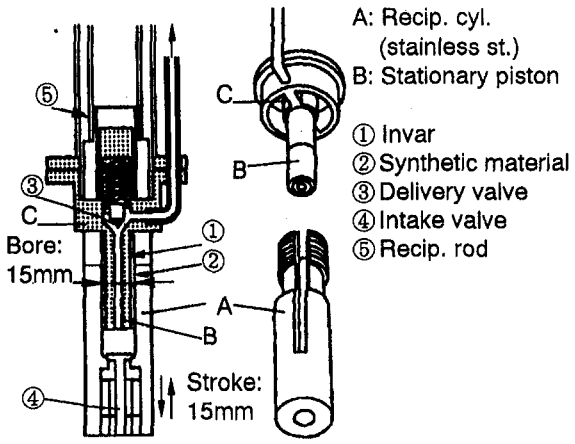

(c) Cylinder recip. LH_2 pump

Fig. 39 Structure of LH_2 pump

1 Improper evaluation has been often made when the future of advanced engines is forecasted. Problems of Wankel rotary engines and those of ceramic engines were pointed out as examples of improper evaluation.

2 The important factor to select appropriate new energy for vehicle use is the weight of fuel and storage device. LH_2 alone can satisfy the requirement.

3 Hydrogen volumetric ratio in the hydrogen/air mixture for a hydrogen engine is significantly larger than the fuel ratio of other engines. Because of this, hydrogen engines with EM have a lower power output, while injection into the cylinder increases the power considerably. BF and PI are additional factors to lower the output.

4 When LPI of cold hydrogen is applied to two-stroke engines, disadvantages of a gasoline two-stroke engine can be prevented, and high engine performance can be obtained.

5 The HPI system realizes high power output without abnormal combustion.

6 Since hydrogen has small density and low viscosity, mixture formation characteristics are different from those of other fuels, and unique optimization is necessary.

7 The amount of NO_x emission for EM is considerably small when λ is larger than 2, whereas the amount increases significantly as the mixture becomes richer. In the case of HPI, unlike EM, EGR and low-temperature hydrogen injection are the methods to reduce NO_x emission.

8 Selection of three different materials for LH_2 pump; its piston outer surface, piston inside and cylinder, enabled no lubricating operation and maintained appropriate piston clearance over the entire temperature range.

9 Increase in supplied hydrogen density by cooling and injection of low-temperature hydrogen, both of which were made possible by LH_2 pump, realized high power output, low NO_x emission, and restraint of abnormal combustion.

10 As a conclusion of the research and development at Musashi Institute of Technology, the following system is most desirable for vehicle use, i.e., the combination of LH_2 tank, LH_2 pump, HPI, spark ignition, and EGR.

References

Eberle, M. K., and Klomp, E. D., 1973, SAE Paper No. 730117.

Fukuma, T., Fujita, T., Pichainarong, P., and Furuhama, S., 1986, "Hydrogen Combustion Study in Direct Injection Hot Surface Ignition Engine," SAE Paper No. 861579.

Fukuma, T., and Furuhama, S., 1987, "Development of 4-Stroke Hydrogen Injection Hot Surface Ignition Engines for Vehicles," *JSAE Transaction,* No. 34, p. 94.

Furuhama, S., 1956a, "A Dynamic Theory of Piston Ring Lubrication (1st report)," *Bulletin of JSME,* Vol. 2, No. 7, p. 423.

Furuhama, S., 1956b, "Gas Leakage From Piston Ring of Small Out Put," *ISME Transactions,* Vol. 22, No. 124, p. 934.

Furuhama, S., 1961, "On the Flow of Gas Through the Piston Ring," *Bulletin of JSME,* Vol. 4, No. 46, p. 691.

Furuhama, S., and Onishi, E., 1973, "Study on the Gas Leakage in Rotary Engines," *JSME Proc.,* No. 730-17, p. 209.

Furuhama, S., 1974, "Gastightness of Rotary Engine," *Science of Machine,* Vol. 26, No. 6, p. 763.

Furuhama, S., 1975, "Drived the Whole Distance by LH_2 Car in the SEED Rally," *Internal Combustion Engine,* Vol. 14-173, p. 73.

Furuhama, S., 1977, "Performance and Exhaust Emission of the LH_2 Hydrogen Engine," JSME Preprint, No. 770-9, p. 61.

Furuhama, S., Yamane, K., and Yamaguchi, I., 1977, "Combustion Improvement in a Hydrogen Fueled Engine," *Int. J. Hydrogen Energy,* Vol. 2, No. 3, p. 329.

Furuhama, S., 1978, "Tribology in Engines (Part 2)," *Journal of JSAM,* Vol. 32, No. 7, pp. 721.

Furuhama, S., and Azuma, H., 1978, "Hydrogen Injection Two-Stroke Spark Ignition Engine," *Proc. of 2nd WHEC,* Vol. 4, p. 1851.

Furuhama, S., 1980, "Rotary Engine (11)," *Internal Combustion Engine,* Vol. 19, No. 232, p. 43.

Furuhama, S., Kobayashi, Y., and Iida, M., 1981, "A LH_2 Engine Fuel System on Board-Cold GH_2 Injection Into Two Stroke Engine With LH_2 Pump," ASME Paper No. 81-HT-81, p. 1.

Furuhama, S., and Kobayashi, Y., 1982, "Hydrogen Cars With LH_2-Tank, LH_2-Pump and Cold GH_2-Injection Two-Stroke Engine," SAE Paper No. 820349.

Furuhama, S., Fukuma, T., and Kobayashi, Y., 1982, "Combustion Improvement in Hot Surface Ignition Hydrogen Diesel Engine," *Proc. ASME–JSME Thermal Eng. Conf.,* p. 261.

Furuhama, S., and Kobayashi, K., 1984, "Development of a Hot-Surface-Ignition Hydrogen Injection Two-Stroke Engine," *Inter. J. Hydrogen Energy,* Vol. 9, No. 3, p. 205.

Furuhama, S., Fukuma, T., and Kashima, T., 1984, "LH_2 Fuel Supply System to Hot Surface Ignition Turbocharged Engine," *Cryogenic Processes and Equipment,* ASME Book No. G00282, p. 105.

Furuhama, S., and Enomoto, 1987, Y., "Heat Transfer Into Ceramic Combustion Wall of Internal Combustion Engines," SAE Paper No. 870153.

Furuhama, S., Koyanagi, K., and Tomisawa, N., 1991, "The Power System of a Computer Controlled Hydrogen Car-GH_2 Injection and Spark Ignition Engine With LH_2 Tank and Pump," *IMechE, C 430/028,* p. 179.

Kobayashi, H., Matsushita, T., and Furuhama, S., 1989, "Study on the Ignition Methods of Engine With Hydrogen Injection Just Before TDC," *JSME Trans.,* Vol. 55-511, p. 895.

Koyanagi, K., Hiruma, M., Yamane, K., and Furuhama, S., 1993, "Effect of Hydrogen Jet on Mixture Formation in a High-Pressure Injection Hydrogen Fueled Engine With Spark Ignition," SAE Paper No. 931811.

Koyanagi, K., Hiruma, M., and Furuhama, S., 1994, "Study on Occurring Mechanism of Backfire in Hydrogen Engines," *Proc. of 72nd JSME Annual Meeting,* Vol. 3, p. 341.

Pichainarong, P., Iwata, T., and Furuhama, S., 1990, "Study of Thermodynamic Analysis in Hydrogen Injection Engines," *Proc. of 8th WHEC,* p. 1087.

Withalm, G., and Gelse, W., 1986, "The Mercedes-Benz Hydrogen Engine for Application in a Fleet Vehicle," *Proc. of 6th WHEC,* p. 1185.

The Hybrid Rich-Burn/ Lean-Burn Engine

D. P. Meyers

J. T. Kubesh

Department of Engine Research,
Southwest Research Institute,
San Antonio, TX 78228

This paper describes a new low-emissions engine concept called the hybrid rich-burn/lean-burn (HRBLB) engine. In this concept a portion of the cylinders of a multicylinder engine are fueled with a very rich natural gas–air mixture. The remaining cylinders are operated with a lean mixture of natural gas and air and supplemented with the rich combustion exhaust. The goal of this unique concept is the production of extremely low NO_x (e.g., 5 ppm when corrected to 15 percent exhaust oxygen content). This is accomplished by operating outside the combustion limits where NO_x is produced. In rich combustion an abundance of hydrogen and carbon monoxide is produced. Catalyst treatment of the rich exhaust can be employed to increase the hydrogen concentration and decrease the carbon monoxide concentration simultaneously. The hydrogen-enriched exhaust is used to supplement the lean mixture cylinders to extend the lean limit of combustion, and thus produces ultralow levels of NO_x. Results to date have shown NO_x levels as low as 8 ppm at 15 percent oxygen can be achieved with good combustion stability and thermal efficiency.

Background

Stationary engines located in the Southern California South Coast Air Basin are facing South Coast Air Quality Management District (SCAQMD) standards that require all stationary power plants that produce more than 500 brake horsepower produce no more than 36 ppm NO_x. However, it has been estimated by SCAQMD that to compete with electric motors, internal combustion engines must generate below 5 ppm NO_x (corrected to 15 percent exhaust oxygen). The impact of switching from stationary natural gas engines to electric motors would have a significant financial impact on gas utilities as well as prime mover operators throughout the U.S.

Southwest Research Institute (SwRI) has recently received a U.S. patent that describes a hybrid rich-burn/lean-burn (HRBLB) engine. This engine requires a portion of the cylinders of a multicylinder engine to be fueled with a very rich natural gas–air mixture. Remaining cylinders operate on an extremely lean mixture of natural gas and air while being supplemented with exhaust from the rich combustion cylinder(s). The result is extremely low emissions of NO_x. This is accomplished by operating outside the combustion limits favorable to NO_x production (i.e., very rich and very lean). In rich combustion an abundance of hydrogen and carbon monoxide is produced, particularly when using natural gas as a fuel. The hydrogen-enriched exhaust augments the lean fuel–air mixture supplied to the other cylinders to extend the lean limit of combustion, thus producing ultralow levels of NO_x [1].

In natural gas-fired engines, ultra-low levels of NO_x are difficult to achieve due to misfire and incomplete combustion when the equivalence ratio (ϕ) falls below 0.6. However, a hydrogen-fueled engine can operate at equivalence ratios well below 0.2 because hydrogen has relatively wide flammability limits and much higher flame speeds than conventional hydrocarbon fuels. In the proposed rich-burn/lean-burn engine, the hydrogen-enriched exhaust from the rich-burn cylinders will supplement very lean fuel–air mixtures in the lean cylinders, thus providing a mixture that will burn efficiently at equivalence ratios well below 0.6. NO_x levels will be exceedingly low in the lean-burn exhaust because combustion products such as CO_2 carried over from the rich-burn cylinders will greatly reduce combustion flame temperatures. This, combined with the leaner equivalence ratio made possible with hydrogen-augmented combustion, is expected to provide the potential of reducing NO_x to the 5 ppm level. A diagram of the overall concept is depicted in Fig. 1.

To date, several areas of initial development have taken place. First, modeling of the rich mixture combustion has been performed to determine cylinder combustion performance and exhaust gas composition as a function of equivalence ratio, bore, stroke, manifold pressure, and manifold temperature. Second, rich combustion experiments have been accomplished on a single-cylinder research engine to determine actual exhaust gas composition as well as appropriate piston geometry, optimum equivalence ratio, and catalyst selection. Finally, lean combustion tests also have been performed by supplementing very lean fuel–air mixtures with various blends of simulated rich exhaust products to determine optimum substitution rates for minimum NO_x formation and maximum efficiency.

Rich Combustion Model

Prior to any experimental work, a computer model was used to predict the performance and emissions of a rich-burn engine. The model was based on a thermodynamic First Law analysis of a piston-cylinder idealization in an internal combustion engine. The piston compresses and expands the cylinder gas based on the kinematics of a typical slider-crank mechanism. At each crank angle a new volume is calculated. The change in temperature from the previous crank angle to the current crank angle is determined by an energy balance. The energy balance includes compression and expansion work, as well as energy changes due to heat transfer and combustion. The amount of mass in the cylinder is determined from the inlet conditions (temperature and pressure) and by estimating the volumetric efficiency using correlations obtained from Taylor [2] and Ferguson [3]. Furthermore, the cylinder charge is also assumed to contain a residual gas fraction and is estimated by the residual gas fraction prediction from Fox [4].

Heat transfer processes are accounted for by using the Woschni heat transfer correlations [5]. Blowby is assumed to be zero. A Wiebe function is used to predict the heat release

Contributed by the Internal Combustion Engine Division and presented at the Internal Combustion Engine Division 1995 Spring Technical Conference, Marietta, Ohio, April 23–26, 1995. Manuscript received by the Internal Combustion Engine Division January 1995. Associate Technical Editor: W. K. Cheng.

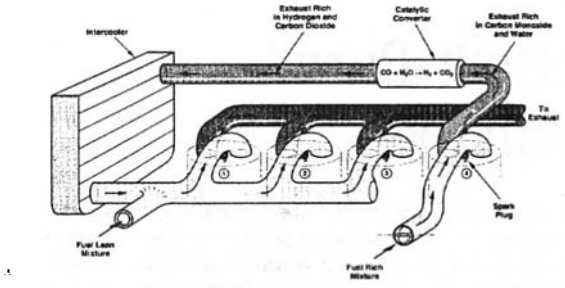

Fig. 1 Hybrid rich-burn/lean-burn engine concept

rate to the combustion chamber [5]. The function determines the fuel mass fraction burned at each crank angle described by four constants. Two of the four constants are the starting angle of combustion and the combustion duration angle. They describe when and how long combustion occurs. The remaining two constants are shape factors that dictate the shape of the mass fraction burned curve.

The start of combustion is determined by spark timing and an induction-time correlation for methane-oxidizer mixtures [6] coupled to an integration scheme based on the work of Livengood and Wu [2]. The combustion duration is taken to be a function of equivalence ratio. This function was derived from experimental rich combustion data obtained in an earlier combustion study at SwRI [7]. The amount of heat release is calculated from the change in mass fraction burned, the heat of combustion of the fuel, and the combustion efficiency. The heat of combustion was assumed to be 44 MJ/kg. The combustion efficiency is also assumed to be a inversely linear function of equivalence ratio, as shown by Heywood [5]. The shape factors used were obtained from typical spark ignition engine mass fraction burned curves [5].

Peak pressure, peak temperature, indicated mean effective pressure, and indicated horsepower were calculated for each set of initial conditions.

The one component that this model could not implicitly account for is apparent flame speed as influenced by in-cylinder gas motion. This model, however, has been calibrated for an engine equipped with a very turbulent piston, and flame speed was indicated by the constants in the Wiebe function.

The Chemical Equilibrium Model. The peak bulk gas temperature and equivalence ratio obtained from the performance model were input into a model that predicted the emissions production of a rich-burn engine. The model used equations developed with the NASA chemical equilibrium code. Results yield exhaust composition dependencies over a variety of engine operating conditions.

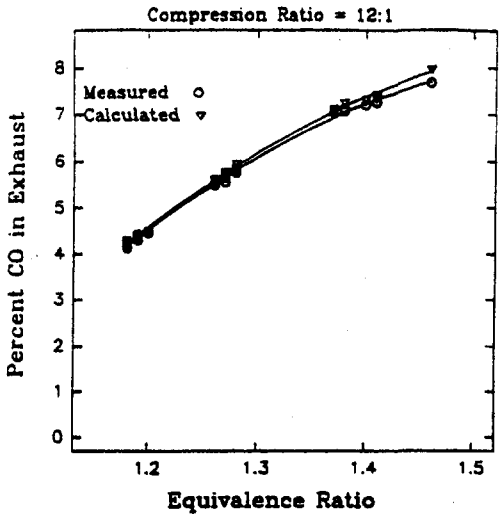

Fig. 2 Comparison of measured CO with equilibrium CO calculated at peak gas pressure and temperature

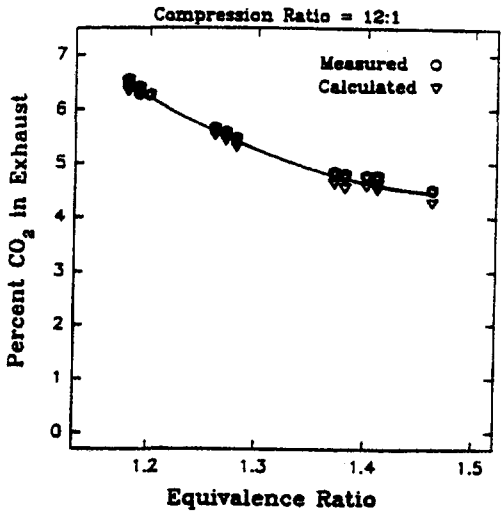

Fig. 3 Comparison of measured CO_2 with equilibrium CO_2 calculated at peak gas pressure and temperature

It was determined that the peak bulk gas temperature could be used in conjunction with the NASA chemical equilibrium code to predict CO_2, CO, H_2O, and H_2 very accurately for a number of different engine operating conditions. This method worked because chemical equilibrium is achieved at the peak bulk gas temperature and essentially freezes at that temperature. Thus, very accurate predictions of the emissions can be obtained by simply knowing peak bulk gas temperature and equivalence ratio.

Figure 2 compares the predicted CO emissions based on the measured peak bulk gas temperature to the measured emissions for the same operating condition as a function of equivalence ratio. Figure 3 compares the predicted CO_2 emissions based on the measured peak bulk gas temperature to the measured emissions for the same operating condition as a function of equivalence ratio. Clearly, these figures exhibit very good agreement between the measured exhaust constituents and the calculated exhaust constituents.

The equations from the NASA equilibrium code were then applied to the results of the combustion model. The equations utilized for predicting the exhaust constituents are as follows:

$$\%\mathrm{CO}_{\mathrm{wet}} = 9.66*10^{-3}*\left(\frac{\Phi^{16.977}}{1+0.222*\Phi^{15}}\right)\times\mathrm{EXP}\left(\frac{376}{T}-\frac{1082210}{T^2}\right)$$

$$\%\mathrm{CO}_{2_{\mathrm{wet}}} = 6.58*10^{-2}*\Phi^{-1.93}*\mathrm{EXP}\left(\frac{531.9}{T}-\frac{214503}{T^2}\right)$$

$$\%\mathrm{H}_{2_{\mathrm{wet}}} = 1.695*10^{-2}*\left(\frac{\Phi^{2.88}}{1+4.99*\Phi^{-13.26}}\right)\times\mathrm{EXP}\left(\frac{862.7}{T}-\frac{89366}{T^2}\right)$$

$$\%\mathrm{H_2O}_{\mathrm{wet}} = 1.89*10^{-1}*\Phi^{-0.39}*\mathrm{EXP}\left(\frac{337}{T}-\frac{492055}{T^2}\right) \quad (2)$$

Table 1 Comparison of model predictions to actual engine data

Parameter	ϕ=1.2		ϕ=1.4	
	Measured	Modeled	Measured	Modeled
Peak Cylinder Pressure (psia)	699	702	583	583
IMEP (psi)	124.6	124.7	116.5	118.0
Peak In-Cylinder Gas Temp. (deg R)	3888*	3929	3787*	3757
Carbon Monoxide (%)	4.47	4.50	7.08	7.25
Carbon Dioxide (%)	6.25	6.24	4.80	4.65

* Calculated from Cylinder Pressure Data

where: Φ = equivalence ratio
T = peak bulk gas temperature (K) from model

It should also be noted that wet and dry exhaust constituents are related by the following equation:

$$\%[N]_{\text{dry}} = \frac{\%[N]_{\text{wet}}}{\left(1 - \frac{\%H_2O}{100}\right)}$$

where: N = exhaust gas species.

Computer Model Results. In order to validate the model, results from the model were compared to actual engine data. Table 1 depicts the results of the Labeco engine operating at an equivalence ratio of 1.2, an engine speed of 1200 rpm, and a spark timing of 14 deg before top-dead-center and a second condition with the engine operating at an equivalence ratio of 1.4, an engine speed of 1800 rpm, and a spark timing of 34 deg before TDC.

From this table it can be seen that the model matches the measured data very closely.

Rich Combustion Experiments

Test Engine. The engine chosen for this investigation was a Labeco CLR (Cooperative Lubrication Research) engine. The stock diesel head was modified to accept a centrally located spark plug and a flush-mounted Kistler model 6121 pressure transducer. The Labeco engine can accommodate either diesel (flat-fire deck) cylinder heads or spark-ignited (bowl-in-head) cylinder heads.

Equivalence Ratio Determination. The biggest problem with testing under rich conditions is predicting the equivalence ratio based on emissions measurements since H_2O is not a measured emission. Under normal circumstances, a constant, known as the water–gas equilibrium constant, is fixed at 3.5. This water–gas equilibrium constant relates the amount of water and hydrogen in the exhaust to known emission measurements of carbon monoxide and carbon dioxide in the following manner [8]:

$$\text{Water gas constant, } K = \frac{x_{CO}x_{H_2O}}{x_{CO_2}x_{H_2}}$$

When operating with extremely rich fuel–air mixtures, this value cannot be assumed to be constant.

It has been determined that for rich combustion the water–gas constant, K_{eq}, freezes at the peak in-cylinder bulk gas temperature. Therefore, the water–gas constant can be determined using a chemical equilibrium code and calculating the peak in-cylinder bulk gas temperature from cylinder pressure data. The water–gas constant, as a function of bulk gas temperature for methane combustion, is given by the following equation:

$$K_{eq} = \exp\left(2.74531 - \frac{1.7805 \times 10^3}{T_{\text{bulk}}} - \frac{1.369 \times 10^6}{T_{\text{bulk}}^2}\right)$$

where: T_{bulk} is the peak bulk gas temperature (k)

Once the water–gas constant, K_{eq}, has been calculated, the equivalence ratio can be determined from the exhaust emissions using the following equations [5]:

$$\phi = \frac{2n_{O_2}}{(n_p)(x_{H_2O}) + n_p(1 - x_{H_2O})(x_{CO} + 2x_{CO_2} + 2x_{O_2} + x_{NO} + 2x_{NO_2}) - r}$$

where:

$$n_p = \frac{n}{x_{CH_{min}} + (1 - x_{H_2O})(x_{CO} + x_{CO_2})}$$

$$x_{H_2O} = \frac{mx_{CO} + x_{CO_2}}{2n[1 + x_{CO}/(K_{eq}x_{CO_2}) + (m/2n)(x_{CO} + x_{CO_2})}$$

for the molecule:

$$C_nH_mO_r$$

Using these equations, the equivalence ratio can then be accurately determined.

Piston Design Strategy. A 12:1 piston was designed to have maximum squish velocities in order to increase air motion/turbulence. The resulting increase in air motion/turbulence would significantly shorten the combustion duration and ultimately increase the thermal efficiency of the engine. Upon completion of testing, it was found that not only was the engine able to run slightly richer, with significantly higher thermal efficiencies, but also at considerably lower NO_x emissions with the 12:1 compression ratio piston compared to a 10:1 compression ratio piston.

Rich Combustion Test Results. Figure 4 depicts NO_x emissions as a function of spark timing for the two pistons at three different equivalence ratios: 1.2, 1.3, and 1.4.

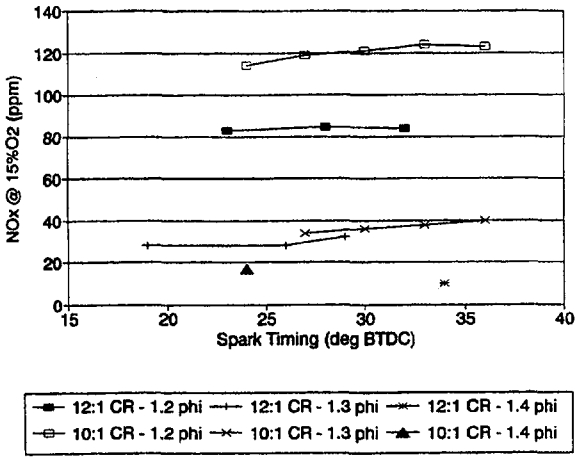

Fig. 4 NO_x at 15 percent oxygen versus spark timing

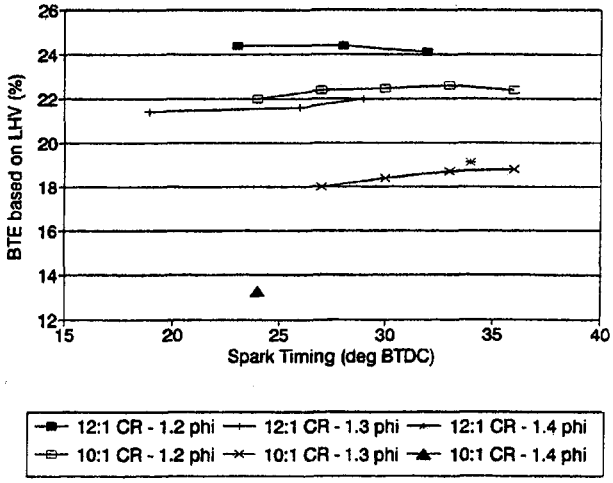

Fig. 5 BTE versus spark timing

Figure 5 shows that in all cases, the 12:1 compression ratio piston had considerably higher thermal efficiency than the 10:1 compression ratio piston. It is important to note that in almost all engines, a tradeoff exists between thermal efficiency and NO_x emissions. However, it was found that the 12:1 high-squish-velocity piston was not only able to achieve lower NO_x emissions but also at higher thermal efficiencies, and even though a tradeoff still exists, it is a better tradeoff than with the 10:1 compression ratio piston, as can be seen in Fig. 6.

These improvements in thermal efficiency and reductions in NO_x levels can be directly attributed to both the higher compression ratio and increased turbulence of the 12:1 piston. This was accomplished through increased air turbulence, which decreased the combustion duration.

It was anticipated that NO_x emissions would be drastically diminished as the equivalence ratio was enriched. The reason for this is twofold. First, combustion temperatures are greatly reduced as equivalence ratios depart from stoichiometry. Second, the amount of oxygen available to convert to NO_x is reduced as the equivalence ratio is increased. Figure 7 depicts NO_x measured in the exhaust prior to entering the catalyst. From this figure it can be seen that NO_x is significantly reduced as the fuel–air mixture is enriched (increasing equivalence ratio). However, spark timing had virtually no effect on NO_x production in the rich region.

Also of interest is the amount of hydrogen and CO produced as the equivalence ratio is varied. Figure 8 depicts CO as a function of rich equivalence ratios and spark timing while Fig. 9 depicts hydrogen production as a function of equivalence ratio and spark timing. It can be seen that both CO and hydrogen increase almost linearly with equivalence ratio. As anticipated, spark timing had no effect on CO or hydrogen.

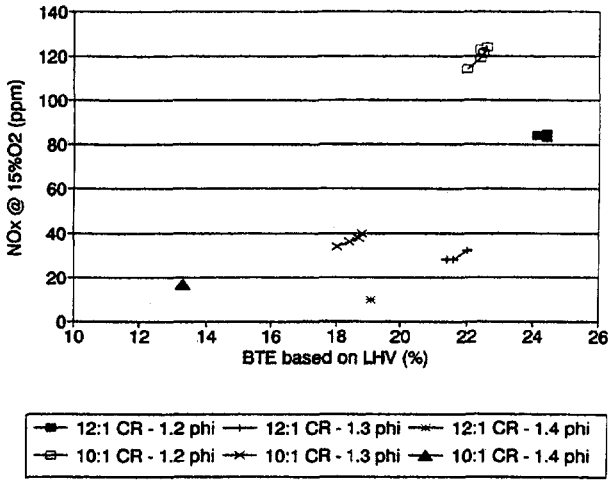

Fig. 6 NO_x at 15 percent oxygen versus BTE tradeoff

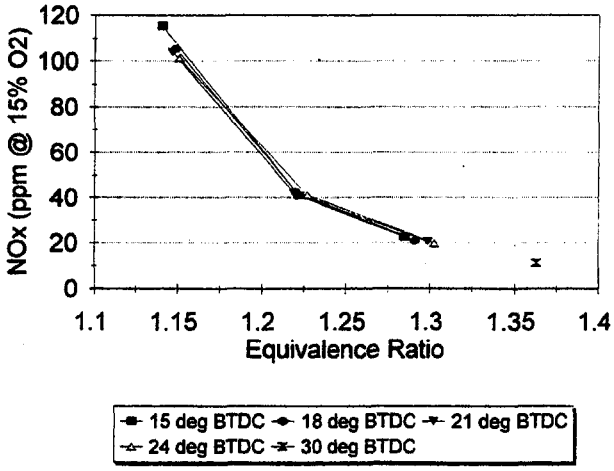

Fig. 7 Effect of equivalence ratio and spark timing on NO_x emissions

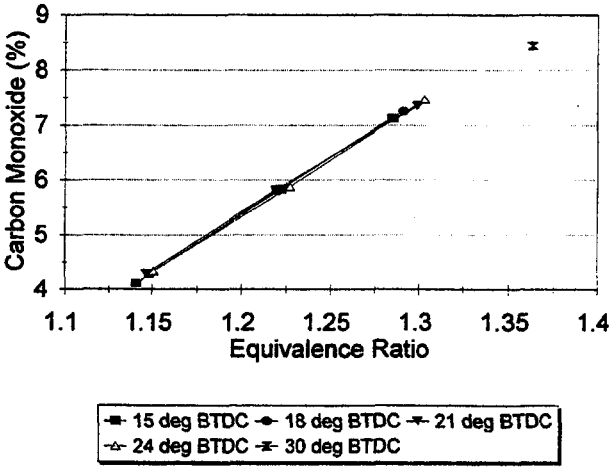

Fig. 8 Effect of equivalence ratio and spark timing on CO emissions

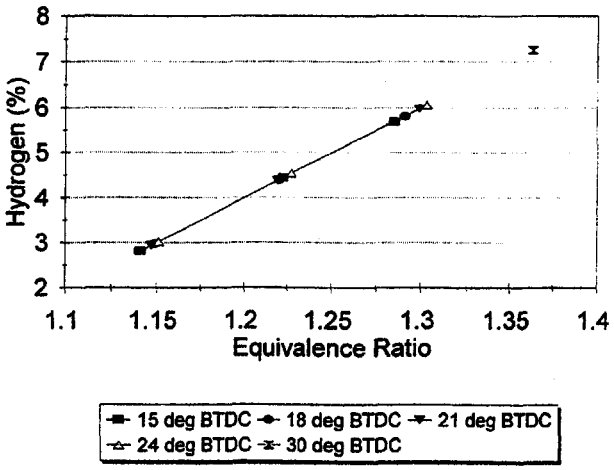

Fig. 9 Effect of equivalence ratio and spark timing on hydrogen emissions

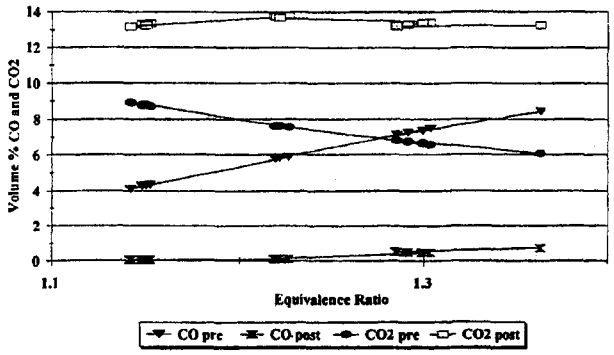

Fig. 10 Pre- and post-catalyst emissions for CO and CO_2 @ 1200 rpm

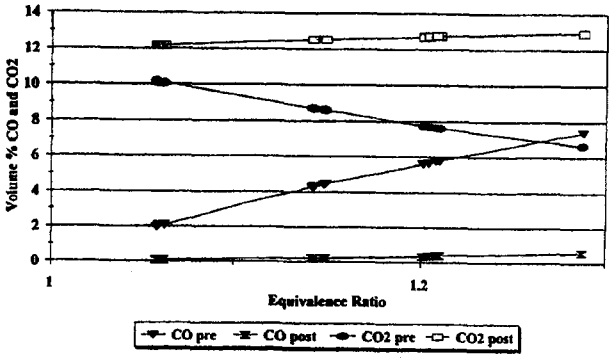

Fig. 12 Pre- and postcatalyst emissions for CO and CO_2 @ 1500 rpm

As established earlier, the products of rich combustion are CO, CO_2, H_2O, and H_2. While CO can be considered a fuel, it does not have the desired characteristics (flammability limits, flame speed, etc.) that hydrogen has. It is possible, however, to reduce the amount of CO in the exhaust catalytically while proportionally increasing the amount of hydrogen. This is accomplished through the water-shift reaction. This reaction is governed by the following equation:

$$CO + H_2O \rightleftharpoons H_2 + CO_2$$

Note that this is a balanced equation; thus, one mole of CO will yield one mole of hydrogen and the reaction is slightly exothermic in the direction shown.

In order to test the practicality of CO to H_2 conversion, a water-shift catalyst was placed in the exhaust system. The engine was then operated at various equivalence ratios and spark timings for 1200 and 1500 rpm. Emissions measurements were taken both upstream and downstream of the catalyst.

The engine was first run at 1200 rpm. Exhaust measurements were taken first upstream and then downstream while the engine remained at a fixed set-point. Figure 10 shows the effect of the catalyst on CO and CO_2. CO was nearly completely eliminated as it is converted to CO_2. Figure 11 shows the effect of the catalyst on hydrogen. It can be seen from these figures the catalyst had a significant effect on converting CO and H_2O to CO_2 and H_2.

The engine was then operated at 1500 rpm. Figure 12 depicts the effect of the catalyst on CO and CO_2, while Fig. 13 depicts the effect on hydrogen. Here again, it can be seen that the catalyst had a tremendous effect on converting CO and H_2O to CO_2 and H_2. In addition, looking at the effects of the catalyst, on NO_x (Fig. 14), note the NO_x was nearly eliminated. It is believed that the increase in engine speed increased the exhaust temperature ahead of the catalyst. This increased temperature caused the catalyst to act like a reduction catalyst, which caused the following reaction to occur:

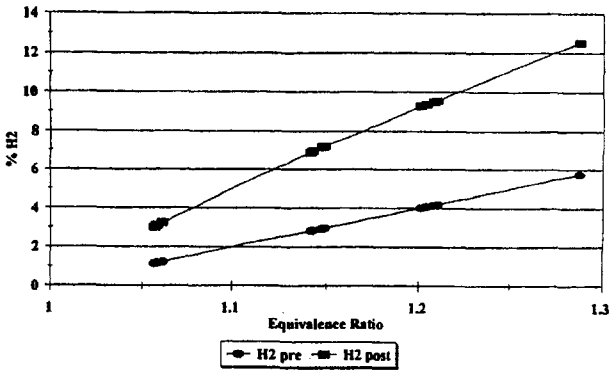

Fig. 13 Pre- and postcatalyst emissions for H_2 @ 1500 rpm

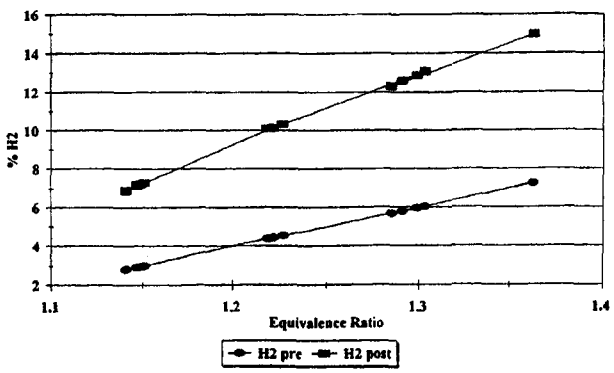

Fig. 11 Pre- and post-H_2 catalyst emissions for H_2 @ 1200 rpm

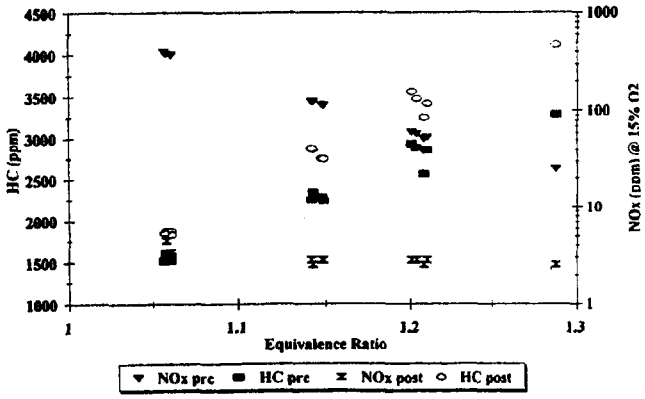

Fig. 14 Pre- and postcatalyst emissions for HC and NO_x at 1500 rpm

$$2CO + 2NO \rightarrow 2CO_2 + N_2$$

Thus, NO_x was virtually eliminated. Temperature data taken on either side of the catalyst indicated that this reaction was plausible.

Lean Combustion Testing

The engine was set up to operate on lean mixtures of natural gas and air augmented with simulated rich exhaust. Several blends of bottled gases were used to simulate postcatalyst rich exhaust compositions corresponding to equivalence ratios of 1.1, 1.2, 1.3, and 1.4.

These blend compositions are identical to those determined during the rich combustion testing and are shown in Table 2.

The engine was equipped with the high-turbulence, 12:1 compression ratio piston originally designed for the rich combustion experiments.

Table 2 Blend compositions for rich combustion testing

Constituent (by vol.)	Blend			
	1.1	1.2	1.3	1.4
H_2 (%)	7.3	10.1	13.0	15.0
CO (%)	0.00	0.10	0.50	0.75
CO_2 (%)	13.3	13.8	13.4	13.2
CH_4 (ppm)	3000	3500	4000	5090
Nitrogen	Bal.	Bal.	Bal.	Bal.

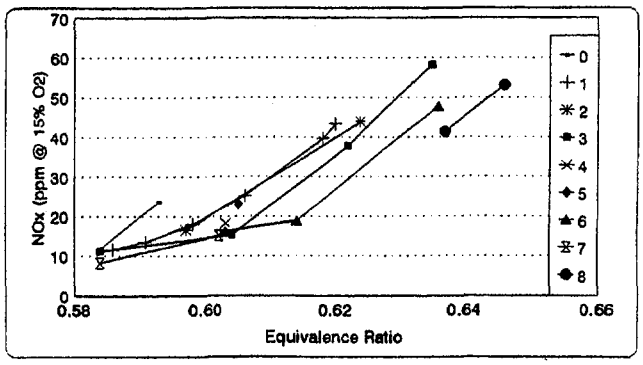

Fig. 15 Rich-burn/lean-burn lean-burn test—NO_x results

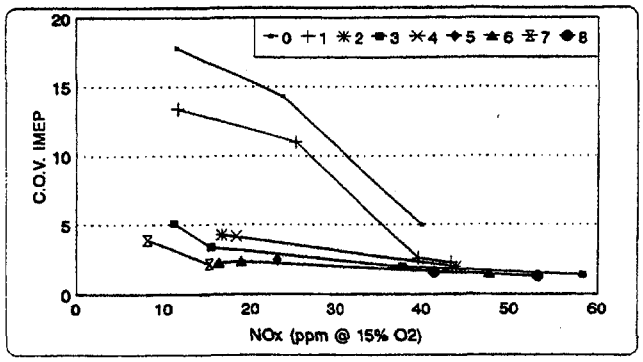

Fig. 16 Rich-burn/lean-burn lean-burn test—combustion results

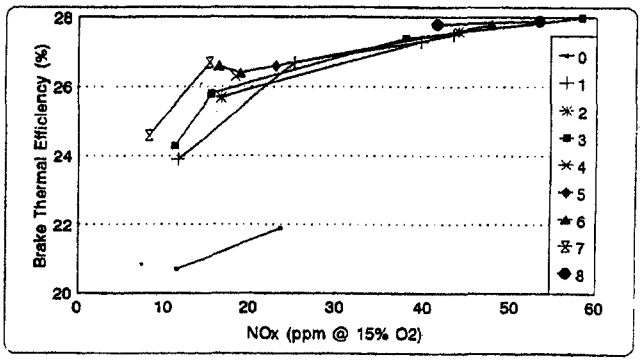

Fig. 17 Rich-burn/lean-burn lean-burn test—efficiency results

Of the four simulated rich combustion exhaust blends, the blend that corresponds to exhaust from an equivalence ratio of 1.4 showed the most promising results. With that blend, corrected NO_x levels were down in the 8 ppm range while maintaining a COV of IMEP less than 4 percent.

Figure 15 depicts corrected NO_x as a function of the overall equivalence ratio. The natural gas equivalence ratio differs from the overall equivalence ratio in that the overall equivalence ratio accounts for the hydrogen, CO, and hydrocarbons in the supplemented rich exhaust. The numbers within the graph denote the percentage of exhaust mass flow to total mass flow. Hence, a higher number denotes higher substitution of rich exhaust. From this figure it can be seen that very low NO_x level (less than 10 ppm) can be achieved with high substitutions of rich exhaust. This is because the hydrogen extends the lean limit of combustion and at the same time increases the amount of inerts, thus lowering the combustion temperatures thereby lowering NO_x production.

While lowering NO_x is the ultimate goal, other aspects cannot be overlooked. Included in these other aspects are efficiency, hydrocarbons, and stable combustion. Good consistent combustion yields good efficiency and minimized hydrocarbons. The coefficient of variation (COV) of indicated mean effective pressure (IMEP) is often used as a measure of combustion stability. As an industry standard, if a measured data point has a COV of IMEP less than 5 percent than the stability is often considered good. The lower the COV the better the consistency of the combustion. Figure 16 depicts the COV of IMEP as a function of corrected NO_x. The numbers within the graph denote the percentage of exhaust mass flow to total mass flow. Hence, a higher number denotes higher substitution of rich exhaust. From this figure it can be seen that very low NO_x levels are achievable with very low COV's of IMEP. It can also be seen that, in general, the higher the substitution rate, the lower the COV for a given NO_x level.

Figure 17 depicts brake thermal efficiency as a function of NO_x. It should be noted that the LABECO engine has very poor efficiency numbers due to high friction and parasitic loads; therefore the data should be compared based on relative magnitude of changes as opposed to absolute values. From this figure it can be seen that the efficiency does tend to fall off as the NO_x levels are reduced. However, the addition of rich exhaust does increase the efficiency. It should also be noted that these efficiencies are based on total flow and therefore include the energy associated with simulated rich exhaust.

Conclusions

In conclusion it has been shown that very low NO_x emissions can be achieved by operating extremely rich. Additionally, rich combustion of natural gas and air at equivalence ratios between 1.35 and 1.40 not only produces low NO_x emissions, but also provides ample amounts of hydrogen to extend the lean limit of combustion when supplemented to lean mixtures of natural gas and air. By extending the lean limit of combustion, ultralow emissions of NO_x are achievable. The results of this early research indicate that ultralow NO_x emissions are achievable on a multicylinder engine where one cylinder operates rich and the remaining cylinders are operated lean and supplemented with the hydrogen enriched exhaust of the rich cylinder.

Acknowledgments

The authors wish to thank Southern California Gas Company and South Coast Air Quality Management District for their continued support of this project.

References

1 MacDonald, J. S., "Evaluation of the Hydrogen Supplemented Fuel Concept With an Experimental Multicylinder Engine," SAE Paper No. 760101, 1976.

2 Taylor, C. F., *The Internal Combustion Engine in Theory and Practice,* Vol. 1, 2nd ed., MIT Press, Cambridge, MA, 1986.
3 Ferguson, C. R., *Internal Combustion Engines,* Wiley, New York, 1986.
4 Fox, J. W., et al., "A Model for Predicting Residual Gas Fraction in Spark-Ignition Engines," SAE Paper No. 931025, 1993.
5 Heywood, J. B., *Fundamentals of Internal Combustion Engines,* McGraw-Hill, New York, 1988.
6 Seery, D. J., and Bowman, C. T., "An Experimental and Analytical Study of Methane Oxidation Behind Shock Waves," *Combustion & Flame,* Vol. 14, 1970, pp. 37–48.
7 Meyers, D. P., and Meyer, R. C., "Open Chamber Combustion Study," GRI-93/0133, GETA 92-03, Apr. 1994.
8 Meyers, D. P., and Naegeli, D., "Characterization of Hydrogen Emissions From a Rich-Burn Natural Gas Engine," Southwest Research Institute Internal Research Project 03-0750-126, 1991.

Measurements of Droplet Velocity and Size Downstream of the Moving Valves of a Four-Valve Engine With Manifold Injection, Operated Under Isothermal Steady Suction Conditions

M. Posylkin

A. M. K. P. Taylor

J. H. Whitelaw

Imperial College of Science, Technology, and Medicine, London, United Kingdom

K. Ishii

M. Miyano

Honda R & D Ltd., Saitama, Japan

The four-valve head of a VTEC engine was mounted on an open cylinder and the valves and fuel injection system operated as in the engine with a rotational speed of 1200 rpm. Local measurements of droplet characteristics were obtained with a phase-Doppler velocimeter and iso-octane injected over 5 ms intervals, corresponding to 36 crank angle degrees, with manifold depression of 20 mbar. The results show that most of the fuel droplets were located close to the liner and on the side of the cylinder adjacent to the exhaust valves. In the plane of the measurement, 10 mm below TDC, the liquid flux diminished as the initiation of injection was advanced before opening of the inlet valves. With injection with the inlet valves closed, there were two waves of droplets, one from each of the two valves and separated by 60 deg CA and both with the Sauter mean diameter of about 120 μm. With injection with the inlet valves open, most of the droplets emerged from the main inlet valve and with Sauter mean diameters of about 50 μm, smaller than those of the unconfined spray.

Introduction

The use of manifold injection is now widespread and can lead to improved mixture control and fuel economy. Control of the distribution of fuel is also important in the reduction of emissions that may arise in the form of unburned hydrocarbons, due to local quenching on the liner, or as a consequence of production of oxides of nitrogen due to long residence times at temperatures close to the adiabatic flame temperatures of the mixture. Recent contributions to the implementation of manifold injection have been reported by Bandel et al. (1989), Horie et al. (1992), Kiyota et al. (1992), and Spiegel and Spicher (1992) and suggestions for the control of the distribution of fuel concentration by injection timing were made by Quader (1982). Also, Arcoumanis et al. (1994) have shown that a rich mixture in the vicinity of the spark assists the formation of the flame kernel and its subsequent propagation in mixtures with air-to-fuel ratios higher than stoichiometric.

The distribution of liquid flux and the trajectories of the corresponding fuel droplets provide the basis for subsequent stratification of the fuel. Measurements within engine cylinders have been reported, for example, by Posylkin et al. (1994a) and Ishii et al. (1995). These papers have shown that injection with the valve closed allowed the liquid fuel to remain in the port with effects of evaporation that depended on the residence time, with remaining fuel to be swept from the liquid film on the surface of the valve by the air flow, but with comparatively low velocities since the interface occurred at the intersection of the liquid and air boundary layers. A simpler approach, albeit with limitations, is to place the cylinder head on an open cylinder, to operate the valves and to provide suction so that air is drawn through the valves and to inject fuel in the same manner as in the engine. The application of this approach is described here and is more realistic than that of the investigations of Kawazoe et al. (1991) and Posylkin et al. (1994b) with stationary and open valves.

The purpose of the present experiment was to determine the distribution, size, and velocity characteristics of fuel droplets as they enter the cylinder of a VTEC engine and as a function of injection timing. The experimental facility is described in the following section, together with the instrumentation, and the results are presented and discussed in the third section with summary conclusions presented in the fourth.

Experimental Arrangement

A photograph of the experimental facility is shown in Fig. 1, together with an indication of the arrangement of valves and spark plug and the definition of positive and negative velocity components; the variations of the valve lifts are also shown. The cylinder head, inlet manifold, fuel injector, and throttle valve are similar to those described by Horie et al. (1992) and were arranged on a 75 mm internal diameter perspex cylinder coupled to a suction fan. The valves were activated as in the engine through a belt-driven transmission, with ratio of two, by a variable speed electric DC motor (GE 1.5 kW). The air was drawn through the inlet valves and the exhaust port was blocked. The fuel injector was timed by a shaft encoder on the motor axis and a magnetic pickup on the camshaft with the signals processed by a computer-controlled timer card (Analogic, model CRTM-5) and subsequently amplified by a custom-built

Contributed by the Internal Combustion Engine Division and presented at the Internal Combustion Engine Division 1995 Spring Technical Conference, Marietta, Ohio, April 23–26, 1995. Manuscript received by the Internal Combustion Engine Division February 1995. Associate Technical Editor: W. K. Cheng. Paper No. 95-ICE-10.

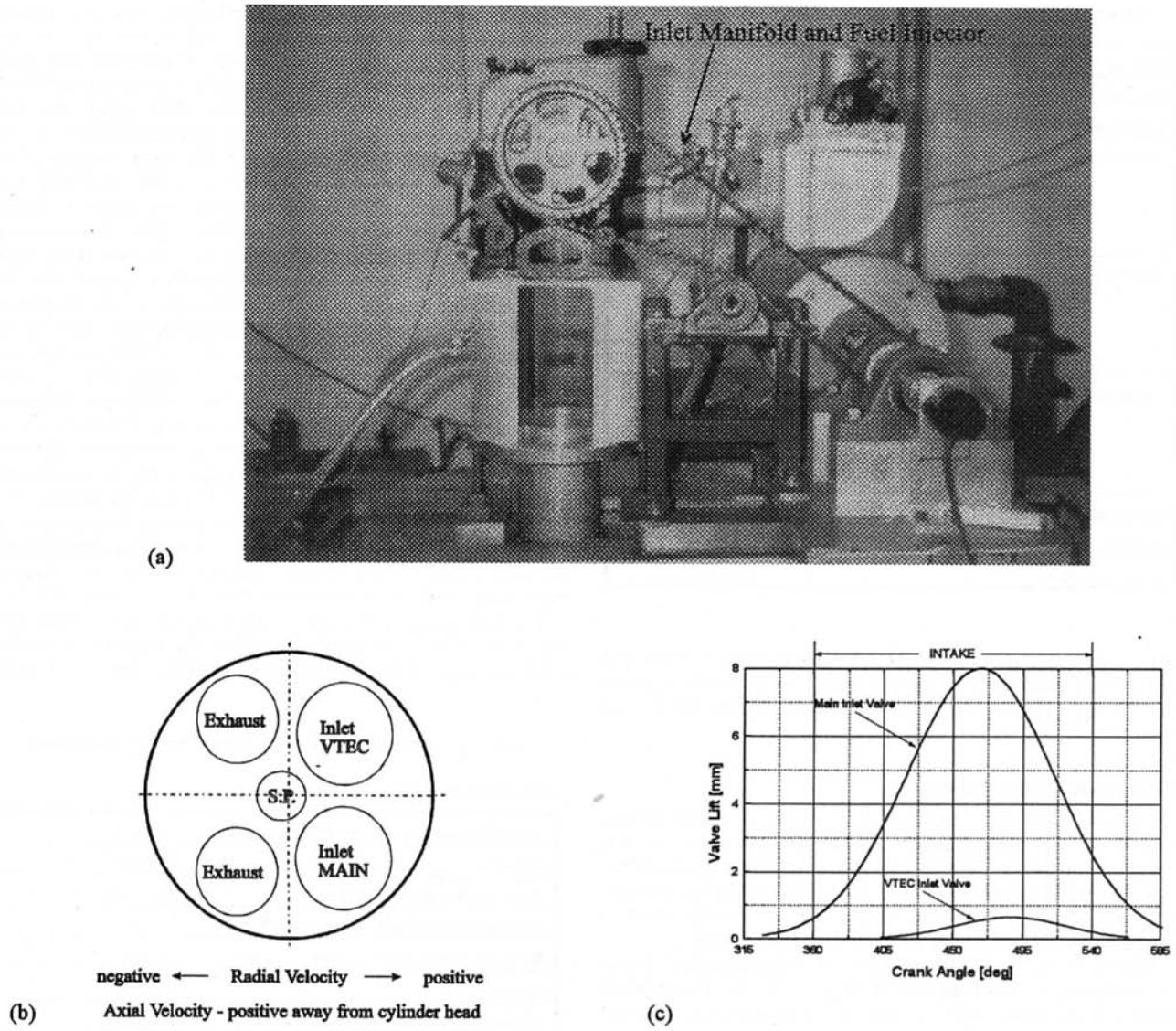

Fig. 1 (*A*) Photograph of the experimental arrangement; (*B*) cross section in plane 10 mm below the cylinder head together with the orientation of the measurements with respect to the cylinder liner and the intake and exhaust valves; and (*C*) inlet valve timing diagram

injector driver module. The fuel was iso-octane (GPR™, type 2,2,4-trimethylpentane) and was chosen to avoid fouling of the transparent perspex cylinder liner. Table 1 records the more important characteristics of the cylinder head and valve timing.

The phase-Doppler instrument was similar to that described by Hardalupas et al. (1989) and had the characteristics of Table 2. The signals from the shaft encoder provided information of the crank angle to the same computer that received signals from the phase-Doppler velocimeter, so that all measurements of droplet velocity and diameter were associated with a crank angle measured from firing top-dead-center. Thus records of droplet velocity and diameter were recorded as a function of crank angle and time, and were ensembled in crank-angle intervals of 0.5 deg.

Measurements of velocity and size were based, wherever possible, on at least 1000 samples, resulting in statistical uncertainties of less than ±5 percent in the mean, ±15 percent in the rms of the velocity signal, and ±5 percent in the cumulative size distribution based on the number of droplets (Tate, 1982). The liquid flux can be inferred, albeit with inaccuracy, from the data rates and droplet diameters. The uncertainty of the timing circuit to assign a crank angle value to each datum was less than 0.51 deg based on the resolution of the shaft encoder and the internal clock frequency of the phase-Doppler counter.

The measurements were made at a crank-shaft equivalent speed of 1200 rpm and manifold depression of −20 mbar gage and in the plane 10 mm below the TDC. The air flow rate was set at 1.04×10^{-3} m^3/s, which corresponded to that of a single-cylinder Honda VTEC engine of Ishii et al. (1995) operating with 30 percent volumetric efficiency and similar speed. Measurements at a small number of locations were also obtained within the pent-roof, at 4 mm above the TDC, through the windows positioned in the cylinder head and shown in the photograph of Fig. 1. The fuel was injected every fourth induction cycle over 36 deg CA, that is, 5 ms, and with a rate of 15 mm^3 per injection, to provide stoichiometric air-to-fuel ratio. The skip injection allowed more convenient dilution of the charge in the exhaust ducting and examination of the time required for stripping of the liquid film on the surfaces of inlet ports. The timing of the start of injection, Θ_{inj}, was at 180, 360, and 420 deg CA after firing TDC and it can be seen from Table 1 that the inlet valves were closed at 180 deg, opening at 360 deg, and fully open at 420 deg. The VTEC valve opened about 60 deg CA after the main valve and closed 40 deg before it. It

Table 1 Characteristics of the cylinder head and valve timing

Bore (mm)	75
Inlet valves diameter (mm)	27.5
Exhaust valves diameter (mm)	23.5
Main inlet valve timing @ 1mm:	
opening	370°
closing	565°
max. lift (mm)	8.0
VTEC inlet valve timing @ 0.21mm:	
opening	430°
closing	548°
max. lift (mm)	0.65
Exhaust valves timing @ 1mm:	
opening	160°
closing	390°
max. lift (mm)	6.5
Crank-shaft equivalent speed	1200 RPM
Injection timing	Variable
Injection duration	36° CA (5ms)

should be noted that the injector has been characterized with injection into atmospheric air and with a Sauter mean diameter of 130 μm, measured as an average across a diameter 60 mm from the nozzle.

Results and Discussion

Measurements were obtained at 46 locations, evenly spaced across the measurement plane, and the results are presented as contour plots of the ensemble averages of Sauter mean diameters, data rate, and axial and radial velocities of droplets between 360 and 720 deg CA. Where necessary, the scatter plots of diameters, axial and radial velocities are also shown.

Figure 2 presents contour plots of cycle-averaged Sauter mean diameters and data rate of droplets in the measurement plane for the three injection timings. The data rate contours show that most of the droplets passed through a small region close to the cylinder liner on the side of the exhaust valves, with the maxima close to the diameter between the exhaust valves for Θ_{inj} = 180 and 360 deg CA and opposite the main inlet valve for Θ_{inj} = 420 deg CA. The number of droplets was smallest with injection with the inlet valves closed, and increased from 0.3 at 180 deg to 8 at 360 deg and 40 at 420 deg CA. The Sauter mean diameter at the locations of the maxima in data rate decreased from about 120 μm at 180 deg to 60 μm at 360 deg and 50 μm at 420 deg CA and these results suggest that the liquid flux passing through the measurement plane increased by factors of approximately 3 and 10, relative to that with start of injection at 180 deg. This confirms that the amount of liquid striking and remaining on solid surfaces upstream of the plane of the measurement increased with earlier injection. The ensemble-averaged axial and radial velocities, not presented here, ranged from +15 m/s to −5 m/s. Large positive radial velocities close to the liner between exhaust and VTEC valves were measured with Θ_{inj} = 420 deg and suggest that some droplets with Sauter mean diameter of around 30 μm acquired the swirling motion of the air flow, with a ratio of about 2.5 for this particular geometry (Horie et al., 1992).

Figure 3 presents diameters, axial and radial velocities of droplets at a location 10 mm from the liner on the side of exhaust valves, and on a diameter between these valves. With commencement of injection at 180 deg CA, that is with the inlet valves closed, droplets emerged in two waves at about 400 and 460 deg CA and with Sauter mean diameters larger than 80 μm in both. The two waves are associated with the droplets originating from the main and VTEC valves, respectively, and are consistent with the profiles of valves opening. The axial velocities of droplets from the main valve were about half those of the droplets from the VTEC valve, with radial velocities mostly toward the axis of the cylinder. Droplets from the VTEC valve had radial velocities toward the liner because they emerged through the narrow gap between the valve and seat, less than 0.65 mm, and followed this trajectory; they were likely to avoid impingement on the solid surfaces of the pent-roof and cylinder liner. The droplet diameters, in particular those from the VTEC valve, show that small droplets emerged some 10 deg CA before large droplets. This difference in time of appearance is even more evident with injection timings closer to the opening of the VTEC valve, that is 320 and 340 deg CA and not shown here. This result suggests an initial flow of small droplets, which remained in suspension with the air, followed by those removed from films on surfaces by the boundary layers. The corresponding difference between the arrival time of small and large droplets is 2 ms, or 14 deg CA, with the assumption of droplet mean velocities of 12 and 7 m/s, respectively, over the 40 mm distance. The larger number of large droplets associated with the first wave and the main valve is unexpected since the time to form a film is shorter, and may be due to the different trajectories of the flow of air and liquid from the two valves.

The two waves occur only with injection with closed inlet valves because these conditions allow the injector to provide equal amounts of fuel to each port, whereas, with open valves,

Table 2 Characteristics of the phase-Doppler velocimeter

Transmitting Optics

300mW (nominal) Ar^+ laser wavelength	514.5 nm
operated at	150 mW
Beam diameter, at e^{-2} intensity	1.25 mm
Shift frequency (nominal) due to rotation of grating	3-5 MHz
Short-term stability of shift frequency (r.m.s.)	0.3 %
Beam separation	27 mm
Measured half-angle of intersection	1.282°
Calculated dimensions of beam intersection volume at $1/e^2$ intensity	4.68 mm 0.104 mm 0.104 mm
Fringe spacing	11.49 μm
Calculated number of fringes within $1/e^2$ intensity	9
Frequency to velocity conversion factor	0.087 MHz/ms^{-1}

Receiving Optics

Location of collection optics from forward scatter	30°
Focal length of collimating lens in receiving optics module	310 mm
Apertures at collimating lens: dimension of rectangular apertures separation between apertures 1 and 2 separation between apertures 1 and 3	 50 x 10 mm 13.3 mm 26.7 mm
Focal length of imaging lens in receiving optics module	160 mm
Width of spatial filter before the photomultipliers	50 μm
Magnification of receiving optics hence effective length of measuring volume	0.53 187.5 μm
Phase angle-to-diameter conversion factor for channel 1 and 3	0.502 μm/degree

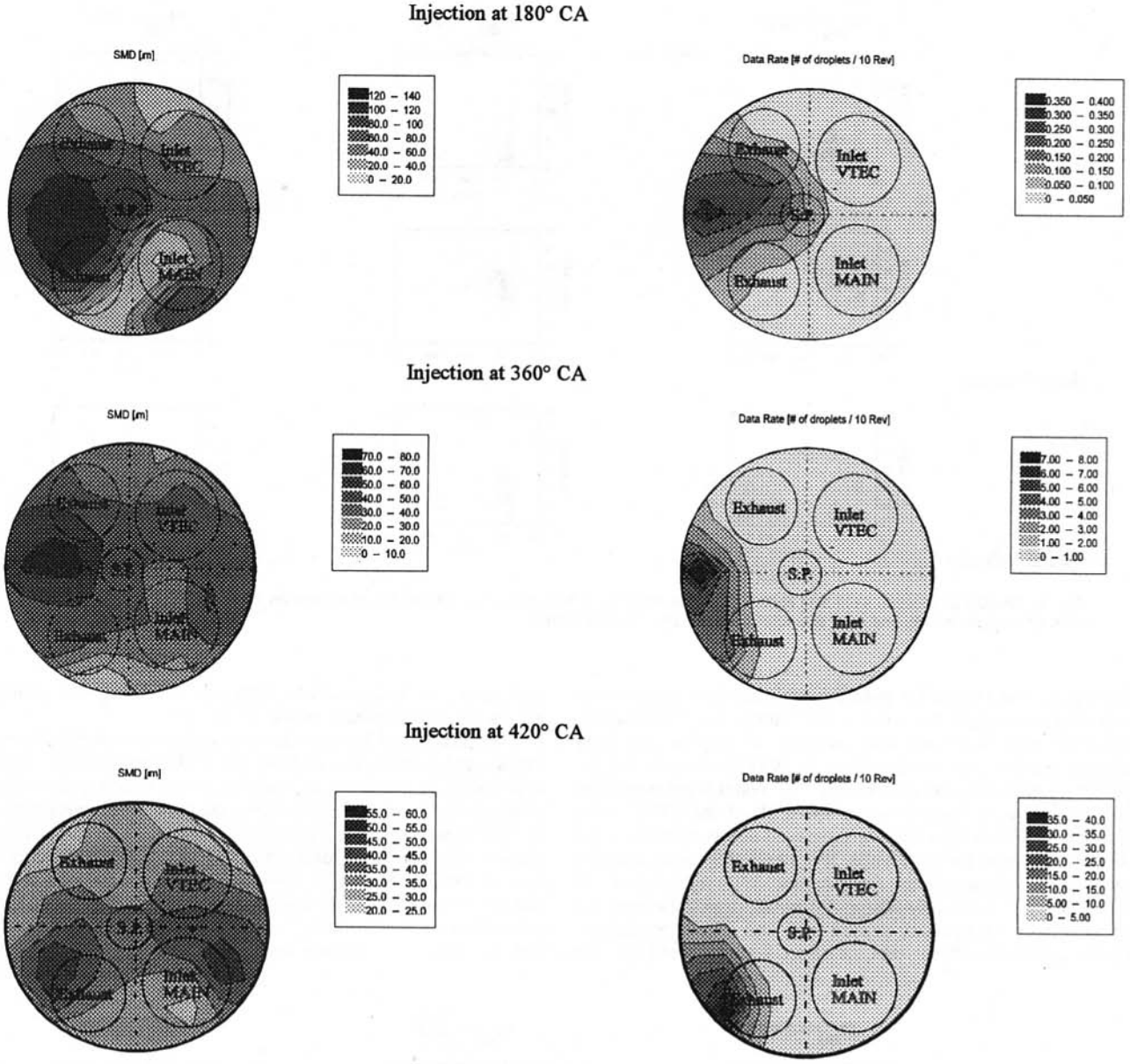

Fig. 2 Cycle-averaged contour plots of Sauter mean diameter and data rates of droplets for three injection timings

the unequal resistance offered by the main and VTEC valves ensured that most of the fuel from the injector entered the port of the main valve. Thus, injection with the main valve opening or open led to a single wave of droplets with a smaller Sauter mean diameter, which was smallest in the latter case at about 40 μm, since the droplets from the injector and with some secondary atomization due to impingement were able to follow the mean flow and pass through the valve gap without formation of liquid films on solid surfaces. The velocities are, as expected, higher with the opening valve so that more droplets were unable to follow the flow, settle on surfaces, and lead to the formation of films and larger, slow moving droplets due to the secondary atomization by stripping. In this case, large droplets emerged early and their size decreased as the valve lift increased so that droplets were able to pass directly to the exit of the valve without formation of films.

The number of droplets with trajectories toward the axis of the cylinder decreased with delay in injection angle to a minimum value of about 3 percent of the total with injection beginning at 420 deg CA. Late injection also caused a decrease in the amount of liquid impinging on solid surfaces and therefore, in the number of small droplets with low axial velocities.

With the VTEC valve disengaged, droplets could enter only through the main inlet valve. Results for this arrangement are shown in Fig. 4 at the same location and injection timings as those of Fig. 3. It was considered possible that the flow from the VTEC valve could have changed the region in which the main flow of air and liquid fuel passed through the measurement plane and this was checked and found not to be the case. With the VTEC valve blocked and injection with the main valve closed, all of the fuel emerged from the main valve and the results of Fig. 4 are similar to those of the first wave of Fig. 3, including the data rates. Estimates of the liquid fluxes of Figs. 3 and 4, at this location, indicate that some droplets emerged from the VTEC valve with injection at 360 deg CA, although they constituted less then 10 percent of the total liquid flux. With injection at 420 deg CA, more than 97 percent of the total liquid flux emerged from the main inlet valve.

The number of droplets that remained in the inlet port and emerged into the cylinder during the subsequent skipped-injec-

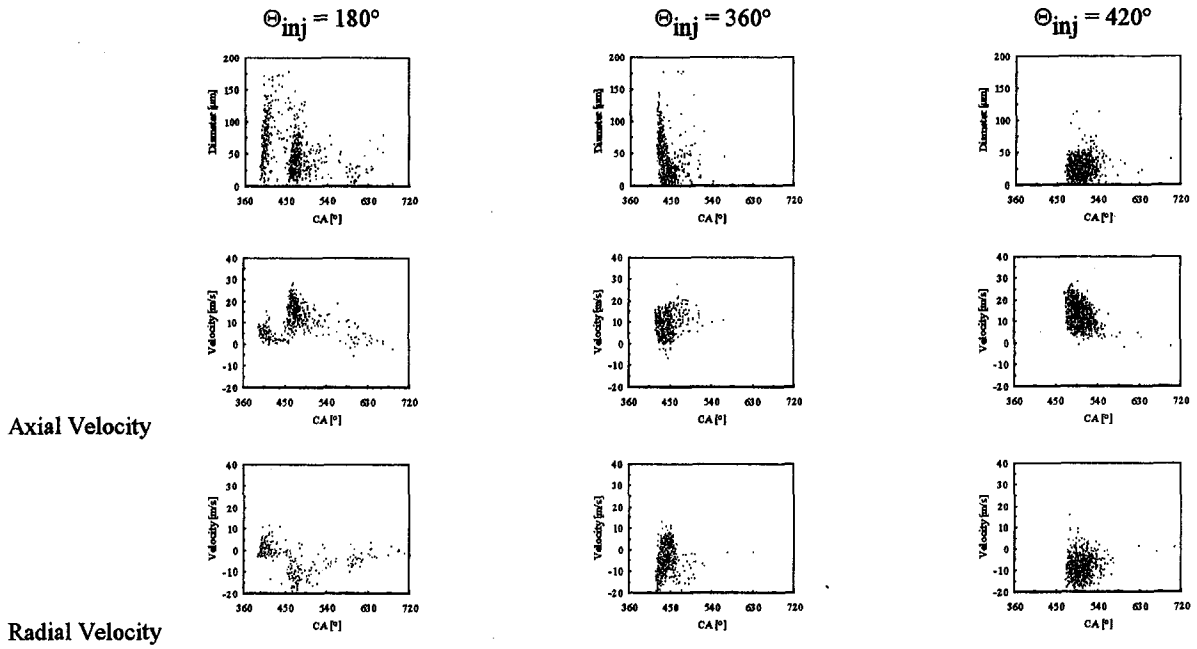

Fig. 3 Droplet diameters, axial and radial velocities with Θ_{inj} = 180, 360, and 420 deg CA at a location 10 mm from the liner on the side of exhaust valves, and on a diameter between the exhaust valves

tion cycles was largest for injection with the inlet valve closed and emerged mainly from the VTEC valve. They represented about 40 percent of the total number of droplets and only slightly less than the number from the VTEC valve during the induction cycle adjacent to injection. This result is not surprising since the short opening time and small lift of the VTEC valve resulted in low air flow rates with limited ability to remove the fuel deposited on the port walls. It is likely, however, that this fuel would evaporate in the firing engine. With injection at 360 and 420 deg CA, the proportion of droplets detected during the skipped-injection cycle decreased to 5 and 3 percent, respectively, and this confirms that the spray was deflected into the main inlet port by the air flow, with only a few droplets impinging on the solid surfaces of the VTEC port.

It should be noted that quantitative comparisons of droplet characteristics and contributions of main and VTEC valves, Figs. 3 and 4, are valid for the particular location where measurements were obtained. However, the relative proportion of a fuel remaining in the VTEC port into the skipped-injection cycle is not expected to change with location. Measurements in the same plane but at a location closer to the VTEC valve have confirmed this and shown that the two-wave structure associated with the closed-valve injection and the relative contributions from the main and VTEC valves with the open-valve injection remained.

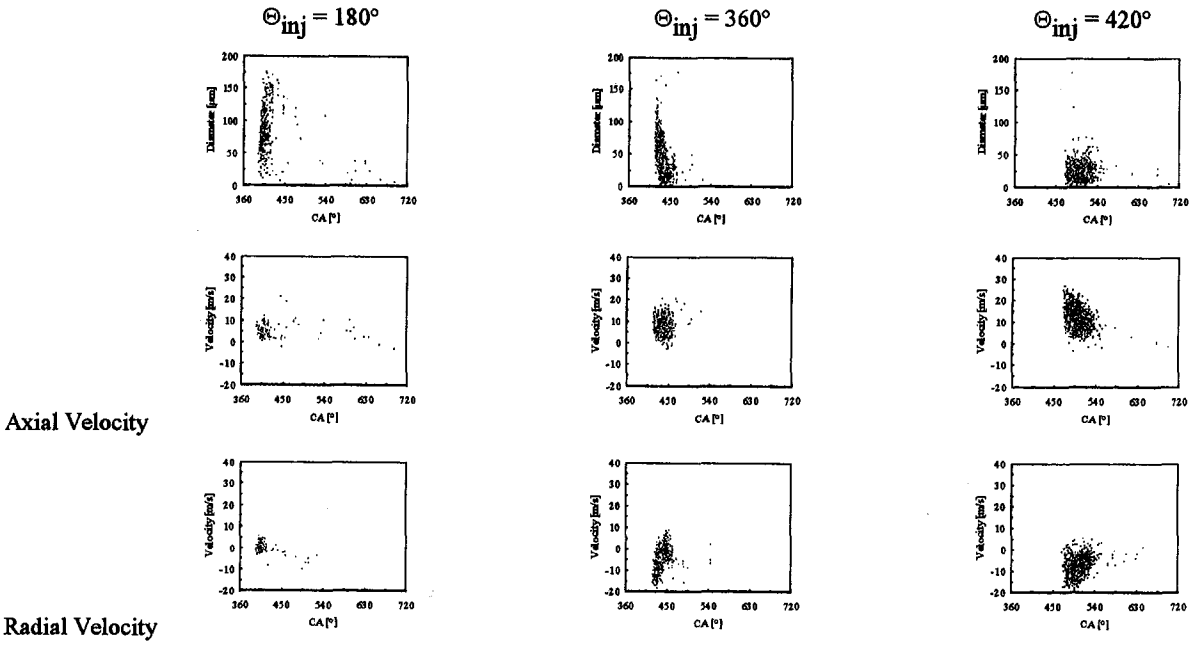

Fig. 4 Droplet diameters, axial and radial velocities with Θ_{inj} = 180, 360, and 420 deg CA at a location 10 mm from the liner on the side of exhaust valves and on a diameter between the exhaust valves; main inlet valve active and VTEC valve disengaged

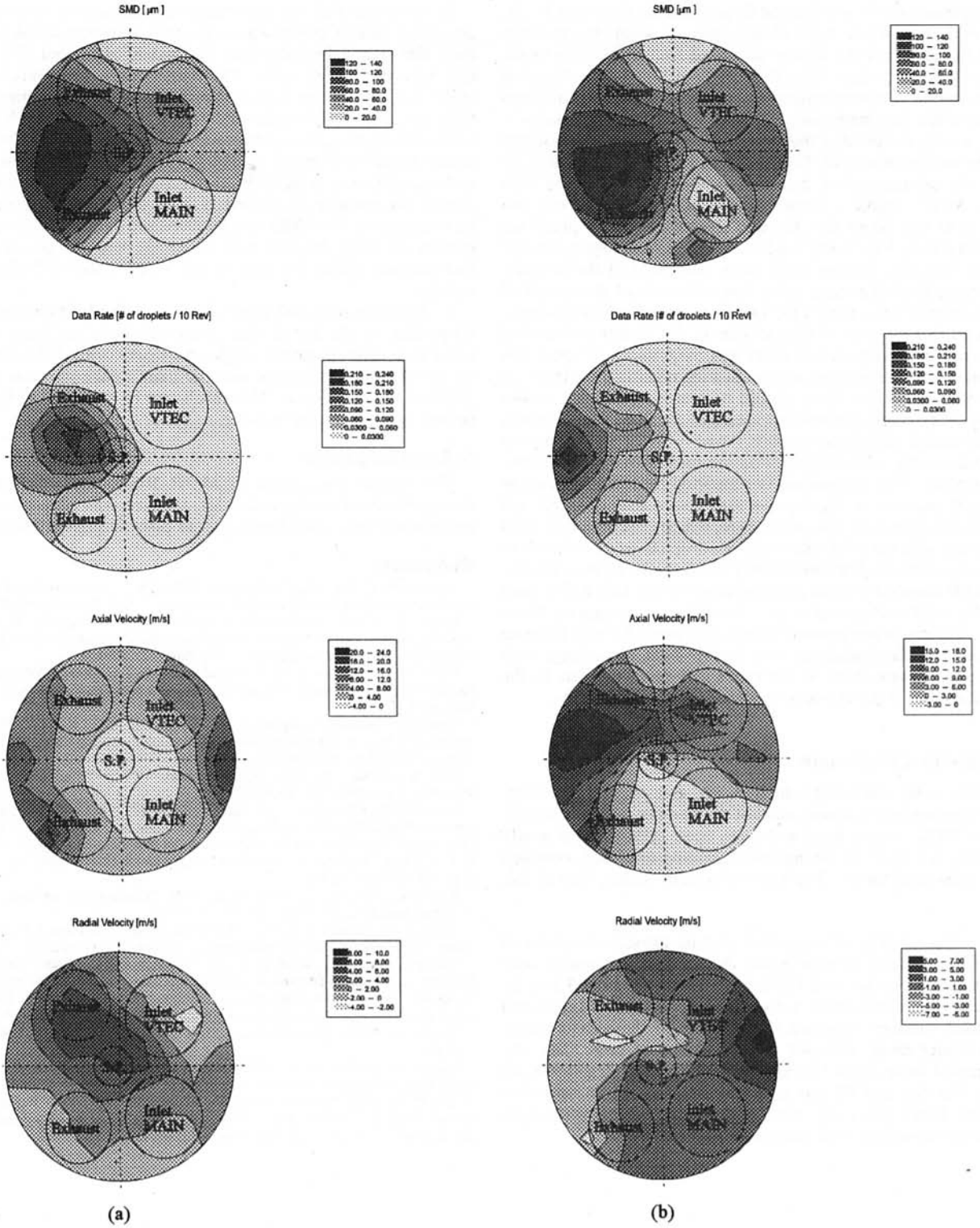

Fig. 5 Contour plots of Sauter mean diameter, data rate, axial and radial velocities of droplets emerging from (*a*) main inlet valve and (*b*) VTEC inlet valve with injection at 180 deg CA. The results represent decomposition of those shown in Fig. 2 for injection with the valves closed.

Due to the time difference between droplets emerging from the main and VTEC valves with injection with the inlet valves closed, it was possible to obtain a decomposition of results of Fig. 2 to provide information on the spatial distribution of characteristics of droplets emerging from the two valves immediately after their opening and this is shown in Fig. 5. The decomposition was made in the crank angle windows of 360 to 430 deg and 431 to 720 deg CA, which correspond to the time intervals over which droplets emerged from the main and VTEC valves, respectively. The SMD of droplets from the two valves were almost similar, typically between 100 and 120 μm at the locations of large data rate, although isolated maximum of up to 140 μm was observed from the VTEC valve. These SMD are similar to those of the free spray. Surveys of the measure-

ment plane have shown that the flows from the main and VTEC valves did not follow identical trajectories as would be expected, with the center of the former displaced from the center of the latter by some 20 mm. Thus the results of Fig. 3 do correspond to the region of maximum data rate of Fig. 2, which was between those of the maximum data rate from each flow. The results of Fig. 4 were obtained at the same location, which was not that of the maximum rate of droplet arrival from the main valve, so that the information of data rates should be considered with care. More reliable estimates of the contribution of the two valves to the liquid flux through the measurement plane are obtained from Fig. 5 and suggest that they were approximately equal. Velocity contour plots show that most of the droplets emerging from the main valve had velocities of about half of these droplets from the VTEC valve with radial velocity component toward the axis of the cylinder in the former and toward the liner in the latter. Direction and magnitudes of axial and radial velocities can provide an indication regarding the trajectories of droplets, but these should be considered with care because of the three-dimensional nature of the flow. The direction of the radial velocities suggests, however, that some droplets from the main valve impinged on the liner above the measurement plane. This suggestion is supported by measurements at a small number of locations 4 mm above that of TDC and within the pent-roof, not shown here, which indicated that, with injection with the inlet valves closed, droplets from both valves moved toward the liner with nearly similar velocity magnitudes. Possible consequences of impingement are that fuel will remain on the solid surfaces and, in a fired engine, evaporate faster than droplets in the gaseous stream and possibly with increase in unburned hydrocarbons due to the local quenching, with subsequent convection of the vapor and small droplets to the other region of the cylinder by swirl and tumble motion.

Summary Conclusions

Sizes, axial and radial velocities, and data rates of fuel droplets were measured downstream of the moving valves of a four-valve VTEC engine head and in an open cylinder with steady suction and injection timing corresponding to closed, opening, and open inlet valves. The more important findings are as follows:

1 The quantity of liquid fuel passing through the plane of the measurement, 10 mm below that of TDC, increased with Θ_{inj} from 180 to 360 and 420 deg by factors of about 3 and 10, respectively. This implies a decreasing proportion of liquid fuel on solid surfaces upstream of the plane of the measurement. The Sauter mean diameter in the regions of large data rate decreased from about 120 μm with Θ_{inj} of 180 deg to 60 μm with 360 deg and 50 μm with 420 deg CA. In an operating engine, liquid films will tend to evaporate so that with early injection more fuel will emerge as vapor.

2 Injection with the inlet valves closed caused droplets to enter the cylinder in two waves, the first at around 400 deg CA from the main inlet valve and the second at around 460 deg CA from the VTEC valve. The Sauter mean diameters were about 120 μm in both waves. Velocities of droplets emerging from the main valve were about half those from the VTEC valve. The short opening times and small lift of the VTEC valve resulted in almost similar amounts of fuel remaining in the port and emerging during the skipped-injection cycle. In an operating engine, the number of droplets in both waves will be reduced by evaporation, the SMD will be increased since a greater proportion of small droplets will evaporate, and the quantity of fuel retained within the port of the VTEC valve will also be reduced.

3 Injection with both inlet valves operating led to more than 90 percent of the liquid flux to emerge from the main inlet valve in a cone of narrow angle, consistent with deflection of the spray from the injector into the main intake port and with SMD of around 50 μm. This result can be expected to be repeated in an operating engine.

Acknowledgments

The authors are grateful to Mr. P. Bruni, who constructed the experimental facility and to Mr. J. Laker, who advised on the implementation of the timer card to provide phased injection.

References

Arcoumanis, C., Hull, D., and Whitelaw, J. H., 1994, "An Approach to Charge Stratification in Lean Burn Spark Ignition Engines," SAE Paper No. 941878.

Bandel, W., Fraidl, G., Mikulic, L. A., Carstensen, H., and Quissek, F., 1989, "Investigation of Mixture Preparation and Charge Motion Effects on the Combustion of Fast-Burn Gasoline Engines," SAE Paper No. 890160.

Hardalupas, Y., Taylor, A. M. K. P., and Whitelaw, J. H., 1989, "Velocity and Particle Flux Characteristics of Turbulent Particle-Laden Jets," *Proc. Roy. Soc.*, Vol. A426, p. 31.

Horie, K., Nishizawa, K., Ogawa, T., Akazaki, S., and Miura, K., 1992, "Development of a High Fuel Economy and High Performance Four-Valve Lean Burn Engine," SAE Paper No. 920455.

Ishii, K., Miyano, H., Urata, Y., Hardalupas, Y., Taylor, A. M. K. P., and Whitelaw, J. H., 1995, SAE Paper No. 950507.

Kawazoe, H., Ohsawa, K., and Kataoka, M., 1991, "LDA Measurement of Gasoline Droplet Velocities and Sizes at Intake Valve Annular Passage in Steady Flow State," *Applications of Laser Techniques in Fluid Mechanics*, R. J. Adrian, D. F. G. Durao, F. Durst, M. Heitor, M. Maeda, and J. H. Whitelaw, eds., Vol. 5, p. 248, Springer Verlag.

Kiyota, Y., Akishino, K., and Ando, H., 1992, "Concept of Lean Combustion by Barrel-Stratification," SAE Paper No. 920678.

Posylkin, M., Taylor, A. M. K. P., Vannobel, F., and Whitelaw, J. H., 1994a, "Fuel Droplets Inside a Firing Spark-Ignition Engine," SAE Paper No. 941989.

Posylkin, M., Taylor, A. M. K. P., and Whitelaw, J. H., 1994b, "Manifold Injection and Origin of Droplets at the Exit of an Inlet Valve," 7th International Symposium on the Applications of Laser Techniques to Fluid Mechanics, Lisbon, paper 33.3; to be published in *Application of Laser Techniques 7*, Springer Verlag.

Quader, A., 1982, "The Axially Stratified Charge Engine," SAE Paper No. 820131.

Spiegel, L., and Spicher, U., 1992, "Mixture Formation and Combustion in a Spark Ignition Engine With Direct Fuel Injection," SAE Paper No. 920521.

Tate, R. W., 1982, "Some Problems Associated With the Accurate Representation of Droplet Size Distributions," in: *Proc. of 2nd Int'l Conf. on Liquid Atomisation and Spray Systems (ICLASS)*, Wisconsin, USA.

Effect of Inertia Variation Due to Reciprocating Parts and Connecting Rod on Coupled Free Vibration of Crankshaft

S. Rajendran[1]

M. V. Narasimhan

Department of Mechanical Engineering,
Indian Institute of Science,
Bangalore 560 012, India

The inertia due to reciprocating parts and connecting rods, as felt by the crankshaft, varies with the crank angle. The effect of inertia variation on torsional free vibration of crankshafts has been studied extensively. In this paper, the effect on combined torsional and bending free vibrations is examined. Single-cylinder engine crankshaft geometry is considered for the study. The results indicate that the inertial coupling, introduced by the reciprocating parts and connecting rod, significantly influences the free vibration characteristics, particularly when the natural frequencies of the crankskahft are closely spaced. The results suggest that, under such conditions, modeling the crankshaft as a pure torsional system would involve considerable error.

1 Introduction

Reciprocating engine crankshafts have been analyzed for a long time as pure torsional vibration systems (Ker Wilson, 1956, 1963; Den Hartog, 1956; Nestorides, 1958). The reciprocating parts and connecting rod are usually modeled as a lumped equivalent mass located at the crankpin center. As the crankshaft rotates, the relative disposition of crank-gear components varies continuously, and hence the equivalent mass is a function of crank angle. The crankshaft, along with piston and connecting rod, is, therefore, an inertia variant system. The frequency of dominant harmonic component of inertia variation is twice that of crankshaft rotational speed. The strength of other harmonic components diminishes quickly as the order increases (Den Hartog, 1956; Ker Wilson, 1963).

In large engines such as in marine applications, the torsional natural frequency of the crankshaft is so low that lower order critical speeds fall within the operating speed range. The lower order harmonic components of inertia variation, being stronger in magnitude, result in strong parametric excitations leading to instability over a wide speed range in the vicinity of $F_n/F_m = \frac{1}{2}$ or 1, where F_n is the natural frequency of the crankshaft and F_m is the frequency of inertia variation. Extensive literature exists on this subject (Goldsbrough, 1925; Kjaer, 1930; Gregory, 1954; Den Hartog, 1956; Ker Wilson, 1963; Draminsky, 1965; Pasricha and Carnegie, 1981).

In contrast, in small engines such as in automotive applications, the torsional natural frequency of crankshaft is comparatively high, and hence only higher order (usually fourth order and above) critical speeds fall within the operating speed range. Since the higher order harmonic components of inertia variation are weaker in magnitude, the resulting parametric excitations will also be weaker. Hence, under such conditions, it is usual to ignore the effects of parametric excitation and compute the free vibration characteristics of crankshaft under pseudo-static conditions, neglecting the rotational speed (Ker Wilson, 1956). The influence of inertia variation in such cases is to cause periodic variation of natural frequency.

With the rapid development of digital computers, there is a renewed interest in crankshaft vibrations. Rao and Sanyal (1980) and Rao (1984) have presented a comprehensive review of literature on crankshaft vibrations up to 1982 and have quoted several papers published between 1970 and 1982. Several other papers on crankshaft vibrations have also appeared in the last 15 years (as for example, Shaw and Richter, 1979; Bargis et al., 1980; Nagaike and Nagamatsu, 1984; Kabele, 1984; Carrato and Fu, 1986; Jhonston and Shusto, 1987; Lacy, 1987; Green, 1987; Heath and McNamara, 1990). However, studies on the effect of inertia variation due to reciprocating parts and connecting rod on coupled vibration of crankshaft have not appeared.

The present paper is aimed at understanding how the free vibration characteristics of crankshafts are influenced by the inertia variation under combined torsional and bending vibrations. The investigation reported in this paper is limited to single-cylinder engine crankshaft geometry. However, a similar approach is also applicable to multicylinder engine crankshafts where all the crank throws lie in a plane. The parametric excitations due to inertia variation and the consequent instability are neglected in the analysis, and the free vibration characteristics are computed under pseudostatic condition of the crankshaft. Such an approach is justified for small engines, where only higher order critical speeds lie in the operating speed range.

2 Mathematical Model

To start with, it is assumed that an eigenanalysis of the bare crankshaft (without including the reciprocating parts and connecting rod) has already been made by a finite element method, for example. The expressions for kinetic and strain energy of the crankshaft are written in terms of its free vibration modes. The reciprocating parts and connecting rod are assumed to be rigid and their kinetic energy is written in terms of modal coordinates. Lagrange's equations are then applied to the crankshaft assembly (crankshaft + reciprocating parts + connecting rod) to obtain the equations of motion.

Alternatively, it is possible to develop a finite element model for the whole assembly consisting of crankshaft, connecting rod, piston, etc., and analyze its free vibration characteristics as a whole. However, for the present work, where the physics of the problem is of prime interest, the modal model described is convenient and hence preferred to an all-finite-element model.

2.1 Kinetic and Strain Energy of Crankshaft. The kinetic energy, T_s, and the strain energy, U_s, of the crankshaft are given by

[1] Current address: Structures Division, National Aerospace Laboratories, Bangalore, India.

Contributed by the Internal Combustion Engine Division for publication in the JOURNAL OF ENGINEERING FOR GAS TURBINES AND POWER. Manuscript received at ASME Headquarters August 1996. Associate Technical Editor: W. K. Chang.

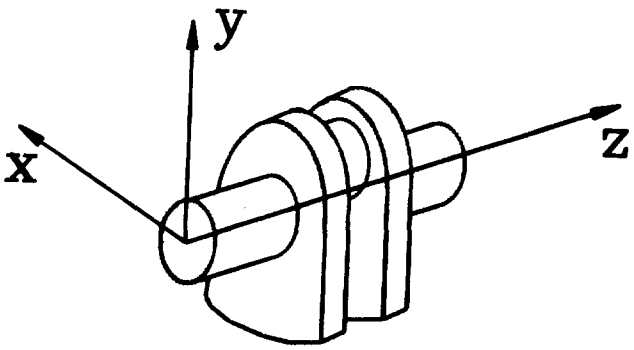

Fig. 1 Coordinate system

$$T_s = \tfrac{1}{2}\,\dot{\mathbf{u}}^T\mathbf{M}\dot{\mathbf{u}} \tag{1}$$

$$U_s = \tfrac{1}{2}\,\mathbf{u}^T\mathbf{K}\mathbf{u} \tag{2}$$

where $\mathbf{u}$ is the displacement vector, the overdot refers to time derivative, and $\mathbf{M}$ and $\mathbf{K}$ are the finite element mass and stiffness matrices, respectively.

The first few modes of a single cylinder engine crankshaft (Fig. 1) can be classified as (*i*) *torsional modes* in which the crankshaft executes predominantly torsional oscillations about the z axis, (*ii*) *in-plane bending modes* in which the crankshaft executes predominantly bending vibration in the y–z-plane, and (*iii*) *out-of-plane bending modes* in which the crankshaft executes predominantly bending vibration in the x–z-plane. The higher modes do not conform strictly to this classification. For instance, the higher torsional modes do have considerable out-of-plane bending, and vice versa.

Expanding $\mathbf{u}$ in terms of mode shape vectors, the expressions for T_s and U_s can be expressed in terms of modal parameters as

$$T_s = \tfrac{1}{2}\Big[\sum_{j=1}^{m_1} m_{tor}^j r_o^2(\dot{\theta}_{tor}^j)^2 + \sum_{j=1}^{m_2} m_{opb}^j(\dot{x}_{opb}^j)^2 + \sum_{j=1}^{m_3} m_{ipb}^j(\dot{y}_{ipb}^j)^2\Big] \tag{3}$$

$$U_s = \tfrac{1}{2}\Big[\sum_{j=1}^{m_1} k_{tor}^j r_o^2(\theta_{tor}^j)^2 + \sum_{j=1}^{m_2} k_{opb}^j(x_{opb}^j)^2 + \sum_{j=1}^{m_3} k_{ipb}^j(y_{ipb}^j)^2\Big] \tag{4}$$

where $m_{tor}^j = (\boldsymbol{\psi}_{tor}^j)^T\mathbf{M}\boldsymbol{\psi}_{tor}^j$, $m_{opb}^j = (\boldsymbol{\psi}_{opb}^j)^T\mathbf{M}\boldsymbol{\psi}_{opb}^j$, $m_{ipb}^j = (\boldsymbol{\psi}_{ipb}^j)^T\mathbf{M}\boldsymbol{\psi}_{ipb}^j$, $k_{tor}^j = (\boldsymbol{\psi}_{tor}^j)^T\mathbf{K}\boldsymbol{\psi}_{tor}^j$, $k_{opb}^j = (\boldsymbol{\psi}_{opb}^j)^T\mathbf{K}\boldsymbol{\psi}_{opb}^j$, $k_{ipb}^j = (\boldsymbol{\psi}_{ipb}^j)^T\mathbf{K}\boldsymbol{\psi}_{ipb}^j$, m_{tor}^j, m_{opb}^j, and m_{ipb}^j are the modal masses, k_{tor}^j, k_{opb}^j, and k_{ipb}^j are the modal stiffnesses, j^{th} is mode number, $\boldsymbol{\psi}_{tor}$, $\boldsymbol{\psi}_{opb}$, and $\boldsymbol{\psi}_{ipb}$ are mode shape vectors of the bare crankshaft, θ_{tor} is the angular displacement of crankpin center in the torsional mode (Fig. 8), x_{opb}^j is the x displacement of crankpin center in the out-of-plane bending mode (Fig. 8), y_{ipb}^j is the y displacement of crankpin center in the in-plane bending mode (Fig. 8), r_o is the crank radius (Fig. 8), and m_1, m_2, and m_3 are the number of torsional, out-of-plane bending, and in-plane bending modes, respectively, in the first m vibration modes. $m_1 + m_2 + m_3 = m$.

In deriving the expressions given by Eqs. (3) and (4), the vibration amplitudes are assumed to be small. For the torsional and out of plane bending modes, the y and z displacements (Fig. 1) of crankpin center are ignored in comparison with the x displacement. For the in-plane bending modes, the x and z displacements of the crankpin center are ignored in comparison with the y displacement. The mode shape vectors are assumed to be scaled in such a way that the x motion of the crankpin center in the torsional and out-of-plane bending modes, and the y motion of the crankpin center in the in-plane bending modes are unity.

2.2 Kinetic Energy of Reciprocating Parts and Connecting Rod. The crankpin center executes both circular and radial motions due to torsional and bending vibrations, respectively. Considering both the tangential and radial velocities of the crankpin center, the expressions for the kinetic energy of reciprocating parts, T_p, and that of connecting rod, T_c, can be obtained (Rajendran, 1993) as in Eqs. (5) and (6). A brief development of these expressions is indicated in Appendix A:

$$T_p = \tfrac{1}{2}\,\mathbf{v}^T\mathbf{M}_p^{eq}\mathbf{v} \tag{5}$$

$$T_c = \tfrac{1}{2}\,\mathbf{v}^T\mathbf{M}_c^{eq}\mathbf{v} \tag{6}$$

where

$$\mathbf{M}_p^{eq} = m_p\begin{bmatrix} C_{tt} & C_{tr} \\ C_{tr} & C_{rr}\end{bmatrix}, \quad \mathbf{M}_c^{eq} = m_c\begin{bmatrix} F_{tt} & F_{tr} \\ F_{tr} & F_{rr}\end{bmatrix},$$

$$\mathbf{v} = \begin{Bmatrix} v_t \\ v_r\end{Bmatrix}, \quad v_t = r\frac{d\theta}{dt}, \quad v_r = \frac{dr}{dt}$$

$$\mathrm{A} = \left[-\sin\theta - \frac{r\sin\theta\cos\theta}{l\left(1 - \frac{r^2}{l^2}\sin^2\theta\right)^{1/2}}\right],$$

$$B = \left[\cos\theta - \frac{r\sin^2\theta}{l\left(1 - \frac{r^2}{l^2}\sin^2\theta\right)^{1/2}}\right],$$

$$C_{tt} = A^2, \quad C_{tr} = AB, \quad C_{rr} = B^2,$$

$$F_{tt} = C_{tt} + D_{tt}\frac{l_g}{l} + E_{tt}\frac{k^2}{l^2},$$

$$F_{rr} = C_{rr} + D_{rr}\frac{l_g}{l} + E_{rr}\frac{k^2}{l^2}, \quad F_{tr} = C_{tr} + D_{tr}\frac{l_g}{l} + E_{tr}\frac{k^2}{l^2},$$

$$D_{tt} = 2A\sin\phi(-B\cos\phi - A\sin\phi),$$

$$D_{rr} = 2B\sin\phi(A\cos\phi - B\sin\phi),$$

$$D_{tr} = A\sin\phi(A\cos\phi - B\sin\phi) + B\sin\phi(-B\cos\phi - A\sin\phi),$$

$$E_{tt} = (-B\cos\phi - A\sin\phi)^2, \quad E_{rr} = (A\cos\phi - B\sin\phi)^2,$$

$$E_{tr} = (E_{tt}E_{rr})^{1/2},$$

$$\sin\phi = \frac{r}{l}\sin\theta,$$

and $\mathbf{M}_p^{eq}$ and $\mathbf{M}_c^{eq}$ are the equivalent mass matrices of reciprocating parts and connecting rod, respectively.

For small vibration amplitudes, θ and r can be expressed in the form

$$\theta = \theta_0 + \theta_{tor} + \frac{x_{opb}}{r_o} \tag{7}$$

$$r = r_o + y_{ipb} \tag{8}$$

where θ_0 is the crank angle (measured from TDC), and θ_{tor}, x_{opb}, and y_{ipb} are the angular, x, and y displacements at the

crankpin center, respectively (Fig. 8). The quantities θ_{tor}, x_{opb}, and y_{ipb} can be written as

$$\theta_{tor} = \sum_{j=1}^{m_1} \theta_{tor}^j \tag{9}$$

$$x_{opb} = \sum_{j=1}^{m_2} x_{opb}^j \tag{10}$$

$$y_{ipb} = \sum_{j=1}^{m_3} y_{ipb}^j \tag{11}$$

Using Eqs. (7)–(11), the tangential and radial velocities of the crankpin center, v_t and v_r, respectively, can be written as

$$v_t = \sum_{j=1}^{m_1} r_o \dot{\theta}_{tor}^j + \sum_{j=1}^{m_2} \dot{x}_{opb}^j \tag{12}$$

$$v_r = \sum_{j=1}^{m_3} \dot{y}_{ipb}^j. \tag{13}$$

Using Eqs. (12) and (13) in Eqs. (5)–(6), the expressions for T_p and T_c can be obtained in terms of the modal coordinates, θ_{tor}^j, x_{opb}^j, and y_{ipb}^j.

2.3 Energy of the Complete System. The crankshaft assembly, consisting of crankshaft, reciprocating parts, and connecting rod, is considered now. The mass matrix of the complete system, $\tilde{\mathbf{M}}$, is given by

$$\tilde{\mathbf{M}} = \mathbf{M} + \mathbf{M}' + \mathbf{M}'' \tag{14}$$

where $\mathbf{M}'$ and $\mathbf{M}''$ are $n \times n$ matrices are additions due to reciprocating parts and connecting rod, respectively.

The total kinetic energy, T, and the total strain energy, U, of the complete system are given by

$$T = \tfrac{1}{2}\, \dot{\mathbf{u}}^T \tilde{\mathbf{M}} \dot{\mathbf{u}} \tag{15}$$

$$U = \tfrac{1}{2}\, \mathbf{u}^T \mathbf{K} \mathbf{u} \tag{16}$$

Expanding $\mathbf{u}$ in terms of mode shape vectors, the expressions for T and U can be expressed as

$$T = T_p + T_c + T_s \tag{17}$$

$$U = U_s \tag{18}$$

where the expressions for T_s, U_s, T_p and T_c are given by Eqs. (3), (4), (5), and (6), respectively.

2.4 Equations of Motion. Using Lagrange's equations, the equations of motion can be derived as

$$\mathbf{P}\ddot{\mathbf{x}} + \mathbf{Q}\mathbf{x} = \mathbf{o} \tag{19}$$

where

$$\mathbf{P} = \begin{bmatrix} \mathbf{M}_{tor} + G_{tt}\mathbf{J}_{m_1\times m_1} & G_{tt}\mathbf{J}_{m_1\times m_2} & G_{tr}\mathbf{J}_{m_1\times m_3} \\ G_{tt}\mathbf{J}_{m_2\times m_1} & \mathbf{M}_{opb} + G_{tt}\mathbf{J}_{m_2\times m_2} & G_{tr}\mathbf{J}_{m_2\times m_3} \\ G_{tr}\mathbf{J}_{m_3\times m_1} & G_{tr}\mathbf{J}_{m_3\times m_2} & \mathbf{M}_{ipb} + G_{rr}\mathbf{J}_{m_3\times m_3} \end{bmatrix},$$

$$\mathbf{Q} = \text{Diag}\,[k_{tor}^1, k_{tor}^2, k_{tor}^3, \ldots, k_{tor}^{m_1}, k_{opb}^1, k_{opb}^2, k_{opb}^3, \ldots, k_{opb}^{m_2}, k_{ipb}^1, k_{ipb}^2, k_{ipb}^3, \ldots, k_{ipb}^{m_3}],$$

$$\mathbf{x}^T = \left[\theta_{tor}^1, \theta_{tor}^2, \theta_{tor}^3, \ldots, \theta_{tor}^{m_1}, \frac{x_{opb}^1}{r_o}, \frac{x_{opb}^2}{r_o}, \frac{x_{opb}^3}{r_o}, \ldots, \frac{x_{opb}^{m_2}}{r_o}, \frac{y_{ipb}^1}{r_o}, \frac{y_{ipb}^2}{r_o}, \frac{y_{ipb}^3}{r_o}, \ldots, \frac{y_{ipb}^{m_3}}{r_o}\right],$$

$\mathbf{o}$ is a $n \times 1$ null vector,

$$\mathbf{M}_{tor} = \text{Diag}\,[m_{tor}^1, m_{tor}^2, m_{tor}^3, \ldots, m_{tor}^{m_1}],$$

$$\mathbf{M}_{opb} = \text{Diag}\,[m_{opb}^1, m_{opb}^2, m_{opb}^3, \ldots, m_{opb}^{m_2}],$$

$$\mathbf{M}_{ipb} = \text{Diag}\,[m_{ipb}^1, m_{ipb}^2, m_{ipb}^3, \ldots, m_{ipb}^{m_3}],$$

$$G_{tt} = C_{tt}m_p + F_{tt}m_c, \quad G_{tr} = C_{tr}m_p + F_{tr}m_c,$$

$$G_{rr} = C_{rr}m_p + F_{rr}m_c,$$

and $\mathbf{J}_{m_i\times m_j}$ is an $m_i \times m_j$ matrix with all entries equal to unity.

3 Free Vibration Analysis

Although Eq. (19) involves several modes, in this paper only a two-mode model is considered. This would be justified for a crankshaft with a pair of natural frequencies isolated sufficiently from all others. Depending on the choice of these two modes, three important cases arise: Case 1—a pair of torsional and in-plane bending modes; Case 2—a pair of out-of-plane bending and in-plane bending modes; Case 3—a pair of torsional and out-of-plane bending modes. Only Case 1 is dealt with in this paper. The procedure is similar for other cases and is discussed elsewhere (Rajendran, 1993).

Considering only a torsional and in-plane bending mode, the equations of motion reduce to the form

$$\mathbf{A}\ddot{\mathbf{u}} + \mathbf{B}\mathbf{u} = \mathbf{o} \tag{20}$$

where

$$\mathbf{A} = \begin{bmatrix} m_{tor} + C_{tt}m_p + F_{tt}m_c & C_{tr}m_p + F_{tr}m_c \\ C_{tr}m_p + F_{tr}m_c & m_{ipb} + C_{rr}m_p + F_{rr}m_c \end{bmatrix},$$

$$\mathbf{B} = \begin{bmatrix} k_{tor} & 0 \\ 0 & k_{ipb} \end{bmatrix}, \quad \text{and} \quad \mathbf{u} = \begin{Bmatrix} \theta_{tor} \\ \dfrac{y_{ipb}}{r_o} \end{Bmatrix}$$

The equations are linear with constant coefficients and hence admit harmonic solutions of the form

$$\theta_{tor} = \Theta_{tor} \cos \sqrt{\lambda} t \tag{21}$$

$$y_{ipb} = Y_{ipb} \cos \sqrt{\lambda} t \tag{22}$$

where Θ_{tor} and Y_{ipb} are the amplitudes of torsional and in-plane vibrations and λ is an eigenvalue. $\lambda = \omega^2$ where ω is the natural frequency in rad/s.

The expressions for the two eigenvalues λ_1 and λ_2 can be derived in a nondimensional form as given below:

$$\frac{\lambda_{1,2}}{\lambda_{tor}} = \frac{\left(C_{22} + \dfrac{\lambda_{ipb}}{\lambda_{tor}} C_{11}\right) \pm \left[\left(C_{22} - \dfrac{\lambda_{ipb}}{\lambda_{tor}} C_{11}\right)^2 + 4\dfrac{\lambda_{ipb}}{\lambda_{tor}} C_{12}C_{21}\right]^{1/2}}{2(C_{11}C_{22} - C_{12}C_{21})} \tag{23}$$

Alternatively,

$$\frac{\lambda_{1,2}}{\lambda_{ipb}} = \frac{\left(\dfrac{\lambda_{tor}}{\lambda_{ipb}} C_{22} + C_{11}\right) \pm \left[\left(\dfrac{\lambda_{tor}}{\lambda_{ipb}} C_{22} - C_{11}\right)^2 + 4\dfrac{\lambda_{tor}}{\lambda_{ipb}} C_{12}C_{21}\right]^{1/2}}{2(C_{11}C_{22} - C_{12}C_{21})} \tag{24}$$

where

$$C_{11} = 1 + C_{tt}a_{tor} + F_{tt}b_{tor}, \quad C_{12} = C_{tr}a_{tor} + F_{tr}b_{tor}$$

$$C_{21} = C_{tr}a_{ipb} + F_{tr}b_{ipb}, \quad C_{22} = 1 + C_{rr}a_{ipb} + F_{rr}b_{ipb}$$

$$\lambda_{tor} = \frac{k_{tor}}{m_{tor}}, \; \lambda_{ipb} = \frac{k_{ipb}}{m_{ipb}}, \quad a_{tor} = \frac{m_p}{m_{tor}}, \quad b_{tor} = \frac{m_c}{m_{tor}},$$

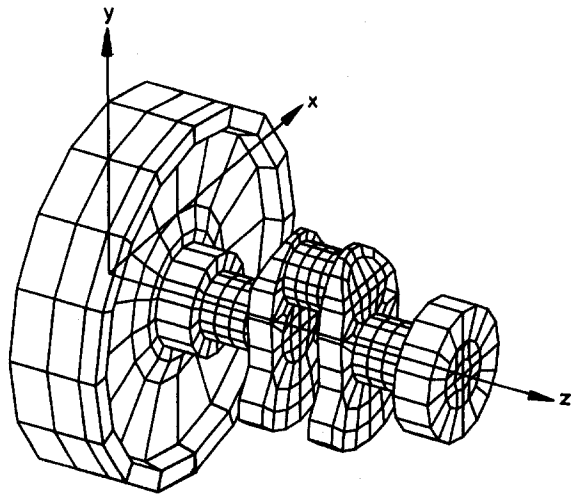

Fig. 2 Finite element mesh of crankshaft. Type of element: 8-node hexahedron. Number of elements = 520. Number of nodes = 961. Number of degrees of freedom per node = 3.

$$a_{ipb} = \frac{m_p}{m_{ipb}}, \quad b_{ipb} = \frac{m_c}{m_{ipb}},$$

$\omega_{tor} = (\lambda_{tor})^{1/2}$, and $\omega_{ipb} = (\lambda_{ipb})^{1/2}$. ω_{tor} and ω_{ipb} are the torsional and in-plane bending natural frequencies, respectively, of the bare crankshaft.

For a given eigenvalue, the ratio $(r_o\Theta_{tor}/Y_{ipb})$ can be computed. This ratio is a measure of the torsional-bending coupling. For pure torsional mode $(r_o\Theta_{tor}/Y_{ipb}) = \infty$, for pure in-plane bending mode $(r_o\Theta_{tor}/Y_{ipb}) = 0$ and for coupled mode $0 < (r_o\Theta_{tor}/Y_{ipb}) < \infty$. This ratio will hereinafter be referred to as the *coupling ratio.*

The expressions for the coupling ratios corresponding to λ_1 and λ_2 can be derived as

$$\left(\frac{r_o\Theta_{tor}}{Y_{ipb}}\right)_{\lambda_i} = \frac{\frac{\lambda_i}{\lambda_{tor}}(C_{tt}a_{tor} + F_{tt}b_{tor})}{1 - \frac{\lambda_i}{\lambda_{tor}}(1 + C_{tt}a_{tor} + F_{tt}b_{tor})}, \quad i = 1, 2 \quad (25)$$

4 Computational Aspects

The values of the parameters a_{tor}, b_{tor}, a_{ipb}, and b_{ipb} depend on the geometry of the crankshaft, and can be computed provided the modal masses, m_{tor} and m_{ipb}, the mass of reciprocating parts, m_p, and the mass of connecting rod, m_c, are known. For the present work, the nominal values have been chosen as: $a_{tor} = b_{tor} = a_{ipb} = b_{ipb} = 0.3$, which is typical of the crankshaft geometry shown in Fig. 2.

The values of other nondimensional parameters used in computation, unless stated otherwise, are as follows: $l_g/l = 0.7$, $k/l = 0.97$, $l/r = 3.5$. Using Eqs. (23), (24) and (25), the nondimensional eigenvalues and coupling ratios have been computed in the range $0 < \theta_o < 360$ deg in steps of 1 deg. The computed eigenvalues λ_1 and λ_2 have been found to be real. Also,

$$\lambda_1 > \lambda_2 > 0 \quad (26)$$

in the range of interest of parameters.

5 Results and Discussion

Figures 3(*a*) and 3(*b*) depict how the natural frequencies of crankshaft assembly (crankshaft + reciprocating parts + connecting rod) fluctuate with crank angle. The closeness of natural frequencies of bare crankshaft, which is characterized by the closeness ratio, R_o (see figure caption for definition), is varied as a parameter. It is seen that the fluctuation of natural frequencies is large when the natural frequencies of bare crankshaft are well separated, i.e., when R_o is close to zero; it is small when the natural frequencies of bare crankshaft are close to each other, i.e., when R_o is close to unity. Typically, for $R_o = 1$, the amplitude of fluctuation of ω_1^* is practically zero (which is very interesting) whereas that of ω_2^* is finite, but small.

Figure 4(*a*) and 4(*b*) (refer to continuous lines) depict how the mean value of natural frequencies taken over one revolution of crank varies with closeness ratio R_o. It seen that the mean values are little influenced by R_o except in a small region close to $R_o = 1$. In this region, however, the mean values show high sensitivity to change in R_o.

By setting the off-diagonal terms of matrix **A** (Eq. (20)) to zero, the plots of mean values of frequencies against R_o are shown in broken lines. These lines are straight, suggesting that the high sensitivity of mean values to changes in R_o at regions close to $R_o = 1$, discussed above, is due to the off-diagonal terms.

Figures 5(*a*) and 5(*b*) (refer to continuous lines) show how the amplitudes of cyclic fluctuation of natural frequencies vary with R_o. It is seen that R_o significantly influences the amplitudes of cyclic fluctuation in a small region close to $R_o = 1$. By setting the off-diagonal terms of matrix **A** (Eq. (20)) to zero, the respective plots are shown in broken lines. Here again it is seen that the high sensitivity of amplitudes of cyclic fluctuation to changes in R_o at regions close to $R_o = 1$ is due to the off-diagonal terms.

Figure 6 shows how the closeness of natural frequencies of crankshaft assembly, which is characterized by the closeness

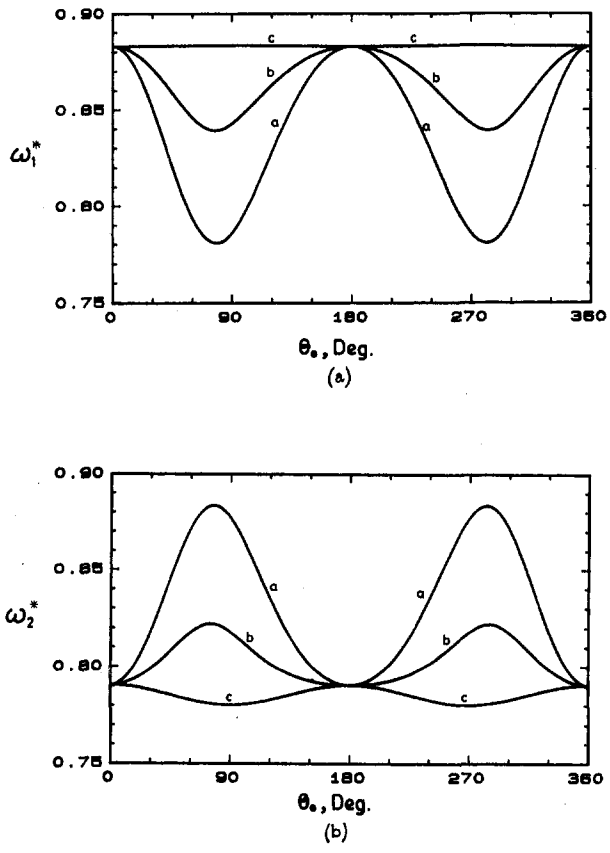

Fig. 3 Periodic fluctuation of natural frequencies of crankshaft assembly with crank angle, θ_o. Curves *a*, *b*, and *c* correspond to $R_o = 0.001$, 0.95, and 1.0, respectively. The natural frequencies have been normalized such that $\omega_1^* = \omega_1/\omega_{tor}$ and $\omega_2^* = \omega_2/\omega_{ipb}$. $R_o = \omega_{ipb}/\omega_{tor}$ and is called the closeness ratio of natural frequencies of bare crankshaft.

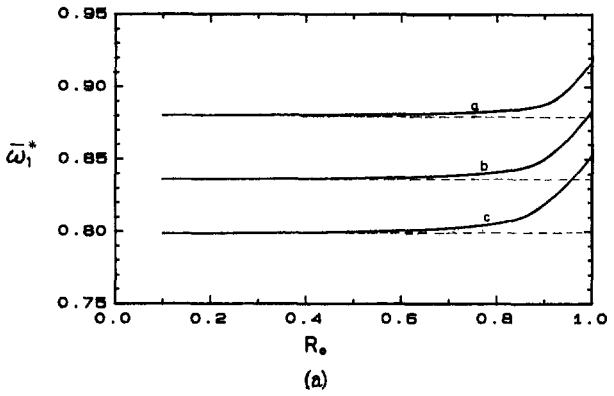

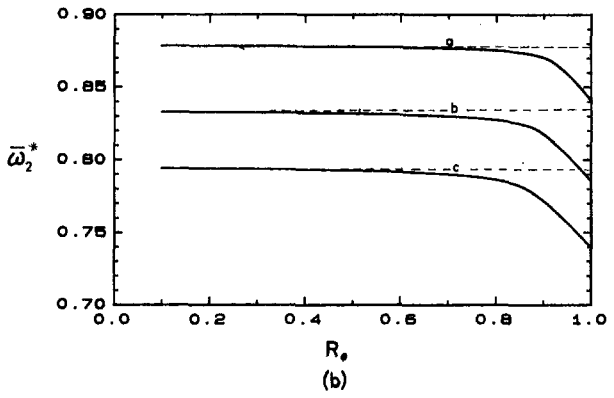

Fig. 4 Influence of closeness ratio, R_o, on mean natural frequencies of crankshaft assembly. Curves *a*, *b*, and *c* correspond to $a_{tor} = b_{tor} = a_{ipb} = b_{ipb} = 0.2$, 0.3 and 0.4, respectively. $\bar{\omega}_i^* = [\sum_{\alpha=1}^{360} (\omega_i^*)_\alpha]/360$, $i = 1, 2$. $R_o = \omega_{ipb}/\omega_{tor}$.

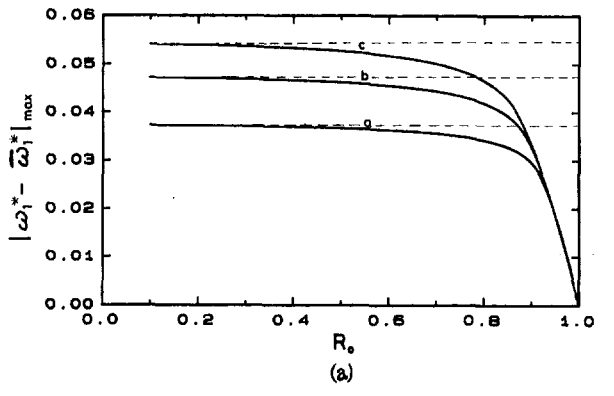

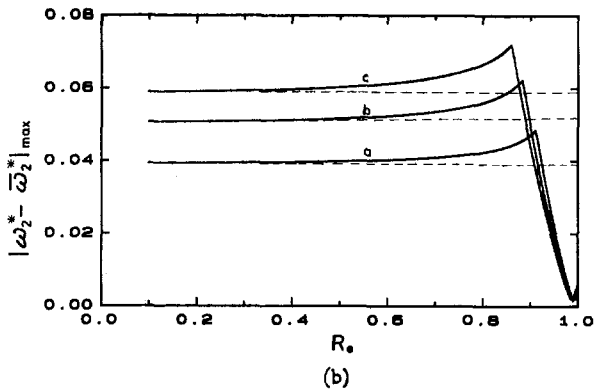

Fig. 5 Influence of closeness ratio, R_o, on the amplitude of fluctuation of natural frequencies of crankshaft assembly. Curves *a*, *b*, and *c* correspond to $a_{tor} = b_{tor} = a_{ipb} = b_{ipb} = 0.2$, 0.3 and 0.4, respectively. $|\omega_i^* - \bar{\omega}_i^*|_{max}$, $i = 1, 2$ stand for amplitudes of fluctuation. $R_o = \omega_{ipb}/\omega_{tor}$.

ratio R_n (see figure caption for definition), varies with the closeness ratio R_o. It is observed from the plot that $R_n \leq R_o$, whatever be the value of R_o. This means that the natural frequencies of crankshaft assembly are better separated than the natural frequencies of bare crankshaft. It is also seen that $R_n \neq 1$ for whatever value of R_o. This suggests that the crankshaft assembly cannot have coincident natural frequencies, even when the natural frequencies of bare crankshaft are coincident.

Figures 7(*a*) and 7(*b*) show how the coupling ratios vary with crank angle. For values of R_o close to zero, the coupling ratio stays close to 90 deg in case of ω_1 (Fig. 7(*a*)) and close to 0 deg in the case of ω_2 (Fig. 7(*b*)), although slight fluctuations are noticed. This would mean that the vibration corresponding to ω_1 remains close to pure torsional and that corresponding to ω_2 remains close to pure in-plane bending. However, for large values of R_o, both the coupling ratios fluctuate between 0 and 90 deg as the crank angle increases, which would mean that the mode of vibration corresponding to ω_1 as well as ω_2 fluctuate between pure torsional and pure in-plane bending as the crank angle is varied.

7 Concluding Remarks

In this paper, the effect of inertia variation due to reciprocating parts and connecting rod on the coupled free vibration of crankshaft has been analyzed. The cyclic fluctuation of natural frequencies due to the inertia fluctuation is influenced significantly by the closeness ratio of the natural frequencies of bare crankshaft. As the closeness increases, the amplitude of cyclic fluctuation decreases. It is interesting to note that, when for a closeness ratio of unity, one of the natural frequencies of crankshaft, i.e., ω_1, does not exhibit cyclic fluctuation at all.

The sensitive dependence of the fluctuation of natural frequencies on the closeness of natural frequencies of bare crankshaft is caused by the off-diagonal terms of the equivalent mass matrices of reciprocating parts and connecting rod. Thus the off-diagonal terms cannot be ignored, particularly when the torsional and bending natural frequencies of bare crankshaft are close to each other (closeness ratio 0.8 to 1.0). This suggests that, for the coupled as well as the pure torsional models, comparable results may be expected when the closeness ratio is typically less than 0.8. Between 0.8 and 1.0, however, the torsional-bending coupling introduced by the reciprocating parts and connecting rod is significant, and hence a coupled vibration model is preferable under these conditions. The results provide

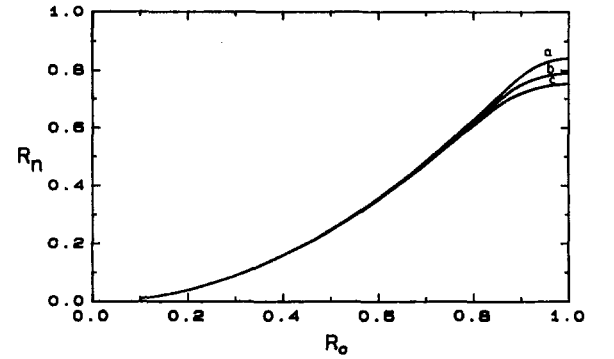

Fig. 6 Variation of R_n with R_o. Curves *a*, *b*, and *c* correspond to $a_{tor} = b_{tor} = a_{ipb} = b_{ipb} = 0.2$, 0.3 and 0.4, respectively. $R_n = \omega_2/\omega_1$ and $R_o = \omega_{ipb}/\omega_{tor}$.

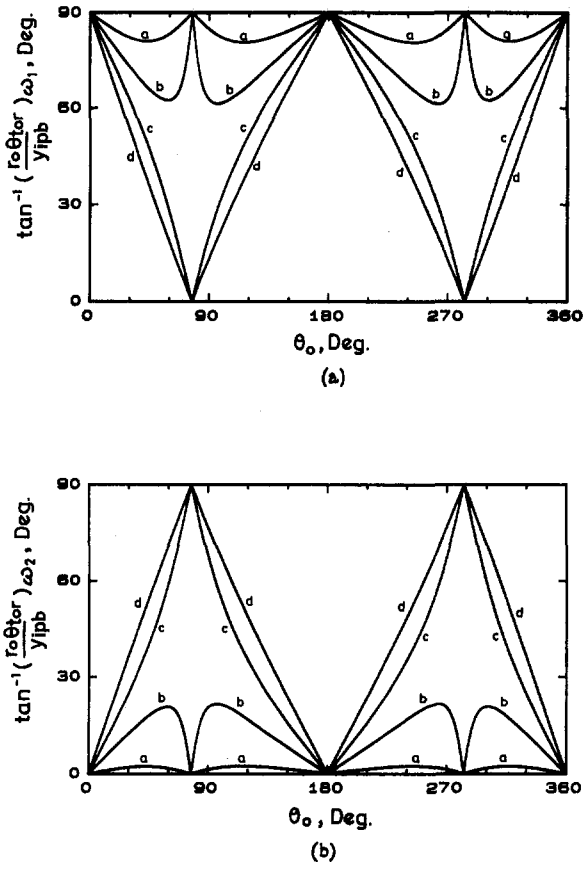

Fig. 7 Periodic fluctuation of coupling ratios with crank angle, θ_o. Curves *a*, *b*, *c*, and *d* correspond to R_o = 0.5, 0.85, 0.95, and 1, respectively.

motivation for studying the effect of reciprocating parts and connecting rod on the forced vibration of crankshaft. Research is in progress.

References

Bargis, E., Garro, A., and Vullo, V., 1980, "Crankshaft Design and Evaluation: Part 1—Critical Analysis and Experimental Evaluation of Current Methods; Part 2—A Modern Design Method: Modal Analysis; Part 3—Modern Design Method: Direct Integration," *Proc. Int. Conf. Reliability, Stress Analysis and Failure Prevention Methods in Mechanical Design,* Aug. 18–21, ASME, pp. 191–218.

Carrato, P. J., and Fu, C. C., 1986, "Modal Analysis Techniques for Torsional Vibration of Diesel Crankshafts," SAE Paper No. 861225.

Den Hartog, J. P., 1956, *Mechanical Vibrations,* 5th ed., McGraw-Hill, New York.

Draminsky, P., 1965, "Extended Treatment of Secondary Resonance," *Shipbuilding and Marine Engineering International,* Vol. 88, pp. 180–186.

Goldsbrough, G. R., 1925, "Torsional Vibration in Reciprocating Engine Shafts," *Proc. Royal Society,* Vol. 190, pp. 99–106.

Green, G. W., 1987, "Design of Crankshaft by the Finite Element Method," SAE Paper No. 870579.

Gregory, R. W., 1954, "Non-linear Oscillations of a System Having Variable Inertia," Ph.D. thesis, University of Durham.

Heath, A. R., and McNamara, P. M., 1990, "Crankshaft Stress Analysis—Combination of Finite Element and Classical Analysis Techniques," ASME *Journal of Engineering for Gas Turbines and Power,* Vol. 112, pp. 268–275.

Jhonston, P. R., and Shusto, L. M., 1987, "Analysis of Diesel Engine Crankshaft Torsional Vibrations," SAE Paper No. 870870.

Kabele, D. F., 1984, "A New Approach in the Simulation of Crankshaft Torsional Vibration," *Proc. I. Mech. E.,* C140/84, pp. 131–139.

Ker Wilson, W., 1956, *Practical Solution of Torsional Vibration Problems: Vol. 1: Frequency Calculations,* 3rd ed. revised, Chapman and Hall Ltd., London.

Ker Wilson, W., 1963, *Practical Solution of Torsional Vibration Problems: Vol. 2: Amplitude Calculations,* 3rd ed., Chapman and Hall Ltd., London.

Kjaer, 1930, "Torsional Vibration in Diesel Crankshafts," *The Motorship,* Aug.

Lacy, D. J., 1987, "Computers in Analysis Techniques for Reciprocating Engine Design," *Proc. I. Mech. E.,* C14/87, pp. 55–68.

Nagaike, M., and Nagamatsu, A., 1984, "Basic Research on Vibration and Noise of Internal Combustion Engine (1st Report, Vibration Analysis of the Piston-Crank System I)," *Bull. JSME,* Vol. 27, pp. 289–294.

Nestorides, E. J., ed., 1958, *A Handbook on Torsional Vibration,* Cambridge University Press, London.

Pasricha, M. S., and Carnegie, W. 1981, "Diesel Crankshaft Failures in Marine Industry—A Variable Inertia Aspect," *Journal of Sound and Vibration,* Vol. 78, pp. 347–354.

Rajendran, S., 1993, "Dynamic Analysis of Crankshaft Using Finite Element Method," Ph.D. thesis, Department of Mechanical Engineering, Indian Institute of Science, Bangalore.

Rao, D. K., and Sanyal, A., 1980, "Torsional Vibration in Ship Engine Shafts," *Shock and Vibrations Digest,* Vol. 12, pp. 3–8.

Rao, D. K., 1984, "Torsional Vibration of Crankshafts in Reciprocating Machines," *Shock and Vibrations Digest,* Vol. 16, pp. 15–23.

Shaw, T. M., and Richter, I. B., 1979, "Crankshaft Design Using a Generalized Finite Element Model," SAE Paper No. 790279.

APPENDIX A

Expressions for the Kinetic Energy of Reciprocating Parts and Connecting Rods in Terms of the Tangential and Radial Velocities of Crankpin Center

In the conventional lumped mass modeling of reciprocating parts and connecting rods for torsional vibration analysis, only circular motion of the crankpin center about the journal axis is usually considered. Under combined torsional and bending vibrations, the crankpin can also move radially due to bending vibration (Fig. 8) in addition to its circular motion due to torsional vibration.

Kinetic Energy of Reciprocating Parts

Considering a slider crank as shown in Fig. 9(*a*), the distance of piston pin center *P* from the crank center *O* for a given crank angle, θ, is given by

$$z = r\cos\theta + l\left(1 - \frac{r^2}{l^2}\sin^2\theta\right)^{1/2} \tag{27}$$

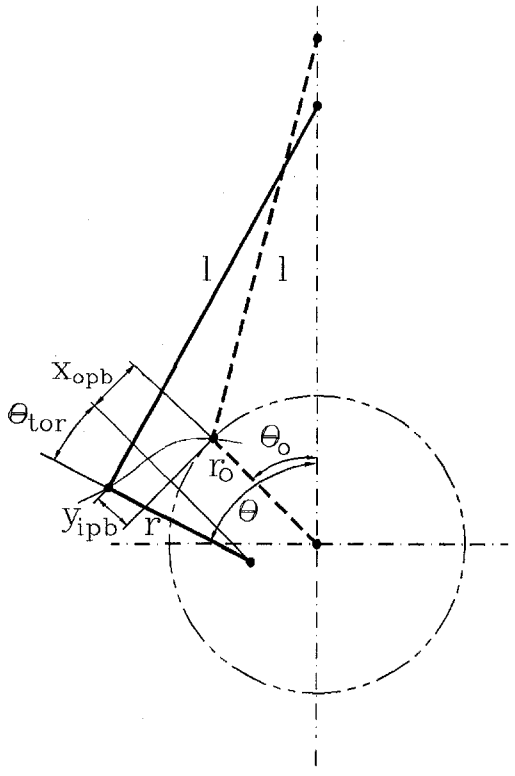

Fig. 8 Kinematics of slider crank under combined torsional and bending vibrations

The velocity of piston pin center toward the crank center is given by

$$v_p = -\frac{\partial z}{\partial t} = -\left[\left(\frac{1}{r}\frac{\partial z}{\partial \theta}\right)\left(r\frac{d\theta}{dt}\right) + \left(\frac{\partial z}{\partial r}\right)\left(\frac{dr}{dt}\right)\right] \quad (28)$$

The quantities $r(d\theta/dt)$ $(\equiv v_t)$, and (dr/dt) $(\equiv v_r)$ represent the tangential and radial velocities, respectively, of the crank pin center.

The kinetic energy of reciprocating parts, T_p, is given by

$$T_p = \tfrac{1}{2} m_p v_p^2 \quad (29)$$

Substituting for v_p using Eq. (28) and rearranging, this can be rewritten as in Eq. (5).

Kinetic Energy of Connecting Rod

The velocity of the piston pin center, and the radial and tangential velocities of the crank pin center (shown in Fig. 9(*a*)) can be resolved into components along and normal to the longitudinal axis of the connecting rod as shown in Fig. 9(*b*). Using Fig. 9, the expressions for these components can be derived in terms of v_p, v_t, θ, and ϕ. Since the connecting rod is assumed to be rigid, $v_{p1} = v_{c1}$. The kinetic energy of the connecting rod due to its longitudinal motion is given by $T_1 = \frac{1}{2} m_c v_{p1}^2 = \frac{1}{2} m_c v_{c1}^2$. The lateral velocity of the connecting rod changes linearly from v_{p2} at the piston pin center to v_{c2} at the crank pin center. Letting $\rho(\xi)$ represent the mass per unit length of the connecting rod at a distance ξ from the piston pin center, the kinetic energy due to lateral motion of the connecting rod is obtained by integration as

$$T_2 = \int_0^l \left[\frac{1}{2}(\rho d\xi)\left(v_{p2} + \frac{(v_{c2} - v_{p2})}{l}\xi\right)^2\right] \quad (30)$$

Rearranging the terms, and identifying that $\int_0^l \rho d\xi \equiv$ mass of the connecting rod, m_c, $\int_0^l \rho \xi d\xi \equiv$ first mass moment of the connecting rod about the piston pin center, $m_c l_g$, and $\int_0^l \rho \xi^2 d\xi \equiv$ the second mass moment of the connecting rod about the piston pin center, $m_c k^2$, the expression for T_2 is rewritten as

$$T_2 = \frac{1}{2} m_c \left[v_{p2}^2 + 2v_{p2}(v_{c2} - v_{p2})\frac{l_g}{l} + (v_{c2} - v_{p2})^2 \frac{k^2}{l^2}\right] \quad (31)$$

The total kinetic energy of the connecting rod, T_c, is given by $T_c = T_1 + T_2$, which on rearrangement yields an expression for the kinetic energy as in Eq. (6).

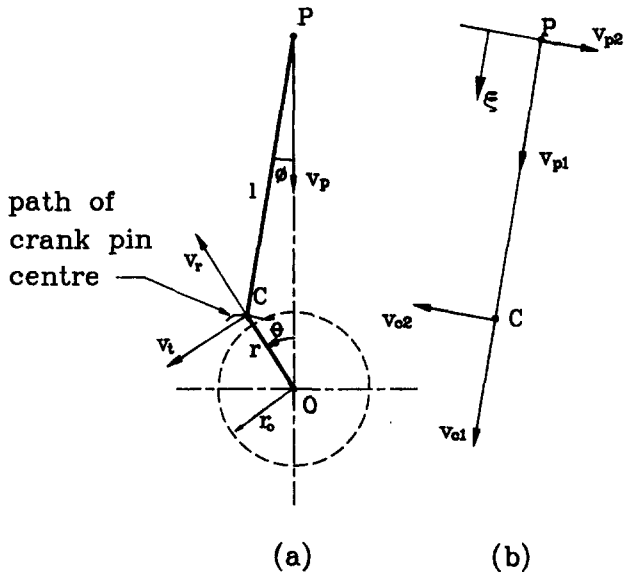

Fig. 9 Components of piston pin center and crankpin center velocities